

DRAFT Technical Reports for Deepwater Horizon Water Column Injury Assessment

WC_TR.13: Application of OILMAP DEEP to the Deepwater Horizon Blowout

Authors: Malcolm Spaulding, Daniel Mendelsohn, Deborah Crowley,
Zhengkai Li, Andrew Bird

Revised: September 30, 2015

Project Number: 2011-144

RPS ASA 55 Village Square Drive, South Kingstown, RI 02879

Table of Contents

Preface	xi
1 Executive Summary	1
1.1 Pipeline Release Model	2
1.2 Blowout Plume Model	2
1.3 Dispersant Treatment Model	3
1.4 Oil Droplet Size Distribution Model	4
1.5 Fountain and intrusion model	5
1.6 Conclusions	6
2 Introduction and Study Objectives	7
3 Overview of OILMAP DEEP	9
3.1 Model System Overview	9
3.2 Overview of Model Components	10
3.2.1 Pipeline release model overview (Appendix D)	12
3.2.2 Blowout model overview (Appendix E)	12
3.2.3 Dispersant treatment model overview (Appendix F)	13
3.2.4 Oil droplet model overview (Appendix G)	13
3.2.5 Fountain and intrusion model overview (Appendix H)	13
4 Blowout Model Development and Application History	14
4.1 OILMAP DEEP Development	14
4.2 Comparison to other blowout models	14
4.2.1 SINTEF's DeepBlow Model (Johansen 1998, 2000)	15
4.2.2 Clarkson University Deep Oil and Gas (CDOG) Model (Yapa et al. 2001)	15
4.2.3 MIT Empirical Model (Socolofsky 2001)	16
4.2.4 API Model Inter-comparison Study	16
5 Application of OILMAP DEEP to Hindcast DWH Spill	20
5.1 Environmental Data	20
5.2 Estimates of Oil Release Rates from Department of Justice (DOJ) Expert Reports	23
5.3 Specifications of the oil and gas release rates; kink and riser flow rates	25
5.4 Specification of dispersant application strategy and amount	32
5.5 Application of pipeline release model	36
5.5.1 Model input	37
5.5.2 Model application	39
5.5.3 Model results	39
5.6 Application of the Dispersant Treatment Model	42

5.6.1	Application strategies	42
5.7	Application of the blowout plume model	46
5.7.1	Plume dynamics and trapping depth	46
5.7.2	Model Input	46
5.7.3	Model Output	51
5.7.4	Gas Dissolution and Methane Concentrations	56
5.7.5	Hydrate formation	57
5.7.6	Comparison to analytical plume solutions	57
5.8	Application of the oil droplet model	61
5.8.1	Volume weighted methodology for multiple release locations	61
5.8.2	Droplet size distributions for the kink and riser releases	63
5.8.3	Impact of dispersant application on droplet size distributions	65
5.8.4	Comparison of model predictions with field observations	67
5.9	Application of the fountain and intrusion model	68
5.9.1	Extent and flow rate of intrusion layer	69
5.9.2	Comparison to in situ concentrations and mass balance estimate	73
6	Sensitivity of model predictions to dispersant treatment case studies	79
6.1	Estimates from Oil Budget Calculator (Lehr et al. 2010)	83
6.2	Chemistry Based Estimates	85
7	Linkage of OILMAP DEEP predictions to SIMAP	88
8	Summary and conclusions	89
9	References	92

List of Figures

Figure E-1. OILMAP DEEP Blowout Modeling Framework and Components	2
Figure 3-1. Overview of OILMAP DEEP integrated blowout model system. Ovals show individual model components and boxes show the required environmental, oil and gas release, and dispersant application data. The blowout plume model is highlighted in yellow as it is the core of OILMAP DEEP. The blowout plume model provides input to the fountain and intrusion model, which in turn provides information on the vertical extent of the intrusion layer where oil droplets are initially placed for the subsequent far field modeling in SIMAP.....	9
Figure 3-2. Visualization of a round, angled, buoyant jet discharging into a stratified ambient environment (Fan 1967). The locations of key features are noted: zone of flow establishment, zone of established flow, buoyant plume, trapping height, fountain peak, and the horizontally spreading intrusion layer.	10
Figure 4-1. Time series comparison of fluorescence measurement (colored dots) with predicted trap height (black dots): upper and lower estimates shown in gray crosses). Size of the colored dots represents the amount of “excess” fluorescence; color of the dots indicates potential density as σ_t (sigma t). (Socolofsky et al. 2011).	16
Figure 5-1. Spatial distribution of all CTD data collected in 2010. Points are color-coded by the date on which the profile of CTD data was collected. Below, a histogram of the number of CTD casts taken per day as a time series, also color-coded by date collected. Data presented in this plot include all data collected onboard Response, NRDA, and Academic cruises.	21
Figure 5-2. Density (kg/m^3), as σ_T (whereby $\sigma_T = \rho - 1000 \text{ kg m}^{-3}$), vs depth (m) for all station casts noted in Figure 5-1 where the data were verified. This includes CTD measurements from May 10 to October 20, 2010 for the Northeastern Gulf of Mexico. Most of the CTD profiles are taken in close proximity to the spill site. The profiles have little variability at depth (below 500 m), but significant seasonal variability near the surface (depths less than 200 m).....	22
Figure 5-3. Flow rates (bbls/day) vs time for the DWH spill from the start to the end of the release (left panel) and the total amount released (millions of bbls) during the spill (right panel) showing low, mean, and high values, if provided. Estimates of the release rates on selected days by DOJ experts are noted as are the estimates by FRTG teams that support the OBC estimates.	24
Figure 5-4. Time history of the estimated total oil release rate based on the Oil Budget Calculator (OBC) (Lehr et al. 2010), with and without adjustment for the amount recovered via the top hat installed on June 3, 2010. Estimates of the oil release rates from the riser and kink are provided. The amount of dispersants applied subsurface to the spill is also provided. All rates in barrels per day.	27
Figure 5-5. Schematic of releases of oil and gas from the end of the riser pipe and from small holes at a kink in the riser pipe above the BOP (McNutt et al. 2011).	28
Figure 5-6. ROV image of the end of the riser pipe taken by <i>MSV Skansi Neptune</i> on May 14, 2010.....	28
Figure 5-7. ROV image of the kink above the BOP taken by Maxx3 May 14, 2010 (Round 1, Packet E).	28

Figure 5-8. Time history of the number of holes in the vicinity of the kink from the start of the spill on April 22, 2010 until the riser was cut above the BOP in early June 2010. The inserts show the ROV imagery that supports the estimates for the number of holes.....	30
Figure 5-9. Photographs of the post cut riser flange (upper), and the recovered section of cut riser pipe (lower) along axis toward the BOP. Both images were taken at the NASA Michoud facility in New Orleans, LA. The riser pipe has been cut longitudinally with half removed. (Photos taken by Andrew Bird, May 2012.)	31
Figure 5-10. Photographs of the kink location, inside to outside (upper left), side (upper right) and outside to inside, (lower center) views taken at the NASA Michoud facility. (Photos taken by Andrew Bird, May 2012.) The holes are identified as A, B, C, D, E, and F (lower center).....	32
Figure 5-11. Dispersant applicator time series, showing observed presence of dispersant application method from sampled ROV video (left axis, when known), and subsea dispersant amounts in barrels (right axis). EPA dispersant testing and riser cutting operation was performed between May 31 and June 3, 2010.	33
Figure 5-12. Photographs from the ROV video of the wand (upper) and trident (lower left and right) dispersant application methods. Wand dispersant application method (upper). Trident application method (lower left and right).....	34
Figure 5-13. Image captured by Maxx3, June 18, 20:06:13 (Round 1, Packet K - DVD 98). The top of this picture indicates the presence of a dispersant ring (or a collar), but it seems that no dispersant is being applied at the specific moment when the image has been captured.	34
Figure 5-14. A sketch of the hooked wand for dispersant application (left) and an image (captured by Millennium22 on 7/11/10 at 14:17), showing its temporary application (right).	35
Figure 5-15. Number of hours per day of dispersant pumping at the specified rates (8, 10, and 12 gpm) to obtain the daily amount of dispersant applied through the spill period.	35
Figure 5-16. Schematic of the pipeline release model application to the DWH blowout.	37
Figure 5-17. Timeline of the number of kink holes and their associated opening area used in the pipeline release model.	40
Figure 5-18. <i>Pipeline release model</i> predicted flow spilt between the kink holes and the riser outlet.	40
Figure 5-19. Fraction treated (solid line, left axis) and DOR (dashed line, right axis) vs number of diameters downstream from the release with varying sector fractions treated. The effective DOR is estimated by dividing the target DOR by the dispersant effectiveness (DE).....	43
Figure 5-20. Fraction treated (solid line, left axis) and DOR (dashed line, right axis) vs height above the origin (m) with varying sector fractions treated. The effective DOR is estimated by dividing the target DOR by the dispersant effectiveness (DE).	44
Figure 5-21. Fraction treated (solid line, left axis) and DOR (stacked column, right axis) during the JF3 cruise for sectors treated 20%, 30%, and 40%, respectively. The estimated DORs for the JF3 dives #5 and #6 are also plotted (filled circles) along with the Dive number and the distance (m) from the wellhead (see Appendix G for additional details).	45
Figure 5-22. Time series of release volumes from reservoir, kink and riser and the amount collected.....	50

Figure 5-23. Vertical profile of water temperature, salinity and density from the R/V Brooks McCall Station 54 observation taken 30 on May, 2010.	51
Figure 5-24. Plume radius and centerline velocities for typical conditions for pre- and post-cut of the riser releases and the kink release.	53
Figure 5-25. Plume centerline gas concentration and relative gas volume for typical conditions for each pre- and post- cut and kink releases.	54
Figure 5-26. Example excess CDOM profiles. Spatial distribution of all CTD data collected in 2010 is the same as displayed in Figures 5-1 and 5-2.	55
Figure 5-27. Model predicted trap height vs. observed CDOM anomaly	56
Figure 5-28. Illustration of conditions for stable hydrate formation for approximately 1,500 m of water (Anderson et al. 2012).	57
Figure 5-29. Estimation of the maximum plume height in a stratified environment as applied to the Deepwater Horizon blowout event using the Carazzo et al. (2008) and Socolofsky et al. (2011) model. The trap height predicted by using a simple plume model is dependent on the buoyancy frequency (s^{-1}), which is a nonlinear function of depth. Shown here is an example of the best estimate of the plume trap height in a non-linearly stratified water column for average pre-cut conditions.	59
Figure 5-30. Fischer et al. (1979) plume model predicted entrained volume flux as a function of height above the source.	60
Figure 5-31. Fischer et al. (1979) plume model predicted trap height above the plume source.	61
Figure 5-32. Total oil droplet size distribution as described by cumulative volume fraction (blue diamonds) and three fractions of the total flow (red square, riser flow treated with dispersant at DOR 1:90; purple cross, kink flow without treatment; and green triangle, riser flow without treatment). The total daily flow rate from the blowout release is assumed to be separated into three volume/mass separate fractions - 25% from the kink, 25% from the riser successfully treated by chemical dispersant, and 50% from the riser that has not been treated by any chemical dispersant. The total cumulative volume distribution is calculated using a volume/mass weighted method.	63
Figure 5-33. Predicted kink release (stages I, II, III) and riser release (I, II, III) flow droplet size individual and cumulative distributions.	64
Figure 5-34. Comparison of the observed oil droplets cumulative volume size distribution and the predicted cumulative volume size distribution for four different dispersant-to-oil ratios (DORs). The observational data are from the two dives (#5 and #6) that were reported to have much oil in deep water (Davis and Loomis, 2014) of the M/V JF3 cruises during June 14-20, 2010. The model distributions are the composite distributions of the chemically and physically dispersed oil droplets, based on an average daily release rate of 38,700 bbls oil to the water column, and a dispersant application rate of 259 bbls Corexit 9500 per day. Dispersant effectiveness was assumed 100% at various simulated DORs.	68
Figure 5-35. Intrusion layer model predicted spreading velocity, layer height, and width as a function of the radial distance from the plume centerline, assuming an entrainment coefficient of 0.083. The upper, middle, and lower panels are for pre-cut, kink, and post-cut conditions, respectively.	71

Figure 5-36. Model predicted intrusion layer volume flux and cross sectional area vs distance downstream for the pre-cut, kink, and post-cut conditions. Values for the volume flux predicted by the plume model for pre and post cut periods are also shown. Insert shows the orientation of the dividing streamline (all releases from the blowout stay within the streamline boundary). 72

Figure 5-37. BTEX observations over the course of the blowout period: (a) BTEX concentrations as a function of distance from the wellhead, (b) BTEX concentrations as a function of date. Pre and post cut values are shown. 74

Figure 5-38. Fountain and intrusion model predicted total entrained volume flux at trap height for the post cut period. 75

Figure 5-39. Fountain and intrusion model predicted percent retention of BTEX in the intrusion layer vs time during the post cut period. 75

Figure 5-40. Application rate of Corexit 9500A dispersant at the well and resultant DOSS mass flux vs time from data in the Oil Budget Calculator (OBC) and Kujawinski et al. (2011). 76

Figure 5-41. DOSS concentrations in the plume layer from NRDA cruise post-cut cruises (upper panel), and the linear correlation of the paired BTEX and DOSS concentrations (lower panel). 77

Figure 5-42. Fountain and intrusion model predicted fraction of DOSS retained in the intrusion layer each day during the post-cut period. 78

Figure 6-1. Typical oil droplet size distribution curves of the four treatment cases (no dispersant, low dispersant, best estimate, and high dispersant application) on a typical day of oil release: (A) upper-left panel, cumulative distribution in the presence of both kink flow and flow at the end of pre-cut riser; (B) upper-right panel, individual distribution in the presence of both kink flow and flow at the end of pre-cut riser; (C) lower-left panel, cumulative distribution in the presence of post-cut riser only; and (D) lower-right panel, individual distribution in the presence of post-cut riser only. 80

Figure 6-2. Oil droplet size distribution curves of the four treatment cases (no dispersant, low dispersant, best estimate, and high dispersant application) of the total oil release throughout the entire oil spill incident: (A) upper panel, cumulative distribution; dashed line indicate the cut-off size (300 μ m) of oil droplets trapped in the plume layer (B) lower panel, individual distributions. 81

Figure 6-3. DWH hydrocarbon mass flow and distribution in different environmental compartments as estimated by Ryerson et al. (2012) according to chemical data. Upper panel, Evaporated hydrocarbon composition after 2 d (A; blue bars), surface oil slick composition after 2 d (B; black bars), and dissolved hydrocarbon composition (C; red bars). The leaking hydrocarbon composition from CH₄ through n-C39 (black line) is shown in each panel for comparison. (D) Schematic (not to scale) of hydrocarbon mass flows in the marine environment; values are calculated for June 10, 2010, in millions of kilograms per day. Lower right panel, Left-hand bar shows DWH hydrocarbon mass flow, in millions of kilograms for June 10, 2010, along different environmental transport pathways calculated using the chemical composition data. The center bar shows the calculated release into the Gulf averaged over the spill duration, and the right hand bar shows the official estimate of total hydrocarbon mass flow averaged over the spill duration. 86

List of Tables

Table 4-1. Comparison of DEEP BLOW and OILMAP DEEP predictions, API Test Cases 9 and 10.....	19
Table 5-1. Mean and standard deviation of ADCP measurements at two stations near the well head. Data collection period, bin depth and number of data points are also provided.	23
Table 5-2. Cumulative volume of oil released (millions of barrels) by DOJ experts and from the OBC report for low, mean, and high values. Overall mean and standard deviation from the expert reports are also noted.	25
Table 5-3. Excerpt from the Macondo Black-Oil Tables (BOT) (Zick 2013)	26
Table 5-4. List of parameters used in the pipeline release model.	38
Table 5-5. <i>Pipeline release model</i> predicted flow split between the kink and riser openings	41
Table 5-6. Summary of <i>blowout plume model</i> input parameters.	47
Table 5-7. Summary of oil release and diameter of riser and kink release for DWH spill event	48
Table 5-9. Summary of minimum, maximum, mean and median flows for each release phase.	53
Table 5-10. Prediction of the number and volume median diameter of droplet size distribution for typical release scenarios.....	65
Table 6-1. Oil droplet rise speed and time to rise from the trapping depth, 1100 m, to the surface at the spill site vs droplet size diameter.	82
Table 6-2. Cumulative oil droplet size distribution for no treatment and low, best estimate, and high treatment cases. The values for 300 μm are highlighted.....	83
Table 6-3. OBC estimates of the total volume and percent of total oil released from the DWH spill for the best, expected, and worst case assumptions. The upper and lower portions of the table include/exclude, respectively the amount of oil recovered at the source.....	85
Table 6-4. Ryerson et al. (2012) Estimates of the total release rate into the environment and into the deep plume	87
Table 6-5. Estimates of the percent oil retained in the water column from various sources	88

List of Appended Reports and Addendum

Appendix A Release Configurations

A1. Introduction

A2. DWH spill event timeline

A2.1. Release configuration details

A2.1.1. Baseline configuration

A2.1.2. Release Configuration 1 (RC1): Leak from end of broken riser only (April 22nd 2010 – April 28th 2010)

A2.1.3. Release Configuration 2 (RC2) – Release from end of broken riser and kink (April 28th 2010 – June 3rd 2010)

A2.1.4. Release Configuration 3 (RC3) – Riser flow only, post riser cut (June 3rd 2010 – June 4th 2010) & (July 10th 2010 – July 11th 2010)

A2.1.5. Release Configuration 4 (RC4) - Riser flow only, post cut, with top hat (June 13th 2010 – July 10th 2010)

A2.1.6. Release Configuration 5 (RC5) - Post riser cut, flange removed (July 11th 2010)

A2.1.7. Release Configuration 6 (RC6) - Transition spool flow (July 11th 2010 – 12th July 2010)

A2.1.8. Release Configuration 7 (RC7) - Three ram capping stack (main flow) (July 12th 2010 – 14th July 2010)

A2.1.9. Release Configuration 8 (RC8) - Three ram capping stack (valve flow) (July 14th 2010 – 15th July 2010)

Appendix B Oil and dispersant application rates

B1. Spreadsheet oil release rate and dispersant application vs time

B2. Spreadsheet of gas release – at depth based on GOR and pressure

B3. Release to the water column of oil and gas – based on collection

Appendix C Physicochemical properties of the source oil

C1. Physical properties of the un-weathered fresh source oil

C2. Bulk chemical properties of the fresh source oil

C3. Detailed chemical properties of the fresh source oil

Appendix D Pipeline release model

D1. Introduction and objective

D2. Multiphase pipe network model

D2.1. Application of model to DWH release rate from well head

D2.2. Predictions of oil and gas release from riser and kink on selected dates

D3. Comparison of model predictions with PIV observation on selected dates

D4. Summary and conclusions

Appendix E Model of blowout plume

E1. Introduction and objective

E2. Blowout plume model

E3. Comparison of model predictions with observations

E4. Summary and conclusion

Appendix F Model of dispersant treatment

- F1. Background
- F2. Model Framework and Assumptions
 - F2.1 Treatment types
 - F2.2 Release scenarios
- F3. Model application and validation
- F4. Summary and conclusions

Appendix G Oil droplet size model

- G1. Introduction and background
- G2. Review of gas and droplet size measurements: laboratory and field observations
 - G2.1. Laboratory experiments
 - G2.1.1. Blowout - University of Hawaii
 - G2.1.2. Subsurface oil release – SINTEF API Study of Droplet Size Distributions and Dispersant Injection Techniques
 - G2.1.3. SL Ross BSEE Subsea Chemical Dispersant Research
 - G2.1.4. Delvigne's natural dispersion and droplet size distribution model
 - G2.1.5. SINTEF wave tank experiments on natural entrainment of weathered high viscosity oil
 - G2.1.6. Bedford Institute of Oceanography
 - G2.2. Deep Spill field experiments on blowout releases of oil and gas
 - G2.2.1. Methane gas bubble size distribution
 - G2.2.2. Diesel oil droplet size distribution
 - G2.3. Deep Water Horizon measurements
 - G2.3.1. ROV Video particle size
 - G2.3.2. *Holocam* (Appendix I)
- G3. Impact of dispersant treatment on oil droplet size distribution
- G4. Review of existing oil droplet size models in existing blowout models
 - G4.1. CDOG DEEP BLOW and OILMAP DEEP
 - G4.1.1. Determining the maximum drop size (d_{95}) based on Weber number method
 - G4.1.2. Determining the Rosin-Rammler type droplet size distribution
 - G4.2. SINTEF Modified Blowout Oil Droplet Size Model
 - G4.2.1. Determining the volume median diameter of drop size (vd_{50}) based on the modified Weber number method
 - G4.2.2. Droplet size distribution
- G5. New OILMAP DEEP oil droplet size model
 - G5.1. Lognormal distribution with Weber number dependent VMD
 - G5.1.1. Definition of dimensionless groups
 - G5.1.2. Volume median diameter formula
 - G5.1.3. Droplet size distribution
 - G5.2. Model validation
 - G5.2.1. Comparison of existing and developed oil droplet model with laboratory testing results
 - G5.2.2. Comparison of lognormal and Rosin- Rammler distributions with laboratory and field data
 - G5.2.3. Comparison of treated and untreated oil droplet size distributions using the new droplet size model

G6. Summary and conclusions
G7. References

Appendix H Fountain and Intrusion Model

H1. Introduction and objective
H2. Blowout plume model
H3. Comparison of model predictions with observations
H4. Summary and conclusion

Appendix I Analysis of Davis Holocam oil droplet size distribution data

I1. Holocam Dive Data
I2. Log normal distribution fit to the data: mean volume diameter and standard deviation
I3. Summary
I4. References

Appendix J OILMAP DEEP Output to SIMAP Input

J1. Blowout Plume Model Output for SIMAP Input
J2. Droplet Size Model Output for SIMAP Input
J3. Model Results Post Processing for SIMAP Input

Addendum 1 Updated Modeling using Court Determined Volumes

1. Introduction
2. Model Predictions
 - 2.1. Daily Release Volumes
 - 2.2. Pipeline Release Model Using Court Total Release Volumes
 - 2.3. Blowout Plume Model Using Court Release Volumes
 - 2.3.1. Black Oil Table Analysis Using Court Release Volumes
 - 2.3.2. Blowout Plume using Court Release Volumes
 - 2.4. Dispersant Treatment Model using Court Release Volumes
 - 2.5. Droplet Size Distributions using Court Release Volumes
 - 2.6. Updated SPT File
3. Summary
4. References

Preface

This report document contains analyses of the Deepwater Horizon oil spill based on estimates of the released oil volume previously established by the Government as documented in the Oil Budget Calculator (Federal Interagency Solutions Group, Oil Budget Calculator Science and Engineering Team, Lehr et al. 2010). In January 2015, the U.S. District Court for Eastern District of Louisiana (Case 2:10-md-02179-CJB-SS Document 14021 Filed 01/15/15) made findings of different release volumes (USDC 2015). The analyses presented in this report and select appendices were updated using the court release volumes and the results of these analyses are summarized in Addendum 1.

1 Executive Summary

OILMAP DEEP, an integrated system of models, was applied to the *Deepwater Horizon* (DWH) oil spill to predict the near field transport and fate of the oil and gas released into the northeastern Gulf of Mexico. The output of the model was provided as input to SIMAP to characterize the subsurface oil release, which is then used to determine the far field transport, fate, exposures, and effects of the oil in the environment (French McCay et al. 2015). OILMAP DEEP blowout modeling system is comprised of five integrated model components that are assembled to predict the near field dynamics of the release of oil and gas to the water column from a subsea blowout, which includes the subsurface application of dispersant (Figure E-1). The model was applied to multiple releases during the DWH event. The system is primarily focused on predicting the dynamics of the plume and the resulting intrusion layer, the dissolution of gas, formation of hydrates, and the oil droplet size distribution and concentration in the plume and the intrusion layer.

The five integrated subcomponents of the system are: pipeline release, blowout plume, dispersant treatment, oil droplet size distribution, and fountain and intrusion. The pipeline release model predicts the release rate of oil and gas from various openings in the riser system. The plume model predicts the characteristics of the plume resulting from the oil and gas release including: its radius, velocity, entrainment rate, and the oil and gas concentrations with distance from the release location, and trapping height/depth (height is measured from the seabed and depth from the water surface). The trapping depth is defined as the vertical location where plume buoyancy is dissipated by entrainment of ambient seawater and gas dissolution. This results in rapid radial spreading of the plume into an intrusion layer. This intrusion layer is modified by the dynamics of the ambient current field. The dispersant treatment model predicts the fraction of oil treated and the effective Dispersant-to-Oil Ratio (DOR) knowing the amount of dispersant applied and the application method. The oil droplet model predicts the oil droplet size distribution, with and without dispersant treatment, for single or multiple release locations. The fountain and intrusion model predicts the geometry (thickness versus distance) of the flow intrusion at the plume trapping depth and the dilution of oil droplets or components with distance from the source. Dissolution and biodegradation of oil are not included in the blowout model but are included in far field fate and transport model. The processes, formulation (governing equations), input and output, and the linkage among the models are provided in this report and associated appendices. This integrated system is an advancement over other existing oil blowout models which typically only include the blowout plume and oil droplet size distribution models for single point-source releases.

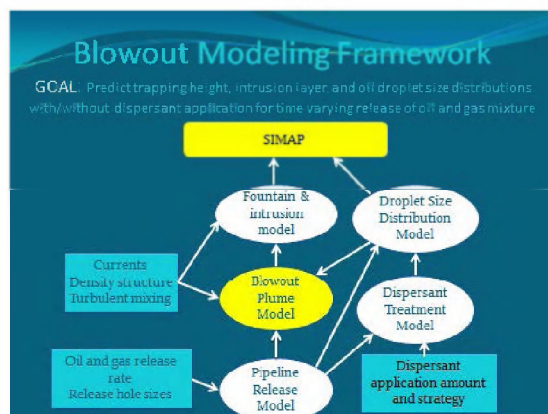


Figure E-1. OILMAP DEEP Blowout Modeling Framework and Components

The OILMAP DEEP suite of models were applied to the DWH blowout spill in the immediate vicinity of the wellhead and validated, to the extent possible, with *in-situ* observations. This report summarizes work accomplished. The major findings by sub-model are provided below:

1.1 Pipeline Release Model

During the course of the DWH spill oil was initially released from both the riser and the kink holes above the wellhead, and after the riser was cut from the riser above the wellhead. The pipeline release model simulates releases from two separate locations: the end of the riser pipe and a number (two increasing to six) of small holes in the vicinity of the kink. The riser release was modeled from the start of the spill on April 22 through June 3, 2010, when the riser was cut immediately above the BlowOut Preventer (BOP). The kink releases did not begin until April 28. From April 28 to June 3, 2010 the model estimated that the amount of oil released from the kink was on the order of 20% of the total amount released in that time period, and increased from 18% initially to 34% immediately before the riser was cut. These predictions are consistent with estimates made by Particle Image Velocimetry (PIV) methods reported by the Flow Rate Technical Group (McNutt et al. 2011) that gave values in the range of 15 to 26% in mid-May (14 to 16) and those based on Acoustic Doppler Current Profiler (ADCP) measurements by Camilli et al. (2011), that gave 31% for May 31, 2010. The increase in flow percentage over time was a result of the number of holes at the kink increasing from two, at the start of the kink releases, to six immediately before the riser was cut. The evolution of the number of holes was based on a detailed analysis of available ROV imagery taken during the spill, as well as inspection of the kink and adjacent sections of the riser when these were retrieved from the seabed and impounded as evidence in the case (Appendix A). The latter inspection allowed estimates to be made of the final number, configurations, and sizes of the holes. The hole size evolution is unknown and hence the analysis assumed hole sizes based on the measured values once the riser was retrieved after the accident.

1.2 Blowout Plume Model

Blowout plume simulations were performed for the kink and riser releases prior to the riser cut, and for the riser only, post the riser cut on June 3, 2010. The water depth at the well location was 1,523 m and at the end of the riser (approximately 210 m northwest of the BOP), pre-cut, 1,509 m (see Table A-2 of Appendix A: Release configuration report). The kink release was approximately 20 m above the seafloor or a water depth of 1,503 m at the well location. The

riser post-cut release was at the same longitude and latitude as the kink release, but was approximately 18 m above the seafloor or a water depth of 1,505 m at the well location. Prior to the riser cut, the blowout plume model predicted a nearly vertical orientation of the plume from the riser, growing in diameter until the plume trapped (defined as rapid spreading horizontally) at approximately 326 m from the release point or at a water depth of approximately 1,183 m on average. The weak mean (0.07 m/s) and variable (0.05 m/s, standard deviation) currents were not strong enough to cause the plume to bend. The kink releases were predicted to trap at a lower elevation than the riser release due to the lower release flow rate. The trap height was predicted to be, on average, 200 m from the kink release location (water depth of 1,303 m). The predicted trap height varied daily due to variations in the amount of oil and gas released to the water column. The oil release rate was adjusted based on the amount of oil recovered. After the riser cut was complete on June 3rd, the trap height was about 304 m above the release location (water depth of 1,201 m). The diameter (2 times half-width) of the plume ranged from 166 m (pre-cut) to 156 m (post-cut) at the trap depth for the riser plume and 138 m for the kink plume. The predicted trapping heights/depths were in very good agreement with fluorescence (as measured by Colored Dissolved Organic Matter, CDOM) and measurements of oil concentration and Benzene, Toluene, Ethylbenzene, and o-, m-, and p-Xylene (BTEX), which showed elevated concentrations at heights of 200 to 500 m above the release prior to the riser cut and 300 to 400 m post the cut. The model was able to correctly estimate the mean trapping depth during the spill and in addition the differential trapping depths, pre and post the riser cut, with time.

The plume model predicted that the majority of the methane gas in the release was dissolved in the water column as the oil/gas mixture rose to the trapping depth. The rise times were on the order of 15-20 min. This result is in agreement with field observations reported by Valentine et al. (2010) and Reddy et al. (2012) that show methane was completely dissolved by the time the plume reached its trapping depth. Model simulations without gas dissolution showed that the predicted trapping height was considerably higher (~100 m) than observed and clearly illustrates the importance of accounting for gas dissolution and the associated loss of buoyancy in the plume model predictions.

The plume model predicted that there was no hydrate formation in the unimpeded oil and gas plumes. This is attributable to the fact that dissolution of methane from the plume had not locally reached saturation concentrations and hence hydrates were not predicted to form (Anderson et al. 2012). This result is consistent with field observations that showed only limited hydrate formation in the oil/gas plumes. This contrasts with conditions inside the various containment devices (e.g., cofferdam) used by BP, where hydrates formed because of the elevated methane concentrations in the confined spaces.

1.3 Dispersant Treatment Model

The dispersant treatment model predicted that the amount of oil effectively treated and the associated dispersant to oil ratio (DOR) varied considerably over the spill period given variations in the dominant dispersant application devices used (i.e., wand and trident/bident (or Y shaped fork)) and the amount and location of dispersant applied. Analysis of the video imagery obtained by Remotely Operated Vehicles (ROV) indicated that dispersants were primarily applied adjacent to the plume and entrained into and mixed into the buoyant plume. The predicted total fraction treated was generally higher post riser cut, compared to pre riser cut, since the principal dispersant application method changed from a single wand (pre-cut), to a two-prong trident (bident) with multiple spray nozzles (post-cut). The trident was predicted to be much more

effective at applying dispersants around the outer circumference of the released jet/plume because of its wider circumferential angular reach. The estimated fraction of oil treated with dispersant and the effective DOR has been shown to vary considerably dependent on the assumptions about the application method and the degree of mixing within the buoyant jet.

Simulations were performed using the dispersant treatment and oil droplet size models to predict the droplet size distributions for a variety of assumed treatment options. Four cases were investigated: no treatment, and low, best estimate, and high efficiency dispersant treatment. All dispersant treatment cases employed all the dispersants that were applied but using different assumptions about their application. For the low application case it was assumed that the dispersants were mixed with the oil that was released from the riser with a dispersant efficiency of 50%. For the high case, the mixing was assumed to be the same as for the low case, but the dispersant efficiency was fixed at 100%. The best estimate case represents the actual application method based on a review of ROV imagery and the type of application device (e.g., wand or trident/bident) employed. A dispersant efficiency of 80% was assumed for this case.

These estimates suggest that during the pre-cut time period, oil dispersion (formation of smaller droplets) was a result of mechanical processes (high exit velocities) at the kink holes and dispersant application at the end of the riser via the wand. During the post-cut period, oil dispersion appears to be primarily due to dispersant treatment via the trident above the BOP and at the outer edge of the top hat. Analysis of the BTEX data does not allow one to distinguish the differential effects of mechanical formation by the kink flow and dispersant application at the end of the riser.

1.4 Oil Droplet Size Distribution Model

The oil droplet size model uses an empirically-based method, dependent on both the Weber and Ohnesorge numbers (Hinze 1955; Masutani and Adams 2000) to determine the Volume Median Diameter droplet size (VMD). The model assumes that the droplets are log-normally distributed. The model parameters were calibrated with data from the *DeepSpill* experiment (Johansen et al. 2001), Delvigne and Sweeney (1988)'s grid column experiments for low and moderate viscosity oils, and Reed et al. (2009)'s wave tank breaking wave experiments for more viscous oils. The model was then validated against several small and large scale laboratory studies on subsurface releases of oil, with and without dispersant treatment (Brandvik et al. 2013; Brandvik et al. 2014 and Belore 2014).

The model was used to estimate the droplet size distributions from the various releases (kink, and pre and post riser cut). The droplet model predicted that the VMD from the untreated riser flow changed from 2,300 μm prior to the riser cut to 3,000 μm during the kink flow period, and finally to 2,700 μm after the riser cut. Simulations of the kink release showed that the VMD ranged from 330-360 μm . The large difference between the riser and kink droplet sizes is a result of the differential flow velocity between the riser flow, with a relatively large cross sectional area, and the kink flow, with multiple holes yet much smaller cross sectional areas. The variability in the riser droplet sizes was due to differences in flow rate; smaller sizes corresponding to higher flow rates. The release from the kink had less variability in the exit velocity and therefore a smaller range of median droplet sizes.

The general trend is that dispersant treatment reduces the droplet size (Li et al. 2009a, b). The treated oil at the riser is therefore predicted to have much smaller droplet sizes than the

untreated oil. The fraction of oil treated is dependent on the treatment application method and the effectiveness and amount of dispersants available. The droplet size of the total release is the volume-weighted distributions of treated and untreated oil. It has not been possible to verify all of the estimates of droplet sizes from the different sources and different treatments, given the fact that no droplet size data is available in the immediate vicinity of each of the riser or kink releases.

To gain insight into the droplet size distribution, the dispersant and droplet size models were applied to predict the distributions observed from the *Holocam* measurements made during the M/V Jack Fitz 3 (JF3) cruise (June 14 to 20, 2010) (Davis and Loomis 2014). The droplet size measurements were made during nine dives, with the maximum depths ranging from approximately 260 to 1,490 m below the sea surface and distances of 1.15 – 9.32 km from the well head. The automatic processing data from dives #5 and #6, which have been verified by a manual processing method to have much oil in the deep water column, and only those particles that were identified as class 1 (i.e., oil droplets) were binned into discrete depth intervals of 100 m each for analysis. The data set was further restricted to dives where manual methods confirmed the automated method and showed significant oil. Dispersants were being applied adjacent to the top hat during this post cut period by the trident, and hence the observed droplet size distribution is a result of both treated and untreated oil droplets.

The model predictions of the droplet size distributions showed very good agreement with observations (see Appendix I Figures I-5 and Figure I-9 for model and data comparison examples). The range of VMD for the two dives (#5, 6) that were reported to have much oil had volume median diameter ranging from 70 to 250 μm . The logarithmic geometric standard deviation ($\log(\text{GSD})$) of the log normal distribution was 0.59 ± 0.08 . This compares to 0.51 ± 0.09 when the model was fit to the Norwegian *Deep Spill* data (Johansen et al. 2001). The present analysis provides a reasonable upper bound to the size of oil droplets that are retained in the water column by the time of *Holocam* sampling. Larger size oil droplets are predicted to travel to the sea surface quite quickly due to their buoyancy. This value is consistent with the results of the lab study on the effects of droplet size on intrusion and subsequent transport of subsurface oil spills (Chan et al. 2014). The authors found that the particle spread increase rapidly as the normalized particle slip velocity becomes smaller for Type 1a* plume (see Figure 6 of Chan et al. 2014), in which the particles are transported within the intrusion layer, suggesting that small oil droplets on the order of several hundred microns will be more widely distributed in the water column, whereas larger droplets on the order of millimeters will rise to the surface within a close range of the wellhead.

Observed VMDs were substantially smaller (70-250 μm) than the model estimates for the untreated post riser cut release (~2,700 μm). Comparison of the model predicted size distributions for the post-cut riser released oil shows that there is very little overlap of the sizes of the dispersant-treated and untreated oil droplets. Simulations were performed with the droplet size model and show that the predicted distributions are in very good agreement with observations if the oil water interfacial tension was reduced, corresponding to those predicted by the dispersant treatment model over the field sampling period (June 14th to 20th, 2010).

1.5 Fountain and intrusion model

Assuming a fixed release rate of 62,000 barrels per day, the fountain and intrusion model predicted a peak thickness of 100 m above the trapping depth. The resulting intrusion layer was predicted to spread radially from the source, in the absence of currents, with a thickness

decreasing from approximately 20 m at a radial distance of 100 m to 4.5 m at 1 km. The velocity in the intrusion layer was similarly estimated to decrease radially from 0.17 m/s at 100 m to 0.08 m/s at 1 km. For comparison the mean ambient currents were approximately 0.07 m/s. The intrusion flow rate predicted by the blowout model for the riser release was approximately 2,200 m³/sec and used as input to the fountain and intrusion model. The final stage of the fountain and intrusion model, including effects of the ambient current and entrainment from the resulting plane wake flow, predicted flow rates on the order of 7000 m³/sec immediately downstream (with several km) of the source. These values are consistent with estimates by Camilli et al. (2010) and Kujawinski et al. (2011). No field measurements were available that could fully resolve the flows and concentrations of the fountain or the intrusion layer. Model results are, however, broadly consistent with observed CDOM profiles taken during the spill and the results of empirical model predictions of the peel height (fountain peak) and intrusion flow rates by Socolofsky et al. (2011).

The fountain and intrusion model and associated intrusion calculations were used to determine the amount of BTEX and the dioctyl sodium sulfosuccinate (DOSS) component of the dispersant that was retained in the intrusion layer. These two tracers (i.e., BTEX and DOSS) were selected for the analysis since both are expected to be associated with the intrusion layer (highly soluble and related to the application of dispersants to the spill) and be conservative tracers in close proximity to the wellhead. The estimates were made by dividing the observed fluxes of these two chemical in the intrusion layer (concentrations multiplied by volume flow rates) by the amounts released at the well head.

BTEX (represents about 1.9 % by weight of the parent oil) collected during the spill, in the near field of the release (≤ 10 s km), show the largest values in the immediate vicinity of the trapping depth, with the highest concentrations in the range of 50 to 100µg/l. The concentrations display strong variability in both space and time, but are systematically higher in pre-cut (mean value - 103 µg/L), compared to post riser cut period (mean value – 51µg/L). Sampling during the pre-cut period was generally restricted to the SW of the well head, while samples collected during the post cut period provided coverage of the entire directional distribution. In addition there were two sources during the pre-cut period (kink and riser) with two separate trapping depths and only one during the post cut period (riser). Given the lack of adequate directional sampling and the issues in dealing with multiple sources during the pre-cut period, analysis of retention was restricted to the post-cut period only. Estimates were made using the observed post-cut BTEX data within 6 km of the well head, and the predictions of the intrusion flows. It was estimated that $27\% \pm 5\%$ of the released BTEX was in the intrusion layer. The upper and lower bounds represent the 95% confidence limits on the retention estimate. Similar estimates were made for, DOSS and predicted that $90\% \pm 23\%$ ¹ of DOSS was in the intrusion layer. This is consistent with the idea that DOSS should be associated with the dispersed fraction of the oil and hence completely trapped in the intrusion layer. The DOSS analysis also supports estimates of the volume flux used in the BTEX analysis.

1.6 Conclusions

In summary, the dispersant treatment and oil droplet model predicted - that 8%, 20%, and 33% of the oil was dispersed (low, best estimate, high) in the intrusion layer. These estimates include small oil droplets formed by mechanical processes due to higher exit velocities at the kink. If no

¹ Confidence interval 67%-100%

treatment is performed 6 % of the oil is predicted to be trapped. Oil droplets below a size of 300 μm are assumed to be trapped. Droplets larger than this size rise to the surface with their rise velocities dependent on the droplet size and oil density. These values are in reasonable agreement with the analyses using the plume and fountain models in conjunction with observed BTEX concentration data which yield a best estimate of $27 \% \pm 5 \%$ during the post-cut period. Estimates based on the Oil Budget Calculator (OBC) (Lehr et al. 2010) range from 20 to 38%, with an expected value of 25%, slightly lower than the present estimates. Similar estimates based on hydrocarbon chemistry data yield values in the range of 28 to 45%, with an average of 36%, somewhat higher than the present estimates as both oil and gas phase hydrocarbons are included (Ryerson et al. 2012).

The blowout model predictions are in good agreement with the available observations for plume trapping height and the major characteristics of the intrusion layer. Predictions of the droplet size distribution are in very good agreement with the *Holocam* observations and clearly show that the dispersant application was effective in retaining oil in the water column and that mechanically induced dispersion of releases from the kink also played a role in dispersing oil during the pre-riser cut period. Model predictions of the percent of oil retained in the intrusion layer are consistent with independent estimates based on field observations and components of the blowout model. The uncertainty in these estimates is reasonable given the limited amount and quality of the data currently available and assumptions made in the analyses.

2 Introduction and Study Objectives

Two fully developed and closely linked models - OILMAP DEEP and SIMAP – were used in hindcasting the transport, fate, and effects of the Deepwater Horizon (DWH) blowout. OILMAP DEEP predicts the oil and gas release from the pipeline, the blowout plume associated with the discharge and its trapping depths, the dissolution of gas from the rising plume into the water column, the oil droplet size distribution, the fraction of oil treated with a specified application method and the associated DOR, and the characteristics of the fountain and intrusion layer. The model addresses both chemically treated (by dispersant) and untreated oil from single and multiple time-varying sources. The model spatial scales typically extend from tens to hundreds of meters above the seabed and within hundreds of meters to a km horizontally from the blowout location, while its temporal scale extends over the time period of the release. SIMAP then uses the results of OILMAP DEEP as input to define the release and then predicts the far field transport, fate, exposure, and effects of the spill. SIMAP spatial scales extend to an area that fully encompasses the subsurface and surface area affected by the spill (on the order of hundreds of square kilometers for a large spill). The separation into two models, SIMAP and OILMAP DEEP, allows one to address the large variation in the spatial scales of the near field blowout release and the far field receiving water environment; this separation also makes it possible to account for the difference in dynamics of the near blowout release versus those that control the far field distribution and fate of contaminants in the ocean.

The objectives of this report are:

- Provide an overview of the integrated deep water oil and gas blowout model system (OILMAP DEEP),
- Describe the application and validation of the model to the DWH spill, and
- Describe how predictions from OILMAP DEEP are linked with SIMAP.

A separate report provides an overview of SIMAP and its application to the spill (French McCay et al. 2015). Section 3 of this report provides an overview of the integrated blowout model OILMAP DEEP including pipeline release, blowout plume, dispersant treatment, oil droplet, and fountain model components. A brief summary of OILMAP DEEP and the application history of the blowout portion of the system are provided in Section 4. This section also includes a brief overview of other blowout models currently in use. Section 5 presents the application and validation of the model to the DWH spill. Predictions of the amount of oil that remains in the water column for various treatment strategies, using the dispersant treatment and oil droplet size model are provided in Section 6. The linkage of OILMAP DEEP to the far field model, SIMAP is outlined in Section 7. Section 8 provides the summary and conclusions, and references are given in Section 9. Appendices A through J give supporting information and additional details on model inputs and results. Appendices A, B, and C provide information on the time line for the spill event, oil release and dispersant application rates, and physiochemical properties of the oil, respectively. Appendices D to H provide details on each of the five model components. Appendix I provides an analysis of *Holocam* data to estimate oil droplet size distributions, and Appendix J describes results used as input to far-field modeling using SIMAP (French McCay et al. 2015).

3 Overview of OILMAP DEEP

3.1 Model System Overview

Based on the most recent developments, OILMAP DEEP is comprised of five integrated model components that are assembled to predict the dynamics of the release of oil and gas to the water column from a subsea blowout, with and without subsurface dispersant treatment. The integrated system is primarily focused on predicting the dynamics of the plume and resulting intrusion layer, the dissolution of gas, formation of hydrates, and the oil droplet size distribution and concentrations. Figure 3-1 shows a schematic of the system with the ovals representing individual model components and the boxes, data inputs. As a conservative assumption, oil droplets are assumed not to undergo dissolution or biodegradation within the blowout plume given the empirically recognized fast rise times. These processes are however included in the far field model (SIMAP). Figure 3-2 shows the location of the key areas of interest for an easily visualized laboratory scale buoyant plume. OILMAP DEEP is focused on predicting the near field dynamics of the release. Output from this model is then provided to SIMAP, which then predicts the far field transport, fate, exposure, and effects of the release.

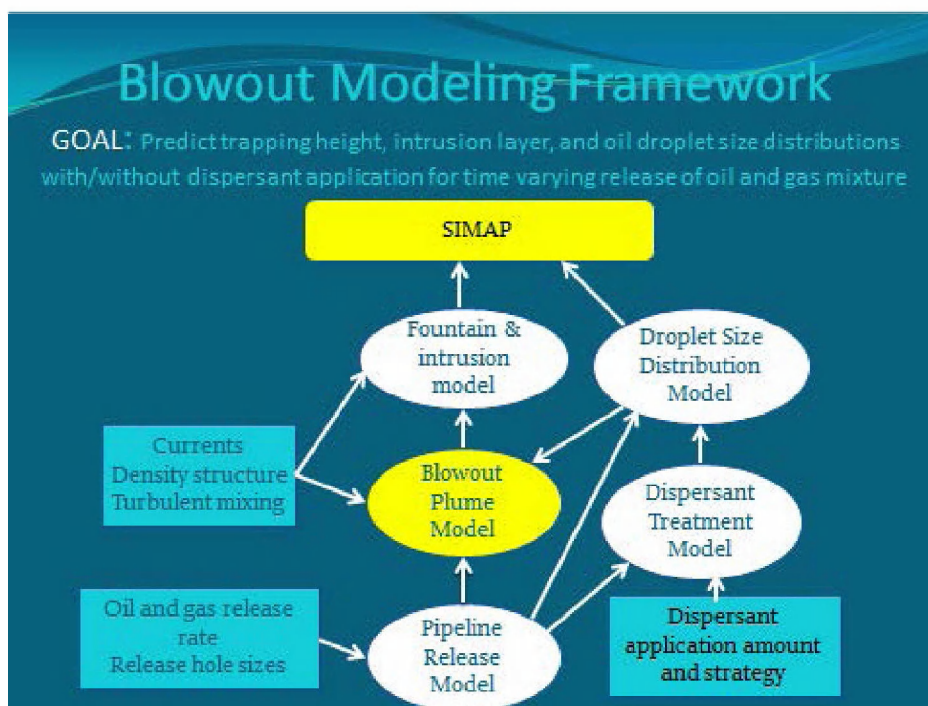


Figure 3-1. Overview of OILMAP DEEP integrated blowout model system. Ovals show individual model components and boxes show the required environmental, oil and gas release, and dispersant application data. The blowout plume model is highlighted in yellow as it is the core of OILMAP DEEP. The blowout plume model provides input to the fountain and intrusion model, which in turn provides information on the vertical extent of the intrusion layer where oil droplets are initially placed for the subsequent far field modeling in SIMAP.

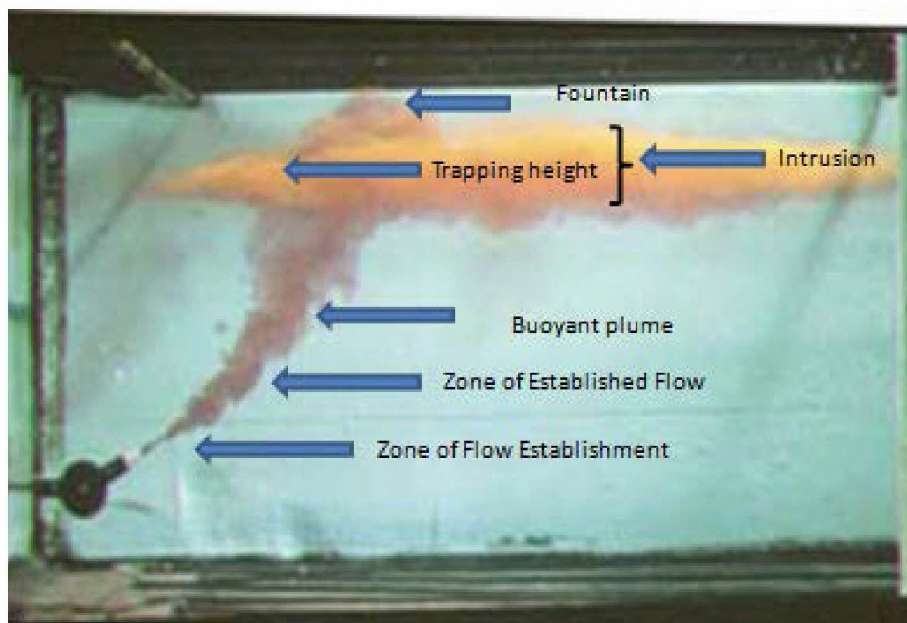


Figure 3-2. Visualization of a round, angled, buoyant jet discharging into a stratified ambient environment (Fan 1967). The locations of key features are noted: zone of flow establishment, zone of established flow, buoyant plume, trapping height, fountain peak, and the horizontally spreading intrusion layer.

3.2 Overview of Model Components

OILMAP DEEP is an integrated blowout model including the following model components: pipeline release, blowout plume, dispersant treatment, oil droplet size, and fountain. The *pipeline release model* predicts the release rate of oil and gas from various openings in a riser system. The *blowout plume model* predicts the characteristics of the plume resulting from the oil and gas release including its orientation, radius, velocity, entrainment rate, and oil and gas concentrations as a function of distance from the release location and the trapping height/depth (height is measured from the release location and depth from the water surface). The trapping depth is the location where plume buoyancy is dissipated by entrainment and gas dissolution, which results in rapid radial spreading of the plume into an intrusion layer. The trapping height/depth is at the center of the intrusion layer. The *dispersant treatment model* predicts the fraction of oil treated and the effective Dispersant to Oil Ratio (DOR) for the specified application method and amount of dispersant applied. The *oil droplet size model* predicts the oil droplet size distribution, with and without dispersant treatment, for single or multiple release locations. The *fountain and intrusion model* predicts the geometry (height and thickness versus distance) of the flow intrusion observed at the trapping depth.

OILMAP DEEP starts with the *pipeline release model* which simulates the distribution of flow from the source through a network of multiple outlet paths based on the characteristics of the source (oil and gas release rates) and receiving water (pressure and density) and the configuration (location and geometry of pipes and outlet orifice(s) (holes)) of the various flow paths. Inputs to the model include information on the oil and gas release rates, and the piping network details, and hole sizes. The model predicts the flow rates and exit velocities, for the various openings through which oil and gas are released to the environment over time.

Wellhead configuration changed throughout the spill and the model addresses multiple releases, through a complex network of interconnected pipes for a multi-phased (i.e., gas and oil) flow.

Output from the *pipeline release model* provides input on oil and gas releases to an integral, *blowout plume model*. This model predicts the plume centerline location and magnitude of the velocity, buoyancy, and gas and oil concentrations. The model also includes the ability to predict the formation of hydrates and the resulting loss of plume buoyancy. The model assumes that the distribution of the predicted variables is self-similar (i.e., same shape) with a Gaussian distribution and treats the discharge as a buoyant plume. If the release is modeled in a stratified water column, the plume may trap and spread horizontally into an intrusion layer. Similarly, if the release is in a region where the ocean currents are sufficiently strong, the plume may be bent as a result of the currents. Multiple releases can be addressed by performing individual plume simulations for each release.

In responding to blowouts one option is to treat the oil and gas release with subsurface dispersants, which is a first-of-its-kind use in the Deepwater Horizon incident. The effect of dispersants is to reduce the oil-water interfacial tension (IFT). This in turn results in a reduction of the oil droplet sizes and an increase in the total oil-water surface area. The *dispersant treatment model* provides a method to predict the fraction of the oil that receives treatment and the dispersant to oil ratio (DOR) of the treated oil. The DOR can be modified by the dispersant effectiveness (DE) to determine an effective DOR. This information is used as input to the *oil droplet size model* in terms of the change in oil water interfacial tension to predict the impact of dispersant treatment on the oil droplet size distribution.

In a typical blowout release only a portion of the oil may be effectively treated by dispersant and the remaining oil released untreated. The dispersants may be applied internally and hence be premixed with the oil. Alternately they may be sprayed, injected, or entrained into the blowout jet or plume. In this case a volume/mass weighted method is used to determine the total oil droplet size distribution. This method was extended to cover time varying treatments of multiple releases, with varying dispersant application rates as recorded during the DWH spill responses.

As the oil is released from the blowout it is broken up into a series of discrete droplets with a size distribution dependent on the mixing energy at the release location and the oil-water interfacial tension; the higher the mixing energy, or the lower the oil water interfacial tension, the smaller the droplet size distribution; dispersed phase (oil) viscosity, on the other hand, counteracts the effect of reduction in oil-water interfacial tension. The *oil droplet size model* allows estimates to be made of the oil droplet size distribution, with and without treatment. Multiple releases may result in different droplet size distributions because of differences in the source and treatment conditions.

In the event that oil droplets or gas bubbles have significant rise rates, the plume may overshoot the trapping depth and result in a fountain like flow, where the flow reaches a peak level and then falls back to the trapping depth. The flow and associated oil droplets and gas bubbles are then transported horizontally into an intrusion layer. These behaviors are addressed by the *fountain and intrusion model*. The resulting intrusion layer increases in thickness from the source due to entrainment of surrounding water. In the presence of ambient currents, the combined flow field displays a “U” shape, where the radial flow is countered by the ambient flow in the upstream direction and in the same direction as the ambient flow in the downstream direction.

Predictions of the *blowout plume model* (trapping height and plume diameter for each release), and the *oil droplet size model* (volume-weighted oil droplet size distribution, with or without dispersant treatment), are provided as input to SIMAP. Predictions from the *fountain and intrusion model* (peak height at release, flow rate and thickness of the intrusion layer as a function of distance from the source) are also available for finer scale evaluations in the area of the wellhead but not typically used as input to SIMAP. The blowout and droplet size simulations are normally performed on a daily time step. This time step is used to match the temporal resolution of the input data of oil release and subsurface dispersant applied.

The output of OILMAP DEEP and the input to SIMAP (far field transport and fate model), contains a list of the locations (latitudes, longitudes, depths) and times of mass releases of varying droplet sizes. The time step of the SIMAP model simulations is a half-hour, and as such the daily release, which was assumed at a constant rate throughout the day, is used to determine the appropriate mass released in each droplet size bin every half hour used in the SIMAP model. While the evaluations of the blowout model predictions are based on evaluating the amount of oil that remains trapped in the water column, with a nominal oil droplet diameter of 300 μm or smaller in this report, the complete oil droplet size range predictions are provided as input to SIMAP. Neither dissolution nor biodegradation process were considered in OILMAP DEEP given the rapid rise times of the plume and hence the amount of oil input to SIMAP was the same as that released from the wellhead.

Sections 3.2.1 to 3.2.5 give a broad overview of each of the five models noted above. The overview is structured to summarize the following for each model: processes addressed, formulation used (i.e., governing equations or empirical approximations), model input, and model predictions (output). The linkage among the various model components was summarized above. Detailed derivations for each model and their application are provided in Appendices D to H.

3.2.1 Pipeline release model overview (Appendix D)

Processes: Model predicts the two-phase flow distribution in a network of pipes with any number of release locations and release exit opening geometries.

Model Formulation: Conservation of oil and gas masses and energy in the flow network for two phase flow.

Input: Branch flow network geometry including interconnections, pipe diameters, lengths, roughness, and release exit openings (hole shape, size, and edge conditions); oil and gas densities, temperatures, and flow rates at origin of flow network; and pressure above blowout preventer (BOP) and ambient pressure at release locations.

Output: Time varying oil and gas flow rate in each branch of the flow network and through each release location.

3.2.2 Blowout model overview (Appendix E)

Processes: Model predicts the location, velocity, buoyancy, oil and gas concentrations, gas dissolution and gas-plume separation, and hydrate formation along the plume centerline. The model assumes self-similar cross plume profiles for all variables. Oil dissolution and biodegradation are not estimated in the current application. Each release location requires separate simulations. The model assumes that the release is a plume and hence has an offset from the release location to account for the transition from jet to plume stages.

Model formulation: Conservation of momentum (with buoyancy), water mass, and oil mass; the change of plume buoyancy is considered from both gas dissolution and/or separation, and gas hydrate formation. The impact of oil concentrations on buoyancy is not considered given its limited influence on plume buoyancy.

Input: Oil and gas release rates and densities, release opening diameters, mean horizontal currents, terminal oil droplet rise velocity, and water column density structure.

Output: Initial exit release exit velocity, plume centerline location, velocity, buoyancy, oil and gas concentrations vs depth, and plume trapping depth.

3.2.3 Dispersant treatment model overview (Appendix F)

Processes: Model predicts the DOR and fraction of oil treated by external application of dispersants. Each release location requires separate simulations.

Model Formulation: Conservation of mass and momentum equations for a buoyant plume, including the entrainment of seawater, with a focus on the area close to the release (10 to 20 diameters from the release). Formulation also includes characterization of the relationship between estimated DOR and oil water interfacial tension, normally based on laboratory experiments for the oil of interest and type of dispersant applied.

Input: Water and oil density, total oil/gas flow rate, geometry at the release locations (diameter of release pipe), dispersant application rate, dispersant effectiveness, and dispersant application method.

Output: Fraction of oil treated, DOR, effective DOR (modified by dispersant effectiveness or DE), and oil water interfacial tension.

3.2.4 Oil droplet model overview (Appendix G)

Processes: Model predicts oil droplet size distribution, reported as volume median diameter (VMD) distribution (d_{50}) with an assumed log normal distribution. Each release location requires separate simulations.

Model formulation: Empirically-based estimate of volume median d_{50} based on Weber number of the release (ratio of mixing energy to interfacial tension) and Ohnesorge number of the oil properties (ratio of viscosity to oil water interfacial tension as impacted by dispersant treatment). Distribution of droplets assumed as lognormal with fixed geometric standard deviation, based on empirical fit to observations.

Input: Oil-water interfacial tension, oil and water density, oil viscosity, and exit velocity from release location.

Output: Oil droplet size distribution (volume median diameter, d_{50} and logarithmic geometric standard deviation).

3.2.5 Fountain and intrusion model overview (Appendix H)

Processes: Model predicts fountain height (optional), and thickness and flow rate of the intrusion layer. Each release location requires separate simulations.

Model formulation: Conservation of mass and momentum equations (with buoyancy).

Input: Oil/gas density, ambient density structure, release flow rate, and ambient currents.

Output: Peak height of fountain, trapping depth, intrusion layer flow rate and thickness, and spreading velocity as impacted by interaction between the release and the ambient current.

4 Blowout Model Development and Application History

4.1 OILMAP DEEP Development

The foundation of what would eventually become OILMAP DEEP was initiated in 1982 when M. Spaulding, one of the principal authors of this report, developed a model to predict oil and gas blowout dynamics based on a model formulation proposed by McDougall (1978). The original integral plume model, developed at that time, numerically solved the conservation of water and oil mass, momentum, and buoyancy equations along the plume center. The distribution of variables across the plume was assumed to be Gaussian and the solutions self-similar (same shape independent of location relative to the discharge). The model predicted the plume center location and width; centerline velocity, buoyancy, and oil concentrations; and plume trapping height if applicable. Spaulding et al. (2000) added hydrate formation to the model framework and performed an application and extensive sensitivity studies to a proposed development off the west coast of Congo (Africa). The paper also presented comparisons of model predicted center line velocities with observations for two shallow (50 m) compressed gas releases off the coasts of Florida and Vancouver Island. Model predictions were observed to be in good agreement with these very limited field observations (Spaulding et al. 2000).

The predecessor to OILMAP DEEP was also applied in a model inter-comparison study as part of the SINTEF *Deep Spill* project. The field experiments were performed in deep water off the coast of Norway. The other blowout models evaluated were DeepBlow and CDOG (description of these models below). Note that DeepBlow and CDOG were validated with and applied to the oil and gas release from *Deep Spill*. An overview of the *Deep Spill* project is provided in Johansen et al. (2001, 2003). A summary of the inter-comparison study is presented in Adams and Socolofsky (2004). No detailed evaluation of the models was made in the inter-comparison study since field data for model validation were lacking.

RPS ASA's blowout model has seen extensive use since 2000 with primary applications in the Gulf of Mexico and off the west coast of Africa for spill response planning and environmental permitting for deep water development. OILMAP DEEP models the near field behavior of the release while OILMAP/SIMAP, using input from blowout, predicts the far field transport, fate, exposures, and effects of the oil in the environment. The most recent version of OILMAP DEEP, developed in 2011, included the ability to predict the dissolution of gas and its feedback on the plume buoyancy. In addition a module was added to allow for simple (percent of oil treated with a given DOR) modeling of dispersant application to blowouts at the source (Crowley et al. 2014). The 2011 version of OILMAP DEEP was the starting model code used for this study.

As part of the current project, OILMAP DEEP has been extended and improved in a number of key areas including: the deployment and addition of pipeline release, dispersant treatment, and fountain and intrusion models, extension of the plume model to handle input from Black Oil Tables (BOT), and development of a new, universal oil droplet size model.

4.2 Comparison to other blowout models

In addition to OILMAP DEEP, there are three other blowout modeling systems that are relatively widely known and published. Two are integral plume type models (SINTEF's DeepBlow and

Clarkson University, Deep Oil and Gas model, CDOG), which both use a similar conceptual framework as OILMAP DEEP, and one empirical model based on dimensional analysis, laboratory observations, and the results of many years of research in buoyant plume dynamics (MIT's empirical blowout model). Each model is described briefly below with a focus on the processes included and the level of model validation and application, if known.

4.2.1 SINTEF's DeepBlow Model (Johansen 1998, 2000)

The foundation for DeepBlow was first documented in a technical report published by Johansen (1998) and introduced into the literature by Johansen (2000). It was based on earlier work reported by Rye (1994). The model is based on an integral plume, Lagrangian concept and applied to multi-phase discharges of water, oil, and gas in a stratified water column with variable currents. The gas may be combined with sea water and converted to hydrate, dissolved into the plume entrained water, or leak out of the plume due to the slip between rising gas bubbles and the plume trajectory. Non-ideal behavior of the gas is addressed through a pressure- and temperature-dependent compressibility z -factor in the equation of state. The model was applied to predict the behavior of experimental releases performed in Norwegian waters and showed qualitative agreement with observed plume dynamics when gas dissolution was included. Simulations were performed for other hypothetical releases in both deep and shallow water. For discharges at intermediate to shallow depths (100 ± 250 m), the two major processes limiting plume rise were predicted to be: (a) dissolution of gas into ambient water, or (b) bubbles rising out of the inclined plume. These processes tend to be self-enforcing, i.e., when gas is lost by either of these processes, plume rise tends to slow and more time is available for gas dissolution. For discharges in deep waters ($700 \pm 1,500$ m depth), hydrate formation, if present, was found to be a dominant process in limiting plume rise.

Johansen et al. (2003) summarized the application of the model to field experiments from a deep water release off the coast of Norway in the *Deep Spill* experiment (Johansen et al. 2001). Comparisons were once again qualitative and showed the importance of gas dissolution in controlling plume trapping and the lack of any hydrate formation. The later was attributed to the fact that dissolved methane concentrations had not reach saturation levels; a precursor for hydrate formation.

4.2.2 Clarkson University Deep Oil and Gas (CDOG) Model (Yapa et al. 2001)

Yapa and Zheng (1997) presented a review of integral plume models and following this work extended the existing model framework to include multi-phase flows to model oil and gas releases from a blowout (Zheng and Yapa 1997a and b). Yapa's group then extended their earlier work in a series of two-part papers, the first (Zheng et al. 2002) describing the theory and model formulation and the second (Chen and Yapa 2003) presenting the application of the model to the *Deep Spill* experiment (Johansen et al. 2001). At this stage of development, the model incorporated the phase changes of gas, associated changes in thermodynamics (cold temperatures and high pressures) and its impact on the hydrodynamics of the jet/plume. Hydrate formation, hydrate decomposition, gas dissolution, non-ideal gas behavior, and possible gas separation from the main plume due to strong cross currents were integrated with the jet/plume hydrodynamics and thermodynamics. Model formulation, comparisons with experimental data, and other ancillary information can be found in Zheng et al. (2003), Yapa et al. (2010), Bandara and Yapa (2011), Chen and Yapa (2004), Chen and Yapa (2007) and Dasanayaka and Yapa (2009). Yapa et al. (2012) provide a brief model development history and summarize the development of a companion model- to predict the far field advection and dispersion of oil and gas (see Dasanayaka and Yapa 2009 for details).

4.2.3 MIT Empirical Model (Socolofsky 2001)

Empirical relationships, characterizing buoyant plumes have been developed from laboratory experiments with air bubbles, glass beads (creating inverted, downward falling plumes), crude oil, and buoyant continuous-phase tracers in stratified and flowing conditions by Akar and Jirka (1995) and Socolofsky and Adams (2002, 2003, 2005). The experiments indicate that plume characteristics are governed by five parameters: horizontal velocity, ambient density gradient, (given in terms of the buoyancy frequency), oil/gas bubble rise velocity, source buoyancy, and height above the discharge. Socolofsky and Adams (2002, 2003, 2005) have developed empirical relations among these five parameters based on laboratory data to predict the plume separation height; peel height; trap height; flow rate, width, and upstream penetration of the first intrusion layer; and peeling fraction.

Socolofsky et al. (2011) applied their empirical method to predict the trap height for the DWH spill and compared model predictions to observations based on fluorescence measurements of Colored Dissolved Organic Matter (CDOM) concentrations. The results are shown in Figure 4-1 (the figure is taken directly from Socolofsky et al. 2011). The black dots represent the empirical model predictions and the colored dots the observations. Model predictions are seen to be in good agreement with the observations, correctly predicting the mean trap height. Prior to the riser cut on June 3, 2010, the observations show a larger variance in the fluorescence, that the model was not able to capture.

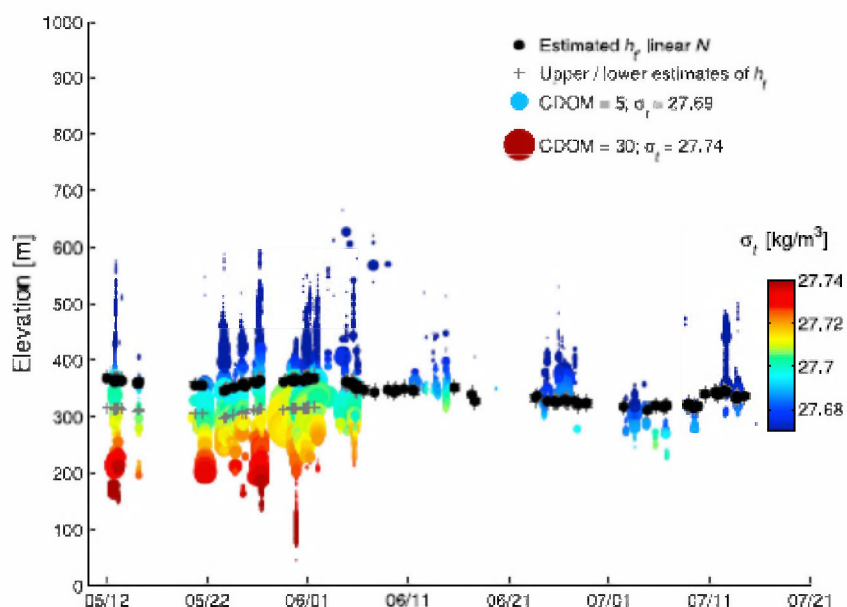


Figure 4-1. Time series comparison of fluorescence measurement (colored dots) with predicted trap height (black dots); upper and lower estimates shown in gray crosses). Size of the colored dots represents the amount of “excess” fluorescence; color of the dots indicates potential density as σ_t (sigma t). (Socolofsky et al. 2011).

4.2.4 API Model Inter-comparison Study

To assess the capabilities of available blowout models and the potential effectiveness of subsea dispersant application as predicted by these models, a model inter-comparison exercise was

sponsored by the American Petroleum Institute (API), through the Joint Industry Task Force, D3 Subsea Dispersant Injection Modeling Team, with co-sponsorship by the BP/Gulf of Mexico Research Initiative through the Gulf Integrated Spill Research (GISR) and Center for Integrated Modeling and Assessment of the Gulf Ecosystem (C-IMAGE) Consortia. Modelers were given a matrix of test cases and presented their modeling results at a workshop conducted in Houston, Texas, USA, on January 31, 2014. The fourteen (14) test (hypothetical) cases explored a range of water depths (200 and 2000 m), gas to oil ratios GORs (500 and 2,000 standard cu ft (ft³) gas/bbl of oil), cross current speeds (0.05 and 0.3 m/sec) and dispersant treatment (none and 2 %). The density stratification was fixed for all cases under conditions characteristic of the northeastern Gulf of Mexico. The oil and gas release rates and properties, including density, composition, viscosity, and interfacial tension, with and without dispersants, were provided. Models were run either by their developers or experienced users. The participating models were:

- SINTEF DEEP BLOW a component of their Oil Spill Contingency and Response (OSCAR) model,
- The National Energy Technology Laboratory (NETL) Blowout and Spill Occurrence Model (BLOSOM)
- The DHI MIKE Model module for subsea oil spills.
- Applied Science Associates (ASA) OILMAP DEEP, a component of their OILMAP and SIMAP spill modeling systems.
- Empirical correlation equation models for the near-field dynamics applied in Socolofsky et al. (2011) to the Deepwater Horizon accident. These results were supplied to two different research-oriented far-field transport models, the Lagrangian Transport (LTRANS) model, run by E. North from the University of Maryland and the Connectivity Modeling System (CMS), run by C. Paris from the Rosenstiel School for Marine and Atmospheric Science, University of Miami.

These models span a range of well developed (DEEP BLOW, OILMAP DEEP, and empirical correlation models) and new modeling systems (BLOSOM and MIKE Subsea oil), from both industry and academia. The inter-comparisons were conducted in two phases. In Phase I modelers were asked to provide predictions of the initial oil and gas bubble size distribution for all cases. Based on a review of these results, the API team leaders released consensus oil and gas bubble sizes to be used in the next phase. Phase II focused on predictions of the plume dynamics and the transport of oil droplets to the sea surface. The transport of oil droplets is normally included in models of the far field and for select models the near field as well. Given the theoretical nature of test cases, the study presents an inter-comparison of model predictions. The results of the inter-comparison study were presented at the workshop and are provided in an overview paper published in Marine Pollution Bulletin (Socolofsky et al. 2015). RPS ASA performed the simulations that were reported at the workshop using the most recent, commercially available version of OILMAP DEEP. Simulations for the far field transport of oil droplets from the release to the surface were performed using a simple advective scheme, consistent with what is included in OILMAP/SIMAP. The version of OILMAP DEEP that was used for the inter-comparison study does not include the major improvements made in the model and reported here. The results from OILMAP DEEP were presented at the workshop by a representative from ExxonMobil.

The major conclusions from the study were:

1. The models used to predict the oil droplet and gas bubble size distributions are all empirical and primarily dependent on the Weber number; however, in some cases a

dimensionless parameter (viscosity number) to represent viscous effects is included. The empirical models represent extrapolations from existing laboratory and very limited field data and hence are highly dependent on what data is used to develop the model coefficients. The droplet size models give predictions that are precise to within $\pm 50\%$ for the volume median diameter.

2. When applied, dispersants give a 200-fold reduction in the interfacial tension between oil and water under test conditions, and are predicted to reduce the mean droplet size by about one order of magnitude.
3. The models used to predict the plume dynamics were all of the integral plume type and predicted a single intrusion layer several hundred meters above the release for the deep water (2,000 m) releases. All models predict intrusion layer flux on the order of 1,000 m³/sec at the trapping depth. The presence of strong cross flow enhances the entrainment and leads to a reduction in the trapping height. For shallow water (200 m) releases the models predict that the oil is transported directly to the sea surface.
4. Plume model predictions were largely insensitive to droplet size distribution within the range of droplets simulated by each model. Because the plume trap height is always close to 300 m above the release for deep water blowouts, the plume stage of the simulation generally represents a small fraction of the oil transport distance. This stage is necessary however to predict the formation of subsurface intrusions, but variability in model predictions is not expected to significantly affect the predictions for oil surfacing.
5. All models use either a simple advective scheme or an advection and diffusion method to predict far field transport, with the specified cross flow currents transporting the oil downstream and the buoyant rise velocity transporting the oil vertically toward the surface. In general, the larger the oil droplet size the closer to the release site where the droplet surfaces. Application of dispersants reduces the oil droplet sizes and hence shifts the oil impacted surface area further from the source, a few 10s kilometers downstream.
6. If oil degradation processes were included in the models they can substantially reduce the amount of oil reaching the surface, particularly for treated oil where the oil droplet sizes have been substantially reduced and the surface area to volume ratio dramatically increased.

To illustrate the consistency of the results for the two most widely, commercially available models (DEEP BLOW and OILMAP DEEP), Table 4-1 summarizes a comparison of model predictions for the volume median oil droplet size, intrusion layer depth, and intrusion layer volume flux for API Test Cases 9 and 10. These cases are the closest to the Deepwater Horizon spill: release rate - 20,000 bbls/day, release depth - 2000 m, GOR - 2000, and ambient cross currents - 5 cm/sec. Case 9 had no dispersant treatment and Case 10 assumed a DOR of 2%.

Table 4-1. Comparison of DEEP BLOW and OILMAP DEEP predictions, API Test Cases 9 and 10.

Case 9: 20,000 bbl/day, 2000 m depth, GOR-2000, U= 0.05 m/sec, DOR-0 %				
	DEEP BLOW*	OILMAP DEEP	Difference	% Difference
Droplet diameter(μm), d_{50}	3800	2750	1050	27.6%
Intrusion layer depth(m)	1700	1770	-70	-4.1%
Intrusion layer volume flux(m^3/sec)	4000	3287	713	17.8%
Case 10: 20,000 bbl/day, 2000 m depth, GOR-2000, U= 0.05 m/sec, DOR-2%				
	DEEP BLOW*	OILMAP DEEP	Difference	% Difference
Droplet diameter(μm), d_{50}	200	110	90	45.0%
Intrusion layer depth(m)	1680	1770	-90	-5.4%
Intrusion layer volume flux(m^3/sec)	3800	3287	513	13.5%
* Values estimated from Socolofsky et al (2015); droplet diameter				
Figure 5, intrusion layer depth - Figure 8, and intrusion volume flux- Figure 9				

Comparing the model predictions the differences are small for intrusion layer depth and layer volume flux, both of which are predicted by the plume model. The differences are more substantial for the median oil droplet size distribution, particularly for the treated case. Belore (2014) has recently compared predictions of the SINTEF DEEP BLOW oil droplet model (Johansen et al. 2013) with extensive observations from laboratory scale and tank scale experiments, with and without dispersant treatment, and concluded that the SINTEF model substantially over predicted the oil droplet sizes for the dispersant treated cases (see Appendix G for additional details).

In summary, the inter-comparison study included several of the most commonly used integrated spill models. While these models agreed reasonably well with each other in many respects (e.g., trapping depth, intrusion water flux), they differ in other respects by an order of magnitude or more (e.g., initial droplet size distribution and far field oil surface metrics). This agreement reflects the commonality in basic model formulation (integral plume models, and advective transport models) and model assumptions. The differences between model predictions are mainly attributed to differences in specifying release conditions (oil and gas release rates and composition), the rates of entrainment in the plume and in the presence of cross flows, presence and rates of gas and oil dissolution within the plume, and whether fate processes are included in the model. The inter-comparison study indicates, especially in deep water release where far field transport can be significant affected, more data and better mechanistic understanding of the initial oil droplet size distribution and the rates of the fate processes are critical to improving confidence in model predictions.

5 Application of OILMAP DEEP to Hindcast DWH Spill

This section describes the application of OILMAP DEEP and its subcomponents to the DWH spill. The first section (Section 5.1) provides an overview of the environmental conditions in the receiving water at the well head. The next two sections provide a specification of the oil and gas release (Section 5.2) rates and dispersant application methods and rates (Section 5.3). The next five sections (Sections 5.4 to 5.8) describe the results of the application of the individual model components.

5.1 Environmental Data

To establish the environmental setting for the model application, information on the receiving water density structure and current was reviewed. Both of these variables play a central role in blowout modeling. The degree of vertical stratification in the water column has an important influence on the plume trapping depth while the currents affect the behavior of the plume and whether it bends over allowing gas bubbles to escape, which can deprive the plume of one of its sources of buoyancy.

Figure 5-1 shows the location of CTD (Conductivity, Temperature, and Depth) measurements made in the Gulf of Mexico between April and November, 2010 (Grennan et al. 2015). The station locations are color coded by date and the histogram at the bottom of the figure shows the number of stations per day. The density of measurements is highest in the vicinity of the spill site. Figure 5-2 shows the density profiles, as σ_T , for all stations where the data were verified (QA/QC'd) as part of the NRDA program. A review of the data shows that the variability in density decreases with depth, with high variability in the surface layer (to depth of 200 m) and then rapidly decreasing variability with depth. In the range of interest (trap depth) for blowout modeling (depths of 900 to 1,300 m) there is little variation in either the structure of the density profile or its values. This analysis suggests assuming a constant density gradient structure in the vicinity of the trapping depth and over the duration of the spill is a very reasonable approximation.

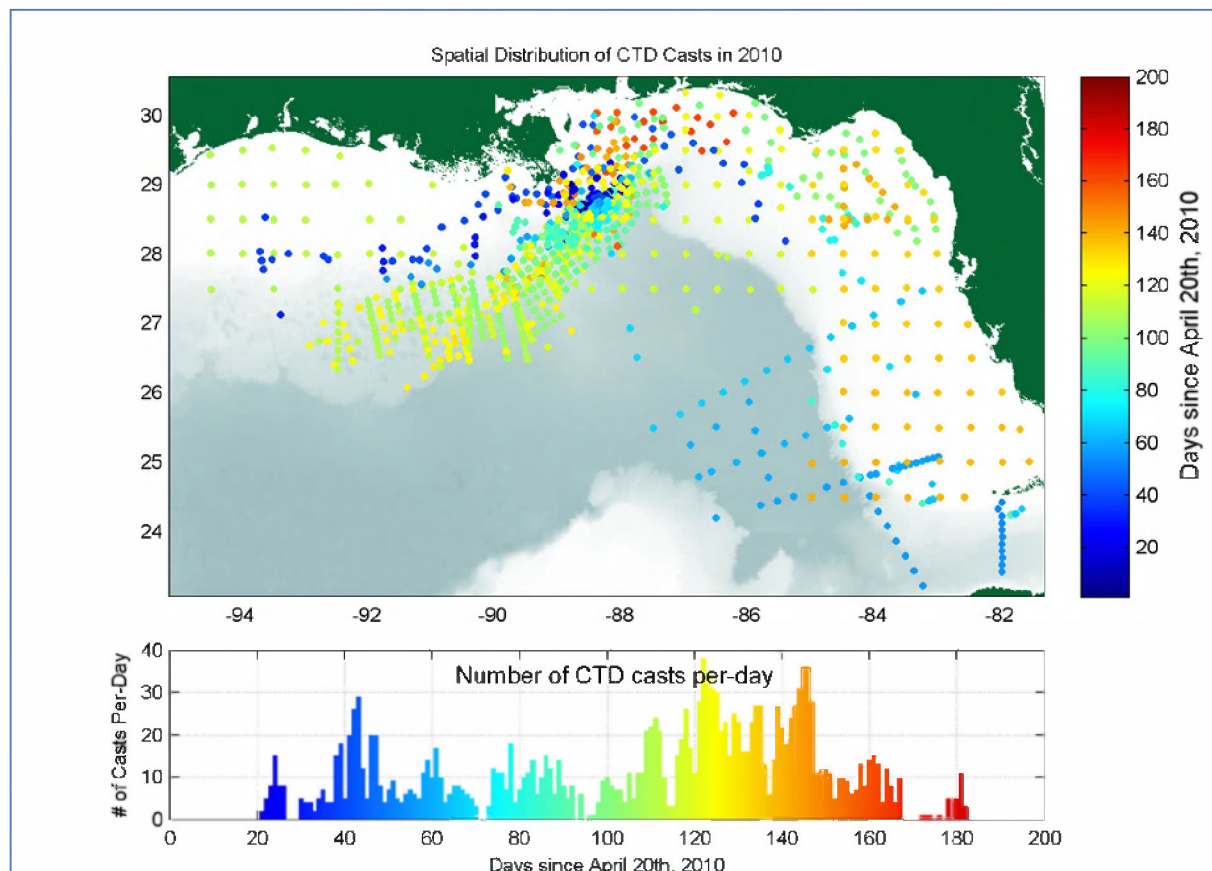


Figure 5-1. Spatial distribution of all CTD data collected in 2010. Points are color-coded by the date on which the profile of CTD data was collected. Below, a histogram of the number of CTD casts taken per day as a time series, also color-coded by date collected. Data presented in this plot include all data collected onboard Response, NRDA, and Academic cruises.

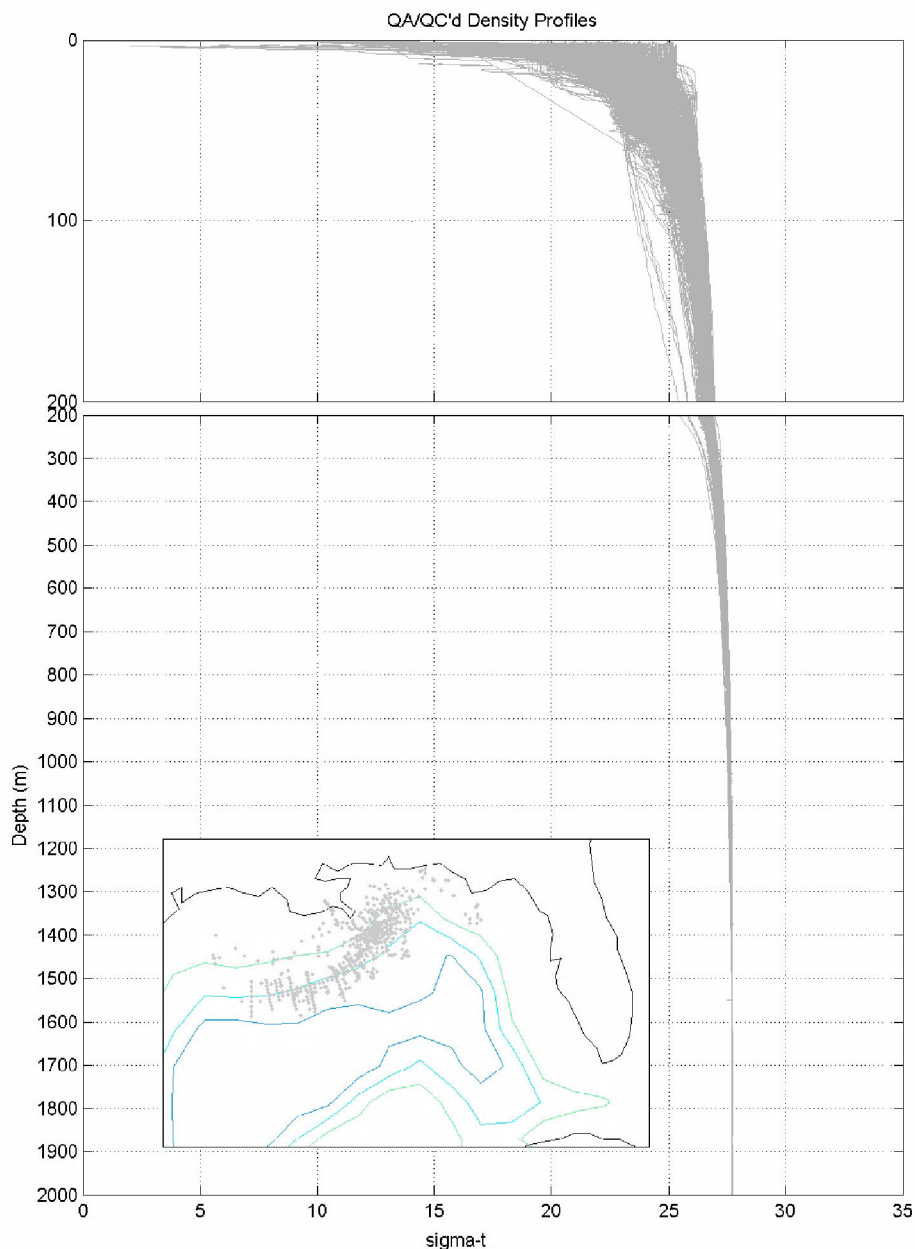


Figure 5-2. Density (kg/m^3), as σ_T (whereby $\sigma_T = \rho - 1000 \text{ kg m}^{-3}$), vs depth (m) for all station casts noted in Figure 5-1 where the data were verified. This includes CTD measurements from May 10 to October 20, 2010 for the Northeastern Gulf of Mexico. Most of the CTD profiles are taken in close proximity to the spill site. The profiles have little variability at depth (below 500 m), but significant seasonal variability near the surface (depths less than 200 m).

Two Acoustic Doppler Current Profilers (ADCP) were deployed in the vicinity of the wellhead from early May through the end of July 2010. Table 5-1 provides a summary of the mean current speed at the ADCP depth bin (depth interval) closest to the trapping height of the plume (~900 m below surface). The stations have mean values of 6.7 to 6.9 cm/sec (0.13 knot) with variances of 4.7 to 5.2 cm/sec. The magnitude of the currents hence is quite low and variable and therefore will not have a substantial impact on plume behavior.

Table 5-1. Mean and standard deviation of ADCP measurements at two stations near the well head. Data collection period, bin depth and number of data points are also provided.

	Station #42916	Station #42868
Mean velocity:	6.7 cm/s	6.9 cm/s
Standard deviation:	4.7 cm/s	5.2 cm/s
Bin depth:	895.9 m	909.9 m
Data period:	5/1 – 7/31/2010	5/9 – 7/31/2010
Data points:	12,139	10,720

The remainder of this section describes the application of OILMAP DEEP and its subcomponents to the DWH spill. The first two sections provide a description of the specification of the oil and gas release rates and dispersant application methods and rates. The next five sections describe the results of the application of the individual model components.

5.2 Estimates of Oil Release Rates from Department of Justice (DOJ) Expert Reports

The U.S. Department of Justice (DOJ) contracted with five experts (Bushnell 2013, Pooladi-Darvish 2013, Dykhuizen 2013, Griffith 2013, Kelkar and Raghavan 2013) to provide estimates of the flow rate and total release from the DWH spill. Their analyses are provided in individual expert reports provided in the list of references and organized by the lead expert's last name. (An additional report was prepared to characterize the oil and gas mixture and provided in the form of an equation of state, as a function of pressure and temperature [Zick 2013], here after referred to as the Black Oil Tables or BOT. A tabulated form (spreadsheet) of the equation of state for the oil and gas mixture is provided in Appendix C of this report.). The typical expert made estimates using their selected methodology for discrete time periods during the release, along with the associated uncertainties. They also provided mean values along with the lower and upper bounds of the total release. Figure 5.3 summarizes the results of the expert's analyses in terms of flow rate vs time during the spill (left panel) and cumulative amounts released (right panel). For reference the flow rate vs time, with and without oil recovery, taken from the NOAA Oil Budget Calculator (OBC) (Lehr et al. 2010) are provided. The estimated flow rates from the various subgroups of the Flow Rate Technical Group (FRTG) (McNutt et al. 2011) that were used in developing the OBC estimates are also given. The OBC cumulative release rates are shown in the right panel to facilitate comparison with DOJ expert's estimates.

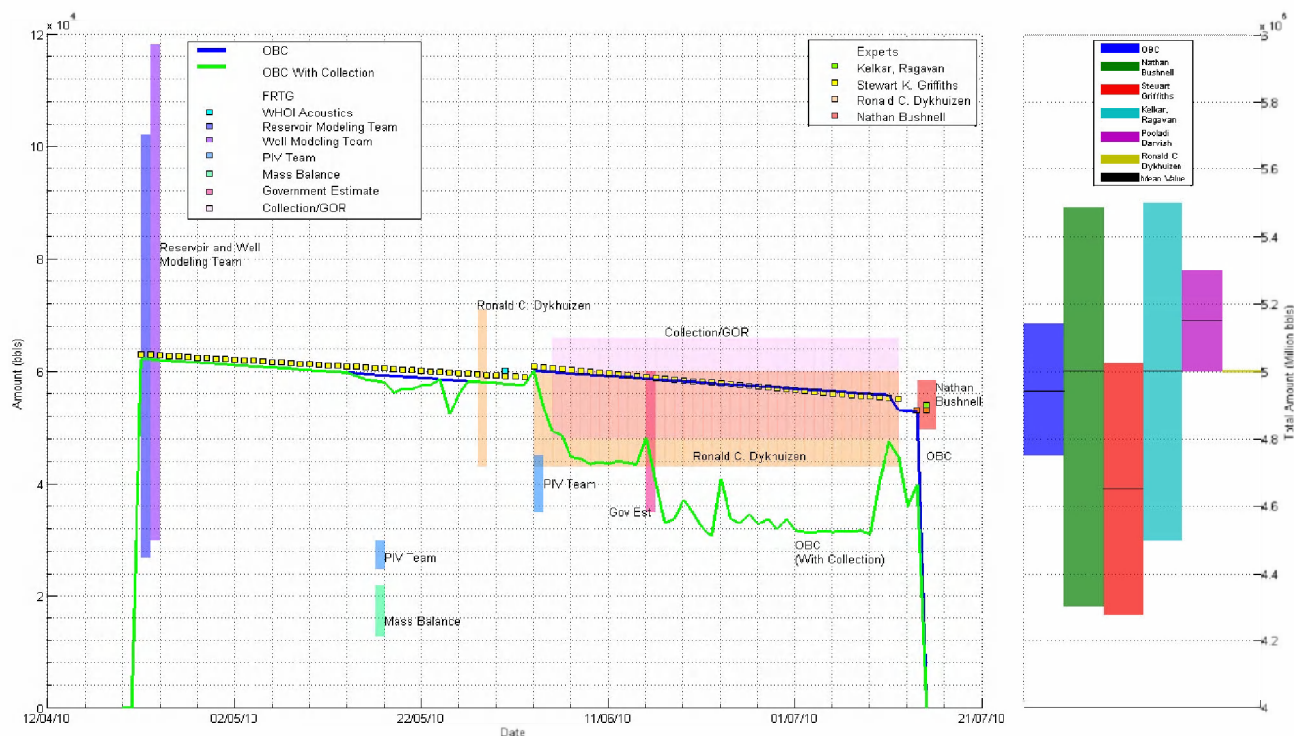


Figure 5-3. Flow rates (bbls/day) vs time for the DWH spill from the start to the end of the release (left panel) and the total amount released (millions of bbls) during the spill (right panel) showing low, mean, and high values, if provided. Estimates of the release rates on selected days by DOJ experts are noted as are the estimates by FRTG teams that support the OBC estimates.

Table 5-2 provides a summary of the total amount of oil released estimated by DOJ experts (average for all DOJ experts) and the OBC report for low, mean, and high estimates. The mean and standard deviation, based on DOJ expert's estimates, are also provided.

The results of the DOJ experts are in very good agreement with the OBC estimates for mean values (DOJ- 4.96 million barrels vs OBC- 4.94 million barrels). The uncertainties for the DOJ estimates are slightly larger (6 to 7%) than those from the OBC (4 %). Given the very good agreement between the results of the various experts and the OBC estimates, the OBC values have been selected for the present application. It should be noted however that the US District Court for Eastern District of Louisiana January 2015 court finding (Case 2:10-md-02179-CJB-SS Document 14021 Filed 01/15/15) of a reduced release volume (4.0 million barrels) was also modeled and is documented in Addendum 1 (USDC 2015).

Table 5-2. Cumulative volume of oil released (millions of barrels) by DOJ experts and from the OBC report for low, mean, and high values. Overall mean and standard deviation from the expert reports are also noted.

Cumulative volume of oil released from DOJ Expert Reports							
Estimated Release (million barrels)							
Expert	Low	Mean	High				
Nathan Bushnell	4.28	4.65	5.02				
Ronald C. Dykhuizen	5	5	5				
Stewart K. Griffiths	4.3	5	5.48				
Ragavan Kelkar	4.5	5	5.5				
Pooladi-Darvish	5	5.15	5.3				
Average	4.62	4.96	5.26				
Variation from mean	6.94%		6.05%				
<table><tr><td>Mean</td><td>4.94</td></tr><tr><td>Standard Deviation</td><td>0.4</td></tr></table>				Mean	4.94	Standard Deviation	0.4
Mean	4.94						
Standard Deviation	0.4						
OBC Report	4.75	4.94	5.14				
Variability from mean	3.85%		4.05%				

5.3 Specifications of the oil and gas release rates; kink and riser flow rates

Figure 5-4 shows the oil release rate to the water column from April 22, 2010 to July 15, 2010 based on the Oil Budget Calculator (OBC) report (Lehr et al. 2010, referred to hereafter as OBC) (solid black line). Based on the OBC, the release rate decreased from just over 60,000 barrels per day at the start of the spill to about 55,000 barrels per day by the time the release stopped. Appendix A provides a summary of the release configurations. Appendix B provides data on release rates based on the OBC total volume flow assumptions, and Appendix C provides the oil and gas properties and ratio based on the Macondo Crude Black Oil Tables (Zick 2013). The time history of daily, total oil release volumes was defined using the values given in the OBC report. Oil was released in one of two different configurations, the first configuration had varying percentages of the total release from two primary locations (Figure 5-5): at the end of the riser (Figure 5-6), and from a number of small holes in the vicinity of a kink that developed in the riser pipe, immediately above the BOP (Figure 5-7), and the second configuration reflected flow only from the cut riser pipe immediately above the BOP. The discrete stepping of the kink release is a result of the change (increase) in the number of holes at the kink. Figure 5-4 also shows estimates of the amount of oil released from the riser and kink for the time period when both release locations were active. These estimates were based on application of the pipeline model described in Section 5.4, using the gas-to-oil ratios estimated at the surface and at depth conditions as provided in Zick (2013).

A phase behavior model – an equation of state fluid characterization – for the Macondo reservoir fluids has been developed (Zick 2013) to predict the Macondo reservoir fluids' physical, thermodynamic, and transport properties as functions of temperature, pressure, and fluid composition. These model predictions can be used to support engineering calculations such as the riser or kink flow of oil from the Macondo well into the Gulf of Mexico, and to evaluate the conversion (through different processes) of reservoir barrels of oil (by which the flow from the reservoir into the well is measured) to stock tank barrels (by which the extent of the Deepwater Horizon oil spill is measured).

The Equation-of-State (EOS) fluid characterization (see details in Zick 2013) can be used as the Macondo fluid model within any engineering software that supports the Peng-Robinson EOS and the Lohrenz-Bray-Clark viscosity model. That includes reservoir simulators, pipe-flow simulators, and surface process simulators. The EOS characterization includes a set of lookup tables of fluid properties as functions of temperature and pressure commonly called *Black-Oil Tables [BOT]* within the industry. These tables were used in the computation of fluid flow from the Macondo reservoir, through the damaged wellbore, to the spill site at the bottom of the Gulf of Mexico. The black-oil tables have been generated under the assumption that the overall flowing composition was constant (at the original, average reservoir composition), but that the liquid and gas phase composition could vary widely as the temperature and pressure changed. For any given combination of temperature and pressure (at regular intervals), the black-oil tables provide the: (1) number of equilibrium phases; (2) molar and volumetric proportions of each phase; (3) molecular weights of each phase; (4) compressibility factor of each phase and of the overall fluid; (5) molar volume of each phase and of the overall fluid; (6) density of each phase and of the overall fluid; (7) viscosity of each phase; and (8) molar composition of each phase. Table 5-3 shows an excerpt from the black-oil tables that were developed from Zick (2013)'s Macondo Equation-of-state model. The complete black-oil tables are provided separately in electronic format in Zick (2013).

Table 5-3. Excerpt from the Macondo Black-Oil Tables (BOT) (Zick 2013)

Temp (F)	Pres (Psia)	Liq Vol Frac	Gas Vol Frac	Liq Den (kg/m ³)	Gas Den (kg/m ³)
200	2000	0.30535	0.69465	710.29	114.63
200	2200	0.33567	0.66433	703.32	127.62
200	2400	0.36486	0.63515	696.63	140.36
200	2600	0.39282	0.60718	690.21	154.31
200	2800	0.41948	0.58052	684.02	167.96
200	3000	0.44482	0.55518	678.04	181.30
200	3200	0.46883	0.53117	672.27	195.32
200	3400	0.49152	0.50848	666.69	210.02
200	3600	0.51292	0.48708	661.28	224.41
200	3800	0.53307	0.46693	656.04	238.98
200	4000	0.55204	0.44796	650.94	253.76
200	4200	0.56990	0.43010	645.97	268.76
200	4400	0.58674	0.41326	641.09	283.98
200	4600	0.60270	0.39730	636.28	299.44
200	4800	0.61797	0.38203	631.47	315.15
200	5000	0.63281	0.36719	626.60	331.12
200	5200	0.64762	0.35238	621.59	347.38
200	5400	0.66300	0.33700	616.31	363.95
200	5600	0.67985	0.32015	610.60	380.39
200	5800	0.69968	0.30032	604.26	398.33
200	6000	0.72526	0.27474	596.96	416.48
200	6200	0.76246	0.23754	588.19	435.76
200	6400	0.82760	0.17240	576.94	457.13
200	6600	1	0	560.31	483.49
200	6800	1	0	562.93	562.93
200	7000	1	0	565.46	565.46
200	7200	1	0	567.92	567.92
200	7400	1	0	570.30	570.30
200	7600	1	0	572.61	572.61
200	7800	1	0	574.86	574.86
200	8000	1	0	577.04	577.04

An analysis of oil flux through the kink and riser flow, based on using the Black-Oil Tables (Zick 2013), is presented in Figure 5-4. The riser release started on April 22, with the kink release beginning on April 28. Both releases were present through June 3, at which point the riser pipe was cut above the BOP eliminating the kink releases. After the riser was cut, a top-hat was installed and a portion of the oil released from the well was recovered. The amount recovered was measured by BP Response on a daily basis and the amount released to the environment estimated by taking the difference between the amounts released and recovered.

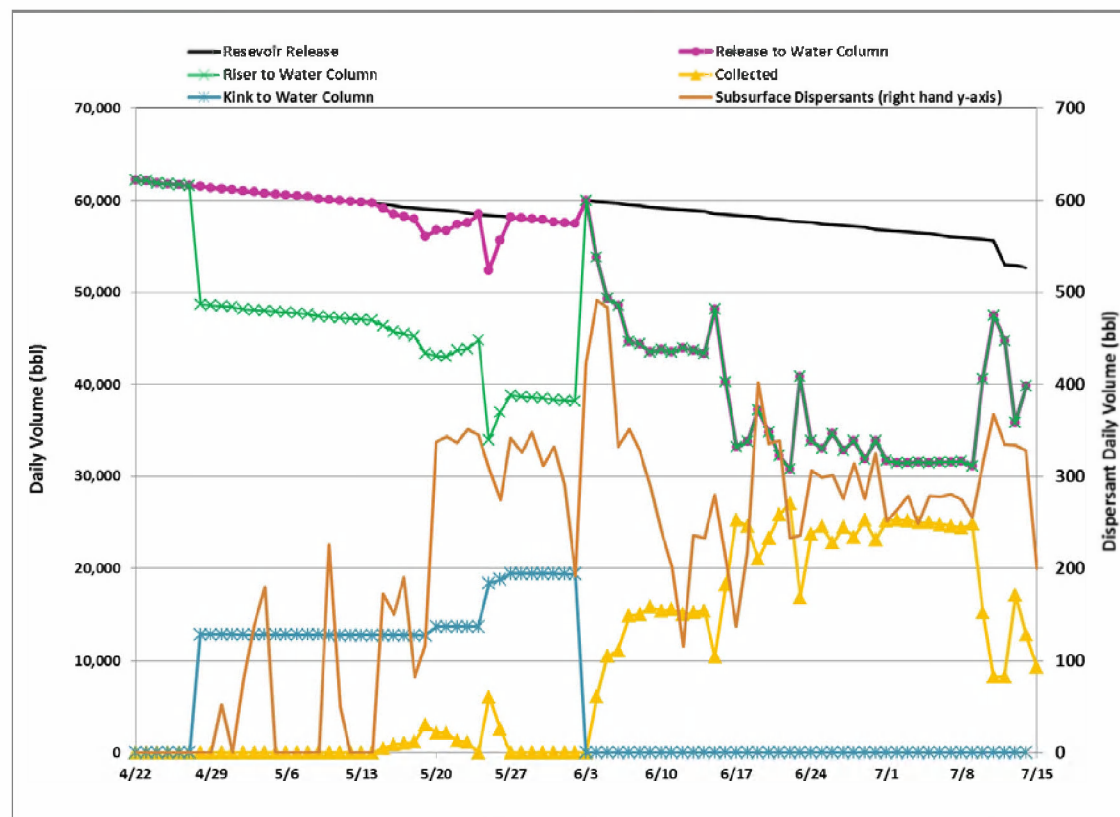


Figure 5-4. Time history of the estimated total oil release rate based on the Oil Budget Calculator (OBC) (Lehr et al. 2010), with and without adjustment for the amount recovered via the top hat installed on June 3, 2010. Estimates of the oil release rates from the riser and kink are provided. The amount of dispersants applied subsurface to the spill is also provided. All rates in barrels per day.

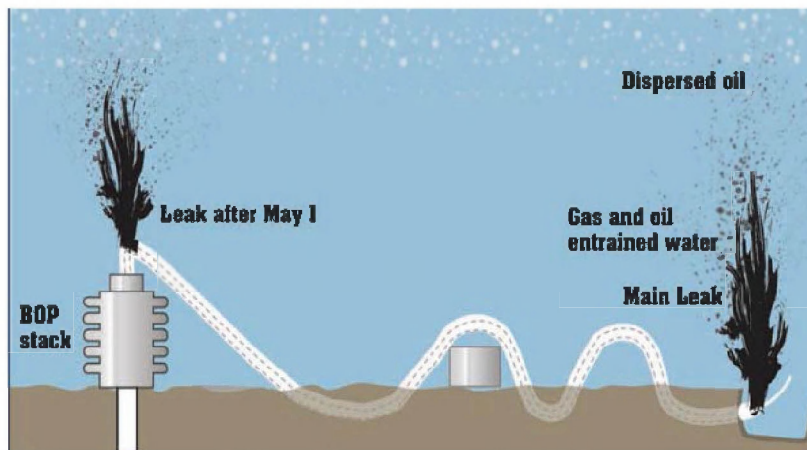


Figure 5-5. Schematic of releases of oil and gas from the end of the riser pipe and from small holes at a kink in the riser pipe above the BOP (McNutt et al. 2011).



Figure 5-6. ROV image of the end of the riser pipe taken by *MSV Skansi Neptune* on May 14, 2010.



Figure 5-7. ROV image of the kink above the BOP taken by Maxx3 May 14, 2010 (Round 1, Packet E).

An in depth review of the available ROV video imagery indicated that the number of holes at the kink increased with time from two (2) beginning on April 28, 2010 to six (6) just before the riser was cut (Figure 5-8). These are documented in Appendix A. Photographs of the cut riser pipe above the BOP (Figure 5-9) and of the riser pipe in the vicinity of the kink (Figure 5-10) were taken during a visit to NASA Michoud facility by RPS ASA employee, Andrew Bird, in May 2012. The photographs clearly document the number of holes in the vicinity of the kink and show that most were elongated in the axial direction (flow direction). Direct kink hole field drawings were made by the U.S. Coast Guard (2011) and used to obtain the final cross sectional areas of each kink hole.



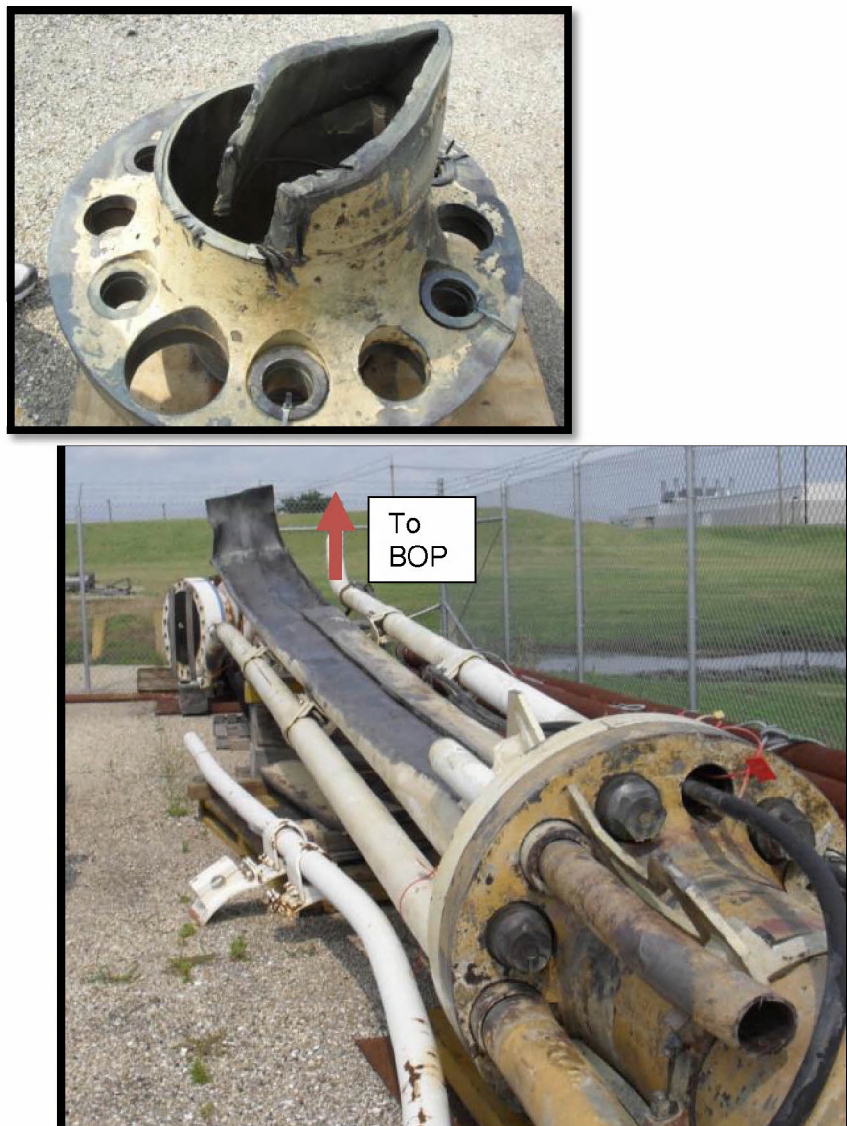


Figure 5-9. Photographs of the post cut riser flange (upper), and the recovered section of cut riser pipe (lower) along axis toward the BOP. Both images were taken at the NASA Michoud facility in New Orleans, LA. The riser pipe has been cut longitudinally with half removed. (Photos taken by Andrew Bird, May 2012.)



Figure 5-10. Photographs of the kink location, inside to outside (upper left), side (upper right) and outside to inside, (lower center) views taken at the NASA Michoud facility. (Photos taken by Andrew Bird, May 2012.) The holes are identified as A, B, C, D, E, and F (lower center).

5.4 Specification of dispersant application strategy and amount

The subsea dispersant applicator time series shown in Figure 5-11 identifies five dispersant applicator types (hook, paddle, collar, trident, and wand). A review of the available ROV video found that two application devices were primarily used: a wand and a trident (forked wand). In both methods, the application device was typically placed adjacent to the oil release and the dispersant entrained into the plume/jet as it exited the riser. The ROV video suggests that a wand was used to apply dispersants at the end of the riser pipe before it was cut, and that the trident was predominantly used post-riser cut (Figure 5-11), while the top-hat was in place. Even

though the wand and trident were the applicator types used predominantly throughout the spill, other application methods and combined methods were also utilized.

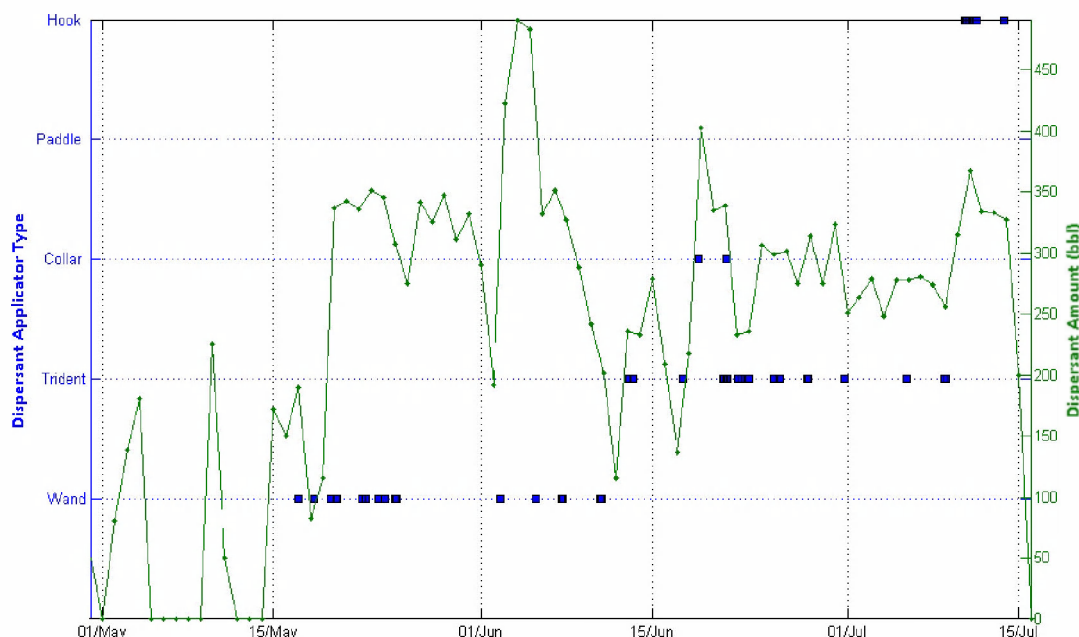


Figure 5-11. Dispersant applicator time series, showing observed presence of dispersant application method from sampled ROV video (left axis, when known), and subsea dispersant amounts in barrels (right axis). EPA dispersant testing and riser cutting operation was performed between May 31 and June 3, 2010.

A wand held by an ROV was used extensively at the outlet end of the riser prior to the cut. In the wand application, dispersant was released through the end of a single pipe held by an ROV (upper panel, Figure 5-12). The dispersant wand was also used in conjunction with the riser insertion tube tool (RITT), a snorkel-type device, which was placed in the broken riser end to capture some of the escaping oil (see details in McNutt et al. 2011). A wand device was also observed post riser cut at the beginning of June until June 13, spanning the early period when the top hat was in place (upper panel, Figure 5-12).

The second device was a two pronged trident (bident) (lower panel, Figure 5-12) where dispersant was sprayed through a series of four small holes on the inner face of each of the trident tines. The trident was placed near the base of the top-hat (post cut). The trident was active starting on June 13, approximately 9 days after the cutting operation was completed on June 3. The trident remained in place approximately 27 days, until the riser adapter flange operations began on July 10. Other types of dispersant application device, such as a ring (Fig. 5-13) or a hooked wand (Fig. 5-14), were observed during the investigation of ROV videos, but were only occasional and on an irregular basis. For instance, inspection of the ROV videos indicated that the hooked wand was used intermittently in the course of capping operation from July 10 to July 15; the hooked wand was sporadically used by inserting it directly into and removing it from the flow aperture (Figure 5-13b) (BP 2010). Given their limited use these devices were not included in the dispersant treatment model simulation.

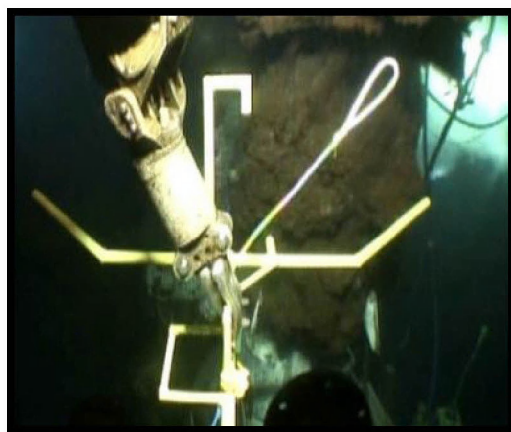


Figure 5-12. Photographs from the ROV video of the wand (upper) and trident (lower left and right) dispersant application methods. Wand dispersant application method (upper). Trident application method (lower left and right).



Figure 5-13. Image captured by Maxx3, June 18, 20:06:13 (Round 1, Packet K - DVD 98). The top of this picture indicates the presence of a dispersant ring (or a collar), but it seems that no dispersant is being applied at the specific moment when the image has been captured.

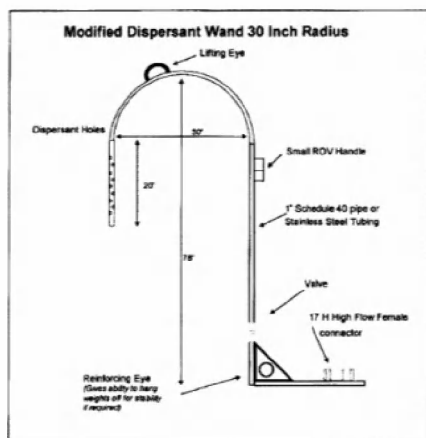


Figure 5-14. A sketch of the hooked wand for dispersant application (left) and an image (captured by Millennium22 on 7/11/10 at 14:17), showing its temporary application (right).

The Oil Budget Calculator (OBC) provides estimates of the amount of dispersants that were applied both at the surface and subsurface. Given the focus here, the daily amount applied subsurface is shown in Figure 5-4. To estimate the subsurface dispersant application rate the daily amount of dispersant applied was divided by three probable pumping rates of 8, 10, and 12 gallon per minute (gpm). This was done to estimate the number of hours per day for an active dispersant application, in order to dispense the amount of dispersant that was applied daily. The results are shown in Figure 5-15. Based on this analysis, it seems likely that a single pump was used to apply dispersants at a nominal pumping rate of 10 gpm; at such rate, for most of the days when dispersant was applied, the dispersant treatment was operating close to 24 hours a day, presumably the limit of time for the treatment operation. This is further substantiated by the directive given by the EPA on a maximum daily volume of 357 bbl/day of dispersant, which is equivalent to 10.4 gpm (Lehr et al. 2010).

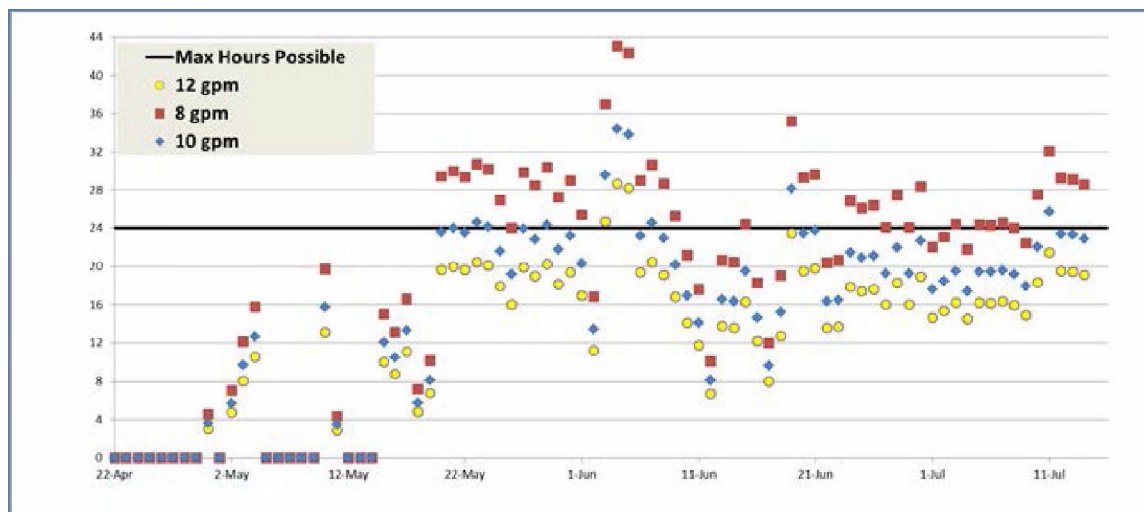


Figure 5-15. Number of hours per day of dispersant pumping at the specified rates (8, 10, and 12 gpm) to obtain the daily amount of dispersant applied through the spill period.

The next five sections provide a summary of the application of the individual model components that comprise **OILMAP DEEP** to the Deepwater Horizon spill.

5.5 Application of pipeline release model

On April 28, 2010, the riser pipe just above the BlowOut Preventer (BOP) began to leak at a point where the pipe had been severely kinked during the riser collapse. Between April 28 and June 3, 2010, the number of holes in the kink area increased from the initial two up to six holes. As the release continued, the holes in the kinked riser increased in size and number, and released a large amount of oil and gas that might otherwise have travelled the length of the riser to the severed end of the pipe several hundred meters away. The oil and gas released through the kink holes was under considerable pressure and was forced through fairly small holes, creating high velocity oil and gas jets. The exiting oil/gas mixture was therefore driven by far greater energy than if it had exited from the much larger riser pipe outlet. The increased energy has the effect of shifting the droplet size distribution to smaller sizes, many more of which could become trapped in the lower water column, changing the oil mass balance between the oil mass surfacing and that remaining at depth. In addition, the amount of oil and gas released affects how the plume of released material behaves in the water column as it rises buoyantly, entraining surrounding waters and finally trapping at some height above the blowout. The *pipeline release model* was employed to determine the flow distribution between the kink holes and the riser outlet; an important factor to consider in understanding the fate of the oil released from the blowout.

The *pipeline release model* is based on the steady state, control volume, first law of thermodynamics energy balance (Appendix D). For the present application, the control volume was specified to contain the riser pipe from the top of the Lower Marine Riser Package (LMRP), above the BOP, to the far end of the riser pipe, where it was laying half buried, but open to the ambient (Figure 5-5). The control volume therefore also contains the kink area where the oil and gas mixture was leaking. A schematic of the model application and the control volume is presented in Figure 5-16.

For the flow calculation through the multiple kink holes, it is assumed the pressure in the pipe at the kink area is the same for all the holes. Similarly the ambient pressure outside the pipe is assumed the same in the kink area. These assumptions are based on the observation that all kink holes are in close proximity. The fraction of the kink flow from each hole out of the total kink flow is set equal to the fraction of the area of each hole to the sum area of all the holes. The head loss is computed for each hole, and the head losses are summed over all kink holes to estimate the total head loss for all the kink holes. The final release rates from the riser and the kink holes are then calculated iteratively to satisfy the governing mass balance and energy conservation equations. Through this method the head losses of the individual holes are reflected in the analysis. In terms of plume modeling, the releases from all kink holes are treated as one release to predict the dynamics of kink plume, while the release from the riser end is treated as a separate release to predict the riser plume dynamics.

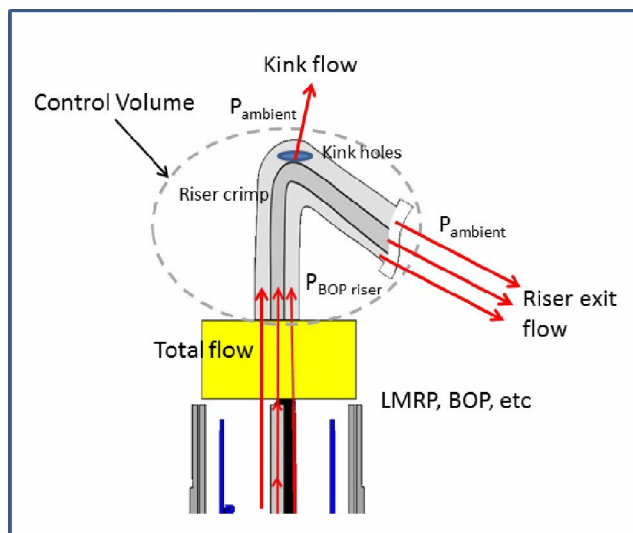


Figure 5-16. Schematic of the pipeline release model application to the DWH blowout.

5.5.1 Model input

Many of the specifications for applying the *pipeline release* model to the DWH blowout are well known, including the riser dimensions, the length of the broken riser between the kink and the outlet, the depths of the well, the kink area and riser outlet, the oil and gas mixture pressure in the BOP and LMRP, and the ambient seawater pressure levels. Some additional parameters are less well known, but estimates have been made, including the pressure inside the pipe after the LMRP, at the kink, and in the riser area downstream of the kink, the oil and gas flow rate, the GOR, the cross-sectional area in the crushed riser at the kink, through which the oil and gas mixture was forced, and finally, the number and sizes of the kink holes themselves. A list of the values used in the model application and the source of the information is presented in Table 5-4.

The ambient seawater pressures outside of the kink-hole area and at the end of the riser pipe were calculated based on the depth of each opening as determined from the ROV surveillance videos, using basic hydrostatic pressure and the density of seawater. The end of the riser pipe, at 15,214 kPa, was slightly deeper than the kink and therefore had a slightly higher pressure than the estimated value at the kink of 15,154 kPa. The pressure in the riser pipe, just above the LMRP, was taken from the Flow Rate Technical Group (FRTG) (McNutt et al. 2011) analysis of conditions in the well, the BOP, and piping system.

The flow rate of oil from the well was also estimated by the FRTG for the duration of the spill and values presented on a daily basis. During the time period of the kink release the total oil flow rate varied between 61,500 and 57,500 bbl/day, decreasing monotonically by 100 bbl/day except every seventh day, which was estimated to drop by 200 bbl/day. The total flow values from the FRTG (as referenced in OBC [Lehr et al. 2010]) were used as input to the pipeline release model and are the basis of the volume flux for the flow distribution (between riser and kink).

Review of the BOT shows that not only the GOR changes with pressure and temperature, but the constituent mass ratio also varied. Since the FRTG volume flow rate of oil was based on

surface conditions, the starting point was to assume that the flow and surface GOR were correct and other calculations would commence from there. Using the BOT, a total mass flux (oil plus gas) at the surface, based on the FRTG numbers was determined. This mass flux number was assumed to be constant due to mass conservation.

Table 5-4. List of parameters used in the pipeline release model.

Parameter Description	Value	Source	Notes
Riser inside cross-sectional area (m ²)	0.1927	BP	Based on 19.5" ID
Riser outlet cross-sectional area (m ²)	0.138	FRTG*	Bent rim at the opening
Internal riser cross-sectional area at kink (m ²)	0.0258	RPS ASA	Crushed riser pipe
Kink depth (m)	1,503	BP	
BOP top depth (m)	1,506	BP	
Riser outlet pipe depth (m)	1,509	BP	
Ambient water pressure at kink (kPa)	15,154	calculated	Based on depth at 1,503 m
Ambient water pressure at riser end (kPa)	15,214	calculated	Based on depth at 1,509 m
Pressure in the pipe above LMRP (kPa)	18,271	FRTG*	2,650 psi
Length of riser pipe after kink (m)	1,500	BP	Approximate
GOR - at the surface (scf/bbl)	2,807	BOT, Zick 2013	Std. Atm.**
GOR - at the surface (m ³ /m ³)	501	BOT, Zick 2013	Std. Atm.**
GOR - at depth (m ³ /m ³) – In-pipe	1.365	BOT, Zick 2013	180 C, 18,271 kPa
Oil density – surface (kg/m ³)	847.58	BOT, Zick 2013	Std. Atm.**
Oil density – in-pipe (kg/m ³)	689.69	BOT, Zick 2013	180 C, 18,271 kPa
Methane density - surface (kg/m ³)	0.9791	BOT, Zick 2013	15 C, 101.3 kPa (1 atm)
Methane density - in-pipe (kg/m ³)	162.53	BOT, Zick 2013	180 C, 18,271 kPa
Liquid volume fraction – surface (-)	0.001992	BOT, Zick 2013	Std. Atm.**
Gas volume fraction – surface (-)	0.998	BOT, Zick 2013	Std. Atm.**
Liquid volume fraction – in-pipe (-)	0.423	BOT, Zick 2013	180 C, 18,271 kPa
Gas volume fraction – in-pipe (-)	0.577	BOT, Zick 2013	180 C, 18,271 kPa

*Flow Rate Technical Group (FRTG) Appendix D: Deepwater Horizon Release Estimate of Rate by PIV Figure 1 pp 24

**Std. Atm. = 60F (15.5C), 14.7psi (101.325kPa)

The total volume flow inside the riser pipe prior to exiting must also be determined from the BOT at the in-pipe pressure and temperature of 18,271 kPa (2,650psi) and 180°C, respectively, resulting in an in-pipe GOR of 1.365 m³/m³. In addition, for the tabulated, in-pipe oil liquid volume fraction of 0.423 and the gas volume fraction of 0.577, and the respective oil and gas densities of 689.69 kg/m³ and 162.53 kg/m³, respectively, a fluid density of 385.43 kg/m³ was estimated. Using this fluid density and the mass flux calculated, in addition to the volume fractions listed, this resulted, for example, in an in-pipe total volume flux of 0.3929 m³/s for an oil flow rate of 61,500 bbl/day.

Despite the fact that there were several ROV units almost constantly monitoring the leakage from the kink holes, it proved to be extremely difficult to measure or even estimate the volume of mixture released to the environment at these locations. This was in part due to the lack of a full understanding of the hole geometries, but also to the difficulty of estimating the flow rate of the jets that were visible to the ROV cameras, not to mention the jet(s) released from holes on the underside of the bent riser, and therefore not directly visible to the cameras.

While oil and gas began to leak after the riser pipe separated from the Deepwater Horizon platform on April 22, 2010, the kink holes did not form and start to leak until April 28 when two holes appear to have formed simultaneously with a noticeable flow of oil and gas from each. Between April 28, 2010 and June 3, 2010 (when the riser cutting operations were completed), the number and size of the holes increased from the initial two at onset to an eventual six holes. A thorough investigation, based on analysis of extensive video imagery and on-site photography provide evidence to understand the chronological enumeration of the kink holes and their shapes with time. For the present application, the number of holes was varied using the time schedule determined from an investigation of ROV imagery, however only the final hole dimensions were used for each time period with different number of kink holes. A timeline of the number of holes and associated cross sectional area for each, which were used in the model, is presented in Figure 5-17.

5.5.2 Model application

The *pipeline release model* application to the DWH blowout was then used to predict release rates from two separate locations: the end of the riser pipe and the small holes in the vicinity of the kink. The process is iterative, and solved by estimating the flow split and then using those values in the first law equation to calculate the flow at the kink and then to back calculate the riser outlet flow. If the new estimates differ from the initial estimate, the process is repeated until a minimum threshold for convergence is reached. The calculations were performed on a daily time step, matching the resolution of the input flow rate data. Additional details, describing the model equations and application method, can be found in Appendix D.

5.5.3 Model results

The *pipeline release model* was run from April 28 through June 2, 2010 to predict the daily flow balance. Figure 5-18 presents the model predicted kink and riser flow rates and the total flow from the well, as a function of time, over that period; note that these values do not take into account any of the collected flow, since this occurs after the release and does not impact the flow distribution analysis. The predicted amount of oil released from the kink was on the order of 11,000 bbl on the first day, increasing to 16,000 bbl immediately before the riser was cut, equating to 18% of the total amount released initially and then increasing to 28%. The predicted flow for each opening and the percent of total are presented in Table 5-5.

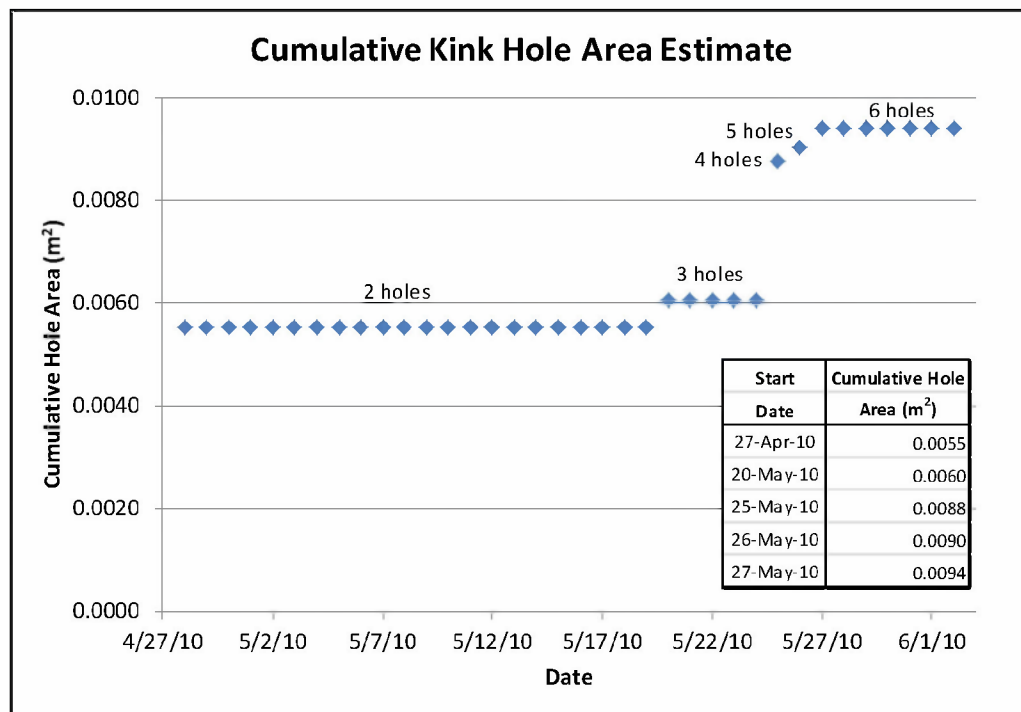


Figure 5-17. Timeline of the number of kink holes and their associated opening area used in the pipeline release model.

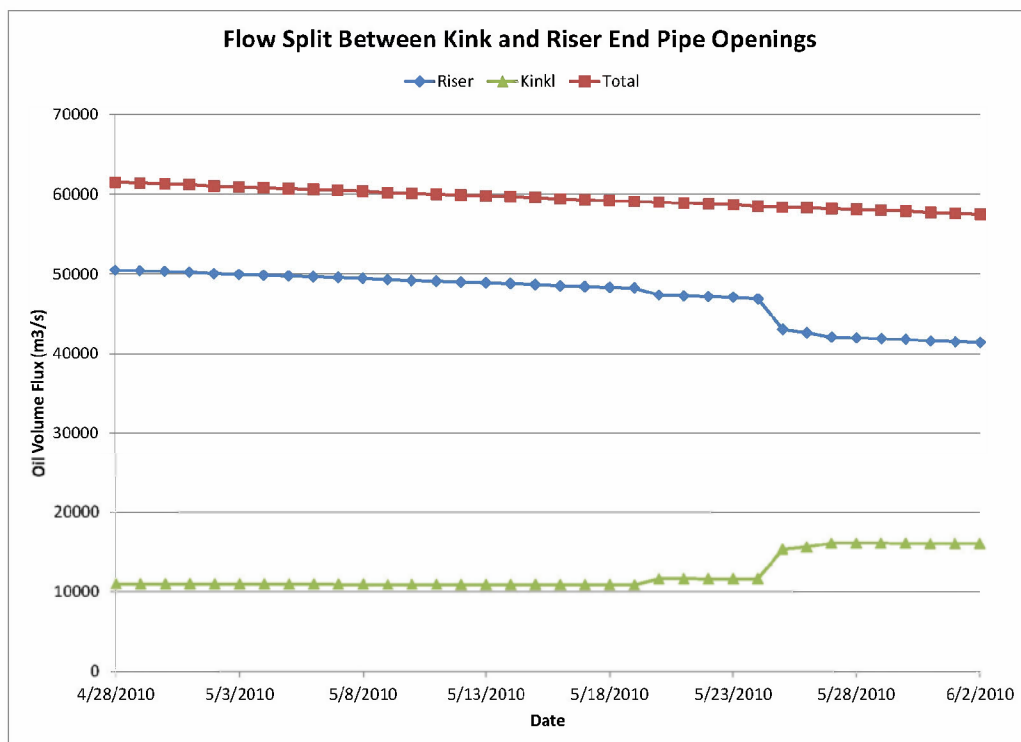


Figure 5-18. Pipeline release model predicted flow split between the kink holes and the riser outlet.

Table 5-5. Pipeline release model predicted flow split between the kink and riser openings

Date	Kink Flow (bbl/day)	Riser Flow (bbl/day)	Total Flow (bbl/day)	Kink as Percent of Total	Date	Kink Flow (bbl/day)	Riser Flow (bbl/day)	Total Flow (bbl/day)	Kink as Percent of Total
4/28/2010	10,980	50,520	61,500	17.9	5/16/2010	10,857	48,543	59,400	18.3
4/29/2010	10,974	50,426	61,400	17.9	5/17/2010	10,851	48,449	59,300	18.3
4/30/2010	10,968	50,332	61,300	17.9	5/18/2010	10,846	48,354	59,200	18.3
5/1/2010	10,962	50,238	61,200	17.9	5/19/2010	10,840	48,260	59,100	18.3
5/2/2010	10,951	50,049	61,000	18	5/20/2010	11,626	47,374	59,000	19.7
5/3/2010	10,945	49,955	60,900	18	5/21/2010	11,621	47,279	58,900	19.7
5/4/2010	10,939	49,861	60,800	18	5/22/2010	11,615	47,185	58,800	19.8
5/5/2010	10,933	49,767	60,700	18	5/23/2010	11,609	47,091	58,700	19.8
5/6/2010	10,927	49,673	60,600	18	5/24/2010	11,598	46,902	58,500	19.8
5/7/2010	10,921	49,579	60,500	18.1	5/25/2010	15,305	43,095	58,400	26.2
5/8/2010	10,915	49,485	60,400	18.1	5/26/2010	15,610	42,690	58,300	26.8
5/9/2010	10,904	49,296	60,200	18.1	5/27/2010	16,085	42,115	58,200	27.6
5/10/2010	10,898	49,202	60,100	18.1	5/28/2010	16,080	42,020	58,100	27.7
5/11/2010	10,892	49,108	60,000	18.2	5/29/2010	16,075	41,925	58,000	27.7
5/12/2010	10,886	49,014	59,900	18.2	5/30/2010	16,070	41,830	57,900	27.8
5/13/2010	10,880	48,920	59,800	18.2	5/31/2010	16,061	41,639	57,700	27.8
5/14/2010	10,874	48,826	59,700	18.2	6/1/2010	16,056	41,544	57,600	27.9
5/15/2010	10,869	48,731	59,600	18.2	6/2/2010	16,051	41,449	57,500	27.9

Early on, while the blowout was still in progress, investigators made estimates of the amount of oil leaking from the kink area. Estimates made by members of the FRTG using Particle Image Velocimetry (PIV) (McNutt et al. 2011) for May 15, 2010, prior to the formation of the FRTG (Wereley 2011), estimated the kink flow at 35% of the riser flow, which corresponds to 26% of the total flow. Additional estimates were made using PIV methods after the formation of the FRTG and gave values ranging 15 to 20% for May 14-16, 2010. Camilli et al. (2011) estimated the flow split, based on ADCP measurements for May 31, 2010, and gave a value of 31%. The estimates, for May 14-16, correspond to the time when only two holes were in existence, whereas by May 31, all six holes were present. The model predictions are in generally good agreement with the observations, both in terms of trend and the percentage of oil released at the kink.

The predicted increase in flow percentage over time was a result of the number of holes at the kink increasing from two, at the start of the spill, to six immediately before the riser was cut. This estimate appears to be reasonable given the observation that the area of the combined openings of the kink holes essentially doubled over the course of the kink leakage. While the flow volumes appear large, the crushed riser pipe in the kink area likely kept the internal pressures on the BOP side extremely high, and caused a considerable reduction in the riser flow. The kink holes were primarily, if not all, between the BOP and the crimp (as opposed to between the crimp and end of riser) which implies that there was a 2,750 kPa (400 psi) pressure drop across the openings to the water column, according to FRTG internal pressure estimates. Given the proximity of the releases, the resulting discharges are clearly interacting with one another. As an engineering approximation the blowout plume model assumed one hole to represent all holes with the area varying to match the total cross sectional area of all holes with time. The loss rates for the flow through each hole were however used in the flow rate analysis.

5.6 Application of the Dispersant Treatment Model

The *dispersant treatment model* (Appendix F) was developed based on the dilution factor of the entrainment of ambient seawater, and the initial and growing fraction of the cross section of the plume where active mixing of the released oil and the applied chemical dispersants occurred. The dilution factor is determined based on calculation through a momentum jet flow or a buoyant plume flow, depending on the distance of dispersant application in comparison with the jet/plume transition length scale. The fraction of the treated cross section of the plume is determined by the dispersant application device; a trident application results in wider contact angle of dispersant with the plume than a wand application, and therefore the fraction treated is proportionally larger with the trident application than the wand application.

The dispersant treatment model was applied to the DWH spill. As a first step, the momentum length scale was calculated for the pre- and post-cut riser releases. This calculation was performed to determine the length scale at which the flow regime changes from a jet to a plume based on the ratio of the momentum to buoyancy of the release. This distinction is of key importance to choosing the proper analytical solution for entrainment calculations. The calculated length scale for the riser ranged from 0.5 to 0.8 m, depending on the assumption about the flow rate and release opening geometry. Estimates were also made for the kink release and gave values of 3 to 5 m, depending on the number of holes and the associated flow rates. Camilli et al. (2011) gave estimates of the momentum length scale for the pre-cut riser of 0.6 m for May 31, 2010, in very good agreement with the analysis presented here. Estimates of the length scale for the kink release are not of interest here since no dispersants were applied at this location. Based on this analysis and the observation from the ROV imagery that the dispersants were typically applied near the end of the riser and that entrainment and subsequent mixing proceeded with distance from the release point, it is reasonable to assume that the release can be best approximated as a buoyant plume, with the buoyancy of the oil and gas driving the plume.

5.6.1 Application strategies

To illustrate the predictions, the *dispersant treatment model* was applied to a simple test case with an oil release rate of 50,000 barrels per day and a dispersant application rate of 300 barrels per day. These values are typical of the ratio of oil to subsurface dispersants used during the spill. If the dispersant is completely mixed with the oil then the DOR is 1:167 (alternately written as 167).

Figure 5-19 shows model predicted fraction treated (solid line, left axis) and DOR (dashed line, right axis) as a function of distance from the release for post riser cut conditions. Distance is measured downstream from the release and non-dimensionalized by the diameter of the release at the source. Figure 5-20 is the same plot but as a function of distance from the origin. Curves are shown assuming 6.25, 10, 12.5, 25, 30, 50, and 100% of the circumferential sector is treated. These values include the azimuthal angle of the original treatment plus an internal growth rate in the plume. As an example, if the dispersant application device has an angular reach of 20 degrees at the application point and the azimuthal internal entrainment rate is 10 degrees, then the total angular sector treated is 40 degrees (20, plus $10+10 = 40$) or in percent of circumference ($40/360$) 11.1%. If the internal growth rate is assumed constant then the sector percentage is independent of distance from the release. The DOR is given in terms of the target DOR divided by the Dispersant Effectiveness (DE). As an example, if the target application DOR is 1:50 and DE is 0.5 then the effective DOR is 1:100. The fraction treated increases with distance from the release and asymptotically approaches a constant value. The amount treated

increases with sector treatment percentage. For low sector ranges (less than 30%) the fraction treated is close to its asymptotic value by 4 to 6 diameters from the release. For higher sector ranges (50 to 100%) asymptotic values are reached at greater distances. The DOR curves all have similar shapes to the fraction treated curves. In general, the fraction treated increases and the DOR decreases, which is reflected by the increase of the denominator, with distance from the release and with increasing percent of sector treated. For analysis purposes it appears that mixing is approximately complete at about 6 diameters. The zone of flow establishment is typically 5-7 diameters from the release. Assuming a DE of 50%, a distance of 6 diameters, and application by the wand, the fraction treated is 6.5 % and the DOR is 1:20 or DOR/DE of 1:40. Similar assumptions for the trident gives a fraction treated of 26% and a DOR of 1:55 or DOR/DE of 1:110.

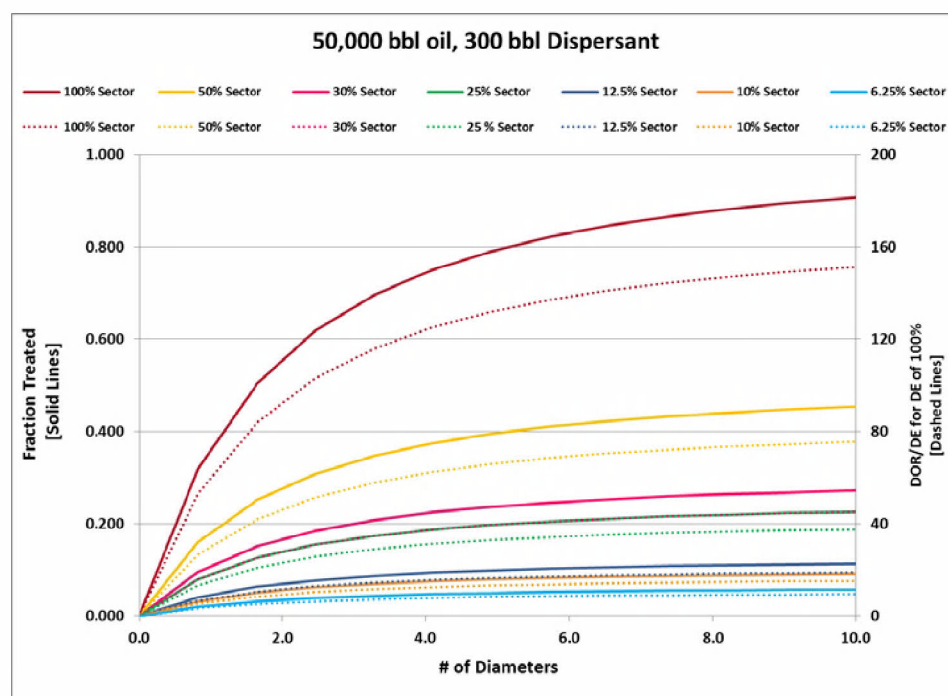


Figure 5-19. Fraction treated (solid line, left axis) and DOR (dashed line, right axis) vs number of diameters downstream from the release with varying sector fractions treated. The effective DOR is estimated by dividing the target DOR by the dispersant effectiveness (DE).

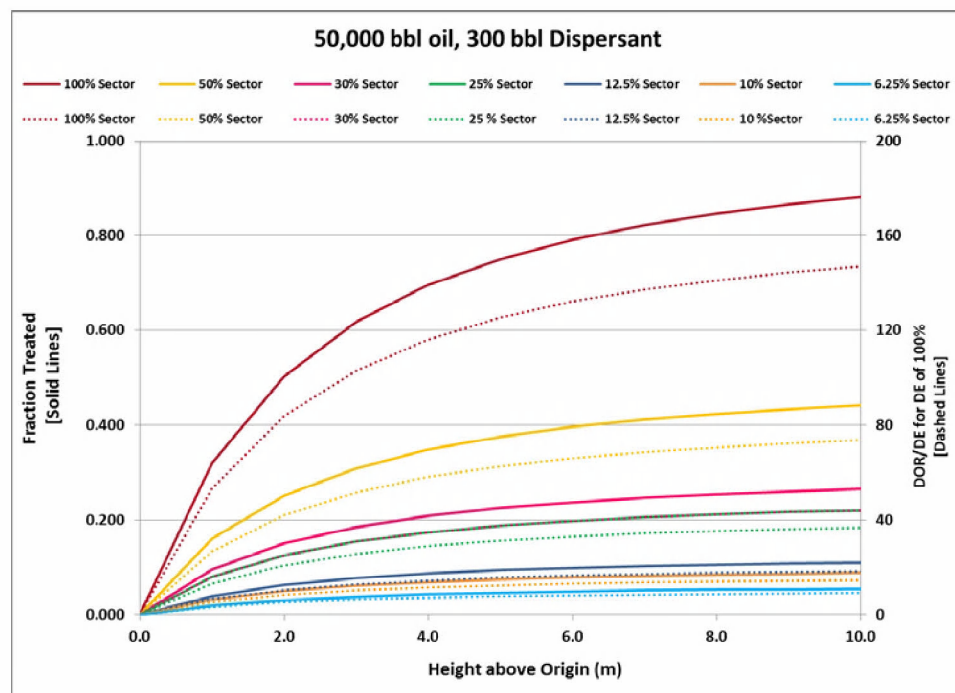


Figure 5-20. Fraction treated (solid line, left axis) and DOR (dashed line, right axis) vs height above the origin (m) with varying sector fractions treated. The effective DOR is estimated by dividing the target DOR by the dispersant effectiveness (DE).

To assess the model's predictive performance, it was applied to predict the fraction treated and DOR during the time period when oil droplet sizes were being measured by *Holocam* during various dives from the R/V Jack Fritz cruises (Davis and Loomis 2014). This droplet size data set is summarized in Section 5.7 and described in detail in Appendix G. The *Holocam* data (Davis and Loomis 2014) is presented in Appendix I. During this period dispersants were primarily being applied via the trident immediately above the release and in close proximity to the mouth of the top hat. *Dispersant treatment model* simulations were performed for June 14 to 20, 2010, with a time step of one day. Daily oil release and dispersant application rates, as provided in Appendix B, were used.

Figure 5-21 shows model predictions of fraction treated and DOR as a function of time assuming 20, 30, and 40% of the sector was treated. The 30% value is a reasonable estimate for the trident. The results are shown at approximately 6 diameters from the release origin. The model predicts fractions treated of 0.16, 0.25 and 0.34 for the 20, 30, and 40% sector cases, respectively. These values are invariant with time. The DOR for each sector case is also shown and varies daily throughout the period; the higher the percent of sector treated, the lower the DOR. The variations are caused by daily variations in the oil release and dispersant application rates. Fraction treated and DOR both scale linearly with percent of sector. The average DORs during the period are 1:33, 1:49, and 1:65 for the 20, 30, and 40% cases, respectively. The DORs for dives #5 and #6, where *Holocam* data were collected, were estimated using the *droplet size model*. Specifically an assumed lognormal distribution was fitted to the observations from each dive and the volume median diameter (VMD) determined for each. The equation that expresses VMD as a function of Weber and Ohnesorge number was then used to estimate the most likely value of the oil-water interfacial tension associated with the observed VMD. This

value in turn was used to determine the DOR based on laboratory based observations of DOR vs oil water interfacial tension for Macondo oil and Corexit dispersant (Venkataraman et al. 2013). The method is outlined in Section 5.8. The DORs for dives #5 and 6 are shown in Figure 5-21. The value to the right of the dive number is the horizontal distance (m) between the sampling site and the well head. The *Holocam* data-based DOR for dives # 5 and 6 were 1:69 and 1:114.5, respectively. Model predictions are hence in reasonable agreement with the very limited observations. The variation of field data is not surprising, given the quite different distances (dive #5 at 1.15 km from the wellhead vs dive #6 at 2.12 km) and depth into the water column (dive #5 at 1,459m vs dive #6 at 1059m). It should be noted that the deepest depth for dive #6 was 1059 m. The dive did not sample the full thickness of the intrusion layer (1,100 to 1,200 m) and hence likely underestimated the effectiveness of the dispersant application. In this case the DOR shown in Figure 5-21 is likely lower than the actual value making it more consistent with the model predictions. As the droplet size data were collected at distance from the wellhead, they may not include much of the release that was in the form of larger droplets, which could have reached the surface before being sampled.

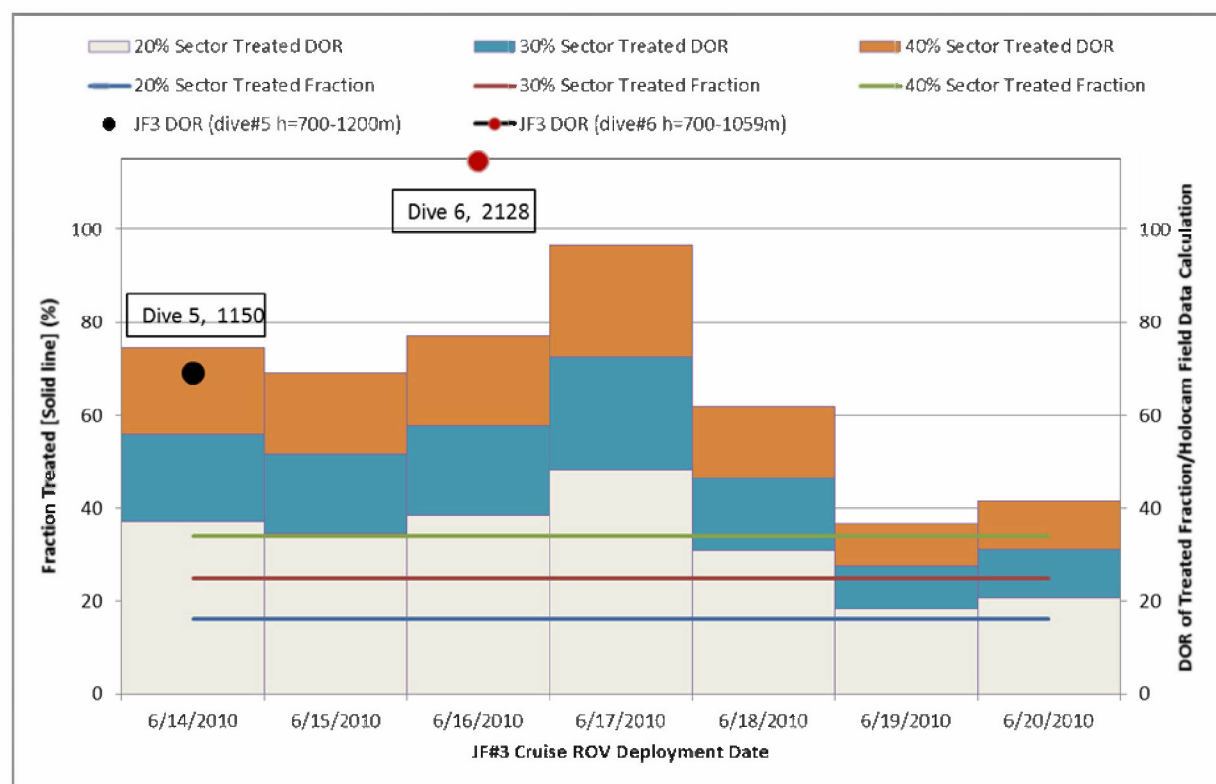


Figure 5-21. Fraction treated (solid line, left axis) and DOR (stacked column, right axis) during the JF3 cruise for sectors treated 20%, 30%, and 40%, respectively. The estimated DORs for the JF3 dives #5 and #6 are also plotted (filled circles) along with the Dive number and the distance (m) from the wellhead (see Appendix G for additional details).

5.7 Application of the blowout plume model

The plume model was applied to predict the plume size and location, the dissolution of gas to the water column, and associated gas concentrations within the plume. The following sections provide a description of the model application and the corresponding results.

5.7.1 Plume dynamics and trapping depth

The *blowout plume model* simulates the release of oil and gas from subsurface release location(s) to predict subsurface plume size and location, as well as the concentration of oil and gas along the plume centerline. The model predictions are largely dependent on the relative density differential between the release and the receiving water; this density differential (buoyant force) causes the plume to ascend vertically and while doing so, entrain water and spread radially. This entrained water mixes with the release resulting in the dilution of the plume oil and gas concentrations, while also slowing the plume ascent and rate of entrainment. The model also simulates the dissolution of gas from bubbles into the entrained water, which also serves to reduce the plume buoyancy. These actions combine to eventually “trap” the plume, meaning the plume (mixture of the oil and gas release with water) eventually reaches a state of neutral buoyancy and no longer ascends through the water column. At this point the ascent of the oil droplets is a function only of their individual buoyancy driven rise velocity (a function of size and density). A full description of the model physics and its application are presented in Appendix E.

5.7.2 Model Input

As described above, the daily release of oil and gas was simulated for the DWH spill event. Throughout the event the release characteristics varied with respect to location, amount, and release exit orifice dimensions. Briefly summarized, the release originated on April 22, 2010 at the site of the broken riser (Site 1 per Appendix A), and for a few days was the only known release, after which on April 28, 2010, a second release began at the kink (Site 2 per Appendix A) just above the LMRP at the wellhead. The kink holes grew over time as did the kink release daily volume until the riser cutting operations eventually finished on June 3, 2010. Note that the cutting operation was completed early in the day and therefore for the analysis June 3rd was considered a ‘post cut’ day. After the cut, the release came from only one location (Site 2 per Appendix A) however the volume released to the water column varied daily depending on the varying reservoir release (gradually decreasing flow) and collection volumes. The *blowout plume model* was used to simulate both the kink and riser release (both pre and post cut riser) separately, resulting in two distinct simulations. Table 5-6 summarizes the input to the *blowout plume model*, and Table 5-7 provides the daily magnitude of the release and release exit diameter for the riser and kink, as these values changed with time through the release. Figure 5-22 shows a time series of the riser release to the water column, the kink release to the water column as well as the total release and collected volumes.

Table 5-6. Summary of *blowout plume model* input parameters.

Input Parameter	Value	Note
Oil Release Rate	Variable See Table 5-5	Appendices A & D
GOR	501 (dimensionless at surface)	Appendix B
Release Depth	Broken Riser 1,509 m Kink 1,503 m Cut Riser 1,505 m	Appendix A
Water Column Profile	See Figure 5-2	Grennan et al. 2015
Release Opening Diameter	Variable See Table 5-4 and Figure 5-17	Appendix A
Oil Density	856 kg/m ³	Appendix G
Reference Pressure	101,325 pa	Estimated
Gas Bubble Slip Velocity	0.21 m/s	Appendix E
Entrainment Coefficient	0.12	Appendix E
Spreading Coefficient	0.20	Appendix E

Table 5-7. Summary of oil release and diameter of riser and kink release for DWH spill event

Date	Day	Riser Location	Riser Release Diameter (m)	Riser Released (bpd of oil)	Kink Equivalent Diameter (m)	Kink Released (bpd of oil)
4/22/2010	1	Site 1 -NW of Wellhead	0.419	62,200	-	-
4/23/2010	2	Site 1-NW of Wellhead	0.419	62,100	-	-
4/24/2010	3	Site 1-NW of Wellhead	0.419	61,900	-	-
4/25/2010	4	Site 1-NW of Wellhead	0.419	61,800	-	-
4/26/2010	5	Site 1-NW of Wellhead	0.419	61,700	-	-
4/27/2010	6	Site 1-NW of Wellhead	0.419	61,600	-	-
4/28/2010	7	Site 1-NW of Wellhead	0.419	50,520	0.084	10,980
4/29/2010	8	Site 1-NW of Wellhead	0.419	50,426	0.084	10,974
4/30/2010	9	Site 1-NW of Wellhead	0.419	50,332	0.084	10,968
5/1/2010	10	Site 1-NW of Wellhead	0.419	50,238	0.084	10,962
5/2/2010	11	Site 1-NW of Wellhead	0.419	50,049	0.084	10,951
5/3/2010	12	Site 1-NW of Wellhead	0.419	49,955	0.084	10,945
5/4/2010	13	Site 1-NW of Wellhead	0.419	49,861	0.084	10,939
5/5/2010	14	Site 1-NW of Wellhead	0.419	49,767	0.084	10,933
5/6/2010	15	Site 1-NW of Wellhead	0.419	49,673	0.084	10,927
5/7/2010	16	Site 1-NW of Wellhead	0.419	49,579	0.084	10,921
5/8/2010	17	Site 1-NW of Wellhead	0.419	49,485	0.084	10,915
5/9/2010	18	Site 1-NW of Wellhead	0.419	49,296	0.084	10,904
5/10/2010	19	Site 1-NW of Wellhead	0.419	49,202	0.084	10,898
5/11/2010	20	Site 1-NW of Wellhead	0.419	49,108	0.084	10,892
5/12/2010	21	Site 1-NW of Wellhead	0.419	49,014	0.084	10,886
5/13/2010	22	Site 1-NW of Wellhead	0.419	48,920	0.084	10,880
5/14/2010	23	Site 1-NW of Wellhead	0.419	48,826	0.084	10,874
5/15/2010	24	Site 1-NW of Wellhead	0.419	48,731	0.084	10,869
5/16/2010	25	Site 1-NW of Wellhead	0.419	48,543	0.084	10,857
5/17/2010	26	Site 1-NW of Wellhead	0.419	48,449	0.084	10,851
5/18/2010	27	Site 1-NW of Wellhead	0.419	48,354	0.084	10,846
5/19/2010	28	Site 1-NW of Wellhead	0.419	48,260	0.084	10,840
5/20/2010	29	Site 1-NW of Wellhead	0.419	47,374	0.088	11,626
5/21/2010	30	Site 1-NW of Wellhead	0.419	47,279	0.088	11,621
5/22/2010	31	Site 1-NW of Wellhead	0.419	47,185	0.088	11,615
5/23/2010	32	Site 1-NW of Wellhead	0.419	47,091	0.088	11,609
5/24/2010	33	Site 1-NW of Wellhead	0.419	49,296	0.088	11,598
5/25/2010	34	Site 1-NW of Wellhead	0.419	43,095	0.106	15,305
5/26/2010	35	Site 1-NW of Wellhead	0.419	42,690	0.107	15,610
5/27/2010	36	Site 1-NW of Wellhead	0.419	42,115	0.110	16,085

Date	Day	Riser Location	Riser Release Diameter (m)	Riser Released (bpd of oil)	Kink Equivalent Diameter (m)	Kink Released (bpd of oil)
5/28/2010	37	Site 1-NW of Wellhead	0.419	42,020	0.110	16,080
5/29/2010	38	Site 1-NW of Wellhead	0.419	41,925	0.110	16,075
5/30/2010	39	Site 1- NW of Wellhead	0.419	41,830	0.110	16,070
5/31/2010	40	Site 1-NW of Wellhead	0.419	41,639	0.110	16,061
6/1/2010	41	Site 1-NW of Wellhead	0.419	41,544	0.110	16,056
6/2/2010	42	Site 1-NW of Wellhead	0.419	41,449	0.110	16,051
6/3/2010	43	Site 2-Wellhead	0.449	60,000	-	-
6/4/2010	44	Site 2-Wellhead	0.449	53,813	-	-
6/5/2010	45	Site 2-Wellhead	0.449	49,304	-	-
6/6/2010	46	Site 2-Wellhead	0.449	48,581	-	-
6/7/2010	47	Site 2-Wellhead	0.449	44,658	-	-
6/8/2010	48	Site 2-Wellhead	0.449	44,394	-	-
6/9/2010	49	Site 2-Wellhead	0.449	43,484	-	-
6/10/2010	50	Site 2-Wellhead	0.449	43,798	-	-
6/11/2010	51	Site 2-Wellhead	0.449	43,546	-	-
6/12/2010	52	Site 2-Wellhead	0.449	43,961	-	-
6/13/2010	53	Site 2-Wellhead	0.449	43,692	-	-
6/14/2010	54	Site 2-Wellhead	0.449	43,379	-	-
6/15/2010	55	Site 2-Wellhead	0.449	48,152	-	-
6/16/2010	56	Site 2-Wellhead	0.449	40,273	-	-
6/17/2010	57	Site 2-Wellhead	0.449	33,105	-	-
6/18/2010	58	Site 2-Wellhead	0.449	33,748	-	-
6/19/2010	59	Site 2-Wellhead	0.449	37,159	-	-
6/20/2010	60	Site 2-Wellhead	0.449	34,809	-	-
6/21/2010	61	Site 2-Wellhead	0.449	32,164	-	-
6/22/2010	62	Site 2-Wellhead	0.449	30,703	-	-
6/23/2010	63	Site 2-Wellhead	0.449	40,834	-	-
6/24/2010	64	Site 2-Wellhead	0.449	33,865	-	-
6/25/2010	65	Site 2-Wellhead	0.449	32,952	-	-
6/26/2010	66	Site 2-Wellhead	0.449	34,642	-	-
6/27/2010	67	Site 2-Wellhead	0.449	32,845	-	-
6/28/2010	68	Site 2-Wellhead	0.449	33,800	-	-
6/29/2010	69	Site 2-Wellhead	0.449	31,877	-	-
6/30/2010	70	Site 2-Wellhead	0.449	33,821	-	-
7/1/2010	71	Site 2-Wellhead	0.449	31,646	-	-
7/2/2010	72	Site 2-Wellhead	0.449	31,409	-	-
7/3/2010	73	Site 2-Wellhead	0.449	31,402	-	-

Date	Day	Riser Location	Riser Release Diameter (m)	Riser Released (bpd of oil)	Kink Equivalent Diameter (m)	Kink Released (bpd of oil)
7/4/2010	74	Site 2-Wellhead	0.449	31,540	-	-
7/5/2010	75	Site 2-Wellhead	0.449	31,418	-	-
7/6/2010	76	Site 2-Wellhead	0.449	31,539	-	-
7/7/2010	77	Site 2-Wellhead	0.449	31,522	-	-
7/8/2010	78	Site 2-Wellhead	0.449	31,621	-	-
7/9/2010	79	Site 2-Wellhead	0.449	31,108	-	-
7/10/2010	80	Site 2-Wellhead	0.546	40,601	-	-
7/11/2010	81	Site 2-Wellhead	0.449	47,465	-	-
7/12/2010	82	Site 2-Wellhead	0.449	44,698	-	-
7/13/2010	83	Site 2-Wellhead	0.449	35,836	-	-
7/14/2010	84	Site 2-Wellhead	0.449	39,857	-	-

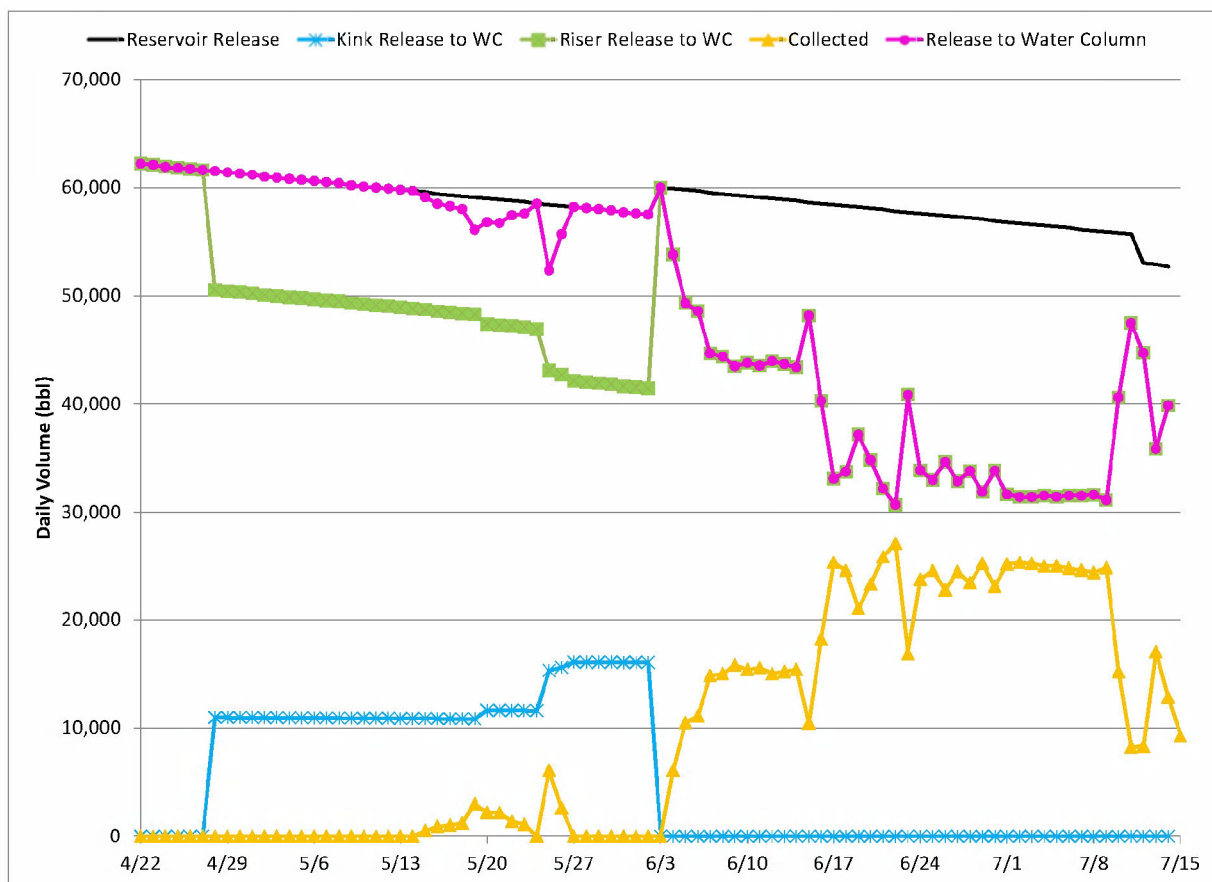


Figure 5-22. Time series of release volumes from reservoir, kink and riser and the amount collected

The preceding input data all describe the oil well blowout and its evolution over the course of the incident. The input data that represents the environment of the Gulf of Mexico and the DWH site in particular is the vertical profile of the water column density. The vertical profile is represented in this case by the water density as a function of depth, which is in turn a function of the temperature and salinity, which are also variable through the water column (Figure 5-2). The vertical profile used for the simulations was derived from a CTD profile taken from the R/V Brooks McCall at Station 54 on 30 May, 2010 and is presented in Figure 5-23. The profile used is representative of the site and while the density profile is not constant it does not vary significantly with time (see Section 5-1). The currents were assumed to be small (based on data summarized in Table 5-1) and hence not included as input to the model, as they have very little impact on trap height (only on the lateral translation of the plume).

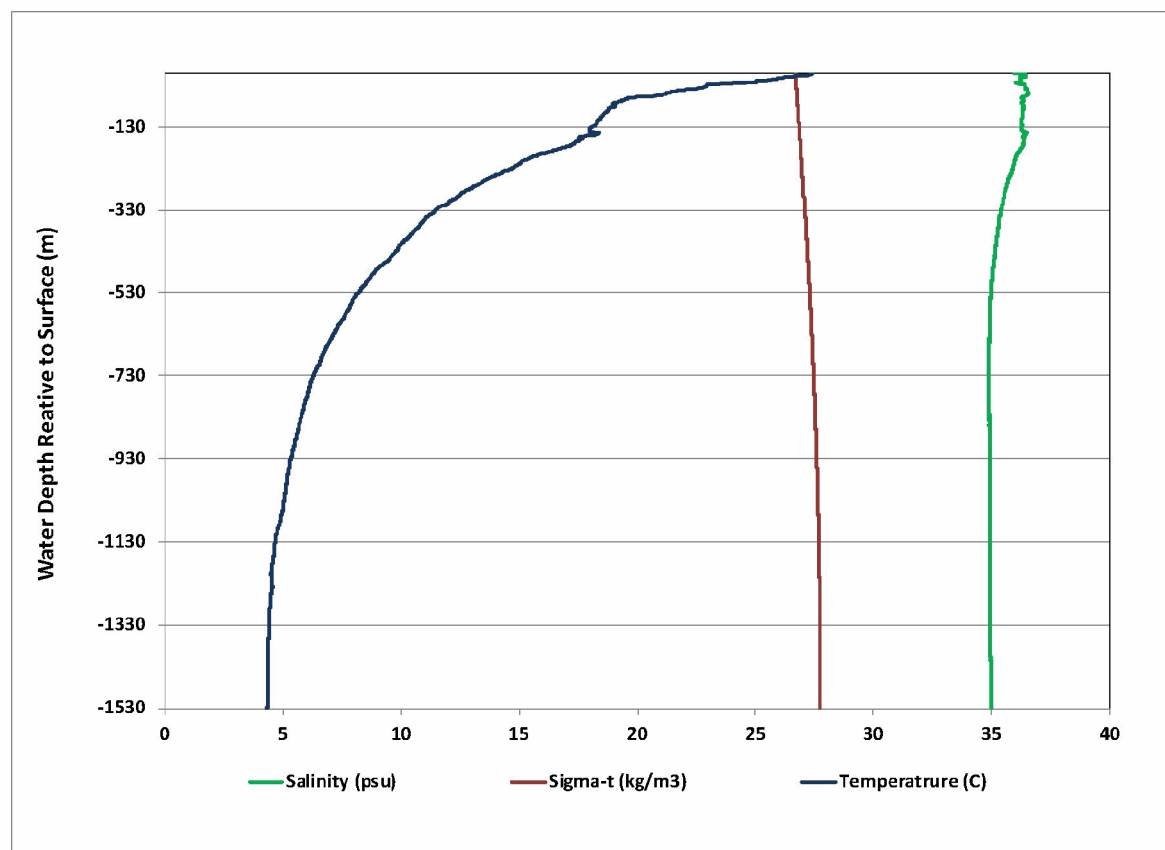


Figure 5-23. Vertical profile of water temperature, salinity and density from the R/V Brooks McCall Station 54 observation taken 30 on May, 2010.

5.7.3 Model Output

Based on the above inputs, the model was run for each day of the 84 total days of the blowout release. The flow rate data is on a daily basis, and hence the model predictions are also daily. For each day, the model provides detailed output of the plume evolution through the water column along with the plume centerline rise velocity, centerline oil and gas concentrations, and plume radius. While there were daily changes in the release specifics (other than discharge rate), the blowout simulation can be separated more broadly into three different phases of

release; (1) release from the broken end of the riser, (2) release from both the broken end of the riser and the kink, and (3) release from the cut riser. The daily discharges, highlighting the range and average flow characteristics for these phases, are shown in Table 5-8.

Figure 5-24 illustrates the model-predicted plume radius and centerline velocity as a function of height above the release for select representative days. Included on the plot are the predictions from both pre-cut and post-cut riser on a day with average flow conditions, as well as the kink flow for initial and final flow conditions. In all cases the centerline velocity decreases and the plume radius increases with increasing height. This figure shows that the predicted plume centerline velocity is typically between 0.7-0.8 m/s initially and decreases with increasing height while the initial kink plume centerline velocity is between 0.5-0.6 m/s. Conversely, the model predicts that the plume radius is initially approximately 10 m for both the kink and riser and gradually increases to approximately 90 m for the riser release and approximately 65 m for the kink at trap height. The initial 10 m plume radius is a result of the initialization process of the plume integral equations. The plume model does not explicitly solve the momentum jet (where momentum forces dominate buoyant forces) and transition to the buoyant plume, but rather initializes the solution based on the physical and numerical properties of a fully developed buoyant plume at a small distance above the plume source. The momentum length scale was calculated for the pre- and post-cut riser releases on a daily basis. This calculation was performed to determine the length scale at which the flow regime changes from a jet to a plume based on the ratio of the release momentum to buoyancy fluxes. The calculated length scale for the transition of flow regime from a jet to a buoyant plume for the riser was estimated ranging from 0.5 to 0.8 m, depending on the flow rate and release opening geometry.

Figure 5-25 illustrates the typical progression of both relative gas volume remaining in the plume and the dissolved gas concentration in the water column as a function of height above the release. The relative gas volume remaining is the instantaneous gas volume in the plume divided by the initial gas volume, all referenced to the surface pressure. In all cases the general trend in dissolution is similar, the amount of gas dissolved increases with increasing height. The trends for dissolved methane concentration are slightly different for the kink compared to the riser. The gas concentration at the plume centerline for the riser increases quickly and then continues to gradually increase with height while the plume centerline concentrations for the kink plume increase quickly initially, to a higher level than the riser, and then gradually decrease with height until the plume traps. It can also be seen that the peak kink plume water column methane concentration occurs when the relative gas volume remaining goes to zero (i.e., no gas bubbles remaining in the plume) and decreases after that. The kink plume continues to rise based on the oil buoyancy alone, from that point upward. Referring to Figure 5-24, it can also be seen that the kink plume centerline velocity levels out from this point as well, since oil either does not dissolve or dissolves but does not lose any in-plume oil mass because of the fast entrainment of ambient water into the plume) and so the oil buoyancy remains constant. The loss to plume rise velocity is due to entrainment and increasing plume density from that point upwards.

The rate of gas dissolution for the kink release is faster than that of the riser release due to the smaller bubble sizes created. The model calculates a constant initial bubble size for each day of the release, picking the smaller of the calculated size based on the energy of the release and the calculated maximum stable bubble size (function of gas and water column properties). The model calculated bubble sizes ranged from approximately 3,700-4,400 μm for the kink and approximately 8,000 μm for the riser, with 11,400 μm the calculated maximum stable methane

bubble size. The kink release has a much larger exit velocity than the riser release due to the small cross sectional area of the openings compared to the volume flow, and therefore has a relatively higher energy associated with it, generating smaller bubble sizes. The smaller gas bubbles in the kink plume dissolve faster due to the larger ratio of surface area to volume compared to the larger bubbles in the riser plume.

Table 5-9 provides a summary of the model predicted minimum, maximum, mean and median flow rates for each stage of the release. Approximately 60% of the flow is pre rise cut and the remaining 40% post cut. During the pre-riser cut period the kink flow is about 24 % of the pre riser cut flow.

Table 5-9. Summary of minimum, maximum, mean and median flows for each release phase.

Release Site	Appendix A Location ID	Min Flow (bbl/day)	Max Flow (bbl/day)	Mean Flow (bbl/day)	Median Flow (bbl/day)
End of Broken Riser (both prior to and after the onset of the kink flow)	1	41,449	62,200*	49,334	48,967
Kink	2	10,840	16,085	12,263	10,957
Post -Cut Riser	2	52,700	60,000	57,490	57,650

*max flow representative of time before Kink flow

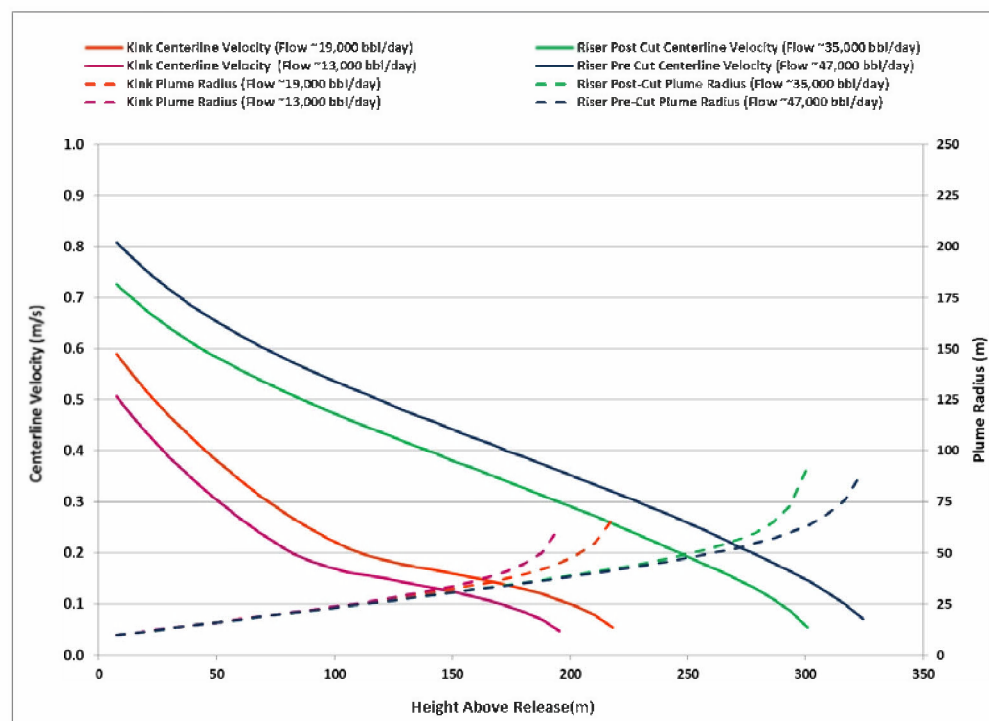


Figure 5-24. Plume radius and centerline velocities for typical conditions for pre- and post-cut of the riser releases and the kink release.

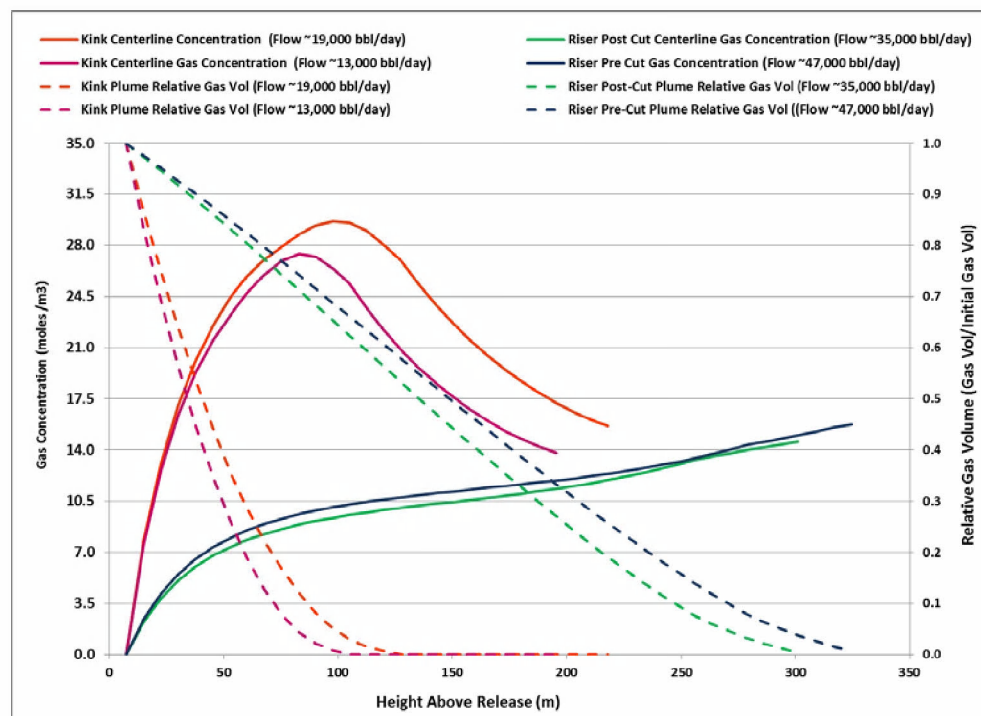


Figure 5-25. Plume centerline gas concentration and relative gas volume for typical conditions for each pre- and post- cut and kink releases.

The model predicted trap heights were compared to observations of excess CDOM in the water column. The CDOM anomaly, characterized by water samples that had greater than 1.5 times the background fluorescence levels, indicates the presence of the trapped plume. A series of example excess CDOM vertical profiles taken in the region of the well is presented in Figure 5-26. Figure 5-27 illustrates model predictions of trap height versus the excess CDOM observations for the period of the blowout. The observations in this figure represent the upper and lower depth bounds of excess CDOM taken from locations close to the wellhead and with sufficient number of samples, as well as the depth of the maximum excess CDOM measured in the profile. Details regarding the background CDOM levels, data analysis, and results are documented in the Physical & Chemical Report (Horn et al. 2015).

As can be seen in Figure 5-27, the model predicted trap depth from the riser release varied from 1,150 to 1,210 m below the surface, and the model predicted trap depth from the kink release varied from 1,275 to 1,310 m below the surface. These predictions compare well to the excess CDOM anomaly which was observed between approximately 800-1,300 m below the surface, with the peak excess CDOM anomaly observed mainly between 1,100-1,300 m below the surface. The model was able to recreate the differing trends between the two releases, as seen with predicted trap height from the kink lower than that of the riser.

Spier et al. (2013) performed an investigation of the distribution and chemical composition of hydrocarbons released from blowout using all available certified hydrocarbon data acquired from NOAA and BP. The analysis identified a deep water plume of hydrocarbons centered at 1,175 m below the surface. This analysis is consistent with the CDOM data presented here and with plume model predictions of trapping height (Figure 5-27). In addition, Spier et al. 2013 also

observed oil at other depths such as 865 m and 265m, but it is likely not fresh oil but remnants of earlier releases after loss by dissolution of the more soluble fractions.

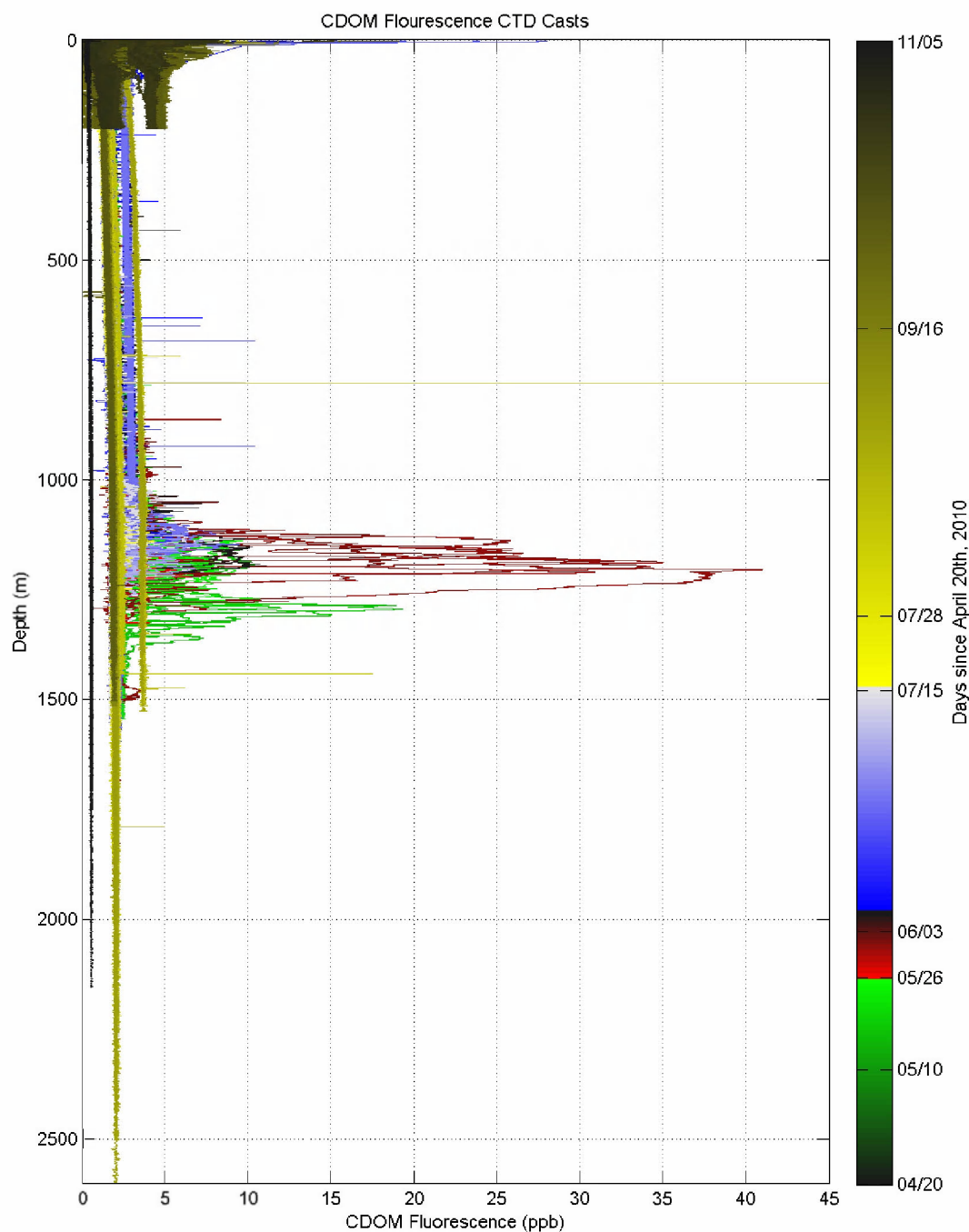


Figure 5-26. Example excess CDOM profiles. Spatial distribution of all CTD data collected in 2010 is the same as displayed in Figures 5-1 and 5-2.

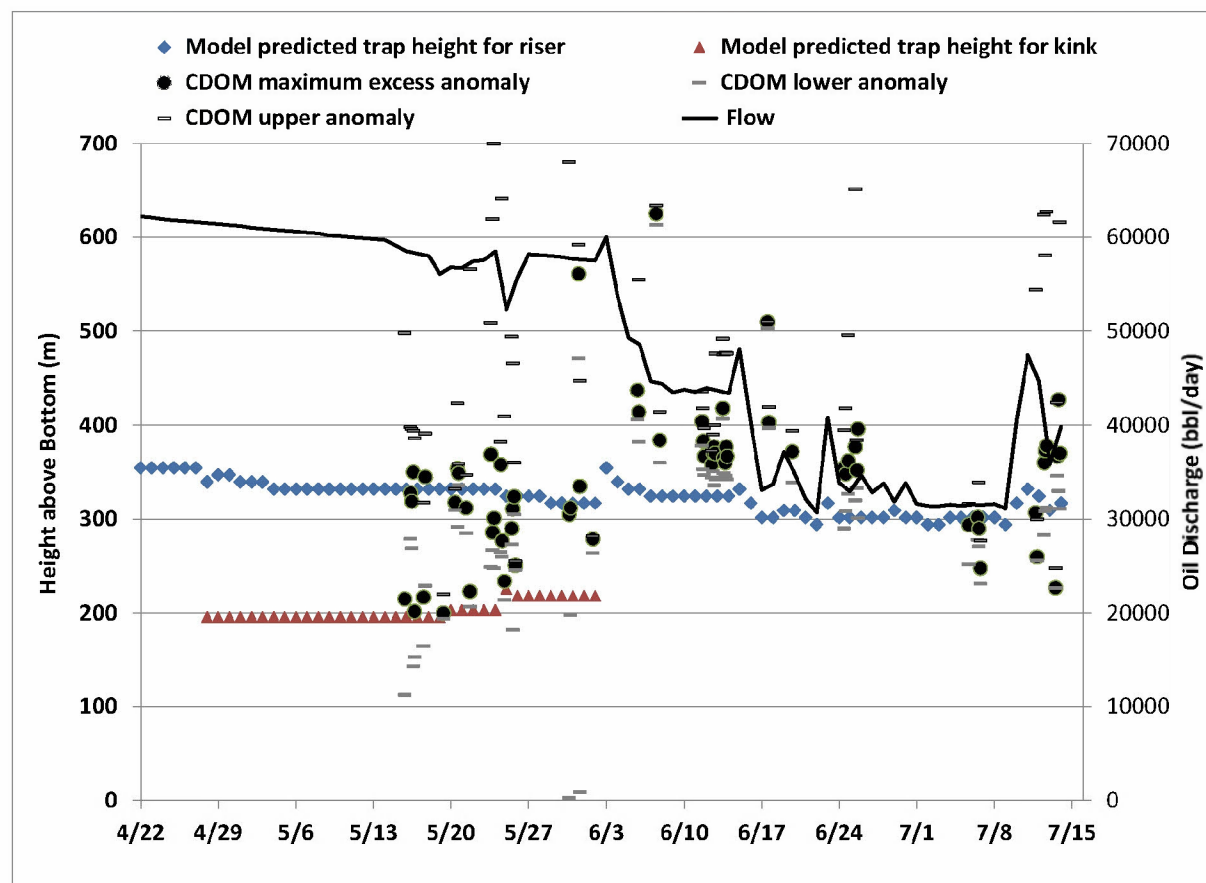


Figure 5-27. Model predicted trap height vs. observed CDOM anomaly

5.7.4 Gas Dissolution and Methane Concentrations

The blowout model formulation includes gas dissolution. In this application the gas is assumed to be primarily methane. The rate of dissolution is primarily a function of the amount of gas in the release and the initial gas bubble size associated with the release. Details on the model gas dissolution algorithm can be found in Appendix E. As the gas dissolves, it reduces the plume buoyancy and changes the dissolved methane concentration in the plume water. The model predicted plume gas volume and the methane concentration at the plume centerline for the riser and the kink are shown in Figure 5-25. Based on the model predictions, it is anticipated that dissolved methane in the plume water would be found above the release up to a vertical extent of approximately 350 m, or approximately 1,150 m below the surface. The model predicted dissolution of methane into the water column is in agreement with the findings of researchers investigating the dissolved oxygen anomaly in the Gulf of Mexico (Kessler et al. 2011). This study reported observations of high water column concentrations of methane at depths between 800-1,200 m. Reddy et al. (2012) suggested that the blowout plume methane gas had completely dissolved (99.99%) by the time it trapped at approximately 1,100 m depth level. These findings are also reflected in the blowout plume model predictions of methane gas dissolution as shown in Figure 5-25, namely that all the gas has dissolved by the time the plume reaches a height of 350 m above the bottom.

5.7.5 Hydrate formation

The *blowout plume model* formulation includes the capability to model the formation and dissolution of methane hydrates, which can form under certain conditions. A combination of pressure and temperature are necessary as well as saturation of the water column with dissolved methane. The temperature and pressure regime at the release sites was sufficient for potential hydrate formation (Anderson et al. 2012); however the methane concentration in the water column was found to be too low to support stable hydrate formation. As shown in Figure 5-25, the model predicted peak methane concentrations are approximately 30 mol/m³ or 0.030 mol/L. Figure 5-28 illustrates the necessary concentration for stable hydrate formation in the range of conditions near the release sites. This figure illustrates that at 4°C (approximately the ambient water temperature at the depth of the blowout); the necessary concentration is a minimum of 0.040 mol/L and increases to over 0.10 mol/L at 18°C. The anticipated temperatures of the water column in the region of the plume (between 1,100 to 1,500 m below the surface) is between 4-6°C, and therefore the plume concentrations are below saturation and stable hydrate formation is not predicted to have taken place. ROV observations show that while hydrates formed on the some parts of the ROV and some of the equipment, including the containment device, they were not extensively observed in the plume.

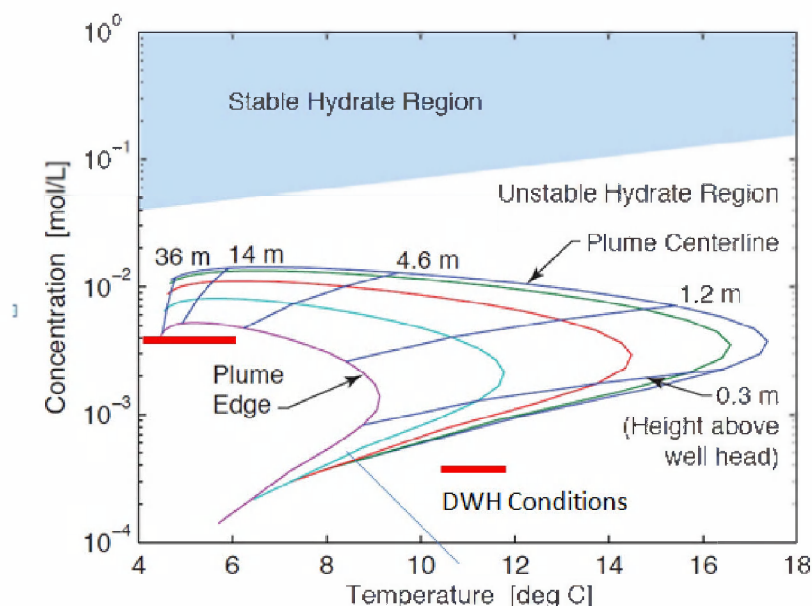


Figure 5-28. Illustration of conditions for stable hydrate formation for approximately 1,500 m of water (Anderson et al. 2012).

5.7.6 Comparison to analytical plume solutions

There are a number of analytical solutions to the buoyant plume problem available in the literature that can be used for comparison to the present application. Simple plume models are the focus here as length scales relating momentum forces in a jet and buoyancy forces in a plume clearly show that a momentum jet solution is only applicable for the first few meters (Section 5.4) and that a fully developed plume forms shortly after that distance. These solutions are simplifications of the plume model used for the analysis here, but allow for some comparisons to gage the order of magnitude of expectations for the various dimensions of the plume model predictions. The plume trap height and the total entrained volume flux at that

height are two of the more important parameters and will be the focus of the comparisons presented here.

Two slightly different formulations were evaluated for the DWH application, the first was based on the work of Morton et al. (1956), one of the seminal works on turbulent buoyant plumes in a linearly stratified environment. One result of their work was a simple non-dimensional solution giving a scaling parameter for the maximum height a plume would attain, before the density difference between the plume and the environment goes to zero and the plume ceases to rise. Following an update of the Morton formula presented by Carazzo et al. (2008) and revised by Socolofsky et al. (2011) adjusted to the Gulf of Mexico conditions the maximum height was formulated in terms of a stratification parameter, an entrainment coefficient, and a buoyancy flux. The trap height prediction equation can be predicted using this equation (Carazzo et al. 2008; Socolofsky et al. 2011):

$$H = 2.9 Fo^{1/4} S^{-3/8}$$

Where, Fo is the source release buoyancy flux (m^4/s^3) and S is the ambient seawater buoyancy flux (s^{-1})

The range of the entrainment parameter varies in the literature from roughly 0.06-0.16, where Carazzo et al. (2008)'s review of the literature suggested 0.125, following the work of Briggs (1969). This is similar to the 0.12 entrainment parameter value used in the *blowout plume model* and is approximately comparable. The stratification parameter is defined for a linearly stratified environment, so in order to use the maximum height equation for the present problem in a variably stratified water column, multiple applications of the equation needed to be made evaluating the calculated trap height based on the local value for the density gradient. The point where the predicted maximum height and the actual height above the bottom for the density gradient used are the same, which should reasonably reflect the best approximation of the trap height using the linear equation.

Figure 5-29 depicts the estimate of the point in the water column where the density stratification predicts a matching maximum height, of about 384 m in this case. The maximum plume height of 384 m is at the upper range of entrained oil observations, based on the CDOM data, and somewhat higher than the *blowout plume model* application results, which were in the range of 350 m above the release location. The simple model presented here however does not include methane gas dissolution as in the *blowout plume model*, and therefore trap height predictions from the simple model are anticipated to be higher than those from the blowout plume model. Sensitivity assessments have illustrated that the net impact of the gas dissolution for a release, with characteristics similar to the DWH spill event, is a reduction of the trap height on the order of 100 m.

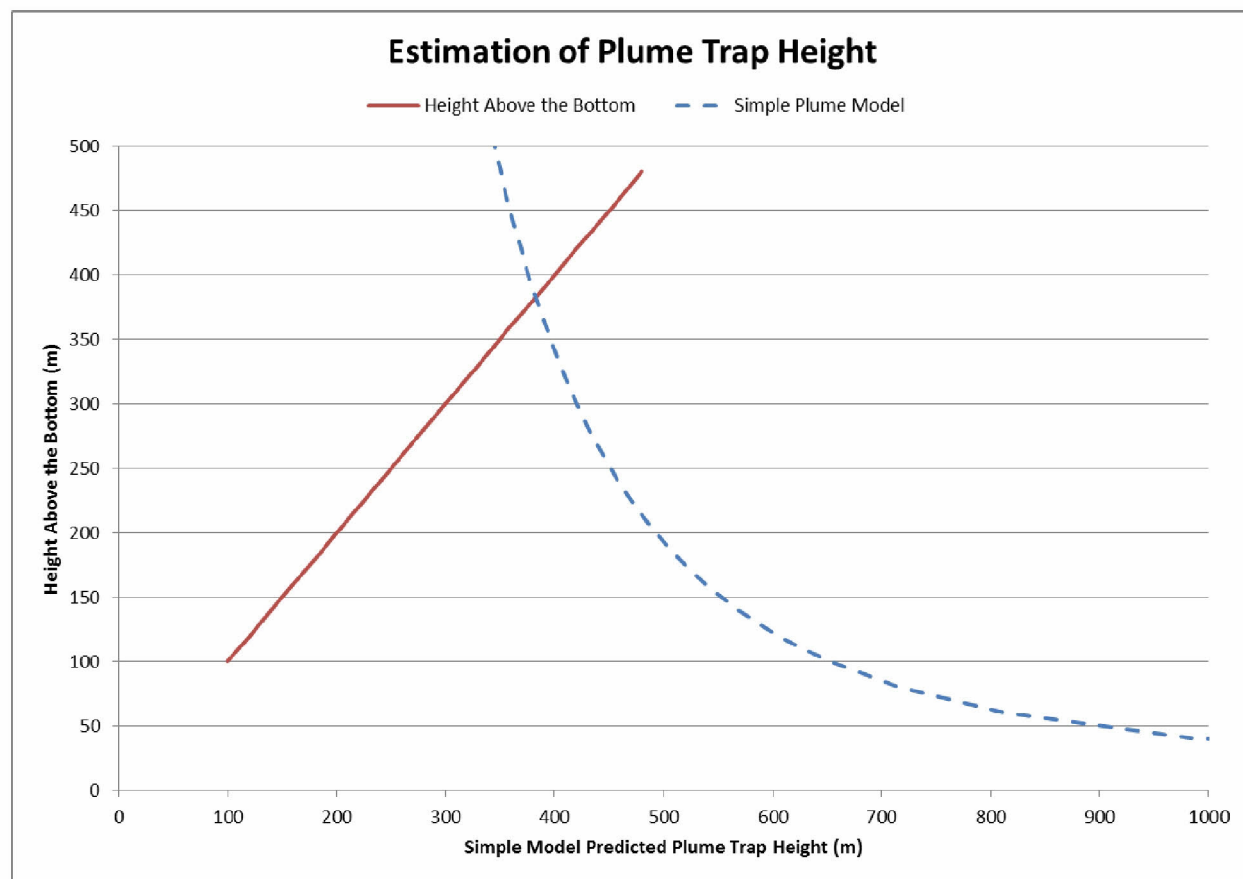


Figure 5-29. Estimation of the maximum plume height in a stratified environment as applied to the Deepwater Horizon blowout event using the Carazzo et al. (2008) and Socolofsky et al. (2011) model. The trap height predicted by using a simple plume model is dependent on the buoyancy frequency (s^{-1}), which is a nonlinear function of depth. Shown here is an example of the best estimate of the plume trap height in a non-linearly stratified water column for average pre-cut conditions.

The second model used for comparison is presented in Fischer et al. (1979). The Fischer simple plume theory model is focused on the total entrainment into the plume as it rises through the water column. Fischer et al. (1979) showed that the growth in the plume volume flux (entrainment) as the plume rises can be determined as a function of the buoyancy flux and the height above the source. A scaling coefficient used in the analysis is approximately equivalent to the entrainment coefficient of the previous plume model. Fischer suggests a value of 0.15 based on experiment. That value was used in the following analysis.

The Fischer formulation presented could be reconfigured to incorporate the ambient density stratification and solved for trap height directly, as done by Socolofsky et al. (2011), but an equivalent numerical approach was adopted here. A series of incremental heights above the plume source were evaluated and the volume flux calculated, as presented in Figure 5-30. At each height, the bulk density of the plume was recalculated based on the initial plume density and volume flux, the density of the surrounding ambient seawater, and the updated plume volume flux. The new plume bulk density is then compared to the ambient. The *blowout plume*

model predicted volume flux for the same source strength is also presented in Figure 5-30 for comparison. The simple model has no constraint on the height or entrainment, but the impact of gas dissolution and the stratified environment are evident in the more complete blowout plume response.

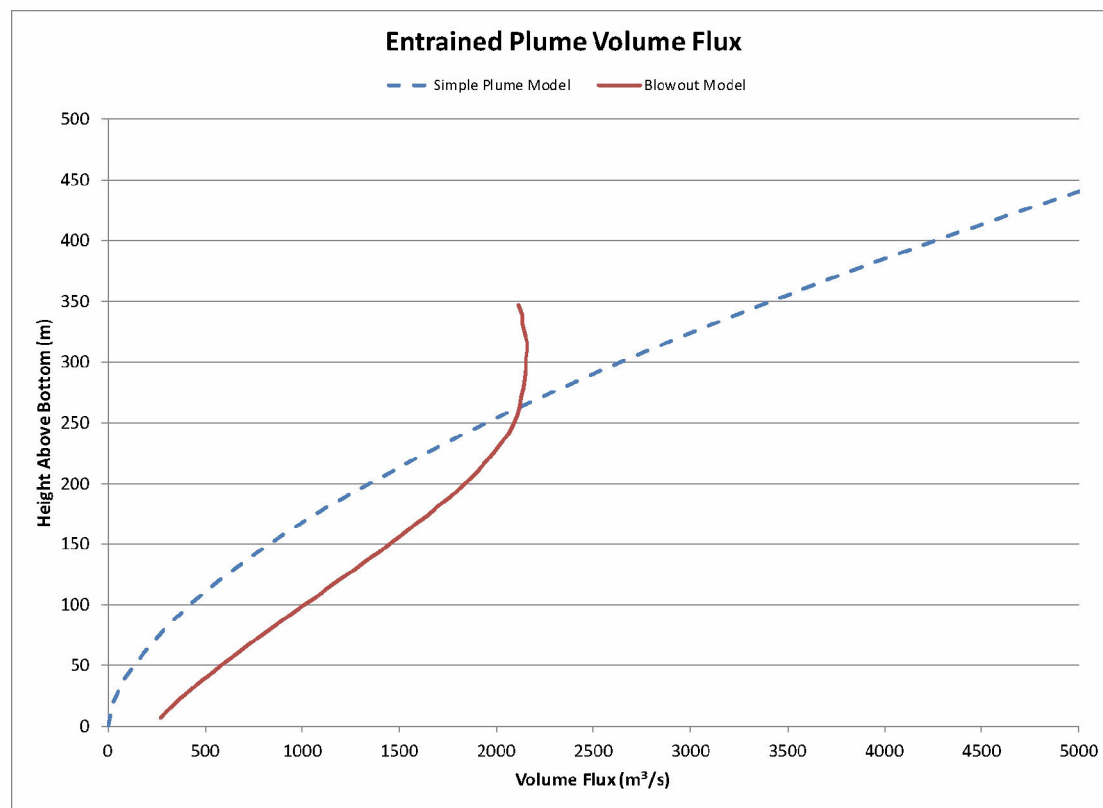


Figure 5-30. Fischer et al. (1979) plume model predicted entrained volume flux as a function of height above the source.

As the plume rises through the water column, the density of the buoyant plume increases as it entrains seawater. At the same time, due to the stratification of the water column, the ambient density experienced by the plume decreases slightly as the plume rises. At the point where the plume density becomes greater than the surrounding ambient density, the plume becomes trapped and no longer rises as shown in Figure 5-31. For the DWH application the simple plume model predicted trap height was 440 m and the total volume flux was estimated to be 5,000 m³/s. The estimated simple plume trap heights are clearly similar, which is not surprising as they are based on the same theory, but they do come at the solution from different points of view. As noted previously, the heights are also greater than predicted by the *blowout plume model* because they do not account for gas dissolution.

The simple model volume flux estimate for the trap height is considerably higher than the blowout model values (in the range of 2,100 m³/sec), partly due to the extended region over which water is entrained, but it should also be noted that the *de-facto* entrainment coefficient of 0.15 is also higher than the value used in the *blowout plume model*. Referring to Figure 5-28, at the *blowout plume model* predicted trap height of 350 m for this oil release rate, the simple

model the predicted flux is just over 3,000 m³/sec, and allowing for the larger entrainment coefficient may explain the discrepancy, but overall the values are very close.

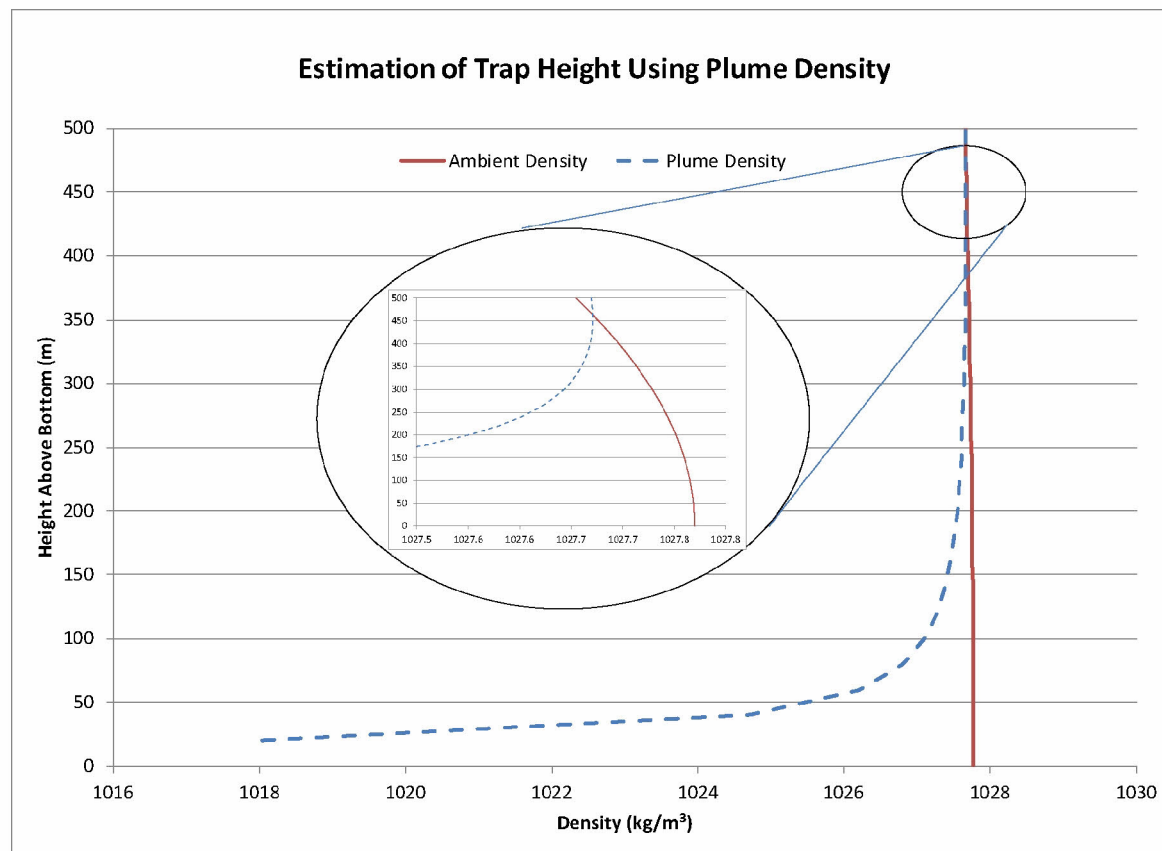


Figure 5-31. Fischer et al. (1979) plume model predicted trap height above the plume source.

5.8 Application of the oil droplet model

This section describes the application of OILMAP DEEP *oil droplet size model* to predict the oil droplet size distribution under a variety of spill release scenarios of the DWH spill. Additional details on the droplet size model are provided in Appendix G. An overview of the *Holocam* based oil droplet size data collected during the M/V Jack Fitz cruise is provided in Appendix I.

5.8.1 Volume weighted methodology for multiple release locations

Release exit velocity and oil-water interfacial tension are the most important parameters in estimating droplet size distributions; with oil-water interfacial tension playing a more significant role in the ranges associated with dispersant treatment applications. As described in Appendix A, multiple release scenarios co-exist in the DWH as oil and gas discharge at different locations during different time periods. The fraction of the flow treated was variable depending on the application method, and the net effect (reduction in oil-water interfacial tension) was dependent on the relative amount of dispersant applied to the fraction of oil treated.

To best describe the complete mass balance given the multiple release scenarios and dispersant treatment, a volume weighted method was developed for describing the overall droplet size distributions. Considering the importance of the parameters influencing droplet size distribution and associated mass released to the water column the spill event, in total, can be thought of as the sum of the different ‘types’ of releases: fraction from the kink and the fraction from the riser, which is further split into a sub-fraction effectively treated by dispersant and another sub-fraction untreated. The relative flow rates from the riser and kink were predicted by the *pipeline release model* (Section 5.4; Appendix D), and verified from the field observation from PIV and ADCP analyses summarized in the flow-rate technical working group report (McNutt et al. 2011).

An example is used to illustrate how to calculate a volume/mass weighted total oil droplet size distribution when the total flow rate is split between the kink and the riser releases. This method is also extendable to the treatment of multiple releases at different dispersant application levels (Appendix F). In this illustrative example, it is assumed that the total volume flow of oil and gas from two sources (i.e., kink and riser) and is separated into three fractions: (A) 25% of the volume flow is released from the kink, (B) 25% of the volume flow is released from the riser which has been successfully treated by chemical dispersant (DOR = 1:40), and (C) 50% of the volume flow is discharged from the riser untreated.

Several steps are taken to predict the overall oil droplet size distribution as a result of multiple release scenarios. The total release rate is assumed to be 60,000 barrels per day with 25% coming from the kink and 75% from the riser. The volume median diameters (VMD) for these fractions are estimated to be 356, 165, and 2,972 μm , for the kink release, the release from the riser treated by dispersant, and the release from the riser untreated, respectively, using the *oil droplet size distribution model* (Appendix G). Oil droplets are assumed to be lognormal distributed. Next, the full range of the lognormal droplet size distribution of each release scenario can be reconstructed based on the *droplet size distribution model*; the model is simple to use given the two known parameters (volume median diameter and geometric standard deviation) of the lognormal droplet size distribution. The droplet size distribution is expressed as either the cumulative volume droplet size distribution or the volume probability density function. Subsequently, the cumulative volume droplet size distribution and the volume probability density distribution within each size bin, is weighted by the volume fraction of each release out of the total flow rate.

Figure 5-32 illustrates the components and final total size distribution of the oil droplets released from the three fractions (riser treated, riser untreated, and kink flows) as calculated by the volume/mass-weighted method. The probability distribution curves are shown for each of the three separate sources. The droplet sizes shift to progressively smaller values, relative to the riser flow, for the kink, and dispersant treated riser flow. The decrease in droplet sizes from the kink release is due to the higher exit velocities while those from the treated riser release are due to the lower interfacial tension. The total probability density curve (blue) shows that there are two peaks in the total droplet size distribution; one between 20 and 500 μm , and the other peak, between 1,000 to 10,000 μm . The first peak is attributed to the droplets produced by the kink flow and the part of the riser flow treated with dispersants, and the second peak of larger droplets is generated by the riser release without dispersant treatment. However, note this distribution may not be measurable in the blowout plume because of the separation of oil droplet

size distribution by transport processes in the environment, including the ambient currents but certainly the higher rise velocities of the larger oil droplets.

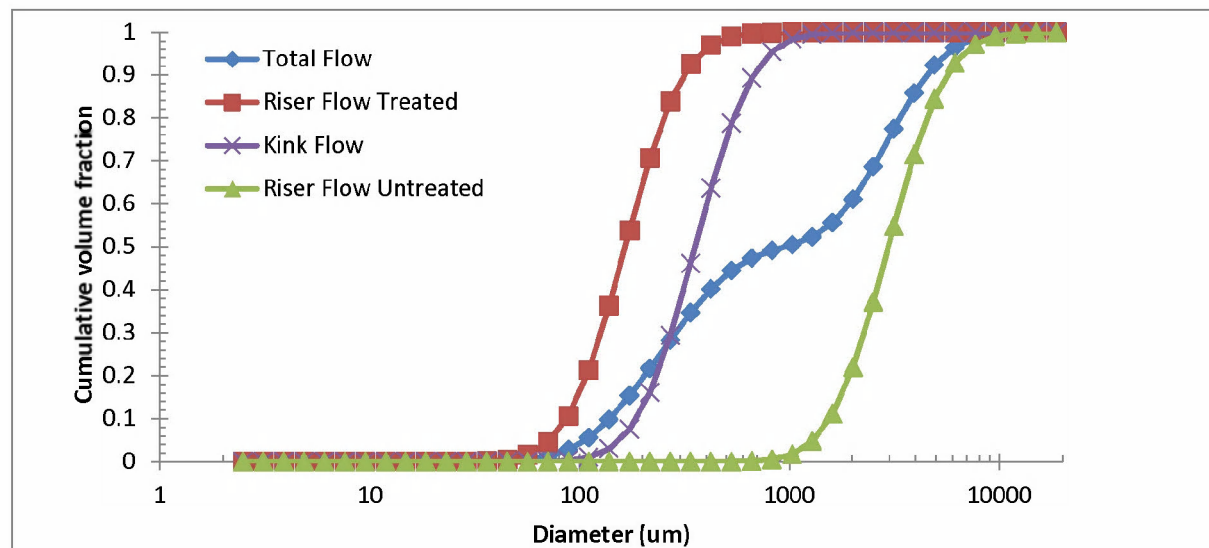


Figure 5-32. Total oil droplet size distribution as described by cumulative volume fraction (blue diamonds) and three fractions of the total flow (red square, riser flow treated with dispersant at DOR 1:90; purple cross, kink flow without treatment; and green triangle, riser flow without treatment). The total daily flow rate from the blowout release is assumed to be separated into three volume/mass separate fractions - 25% from the kink, 25% from the riser successfully treated by chemical dispersant, and 50% from the riser that has not been treated by any chemical dispersant. The total cumulative volume distribution is calculated using a volume/mass weighted method.

5.8.2 Droplet size distributions for the kink and riser releases

In this section, predictions of the released oil droplet size distribution at the kink and the riser release using the *droplet size distribution model* for the following scenarios are presented: (a) kink flow stage I, minimum kink flow rate, (b) kink flow stage II, average kink flow rate, (c) kink flow stage III, maximum kink flow rate, (d) riser flow prior to the cut and before the kink flow started, (e) riser flow from the end of the pipe without dispersant treatment, in the presence of a simultaneous kink flow at the average kink flow rate, and (f) riser flow from the LMRP after the horizontal riser pipe was cut. All the riser flow was assessed without dispersant treatment; this is a hypothetical scenario as most of the time riser flow was partially treated. The impact of dispersant treatment on the droplet size distribution is evaluated in Section 5.8.3 and Appendix F, dispersant treatment model in greater detail.

The *droplet size distribution model* assumes a lognormal droplet size distribution in both number and volume droplet size distribution. The logarithm of particle size is plotted along the x-axis, and the frequency or cumulative fraction is plotted along the y-axis. The prediction of lognormal size distribution is performed by taking the following steps: (a) compute the representative velocity (release exit velocity), (b) compute the Weber number, which represents the ratio of the release dynamic momentum to the interfacial tension forces surrounding the droplets; (c) compute the Ohnesorge number, which represents the ratio of the dispersed phase viscosity

and the square root of the product of oil density, oil-water interfacial tension, and the characteristic length scale; (d) compute the volume median diameter (VMD) through its empirical relationship with the Weber and Ohnesorge number, and a characteristic length scale (the characteristic length scale is either the maximum stable size under quiescent conditions, or the size of the discharge opening, whichever is smaller); and (e) reconstruct the lognormal oil droplet size distribution based on the volume median diameter and the geometric standard deviation.

Following the procedures described above, to predict the released oil droplet size distribution, one needs to know the release hydrodynamic conditions, including the release flow rate, the release mean velocity, the density of the released oil and the ambient seawater, and the oil and seawater interfacial tension. These variables are then used as input to the *droplet size distribution model* to calculate the volume median diameters. Table 5-10 lists the six release scenarios, the input variables, the calculated Weber and Ohnesorge numbers, and the estimated volume median diameters. The predicted volume droplet size distribution for the three kink flows and the three riser flows are reconstructed by using the lognormal droplet size model. Figure 5-33 presents the predicted droplet size distributions for the different kink and riser release scenarios (i.e., kink and riser, at various stages), with the upper panel showing the droplet size distribution and lower panel the cumulative distributions. For the kink release (Figure 5-33, left panels), the predicted volume median diameters for these different stages were 328, 356, and 361 μm , for the minimum, average, and maximum kink flow rates, respectively.

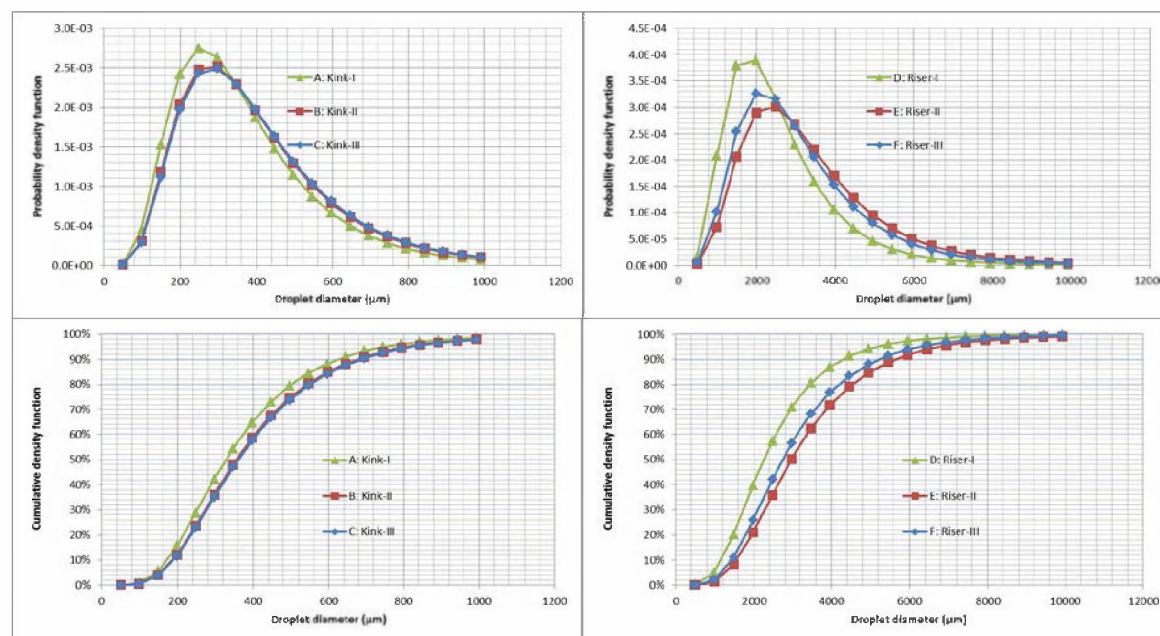


Figure 5-33. Predicted kink release (stages I, II, III) and riser release (I, II, III) flow droplet size individual and cumulative distributions.

Table 5-10. Prediction of the number and volume median diameter of droplet size distribution for typical release scenarios

Scenario	Release description	Release opening diameter (cm)	ρ_w (kg/m ³)	σ_{o-w} (N/m)	u (m/s)	d _o (m)	Weber #	Oh #	VD ₅₀ (μm)
A	Kink release, Stage I	2.0	1027	0.023	14.89	0.013650	146689	0.02	328
B	Kink release, Stage II	2.2	1027	0.023	13.79	0.013650	125713	0.02	356
C	Kink release, Stage III	2.6	1027	0.023	13.61	0.013650	122563	0.02	361
D	Riser release, end of pipe, prior to kink onset	50	1027	0.023	2.32	0.013650	3552	0.02	2257
E	Riser release, end of pipe, split with kink release at stage II	50	1027	0.023	1.78	0.013650	2088	0.02	2972
F	Riser release, LMRP, post-cut, without dispersant	25	1027	0.023	1.92	0.013650	2436	0.02	2744

For the riser flow (Figure 5-33, right panels), the predicted volume median diameters of the three scenarios were 2,257, 2,972, and 2,744 μm, respectively. The median diameters of the riser flows droplets are significantly larger (7.5 times) than those predicted from the kink release, due to the much higher release velocity from the kink holes. The distributions from the riser without dispersant treatment were similar to the diesel droplet distributions observed during the *Deep Spill* experiment (Johansen et al. 2000), as shown in Appendix G. These large droplets are expected to ascend in the immediate vicinity of the riser release due to their large size and buoyancy, and therefore not captured by observations made at distances outside the immediate release site. For example, a droplet of 2,000 μm rises at a terminal velocity of 7.0 cm/s, and travels from a trap depth of 1,100 m to the surface in a few hours. By comparison, a droplet of 500 μm, rises at 1.26 cm/s and takes 24 hours to reach the surface. At a deep sea average current flow speed of ~7 cm/s (Table 5-1), meaning that if an exclusion zone of 1 mile (1,609 m) was executed during monitoring, it would be impossible to detect droplets with sizes larger than 1000 μm.

5.8.3 Impact of dispersant application on droplet size distributions

The overall effectiveness of oil chemical dispersion is dependent on the following three components (Clayton et al. 1993; NRC 2005):

- *Operational effectiveness*, which describes the encounter probability of the dispersant application and the ability of the dispersant to become incorporated into the 'floating' (subsurface) oil,
- *Chemical effectiveness*, which is measured by the fraction of treated 'surface' (subsurface) oil that becomes stably entrained as small droplets in the water column, and

- *Hydrodynamic effectiveness*, which describes the transport of chemically dispersed oil plume and its dilution by turbulent diffusion through horizontal and vertical mixing processes.

Prior to DWH spill, dispersants have never been directly applied at the subsurface (Li et al. 2009a, b); it is therefore not surprising that no report of subsurface dispersant effectiveness is available in literature, other than some initial concept of dispersant application to blowouts (Johansen & Carlsen 2002; NRC 2005). It is possible, however, to gain some insight on the subsurface dispersant effectiveness based on the three components of Clayton et al. (1993) presented above by analyzing the jet/plume fluid dynamics and dispersant and oil effectiveness chemistry. The operational effectiveness of subsurface dispersant application for this model application was quantified in terms of the sector of the plume treated and is described in depth in Appendix F.

The chemical effectiveness in this modeling study is expressed as a percentage, representing the percentage of the applied dispersant that is effectively applied to the oil; multiplying the total amount of subsurface dispersant applied by the chemical effectiveness gives the equivalent amount of dispersant that can be assumed to work at 100% effectiveness. Laboratory dispersant effectiveness tests provide some insight into the chemical effectiveness. A list of lab tests on the effectiveness of dispersant (Corexit 9500 and similar products) on MC252 (or similar) crude oil has been compiled and reported in Appendix F (List of Lab test of MC252 like crude oil chemical dispersant effectiveness reported in laboratory tests; the mean chemical or dispersant effectiveness [DE] in Table F-1 is 52%, median DE is 55%, and the standard deviation 22%).

The hydrodynamic effectiveness is a measure of the oil, dispersant, water mixture which is calculated based on the plume hydrodynamic characteristics; the metric used to represent this consideration is referred to as the hydrodynamic fraction treated. This hydrodynamic fraction treated is an estimate of the fraction of the plume (for a given sector) that gets effectively mixed. As the buoyant plume ascends it entrains water, the dispersant is applied relatively close to the source which allows for efficient mixing prior to entraining large amounts of water. The entrainment of water is important as it is necessary to allow for the treated oil to actually disperse and break into smaller droplets without re-coalescence. This is analogous to the need for vertical mixing of a treated oil slick with the surface water. Given the high mixing energy at the blowout release, and the fast dilution of the plume, it is reasonable to assume that the *in situ* hydrodynamic dispersion effectiveness is almost 100% within the impacted sector. This expectation was confirmed in the solution of the hydrodynamic entrainment calculation as documented in Appendix F which showed that at the point of established flow the fraction treated is 83% (See Figure 5-19 above, value was obtained for 100% sector treatment and distance of 6 diameters downstream of the release opening diameter). The effectiveness that would be realized during oil spill response operations at sea, however, is determined by the combination of the effectiveness achieved from all three components.

On average, the amount of oil released into the water column from the riser (post-cut) during the JF3 cruise period was about 37,000 bbl per day, and the amount of dispersant applied at the subsurface during this period was approximately 250 bbl per day. Assuming complete mixing of the total amount of oil released and the total amount of dispersant injected subsurface on a day to day basis, the apparent dispersant-to-oil ratio for this application would have been 1:150. Given a hydrodynamic effectiveness of 100%, an operational effectiveness of 30% and an

assumed chemical dispersant effectiveness of 50% (based on the analysis made above), it is estimated that the fraction of oil treated could have been 30%, and this fraction would have been treated at an *in situ* DOR of $(250 \times 50\%)/(37,000 \times 30\%) = 1/90 = 1:90$. If the dispersant effectiveness is increased to 80%, this would lead to an *in situ* DOR of 1:56, where 100% DE would correspond to an *in situ* DOR of 1:44.

In the *droplet size distribution model*, the impact of dispersant treatment on oil droplet size distribution is addressed through the variation of oil-water interfacial tension as a function of the type of dispersant applied and the dispersant-to-oil ratio (DOR). The use of dispersant will reduce the dispersed oil droplet size, which is expressed through the calculation of the Weber number, a dimensionless parameter representing the ratio of the disruptive forces and the restorative interfacial tension forces, and Ohnesorge number, a dimensionless number representing the ratio of viscosity and interfacial tension. As more dispersants are applied, the oil-water interfacial tension tends to decrease with decreasing DOR in a highly non-linear relationship (Khelifa and So 2009; Venkataraman et al. 2013) within the operationally meaningful range of DOR (Appendix F). Subsequently, the Weber number is increased; and then the median droplet diameter of the dispersed oil droplets is decreased; the effect of the oil-water interfacial tension reduction, however, would be partially counteracted by the increasing Ohnesorge number, corresponding to an increase in the restoring force due to the dispersed phase viscous force as the oil-water interfacial tension reduces. The geometric standard deviation of the droplet distribution, on the other hand, was assumed to be constant regardless of dispersant treatment.

5.8.4 Comparison of model predictions with field observations

The oil droplet size model was applied to DWH spill for the Jack Fritz (JF) 3 cruise time period, June 14 to 20, 2010, to compare the model prediction and the observation through *in situ* deployment of a digital holographic camera (*Holocam*) mounted on a remotely operating vehicle (ROV). The *Holocam* data (Davis and Loomis 2014) are described in detail in Appendix I.

Simulations were performed assuming DORs of 1:40, 1:90, 1:100, and 1:150, with fraction treated ranging from 0 to 100%. The first two values represent DOR cases explored in the Oil Budget Calculator (Lehr et al. 2010) and the last is representative of the approximate average value assuming all oil is treated for the JF3 cruise period. Given the dispersants that were available, and assuming a complete (100%) effectiveness, these DORs imply that 26.5% (1:40), 60% (1:90), 67% (1:100), and 100% (1:150) of the oil was treated. Note these high treatment fractions ($\geq 60\%$) are much greater than the treated fraction predicted in the dispersant treatment model (Section 5.5 and Appendix F). These values are controlled by the amount of dispersant available, and under the assumption of 100% dispersant effectiveness. Figure 5-34 shows that the predicted droplet size distribution at a DOR of 1:40 -100 matches reasonably well with the data observed from the JF3 field measurements (dives #5 and 6). A DOR of 1:40 predicts a smaller fraction of oil droplets matching the majority of the size distributions from the field observations than those at a DOR of 1:90 and 1:100. A DOR of 1:150 results in most oil droplet sizes larger than those observed in the field.

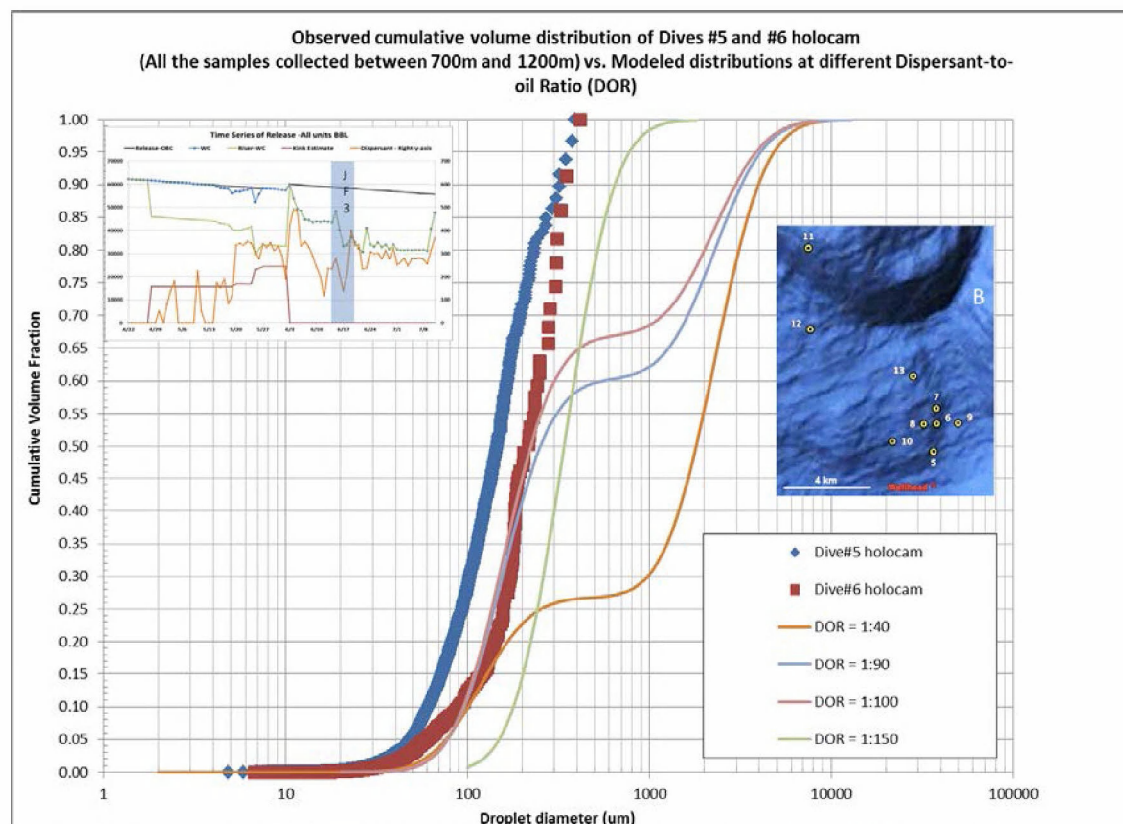


Figure 5-34. Comparison of the observed oil droplets cumulative volume size distribution and the predicted cumulative volume size distribution for four different dispersant-to-oil ratios (DORs). The observational data are from the two dives (#5 and #6) that were reported to have much oil in deep water (Davis and Loomis, 2014) of the M/V JF3 cruises during June 14-20, 2010. The model distributions are the composite distributions of the chemically and physically dispersed oil droplets, based on an average daily release rate of 38,700 bbls oil to the water column, and a dispersant application rate of 259 bbls Corexit 9500 per day. Dispersant effectiveness was assumed 100% at various simulated DORs.

5.9 Application of the fountain and intrusion model

One of the key questions in understanding the effects of the blowout is how much of the oil rose to the surface and how much remained trapped at depth and was transported in the intrusion layer. As shown in the previous sections, early stages of the oil transport and fates is energetic, where the initial plume rises rapidly through surrounding seawater as it is driven upwards by buoyancy forces. Within a few hundred meters of the release, the plume has entrained enough water to become neutrally buoyant and traps (i.e., stops rising). There is still a substantial volume flux associated with the plume however, which is forced laterally in what is called an intrusion layer (Figure 3-2). The transport and fate of the oil in the intrusion layer is the focus of this section. There are a number of analytical methods for evaluating the characteristics of the intrusion layer, one of which is a fountain and intrusion model approach. There are many similarities between the trapping of the plume, its initial overshoot and subsequent development of an intrusion layer and a traditional fluid fountain in a stratified environment, reaching a maximum height and falling back and forming an intrusion layer. In the present effort the fountain and intrusion model focuses on the prediction of the radial spreading and the

entrainment of sea water in the presence of an ambient current. These similarities will be used to further evaluate the fate of material in the trapped plume.

In addition, during the course of the spill event, a significant amount of data was collected, measuring concentrations in the water column of various chemicals associated with oil and the dispersants applied at the blowout in order to track the oil. Validating the model predictions with observations will provide confidence in using the model to estimate the total amount of oil that must have remained in the intrusion layer to create the observed concentrations. In order to accomplish this, an understanding of the bounding values of the thickness, width and spreading of the intrusion layer must be determined, over which the concentrations of oil and dispersant related chemicals can be estimated. The following sections provide a description of the *fountain and intrusion model* development and application and a comparison of the model predicted results to DWH spill observations. Additional details on the development and application of the fountain and intrusion model, with a focus on the intrusion layer are provided in Appendix H.

5.9.1 Extent and flow rate of intrusion layer

An estimate of the thickness of the intrusion layer and the flow rate in a quiescent environment can be determined using a simple fountain and intrusion model approach. Based on the work of Ansong et al. (2008), a relationship is developed between the intrusion layer spreading velocity, the initial buoyancy flux of a fountain impinging on a density interface, and the radial distance from the fountain centerline. Ansong et al. (2008) also related the height of the intrusion layer as it spreads outward and extrudes, to the spreading velocity and the total plume volume flux (initial plus entrained) of a fountain, where the return flow redirects from a vertical (downward) to a horizontal flow.

As an example, assuming a fixed release rate of 62,000 barrels per day ($0.114 \text{ m}^3/\text{s}$), which is an estimate made by McNutt et al. (2011) for flow from the well in the early stages of the blowout, the *blowout plume model* predicted a trap height of approximately 350 m above the bottom. The total entrained volume flow rate at that trap height was predicted by the *blowout plume model* to be approximately $2,200 \text{ m}^3/\text{sec}$. This volume flux was used as input to the *fountain and intrusion model* to predict the plume behavior for this case.

The average ambient currents at the 350 m trap height above the bottom are in the range of 0.07 m/s so the spreading intrusion layer is expected to be deformed and forced in the direction of the ambient flow (Figure 5-36, lower panel). Kolluru (1993) developed a horizontal spreading plume model that accounted for entrainment, using a coefficient similar to the buoyant plume entrainment value, and recommended a value of 0.083. In the present situation, once the fountain reaches its peak, it descends due to buoyant forces (negative), spreads radially in the form of a plane jet, and ultimately transitions to a plane wake in the far field when the jet momentum is small compared to the momentum of the ambient currents. The ambient flow directs the resulting intrusion layer downstream. The entrainment coefficient varies in each of these three regimes: round buoyant plume (0.083), plane jet (0.0625), and plane wake 0.094. A sensitivity analysis was performed to assess the impact of entrainment coefficient on intrusion layer volume flow and shows that the volume flow rate increases with increasing entrainment coefficient (Appendix H). The volume flow rates in all cases asymptotically approach an upper limit (within 5 to 7 km of the release location) as the flow rate per unit area in the intrusion layer matches that of the ambient flow. Based on the sensitivity analysis a value of 0.083 was selected for the entrainment coefficient since it represents the median value used in the sensitivity study and represents the best estimate if a single entrainment value is selected.

Figure 5-35 shows the model predicted intrusion layer width, height, and velocity vs distance downstream for the pre-cut (upper panel), kink (center panel), and post cut (lower panel) time periods, respectively. Average values of oil release rate are used for each time period, i.e. pre-cut 49,334 bbls/day, post-cut 38,548 bbls/day, and kink release 12,263 bbls/day. Predictions are presented starting at a distance of 500 m from the source, at the end of the fountain stage. In all cases, the predicted widths and heights increase with distance, asymptotically approaching an upper limit. The velocities show a similar trend, but decreasing with distance asymptotically approaching the ambient currents. The velocity in all cases approaches the background current speed, while the heights and widths scale with the release rate. The greater the release rates the higher the values. The asymptotic limit is typically reached within 5 to 7 km of the release.

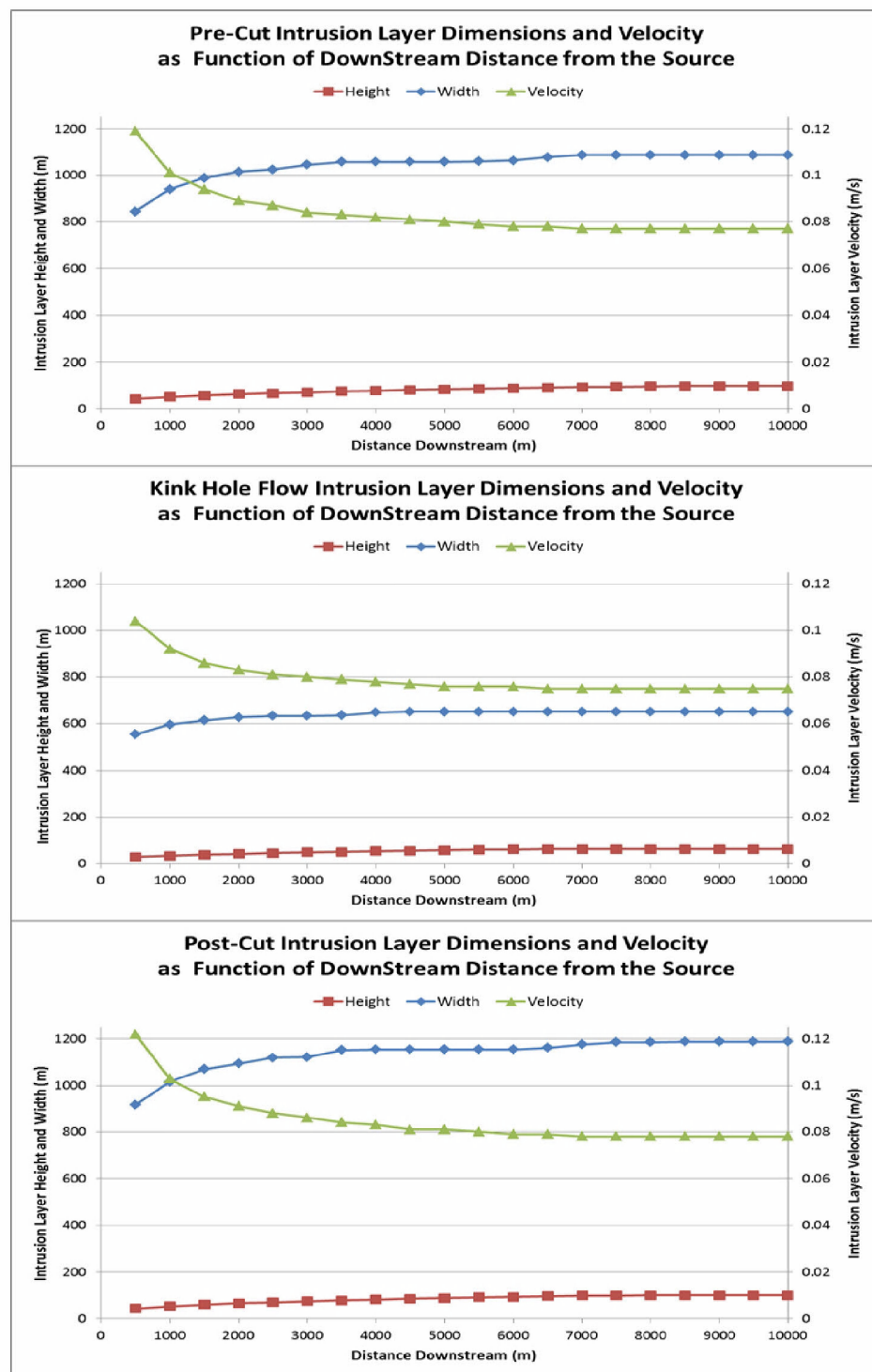


Figure 5-35. Intrusion layer model predicted spreading velocity, layer height, and width as a function of the radial distance from the plume centerline, assuming an entrainment coefficient of 0.083. The upper, middle, and lower panels are for pre-cut, kink, and post-cut conditions, respectively.

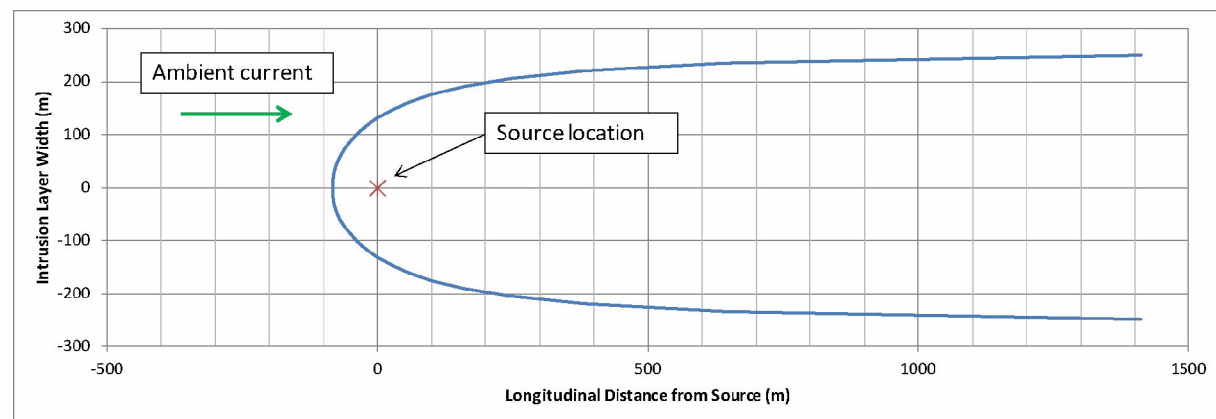
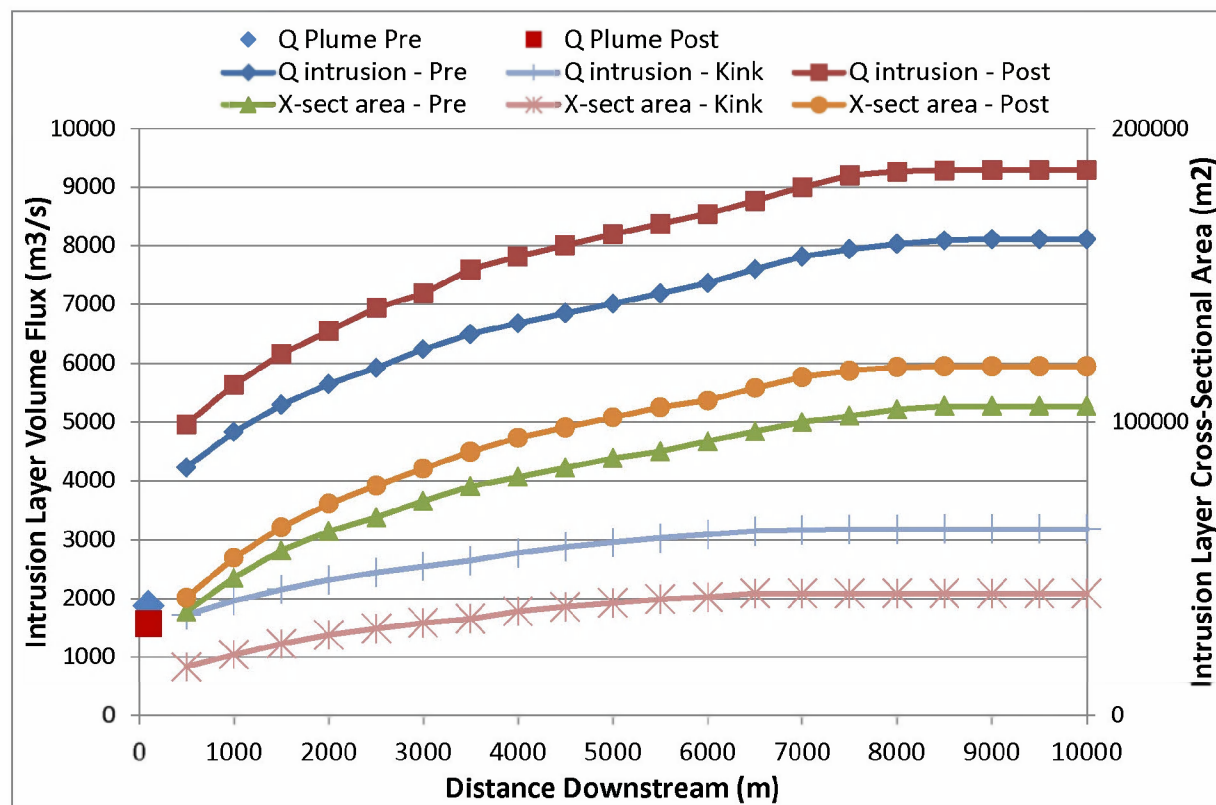


Figure 5-36. Model predicted intrusion layer volume flux and cross sectional area vs distance downstream for the pre-cut, kink, and post-cut conditions. Values for the volume flux predicted by the plume model for pre and post cut periods are also shown. Insert shows the orientation of the dividing streamline (all releases from the blowout stay within the streamline boundary).

Figure 5-36 shows the model predicted intrusion layer volume flux and cross sectional area vs distance downstream for pre-cut, kink, and post-cut conditions. The insert shows a plan view of the release reflecting the downstream transport of the intrusion layer due to the ambient currents. The dividing streamline separating ambient from blowout release flows is also shown.

Cross flow is included in the model formulation using a potential flow solution as shown in Appendix H (Equation H21-25). Both the cross sectional area and the volume flux are predicted to increase with distance downstream and asymptotically approach background conditions at a distance of approximately 5 - 7 km. The volume fluxes scale with magnitude of the release so that kink flow has the smallest values, the pre-cut riser the next largest, and the post riser cut the greatest flow.

The predicted plume volume fluxes range from 6,000 to 10,000 m³/s, depending on the oil release rate. The asymptotic flux was predicted to be 8,105 m³/s and 9,283 m³/s, respectively, for the pre-cut and post-cut period, with an entrainment coefficient of 0.083. These values compare reasonably well with the corresponding near field deep water plume volume flux values estimated by Camilli et al. (2010) (7,040 m³/s) and Kujawinski et al. (2011) (7,800 m³/s). Model results are broadly consistent with observed CDOM and BTEX profiles taken during the spill and the results of empirical model predictions of the peel height (fountain peak) and intrusion flow rates by Socolofsky et al. (2011) (see Figure 4-1). The CDOM measurements found an extended layer of excess CDOM and BTEX, above the background, which is similar in vertical dimension to the intrusion layer thickness described above. The results are also consistent with the API blowout model inter-comparison study presented in Section 4.2.4.

5.9.2 Comparison to in situ concentrations and mass balance estimate

BTEX measurements (BTEX represent about 1.9% of the parent oil, Appendix C) collected during the spill, in the immediate vicinity of the release (≤ 10 km), show the largest values are at the trapping depth, with the highest concentrations scattered in the range of 4 to 230 $\mu\text{g/l}$ (Figure 5-37). The concentrations display strong variability in both space and time, but are systematically higher in pre, compared to post, riser cut periods. The post riser cut releases were substantially reduced compared to the pre-cut releases due to oil recovery operations via the top hat containment system. Reviewing the concentrations in Figure 5-37, the average in the pre-cut time period is 103 $\mu\text{g/L}$ and 51 $\mu\text{g/L}$ in the post cut period, excluding zero and non-detect readings. This suggests that the measurement of higher concentrations is relatively rare and that there is a significant variation of the BTEX concentrations in the intrusion layer.

The present analysis shows that during the pre-riser cut time period, oil dispersion (formation of smaller droplets) and subsequent retention in the intrusion layer, was a result of mechanical processes (e.g., high exit velocities) at the kink holes and, to a more limited extent, dispersant application at the end of the riser via a wand. During the post-cut period, oil dispersion is predicted to be primarily due to dispersant treatment via the trident above the BOP. Analysis of the BTEX data unfortunately does not allow one to distinguish the differential effects of mechanical formation by the kink flow and dispersant application at the riser.

A review of the BTEX data shows a strong directional bias in pre-cut compared to post cut sampling. In addition there were two releases during the pre-cut period (kink and rise) and only one during the post cut period. The model predictions and CDOM data show two separate trapping heights pre-cut and only one post cut. Given these concerns an analysis of the percent of BTEX retained in the intrusion layer was performed only for the post cut period.

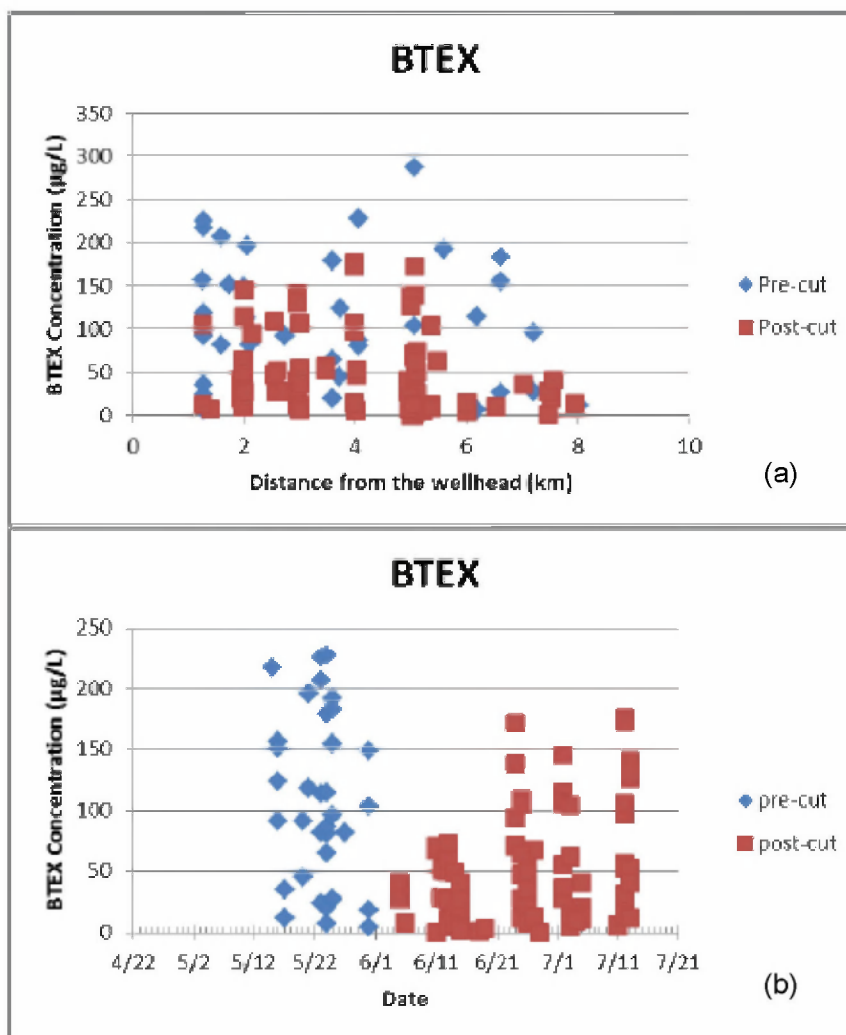


Figure 5-37. BTEX observations over the course of the blowout period: (a) BTEX concentrations as a function of distance from the wellhead, (b) BTEX concentrations as a function of date. Pre and post cut values are shown.

Model predicted volume fluxes in the intrusion layer for the post cut period vs time are provided in Figure 5-38. The time varying volume flux was multiplied by the mean concentrations to yield the BTEX flux. This value was then divided by the BTEX release rate at the source to obtain the percent of BTEX retained in the intrusion layer. Figure 5-39 show the percent retained vs time during the post cut period. The average value retained is $27\% \pm 5\%$, the latter being the 95% confidence limit.

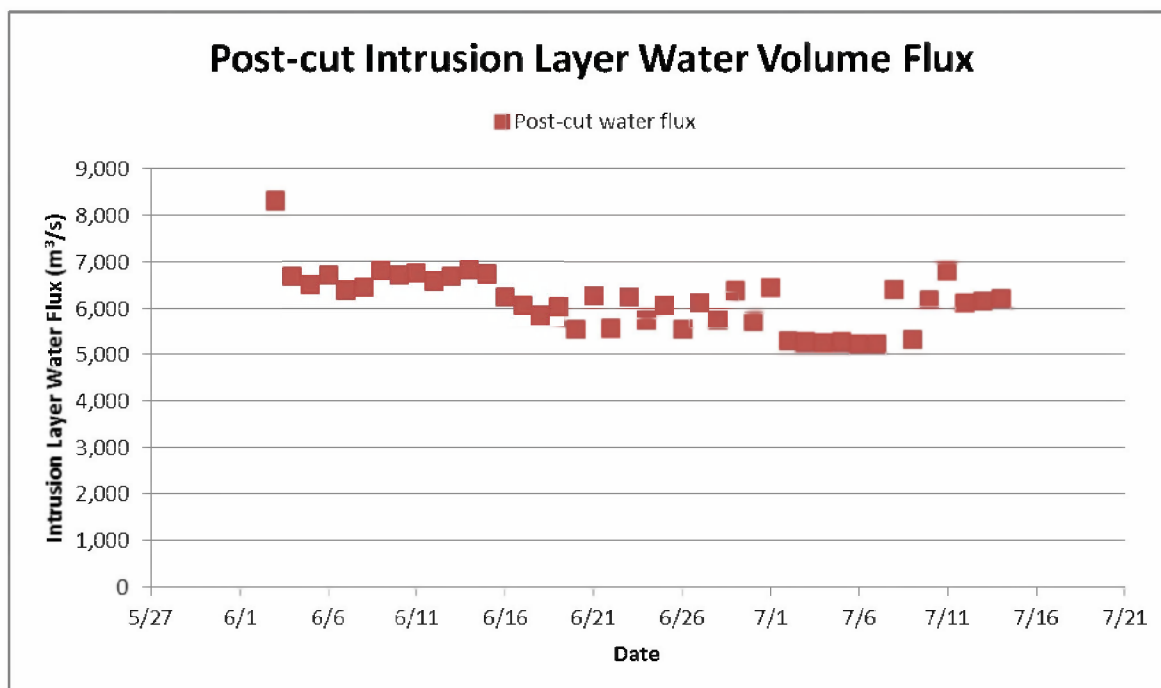


Figure 5-38. Fountain and intrusion model predicted total entrained volume flux at trap height for the post cut period.

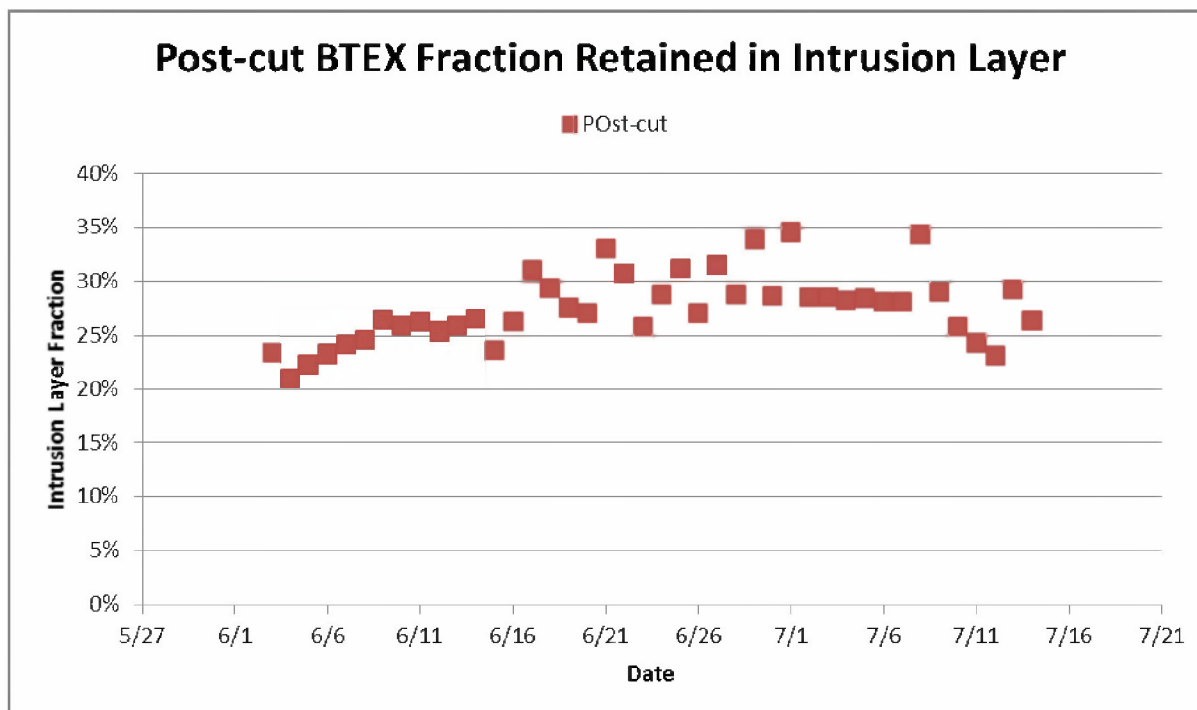


Figure 5-39. Fountain and intrusion model predicted percent retention of BTEX in the intrusion layer vs time during the post cut period.

DOSS Based Estimate

An independent assessment of the amount of mass trapped in the intrusion layer was also made using one ingredient of dispersant, the anionic surfactant DOSS (dioctyl sodium sulfosuccinate), associated with application of subsurface dispersant Corexit 9500A. Measurements were made in the May-June 2010 time period, during the blowout, primarily within 10 km of the well head, and farther afield in September 2010 (Kujawinski et al. 2011). Only the May-June data were used here. A benefit of using DOSS is that the source strength is well documented, as it is a direct function of the amount of dispersant applied. Time series of the dispersant application rate and the resulting mass flux of DOSS are presented in Figure 5-40, where the average DOSS application mass flux was reported as 4,376 kg/day (Kujawinski et al. 2011). The DOSS concentrations in the water column within 10 km of the well and at the depth of the trap height are presented in Figure 5-41, where the average value is 7.9 µg/L. The DOSS concentrations generally decrease with distance; however, the data is highly variable. The bottom panel of the figure shows that the DOSS concentrations are weakly but still significantly correlated with BTEX.

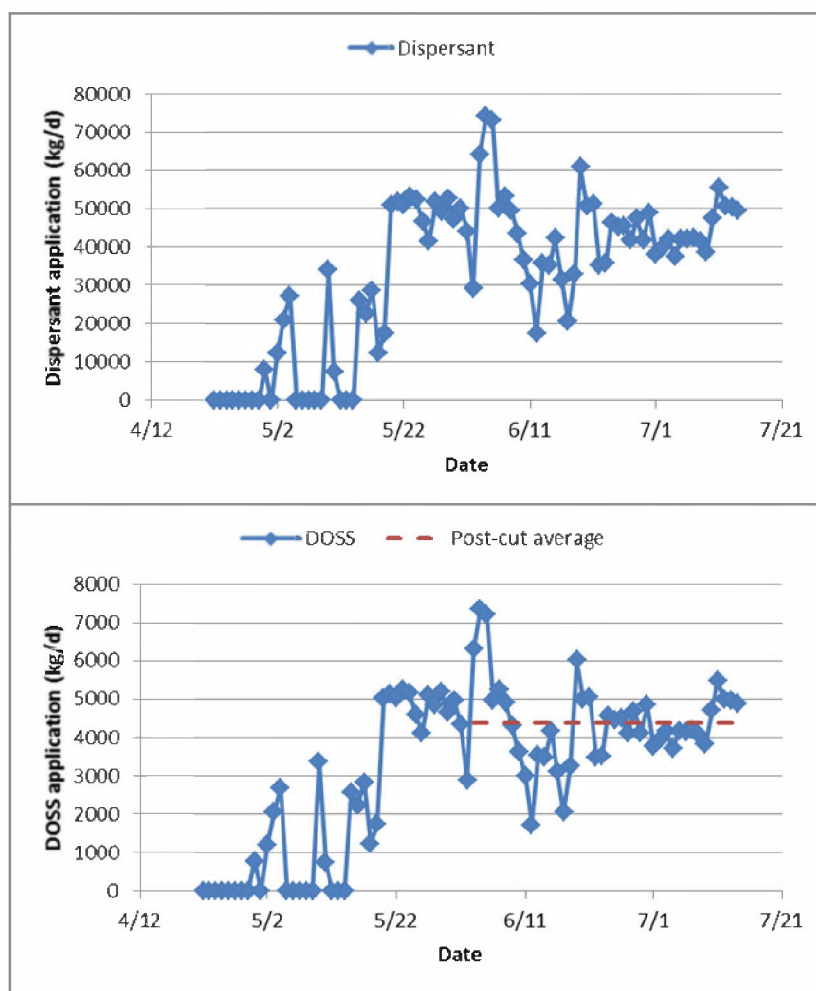


Figure 5-40. Application rate of Corexit 9500A dispersant at the well and resultant DOSS mass flux vs time from data in the Oil Budget Calculator (OBC) and Kujawinski et al. (2011).

To make an estimate of the percent of oil released that remained in the water column using the DOSS observations, a similar analysis was performed as with the BTEX assessment. The estimate was obtained by using the predicted the intrusion layer flow, and assuming that the DOSS is distributed normally over the cross section of the intrusion layer. The analysis was restricted to the post riser cut period, given the fact that DOSS data pre-cut was very limited.

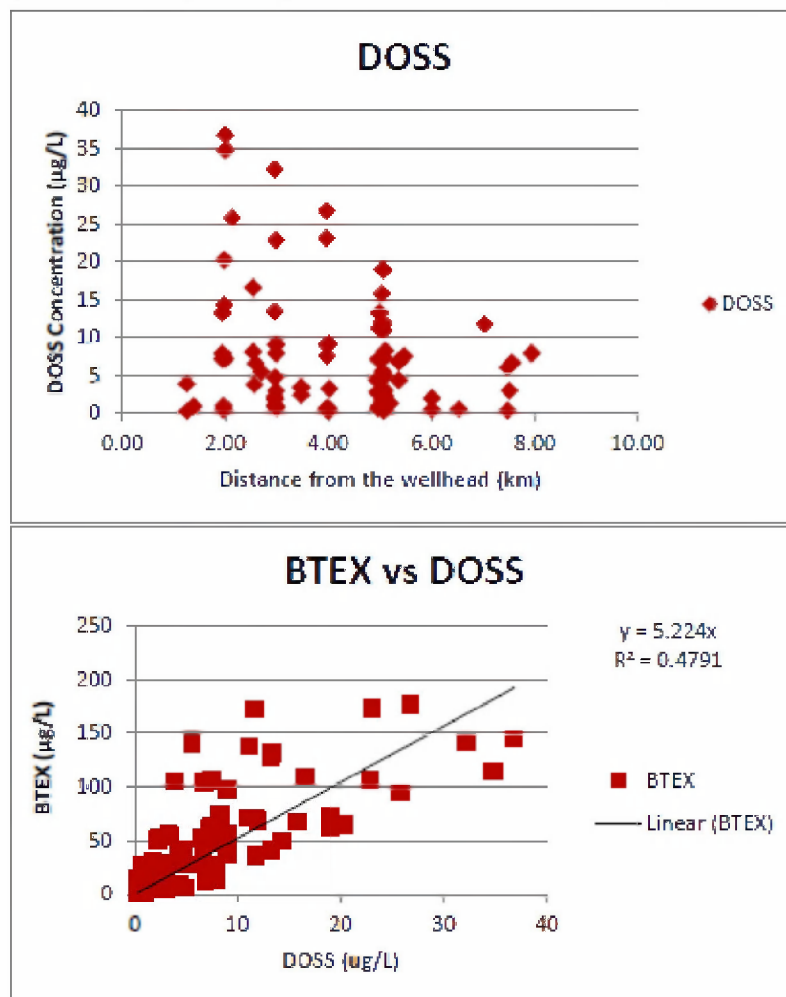


Figure 5-41. DOSS concentrations in the plume layer from NRDA cruise post-cut cruises (upper panel), and the linear correlation of the paired BTEX and DOSS concentrations (lower panel).

Assuming that the dispersant is thoroughly entrained and completely mixed with the oil in the plume, (i.e., the dispersant goes where the dispersed oil goes), the amount of DOSS mass flux that produced the observed water column concentrations, and its proportion to the initial flux, can be used to estimate the DOSS mass that was trapped in the intrusion layer. Figure 5-42 shows the percent retention vs time during the post cut period. The mean value over the entire period is $90\% \pm 23\%^2$, the latter being the 95% confidence limit value.

² Confidence interval 67%-100%

There is some discussion in the literature as to whether DOSS is conservative or not. Kujawinski et al. (2011) found that the degradation rate of DOSS was slow in the deep ocean, behaving essentially as a conservative tracer. Later studies (Campo et al. 2013) however found that there was measurable biodegradation of DOSS at room temperature. More recently, studies by scientists at the Woods Hole Oceanographic Institute (WHOI) and Haverford College (White et al. 2014) reported that DOSS was found in DWH oil samples from 6 to more than 24 months after the spill, and therefore provided evidence that DOSS is indeed persistent in the environment. If degradation is assumed to be significant during the time scale of the intrusion, the values estimated in the preceding analysis should be considered as a lower limit of potential retention levels.

This analysis shows that the DOSS released from the wellhead was retained in the intrusion layer and also serves to validate the value used to approximate the volume flux used in the BTEX analysis presented above.

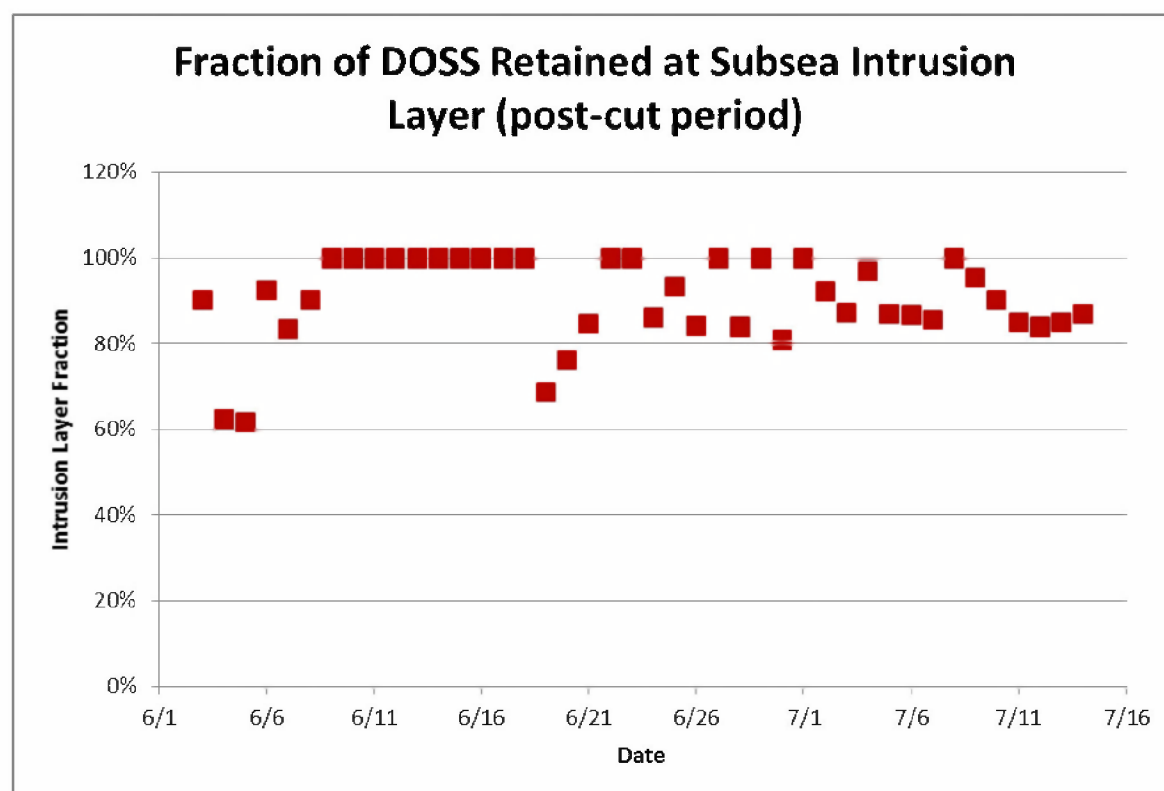


Figure 5-42. Fountain and intrusion model predicted fraction of DOSS retained in the intrusion layer each day during the post-cut period.

In summary, this analysis estimates that $27\% \pm 5\%$ of BTEX and $90\% \pm 23\%^3$ of DOSS were retained in the intrusion layer during the post cut period. The estimate for DOSS is consistent with the assumption that one of the soluble components of dispersant that was used to treat the oil was principally retained in the intrusion layer.

³ Confidence interval 67%-100%

6 Sensitivity of model predictions to dispersant treatment case studies

To understand the impact of various assumptions about the efficacy of dispersant treatment on the oil droplet size distribution a number of individual simulation cases were performed using OILMAP DEEP. In all cases, the oil release and dispersant application rates were as specified in the OBC report. The relative amounts from the kink and riser, pre the riser cut, were obtained from the pipeline release model. The time step in the analysis was daily. In each case a variation of the *dispersant treatment model* was run, as appropriate, to predict the amount of oil treated on a daily basis and the resulting dispersant to oil ratio (DOR). The *droplet size model* was then used to predict the size distributions for both treated and untreated releases, including riser and kink flow, and for both pre and post riser cut periods. Finally the volume weighting procedure was then used to estimate the total oil droplet size distribution for each case. The results are reported in the form of cumulative percent of oil as a function of droplet diameter for each individual component (i.e., the kink, the treated riser, and the untreated riser) of the release and the total release.

Simulation cases were performed to bound the problem, in terms of the oil droplet size distribution and by varying the relative success in the use of dispersants to treat the oil. The reference or base case assumes no dispersant treatment. A brief description of the treatment cases follows. Low, best estimate, and high dispersant application refer to the assumed ascending success levels in the use of the dispersant in treating oil. In all cases the amount of dispersant applied each day was used.

Low dispersant application. This case assumes that all of the dispersant was mixed with the riser flow that was not collected with a 50% dispersant efficiency.

Best estimate dispersant application. This case represents the best estimate of the application of dispersant to the riser release during the spill based on observations (e.g. remotely operated vehicle or ROV) during the spill.

The *dispersant treatment model* assumptions were:

- The fraction treated was estimated at the end of the flow establishment zone (6D).
- Dispersant effectiveness of 80%.
- The volume of oil treated for the DOR calculation was estimated for dispersant applied by single wand pre-riser cut and by trident (bident) post-riser cut with a 29.5 (8.2%) and 108 (30%) degree (percent of total degrees) sector treated, respectively.
- Determination of which application method was employed was based on a review of ROV video.

High dispersant application. This case assumes that all of the dispersant was mixed with the riser flow that was not collected with a 100% dispersant efficiency

Figure 6-1 shows the cumulative and individual oil volume droplet size distributions on two representative days, May 30, 2010 (upper panels) immediately before the riser was cut and June 10, 2010 (lower panels), shortly after it was cut. These two dates were selected to be representative of pre and post riser cut periods. The panels on the left are the cumulative distributions, while those on the right are the individual distributions. The results of all four treatment cases are provided. The vertical dashed

line in the cumulative distribution plot shows the location of 300 μm droplet diameter as a reference oil fraction. Droplet sizes below 300 μm were assumed to remain in the water column while those above were assumed to rise to the sea surface. The distributions are based on droplet volume and not number of droplets.

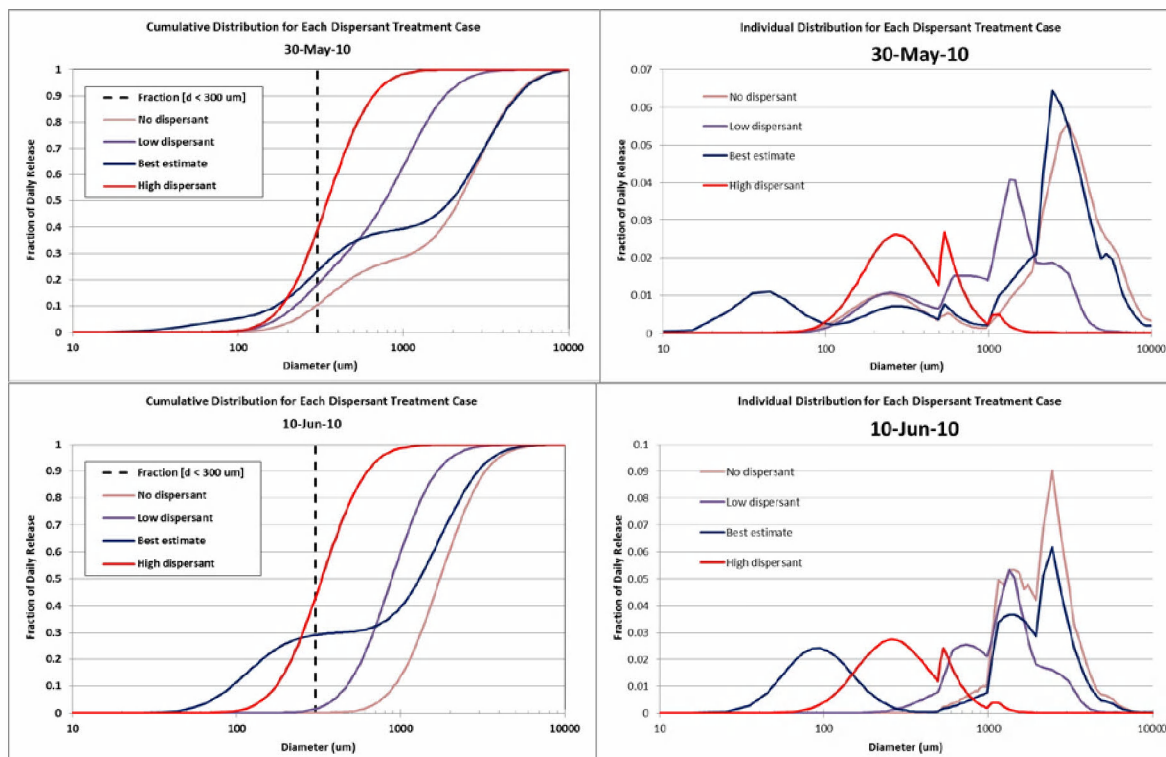


Figure 6-1. Typical oil droplet size distribution curves of the four treatment cases (no dispersant, low dispersant, best estimate, and high dispersant application) on a typical day of oil release: (A) upper-left panel, cumulative distribution in the presence of both kink flow and flow at the end of pre-cut riser; (B) upper-right panel, individual distribution in the presence of both kink flow and flow at the end of pre-cut riser; (C) lower-left panel, cumulative distribution in the presence of post-cut riser only; and (D) lower-right panel, individual distribution in the presence of post-cut riser only.

As dispersants are applied to treat the oil, the droplet size distributions move from right to left; from larger to smaller droplet sizes. This is most clearly seen by comparing the untreated and high treatment cases in both the individual and cumulative distribution plots.

The size distributions for the low and untreated cases are comparable for the pre riser cut example but substantially different post cut (see cumulative distribution plot). During the pre-cut period the cumulative distribution shows a mixture of two discrete populations; small and large droplets (as evidenced by the compound shape of the distribution curve). This characteristic disappears for both the untreated and low treatment cases, post riser cut. The difference in behavior pre and post riser cut is a result of the fact that the kink releases that existed pre riser cut were generating a population of small droplets (without treatment) because of the high kink exit velocities. After the riser cut, this source of small droplets disappeared and thus the

compound shape of the cumulative distribution was present pre-cut and absent post-cut. At the highest treatment levels, the shapes of the cumulative distribution curves for the pre and post cut cases are comparable. For the pre-cut example, small droplets are generated by both the kink flow and dispersant treatment of the riser release, while post-cut the smaller droplets are primarily a result of dispersant treatment. While the mechanisms for moving the droplet size distributions to smaller values are different, the results are comparable.

As expected the distribution for the best estimate case gives droplet sizes to the left of the untreated and low treatment cases, but to the right of the high treatment case. The shape of the cumulative distribution shows the characteristic compound shape, pre- and post-cut. The pre riser cut distribution is comprised of smaller droplets generated both by the kink flow and dispersant treatment of the riser flow, while post riser cut only dispersant treatment is responsible for generating these smaller droplets since the kink flow has been eliminated.

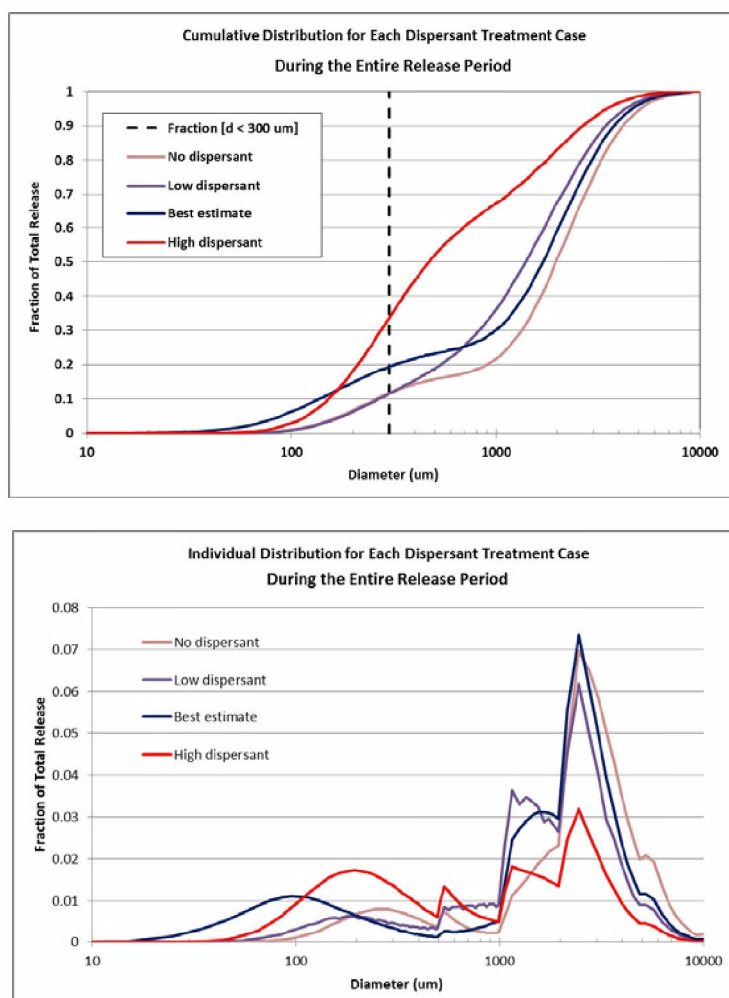


Figure 6-2. Oil droplet size distribution curves of the four treatment cases (no dispersant, low dispersant, best estimate, and high dispersant application) of the total oil release throughout the entire oil spill incident: (A) upper panel, cumulative distribution; dashed line indicate the cut-off size (300 μ m) of oil droplets trapped in the plume layer (B) lower panel, individual distributions.

To develop a sense of the mean conditions during the spill, Figure 6-2 shows plots of cumulative (upper panel) and individual (lower panel) droplet size distributions over the entire release period for each case. These were generated by weighting the daily values by the volumes released. The oil droplet size distributions are predicted to move to smaller sizes as a result of treatment; the more effective the dispersant treatment the greater the shift in value. The effect of the riser cut and elimination of the kink as a source of smaller droplets is masked here since it is included in all cases.

In evaluating the results, it is useful to understand the impact of the droplet size on the droplet rise velocities. For the DWH oil the rise velocities by droplet diameter are provided in Table 6-1. The times for the droplets to reach the surface from 1100 m, the nominal depth at the upper end of the trapping depth are provided as well. As a reference point, let us assume that droplets smaller than 300 μm , which take several days to rise to the surface, remain effectively trapped in the water column while those larger than this size rise to the surface. This is consistent with analysis of the JF-3 data which show d_{95} (388 μm in volume distribution) for dive #5 and 350 μm for dive #6. This is also consistent with the results of the effects of droplet sizes on the intrusion and subsequent transport of oil droplets from a recent lab study (Chan et al. 2014).

Table 6-1. Oil droplet rise speed and time to rise from the trapping depth, 1100 m, to the surface at the spill site vs droplet size diameter.

Lower Bin Size (μm)	Upper Bin Size (μm)	Representative Size (μm)	Rise Velocity Representative Size (cm/s)	Rise Velocity (m/day)	Hours to rise 1,100 m (hours)
0	40	20	0.0026	2.2	11982.6
40	60	50	0.0160	13.8	1914.5
60	80	70	0.0312	27.0	978.1
80	100	90	0.0516	44.5	592.7
100	200	150	0.1415	122.2	216.0
200	300	250	0.3723	321.6	82.1
300	400	350	0.6557	566.5	46.6
400	500	450	0.9719	839.7	31.4
500	600	550	1.3191	1139.7	23.2
600	700	650	1.6543	1429.3	18.5
700	1000	850	2.2939	1981.9	13.3
1000	10000	1500	4.8823	4218.3	6.3

Table 6-2. Cumulative oil droplet size distribution for no treatment and low, best estimate, and high treatment cases. The values for 300 μm are highlighted.

Droplet Size μm	Dispersant Treatment			
	None	Low	Best	High
100	0.00	0.00	0.06	0.02
200	0.03	0.03	0.15	0.17
300	0.06	0.08	0.20	0.33
400	0.08	0.13	0.22	0.44
500	0.10	0.19	0.24	0.52
1000	0.18	0.44	0.30	0.67
2000	0.51	0.74	0.58	0.83
5000	0.95	0.98	0.96	0.98
10000	1.00	1.00	1.00	1.00

Table 6-2 shows the cumulative oil droplet size distributions for the four cases. These values represent the mean over the total release period and hence are the same values shown in Figure 6-2.

For the untreated base case and using 300 μm as the reference point most of the oil (94%) rises to the surface, with about 6% remaining in the water column. Eighty two percent (82%) of the oil is predicted to have droplet sizes greater than 1 mm. As the level of dispersant treatment increases, the percent of oil at or below 300 μm increases with level of treatment: 8% for the low treatment level case, 20% for the best estimate, and 33% for the highest level of treatment. The corresponding values for the percent of oil above 1 mm are 56%, 70%, and 33%, respectively. As dispersant treatment becomes more effective the oil droplet size distribution shifts to the left to smaller sizes (Figure 6-2).

While the analysis presented uses 300 μm as a nominal reference for oil droplets that remain in the water column, in application, simulations were performed on a daily basis and the predicted complete oil droplet size distribution (as result of all sources and treatment) provided to the far field oil transport and fate model.

To validate the model predicted estimate of oil that is dispersed in the water column, it would be ideal to have independent measurements made of the amount of oil in the water column. This of course was not possible given the problem of sampling total oil concentrations at depth over very large spatial and temporal scales. Some information is however available that can provide insight into the model performance. Estimates of the percent of oil dispersed from a variety of sources and methods are provided below. This is followed by a comparison of the model predictions with estimates from these various sources.

6.1 Estimates from Oil Budget Calculator (Lehr et al. 2010)

The Federal Interagency Solutions Group, Oil Budget Calculator Science and Engineering Team performed a first order estimate of the oil mass balance for the spill as a component of

the Incident Action Plan. The Oil Budget Calculator was designed to assist the Situation Unit of the Incident Command System (ICS). Estimates were made of the amount of oil skimmed, burned, chemically dispersed, evaporated or dissolved, naturally dispersed, recovered from the well head, and other. Table 6-3 provides a summary of the results in terms of the amounts and percent of the total, with the upper and lower portion showing the total amount of oil, including and excluding the amount recovered, respectively. Estimates are provided for best, expected, and worse case assumptions. Best is defined as results that have the largest amounts of oil that are treated or removed by the response activity (burned, skimmed, and chemically dispersed). The analysis however does not provide an estimate of the amount of oil that is effectively trapped in water column. The amounts chemically dispersed come from both surface and subsurface application of dispersants. Restricting attention to the percent chemically dispersed and based on the actual amount released to the environment (lower portion of table), the best, expected, and worst case values are 36%, 19%, and 12%, respectively. The best and worst cases have oil releases that are approximately 5% larger and smaller, respectively than the mean value. It is important to note that both the total amount released and the amount in each mass category both vary with best, expected, and worst cases.

It would be helpful to have some approximate sense of the amount of oil that was chemically dispersed from the subsurface application. In the budget calculator the DORs for the surface application were assumed to be 1:20, 1:10, and 1:5 for best, expected, and worse cases and with corresponding values for the subsurface application of 1:90, 1:40, and 1:20. The assumed subsurface DORs were therefore typically four times the surface values. During the spill there was a total of 43,894 barrels of dispersant applied: 25,531 barrels at the surface (58.1 % of the total) and 18,363 barrels (41.9%) subsurface, hence 1.38 times as much dispersant was applied at the surface than subsurface. The total amount of chemically dispersed oil can therefore be approximately pro-rated between surface and subsurface considering the relative DORs and dispersants applied. The fraction dispersed by subsurface application is approximately four times that for the surface and adjusting for relative amount of dispersants applied (1.38) the ratio of oil dispersed from the subsurface to surface is 2.88. The chemically dispersed category is hence approximate $\frac{1}{4}$ surface and $\frac{3}{4}$ subsurface ($1/(1+2.88)=0.257$ and $2.88/(1+2.88)=0.742$).

Based on this analysis, the best estimate for the amount of oil chemically dispersed subsurface oil is $\frac{3}{4}$ of the values reported in the Oil Budget calculator or 27%, 14.2%, and 9% for the best, expected, and worst cases, respectively.

Estimates for the amount of oil that is naturally dispersed are provided in the Budget Calculator as well (Table 6-3). The values are typically 15% of the spill. This includes estimates for both natural dispersion at the sea surface as well as dispersion attributed to the generation of fine droplets as a result of strong turbulent mixing at the release locations (at the kink). Assuming that natural dispersion is limited to about 3 to 4% due to breaking wave limitations the amount of naturally dispersed oil attributed to jet mixing is 11 to 12%. Combining the percent chemically dispersed subsurface with the amount dispersed by the jet release the total amount subsurface is estimated to be approximately 38%, 25%, and 20%, for the best, expected, and worst cases, respectively. It should be noted that this analysis was based on rapid and simple estimates and did not benefit from any observations made during the spill.

Table 6-3. OBC estimates of the total volume and percent of total oil released from the DWH spill for the best, expected, and worst case assumptions. The upper and lower portions of the table include/exclude, respectively the amount of oil recovered at the source.

Total Released Including Amount Recovered at Source				Percentage of total released		
	Best	Expected	Worst	Best	Expected	Worst
	1000s of barrels	1000s of barrels	1000s of barrels			
Skimmed	190	160	130	4%	3%	3%
Burned	260	260	260	5%	5%	5%
Chemically Dispersed	1400	770	500	29%	16%	10%
Evaporated or Dissolved	930	1200	1300	20%	24%	25%
Naturally Dispersed	630	630	630	13%	13%	12%
Direct recover from wellhead	820	820	820	17%	17%	16%
Other	520	1100	1500	11%	22%	29%
Total	4750	4940	5140	100%	100%	100%
Total Released Adjusted by Amount Removed at Source						
Skimmed	190	160	130	5%	4%	3%
Burned	260	260	260	7%	6%	6%
Chemically Dispersed	1400	770	500	36%	19%	12%
Evaporated or Dissolved	930	1200	1300	24%	29%	30%
Naturally Dispersed	630	630	630	16%	15%	15%
Other	520	1100	1500	13%	27%	35%
Sedimented						
Total	3930	4120	4320	100%	100%	100%

6.2 Chemistry Based Estimates

Additional analysis of the treated fraction of oil can be made from the reported chemistry data from field sampling and analysis (Camilli et al. 2010; Hazen et al. 2010; Camilli et al. 2011; Reddy et al. 2012; Ryerson et al. 2012; Spier et al. 2013).

Ryerson et al. (2012) used chemical analysis of hydrocarbon data to quantify DWH hydrocarbon flow rate and environmental distribution (Figure 6 -3); and reported that approximately 10.1 ± 2.0 million kg of total oil and gas were released into the subsurface on June 10, 2010, which is comparable with the official federal estimate of the average flow rate (10.2 ± 1.0 million kg /d) using physical and optical data (McNutt et al. 2011). Among the total released mass, approximately 27% was either flared or recovered; in addition to the fractions burned and recovered, about 5% insoluble and volatile fraction evaporated (after 2 days), 10% insoluble and non-volatile fraction was retained in surface oil slick (after 2 days of evaporation), and about 36% of the leaking mass, primarily as soluble mixture, was detected in subsurface plumes.

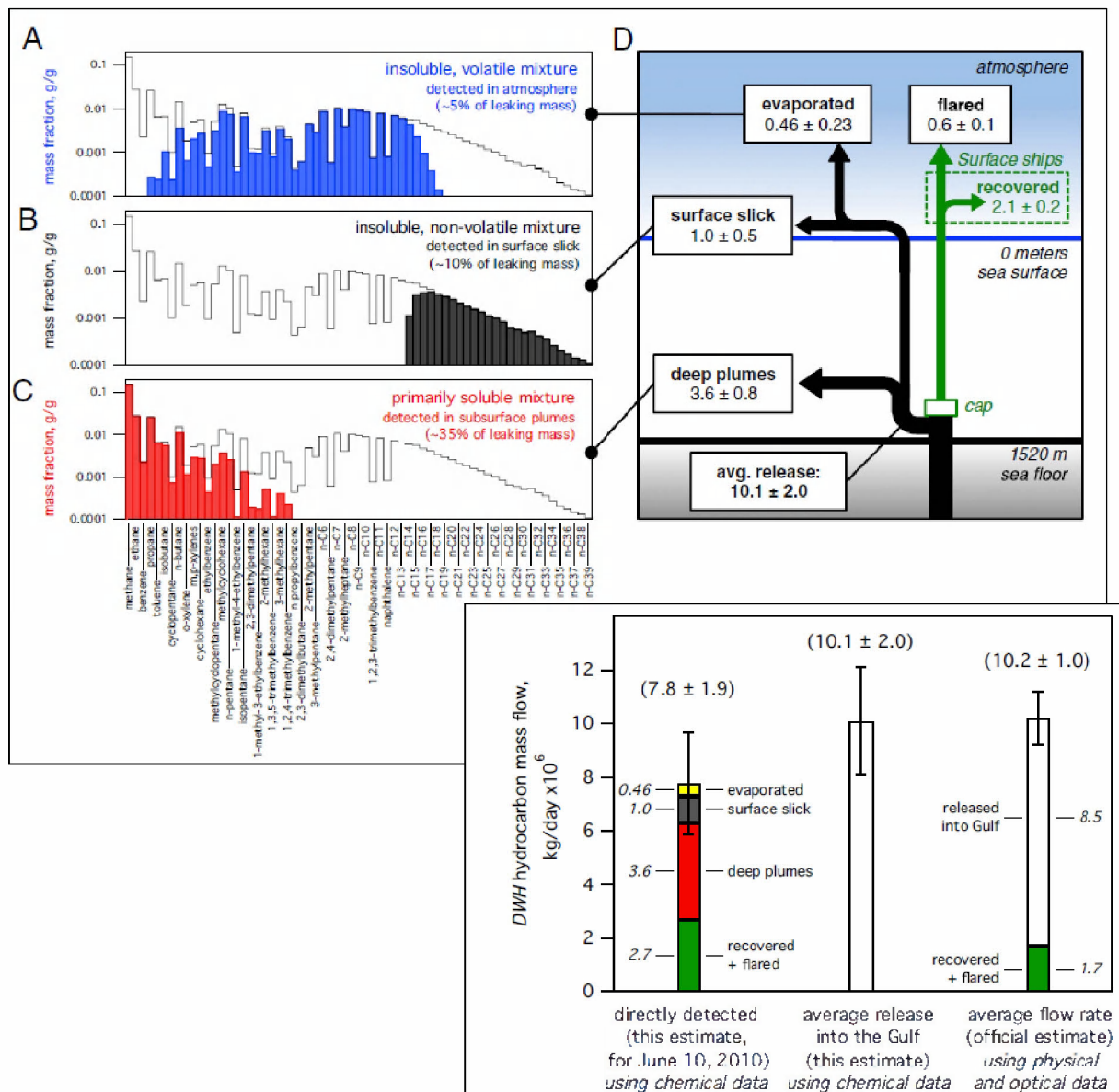


Figure 6-3. DWH hydrocarbon mass flow and distribution in different environmental compartments as estimated by Ryerson et al. (2012) according to chemical data. Upper panel, Evaporated hydrocarbon composition after 2 d (A; blue bars), surface oil slick composition after 2 d (B; black bars), and dissolved hydrocarbon composition (C; red bars). The leaking hydrocarbon composition from CH₄ through n-C39 (black line) is shown in each panel for comparison. (D) Schematic (not to scale) of hydrocarbon mass flows in the marine environment; values are calculated for June 10, 2010, in millions of kilograms per day. Lower right panel, Left-hand bar shows DWH hydrocarbon mass flow, in millions of kilograms for June 10, 2010, along different environmental transport pathways calculated using the chemical composition data. The center bar shows the calculated release into the Gulf averaged over the spill duration, and the right hand bar shows the official estimate of total hydrocarbon mass flow averaged over the spill duration.

Table 6-4 (citation from Table S01 of Online Supporting Information of Ryerson et al. 2012) indicates that among the mass of 3.6 million kg of total hydrocarbon released daily into the deep plumes (Figure 6-3, upper panel, D), Ryerson et al. (2012) estimated that the total insoluble hydrocarbon mass flow rate into deep plume is 1.09 million kg/d and the total soluble hydrocarbon mass flow rate into deep plume is 2.50 million kg/d. Given these release rates, the best estimate of the fraction of hydrocarbon mass flow into the deep plume would be equal to $3.594 \text{ E}+6 / 10.07 \text{ E}+6 = 35.7\%$. The low estimate of the deep plume retained fraction = $((3.594 - 0.3562) * \text{E}+6) / ((10.07+1.313)*\text{E}+6) = 28.4\%$. And the high estimate of the deep plume retained fraction = $((3.594 + 0.3562)*\text{E}+6) / ((10.07-1.313)*\text{E}+6) = 45.1\%$. Note that these estimates are based on both oil and gas phase releases of petroleum hydrocarbons, and therefore it is not surprising to predict values higher than the preceding estimates based solely on oil mass.

Table 6-4. Ryerson et al. (2012) Estimates of the total release rate into the environment and into the deep plume

Estimated Release Rate	Low estimate (kg/day)	High estimate (kg/day)	Average (kg/day)	Plus minus (kg/day)
Total environmental release rate	8.753 E+06	1.138 E+07	1.007 E+07	1.313 E+06
Total soluble hydrocarbon mass flow rate into deep plume	2.177 E+06	2.830 E+06	2.503 E+06	3.265 E+05
Total insoluble hydrocarbon mass flow rate into deep plume	9.480 E +05	1.232 E+06	1.090 E+06	1.422 E+05
Total deep plume mass			3.594 E+06	3.562 E+05

Table 6-5 summarizes estimates of the percent of oil retained in the water from various sources. The individual estimates provided are from the model predictions summarized in Sections 5.9.2, 6.1, and 6.2. The model predicted values are 8%, 20%, and 33% for low, best estimate, and high efficiency treatment cases (6% for the untreated case). These values are consistent with estimates made based on the application of the plume and intrusion models using BTEX ($27 \pm 5\%$). The results are also consistent with the OBC, if estimates of the chemically and mechanically dispersed subsurface oil are used (20, 25, and 38%, worst, expected and best, respectively). The prediction is however below estimates when based on petroleum hydrocarbon (both oil and gas) chemistry data (low 28%, average 36%, high 45%). The average of all expected or best estimate values is 25.5%, in reasonable agreement with the model predicted best estimate of 22%.

Table 6-5. Estimates of the percent oil retained in the water column from various sources

	Source	Percent Oil Dispersed (%)
	OILMAP DEEP Predictions	No treatment -6, low -8, best estimate-20, high treatment -33
	Data Based Estimates	
1	Fountain and intrusion model with entrainment and BTEX data	27 ± 5 post cut
2	Oil Budget Calculator (Section 6.1.1) (mechanically and chemically dispersed subsurface)	low - 20, expected-25, and high-38
3	Oil Budget Calculator (only chemically dispersed subsurface)	low -9, expected -14, and high -27
4	Hydrocarbon chemistry (Section 6.1.2)	Low – 28, average – 36, and high - 45
	Range of Estimates	9 to 45
	Average of Estimates	25.5

7 Linkage of OILMAP DEEP predictions to SIMAP

OILMAP DEEP predictions serve as input to SIMAP to specify the oil and gas release and oil droplet size distributions. The *blowout plume model* provides the following variables, separated by major categories that maybe used as inputs to SIMAP, the far field fate and transport model.

Release geometry: trapping depth (distance above the sea bed representing the lower bound to plume trapping) if trapping occurs, the peak height of the fountain above the seabed, and the thickness, velocity, and flow rate in the intrusion layer as a function of distance from the source. *Oil and gas releases:* dissolved oil and gas concentrations in the plume (if estimated) and the volume weighted oil droplet size distribution at the trapping depth. The model predicted droplet size distributions from the blowout model, divided into discrete bins covering the full range of sizes. The oil droplet size distributions were adjusted to group large oil droplet sizes that very quickly rise to the surface (in times less than the time step in SIMAP) in order to reduce the number of size classes that needed to be tracked.

The assumption made in the linkage between the two models is that the impacts of the blowout oil and gas in terms of fluid or buoyancy are small and do not fundamentally alter the circulation or mixing processes in the receiving water. To account for the interaction between the intrusion layer and ambient flow, a potential flow model was used to predict the shape of the areas of the release. The release takes on a characteristic “U” shape where the lowest part of the U is upstream and represents the location where the intrusion flow and ambient currents are in opposite directions whereas the open part of the “U” is in the same direction as the ambient

currents (Figure 5-35). The orientation of the U changes with the current direction and the size scales with the current speed and oil release rate. This is only necessary if the area of interest is limited to the immediate vicinity of the spill site (≤ 1 km) and ambient currents are strong.

In the present application predictions from the *blowout plume model* (trapping height) and the *oil droplet size model* (volume-weighted oil droplet size distribution), are provided as input to SIMAP. This is done for each separate release (riser and kink). All the oil was assumed to be released at the trapping depth with no dissolution or biodegradation of oil in the blowout model. Far-field model simulations show that the predicted concentrations fields are insensitive to whether the oil is released at a discrete level or distributed over the intrusion layer thickness. The model is similarly insensitive to small variations in the horizontal location since the blowout sizes at the trapping height are small compared to the concentration grid size of the far field model (100s of meters compared to ~ 1 kilometer). The blowout and droplet size simulations were performed on a daily time step.

This time step was used to match the temporal resolution of the input data of oil release and subsurface dispersant applied. The SIMAP input file contains a list of the location (latitude, longitude, depth) and time of mass released varying droplet sizes. The time step of the SIMAP modeling is nominally a half-hour, and as such the daily release, which was assumed at a constant rate throughout the day, was used to determine the appropriate mass released on a half hour basis in each droplet size used in the SIMAP modeling. Details of the process for using the blowout plume modeling results to generate SIMAP input files are in Appendix J.

8 Summary and conclusions

The updated version of OILMAP DEEP, with new features and components as outlined in the report, has been applied to the DWH spill to hindcast the release of oil and gas during the blowout into the water column. Comparisons between model predictions and observations have been made when data is available. The major conclusions of the study are as follows:

- The DWH release is significantly more complicated than what most blowout simulations have addressed in that the release occurred from two separate locations (kink and riser) pre the riser cut and one location (riser) post riser cut. The relative flow rates between the kink and riser varied with time as the number of holes and size of the openings at the kink increased with time and the oil flow rate varied. The *pipeline release model* reasonably captured the relative flow rates between the two sources, pre riser cut, based on observations of the releases using Particle Image Velocimetry (PIV) and Acoustic Doppler Current Profiler (ADCP) methods.
- The *blowout plume model* was used to predict the trapping height for both riser and kink and the riser, post riser cut. As a result of the multiple sources and the varying flow rates the model predicted three trapping depths; riser and kink, pre riser cut, and post riser cut, each varying with time as the oil and gas release rate varied. The multiple trapping depths predicted by the model are consistent with extensive CDOM, BTEX, and DOSS measurements of oil and dispersant concentrations in the water column.
- The *blowout plume model* also clearly showed that the gas that was released during the blowout was entirely dissolved by the trap depth. Accounting for gas dissolution from the plume is important for accurate predictions of trapping depth. If dissolution is not considered the model overestimates the height of trapping. The model predictions are consistent with measurements of gas in the plume and at trapping depths.

- The *blowout plume model* also predicted that gas concentrations in the water column did not reach saturation levels and hence hydrates were not predicted to form. This is consistent with ROV observations of the plumes from both the kink and riser and the plume trapping depth which showed no evidence of being limited by loss of buoyancy due to hydrate formation.
- The *dispersant treatment model* (using momentum length scale estimates) showed that the releases from the riser both pre and post cut rapidly transitioned from jets to buoyant plumes within a distance of 4 to 6 pipe diameters of the release location. This is consistent with ROV observations of the kink and riser releases and independent analyses using Particle Image Velocimetry (PIV) and Acoustic Doppler Current Profiler (ADCP) methods.
- Based on ROV observations, dispersants were typically applied at the edge of the blowout plume and the dispersant entrained into the rising plume. A single wand (single opening) was principally used during the pre-cut period on the riser release, while a trident (bident) (multiple openings) adjacent to the top hat, was used during the post cut period. No treatment was used on the kink releases. The multi-pronged trident impacted a significantly larger sector of the release than the wand.
- The *dispersant treatment model* predicts that approximately 30% of the oil released was treated during the post cut period with an effective DOR of about 1:45 ~ 1:56. This assumes a dispersant efficiency of 80% ~100%. This value for DOR is in reasonable agreement when the oil droplet size distribution model is fit to *Holocam* observations taken during the Jack Fitz 3 cruise.
- A new empirical, universal *oil droplet size model* was developed with dependence on both the Weber and Ohnesorge numbers, the later representing viscous effects important for dispersant treated oils. The model was validated against the most recently available small and large laboratory scale experimental data and shows an excellent ability to estimate oil droplet sizes for both treated and untreated oils.
- When applied to the spill, the *oil droplet size model* provides an excellent agreement with the *Holocam* oil droplet data taken during the DWH spill (dives # 5 and 6) with very high R^2 values when fitted with its lognormal distribution function for the deep dives. The droplet size model is also able to account for the impact of both treated and untreated oil on the total oil droplet size predictions.
- The *Holocam* data (dive #5 and 6 in particular) (Davis and Loomis, 2014) support the general conclusion that oil droplets, with sizes smaller than 300 μm , remained in the water column at the locations sampled (up to 2 km from the wellhead). Due to the distance of the *Holocam* observation from the release, droplets larger than this size are rarely observed, presumably the larger droplets having moved out of the intrusion layer due to their buoyancy.
- The *fountain and intrusion model* predicts a relatively thin intrusion layer that increases in thickness with distance from the source due to entrainment and is modified by the presence of ambient cross flow. The intrusion layer is consistent with observations of CDOM, BTEX, and DOSS in the water column at the plume trapping depth.
- A series of simulations using the *dispersant treatment* and *droplet size model*, with a focus on oil that is dispersed and remains in the water column, shows that even if there is no treatment, 6% of the oil is dispersed mechanically by the very energetic kink flow and to a much more limited extent the pre-cut riser flow. The present estimates assume that all droplets initially less than 300 μm are considered to be in the intrusion layer and close to the source (<2 km). For the low, best estimate, and high efficiency dispersant treatment cases, the amount retained was predicted to be 8, 20, and 33%, respectively.

- To validate these results, estimates were made of the amount of oil retained in the intrusion layer using the results of the *fountain* and *blowout plume model* predictions of the flow rates in the intrusion layer, and BTEX (components of the source oil) and DOSS (a component of dispersants) measurements at the trapping depth. The model estimates that $27\% \pm 5\%$ of the BTEX and $90\% \pm 23\%$ ⁴ of the DOSS were retained in the intrusion layer (based on post cut analysis only). The very high level of retention of DOSS is consistent with the idea that dispersant and dispersant treated oil is primarily retained in the intrusion layer. Estimates from the Oil Budget Calculator (OBC) for retention of both chemically and mechanically dispersed oil ranged from 20 to 38% with an expected value of 25%. Estimates from hydrocarbon chemistry ranged from 28 to 45%, with an average value of 36%. Predictions from the present simulations (8 to 33%, with a best estimate of 20%) are in good agreement with the various independent estimates, in terms of both the mean values as well as the range.

⁴ Confidence interval 67%-100%

9 References

- Adams, E. and S. Socolofsky. 2004 (revised 2005). Deep oil spill modeling activity, supported by the DeepSpill JIP and Offshore Operators Committee.
- Akar, P.J., and G.H. Jirka. 1995. Buoyant spreading processes in pollutant transport and mixing part 2: Upstream spreading in weak ambient current, *J. Hydraul. Res.* 33, 87–100, doi:10.1080/00221689509498686.
- Anderson, K., G. Bhatnagar, D. Crosby, G. Hatton, P. Manfield, A. Kuzmicki, N. Fenwick, J. Pontaza, M. Wicks, S. Socolofsky, C. Brady, S. Svedeman, A. K. Sum, C. Koh, J. Levine, R. P. Warzinski and F. Shaffer. 2012. Hydrates in the Ocean beneath, around, and above Production Equipment. *Energy & Fuels* 26(7):4167-4176.
- Ansong, J, P. J. Kyba, and B. R. Sutherland. 2008. Fountains impinging on a density interface, *J. Fluid Mech.* (2008), vol. 595, pp. 115–139. c 2008 Cambridge University Press
- Bandara, U.C. and P.D. Yapa. 2011. Bubble sizes, break-up and coalescence in deepwater gas/oil plumes. *Journal of Hydraulic Engineering, ASCE* 137, 729e738.
- Belore, R. 2014. Subsea chemical dispersant research. Proceedings of The 37th AMOP Technical Seminar on Environmental Contamination and Response, Environment Canada, Canmore, Alberta, Canada. Pp. 618-650.
- Brandvik, P.J., Ø. Johansen, F. Leirvik, U. Farooq and P.S. Daling. 2013. Droplet breakup in subsurface oil releases – Part 1: Experimental study of droplet breakup and effectiveness of dispersant injection. *Marine Pollution Bulletin* (73):319-326.
- Brandvik, P.J., Ø. Johansen, U. Farooq, G. Angell and F. Leirvik. 2014. Sub-surface oil releases – Experimental study of droplet distributions and different dispersant injection techniques- version 2. A scaled experimental approach using the SINTEF Tower basin. SINTEF report no: A26122. Trondheim Norway 2014. ISBN: 9788214057393.
- Briggs, G.A. 1969. Optimum formulas for buoyant plume rise, *Philos.Trans. R. Soc. Lond.* 265: 197–203.
- BP. 2010. GoM Dilling, Completions and Interventions – Mc252, Guidance on Subsea Dispersant Application, Ops note #4. Round 6, Procedure's folder, pp. 298-307, 2200-T2-DO-PR-4453-0.
- Bushnell, N. 2013. Oil spill by the oil rig “Deepwater Horizon” in the Gulf of Mexico – capping stack flow calculations, July 12 to 15, 2010, Expert report in matter of US vs BP Exploration & Production, Inc. et al, submitted to the U.S. Department of Justice, March 22, 2013.
- Camilli, R., D. Di Iorio, A. Bowen, C. M. Reddy, A.H. Techet, D.R. Yoerger, L.L. Whitcomb, J.S. Seewald, S.P. Sylva and J. Fenwick. 2011. Acoustic measurement of the Deepwater Horizon Macondo well flow rate, *Proceedings of the National Academy of Sciences*. www.pnas.org/cgi/doi/10.1073/pnas.1100385108.
- Camilli, R., C.M. Reddy, D.R. Yoerger, B.A.S. Van Mooy, M.V. Jakuba, J.C. Kinsey, C.P. McIntyre, S.P. Sylva and J.V. Maloney. 2010. Tracking hydrocarbon plume transport and biodegradation at Deepwater Horizon. *Science* 330:201-204.

- Campo, P., A. D. Venosa and M. T. Suidan. 2013. Biodegradability of Corexit 9500 and Dispersed South Louisiana Crude Oil at 5 and 25 °C. *Environmental Science & Technology* 47(4):1960-1967.
- Carazzo, G., E. Kaminski, and S. Tait. 2008. On the rise of turbulent plumes: Quantitative effects of variable entrainment for submarine hydrothermal vents, terrestrial and extra terrestrial explosive volcanism, *J. Geophys. Res.* 113, B09201, doi:10.1029/2007JB005458.
- Chan, G.K.Y., A.C. Chow and E.E. Adams. 2014. Effects of droplet size on intrusion of sub-surface oil spills. *Environmental Fluid Mechanics* 14(5):1-15.
- Chen, F.H. and P.D. Yapa. 2003. A model for simulating deepwater oil and gas blowouts - Part II: comparison of numerical simulations with “Deepspill” field experiments. *Journal of Hydraulic Research, IAHR* 41 (4):353-365.
- Chen, F.H. and P.D. Yapa. 2004. Modeling gas separation from a Bent deepwater oil and gas Jet/Plume. *Journal of Marine Systems, Elsevier, the Netherlands* 45 (3e4), 189e203.
- Chen, F.H. and P.D. Yapa. 2007. Estimating the oil droplet size distributions in deep water spills, *Journal of Hydraulic Engineering*, Vol. 133, No. 2: 197-207.
- Clayton, J.R.J, J.R. Payne and J.S. Farlow. 1993. *Oil Spill Dispersants: Mechanisms of Action and Laboratory Tests*. CRC Press, Inc. Boca Raton, FL.
- Crowley, D., D. Mendelsohn, N.W. Mulanaphy, Z. Li, and M.L. Spaulding. 2014. Modeling subsurface dispersant applications for response planning and preparation, *International Oil Spill Conference*. Paper 300204.
- Dasanayaka, L.K. and P.D. Yapa. 2009. Role of plume dynamics on the fate of oil and gas released underwater. *Journal of Hydro-Environment Research, IAHR/Elsevier*: 243-253.
- Davis, C. S. and N. C. Loomis. 2014. Deepwater Horizon Oil Spill (DWHOS) Water Column Technical Working Group, Image Data Processing Plan: *Holocam* description of data processing methods used to determine oil droplet size distributions from in situ holographic imaging during June 2010 on cruise M/V Jack Fitz 3. Woods Hole Oceanographic Institution and MIT/WHOI Joint Program in Oceanography. 15 pages + Appendices.
- Delvigne, G.A.L and C.E. Sweeney. 1988. Natural dispersion of oil. *Oil and Chemical Pollution* 4: 281-310.
- Dykhuizen, R. C. 2013. Flow rates from the Macondo MC252 well, Expert report in matter of US vs BP Exploration & Production, Inc. et al, submitted to the U.S. Department of Justice, March 22, 2013.
- Fan, L.-N. 1967. Turbulent buoyant jets into stratified or flowing ambient fluids. Technical Report. KH-R-15, W.M. Keck Laboratory of Hydraulics and Water Resources, California Institute of Technology, Pasadena, California.
- Fischer, H.B., E.J. List, R.C.Y. Koh, J. Imberger, and N. H. Brooks (Eds.). 1979, *Mixing in Inland and Coastal Waters*, Academic, New-York.
- French McCay, D., K. Jayko, Z. Li, M. Horn, Y. Kim, T. Isaji, D. Crowley, M. Spaulding, L. Decker, C. Turner, S. Zamorski, J. Fontenault, R. Shmookler and J. Rowe. 2015. Technical Reports for Deepwater Horizon Water Column Injury Assessment, WC_TR.14: Modeling oil fate and exposure concentrations in the Deepwater plume and rising oil

- resulting from the Deepwater Horizon Oil Spill. Project No, 2011-144. RPS ASA, 55 Village Square Drive, South Kingstown, RI 02879.
- Grennan, M., S. Zamorski, L. Decker, M. Horn, and Y. Kim. 2015. Technical Reports for Deepwater Horizon Water Column Injury Assessment – FE_TR.39: Volume II. Water Column CTD and Sensor Data from the Deepwater Horizon Oil Spill. RPS ASA, South Kingstown, RI, USA.
- Griffith, S. K. 2013. Oil release from the Macondo MC252 well, Expert report in matter of US vs BP Exploration & Production, Inc. et al, submitted to the US Department of Justice, March 22, 2013.
- Hazen, T.C., E.A. Dubinsky, T.Z. DeSantis, G.L. Andersen, Y.M. Piceno, N. Singh, J.K. Jansson, A. Probst, S.E. Borglin, J.L. Fortney, W.T. Stringfellow, M. Bill, M.E. Conrad, L.M. Tom, K.L. Chavarria, T.R. Alusi, R. Lamendella, D.C. Joyner, C. Spier, J. Baelum, M. Auer, M.L. Zemla, R. Chakraborty, E.L. Sonnenthal, P. D'haeseleer, H.Y.N. Holman, S. Osman, Z. Lu, J.D. Van Nostrand, Y. Deng, J. Zhou, and O.U. Mason. 2010. Deep-sea oil plume enriches indigenous oil-degrading bacteria. *Science* 330: 204-208.
- Hinze, J.O. 1955. Fundamentals of the hydrodynamic mechanism of splitting in dispersion processes. *Journal of AIChE* 1:289-295.
- Horn, M., M. Grennan, L. Decker, S. Zamorski, D. French McCay, Z. Li. 2015. Technical Reports for Deepwater Horizon Water Column Injury Assessment –Water Column Chemistry Data from the Deepwater Horizon Blowout. RPS ASA, South Kingstown, RI, USA.
- Johansen, Ø. 1998. Subsea Blowout Model for Deep Waters. SINTEF Report STF66 F98105, SINTEF Applied Chemistry, Environmental Engineering, Trondheim, p. 33.
- Johansen, Ø. 2000. DeepBlow: a Lagrangian plume model for deep water blowouts, *Spill Science & Technology Bulletin*, Vol. 6, No. 2:103-111
- Johansen, Ø., P.J. Brandvik and U. Farooq. 2013. Droplet breakup in subsea oil releases – Part 2: Predictions of droplet size distributions with and without injection of chemical dispersants. *Marine Pollution Bulletin* 73(1):327-335.
- Johansen, Ø. and I. M. Carlsen. 2002. Assessment of methods for dispensing dispersant into subsea blowouts. SINTEF Applied Chemistry, Trondheim, Norway, pp. 46.
- Johansen, Ø., H. Jensen, and A. Melbye. 2000. ROV Sonar and Visual Pictures from the Field Trial 'Deep Spill', June 2000, Technical Report, SINTEF Applied Chemistry, Trondheim, Norway.
- Johansen, Ø., H. Rye, and C. Cooper. 2003. DeepSpill Field Study of a simulated gas blowout in deepwater, *Spill Science & Technology Bulletin* 8: 433-443.
- Johansen, Ø., H. Rye, A.G. Melbye, H.V. Jensen, B. Serigstad, T. Knutsen. 2001. DeepSpill JIP—Experimental discharges of gas and oil at Helland Hansen—June 2000. Technical Report, SINTEF Report STF66 F01082, SINTEF Applied Chemistry, Trondheim, Norway, p. 159.
- Kelkar, M. and R. Raghavan. 2013. Rate prediction from the Macondo well, Expert report in matter of US vs BP Exploration & Production, Inc. et al, submitted to the US Department of Justice, March 22, 2013.

- Kessler, J.D., D.L. Valentine, M.C. Redmond, M. Du, E.W. Chan, S.D. Mendes, E.W. Quiroz, C.J. Villanueva, S.S. Shusta, L.M. Werra, S.A. Yvon-Lewis, and T.C. Weber. 2011. A Persistent Oxygen Anomaly Reveals the Fate of Spilled Methane in the Deep Gulf of Mexico. *Science* 331: 312-315.
- Khelifa, A, and L.L.C So. 2009. Effects of chemical dispersants on oil-brine interfacial tension and droplet formation. In: 32nd Proceedings of Arctic and Marine OilSpill Program Technical Seminar, Environment Canada, Ottawa, Canada, pp. 383-396.
- Kolluru, V.S. 1993. Oil blowout model, Applied Science Associates, Inc., Narragansett, RI 02882.
- Kujawinski, E.B., M.C.K. Soule, D.L. Valentine, A.K. Boysen, K. Longnecker, and M.C. Redmond. 2011. Fate of Dispersants Associated with the Deepwater Horizon Oil Spill. *Environ. Sci. & Technol.*, American Chemical Society Publications. American Chemical Society, 2011
- Lehr, B., S. Bristol and A. Possolo. 2010. Deepwater horizon oil budget calculator: A report to the national incident command. The Federal Interagency Solutions Group, Oil Budget Calculator Science and Engineering Team. http://www.restorethegulf.gov/sites/default/files/documents/pdf/OilBudgetCalc_FuII_HQ-Print_111110.pdf (Accessed on April 1, 2012).
- Li Z, K. Lee, T. King, M.C. Boufadel and A.D. Venosa. 2009a. Evaluating crude oil chemical dispersion efficacy in a flow-through wave tank under regular non-breaking wave and breaking wave conditions. *Marine Pollution Bulletin* 58: 735-744.
- Li, Z., K. Lee, T. King, M. C. Boufadel, and A. D. Venosa, 2009b. Evaluating Chemical Dispersant Efficacy in an Experimental Wave Tank: 2—Significant Factors Determining In Situ Oil Droplet Size Distribution, *Environmental Engineering Science*, Volume 26, Number 9, 2009.
- Masutani, S.M. and E.E. Adams. 2000. Experimental study of multiphase plumes with application to deep ocean oil spills. Final report to U.S. Department of Interior, Minerals Management Service, Contract no. 1435-01-98-CT-30946. Pp147.
- McDougall, T. J. 1978. Bubble plumes in stratified environments, *Journal of Fluid Mechanics*, Vol. 85, Part 4, pp 655-672.
- McNutt, M., R. Camilli, G. Guthrie, P. Hsieh, V. Labson, B. Lehr, D. Maclay, A. Ratzel and M. Sogge. 2011. Assessment of Flow Rate Estimates for the Deepwater Horizon / Macondo Well Oil Spill. Flow Rate Technical Group report to the National Incident Command, Interagency Solutions Group. Appendix D – Plume Calculation Team 2010; Particle Image Velocimetry Report. March 10, Available online: <https://www.doi.gov/sites/doi.gov/files/migrated/deepwaterhorizon/upload/FRTG-report-Appendix-D-Plume-Analysis-Report.pdf>
- Morton, B.R., G.I. Taylor, and J.S. Turner. 1956. Turbulent gravitational convection from maintained and instantaneous source, *Proc. R. Soc. London*. 234: 1 – 23.
- National Research Council (NRC). 2005. National Research Council: *Understanding Oil Spill Dispersants: Efficacy and Effects*, National Academies Press, Washington, D.C.
- Pooladi-Darvish. 2013. Estimate of cumulative volume of oil released from the MC252 Macondo well. Rebuttal expert report US v BP Exploration & Production, Inc. et al. TRES-

- 011654R. <http://www.mdl2179trialdocs.com/releases/release201311071200013/TREX-011654R.PDF>
- Reddy, C.M., J.S. Arey, J.S. Seewald, S.P. Sylva, K.L. Lemkau, R.K. Nelson, M.a.S. Van Mooy and R. Camilli. 2012. Composition and fate of gas and oil released to the water column during the Deepwater Horizon oil spill. *Proceedings of National Academy of Sciences* 109(5):20229-20234.
- Reed, M., Ø. Johansen, F. Leirvik, and B. Brors. 2009. Numerical algorithm to compute the effects of breaking waves on surface oil spilled at sea. Final report submitted to NOAA/UNH Coastal Response Research Center. Vol. 19 + appendices. SINTEF Institute for Materials and Chemistry.
- Rye, H. 1994. Model for calculation of underwater blowout plume, *Proceedings of the 17th Arctic and Marine Oilspill Program Technical Seminar, Canada*, p. 849-865.
- Ryerson T.B., R. Camilli, J.D. Kessler, E.B. Kujawinski, C.M. Reddy, D.L. Valentine, E. Atlas, D.R. Blake, J. de Gouwa, S. Meinardi, D.D. Parrish, J. Peischl, J.S. Seewald, and C. Warneke. 2012. Chemical data quantify Deepwater Horizon hydrocarbon flow rate and environmental distribution, *Proceedings of the National Academy of Sciences*, www.pnas.org/cgi/doi/10.1073/pnas.1110564109
- Socolofsky, S.A. 2001. Laboratory experiments of multi-phase plumes in stratification and crossflow. Ph.D. Thesis, Massachusetts Institute of Technology, USA, p. 233.
- Socolofsky, S. A., and E. E. Adams. 2002. Multi-phase plumes in uniform and stratified crossflow, *J. Hydraul. Res.* 40(6): 661–672.
- Socolofsky, S. A. and E. Adams. 2003. Liquid volume fluxes in stratified multiphase plumes, *Journal of Hydraulic Engineering* 129(11): 905-914.
- Socolofsky, S. A. and E. Adams. 2005. Role of slip velocity in the behavior of stratified multiphase plumes, *Journal of Hydraulic Engineering*, 131(4): 273-282.
- Socolofsky, S.A., E. E. Adams, and C.R. Sherwood. 2011. Formation dynamics of subsurface hydrocarbon intrusions following the Deepwater Horizon blowout. *Geophys. Res. Lett.* 38(9): L09602. doi:10.1029/2011GL047174.
- Socolofsky, S. A., E. E. Adams, M. C. Boufadel, Z. M. Aman, Ø. Johansen, W. J. Konkel, D. Lindo, M. N. Madsen, E. W. North, C. B. Paris, D. Rasmussen, M. Reed, P. Rønningen, L. H. Sim, T. Uhrenholdt, K. G. Anderson, C. Cooper and T. J. Nedwed. 2015. Intercomparison of oil spill prediction models for accidental blowout scenarios with and without subsea chemical dispersant injection. *Marine Pollution Bulletin* 96(1–2):110-126.
- Socolofsky, S.A., E.E. Adams, and C.R. Sherwood. 2011. Formation dynamics of subsurface hydrocarbon intrusions following the Deepwater Horizon blowout, *Geophys. Res. Lett.*, 38, L09602, doi:10.1029/2011GL047174.
- Spaulding, M.L., P.R. Bishnoi, E. Anderson, and T. Isaji. 2000. An integrated model for prediction of oil transport from a deep water blowout, 23rd Arctic and Marine Oil Spill Program (AMOP) Technical Seminar, June 14-16, 2000, Vancouver, British Columbia, Canada, pp.611-636.

- Spier, C., W.T. Stringfellow, T.C. Hazen, and M. Conrad. 2013. Distribution of hydrocarbons released during the 2010 MC252 oil spill in deep offshore waters, *Environmental Pollution* 173: 224-230.
- U.S. Coast Guard. 2011. BP Deepwater Horizon Oil Spill: Incident Specific Preparedness Review (ISPR), Final Report. Department of Homeland Security, Washington DC. 2011. Available at <http://www.uscg.mil/foia/docs/DWH/BPDWH.pdf>.
- USDC. 2015. The U.S. District Court for Eastern District of Louisiana, Case 2:10-md-02179-CJB-SS Document 14021 Filed 01/15/15, Findings of fact and conclusions of law phase two trial. Pp 1-44. (<http://www2.epa.gov/sites/production/files/2015-01/documents/phase2ruling.pdf>)
- Valentine, D.L K., J.D. Kessler, M.C. Redmond, S.D. Mendes, M.B. Heintz, C. Farwell, L. Hu, F.S. Kinnaman, S. Yvon-Lewis, M. Du, E.W. Chan, F.G. Tigreros, C.J. Villanueva. 2010. Propane respiration jump-starts microbial response to a deep oil spill. *Science* 330:208-211
- Venkataraman, P., J. Tang, E. Frenkel, G.L. Mcpherson, J. He, S.R. Raghavan, V.L. Kolesnichenko, A. Bose and V.T. John. 2013. Attachment of a Hydrophobically Modified Biopolymer at the Oil-Water Interface in the Treatment of Oil Spills. *Applied Materials & Interfaces* 5(9):3572-3580.
- Wereley, S. 2011. Gulf oil spill Particle Image Velocimetry (PIV) analysis, Appendix 5, Appendix D Plume Calculation Team, PIV report, from McNutt M., R. Camilli, G. Guthrie G, et al. 2011. Assessment of Flow Rate Estimates for the Deepwater Horizon / Macondo Well Oil Spill. Flow Rate Technical Group report to the National Incident Command, Interagency Solutions Group, March 10, 2011.
- White, H.K., S.L. Lyons, S.J. Harrison, D.M. Findley, Y. Liu, and E.B. Kujawinski. 2014. Long-Term Persistence of Dispersants following the Deepwater Horizon Oil Spill. *Environ. Sci. Technol. Lett.* 2014, 1, 295–299, Am. Chem. Soc, 2014
- Yapa, P.D., L.K. Dasanayaka, U.C. Bandara, and K. Nakata. 2010. A model to simulate the transport and fate of gas and hydrates released in deepwater, *Journal of Hydraulic Research*, IAHR. October, 48(5): 559-572.
- Yapa, P., M. Wimalarante, A. Dissanayake, and J. DeGraff. 2012. How does oil and gas behave in deepwater releases, *Journal of Hydro-environmental Research* 6(4): 275-285.
- Yapa, P.D. and L. Zheng. 1997. Modelling oil and gas releases from deep water: A review. *Spill Science & Technology Bulletin* 4:189-198.
- Yapa, P.D., L. Zheng, and F.H. Chen. 2001. A model for deepwater oil/gas blowouts. *Marine Pollution Bulletin* 43: 234–241.
- Zheng, L. and P.D. Yapa. 1997a. Simulation of oil spills from deep water blow-outs. XXVIIth Congress of the International Association for Hydraulic Research, IAHR and ASCE Conference, San Francisco.
- Zheng, L. and P.D. Yapa. 1997b. A numerical model for buoyant oil jets and smoke plumes. In: *Proceedings of the 20th Arctic and Marine Oil Spill Program (AMOP) Technical Seminar*, Vancouver, Canada, pp. 963-979.

- Zheng, L., P. D. Yapa, and F. Chen. 2002. A model for simulating deepwater oil and gas blowouts, Part I Theory and model formulation, *Journal of Hydraulic Research*, 41(4): 339-351.
- Zick, A. 2013. Equation of state fluid characterization and analysis of the Macondo reservoir fluids, Expert report in matter of U.S. vs BP Exploration & Production, Inc. et al, submitted to the U.S. Department of Justice, March 22, 2013.

Technical Reports for Deepwater Horizon Water Column Injury Assessment

WC_TR.13: Application of OILMAP DEEP to the Deepwater Horizon Blowout

Addendum 1: Updated Modeling using Court Determined Volumes

Authors: Malcolm Spaulding, Daniel Mendelsohn, Deborah Crowley,
Zhengkai Li, Andrew Bird

Revised: September 30, 2015

Project Number: 2011-144

RPS ASA 55 Village Square Drive, South Kingstown, RI 02879

Table of Contents

1. Introduction	1
2. Model Predictions	2
2.1 Daily Release Volumes	2
2.2 Pipeline Release Model Using Court Total Release Volumes	3
2.3 Blowout Plume Model Using Court Release Volumes	4
2.3.1 Black Oil Table Analysis Using Court Release Volumes	4
2.3.2 Blowout Plume Using Court Release Volumes	5
2.4 Dispersant Treatment Model Using Court Release Volumes	6
2.5 Droplet Size Distributions Using Court Release Volumes	8
2.6 Updated SPT File	12
3. Summary	12
4. References	13

List of Figures

Figure 1. Time series of OBC and court daily release of oil from the reservoir.	2
Figure 2. Time series of OBC and court daily release of oil to the water column.	2
Figure 3. Time series of OBC and Court cumulative daily release of oil to the water column.....	3
Figure 4. Time series of daily oil volumes based on pipeline release model using the court (top) and OBC estimated volumes (bottom).	4
Figure 5. Time series of daily exit velocities from the riser and kink based on the pipeline release model volume flow rates and the BOT analysis using court and OBC estimated volumes.	5
Figure 6. Time series of riser and kink trap heights using OBC and court release volumes.....	6
Figure 7. Time series of daily oil volumes based on pipe leak analysis using court and OBC estimated total release volumes.	7
Figure 8. Time series of dispersant to oil ratio (DOR) and interfacial tension for court and OBC releases.	8
Figure 9. Time history of mass within droplet size bin classes throughout the spill event using the OBC (top) and court (bottom) total volume. Note the fractional mass is relative to the daily release which differs between OBC and court specification.	9
Figure 10. Cumulative droplet size distributions for the spill event from each of the three sources (riser untreated, riser treated, and kink) as well as the total. Note the x-axis is logarithmic. The top plot illustrates the entire distribution while the bottom plot y-axis is cutoff at 20% level to facilitate viewing the kink and riser treated curves.....	10
Figure 11. Cumulative droplet size distributions in terms of percent of total for the entire spill event based for the court and OBC total release volumes. Note the x-axis is logarithmic.....	11

Figure 12. Cumulative droplet size distributions in terms of mass for the entire spill event for the court and OBC total release volumes. Note the x-axis is logarithmic. 12

List of Tables

Table 1. Summary of release and collection volumes from previous (OBC) assessment and present (court specified) determination. 1

Table 2. Maximum cumulative fraction by source for court and OBC volumes. 11

1. Introduction

In performing simulations of the DWH blowout (Spaulding et al. 2015) estimates of the oil release rate vs time were developed based on the Oil Budget Calculator (OBC) (Lehr et al. 2010) and validated with independent estimates made by Department of Justice (DOJ) flow rate experts. The total volume of oil released from the reservoir was estimated at 4.9 million barrels. The total amount recovered was estimated to be 0.82 million barrels, for a total release to the water column of 4.11 million barrels (Table 1). In January 2015, the U.S. District Court for Eastern District of Louisiana (Case 2:10-md-02179-CJB-SS Document 14021 Filed 01/15/15 (USDC 2015)) found that 4 million barrels of oil were released from the reservoir, and based on the parties stipulation that 0.81 million barrels were recovered, determined that 3.19 million barrels of oil were released to the water column (Table 1). The court made no determination on the daily rate of release, only the total amount released during the spill. The court specified values are about 19% lower than OBC total release from the reservoir and 22% lower than OBC estimates to the water column.

Table 1. Summary of release and collection volumes from previous (OBC) assessment and present (court specified) determination.

	Reservoir Release (bbl)	Collected (bbl)	Release to the Water Column (bbl)
OBC	4,928,100	817,739	4,110,361
Court	4,000,000	810,000	3,190,000

To understand the implications of the reduced flow rate on blowout model predictions, simulations using the blowout model were repeated for the court specified volumes. The release rate pattern was assumed to be the same as in the original OBC based simulations. Simulations were performed for the best estimate for the dispersant application case. The principal implications of the reduced total release volumes are: (1) the distribution of flow between the riser and kink is altered due to the new volume and (2) the droplet size distributions have changed due to the modified release flows (and associated release exit velocities) and the modified dispersant to oil ratio (DOR) of the treated fraction (since the amount of dispersant applied remained unchanged while the oil volume decreased). To address these issues the Pipeline Release Model, Blowout Plume Model, Dispersant Treatment Model and Droplet Size Model (Spaulding et al. 2015) were re-run with the court specified volumes but using the OBC daily release rate pattern.

The end product was new SPT files that were used as input to the far field model (SIMAP). The SPT file defines the time history of the release of oil to the water column by location (riser, kink and riser post cut) and mass of oil by droplet sizes based on the blowout model predictions.

2. Model Predictions

2.1 Daily Release Volumes

The previous modeling implemented time varying (daily timestep) oil discharge rate based on the volumes of oil released and collected as provided in the Oil Budget Calculator (Lehr et al. 2010). Given the assumption of similarity in release pattern, the OBC daily volumes were used to establish the court daily volumes through simple scaling. For comparison Figure 1, 2 and 3 present the daily reservoir release volumes, daily water column release volumes, and cumulative volume release to the water column (i.e., accounting for collection), for the OBC and court volume estimates with time, respectively.

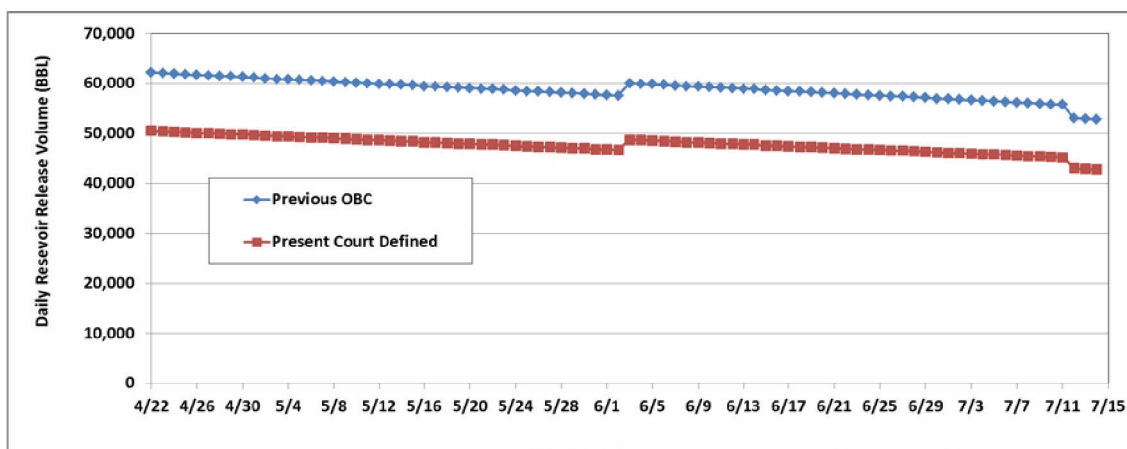


Figure 1. Time series of OBC and court daily release of oil from the reservoir.

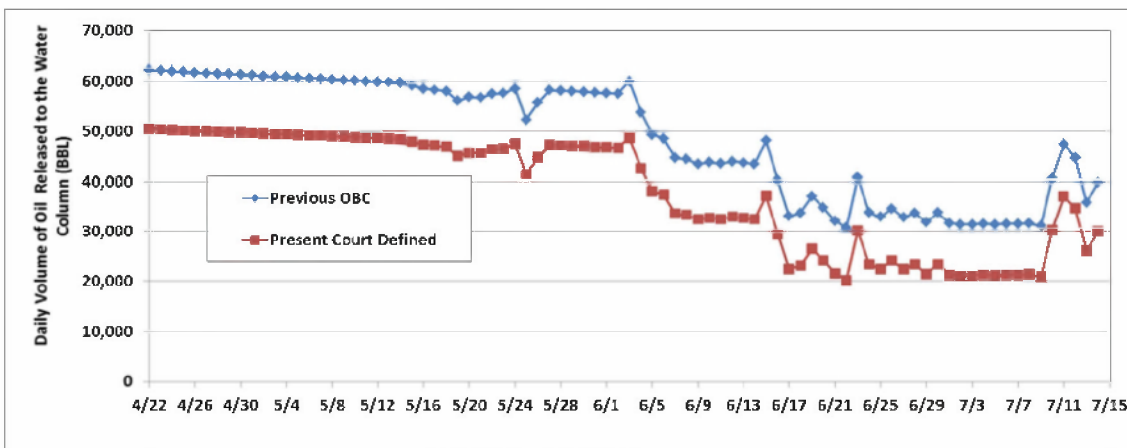


Figure 2. Time series of OBC and court daily release of oil to the water column.

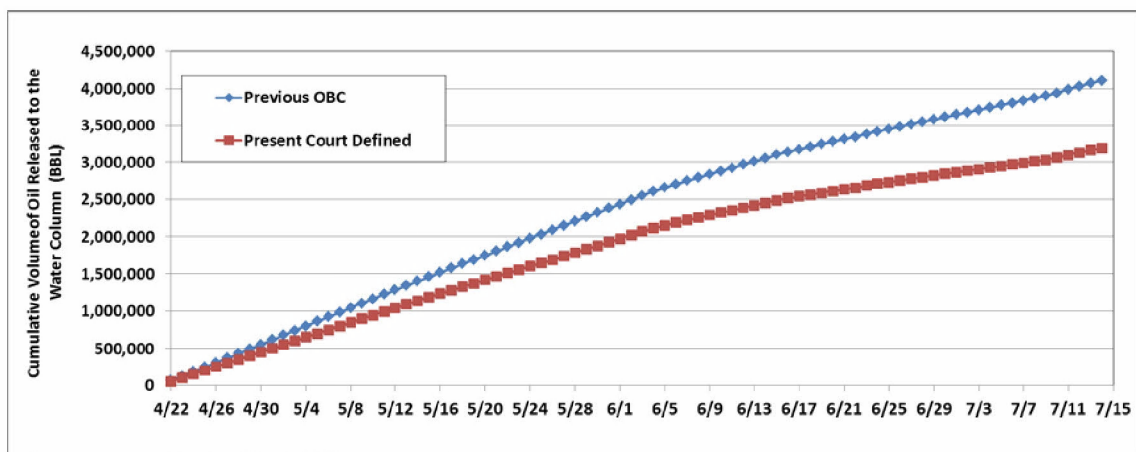


Figure 3. Time series of OBC and Court cumulative daily release of oil to the water column.

2.2 Pipeline Release Model Using Court Total Release Volumes

The pipeline release model (Spaulding et al. 2015, Appendix D) was used to determine the distribution of flow between the end of the broken riser and the kink for the time period after the onset of the kink flow and prior to the riser cut, using the court specification of release volumes. The input included the modified reservoir release rates (daily volumes) and the output was a time history of the flow from the end of the riser and the kink. The daily time history of the release volumes from the reservoir, riser, and kink are illustrated in Figure 4 for court (upper panel) and OBC (lower panel) volumes. The figure also includes the time periods prior to the onset of the kink flows and after the riser was cut, terminating the kink flow. The riser flow is equal to the total reservoir flow for time periods when the kink was absent.

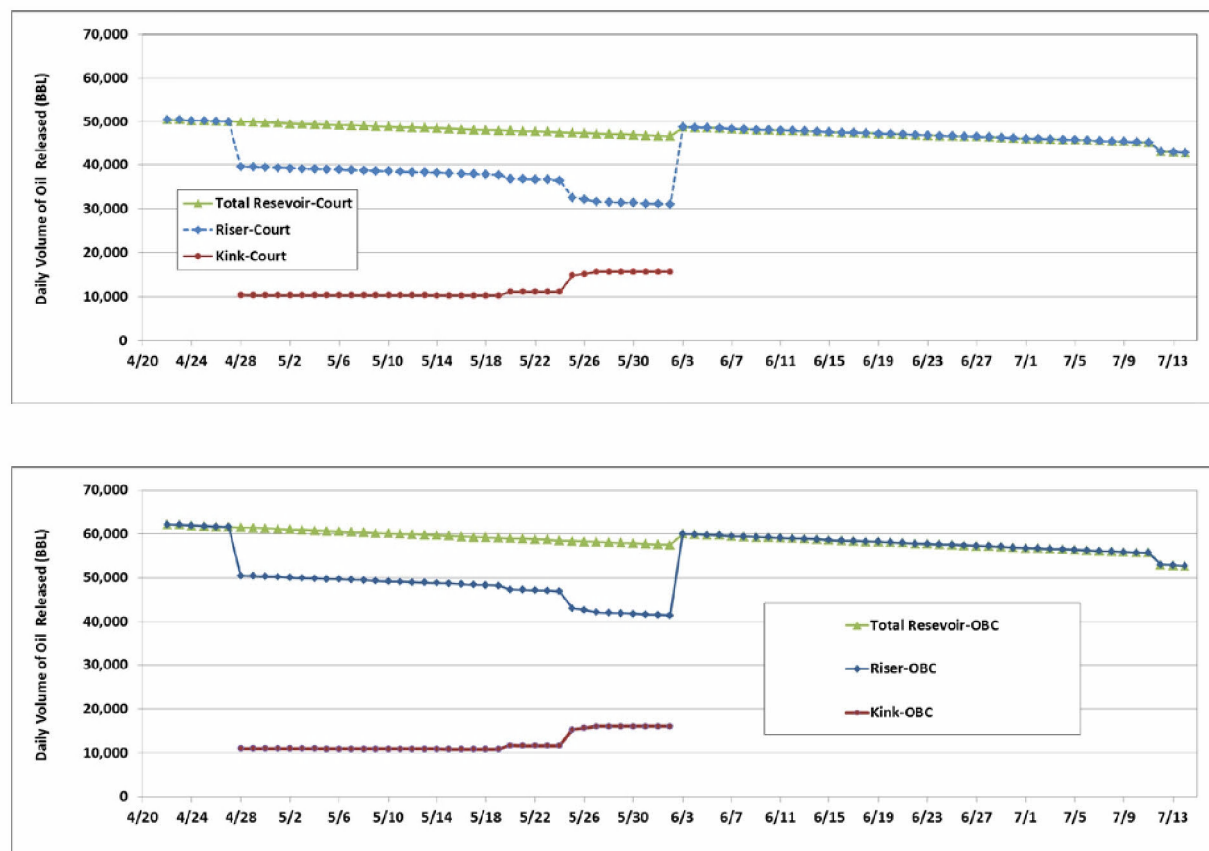


Figure 4. Time series of daily oil volumes based on pipeline release model using the court (top) and OBC estimated volumes (bottom).

2.3 Blowout Plume Model Using Court Release Volumes

The blowout plume model (Spaulding et al. 2015, Appendix E) was rerun with the court release volumes. Consistent with the most recent modeling that implemented the Black Oil Tables (Zick 2013), the gas to oil ratio (GOR) and density of oil at standard conditions, were assumed to be $501 \text{ m}^3/\text{m}^3$ and $847.58 \text{ kg}/\text{m}^3$, respectively. The black oil table analysis was updated using the court volume flows from the pipeline release model to predict new exit velocities and the plume model was then run to predict new trap heights.

2.3.1 Black Oil Table Analysis Using Court Release Volumes

The Black Oil Table (BOT) analysis was updated reflecting the modified flow volumes in order to estimate the exit velocities associated with oil (and gas) flow through the riser and kink. The model predicted exit velocities, based on the OBC and court volumes, are shown in Figure 5. These updated velocities were then used as input to the droplet size model. As expected, given the decrease in flow rate, the court based exit velocities are lower than the OBC based values.

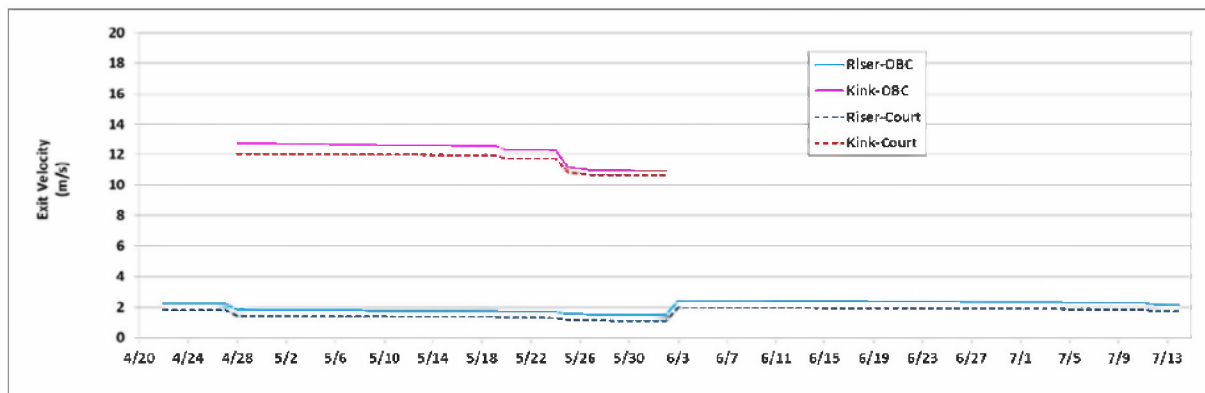


Figure 5. Time series of daily exit velocities from the riser and kink based on the pipeline release model volume flow rates and the BOT analysis using court and OBC estimated volumes.

2.3.2 Blowout Plume Using Court Release Volumes

- The blowout plume model was run to estimate the plume trap height from the riser and kink for the court volume. Figure 6 shows the blowout plume model predictions of trap height for plumes from the riser and the kink based on the OBC and court estimates of release volumes. The trap heights for the court volumes are lower than for the OBC based estimates. The predicted trap heights do not change significantly for the kink release, remaining within 10 m (~4%) of the OBC based estimate. The riser trap heights remain within 40 m (~12%) of the OBC based estimates. This is within the uncertainty of analysis of field CDOM data used to experimentally determine the trap height.

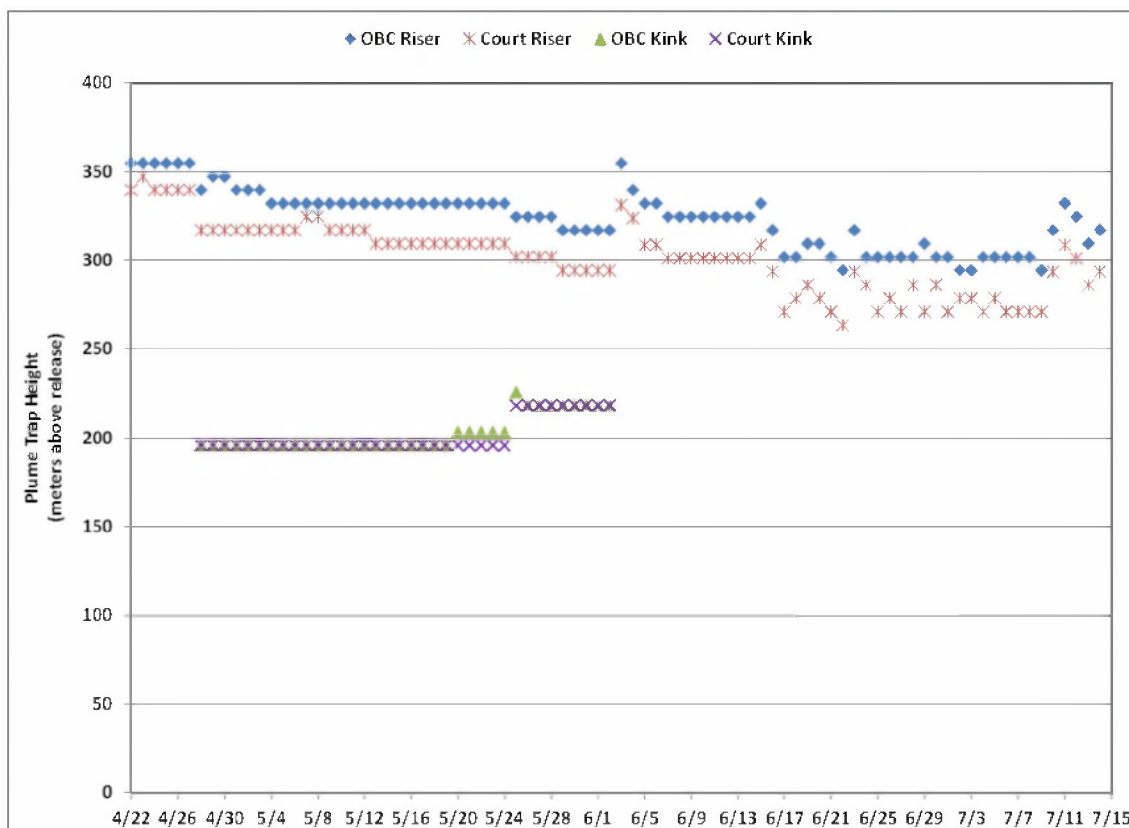


Figure 6. Time series of riser and kink trap heights using OBC and court release volumes.

2.4 Dispersant Treatment Model Using Court Release Volumes

The dispersant treatment model (Spaulding et al. 2015, Appendix F) was updated reflecting the modified flow volumes in order to estimate the fraction of the release from each of the three effective sources (riser untreated, riser treated, and kink) as well as the dispersant to oil ratio associated with the treated fraction of oil. The riser fraction treated (relative to the riser total) was not modified based on new flow volumes, however, the fraction from each of the three sources did change in response to the new flow distribution between the riser and the kink. The daily amount of dispersant applied remained the same as previously established and documented in the Oil Budget Calculator (Lehr et al. 2010). In addition any subsurface oil collection prior to the riser cut was assumed to be associated with the oil originating from the end of the broken riser, consistent with the previous analysis. The estimated source fractions are illustrated in Figure 7 and the treated fraction dispersant to oil ratio (DOR- presented as ratio consequent) and corresponding interfacial tension (IFT) are shown in Figure 8. These updated IFT values were then used as input to the droplet size model and the effective source fractions were used as input to making the SPT file.

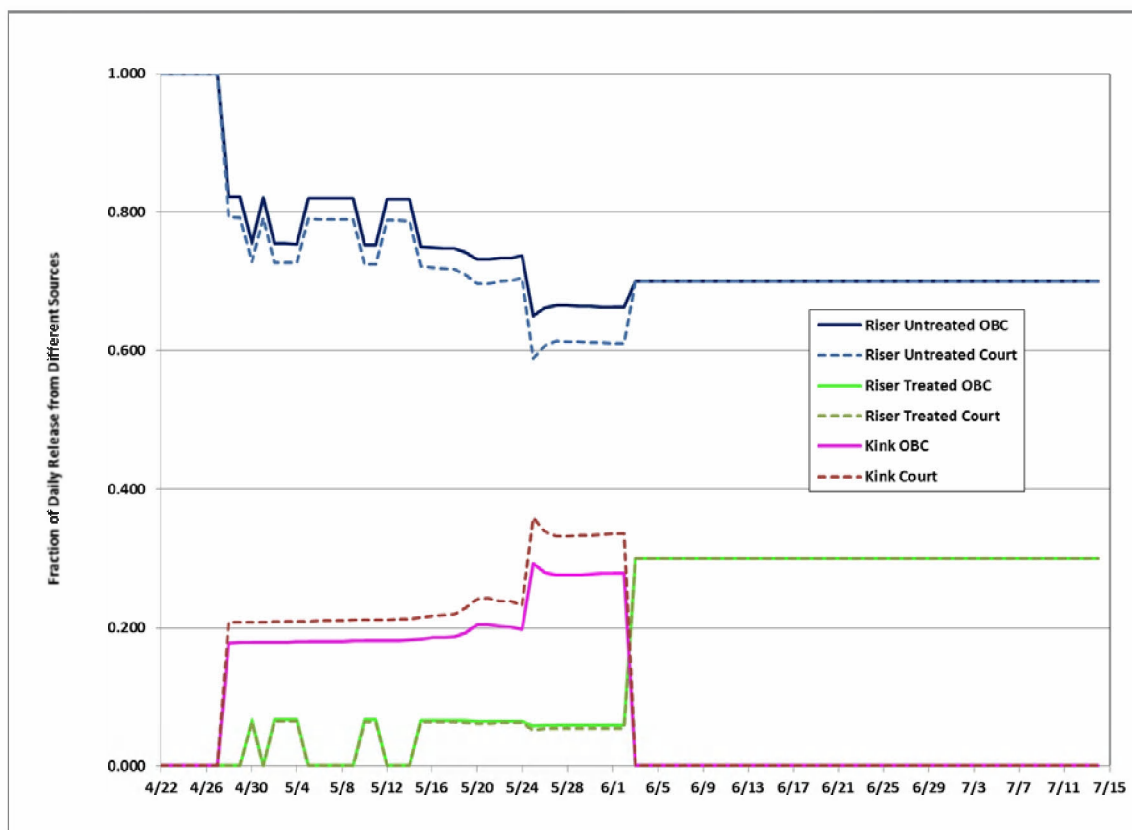


Figure 7. Time series of daily oil volumes based on pipe leak analysis using court and OBC estimated total release volumes.

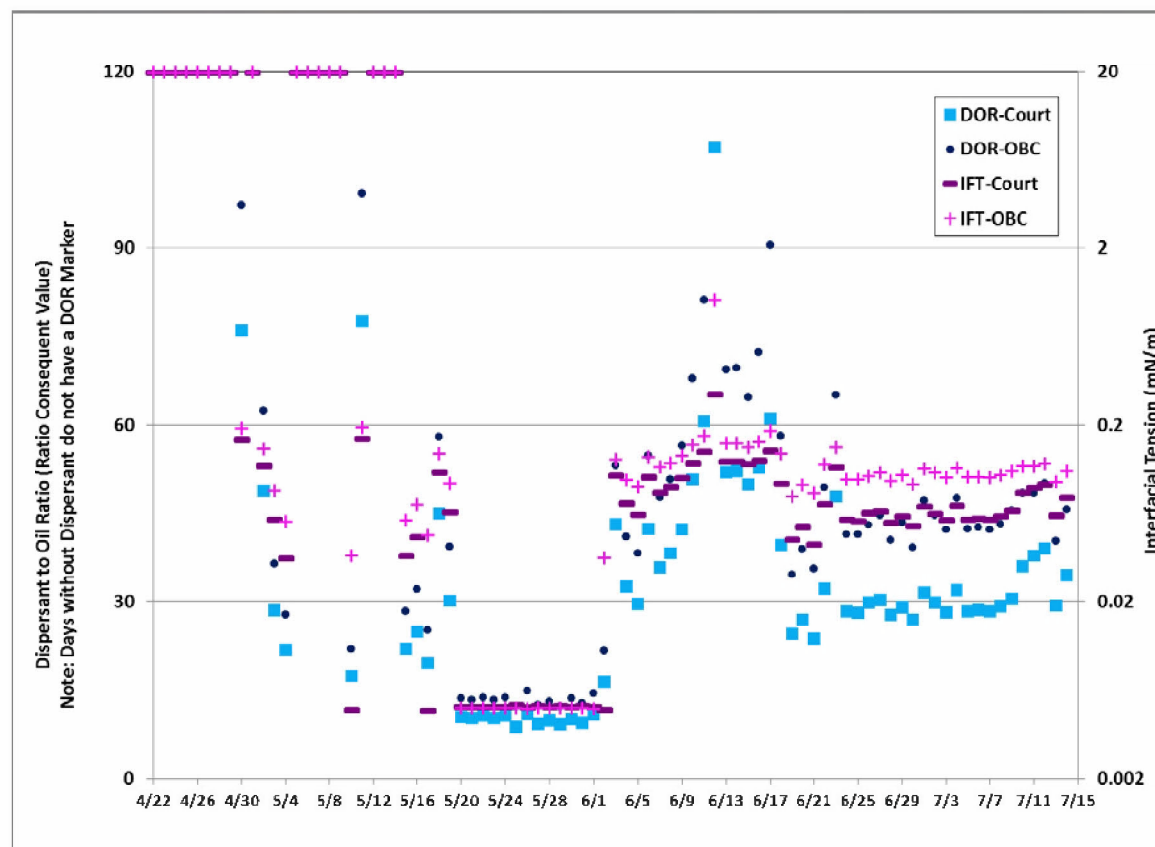


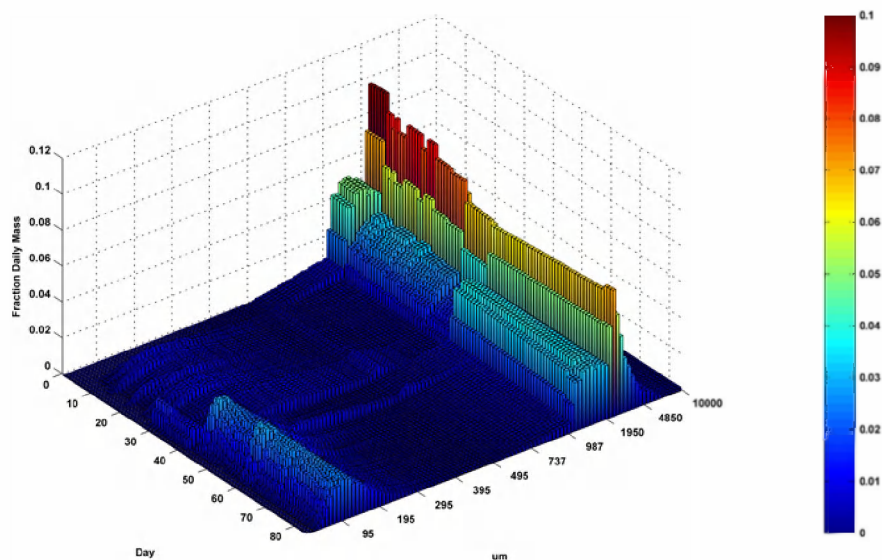
Figure 8. Time series of dispersant to oil ratio (DOR) and interfacial tension for court and OBC releases.

Figure 8 shows that the dispersant-to-oil ratio (DOR) increases and the interfacial tension decreases for the court vs OBC volumes; a direct reflection of the decrease in oil volume and the same amount of dispersant being applied. As an example for DOR, for the post riser cut period the DOR for the OBC volume is approximately 1:45 while the value for the court volume is 1:30.

2.5 Droplet Size Distributions Using Court Release Volumes

The droplet size model (Spaulding et al. 2015, Appendix G) was used to update the predictions of droplet size distributions based on the new exit velocities from the BOT analysis and new mass distribution and IFT values from the dispersant treatment model all stemming from the update of total release volume. Figure 9 illustrates the fraction of daily mass as a function of droplet bin sizes throughout the spill event for the OBC (top) and court (bottom) volumes. Note that the figure shows the relative fraction within each bin per day, though each day had a different release of mass to the water column.

OBC



Court

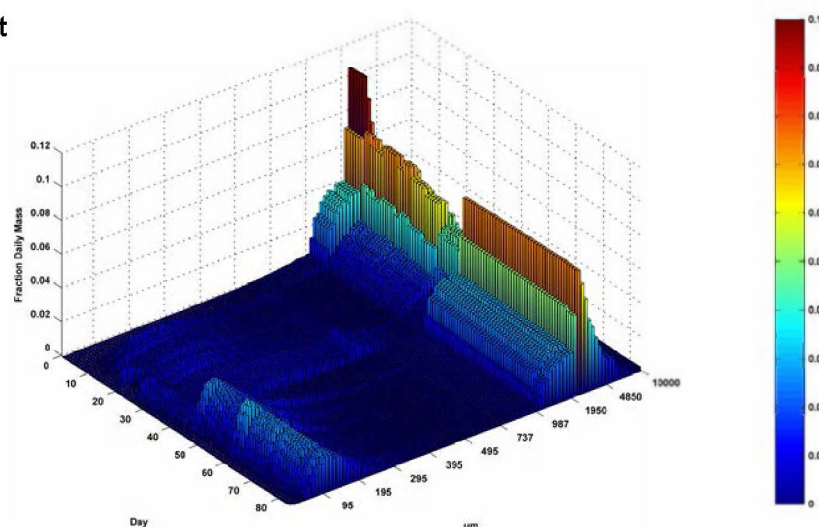


Figure 9. Time history of mass within droplet size bin classes throughout the spill event using the OBC (top) and court (bottom) total volume. Note the fractional mass is relative to the daily release which differs between OBC and court specification.

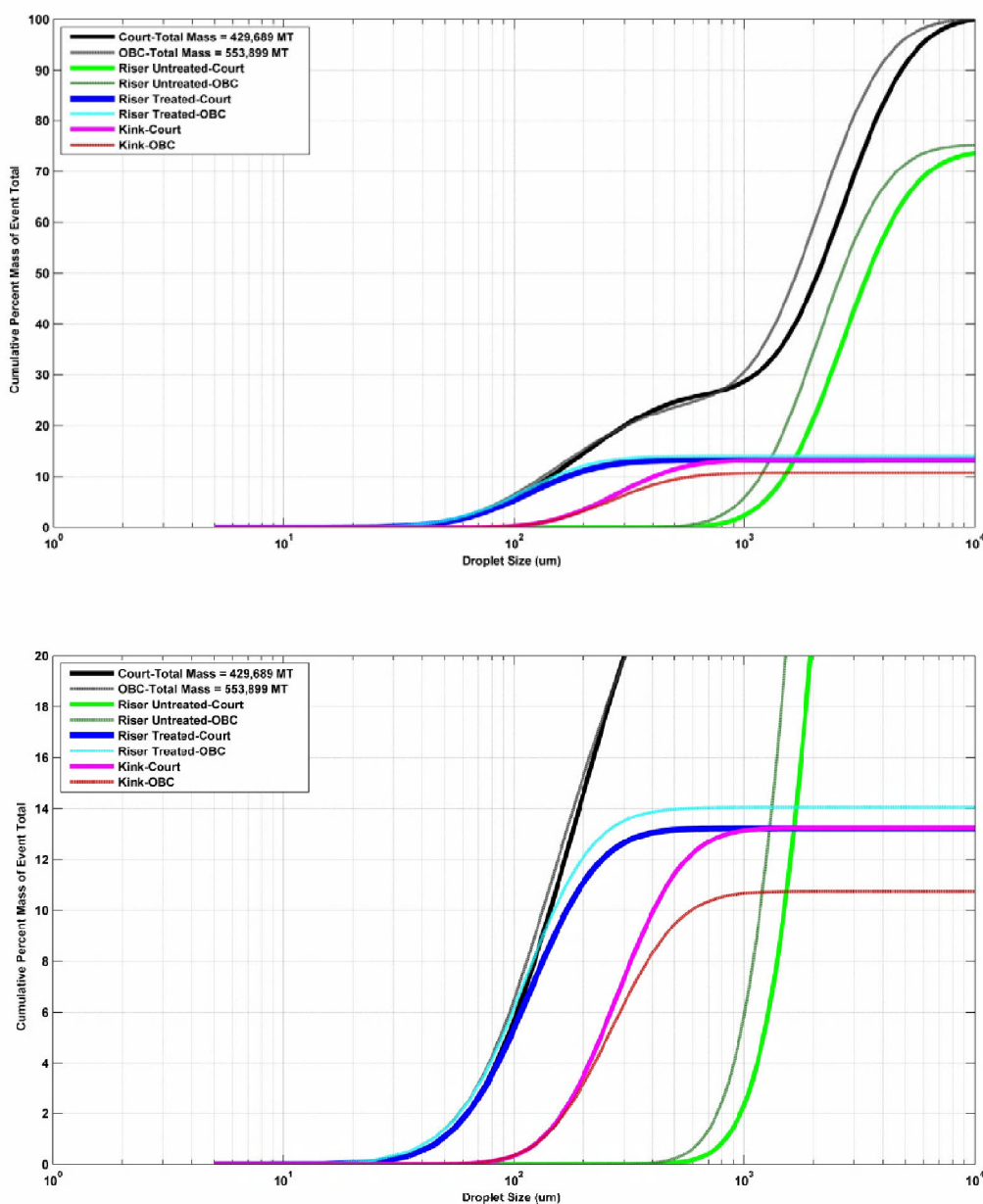


Figure 10. Cumulative droplet size distributions for the spill event from each of the three sources (riser untreated, riser treated, and kink) as well as the total. Note the x-axis is logarithmic. The top plot illustrates the entire distribution while the bottom plot y-axis is cutoff at 20% level to facilitate viewing the kink and riser treated curves.

Figure 10 shows the model predicted cumulative percent of oil droplet sizes by source (kink, riser treated and untreated) and for the total release for court and OBC volume estimates. The upper portion of the figure shows the entire range of droplet sizes and fraction while the lower portion is focused on the kink and treated riser releases. Figure 11 clearly shows that the kink

and treated riser flows dominate the droplet size distribution below 800 μm , while the untreated riser flow dominates the behavior above this droplet size. The court and OBC treated riser flows have very similar values for cumulative percent of mass vs droplet size, while the court based kink flows have a smaller value than the OBC based estimates. The court based value is larger than for OBC for the untreated riser source.

Table 2 shows the maximum cumulative fraction treated by source for both court and OBC volumes taken from Figure 10. For the riser treated flows the court value is 13 % compared to 14 % for OBC. The riser treated flows are 73.5 % for the court value and 75.2 % for OBC. Finally the kink flows have a value of 13.2 % for the court value and 10.7 % for OBC. The differences between the two estimates for all sources are typically no more than a few percent.

Table 2. Maximum cumulative fraction by source for court and OBC volumes.

Source	Court	OBC
Riser Treated	13.2%	14.0%
Riser Untreated	73.5%	75.2%
Kink	13.2%	10.7%

For comparison the cumulative droplet size distributions associated with the OBC and court release volumes are presented in Figure 11 (in terms of percent of total) and Figure 12 (in terms of mass). These figures show that for droplet sizes below about 800 μm the cumulative percentages are very similar for both release volumes while for droplet sizes above this value the court based estimates show generally larger droplet sizes. This is primarily a result of the difference in the riser untreated releases as shown in Figure 10.

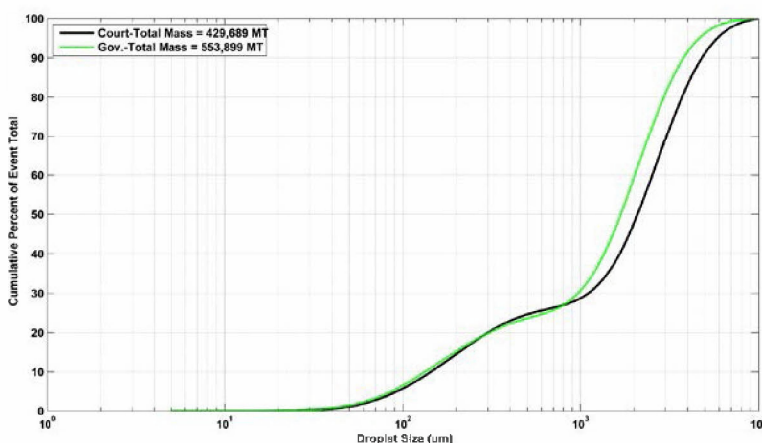


Figure 11. Cumulative droplet size distributions in terms of percent of total for the entire spill event based for the court and OBC total release volumes. Note the x-axis is logarithmic.

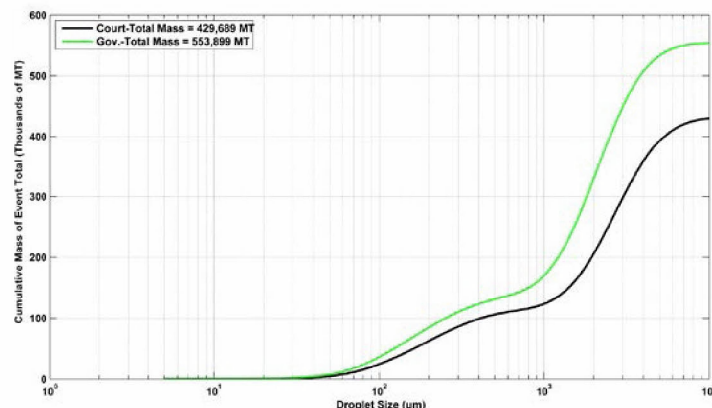


Figure 12. Cumulative droplet size distributions in terms of mass for the entire spill event for the court and OBC total release volumes. Note the x-axis is logarithmic.

2.6 Updated SPT File

The new droplet size distributions and associated mass based on the court flow volume estimate were used to make new SPT files. The plume trap height (and ‘z’ positioning within the water column) was not updated due to the insignificant difference from the OBC estimate. A random lateral positioning of the droplets within a specified radius at the trap height was implemented for initializing the oil droplets within the water column. Droplets were positioned within a 130 m radius from the kink and 180 m radius from the riser; these radii were based on an estimate of the end of the near field intrusion based on Fannelop and Sjoen (1980) as two times the plume radius at trap height where the average plume radius for the kink and riser were 65 m and 90 m, respectively.

3. Summary

The key findings of this analysis are as follows:

- The court specified spill volume released to the water column is approximately 22 % lower than the amount from prior simulations based on OBC estimates. The amount of oil recovered is very similar for both court specified and OBC estimates.
- The lower volume release rate in the court specified volume leads to a reduction in the trap height of about 40 m (12% of the OBC estimate). This is within the uncertainty of analysis of field CDOM data used to experimentally determine the trap height.
- The cumulative oil droplet size distribution based on the court specified volume flow rate shows generally larger sizes than the OBC based estimate above 800 μm and directly attributable to the increase in droplet size for the untreated oil. Below 800 μm the distributions are very similar.
- The cumulative fraction vs droplet size analysis shows that the droplet size distributions are very similar for both the court and OBC volumes. The differences are typically on the order of a few percent. The most substantial difference between the two is simply due to the differences in release volumes.

4. References

- Lehr, B., S. Bristol and A. Possolo. 2010. Deepwater horizon oil budget calculator: A report to the national incident command. The Federal Interagency Solutions Group, Oil Budget Calculator Science and Engineering Team. http://www.restorethegulf.gov/sites/default/files/documents/pdf/OilBudgetCalc_FullHQ-Print_111110.pdf (Accessed on April 1, 2012).
- Spaulding, M., D. Mendelsohn, D. Crowley, Z. Li, and A. Bird. 2015. Technical Reports for Deepwater Horizon Water Column Injury Assessment – WC_TR.13: Application of OILMAP DEEP to the Deepwater Horizon Blowout. RPS ASA, 55 Village Square Drive, South Kingstown, RI 02879, August 2015.
- USDC. 2015. The U.S. District Court for Eastern District of Louisiana, Case 2:10-md-02179-CJB-SS Document 14021 Filed 01/15/15, Findings of fact and conclusions of law phase two trial. Pp 1-44. (<http://www2.epa.gov/sites/production/files/2015-01/documents/phase2ruling.pdf>)
- Zick, A. 2013. Equation of state fluid characterization and analysis of the Macondo reservoir fluids, Expert report in matter of US vs BP Exploration & Production, Inc. et al, submitted to the US Department of Justice, March 22, 2013.

Technical Reports for Deepwater Horizon Water Column Injury Assessment

WC_TR.13: Application of OILMAP DEEP to the Deepwater Horizon Blowout

Appendix A: Release Configuration Report

Authors: Malcolm Spaulding, Daniel Mendelsohn, Deborah Crowley,
Zhengkai Li, Andrew Bird

Revised: September 30, 2015

Project Number: 2011-144

RPS ASA 55 Village Square Drive, South Kingstown, RI 02879

Table of Contents

A1.	Introduction	1
A1.1.	DWH Spill Event Overview and Timeline	1
A2.	Release Configuration Details	4
A2.1.	Baseline Configuration.....	5
A2.2.	Release Configuration 1 (RC1): Release from end of broken riser only (April 22, 2010 through April 28, 2010)	7
A2.3.	Release Configuration 2 (RC2): Release from end of broken riser and kink (April 28, 2010 through June 3, 2010).....	8
A2.4.	Release Configuration 3 (RC3): Riser flow only, post riser cut (June 3, 2010 through June 4, 2010 & July 10, 2010 through July 1, 2010)	15
A2.5.	Release Configuration 4 (RC4): Riser flow only, post cut, with top hat (June 13, 2010 through July 10, 2010)	18
A2.6.	Release Configuration 5 (RC5): Post riser cut, flange removed (July 11, 2010)	21
A2.7.	Release Configuration 6 (RC6): Transition spool flow (July 11, 2010 through July 12, 2010)	22
A2.8.	Release Configuration 7 (RC7): Three ram capping stack - main flow (July 12 through July 14, 2010)	23
A2.9.	Release Configuration 8 (RC8): Three ram capping stack –valve flow (July 14, 2010) 24	
A3.	References	26

List of Figures

Figure A-1: Illustration of release locations: well head and end of broken riser.	4
Figure A-2: Illustration of DWH Blow Out Preventer (BOP) stack (Transocean 2011).	6
Figure A-3: Graphic showing flow from riser indicating main leak, modified from (FRTG, 2010).	7
Figure A-4: Images showing the end of the riser pipe, left image showing riser pipe with oil flowing, right image shows end of riser with no oil flowing (FRTG 2010).	7
Figure A-5: Left image shows riser pipe outlet with oil flowing highlighting its reduced cross sectional area, right image shows end of broken riser with no oil flowing (FRTG 2010).	8
Figure A-6: Riser kink overview modified from FRTG (2010).	9
Figure A-7: Time history of the number of holes in the vicinity of the kink from the start of the spill on April 22, 2010. The inserts show the ROV imagery that supports the estimates for the number of holes.	10
Figure A-8: Visible number of holes at the riser kink (blue) as a function of time. Magenta vertical lines indicate visually confirmed holes forming, red vertical line indicates riser cut.	11
Figure A-9: Labeled image mosaic of kink holes (A, B, C, D, E and F) at riser kink, bottom of image towards BOP. Images were taken at the NASA Michoud facility in New Orleans, LA. (Photos courtesy of Andrew Bird, May 2012).	11
Figure A-10: Gray scale kink hole (A) field drawing (left) from USCG (U.S. Coast Guard 2010), black and white binary image (right).	12
Figure A-11: Time series of kink equivalent diameter and cross sectional area.	14
Figure A-12: Riser insertion tube (RITT), modified from Energy (2012) (Riser Insertion Tube).	14
Figure A-13: Riser flange images, side view (left), top view (middle), side view (right).	15
Figure A-14: Flange section 1 (left), flange section 2 (right).	16
Figure A-15: Calculated cross sectional areas for sections 1 and 2 using pixel/inch length.	17
Figure A-16: Calculated cross sectional areas for sections 1 and 2 using pixel/inch length, includes fitted circle estimates.	17
Figure A-17: Top hat (left) with dimensions, (right) side view of a cross section of top hat on riser adapter flange (Energy 2010).	18
Figure A-18: Top down view, cross section of top hat on riser flange (Energy 2010).	19
Figure A-19: Screen shot captured from ROV video showing bottom of the top hat, section of rubber gasket missing on right side of image, section of rubber gasket present on left side of image (Maxx3 June 11, 2010).	20
Figure A-20: RC5, riser adapter with the flange removed. Photograph from Millennium 21 ROV, July 11, 2010.	21
Figure A-21: Sealing cap installation overview (BP 2010).	23
Figure A-22: Top of three ram capping stack, observed flow in image center is from capping stack mandrel. Photograph from Millennium 42, July 13, 2010.	24

Figure A-23: Valve on top of three ram capping stack, observed flow (left, Photo from Millennium 21 July 14, 2010), side view no flow (middle, Photo from Millennium 22 July 15, 2010), top view no flow (right, Photo from Millennium 22 July 15, 2010).25

List of Tables

Table A-1. DWH spill event timeline broken into phases for NRDA analysis.	2
Table A-2. Coordinates of release locations used in the spill simulations.	4
Table A-3. Summary of key depths.	5
Table A-4. Area and release depth of RC1.....	8
Table A-5. Calculated riser kink hole final areas using binary images.	13
Table A-6. Area and release depth of RC2.....	15
Table A-7. Area and release depth of RC3.....	18
Table A-8. Area and release depth of RC4.....	20
Table A-9. Area and release depth of RC5.....	22
Table A-10. Area and release depth of RC6.....	23
Table A-11. Area and release depth of RC7.....	24
Table A-12. Area and release depth of RC8.....	25

A1. Introduction

This appendix contains a summary of the various oil release and treatment configurations observed during the Deepwater Horizon (DWH) spill event release in support of modeling and assessment of the spill. This appendix also includes a timeline of events throughout the spill, broken into phases characterized by similarity in release conditions, both physical and operational. It provides details of the physical configuration during these phases, including a description of the basis for use of pertinent modeling parameters values. This appendix is intended to serve as a reference for the main text of the report and other appendices documenting the analysis performed in support of the NRDA.

A1.1.DWH Spill Event Overview and Timeline

The DWH spill event started with an explosion of the DWH drilling rig located above the Macondo Well in the Mississippi Canyon Block 252 in the Gulf of Mexico. The explosion occurred on April 20, 2010, after which point the rig sank, damaging the riser pipe, which was the main connection between the drilling rig and the oil and gas reservoir through a series of mechanical apparatus close to the sea bottom. Subsequent to the collapse and settling of the riser pipe it was determined through ROV inspection that oil was leaking from the well through the damaged riser. Over the course of the 87 days, following the initial explosion, the source of the leak varied in position, volume flow, and exit orifice configuration(s); furthermore the response operations over this period also varied including attempts at mitigation, collection, and subsurface dispersant application. For modeling purposes, the release configurations were grouped into phases, reflecting relatively constant release physical characteristics, hereafter referred to as Release Configuration Phases. The response and operational conditions generally tracked the release configuration phases, though were not completely synoptic.

Table A-1 contains a summary of the different phases of the DWH spill event, denoting the relevant Release Configuration Phase as well as the various operational conditions that took place during the phase. Details of the different release configurations are documented in later sections of this appendix.

In addition to the release and operational variability, the observed conditions varied throughout the spill event. Analysis of the water column chemistry data from the event (Horn et al. 2015) did show that there were different intervals of time with similar observed conditions; these intervals are hereafter referred to as the Observed Chemistry Intervals.

Table A-1 also includes the appropriate Observed Chemistry Interval (OCI) for the various event phases. Figure A-1 illustrates the location of the different release sites, and Table A-2 summarizes the coordinates of the locations of the release points used in the NRDA. The location of the wellhead along with the two different leak points (end of broken riser and kink above the blowout preventer (BOP)) were illustrated in a figure, originally from BP, documented in a report dedicated to flow estimations by the Flow Rate Technical Group (FRTG 2010). Based on that schematic and coordinates provided by the NOAA response team (Beegle-Krause 2010) regarding the location, it was determined that the kink above the BOP and the cut riser had the same coordinates as the wellhead and that the release from the end of the broken riser was located approximately 210 m northwest of the wellhead.

Table A-1. DWH spill event timeline broken into phases for NRDA analysis.

Phase	Start Date (mm/dd/yyyy) (HH:MM)	End Date (mm/dd/yyyy) (HH:MM)	Days	Description	Release Config. Phase	Operational: Collection	Operational: Subsea Dispersant	Observed Chemistry Interval
1	4/20/2010	4/20/2010	-	Explosion at Rig	-	-	-	-
2	4/20/2010	4/22/2010	2	Rig sinks, damaging riser	-	-	-	-
3	4/22/2010	4/28/2010 15:33	6	Leak from end of broken riser only	RC1	-	-	OCI 1
4	4/28/2010 15:33	5/26/2010	28	Release from end of broken riser & Kink	RC2	RITT collection small volumes, typ. < 5,000 bbl/day	wand at riser, highly variable use and volume	OCI 1
5	5/26/2010	5/29/2010	3	Release from broken riser & kink, Top Kill	RC2	none	-	OCI 2
6	5/29/2010	6/3/2010 9:05	5	Release from broken riser and kink. Cutting operations	RC2	none	wand at the riser, consistent use, variable volumes	OCI 2
7	6/3/2010 9:05	6/4/2010	1	Riser flow only, post riser cut	RC3	none	-	OCI 2
8	6/4/2010	6/6/2010	3	Riser flow only, post cut, Tophat #4	RC4	consistent use, volume ramped up to ~11,000 bbl/day	Predominantly single wand, consistent use, variable large volumes	OCI 2
9	6/6/2010	6/13/2010	7	Riser flow only, post cut, Tophat #4	RC4	consistent use, at ~ 15,000 bbl oil/day	Predominantly single wand, highly variable volumes	OCI 3
10	6/13/2010	7/10/2010 12:35	27	Riser Flow only, post cut, Tophat #4	RC4	steady, increases to ~ 22,000 bbl/day	Predominantly two- pronged applicator, consistent use & volumes	OCI 3

Phase	Start Date (mm/dd/yyyy) (HH:MM)	End Date (mm/dd/yyyy) (HH:MM)	Days	Description	Release Config. Phase	Operational: Collection	Operational: Subsea Dispersant	Observed Chemistry Interval
11	7/10/2010 12:35	7/11/2010 02:50	<1	Riser Flow only, post cut, Tophat Removed	RC3	decreases ~10,000 bbl/day	Hooked wand in riser, dispersant volume high	OCI 3
12	7/11/2010 02:50	7/11/2010 14:32	<1	Riser Flow only, post cut, no flange	RC5	~8,000 bbl/day	Hooked wand in riser, dispersant volume high	OCI 3
13	7/11/2010 14:32	7/12/2010 18:17	<1	Riser Flow only, post cut, Transition spool	RC6	~8,000 bbl/day	Hooked wand in riser, dispersant volume high	OCI 3
14	7/12/2010 18:17	7/14/10 17:00	<2	Riser Flow only, post cut, capping stack	RC7	~16,000 bbl/day	Hooked wand in riser, dispersant volume high	OCI 3
15	7/14/10 17:00	7/15/2010 14:27	<1	Riser Flow only, post cut, capping stack	RC8	-	-	OCI 3
16	7/15/2010 14:27	-	-	Oil Ceases To Flow	-	-	-	OCI 3
17	After 7/15/2012	-	-	Post cap observation	-	-	-	OCI 4

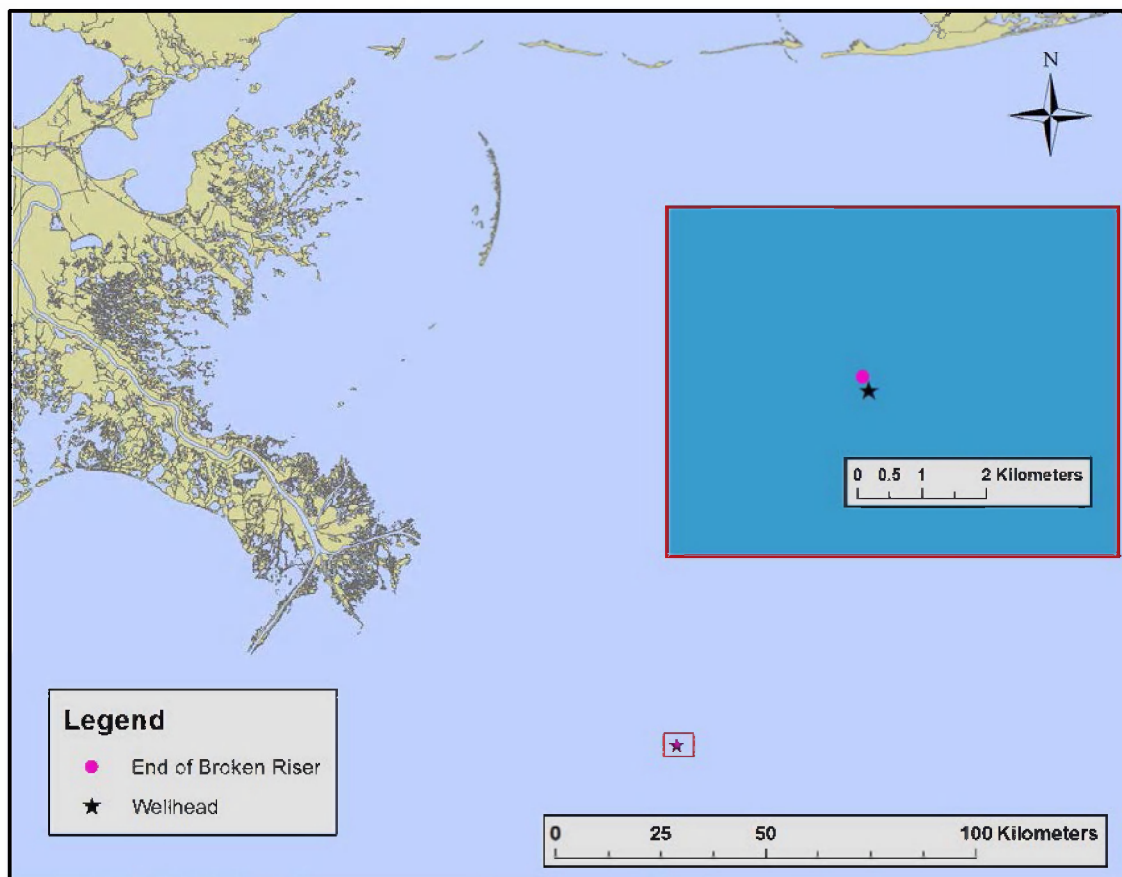


Figure A-1: Illustration of release locations: well head and end of broken riser.

Table A-2. Coordinates of release locations used in the spill simulations.

Location ID	Location	Latitude (N)	Longitude (W)	Water Column Depth (meters)
2	Well	28.73814	88.3569453	1,523
2	Kink - Above BOP	28.73814	88.3569453	1,503
1	End of Broken Riser	28.74002144	88.36686178	1,509
2	Cut Riser	28.73814	88.3569453	1,505

A2. Release Configuration Details

In order to assess the impact of the spill event, it is necessary to adequately characterize the conditions of the initial release of oil and gas as these have a large influence on the ultimate fate and transport of oil and gas within the marine environment. Ultimately, the initial release is characterized in terms of the amount of oil mass released to the water column in different droplet size increments (bins) at the appropriate position (latitude, longitude, depth) in the water column. The parameters that have the largest influence on this initial characterization, outside the volume of release of oil and gas, are the release orifice dimensions, and the dispersant

treatment effectiveness which is largely dependent on the dispersant injection configuration. The dispersant injection configuration is defined by the geometry of the dispersant applicator and the physical characteristics of its application near the injection point, including obstacles which affect the flow in this nearfield area. The physical conditions (position and dimensions) of the release have been determined either through available information or developed through methodologies documented in this appendix. The following sections detail the baseline configuration and eight different release configurations that occurred over the course of the spill event.

A2.1. Baseline Configuration

There were multiple mechanical structures associated with the wellhead including the BOP, lower marine riser package (LMRP), and the riser pipe as well as many extensions, flanges, joints, and adapters. General information on the configuration of these major pieces is provided for background. In simplified form, oil and gas travel through an underground conduit, through the BOP and LMRP and eventually the riser pipe which is attached to the LMRP via the riser adapter. Figure A-2 illustrates the system from the wellhead connection point (at the seabed) to the riser adapter. Table A-3 summarizes the depths for the different features relative to the water surface.

Table A-3. Summary of key depths.

Location	Depth (ft.)	Depth (m)
Seabed	4,996.0	1,522.8
Height from Wellhead Connector to Riser Adapter	53.75	16.4
Depth to Riser Adapter	4,942.3	1,506.4

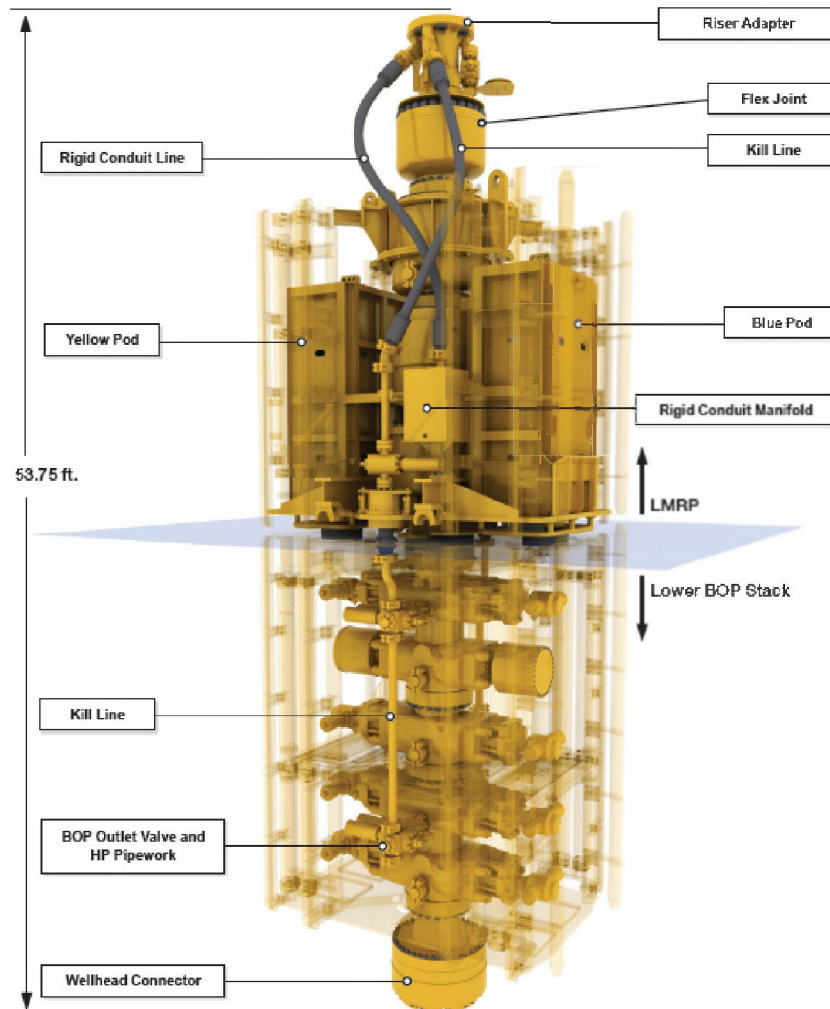


Figure A-2: Illustration of DWH Blow Out Preventer (BOP) stack (Transocean 2011).

A2.2. Release Configuration 1 (RC1): Release from end of broken riser only (April 22, 2010 through April 28, 2010)

Release Configuration Details: Release Location

The explosion and sinking of the DWH rig on April 22 caused the riser pipe to descend to the ocean bottom and break the riser connection to the DWH rig. This caused the riser to fall to the sea floor, however the riser did not simply lay flat on the seabed, rather it buckled and bent in places such that bumps were formed that were positioned at different elevations relative to the sea floor with some sections submerged within the sediments. The riser pipe extended away from the BOP to the sea floor leaving a kink at the BOP riser adapter just above the BOP flex joint (Figure A-3). During RC1, the release of oil and gas was primarily observed from the end of the broken riser pipe, which was partially submerged in the sediment and therefore at a depth equal to the water column depth of 1,513 m (4,963.9 ft) at this location.

Another point of flow was observed along the broken riser between the BOP stack and the main leak point. This release was substantially smaller than the main leak and was caused from a protruding drill. The leak was subsequently capped on May 5, and was deemed negligible in comparison to the main leak, and as such was not explicitly treated as a separate source. Images of the broken end of the riser both with and without flow are shown in Figure A- 4.

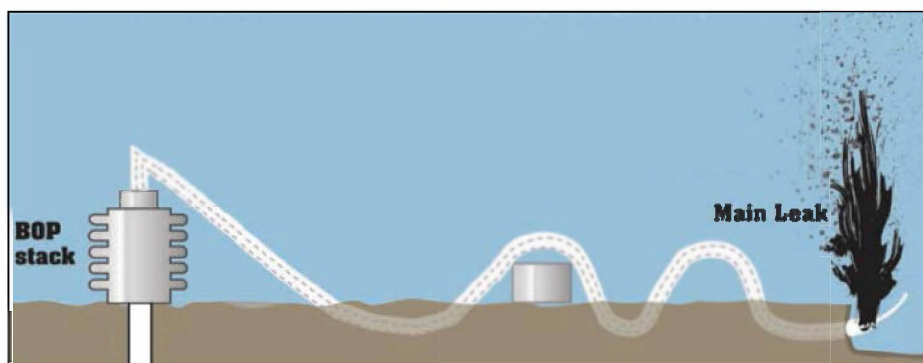


Figure A-3: Graphic showing flow from riser indicating main leak, modified from (FRTG, 2010).



Figure A-4: Images showing the end of the riser pipe, left image showing riser pipe with oil flowing, right image shows end of riser with no oil flowing (FRTG 2010).

Release Configuration Details: Release Cross Sectional Area

Numerous cross sectional area analyses were performed on the end of the riser as part of the Flow Rate Technical Group report (FRTG 2010). The report included appendices from various sources that approximate the cross sectional area of the broken riser pipe, ranging from 150 in² (0.096 m²) to 214 in² (0.138 m²). Figure A-5 below shows two images used in the cross sectional area estimation in the FRTG report. The main text of the FRTG report specifies a cross sectional area of 214 in² (0.138 m²). This value was used in this assessment to represent the cross sectional area of the end of the broken riser pipe. Table A-4 summarizes the details of this release configuration.

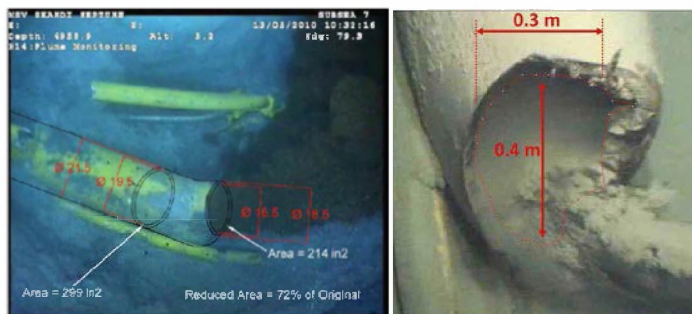


Figure A-5: Left image shows riser pipe outlet with oil flowing highlighting its reduced cross sectional area, right image shows end of broken riser with no oil flowing (FRTG 2010).

Table A-4. Area and release depth of RC1.

Release Configuration	Cross sectional area in ²	Cross sectional area m ²	Depth (ft)	Depth (m)
RC1	214	0.138	4,950.8	1,509

A2.3.Release Configuration 2 (RC2): Release from end of broken riser and kink (April 28, 2010 through June 3, 2010)

Release Configuration Details: Release Location

On April 28 oil and gas was observed flowing from a location just above the BOP riser adapter, at the point where the riser had kinked. Due to this additional release, oil and gas was now flowing from two locations, the end of the broken riser and the kink. This configuration is illustrated in Figure A-6. The height of the kink release above the riser adapter was estimated to be approximately 2 m (6.56 ft), therefore the release depth of the kink flow was approximately 1,503 m (4,931 ft).

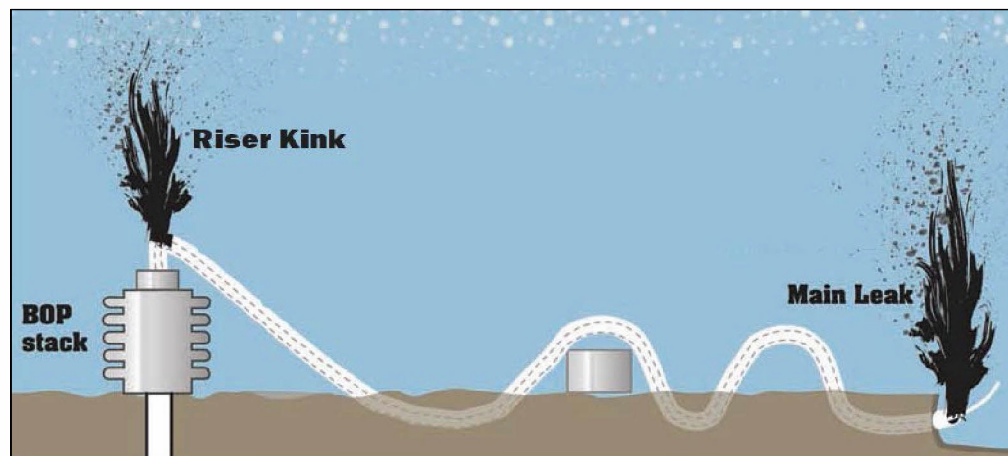


Figure A-6: Riser kink overview modified from FRTG (2010).

Release Configuration Details: Release Cross Sectional Area

The kink leak was first observed through two holes on April 28 with the number of holes and total cross sectional area of the kink release increasing with time. The flow from these kink holes was monitored by numerous ROV's. The imagery captured the evolution of multiple holes until the riser was subsequently cut (below the kink). The cutting operations on the kink began on June 1 and ended on June 3. An overview of the relative change in the kink flow created from ROV imagery stills is shown in Figure A-7. Figure A- 8 displays a time series plot of the number of visible kink holes. The number of holes shown in Figure A-8 was determined from an analysis of over 140 time periods and image stills from ROV video data. The final number of holes determined from the video analysis on June 3, just prior to the cut, was six. This number was confirmed as the maximum number of holes both in a report by the United States Coast Guard (USCG) (U.S. Coast Guard 2010), as well as visual inspection of the recovered cut section of riser, at the evidence yard at the NASA Michoud facility in New Orleans, Louisiana by RPS ASA in May 2012. Figure A-9 displays a labeled image mosaic of the riser kink holes obtained from the RPS ASA visit to the evidence facility. The alphabetized kink hole labeling is consistent with the kink hole labeling in the USCG report (U.S. Coast Guard 2010).

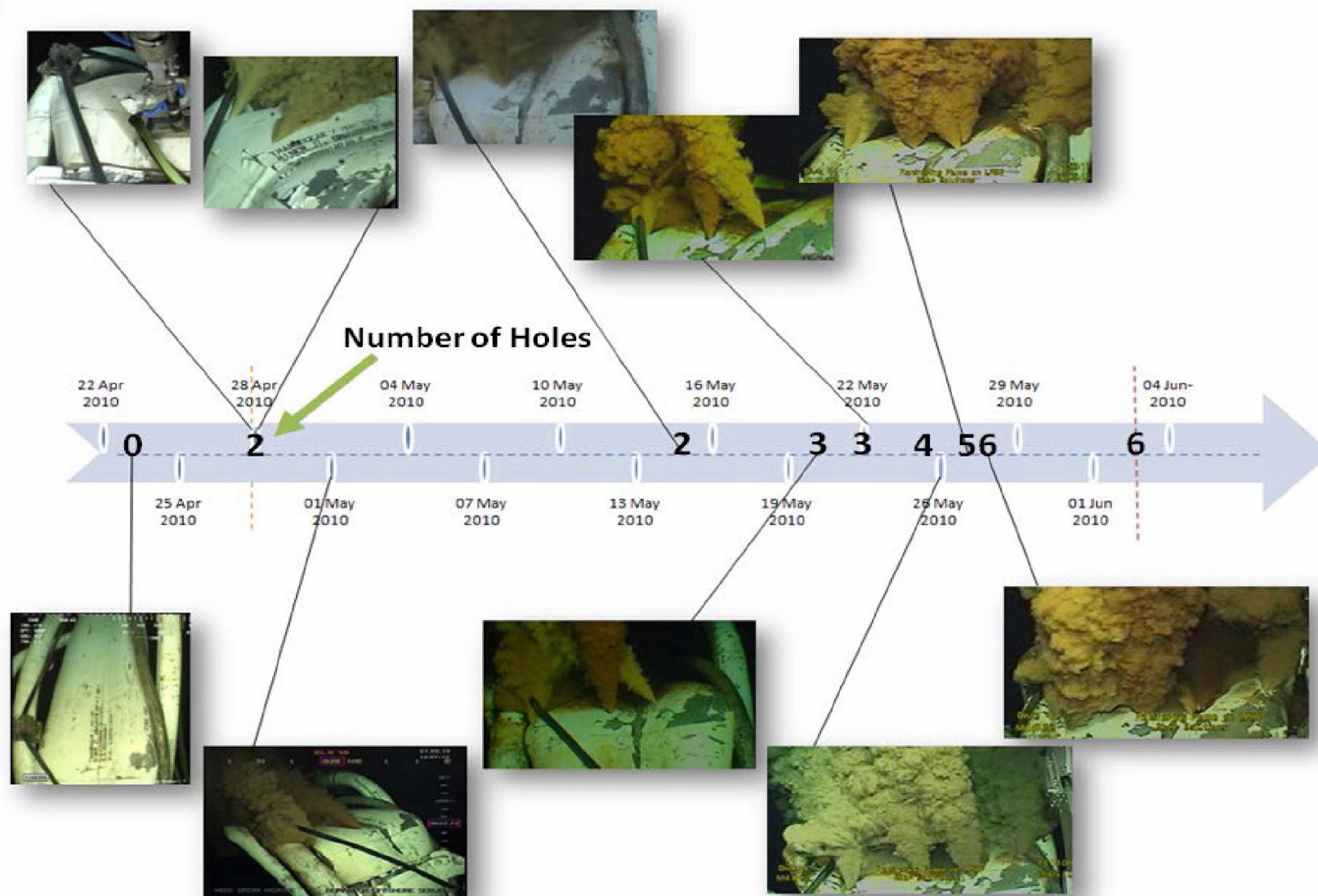


Figure A-7: Time history of the number of holes in the vicinity of the kink from the start of the spill on April 22, 2010. The inserts show the ROV imagery that supports the estimates for the number of holes.

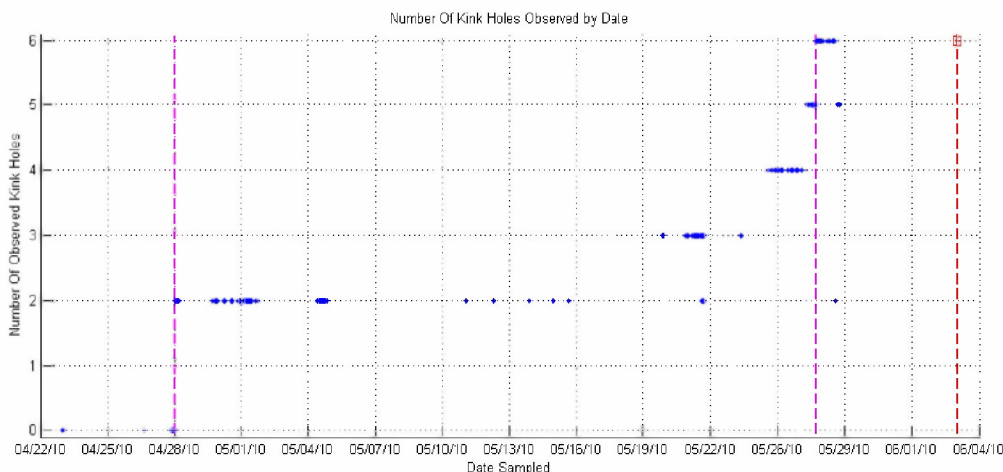


Figure A-8: Visible number of holes at the riser kink (blue) as a function of time. Magenta vertical lines indicate visually confirmed holes forming, red vertical line indicates riser cut.

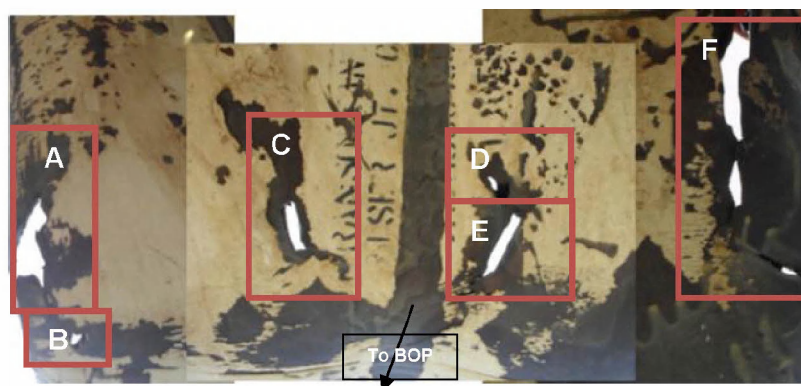


Figure A-9: Labeled image mosaic of kink holes (A, B, C, D, E and F) at riser kink, bottom of image towards BOP. Images were taken at the NASA Michoud facility in New Orleans, LA. (Photos courtesy of Andrew Bird, May 2012).

As a result of the increase in number of holes at the riser kink, the cross sectional area at the kink increased as well. The video evidence record of the kink did not allow for measurement of the kink hole sizes; however the final cross sectional area was obtained from imagery taken at the NASA Michoud facility of the kink holes. The final area for the individual kink holes was obtained through common image processing and analyses techniques. Each individual kink hole field drawing provided in the USCG report (U.S. Coast Guard 2010) was transcribed on $\frac{1}{4}$ inch (0.00635 m) square graph paper. The advantage to this approach was that the scale along with the kink boundary was preserved. By converting each of the individual kink hole field drawings to black and white (binary) images, the boundary edge for each hole was extracted and used to create a filled binary image (Figure A-10). The binary image was created by first creating a

grayscale copy. The grayscale image then has an automatic threshold applied to create the binary image. A reference scale was computed by first sampling the number of pixels for the scale grid, $\frac{1}{4}$ inch (0.00635 m), and then multiplying it by 4 (per inch) for each of the kink hole images. The mean number of pixels from the sampled lengths was used to create a relative pixel/inch scale. By combining this with the binary image created, an estimate of the cross sectional area was calculated for each kink hole.

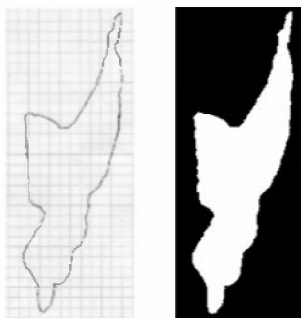








Figure A-10: Gray scale kink hole (A) field drawing (left) from USCG (U.S. Coast Guard 2010), black and white binary image (right).

Table A-5 provides the maximum cross sectional areas for each of the kink holes identified in Figure A-9 estimated using the image processing approach described above. While there is ROV video evidence that indicated that the kink holes evolved (grew) over time, there was insufficient information to estimate the progression of hole growth. Therefore the cross sectional area at any given time was estimated to be equal to the final hole size of each of the kink holes. Figure A-11 illustrates the total cross sectional area, as well as equivalent diameter of the cross sectional area if it were to be represented as a singular circular hole, as a function of time during this release period.

Table A-5. Calculated riser kink hole final areas using binary images.

Hole	Sample Binary Image	Area Estimate (in ²)	Mean pixels per inch	Standard deviation of sampled pixel lengths
A		7.81	77.97	1.28
B		0.61	69.92	1.85
C		0.74	69.59	1.29
D		0.39	70.19	2.08
E		0.82	69.86	1.52
F		4.23	78.38	1.44

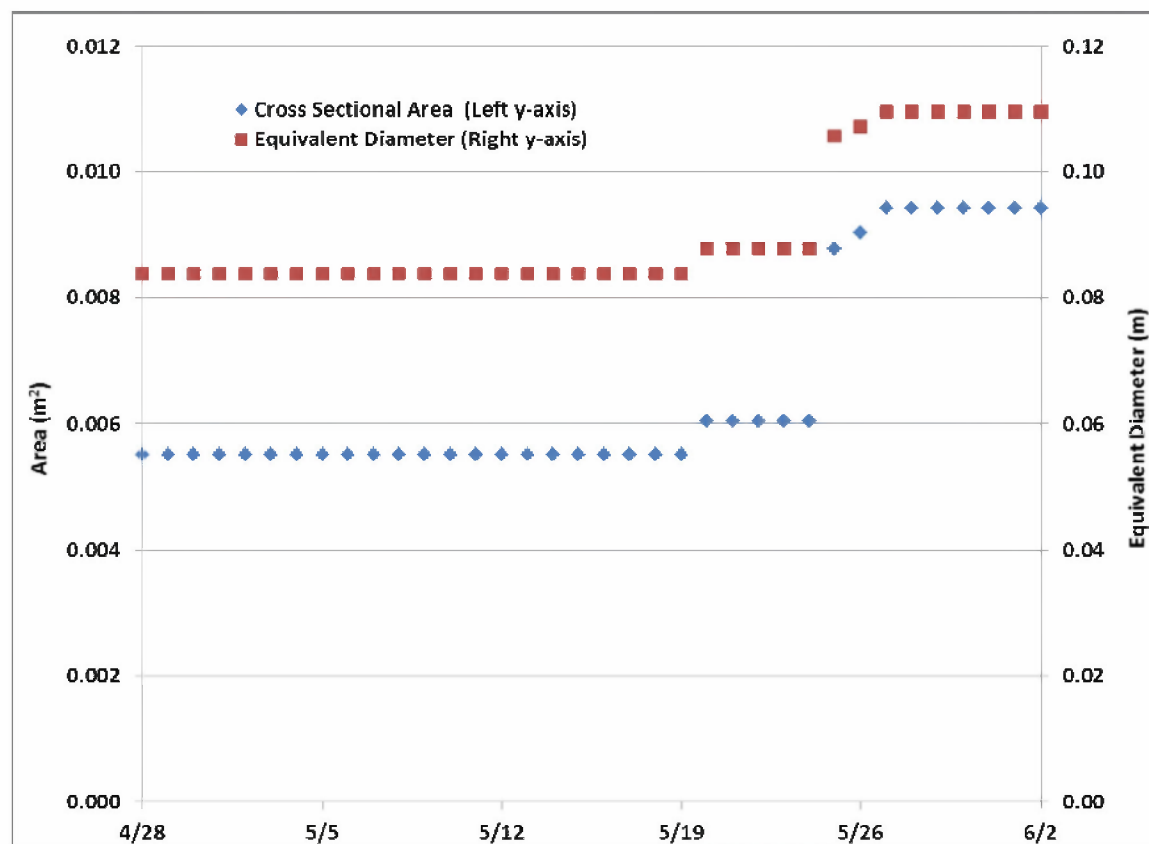


Figure A-11: Time series of kink equivalent diameter and cross sectional area.

Operational: Collection

While the release was in this configuration, the collection operations began through use of the Riser Insertion Tube (RITT). The riser insertion tube (RITT) was first inserted into the riser on May 16, 2010 to collect hydrocarbons coming from the broken riser pipe. Figure A-12 shows the RITT in position within the riser, as well as an outline to its operation. The use of the RITT was intermittent and furthermore had negligible impact on the open cross sectional area of the release. The impact of collection was accounted for in the reduction of flow of oil and gas from the riser.

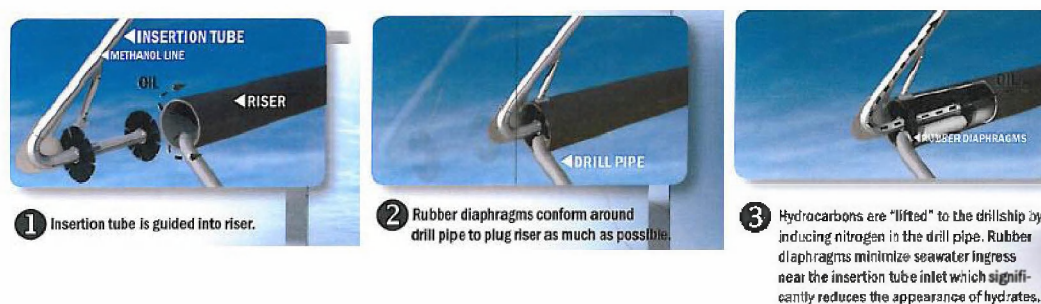


Figure A-12: Riser insertion tube (RITT), modified from Energy (2012) (Riser Insertion Tube).

Operational: Dispersant

This release configuration also included dispersant application utilizing the dispersant wand. The dispersant wand was held next to the riser flow by a ROV.

Table A-6 summarizes the details of this release configuration.

Table A-6. Area and release depth of RC2.

Release Configuration	Cross sectional area in ²	Cross sectional area m ²	Depth (ft)	Depth (m)
RC2	14.6 (kink Holes)	0.0094 (kink Holes)	4,931.1	1,503
	214 (RC 1)	0.138 (RC 1)	4,950.8	1,509

A2.4.Release Configuration 3 (RC3): Riser flow only, post riser cut (June 3, 2010 through June 4, 2010 & July 10, 2010 through July 1, 2010)

This configuration was in operation at two different times, in both instances for approximately one day. The first time was just after the riser cutting operations ceased, and the second time was in between different containment configurations (between top hat and Transitional Spool).

Release Configuration Details: Release Location

The release from this location was from the cut riser, at a location just above the riser adapter. The height of the cut above the riser adapter was small and therefore the release depth was simulated at 1,506.4 m (4,942.3 ft) below the surface outlined in Table A-7.

Release Configuration Details: Release Cross Sectional Area

The cross sectional area of the post cut riser was obtained from direct observations at the NASA Michoud facility and from information available in the FRTG report (FRTG 2010). A number of the images were captured at the facility and used to obtain the cross sectional area of the cut section of riser above the BOP. The cutting operations resulted in an obstruction of the deformed, partially sheared riser pipe from a previous cut attempt, which can be seen in Figure A-13. As the obstruction spans the entire width of the flange opening a cross sectional area for each side of the obstruction was obtained and combined to create a total cross sectional area. Each labeled section of the cut flange can be seen in Figure A-14.

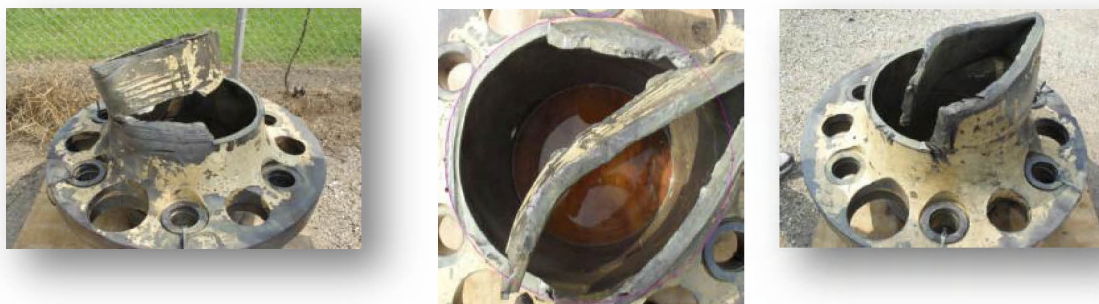


Figure A-13: Riser flange images, side view (left), top view (middle), side view (right).

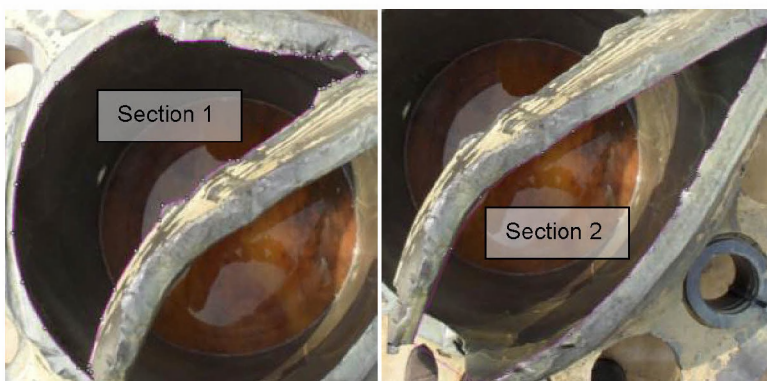


Figure A-14: Flange section 1 (left), flange section 2 (right).

The cross sectional area of the cut just above the flange was estimated using two methods, both used a captured top-down image (Figure A-13 (top view, middle)) of the riser flange and image processing techniques. The first method used sampled pixel lengths of the flange known to be 1 inch (0.0254 m) thick (U.S. Coast Guard 2010) sampled from the top down image to create a pixel/inch scale which was subsequently used to estimate the cross section area of both sections. Figure A- 15 shows the extracted per pixel length, along with an estimated cross section area of each section, and the total estimated cross sectional area. The variation in sampled pixel/inch lengths is due in part to the flange geometry and the obstruction on a portion of the flange edges.

The second method used to estimate the cross sectional area utilized the outside diameter (OD = 21.5 in (0.5461m)) and inside diameter (ID = 19.5 in (0.4953m)) riser pipe estimates obtained from the FTRG report (FRTG, 2010) to estimate additional unit pixel lengths based on circles fitted to the top down image of the riser pipe (Figure A-13). One circle was fit to the best estimate of the curvature of the OD of the riser pipe, and another circle was fit the best estimate of the curvature of the ID of the riser pipe. By using the aforementioned riser geometry a cross sectional area for both sections of the obstructed riser flange could be estimated using the pixel/inch scale obtained from the overlaid circles. Figure A-16 displays the cross sectional area estimates previously shown in Figure A-15, with the addition of the cross-sectional areas estimates for both sections 1 and 2 using the relative scale obtained from the fitted circles. The total mean cross sectional area based on data from both methods for sections 1 and 2 is 245.3 in² (0.1583 m²), with a standard deviation of 24 in² (0.0155 m²). Based on this analysis the final estimate of cross sectional area of the post cut riser was 245.3 in² (0.1583 m²) which has a corresponding equivalent diameter of 0.449 m (1.473 ft).

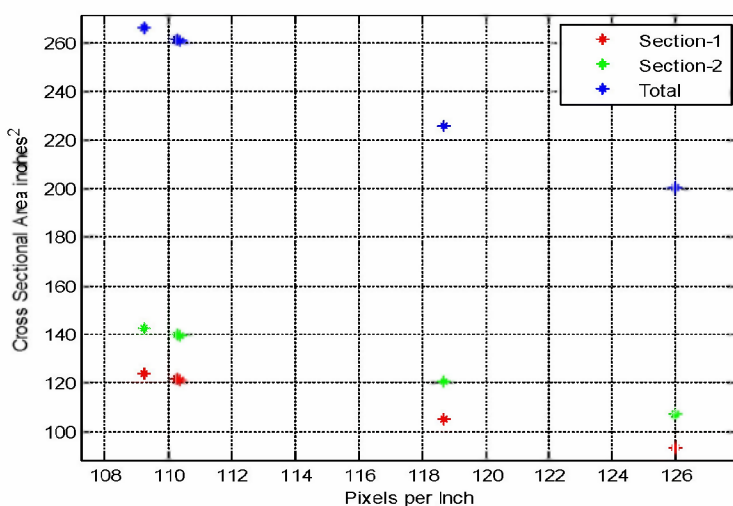


Figure A-15: Calculated cross sectional areas for sections 1 and 2 using pixel/inch length.

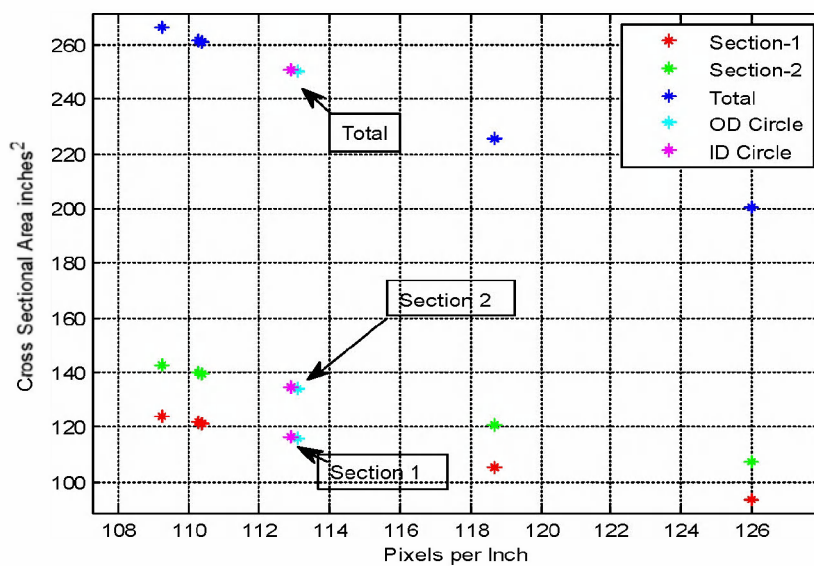


Figure A-16: Calculated cross sectional areas for sections 1 and 2 using pixel/inch length, includes fitted circle estimates.

Operational: Collection

There was no oil collection during this release configuration phase for the first time period (June 3, 2010), however there was collection during the second time period (July 11, 2010) when this configuration was in place.

Operational: Dispersant

Records of daily subsurface dispersant volumes (Appendix B) indicated that dispersants were discharged during both time periods of this release configuration. There is insufficient video evidence to determine the dispersant application method for the June 3, 2010 to June 4, 2010 period. The July 10, 2010 to July 11, 2010 periods however utilized the hooked dispersant wand.

Table A -7 summarizes the details of this release configuration.

Table A-7. Area and release depth of RC3.

Release Configuration	Cross sectional area in ²	Cross sectional area m ²	Depth (ft)	Depth (m)
RC3	245.3	0.158	4,942.3	1,506.4

A2.5.Release Configuration 4 (RC4): Riser flow only, post cut, with top hat (June 13, 2010 through July 10, 2010)

Release Configuration: Release Location

This release configuration reflects the period post riser cut where the flow mitigation apparatus top hat was in place.

The top hat (top hat #4) was placed over the riser flange on the BOP in an attempt to collect some portion of the oil flowing from the cut riser. Figure A-17 illustrates top hat dimensions (left) as well as a cross section of the installed top hat over the riser (right).

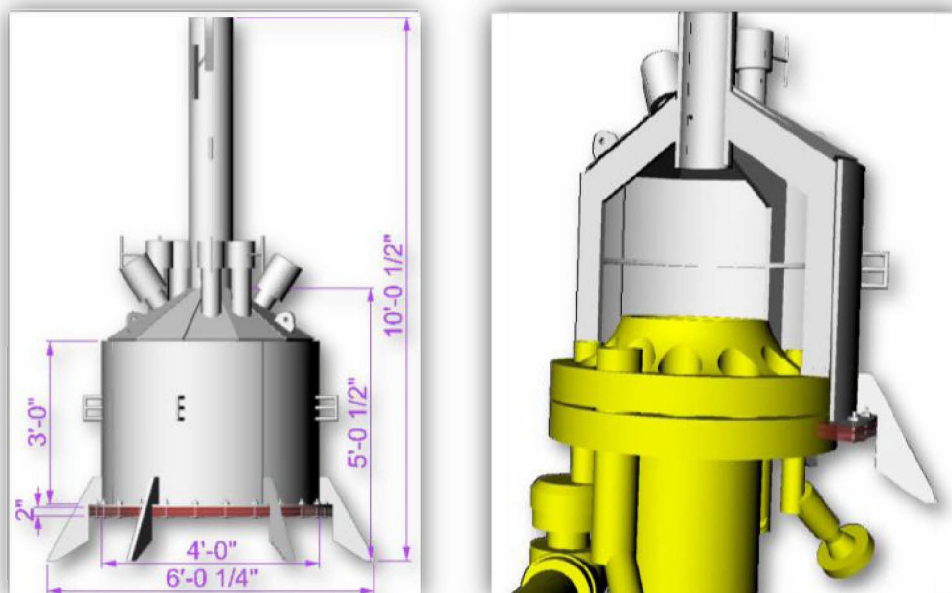


Figure A-17: Top hat (left) with dimensions, (right) side view of a cross section of top hat on riser adapter flange (Energy 2010).

Release Configuration: Cross Sectional Area

During this time period the oil and gas flowed out the cut riser (characteristics as defined in RC 3). Just above the release, a portion of the flow was captured and collected via the collection pipe at the apex of the top hat. The remaining oil and gas was forced down and out through the bottom seal between the outer riser flange and the top hat rubber gasket. The top hat was designed to be placed on top of the cut riser, with the bottom of the top hat surrounding the riser flange. From the available CAD drawings of the top hat (Energy 2010) it is known that the top hat was designed with a few interior sections with a smaller diameter. The sections within the interior of the top hat are believed to have aided in stabilizing the top hat, keeping it in place on the riser flange (Figure A-18).

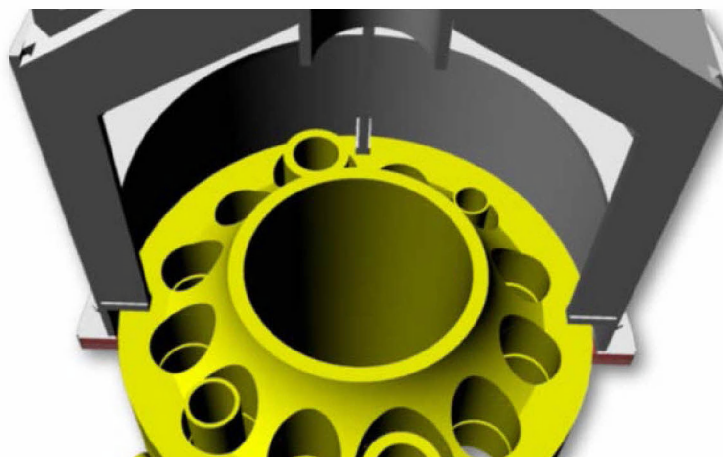


Figure A-18: Top down view, cross section of top hat on riser flange (Energy 2010).

The measurements obtained from the work conducted as part of the FRTG analysis (FRTG 2010) indicated that the OD of the outermost portion of the riser flange is 43 in (1.1 m). The top hat was aligned over the riser, with an ID of 46.5 in (1.181 m). This configuration results in a gap between the OD of the riser and the ID of the top hat. The gap was filled with two rubber gaskets that were stacked on top of each other and mounted to the bottom of the top hat, designed to create a seal between the riser OD and the top hat ID. The gaskets had an OD of 54 in (1.372 m) that was larger in diameter than the rest of the top hat (Figure A-17 (right)), which was 48 in (1.2191 m) and an ID of 41 in (1.04 m). The ID of the gasket is larger than the OD of the riser and therefore the gasket fit was based on this geometry mismatch which would cause the gasket to deflect to create the desired seal. Figure A-19 was captured by the Maxx3 ROV on June 11, approximately eight days after the top hat was installed. The image shows both a section of the bottom of the top hat with and without the presence of the rubber gasket. Due to the lack of visibility of the top hat caused by the flow of oil along the side of the top hat, estimating an approximate cross sectional area based on the presence of the gasket is not possible.

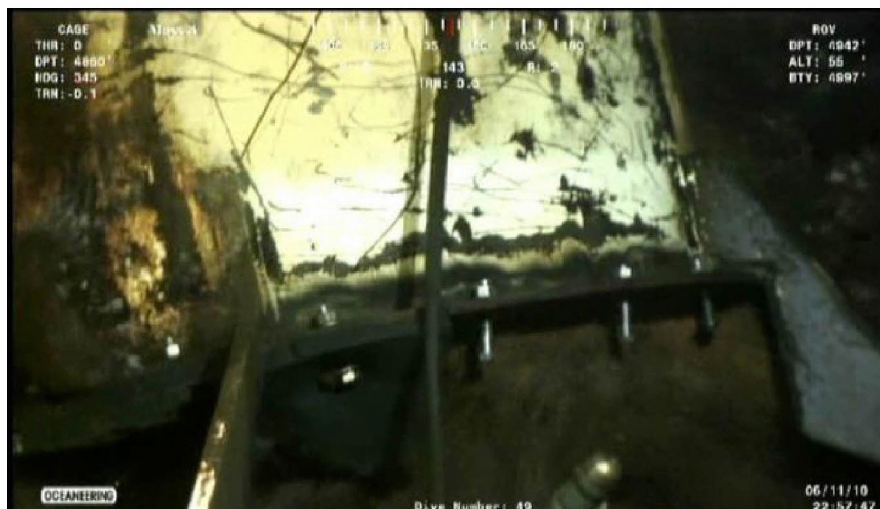


Figure A- 19: Screen shot captured from ROV video showing bottom of the top hat, section of rubber gasket missing on right side of image, section of rubber gasket present on left side of image (Maxx3 June 11, 2010).

The maximum cross-sectional area that could be available for flow can however be estimated using the flange and top hat geometry already stated. The following simplified approximation of the cross sectional area considers that no rubber gasket is present on the bottom of the top hat thereby offering the maximum amount cross sectional area for oil and gas to flow through. The riser flange (assuming circular) has a cross sectional area of 1,452.2 in² (0.937 m²) based on the riser flange ID above. The available area on the bottom of the top hat using the ID provided above is 1,698.2 in² (1.096 m²). By removing the flange cross-sectional area from the total available at the top hat, the maximum available cross section area for flow is estimated at 246 in² (0.159 m²).

Operational: Collection

Collection during this configuration was carried out through the collection pipe at the apex of top hat.

Operational: Dispersant

Dispersant was applied during this release configuration period. Dispersant use was consistent during this phase, however in varying volumes. Dispersant application methods predominantly included the dispersant wand as well as the two pronged trident.

Table A-8 summarizes the details of this release configuration.

Table A-8. Area and release depth of RC4.

Release Configuration	Cross sectional area in ²	Cross sectional area m ²	Depth (ft)	Depth (m)
RC4	246	0.1587	4,942.3	1,506.4

A2.6.Release Configuration 5 (RC5): Post riser cut, flange removed (July 11, 2010)

Release Configuration: Release Location

This release configuration reflects the period post riser cut where the mitigation apparatus top hat #4 was not in place and the flange had been removed from the riser adapter using the flange overshot removal tool. The flange is approximately 5.025 in (0.128 m) tall (FRTG 2010) therefore making the release depth 1,506.4 m (4,942.3 ft) below the surface outlined in Table A-9.

Release Configuration: Cross Sectional Area

Figure A-20 displays the riser adapter after the flange had been removed. The remaining sections of drill pipes were visible in the center of the riser adapter. The OD of the flange is known from the prior analysis used to estimate the cross-sectional area in RC 3. The ID of the riser adapter seen in Figure A-20 must be equal or less than that of the OD of the recovered riser flange, in order for the two pieces of hardware to fit together seamlessly. The ID was therefore assumed to be the same size as the riser ID without the flange (21.5 in (0.5461 m)). The USCG report (U.S. Coast Guard 2010) indicated that two drill pipes were present inside the riser at the kink after the cutting operation was completed. From direct measurements at NASA Michoud Facility, the drill pipes are known to have a thickness of 0.5 inches (0.0127 m), with an ID of 4.5 inches (0.1143 m) and an OD of 5.5 in (0.1397 m). The cross sectional area reduction caused by the drill pipes presence, assuming no material has been lost is therefore at maximum 15.71 in² (0.01 m). Resulting in a minimum overall cross sectional area of 347.3 in² (0.2241 m) for the release configuration.

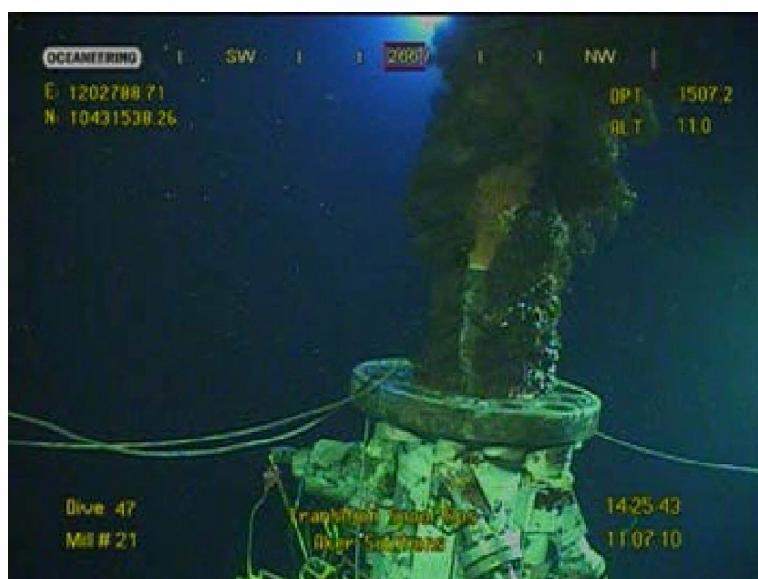


Figure A-20: RC5, riser adapter with the flange removed. Photograph from Millennium 21 ROV, July 11, 2010.

Operational: Collection

There was no observed collection during this configuration phase.

Operational: Dispersant

Dispersant was applied during this release configuration period. The dispersant application method as observed from ROV video was predominantly a hooked dispersant wand inserted in to the riser aperture.

Table A-9 summarizes the details of this release configuration.

Table A-9. Area and release depth of RC5.

Release Configuration	Cross sectional area in ²	Cross sectional area m ²	Depth (ft)	Depth (m)
RC5	347.3	0.2241	4,942.3	1,506.4

A2.7.Release Configuration 6 (RC6): Transition spool flow (July 11, 2010 through July 12, 2010)

Release Configuration: Release Location

This release configuration reflects the period post riser cut where the flange had been removed from the riser adapter, and the transition spool was inserted 31 inches (0.7874 m) into the riser aperture. The transition spool, in total, is approximately 131 ¾ inches (3.35 m) tall before insertion (BP, Plug and Abandonment Project) therefore making the release depth 1,503.85 m (4,933.9 ft) below the surface (Table A-10).

Release Configuration: Cross Sectional Area

The transition spool was the third step in a process to install the three cam capping stack to stem the flow of oil. Figure A-21 outlines the capping stack installation process. The transition spool was inserted and encompassed the protruding drill pipes observed in the riser (Figure A-20). A technical schematic of the transition spool (BP, Plug and Abandonment Project) indicated that the OD of the inserted section of the transition spool is approximately 18 inches (0.4572 m). The schematic shows that the aperture at the top of the transition spool is slightly larger than that of the inserted section of the transition spool. Based on additional technical schematics of the capping stack (Transocean Deepwater Horizon Incident, Cap Stack Team 2010), the transition spool cross sectional area is assumed to be the same size as RC7 which is described in the next section.

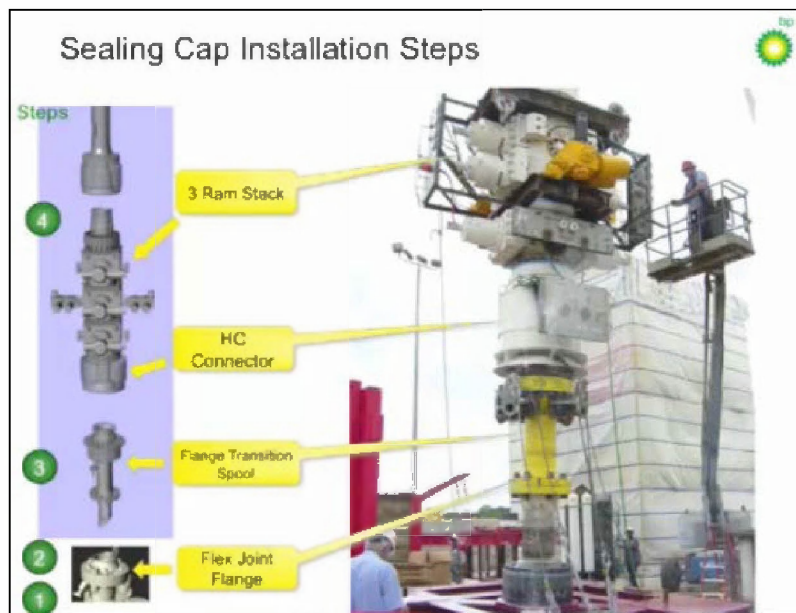


Figure A-21: Sealing cap installation overview (BP 2010).

Operational: Collection

There was no observed collection during this configuration phase.

Operational: Dispersant

Dispersant was applied during this release configuration period. The dispersant application method as observed from ROV video was predominantly a hooked dispersant wand inserted in to the transition spool aperture.

Table A -10 summarizes the details of this release configuration.

Table A-10. Area and release depth of RC6.

Release Configuration	Cross sectional area in ²	Cross sectional area m ²	Depth (ft)	Depth (m)
RC6	276.117	0.1781	4,933.9	1,503.85

A2.8.Release Configuration 7 (RC7): Three ram capping stack - main flow (July 12 through July 14, 2010)

Release Configuration: Location

This release configuration reflects the period post riser cut after the transition spool had been inserted into the riser aperture, and the three ram capping stack had been placed on top. The capping stack aperture was approximately 27 m (89 ft) above the mudline at a depth of approximately 1,496 m (4,907 ft).

Release Configuration: Cross Sectional Area

The three ram capping stack had a central circular release on the top. The central release location had a diameter of 18 ¾ inches (0.4763 m) (Transocean Deepwater Horizon Incident, Cap Stack Team 2010), resulting in a cross sectional area of 276.117 in² (0.1781 m²).

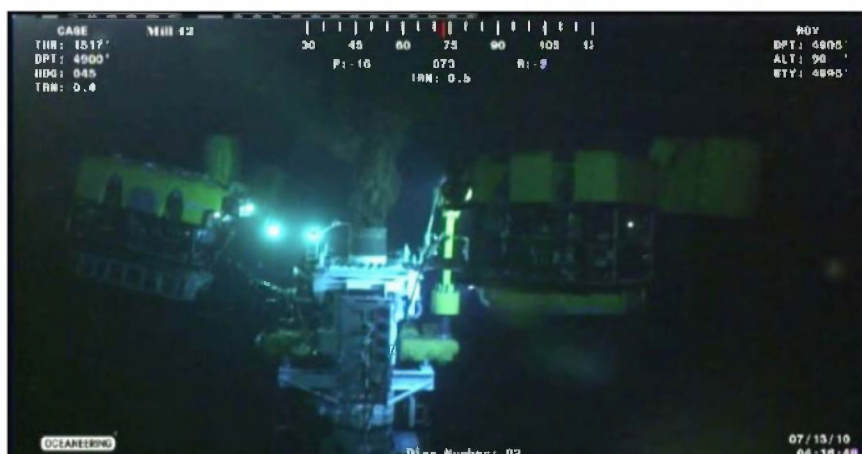


Figure A-22: Top of three ram capping stack, observed flow in image center is from capping stack mandrel. Photograph from Millennium 42, July 13, 2010.

Operational: Collection

There was no observed collection during this configuration phase.

Operational: Dispersant

Dispersant was applied during this release configuration period. The dispersant application method as observed from ROV video was predominantly a hooked dispersant wand inserted in to the central capping spool aperture.

Table A-11 summarizes the details of this release configuration.

Table A-11. Area and release depth of RC7.

Release Configuration	Cross sectional area in ²	Cross sectional area m ²	Depth (ft)	Depth (m)
RC7	276.117	0.178	4,907	1,495.7

A2.9.Release Configuration 8 (RC8): Three ram capping stack – valve flow (July 14, 2010)

Release Configuration: Location

This release configuration reflects the period post riser cut after the transition spool had been inserted in to the riser aperture, and the three ram capping stack had been placed on top. The smaller capping stack aperture (release valve) was approximately 27.127 m (89 ft) above the mudline sitting at a depth of approximately 1,497 m (4,911 ft).

Release Configuration: Cross Sectional Area

The three ram capping stack had two release valves on either side (choke and kill) (BP – BOP connections and capping 2010). After the choke valve assembly (Cameron DR30) was installed one valve was left open. The capping stack schematic noted previously in RC7 (Transocean Deepwater Horizon Incident, Cap Stack Team 2010) shows the diameter of the bore hole reduce to $3\frac{1}{16}$ inches (0.0778 m) inside the capping stack. The release cross sectional area was

modeled to be the same as the bore hole size in the capping stack for the release valves, resulting in a diameter of 29.465 in² (0.019 m). Figure A-23 illustrates the three ream capping stack with and without flow from different angles.



Figure A-23: Valve on top of three ram capping stack, observed flow (left, Photo from Millennium 21 July 14, 2010), side view no flow (middle, Photo from Millennium 22 July 15, 2010), top view no flow (right, Photo from Millennium 22 July 15, 2010).

Operational: Collection

There was no observed collection during this configuration phase.

Operational: Dispersant

Records of daily subsurface dispersant volumes (Appendix B) indicated that dispersants were discharged during this release configuration. At present, there is insufficient video evidence to determine the dispersant application method.

Table A-12 summarizes the details of this release configuration.

Table A-12. Area and release depth of RC8.

Release Configuration	Cross sectional area in ²	Cross sectional area m ²	Depth (ft)	Depth (m)
RC8	29.465	0.019	4,911	1,497

A3. References

- Beegle-Krause, C.J. 2010. Coordinates of Second Leak Point. (D. French McCay, RPS ASA, Interviewer).
- BP - BOP connections and capping. 2010. Capping Stack Integrity Monitoring Procedure. 2200-T2-DO-PR-4512.
- BP. 2010. Sealing Cap Installation Overview. Retrieved from <http://bp.concerts.com/gom/sealingcapinstallationoverviewwithkentwells070910.htm>
- BP, Plug and Abandonment Project. (n.d.). Transition Spool Assembly Schematic. 2200-T2-DO-PR-4744: Attachment 3: Transition Spool Assembly Schematic - Transition Spool with M/D adapter spool (Mandrel).
- Energy, D.O. 2010. Top Hat #4. Retrieved from http://energy.gov/sites/prod/files/edg/open/documents/1.3_Item_2_Top_Hat_4_03_JUN_1130.pdf
- Energy, D.O. 2012. from Riser Insertion Tube: http://energy.gov/sites/prod/files/edg/open/documents/1.1_Item_11_RITT_07_Jun_1900_NL.pdf
- FRTG, P.T. 2010. Deepwater Horizon Release Estimate of Rate by PIV.
- Horn, M., M. Grennan, L. Decker, S. Zamorski, D. French McCay, Z. Li. 2015. Technical Reports for Deepwater Horizon Water Column Injury Assessment –Water Column Chemistry Data from the Deepwater Horizon Blowout. RPS ASA, South Kingstown, RI, USA.
- Transocean. 2011. Macondo Well Incident. Transocean Investigation Report - Volume I.
- Transocean Deepwater Horizon Incident, Cap Stack Team. 2010. Cap Stack Cross Section For Flowpath Clarification. FRTG.
- U.S. Coast Guard. 2010. DH Riser Kink Holes - Measurements with Field Drawing and Images. U.S. Coast Guard - Research & development center.

Technical Reports for Deepwater Horizon Water Column Injury Assessment

WC_TR.13: Application of OILMAP DEEP to the Deepwater Horizon Blowout

Appendix B: Oil, gas, and dispersant release rates

Authors: Malcolm Spaulding, Daniel Mendelsohn, Deborah Crowley,
Zhengkai Li, Andrew Bird

Revised: September 30, 2015

Project Number: 2011-144

RPS ASA 55 Village Square Drive, South Kingstown, RI 02879

Table of Contents

B1.	Time History of DWH Spill Event Parameters	1
B2.	Estimate of Gas Release	4
B3.	References	5

List of Figures

Figure B-1: Time series of daily release volume from reservoir, released to the water column, amount collected and amount of dispersant applied subsurface.	4
--	---

List of Tables

Table B-1. Summary of OBC daily estimates of the oil release rate, oil collection rate and rate of oil released to the water column. Daily volume of surface and subsurface dispersants applied to the spill.....	1
---	---

B1. Time History of DWH Spill Event Parameters

Estimates of total oil release volume, oil collection volumes, dispersant application volume on a daily basis throughout the duration of the DWH spill event were made based on the findings of the Oil Budget Calculator (Lehr et al. 2010). The daily release of oil to the water column was determined by subtracting the subsurface collected volume from the total released volume each day. Table B-1 summarizes the total estimated release, collection from each individual source, the total daily collected, the total released to the water column (total release – total collected), release volume of surface and subsurface dispersants. The time series of total reservoir release, total collected, release to the water column, and subsurface dispersant application are illustrated in Figure B-1.

Table B-1. Summary of OBC daily estimates of the oil release rate, oil collection rate and rate of oil released to the water column. Daily volume of surface and subsurface dispersants applied to the spill.

Date	Released (bbl)	Collected Enterprise (bbl)	Collected Q400 (bbl)	Collected Helix Producer (bbl)	Collected Total (bbl)	Release to the Water Column (bbl)	Subsea Dispersants (gallons)	Surface Dispersants (gallons)
4/20/2010	0				0	0	0	0
4/21/2010	0				0	0	0	0
4/22/2010	62200				0	62200	0	1701
4/23/2010	62100				0	62100	0	0
4/24/2010	61900				0	61900	0	0
4/25/2010	61800				0	61800	0	9818
4/26/2010	61700				0	61700	0	14486
4/27/2010	61600				0	61600	0	27078
4/28/2010	61500				0	61500	0	42143
4/29/2010	61400				0	61400	0	40913
4/30/2010	61300				0	61300	2196	4900
5/1/2010	61200				0	61200	0	11653
5/2/2010	61000				0	61000	3399	0
5/3/2010	60900				0	60900	5812	0
5/4/2010	60800				0	60800	7580	34273
5/5/2010	60700				0	60700	0	49575
5/6/2010	60600				0	60600	0	28770
5/7/2010	60500				0	60500	0	7270
5/8/2010	60400				0	60400	0	41690
5/9/2010	60200				0	60200	0	55932
5/10/2010	60100				0	60100	9460	56220
5/11/2010	60000				0	60000	2100	7940
5/12/2010	59900				0	59900	0	39710
5/13/2010	59800				0	59800	0	41620

Date	Released (bbl)	Collected Enterprise (bbl)	Collected Q400 (bbl)	Collected Helix Producer (bbl)	Collected Total (bbl)	Release to the Water Column (bbl)	Subsea Dispersants (gallons)	Surface Dispersants (gallons)
5/14/2010	59700				0	59700	0	44031
5/15/2010	59600	500			500	59100	7222	14208
5/16/2010	59400	900			900	58500	6300	670
5/17/2010	59300	1030			1030	58270	7980	13213
5/18/2010	59200	1200			1200	58000	3450	12386
5/19/2010	59100	3000			3000	56100	4879	3352
5/20/2010	59000	2200			2200	56800	14151	1
5/21/2010	58900	2175			2175	56725	14400	29892
5/22/2010	58800	1361			1361	57439	14130	52946
5/23/2010	58700	1120			1120	57580	14738	18104
5/24/2010	58500	0			0	58500	14494	630
5/25/2010	58400	6078			6078	52322	12925	200
5/26/2010	58300	2596			2596	55704	11529	7752
5/27/2010	58200	0			0	58200	14347	1029
5/28/2010	58100	0			0	58100	13670	18445
5/29/2010	58000	0			0	58000	14588	2900
5/30/2010	57900	0			0	57900	13073	17631
5/31/2010	57700	0			0	57700	13936	11686
6/1/2010	57600	0			0	57600	12201	0
6/2/2010	57500	0			0	57500	8073	3375
6/3/2010	60000	0			0	60000	17753	6200
6/4/2010	59900	6087			6087	53813	20655	13701
6/5/2010	59800	10496			10496	49304	20306	125
6/6/2010	59700	11119			11119	48581	13937	0
6/7/2010	59500	14842			14842	44658	14732	10744
6/8/2010	59400	15006			15006	44394	13763	8324
6/9/2010	59300	15816			15816	43484	12112	2100
6/10/2010	59200	15402			15402	43798	10163	5872
6/11/2010	59100	15554			15554	43546	8447	14305
6/12/2010	59000	15039			15039	43961	4852	10356
6/13/2010	58900	15208			15208	43692	9916	36012
6/14/2010	58800	15421			15421	43379	9800	10741
6/15/2010	58600	10448			10448	48152	11726	2768
6/16/2010	58500	14752	3475		18227	40273	8777	13593
6/17/2010	58400	16026	9269		25295	33105	5763	12423
6/18/2010	58300	14446	10106		24552	33748	9148	15711

Date	Released (bbl)	Collected Enterprise (bbl)	Collected Q400 (bbl)	Collected Helix Producer (bbl)	Collected Total (bbl)	Release to the Water Column (bbl)	Subsea Dispersants (gallons)	Surface Dispersants (gallons)
6/19/2010	58200	11047	9994		21041	37159	16911	8510
6/20/2010	58100	14574	8717		23291	34809	14070	19576
6/21/2010	58000	15566	10270		25836	32164	14233	11217
6/22/2010	57800	16668	10429		27097	30703	9793	2008
6/23/2010	57700	8329	8537		16866	40834	9891	5099
6/24/2010	57600	15789	7946		23735	33865	12871	21088
6/25/2010	57500	16338	8210		24548	32952	12540	4633
6/26/2010	57400	14734	8024		22758	34642	12654	23022
6/27/2010	57300	16277	8178		24455	32845	11558	6626
6/28/2010	57200	15313	8087		23400	33800	13174	0
6/29/2010	57100	17027	8196		25223	31877	11560	324
6/30/2010	56900	14875	8204		23079	33821	13609	0
7/1/2010	56800	16918	8236		25154	31646	10558	17852
7/2/2010	56700	16992	8299		25291	31409	11065	14210
7/3/2010	56600	17022	8176		25198	31402	11698	432
7/4/2010	56500	16924	8036		24960	31540	10429	3079
7/5/2010	56400	16759	8223		24982	31418	11688	803
7/6/2010	56300	16536	8225		24761	31539	11655	473
7/7/2010	56100	16659	7919		24578	31522	11770	1245
7/8/2010	56000	16308	8071		24379	31621	11512	0
7/9/2010	55900	16543	8249		24792	31108	10748	0
7/10/2010	55800	7096	8103		15199	40601	13210	0
7/11/2010	55700	0	8235		8235	47465	15420	0
7/12/2010	53000	0	7291	1011	8302	44698	14038	0
7/13/2010	52900	0	7888	9176	17064	35836	13997	999
7/14/2010	52700	0	5163	7680	12843	39857	13746	0
7/15/2010	0	0	3431	5876	9307	0	8391	0

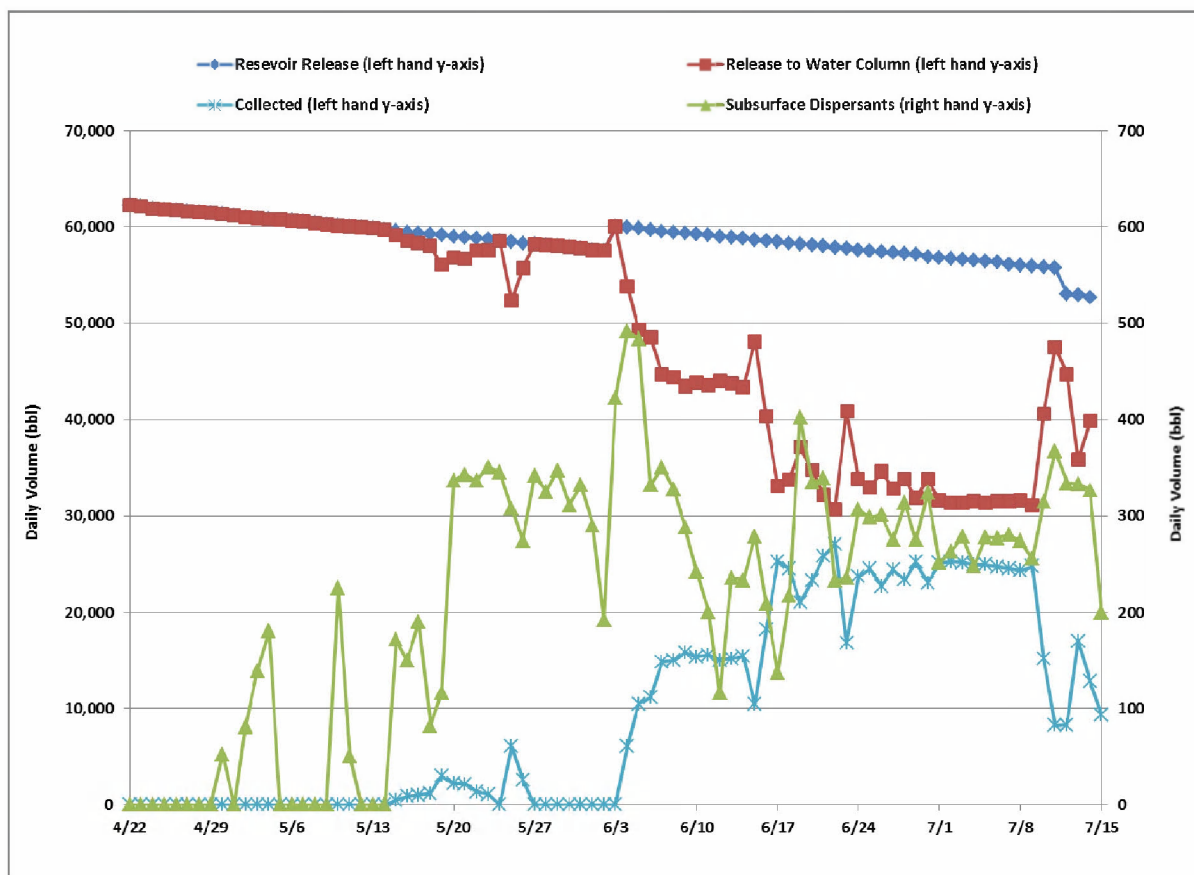


Figure B-1: Time series of daily release volume from reservoir, released to the water column, amount collected and amount of dispersant applied subsurface.

B2. Estimate of Gas Release

The volume flow rate and total release of gas associated with the blowout was estimated using the oil release rates (described above) and the gas to oil ratio (GOR) from the Black Oil Tables (Zick 2013). The GOR is (typically) expressed relative to standard atmospheric conditions, and multiple components of the **OILMAP DEEP** model require input of GOR at standard temperature and pressure. Based on the input of oil release rate (volume flux) and GOR, **OILMAP DEEP** calculates gas volume flux at surface conditions and subsequently adjusts this gas flux to account for gas compressibility and fugacity in order to represent the initial release conditions at depth. Appendix C provides details of GOR estimates based on the oil and gas properties based on the Macondo Crude Black Oil Tables (Zick 2013).

B3. References

- Lehr, B., S. Bristol and A. Possolo. 2010. Deepwater horizon oil budget calculator: A report to the national incident command. The Federal Interagency Solutions Group, Oil Budget Calculator Science and Engineering Team.
http://www.restorethegulf.gov/sites/default/files/documents/pdf/OilBudgetCalc_Full_HQ-Print_111110.pdf (Accessed on April 1, 2012).
- Zick, A. 2013. Equation of state fluid characterization and analysis of the Macondo reservoir fluids, Expert report in matter of US vs BP Exploration & Production, Inc. et al, submitted to the U.S. Department of Justice, March 22, 2013.

Technical Reports for Deepwater Horizon Water Column Injury Assessment

WC_TR.13: Application of OILMAP DEEP to the Deepwater Horizon Blowout

Appendix C: Physical-Chemical Properties of the Source Oil and the Black-Oil Tables of the Macondo Reservoir Fluids

Authors: Malcolm Spaulding, Daniel Mendelsohn, Deborah Crowley,
Zhengkai Li, Andrew Bird

Revised: September 30, 2015

Project Number: 2011-144

RPS ASA 55 Village Square Drive, South Kingstown, RI 02879

Table of Contents

C1.	Introduction	1
C2.	Physical properties of the unweathered fresh source oil	1
C3.	Chemical properties of the fresh source oil	1
C4.	Equation-of-State (EOS) Characterization of Macondo Reservoir Fluids	2
C5.	Macondo Black-Oil Tables.....	4
C6.	Summary.....	5
C7.	References.....	6

List of Figures

Figure C-1: Pressure-temperature phase envelope for the average Macondo reservoir fluid, comparing EOS predictions with experimental saturation pressure data (Zick 2013).....	4
--	---

List of Tables

Table C-1: Macondo EOS fluid characterization (for the 1978 Peng-Robinson EOS) from Zick (2013)	3
Table C-2: Excerpt from the Macondo Black-Oil Tables (Zick 2013)	5

C1. Introduction

Sections C2 and C3 of this appendix summarize the physical and chemical properties of the fresh MC252 Macondo-1 Well crude oil (Stout 2015a,b).

Sections C4 and C5 of this appendix summarize the Equation-of-State (EOS) fluid characterization and the Black-oil Tables (BOT) of the Macondo reservoir fluids. These reservoir oil and gas phase fluid compositions and characterization were provided by the United States Department of Justice (DOJ) Expert Report, entitled “Equation-of-State Fluid Characterization and Analysis of the Macondo Reservoir Fluids”, prepared by Dr. A.A. Zick of the Zick Technologies, Inc. More details can be found in Zick (2013).

C2. Physical properties of the unweathered fresh source oil

The physical analyses conducted by Stout (2015b) indicate that the MC252 Macondo-1 source oil had a density of 0.8483 g/ml at 15°C, which corresponds to an API gravity of 35 degrees. As such, this density indicates that MC252 is a “light” crude oil. The dynamic viscosity of the fresh oil at 15°C was 7.145 cP; typical of lighter crude oil. The oil’s density and viscosity exhibit a typical relationship with temperature, with both parameters being slightly higher at 5°C and slightly lower at 30°C. The oil-water interfacial and surface tensions of the fresh oil at 20°C were 19.63 and 3.43 mN/m, respectively.

C3. Chemical properties of the fresh source oil

The high temperature simulated distillation profile for the Macondo-1 oil (Stout 2015b) indicates that nearly all highly volatile gaseous compounds below C5 were lost from the source oil during its collection and handling. The oil exhibits a typical pattern for fresh, light crude oil wherein there is a steady decrease in mass percentages for boiling fractions ranging from a maximum of 24 wt% in the C5-C10 fraction to 5 wt% in the C35-C40 fraction. Approximately 14 wt% of the fresh source oil is contained in the C40+ fraction.

A representative GC/FID chromatogram for the fresh Macondo-1 source oil (Stout 2015a) indicates that the oil is dominated by a series of *n*-alkanes that steadily decrease in concentration with increasing carbon number – as is typical of most crude oils. The average TPH concentration of the source oil is 681,389 µg/g oil. This means that about 68.1 wt% of the oil ranged from C9 to C44. The balance of the oil’s mass resides in the volatile fraction below C9 and in non-chromatographable compounds with boiling points above C44. Approximately 15% of the measured TPH was comprised of *n*- alkanes. This relatively high percentage indicates that the Macondo-1 oil was relatively waxy or paraffin-rich oil.

Some of the volatile fraction below C9 (and above C5) was characterized in the PIANO analysis of the source oil (Stout 2015a), showing that the fresh source oil contained 17.4 wt% of total targeted PIANO compounds. Only 13.5 wt% of the oil boiled between C5 and C9, which when added to the 68.1 wt% TPH (C9-C44), indicates that approximately 81.6 wt% of the oil boiled between C5 and C44. Because gases below C5 were lost from the oil during sampling/handling, the combined PIANO and TPH analysis indicate that the balance of the fresh oil (18.4 wt %) boils above C44. The composition of the VOCs was dominated by aliphatic hydrocarbons – paraffin, iso-paraffins, and naphthenes – they comprised 14.3 wt% of the oil (Stout 2015a). The total targeted volatile aromatics comprised 3.16 wt % of the oil, which included 1.9 wt % total BTEX, which in turn included 0.24 wt % benzene.

The concentrations of decalins, parent and alkylated PAHs, and sulfur-containing aromatics detected in the un-weathered Macondo-1 oil are given in Stout (2015a). The oil contained 1.33 wt % of total PAHs (TPAH), of which 1.19 wt % was 2- and 3- ring low molecular weight PAHs (LPAH) and 0.14 wt % was 4- to 6-ring high molecular weight PAHs. The LPAH were dominated by C0-C4 naphthalenes (0.76 wt %), which comprised more than half of the TPAH. Naphthalene was present at an average concentration of 964 µg/g oil. Although the sulfur content of the Macondo-1 source oil was not measured, the relative abundance of sulfur-containing aromatic compounds measured (benzothiophenes, dibenzothiophenes, and naphthobenzothiophenes) was relatively low.

C4. Equation-of-State (EOS) Characterization of Macondo Reservoir Fluids

A phase behavior model – an equation of state fluid characterization – for the Macondo reservoir fluids has been developed by DOJ expert Dr. Aaron A. Zick (Zick 2013) from the assessment of the available Macondo fluid PVT (pressure, volume, temperature) laboratory data. The model can be used to predict the Macondo reservoir fluids' physical, thermodynamic, and transport properties as functions of temperature, pressure, and fluid composition. These model predictions can be used to support engineering calculations such as the total flow of oil from the Macondo well into the Gulf of Mexico. The model can also be used to evaluate the conversion (through different processes) of reservoir barrels of oil (by which the flow from the reservoir into the well is measured) to stock tank barrels (by which the extent of the Deepwater Horizon oil spill is measured).

Engineering calculations involving fluids require a model of the fluid's properties and phase behavior under different conditions of pressure, volume, temperature, and/or overall composition. The relevant fluid properties might include molecular weight, density, and viscosity. The fluid's phase behavior describes when and how the fluid will partition into different phases (gas, liquid, and/or solid) and what the compositions of those phases might be, which in turn will determine the properties of those phases. An equation of state such as the Peng-Robinson EOS (Robinson and Peng 1978), together with an equation-of-state fluid characterization, can provide such a model. Through the laws of thermodynamics, such an EOS can also predict the equilibrium phase behavior of a modeled fluid system for any given set of independent state variables, such as temperature, pressure, and overall composition.

An EOS fluid characterization consists of four elements: (a) the set of components that constitute the fluids of interest, (b) the estimated physical and thermodynamic properties of each

component, (c) a matrix of binary interaction parameters (BIPs) to account for possible interactions between every unique pair of components, and (d) compositions of the fluids of interest, expressed as relative amounts of the characterization's components.

The process of building an EOS fluid characterization consists of choosing or defining an appropriate suite of components, estimating the initial properties for each component and the BIPs for all component pairs, casting the fluid compositions of interest in terms of the defined suite of components, and tuning the EOS parameters to optimize the prediction of available phase behavior data. In most cases, the tuning of the EOS fluid characterization is followed by the estimation (and possible tuning) of parameters for auxiliary models that are often used together with the EOS fluid model to predict additional, non-EOS fluid properties, such as viscosity and interfacial tension, which can be important for multiphase fluid flow calculations.

Table C-1: Macondo EOS fluid characterization (for the 1978 Peng-Robinson EOS) from Zick (2013)

Component	MW	Tc (R)	Pc (psia)	AF	VS	ZcVis	Pchor					
N2	28.014	227.16	492.04	0.03700	-0.16750	0.29170	55.10					
CO2	44.010	547.42	1069.51	0.22500	0.00191	0.27433	80.00					
C1	16.043	343.01	667.03	0.01100	-0.14956	0.28620	71.00					
C2	30.070	549.58	706.62	0.09900	-0.06260	0.27924	111.00					
C3	44.097	665.69	616.12	0.15200	-0.06381	0.27630	151.00					
C4-C5	63.370	767.52	521.40	0.21328	-0.05005	0.27048	204.93					
C6-C7	89.779	941.56	449.50	0.27691	0.00117	0.26458	250.47					
C8-C9	113.271	1041.98	397.68	0.33414	0.02830	0.26393	306.85					
C10-C12	151.237	1171.61	337.32	0.42755	0.05856	0.26340	397.97					
C13-C19	215.517	1330.41	270.20	0.57931	0.08930	0.26000	552.24					
C20+	441.107	1606.72	182.26	1.09027	0.00369	0.28268	1093.66					
BIPs	N2	CO2	C1	C2	C3	C4-C5	C6-C7	C8-C9	C10-C12	C13-C19	C20+	
N2	0	0.00300	0.02500	0.01000	0.09000	0.09943	0.11000	0.11000	0.11000	0.11000	0.09453	
CO2	0.00000	0	0.10500	0.13000	0.12500	0.11587	0.11500	0.11500	0.11500	0.11500	0.09962	
C1	0.02500	0.10500	0	0.00097	0.00319	0.00689	0.01123	0.01478	0.01981	0.02690	0.06074	
C2	0.01000	0.13000	0.00097	0	0.00000	0.00000	0.00000	0.00000	0.00000	0.00000	0.02106	
C3	0.09000	0.12500	0.00319	0.00000	0	0.00000	0.00000	0.00000	0.00000	0.00000	0.02106	
C4-C5	0.09943	0.11587	0.00689	0.00000	0.00000	0	0.00000	0.00000	0.00000	0.00000	0.02106	
C6-C7	0.11000	0.11500	0.01123	0.00000	0.00000	0.00000	0	0.00000	0.00000	0.00000	0.02106	
C8-C9	0.11000	0.11500	0.01478	0.00000	0.00000	0.00000	0.00000	0	0.00000	0.00000	0.02106	
C10-C12	0.11000	0.11500	0.01981	0.00000	0.00000	0.00000	0.00000	0.00000	0	0.00000	0.02106	
C13-C19	0.11000	0.11500	0.02690	0.00000	0.00000	0.00000	0.00000	0.00000	0.00000	0	0.02106	
C20+	0.09453	0.09962	0.06074	0.02106	0.02106	0.02106	0.02106	0.02106	0.02106	0.02106	0	

Table C-1 gives the Macondo EOS fluid characterization (for the 1978 Peng-Robinson EOS) developed by Zick (2013). The first part of the table lists the components, their essential EOS properties (molecular weight, critical temperature, critical pressure, acentric factor, and volume shift parameter), their critical z-factors for use in the Lohrenz-Bray-Clark viscosity model (Lohrenz et al. 1964), and the parachors for use in the Weinaug-Katz interfacial tension model (Weinaug and Katz 1943). The second part of the table shows the matrix of binary interaction parameters (BITS) – parameters that account for interactions between given pairs of components.

Figure C-1 shows the PT diagram, or pressure-temperature phase envelope, for the average Macondo reservoir fluid from Table C-1. This type of diagram shows the saturation pressure as a function of temperature. Inside the envelope, the fluid will separate into two equilibrium phases. Outside of the envelope (above, below, and to the right in the figure), the fluid will remain in a single phase state. At a given temperature, the saturation pressure can be either a bubble point, a dew point, or a critical point. When the two-phase region is entered from a bubble point, the first appearance of the second, incipient phase will be a bubble of a less dense phase (more vapor-like). Conversely, when the two-phase region is entered from a dew point, the first appearance of the second, incipient phase will be a droplet of a denser phase (more liquid-like). When the two-phase region is entered from a critical point, however, the first appearance of the second, incipient phase will be indistinguishable from the primary phase.

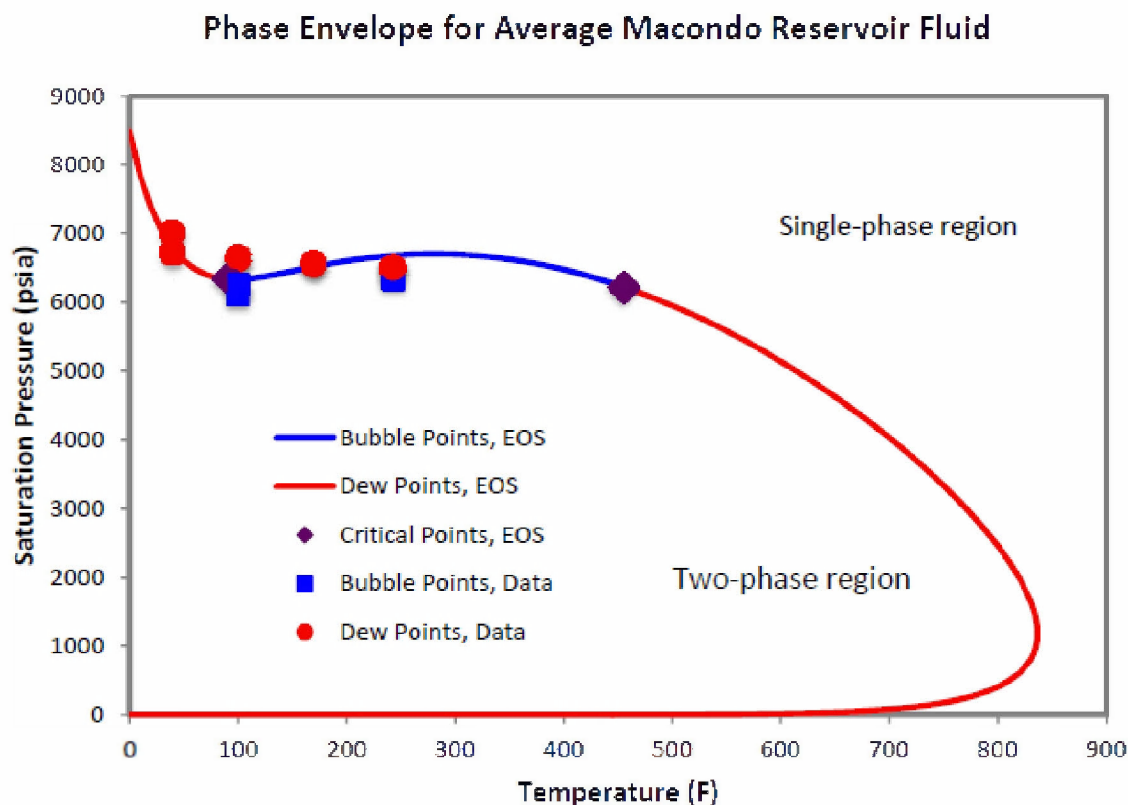


Figure C-1: Pressure-temperature phase envelope for the average Macondo reservoir fluid, comparing EOS predictions with experimental saturation pressure data (Zick 2013).

C5. Macondo Black-Oil Tables

The EOS fluid characterization (summarized above and details are given in Zick 2013) can be used as the Macondo fluid model within any engineering software that supports the Peng-Robinson EOS and the Lohrenz-Bray-Clark viscosity model. That includes reservoir simulators, pipe-flow simulators, and surface process simulators. A set of lookup tables of fluid properties as functions of temperature and pressure (commonly called *black-oil tables* within the industry) for use in the computation of fluid flow from the Macondo reservoir, through the damaged wellbore, to the spill site at the bottom of the Gulf of Mexico. The black-oil tables have been generated under the assumption that the overall flowing composition was constant (at the original, average reservoir composition), but that the liquid and gas phase composition could vary widely as the temperature and pressure changes. For any given combination of temperature and pressure (at regular intervals), the black-oil tables provide: (1) The number of equilibrium phases; (2) The molar and volumetric proportions of each phase; (3) The molecular weights of each phase; (3) The compressibility factor of each phase and of the overall fluid; (4) The molar volume of each phase and of the overall fluid; (5) The density of each phase and of the overall fluid; (6) The viscosity of each phase, and (7) The molar composition of each phase. Table C-2 shows a small excerpt from the black-oil tables that were built from Zick (2013)'s

Macondo Equation-of-state (EOS) model. The complete black-oil tables are provided separately in electronic format in Zick (2013).

Table C-2: Excerpt from the Macondo Black-Oil Tables (Zick 2013)

Temp (F)	Pres (Psia)	Liq Vol Frac	Gas Vol Frac	Liq Den (kg/m3)	as Den (kg/m3)
200	2000	0.30535	0.69465	710.29	114.63
200	2200	0.33567	0.66433	703.32	127.62
200	2400	0.36486	0.63515	696.63	140.86
200	2600	0.39282	0.60718	690.21	154.31
200	2800	0.41948	0.58052	684.02	167.96
200	3000	0.44482	0.55518	678.04	181.80
200	3200	0.46883	0.53117	672.27	195.82
200	3400	0.49152	0.50848	666.69	210.02
200	3600	0.51292	0.48708	661.28	224.41
200	3800	0.53307	0.46693	656.04	238.98
200	4000	0.55204	0.44796	650.94	253.76
200	4200	0.56990	0.43010	645.97	268.76
200	4400	0.58674	0.41326	641.09	283.98
200	4600	0.60270	0.39730	636.28	299.44
200	4800	0.61797	0.38203	631.47	315.15
200	5000	0.63281	0.36719	626.60	331.12
200	5200	0.64762	0.35238	621.59	347.38
200	5400	0.66300	0.33700	616.31	363.95
200	5600	0.67985	0.32015	610.60	380.89
200	5800	0.69968	0.30032	604.26	398.33
200	6000	0.72526	0.27474	596.96	416.48
200	6200	0.76246	0.23754	588.19	435.76
200	6400	0.82760	0.17240	576.94	457.13
200	6600	1	0	560.31	483.49
200	6800	1	0	562.93	562.93
200	7000	1	0	565.46	565.46
200	7200	1	0	567.92	567.92
200	7400	1	0	570.30	570.30
200	7600	1	0	572.61	572.61
200	7800	1	0	574.86	574.86
200	8000	1	0	577.04	577.04

C6. Summary

In summary:

- The Macondo-1 oil was a light ($\rho = 0.8483$ g/ml @ 15°C), low viscosity (7.145 cP @ 15°C) paraffinic crude oil. Both the density and viscosity of the oil were higher at low temperatures (5°C), such as existed near the well head.
- The Macondo-1 oil contained about 13.5 wt % volatiles (C5-C9) and 68.1 wt % semi-volatiles (C9-C44). Because gases below C5 were lost from the analyzed oils during sampling/handling, the balance of the mass (approx. 18.4 wt %) boils above C44.
- The Macondo-1 oil contained volatiles that were mostly aliphatic hydrocarbons, although volatile aromatic hydrocarbons comprised 3.16 wt % of the oil which included 1.9 wt% total BTEX (19,124 $\mu\text{g/g oil}$), which in turn included 0.24 wt % (2351 $\mu\text{g/g oil}$) benzene.
- The Macondo-1 oil contained semi-volatiles that included 1.33 wt % of total PAHs (TPAH, i.e., sum of all analytes from naphthalene to benzo[g,h,i]perylene), with the C0-C4 naphthalenes (0.76 wt %), comprising more than half of the TPAH. Naphthalene was present at an average concentration of 964 $\mu\text{g/g oil}$.

A specific type of phase behavior model—an equation-of-state fluid characterization—has been developed for the Macondo reservoir fluids by Zick (2013). A set of lookup *black-oil tables* are provided to represent the fluid properties as functions of temperature and pressure. The black-

oil tables, including oil and gas phase compositions and properties under various temperature and pressure conditions, are used in blowout plume model and pipeline release model and fountain model of the Application of OILMAP DEEP to the Deepwater Horizon Blowout report.

C7. References

- Lohrenz, J., Bray, B. G., and Clark, C. R. 1964. Calculating Viscosities of Reservoir Fluids from their Compositions, JPT, 1171, Trans., AIME 231.
- Robinson, D. B. and Peng, D. Y. 1978. The Characterization of the Heptanes and Heavier Fractions, Research Report 28, Gas Producers Association, Tulsa, OK.
- Stout, S.A. 2015a. Physical and chemical properties of the fresh MC252 Macondo-1 well crude oil. NewFields Technical Report to the Trustees in support of the PDARP.
- Stout, S.A. 2015b. Bulk chemical and physical properties of fresh and weathered Macondo crude oil. NewFields Technical Report to the Trustees in support of the PDARP.
- Weinaug, C.F. and Katz, D.L. 1943. Surface Tensions of Methane-Propane Mixtures. Ind.&Eng.Chem. 35, 239.
- Zick, A. A. 2013. Expert Report, U.S. v. BP Exploration & Production, Inc. et al., Equation-of-State Fluid Characterization and Analysis of the Macondo Reservoir Fluids. Prepared on behalf of the United States. Prepared by: Aaron A. Zick, Zick Technologies, Inc., 6335 SW Dolph Drive, Portland, OR. March 22, 2013.

Technical Reports for Deepwater Horizon Water Column Injury Assessment

WC_TR.13: Application of OILMAP DEEP to the Deepwater Horizon Blowout

Appendix D: Pipe Leak Model Development

Authors: Malcolm Spaulding, Daniel Mendelsohn, Deborah Crowley,
Zhengkai Li, Andrew Bird

Revised: September 30, 2015

Project Number: 2011-144

RPS ASA 55 Village Square Drive, South Kingstown, RI 02879

Table of Contents

D1.	Introduction	1
D2.	Pipe Leak Model Theory.....	1
D3.	Application to the Deepwater Horizon Blowout	3
D3.1	Model Input	4
D3.2	Head Loss in the Pipe	7
D3.3	Model Results	10
D4.	Discussion.....	12
D5.	References.....	13

List of Figures

Figure D-1.	Schematic of the pipeline leak model application to the DWH blowout.	3
Figure D-2.	Interpretation of the flow structure at the exit of the kink holes on May 15, 2010 by Omer Savas, University of California, Berkeley (Appendix 4, McNutt et al. 2010). J refers to jet and E to entrainment with the subscript referring to jet number. (Figure 4, McNutt et al. 2010)..	6
Figure D-3.	Timeline of the number of kink holes and their associated opening area used in the pipeline leak model.	7
Figure D-4.	ROV image of the end of riser pipe on May 5, 2010 showing the crimping and reduced area (Figure 2, McNutt et al. 2010).	10
Figure D-5.	Pipeline release model predicted flow spilt between the kink holes and the riser outlet.	11

List of Tables

Table D-1.	List of parameters used in the pipeline leak model.	4
Table D-2.	Pipeline release model predicted flow split between the kink and riser openings.	11

D1. Introduction

Beginning on April 28, 2010, the riser pipe just above the Blowout Protector (BOP) began to leak where the pipe had been severely kinked as it fell to the sea floor during the collapse. Between April 28 and June 3, 2010, approximately six holes formed, increasing in area over time, releasing a large amount of oil and gas that would otherwise have travelled the length of the riser, to the severed end of the pipe before being released to the environment. The oil and gas released through the kink holes was under considerable pressure, creating oil/gas jets exiting at high velocity from each of the holes.

As a result of the high exit velocity and therefore high energy, it has been predicted that the oil droplets created in the process would be considerably smaller than those created as a result of exiting from the opening at the end of the riser pipe which had a much larger opening and therefore lower exit velocity. The droplet size range created at the kink hole opening is expected to be small enough that a large amount of them would easily be trapped, along with the entrained volume of the plume created by the blowout leakage at the kink, as it became neutrally buoyant. It is therefore important to understand the volume of oil and gas that leaked through the kink holes in order to understand the fate of that oil and the overall amount of oil in the water column.

At the time of the blowout, while some visual method-based estimates were made (Lehr et al. 2010, McNutt et al. 2011), it was not possible to directly measure the flow of oil and gas from the kink holes. Therefore an alternative method to estimate the flow rate was needed to evaluate leakage from the kink area and develop a full understanding of the flow split between the kink holes and the end of the riser pipe, prior to when the collapsed riser was cut and removed from the top of the Lower Marine Riser Package (LMRP).

D2. Pipe Leak Model Theory

The RPS ASA pipe leak model is designed to predict the single phase oil/gas mixture flow distribution in a network of pipes with any number of release locations and hole geometries, with the purpose of determining the potential leak rate for an accidental fracture or hole in an oil transport pipe. If the pressure, flow, and constituency of the oil/gas mixture (GOR) are known, in addition to the pipeline configuration and geometries, it is possible to calculate the flow distribution between the various openings through which the oil and gas can escape.

The pipe leak model is based on first principles, incorporating the steady state, control volume first law of thermodynamics (Van Wylen and Sontag 1973). The control volume is specified to surround the opening with the unknown flow, extending to such a point that known characteristics of the pipe and flow can be specified as boundary conditions for the port of the flow network of interest.

Employing the description of the control volume, there are three basic openings through which the oil and gas mixture flows; flow into the system from the source, flow exiting the system through a fissure or open holes, and flow exiting the system through the end of the pipe. This analysis assumes that the releases at the kink can be lumped into one release representative of the individual releases. Therefore, an energy balance for the system can be written as energy flux equals the sum of the energy flux out. The steady state, steady flow first law equation for a control volume described above, can be written as follows:

$$\dot{m}_s \left(\frac{P_s}{\rho} + \frac{u_s^2}{2} + g(h_s + z_s) \right) = \dot{m}_k \left(\frac{P_k}{\rho} + \frac{u_k^2}{2} + g(h_k + z_k) \right) + \dot{m}_r \left(\frac{P_r}{\rho} + \frac{u_r^2}{2} + g(h_r + z_r) \right) \quad D.1$$

where \dot{m}_s = source mass flux (kg/s)
 \dot{m}_k = mass flux through the leak (kg/s)
 \dot{m}_r = mass flux at the outlet end of the pipe (kg/s)
 g = acceleration due to gravity (m/s²)
 ρ = gas/oil fluid density at depth (kg/m³)
 P_i = pressure (Pa)
 u_i = velocity (m/s)
 h_i = head loss (m)
 z_i = height above the bottom (m)

and the subscript refers to:

s = at the upstream source opening of the pipe
 k = at the leak site openings
 r = at the downstream (end) outlet opening of the pipe

If we let

$$\begin{aligned} a &= \left(\frac{P_s}{\rho} + \frac{u_s^2}{2} + g(h_s + z_s) \right) \\ b &= \left(\frac{P_k}{\rho} + \frac{u_k^2}{2} + g(h_k + z_k) \right) \\ c &= \left(\frac{P_r}{\rho} + \frac{u_r^2}{2} + g(h_r + z_r) \right) \end{aligned} \quad D.2$$

then Equation D.1 simplifies to:

$$a\dot{m}_s = b\dot{m}_k + c\dot{m}_r \quad D.3$$

Assuming this is a steady state process, mass balance in the control volume dictates that:

$$\dot{m}_r = \dot{m}_s - \dot{m}_k \quad D.4$$

then

$$a\dot{m}_s = b\dot{m}_k + c(\dot{m}_s - \dot{m}_k)$$

This equation can then be solved for the unknown mass flow rate at the kink (\dot{m}_k), giving:

$$\dot{m}_k = \dot{m}_s \left(\frac{a-c}{b-c} \right) \quad D.5$$

Assuming the mass flux from the source, \dot{m}_s , is known, the mass flux for the kink holes can be estimated using Equation D.5. Equation D.4 can then be used to calculate the mass flux through the downstream riser pipe.

D3. Application to the Deepwater Horizon Blowout

The amount of oil and gas flow from the end of the riser pipe is necessarily influenced by the amount of flow leaking from the kink area, where the flow rate from the riser is decreased directly by the amount of leakage from the kink holes, assuming that the flow from the well itself remains unaffected by the formation and leakage of the holes. Using these hypotheses for the Deepwater Horizon (DWH) event, the pipe leak model was applied to the fallen riser to determine the flow spilt between the kink holes and the end of the riser pipe. The application focused on the time between the time of the onset of the kink area leakage and the final cutting of the riser at the kink.

The control volume for the application (Figure D-1) was specified to contain the riser pipe from the top of the Lower Marine Riser Package (LMRP), above the BOP, to the far end of the riser pipe where it was lying, half buried but open to the ambient. The control volume therefore contained the kink area where the oil and gas mixture was leaking at an undetermined rate. The pipe leak model source input and outlet locations are then the flow into the system from the well at the LMRP, flow exiting the system through the kink holes, and flow exiting the system through the end of the riser pipe approximately 1,500 m farther along the riser, respectively (McNutt et al. 2011).

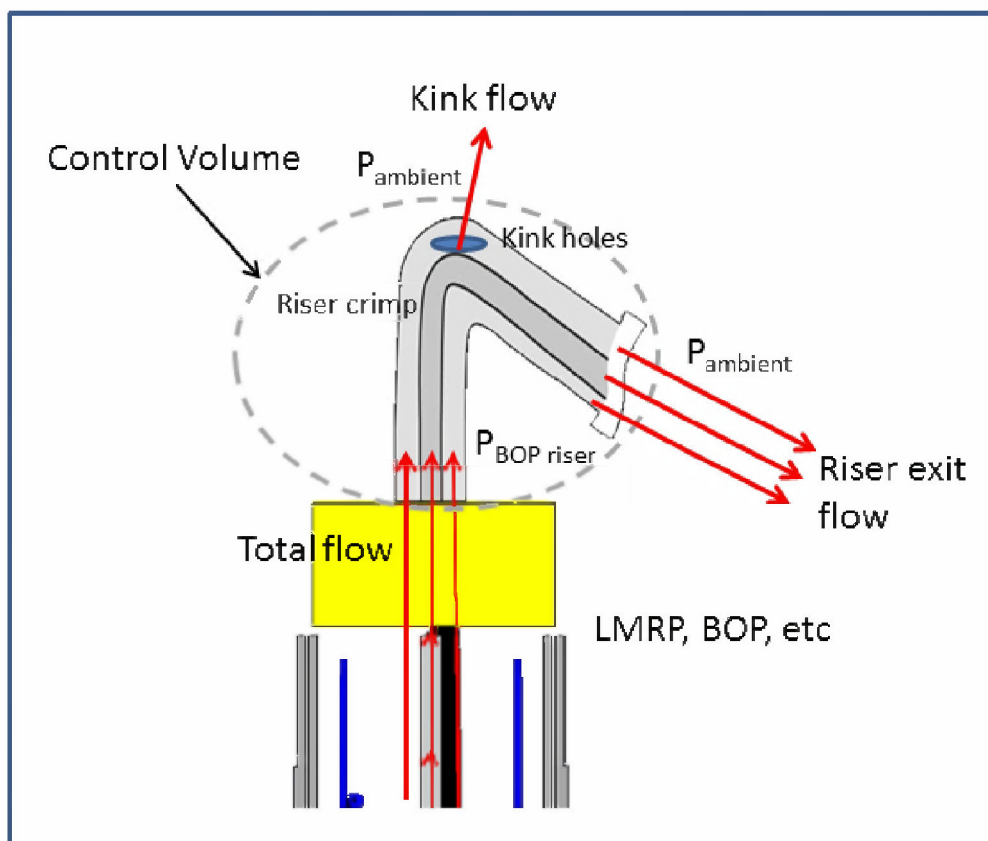


Figure D-1. Schematic of the pipeline leak model application to the DWH blowout.

D3.1 Model Input

Many of the specifications for applying the *pipeline release model* to the DWH blowout are well known, including the riser dimensions, the length of the broken riser between the kink and the outlet, the depths of the well, the kink area and riser outlet, the oil and gas mixture pressure in the BOP and LMRP, and the ambient seawater pressure levels. Some additional parameters are less well known, but estimates have been made, including the pressure inside the pipe after the LMRP, at the kink, and in the riser area downstream of the kink, the oil and gas flow rate, the GOR, the cross-sectional area in the crushed riser at the kink, through which the oil and gas mixture was forced, and finally, the number and sizes of the kink holes themselves. A list of the values used in the model application is presented in Table D-1.

Table D-1. List of parameters used in the pipeline leak model.

Parameter Description	Value	Source	Notes
Riser inside cross-sectional area (m ²)	0.1927	BP	Based on 19.5" ID
Riser outlet cross-sectional area (m ²)	0.138	FRTG*	Bent rim at the opening
Internal riser cross-sectional area at kink (m ²)	0.0258	RPS ASA	Crushed riser pipe
Kink depth (m)	1,503	BP	
BOP top depth (m)	1,506	BP	
Riser outlet pipe depth (m)	1,509	BP	
Ambient water pressure at kink (kPa)	15,154	calculated	Based on depth at 1,503 m
Ambient water pressure at riser end (kPa)	15,214	calculated	Based on depth at 1,509 m
Pressure in the pipe above LMRP (kPa)	18,271	FRTG*	2,650 psi
Length of riser pipe after kink (m)	1,500	BP	Approximate
GOR - at the surface (scf/bbl)	2807	BOT, Zick 2013	Std. Atm.**
GOR - at the surface (m ³ /m ³)	501	BOT, Zick 2013	Std. Atm.**
GOR - at depth (m ³ /m ³) – In-pipe	1.365	BOT, Zick 2013	180 C, 18,271 kPa
Oil density – surface (kg/m ³)	847.58	BOT, Zick 2013	Std. Atm.**
Oil density – in-pipe (kg/m ³)	689.69	BOT, Zick 2013	180 C, 18,271 kPa
Methane density - surface (kg/m ³)	0.9791	BOT, Zick 2013	15 C, 101.3 kPa (1 atm)
Methane density - in-pipe (kg/m ³)	162.53	BOT, Zick 2013	180 C, 18,271 kPa
Liquid volume fraction – surface (-)	0.001992	BOT, Zick 2013	Std. Atm.**
Gas volume fraction – surface (-)	0.998	BOT, Zick 2013	Std. Atm.**
Liquid volume fraction – in-pipe (-)	0.423	BOT, Zick 2013	180 C, 18,271 kPa
Gas volume fraction – in-pipe (-)	0.577	BOT, Zick 2013	180 C, 18,271 kPa

*Flow Rate Technical Group (FRTG 2010) Appendix D: Deepwater Horizon Release Estimate of Rate by PIV Figure 1 pp 24.

**Std. Atm. = 60F (15.5C), 14.7psi (101.325kPa)

The ambient seawater pressures outside of the kink hole area and at the end of the riser pipe were calculated based on the depth of each opening as determined from the ROV surveillance

videos, using basic hydrostatic pressure and the density of seawater. The end of the riser pipe, at 15,214 kPa, was slightly deeper than the kink which had a slightly higher pressure than the estimated value at the kink of 15,154 kPa. The pressure in the riser pipe, just above the LMRP, was taken from the Flow Rate Technical Group (FRTG) (McNutt et al. 2011) analysis of conditions in the well, the BOP, and piping system.

The flow rate of oil from the well was also estimated by the FRTG for the duration of the spill and values presented on a daily basis. According to the FRTG (McNutt et al. 2011), during the time period of the kink leak, the oil flow rate varied between 61,500 and 57,500 bbl/day, decreasing monotonically by 100 bbl/day, except every seventh day estimated to drop by 200 bbl/day. The total flow values from the FRTG were used as input to the pipeline release model and are the basis of the volume flux for the flow spilt.

Review of the Black Oil Tables (BOT) (Zick 2013) shows that not only is the GOR variable with pressure and temperature, but the constituent mass ratio also varies. Therefore, the total volume flow inside the riser pipe prior to exiting must to be determined from the BOT at the in-pipe pressure and temperature of 18,271 kPa (2,650 psi) and 180°C, respectively, resulting in an in-pipe GOR of 1.365. In addition, for the tabulated, in-pipe oil liquid volume fraction of 0.423 and the gas volume fraction of 0.577, and the respective oil and gas densities of 689.69 kg/m³ and 162.53 kg/m³, respectively, a fluid density of 385.43 kg/m³ was estimated. This resulted, for example, in an in-pipe total volume flux of 0.3929 m³/s for the initial flow of 61,500 bbl/day.

Despite the fact that there were several ROV (remotely operated vehicle) units almost constantly monitoring the leakage from the kink holes, it proved to be extremely difficult to measure or even estimate the volume of mixture released to the environment at these locations. This was in part due to the lack of a full understanding of the holes geometries, but also to the difficulty of estimating the flow rate of the jets that were visible to the ROV cameras, not to mention the jet(s) emanating from holes on the underside of the bent riser, and therefore not visible to the ROV cameras.

While oil and gas began to leak after the riser pipe separated from the DWH platform on April 22, 2010, the kink holes did not form and start to leak until April 28, 2010 when two holes appear to have formed simultaneously with a noticeable flow of oil and gas from each (Appendix A). Between April 28, 2010 and June 3, 2010 (when the riser cutting operations were completed), the number and size of the holes increased from the initial onset of two to an eventual six holes. The evolution of the number of holes was based on a detailed analysis of available ROV imagery taken during the spill and the inspection of the kink and riser sections (after they were retrieved from the seabed and impounded as evidence, see Appendix A for details). By that time however, the number, size and geometry of the holes had been evolving almost continuously, so the actual progressions of the sizes and configurations were approximated; however the video evidence does provide confidence that the overall trend was captured. For the present application, the number of holes was varied along the time schedule determined from the investigation; however only the final hole dimensions were used for each. A timeline of the number of holes and associated area used in the model is presented in Figure D-3.

In addition to the evolving number, locations, and time varying sizes of the holes the jet discharges from the kink showed considerable interaction in the immediate vicinity of the release. Figure D-2 shows the flow field near the kink on May 15, 2010 viewed by the ROV. The figure has been annotated by Omer Savas, Mechanical Engineering, University of California, Berkeley and provided in Appendix 4 (McNutt et al. 2011). The Js refer to jets and E to entrained flows. The subscripts designate the jet numbers. At this point there are two substantial

releases (on the left side, J_2 , and the center of the image, J_1) and one emerging release (on the right side, J_0). It is clear from the flow interpretation that there is complex interaction among the releases from the various holes, thus complicating the modeling of their releases. Given the proximity of the releases, the resulting discharges are clearly interacting with one another. As an engineering approximation the model assumed one hole to represent all holes with the area varying to match the total cross sectional area of all holes with time.

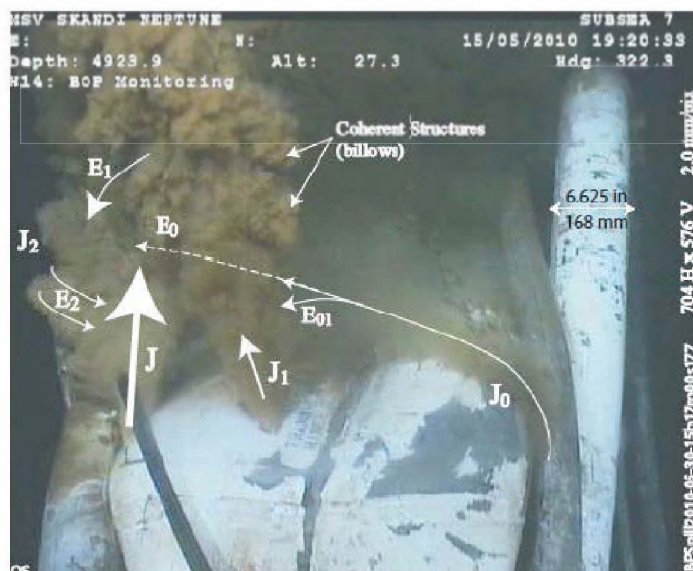


Figure D-2. Interpretation of the flow structure at the exit of the kink holes on May 15, 2010 by Omer Savas, University of California, Berkeley (Appendix 4, McNutt et al. 2011). J refers to jet and E to entrainment with the subscript referring to jet number. (Figure 4, McNutt et al. 2010).

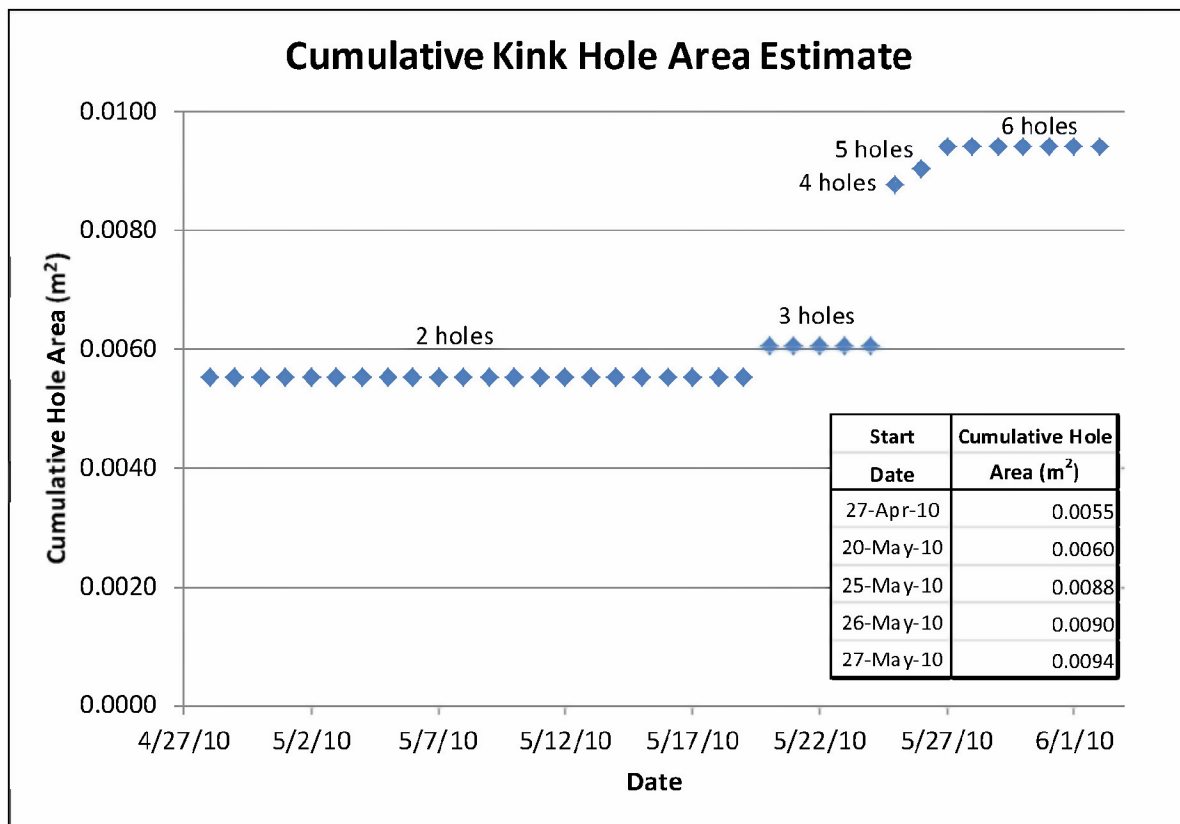


Figure D-3. Timeline of the number of kink holes and their associated opening area used in the pipeline leak model.

D3.2 Head Loss in the Pipe

There are a number of aspects of the collapsed riser that would certainly have affected the flow through the pipes and the kink holes in addition to the riser pipeline characteristics, the oil and gas properties, and the boundary conditions for the source flow and pressure. These influences needed to be accounted for in the DWH simulations, and were implemented in the model application primarily as head loss terms in the energy balance equation. The total head loss in the pipe is a sum of the friction loss associated with flow through the riser pipe, and minor losses due to bends, crimps, contractions, flow through the openings and the like in the pipe. The pipe friction head loss can be estimated by the Darcy equation (White 1979):

$$h_f = \frac{f L v^2}{2gD} \quad \text{D.6}$$

where h_f = head loss due to friction (m)
 f = friction coefficient (-)
 L = length of the pipe (m)
 v = flow velocity in the pipe (m/s)
 g = acceleration due to gravity (m/s²)
 D = pipe diameter (m)

The head loss at an obstruction (minor head loss) can be determined as (White 1979):

$$h_L = K_i \frac{v^2}{2g} \quad D.7$$

where h_K = obstruction head loss (m)

K_i = loss coefficient associated with obstruction i (-)

The total head loss associated with flow through the pipe and obstructions are then summed to give (White, 1979):

$$h_{total} = \frac{v^2}{2g} \left(\frac{fL}{D} + \sum K_i \right) \quad D.8$$

For implementation in the model application, the head losses also need to be divided appropriately among the three coefficients a, b and c from Equations D.2 above. The following head loss estimates were developed based on White (1979) for minor head loss in pipes.

The first head loss was due to a major constriction at the kink in the riser pipe, a few meters above the LMRP, where the pipe was bent at an angle greater than 90°, crushing the riser as well as the two drill pipes inside the riser, severely restricting the area through which the oil and gas mixture could flow. The extreme pressure on the well side of the kink was sufficient to force a significant amount of flow through the area, accelerating the fluid, which may have contributed to the formation and growth of the kink holes. The flow area restriction would also have caused a pressure drop, and as the holes were primarily upstream of the crimp, may also have also contributed to the large volume of flow estimated to have been released at the kink site. The impact of this restriction was implemented as a sudden contraction, a sudden expansion, and flow around a bend in the pipe, as follows:

$$K_{sc} = 0.42 \left[1 - \left(\frac{d_{crimp}}{D} \right)^2 \right] \quad D.9$$

$$K_{se} = 1.00 \left[1 - \left(\frac{d_{crimp}}{D} \right)^2 \right]^2 \quad D.10$$

$$K_{90} = 0.95 \quad D.11$$

$$h_c = \frac{v^2}{2g} (K_{sc} + K_{se} + K_{90}) \quad D.12$$

where K_{sc} = sudden contraction coefficient (-)

K_{se} = sudden expansion coefficient (-)

K_{90} = 90° bend coefficient (-)

d_{crimp} = crimped riser pipe effective diameter (m)

h_c = head loss due to the kink (m)

The effective diameter of the crimped area was determined from the measured area as presented in Table D-1 for model input parameters. The head loss due to the kink area crimping of the rise pipe was implemented in coefficient “b” (Equation D2), as it was determined that the kink holes were upstream of or in the immediate area of the crimp. A similar set of loss coefficients was defined for the flow through the kink holes and also implemented in coefficient “b”:

$$K_{sc} = 0.42 \left[1 - \left(\frac{d_k}{D} \right)^2 \right] \quad \text{D.13}$$

$$K_{se} = 1.00 \left[1 - \left(\frac{d_k}{D} \right)^2 \right]^2 \quad \text{D.14}$$

$$h_k = \frac{v_k^2}{2g} (K_{sc} + K_{se}) \quad \text{D.15}$$

where d_k = effective diameter of the combined kink holes (m)

v_k = velocity through the kink holes (m)

h_k = head loss through the kink holes (m)

The velocity through the kink holes is also one of the dependent variables and must be solved for simultaneously in the final solution, remembering that

$$v = \frac{\dot{m}}{\rho A} \quad \text{D.16}$$

For the flow calculation through the multiple kink holes, it is assumed the pressure in the pipe at the kink area is the same for all the holes. Similarly the ambient pressure outside the pipe is assumed the same in the kink area. These assumptions are based on the observations that all kink holes are in close proximity. The fraction of the kink flow from each hole out of the total kink flow is set equal to the fraction of the area of each hole to the sum area of all the holes. The head loss is computed for each hole, and the head losses are summed over all kink holes to estimate the total head loss for all the kink holes. The final release rates from the riser and the kink holes are then calculated iteratively to satisfy the governing mass balance and energy conservation equations. Through this method the head losses of the individual holes are reflected in the analysis. In terms of plume modeling, the releases from all kink holes are treated as one release to predict the dynamics of kink plume, while the release from the riser end is treated as a separate release to predict the riser plume dynamics.

The head losses associated with the flow down the remaining 1,500 m riser pipe after the kink and the final exit through the open end of the collapsed riser, which was also crushed marginally at its end (Figure D-4) completes the loss estimates. The loss coefficients for the long riser and exit are:

$$K_{pf} = \frac{fL}{D} \quad \text{D.17}$$

$$K_{sc} = 0.42 \left[1 - \left(\frac{d_{re}}{D} \right)^2 \right] \quad \text{D.18}$$

$$K_{se} = 1.00 \left[1 - \left(\frac{d_{re}}{D} \right)^2 \right]^2 \quad \text{D.19}$$

$$h_{re} = \frac{v_r^2}{2g} (K_{pf} + K_{sc} + K_{se}) \quad \text{D.20}$$

where K_{pf} = pipe friction loss coefficient (-)

d_{re} = effective diameter of the crushed riser exit opening (m)

v_{re} = velocity through the long riser (m)

h_{re} = head loss due to friction along the riser and exit flow (m)

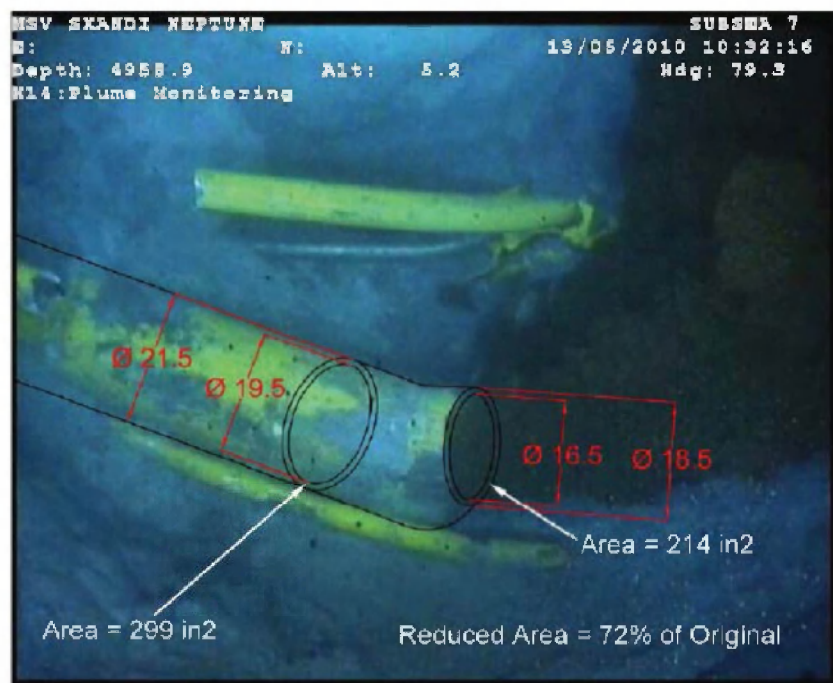


Figure D-4. ROV image of the end of riser pipe on May 5, 2010 showing the crimping and reduced area (Figure 2, McNutt et al. 2011).

These final loss factors were implemented in coefficient “c” (Equation D2), associated with the flow after the kink area, through the long riser pipe and exit. As with the kink flow velocity, the downstream riser flow velocity must be solved for simultaneously, but is similarly a function of the mass flux through downstream riser.

The model application was then used to predict unknown release rates from the two locations: the end of the riser pipe and the kink holes. The process was iterative, and solved by estimating the flow split and then using those values in the first law equation to calculate the flow at the kink and then to back calculate the riser outlet flow. If the new estimates differed from the initial estimate, the process was repeated until a minimum threshold for convergence was reached. The calculations were performed on a daily time step, matching the resolution of the input flow rate from the source as estimated by the FRTG.

D3.3 Model Results

The pipeline release model was run from April 28 through June 2, 2010 to predict the daily flow balance. Figure D-5 presents the model predicted kink and riser flow rates and the total flow from the well, as a function of time, over that period; note that these values do not take in account any of the collected flow, since this occurs after the release and does not impact the flow distribution analysis. The predicted amount of oil released from the kink was on the order of 11,000 bbl on the first day, increasing to 16,000 bbl immediately before the riser was cut, equating to 18% of the total amount released and then increasing to 28%, respectively. The

predicted flow for each opening and the percent of total are presented in Figure D-5 and Table D-2.

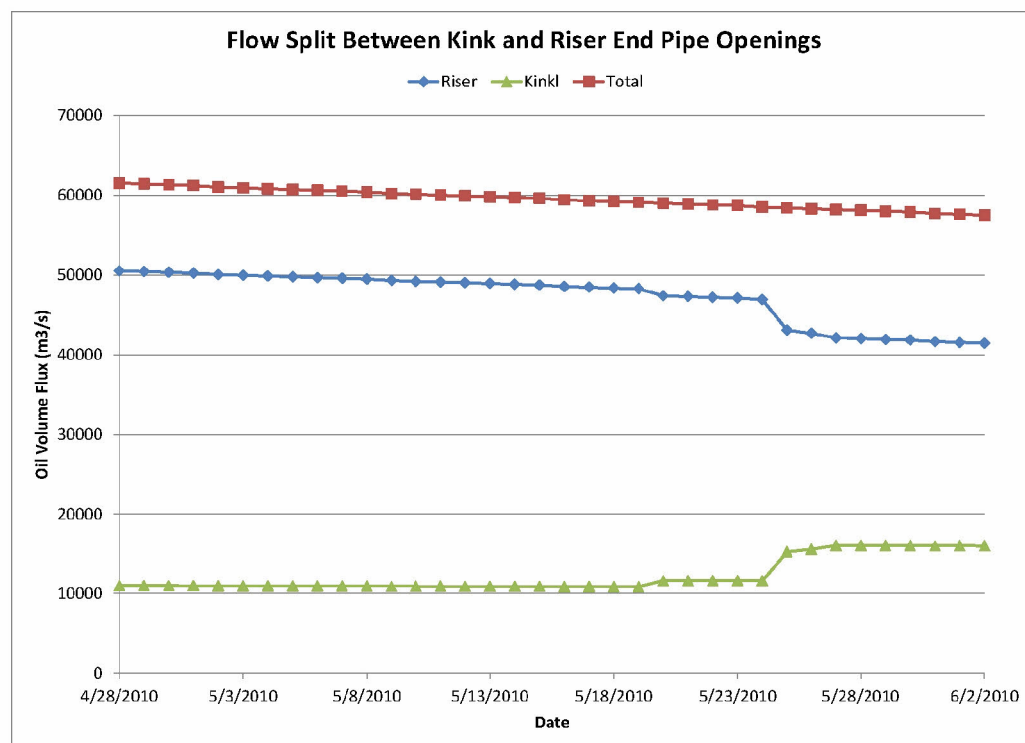


Figure D-5. Pipeline release model predicted flow split between the kink holes and the riser outlet.

Table D-2. Pipeline release model predicted flow split between the kink and riser openings.

Date	Kink Flow (bbl/day)	Riser Flow (bbl/day)	Total Flow (bbl/day)	Kink as Percent of Total	Date	Kink Flow (bbl/day)	Riser Flow (bbl/day)	Total Flow (bbl/day)	Kink as Percent of Total
4/28/2010	10980	50520	61500	17.9	5/16/2010	10857	48543	59400	18.3
4/29/2010	10974	50426	61400	17.9	5/17/2010	10851	48449	59300	18.3
4/30/2010	10968	50332	61300	17.9	5/18/2010	10846	48354	59200	18.3
5/1/2010	10962	50238	61200	17.9	5/19/2010	10840	48260	59100	18.3
5/2/2010	10951	50049	61000	18	5/20/2010	11626	47374	59000	19.7
5/3/2010	10945	49955	60900	18	5/21/2010	11621	47279	58900	19.7
5/4/2010	10939	49861	60800	18	5/22/2010	11615	47185	58800	19.8
5/5/2010	10933	49767	60700	18	5/23/2010	11609	47091	58700	19.8
5/6/2010	10927	49673	60600	18	5/24/2010	11598	46902	58500	19.8
5/7/2010	10921	49579	60500	18.1	5/25/2010	15305	43095	58400	26.2
5/8/2010	10915	49485	60400	18.1	5/26/2010	15610	42690	58300	26.8

Date	Kink Flow (bbl/day)	Riser Flow (bbl/day)	Total Flow (bbl/day)	Kink as Percent of Total	Date	Kink Flow (bbl/day)	Riser Flow (bbl/day)	Total Flow (bbl/day)	Kink as Percent of Total
5/9/2010	10904	49296	60200	18.1	5/27/2010	16085	42115	58200	27.6
5/10/2010	10898	49202	60100	18.1	5/28/2010	16080	42020	58100	27.7
5/11/2010	10892	49108	60000	18.2	5/29/2010	16075	41925	58000	27.7
5/12/2010	10886	49014	59900	18.2	5/30/2010	16070	41830	57900	27.8
5/13/2010	10880	48920	59800	18.2	5/31/2010	16061	41639	57700	27.8
5/14/2010	10874	48826	59700	18.2	6/1/2010	16056	41544	57600	27.9
5/15/2010	10869	48731	59600	18.2	6/2/2010	16051	41449	57500	27.9

D4. Discussion

Early on, while the blowout was still in progress, investigators made estimates of the amount of oil leaking from the kink area. Estimates made by members of the FRTG using Particle Image Velocimetry (PIV) for May 15, 2010 prior to the formation of the FRTG (Wereley 2010) estimated the kink flow at 35% of the riser flow, which corresponds to 26% of the total flow. Additional estimates were made using PIV methods after the formation of the FRTG and gave values ranging from 15 to 20% for May 14-16, 2010 (McNutt et al. 2011). Camilli et al. (2011) estimated the flow split, based on ADCP measurements, for May 31, 2010 and gave a value of 31%. The estimates, for May 14-16, correspond to the time when only two holes were in existence, whereas by May 31, all six holes were present. The model predictions are in generally good agreement with the observations, both in terms of trend and the percentage released.

The predicted increase in flow percentage over time was a result of the number of holes at the kink increasing from two, at the start of the spill, to six immediately before the riser was cut. This estimate appears to be reasonable given the observation that the area of the combined openings of the kink holes essentially doubled over the course of the kink leakage. While the flow volumes appear large, the crushed riser pipe in the kink area likely kept the internal pressures on the BOP side extremely high, and caused a considerable reduction in the riser flow. The kink holes were primarily, if not all, between the BOP and the crimp (as opposed to between the crimp and end of riser of the crimp) which implies that there was a 2,750 kPa (400 psi) pressure drop across the openings to the water column, according to FRTG internal pressure estimates (McNutt et al. 2011).

D5. References

- Camilli R., D. Di Iorio, A. Bowen, C. M. Reddy, A. H. Techet, D. R. Yoerger, L. L. Whitcomb, J. S. Seewald, S. P. Sylva and J. Fenwick. 2011. Acoustic measurement of the Deepwater Horizon Macondo well flow rate, *Proceedings of the National Academy of Sciences*. www.pnas.org/cgi/doi/10.1073/pnas.1100385108.
- Flow Rate Technical Working Group (FRTG). 2010. Assessment of flow rate estimates for the Deepwater Horizon/Macondo Well, Plume Team Deepwater Horizon Release Estimate of Rate by PIV, US Department of Interior, July 21, 2010. p. 216.
- Lehr, B., S. Bristol and A. Possolo. 2010. Deepwater horizon oil budget calculator: A report to the national incident command. The Federal Interagency Solutions Group, Oil Budget Calculator Science and Engineering Team. http://www.restorethegulf.gov/sites/default/files/documents/pdf/OilBudgetCalc_Full_HQ-Print_111110.pdf (Accessed on April 1, 2012).
- McNutt, M., R. Camilli, G. Guthrie, P. Hsieh, V. Labson, B. Lehr, D. Maclay, A. Ratzel and M. Sogge. 2011. Assessment of Flow Rate Estimates for the Deepwater Horizon / Macondo Well Oil Spill. Flow Rate Technical Group report to the National Incident Command, Interagency Solutions Group. Appendix D – Plume Calculation Team 2010; Particle Image Velocimetry Report. March 10, Available online: <https://www.doi.gov/sites/doi.gov/files/migrated/deepwaterhorizon/upload/FRTG-report-Appendix-D-Plume-Analysis-Report.pdf>
- Van Wylen, G. J. and R. E. Sontag. 1973. Fundamentals of Classical Thermodynamics, Wiley and Sons.
- Wereley, S. 2010. Congressional Testimony. May 2010.
- White, F.M. 1979. Fluid Mechanics, McGraw-Hill, Inc.
- Zick, A. A. 2013. Expert Report, U.S. v. BP Exploration & Production, Inc. et al., Equation-of-State Fluid Characterization and Analysis of the Macondo Reservoir Fluids. Prepared on behalf of the United States. Prepared by: Aaron A. Zick, Zick Technologies, Inc., 6335 SW Dolph Drive, Portland, OR. March 22, 2013.

Technical Reports for Deepwater Horizon Water Column Injury Assessment

WC_TR.13: Application of OILMAP DEEP to the Deepwater Horizon Blowout

Appendix E: Model of the Blowout Plume

Authors: Malcolm Spaulding, Daniel Mendelsohn, Deborah Crowley,
Zhengkai Li, Andrew Bird

Revised: September 30, 2015

Project Number: 2011-144

RPS ASA 55 Village Square Drive, South Kingstown, RI 02879

Table of Contents

E1.	Introduction.....	1
E1.1	Description of Blowout.....	1
E1.2	Background on Modeling Blowouts.....	4
E2.	Blowout Model.....	5
E2.1	Model Theory	5
E2.2	Conservation of water mass	6
E2.3	Conservation of oil mass	6
E2.4	Conservation of momentum.....	7
E2.5	Conservation of buoyancy	7
E2.6	Gas Dissolution	8
E2.7	Hydrate Formation.....	10
E2.8	Plume Separation.....	13
E2.9	Droplet Size Distribution.....	14
E3.	Model Implementation	14
E3.1	Model Parameters	15
E3.2	Implementation of the Macondo Crude Black Oil Tables	18
E3.3	Initialization of the Plume Model	21
E4.	References	22

List of Figures

Figure E-1.	Blowout plume example showing the various stages of the plume in the water column.	1
Figure E-2.	Schematic of the blowout plume in shallow water.	3
Figure E-3.	Illustration of a blowout plume development and subsurface trapping.	4
Figure E-4.	Methane phase equilibrium plot as a function of water depth and temperature for the formation of methane hydrates.....	11
Figure E-5.	Example of plume trapping height with and without hydrate formation.	12
Figure E-6.	Illustration of conditions for stable hydrate formation for approximately 1,500 m of water (Anderson et al. 2012).	13
Figure E-7.	Blowout plume in a cross-flow, showing bubble plume separation.	14
Figure E-8.	Flowchart of the OILMAP Deep blowout plume model runtime execution.	17
Figure E-9.	Example plume half width and centerline rise velocity as a function of distance above the blowout.	18

List of Tables

Table E-1. Blowout plume model parameters.....	16
Table E-2. Black Oil Tables properties for “standard” surface conditions (Zick, 2013).....	19
Table E-3. Example oil and gas flow rates determined using Black Oil Tables properties for NOAA estimated blowout release rates at “standard” surface conditions	19
Table E-4. Black Oil Tables properties for the two conditions estimated at depth (Zick, 2013). Top line is for conditions in equilibrium with ambient; bottom line for in-pipe conditions.	20
Table E-5. Calculations of the oil/gas fluid exit velocity, transition height and plume half width. Top line is for conditions in equilibrium with ambient; bottom line for in pipe conditions.	21

E1. Introduction

OILMAP DEEP's plume model estimates the characteristics of the plume associated with a subsurface blowout release of oil and gas. Figure E-1 presents a schematic of the various stages of a subsurface release in the water column. The blowout model estimates the size and location of a buoyant oil and gas plume in response to the release parameters and environmental characteristics, tracking the development of the plume until the point where the density of the plume matches the ambient, through entrainment, and the buoyancy has decreased such that the oil and gas mixture no longer rises. In addition, the model includes a formulation used to estimate the oil droplet size distribution and associated droplet rise velocity resulting from the release. The droplet size model is provided in Appendix G.

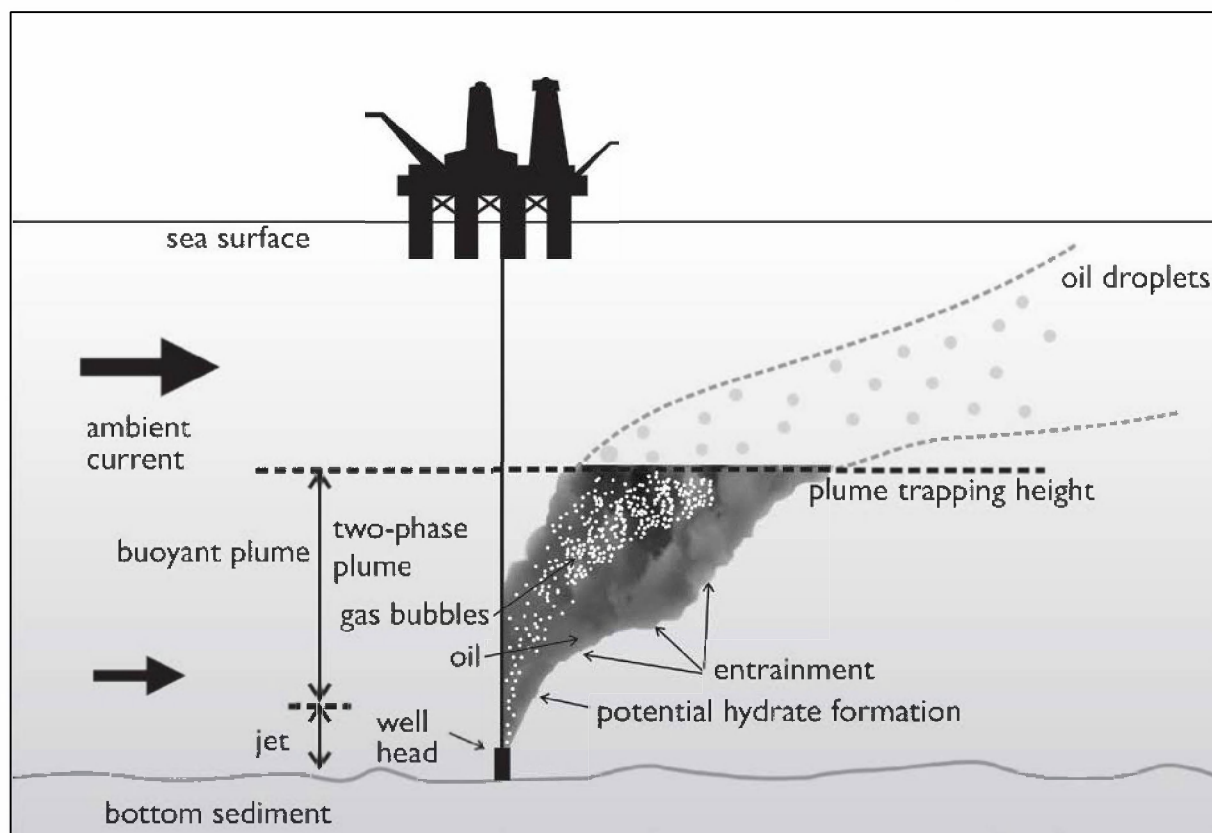


Figure E-1. Blowout plume example showing the various stages of the plume in the water column.

E1.1 Description of Blowout

In a subsurface well blowout, discharged materials consisting of a mixture of gaseous and liquid hydrocarbons go through three phases (illustrated schematically in Figure E-2):

1) Momentum jet

The immediate pressure difference between inside the well and the ambient water drives the discharge in a momentum jet exiting the blowout orifice. The momentum jet

dissipates relatively quickly as it entrains surrounding water, and is confined to the vicinity of the wellhead, or blowout site (typically on the order of meters).

At the blowout opening, the oil in the release is exposed to significant turbulent energy, resulting in a break up into small droplets. These droplets (typically micrometers to millimeters in diameter) are transported upward with the rising plume.

2) Buoyant density plume

As the discharge moves upward, the density difference between the gas bubbles in the plume and the ambient waters results in a buoyant force which drives the plume. As the plume rises, it continues to entrain sea water, increasing the plume's density, reducing the velocity and buoyancy, and increasing its radius. The dissolution from gas bubbles in the plume may deprive the plume of some of its buoyancy. If the ambient currents are strong enough the plume maybe bent as shown in Figure 1. Gas bubbles may also separate from the plume if their rise rates exceed the plume's rise rate. The oil droplets continue to be transported upwards with the plume but their individual rise velocities contribute little to their upward motion.

3) Free rise and advection-diffusion

When the plume reaches the sea surface or its *termination or trap height* (all momentum is lost), it can be deflected in a radial pattern, within a horizontal flow zone, without appreciable loss of momentum (intrusion). This radial flow carries the oil particles rapidly away from the center of the plume, while the velocity and oil concentrations in this flow zone decrease with distance from the release.

Subsequently, oil particles ascend to the surface solely by their own buoyancy. Rise velocities of oil droplets are much slower than the velocity of a buoyant gas-liquid plume, resulting in particle transport that may take considerably longer to reach the surface and result in transport farther (horizontally) from the release site due to ambient currents.

Of the three phases described above, the blowout plume model simulates only phase two, the buoyancy driven portion. The assumption is that Phase 1, the momentum jet, is very limited in distance from the release (numbers of diameters of the orifice from the release) and hence relatively insignificant in the development of the overall plume and prediction of the trap height. Phase 3, the passive oil droplet transport and fate, is simulated using the far field oil particle transport and fate model, **SIMAP**.

In shallow water (<200 m) oil and gas released from the sea bed are driven into the water column as a jet due to the momentum of the discharge (Figure E-1). The jet region is confined to the vicinity of the seabed and is relatively short in length (< several meters). As the discharge moves upward the density difference between the expanding gas bubbles in the plume and the receiving water result in a buoyant force which drives the plume. The resulting plume is analogous to a thermal plume, with the important exception that for blowouts the plume is bubble starved, because the bubbles are few in number and large. The presence of the bubbles leads to a two-layer structure with an inner core bubble plume and an outer ring of mostly entrained water.

As the plume rises, it continues to entrain ambient sea water due to the velocity difference between the rising plume and the receiving water. This entrainment reduces the plume's velocity and buoyancy, and increases its radius. The oil in the release is rapidly mixed by the turbulence in the rising plume causing it to break up into small droplets. These droplets (typically a few micrometers to millimeters in diameter) are rapidly transported upward by the rising

plume; their individual rise velocities contributing little to their upward motion. As the plume reaches the sea surface, it is deflected in a radial, surface flow zone without appreciable loss of momentum as can be seen in Figure E-2. This radial jet, with its origin at the surface directly above the blowout, carries the oil particles rapidly away from the center of the plume. The velocity and oil concentrations in this surface flow zone decrease with distance from the plume centerline while the depth of the zone increases. Finally in the far field, where the plume buoyancy has been dissipated, ambient currents and/or wind generated waves determine the subsequent transport and dispersion of the oil.

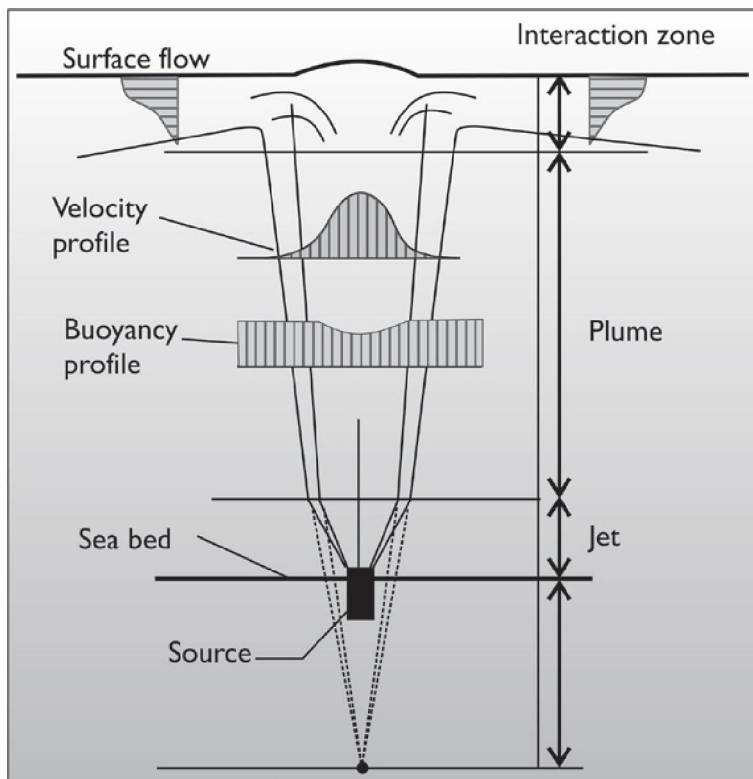


Figure E-2. Schematic of the blowout plume in shallow water.

There are several important processes that may alter this basic description of jet and plume behavior. If the buoyant driving force for the plume is dissipated by entrainment before it reaches the surface, the oil droplets in the plume will be carried to the surface solely by their own rise velocities and the surface interaction zone will effectively disappear. The plume behavior can also be altered by variations in the ambient density field, which can cause trapping of the plume in the water column as seen in Figure E-3. Finally in the presence of strong ambient currents, the plume path can be substantially altered as the current forces the jet to bend from its preferred vertical direction (Figure E-1). If the current velocity profile with depth varies with time, the path of the plume can become very complicated.

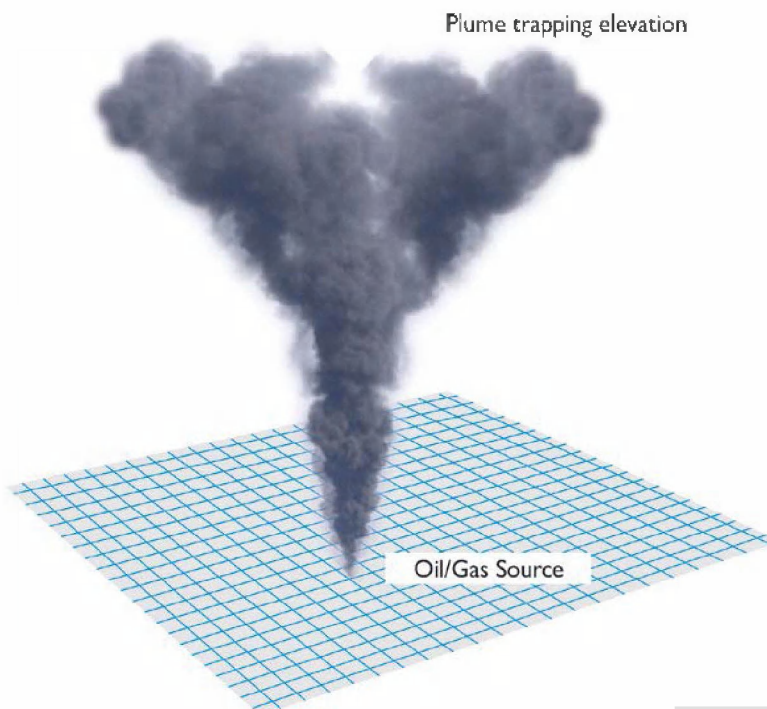


Figure E-3. Illustration of a blowout plume development and subsurface trapping.

As water depths increase (>200 m) the basic dynamics of the oil/gas jet/plume become more complicated, principally due to the increase in hydrostatic pressure at the seabed which leads to the possibility of rapid gas dissolution and formation of gas hydrate solids. The behavior of gas is altered significantly in the higher pressures associated with deep water, and deviates from ideal. In addition, the solubility of the gas in water is also affected by the ambient pressure, temperature, and salinity. In the deeper waters, the expansion rate of the gas bubbles is exceeded by the gas dissolution rate indicating that there is a potential for a significant portion of the gas to dissolve as the plume rises, decreasing the buoyancy forces driving the plume upwards.

E1.2 Background on Modeling Blowouts

A review of the literature shows that our understanding and ability to model the dynamics of rising oil and gas plumes in shallow water is extensively developed. Early work by McDougall (1978), Fanneløp and Sjøen (1980a,b), and Milgram (1983), using integral plume theory, has been extended by Rye (1994) and Kolluru (1993) into operational models to predict plume dynamics and oil concentrations. Zheng and Yapa (1997,1998) have further developed and refined this basic approach for buoyant oil jets and smoke plumes. Their model has been extensively tested against analytic and theoretical results and laboratory and field experiments. Rye et al. (1996) describe a 1995 experiment in the North Sea. In all cases, the models performed well against theory and field observations. They also correctly predicted the height of the transition zone from when oil transport was dominated by plume dynamics to when oil droplet rise velocities dominated its movement.

Early work on the formation rate of gas hydrates under the gas/oil flow rates, hydrostatic pressures, temperatures, and salinity at typical blowout sites was performed by Topham (1975,

1977) in the form of field experiments. For those experiments, natural gas was used at a release depth of 650 m, with and without oil, and observations of the formation of hydrates in both cases were made. He was unable to determine the rates of formation but did note that hydrates did not form at depths shallower than about 300 m. Bishnoi and Maini (1979) performed a set of laboratory experiments using a high pressure test facility (2,000 psi) (equal to a seawater depth of 1,370 m). According to their work, gas to hydrate conversion was complete when starting pressures were in excess of 700 psi (480 m) and ceased when the pressure was lower than 450 psi (310 m). It is noted that the hydrate formation pressures are highly dependent on the gas or hydrocarbon liquid compositions. For very light condensate oils or oil and gas mixtures rich in gas the pressure could be even lower than 450 psi. Quantitative estimates of the rates were not provided. Zheng and Yapa (1999) have extended their model to include a simplified hydrate formation component. The approach ignored the kinetics of hydrate formation, assuming that all hydrates were formed at the very beginning of the release and that the conversions are based on ideal gas laws. Since, Chen and Yapa (2001) have added hydrate formation and decomposition kinetics in the CDOG (Clarkson Deepwater Oil & Gas) model (Yapa and Chen, 2003). More recently, Anderson et al. (2012) have adopted an approach based on characterizing dissolved gas concentration versus temperature.

E2. Blowout Model

E2.1 Model Theory

RPS ASA's oil blowout model is based on the work of McDougall (1978), Kolluru (1993), Fanneløp and Sjøen (1980b) and Spaulding et al. (2000) for the gas plume, Fanneløp and Sjøen (1980a) for plume/free surface interaction, Kolluru (1993) for oil concentration, Spaulding et al. (2000) for hydrate formation and Zheng et al. (2002) and Zheng and Yapa (2002) for gas dissolution. A simplified integral jet theory is employed for the vertical as well as for the horizontal motions of the gas-oil plume. The necessary model parameters defining the rates of entrainment and spreading of the jet are obtained from laboratory studies (Fanneløp and Sjøen 1980a). The gas plume analysis is described in McDougall (1978) and Fanneløp and Sjøen (1980b). The hydrate formation and dissociation is formulated based on a unique equilibrium kinetics model developed by R. Bishnoi and colleagues at the University of Calgary. A brief description of the governing equations used in the model and the solution methodology is given below.

The steady state gas flow rate $Q(z)$, at any height z , (measured positively upward from the source) can be related to the value of flow rate at the surface (atmospheric pressure) Q_o by

$$Q(z) = \left[\frac{Q_o P_a}{(H - z) \rho_r g} \right]^{1/n} \quad (2-1)$$

where $Q(z)$	=	steady state gas flow rate at depth (m^3/s)
Q_o	=	steady state gas flow rate at surface pressure (m^3/s)
z	=	height above blowout (m)
P_a	=	atmospheric pressure (Pa)
g	=	acceleration due to gravity (m/s^2)
ρ_r	=	reference density of sea water (kg/m^3)
H	=	total static pressure head at the blow out location (m)

The exponent n lies between the isothermal and adiabatic values. In this case, the expansion process is assumed to be isothermal and therefore $n=1$.

Earlier work (McDougall 1978; Spaulding et al. 2000) shows that the average vertical velocity v and density deficiency g' in the plume vary, according to a Gaussian curve across the plume width. These variations are given by

$$v(r, z) = v(z) \exp\left(\frac{-r^2}{b^2}\right) \quad (2-2)$$

$$g'(r, z) = g'(z) \exp\left(\frac{-r^2}{\lambda^2 b^2}\right) \quad (2-3)$$

where $v(r, z)$ = vertical velocity in the plume at height z and radius r , (m/s)
 $v(z)$ = vertical velocity at the centerline at height z , (m/s)
 b = effective radius of the plume, (m)
 $g'(r, z)$ = $g(\rho_o(z) - \rho(r, z))/\rho_r$ is the reduced gravity, (m/s²)
 $\rho_o(z)$ = density of the environment at height z , (kg/m³)
 $\rho(r, z)$ = plume density at r and z caused by mixing of ambient seawater and gas bubbles, (kg/m³)
 λ = empirically derived spreading parameter ($\lambda \approx 0.2$),

A similar assumption is made for oil concentration in the plume and can be expressed as

$$C(r, z) = C(z) \exp\left(\frac{-r^2}{\lambda_c^2 b^2}\right) \quad (2-4)$$

where $C(r, z)$ and $C(z)$ (in ppt) are analogous to Eq. 2-2 and 2-3 and λ_c is the oil concentration plume spreading parameter. The oil spreading coefficient (λ_c) values vary between 0.2 and 0.5 (Fannelop and Sjoen 1980a).

The plume equations are derived by applying the conservation laws of water mass, momentum, oil mass, and buoyancy and using the relationships noted for velocity, density, and concentration (McDougall 1978). The governing equations are applied for an element along the plume centerline. The equations are given in the following sections.

E2.2 Conservation of water mass

The conservation of water mass in the plume is given by:

$$\frac{d}{dz}(b^2 v) = 2\alpha b v \quad (2-5)$$

where the entrainment constant α has been employed to relate the plume velocity v to the amount of fluid entrained, similar to thermal plumes. The entrainment coefficient ranges in value between 0.06 and 0.12 (Yapa and Zheng 1997).

E2.3 Conservation of oil mass

The conservation of oil mass in the plume is given by:

$$\frac{d}{dz} \left[\left(\frac{\pi(\lambda_c b)^2 v}{\lambda_c + 1} + \pi(\lambda_c b)^2 W_s \right) C_c \right] = 0 \quad (2-6)$$

where W_s is the terminal rise velocity for a given oil droplet. This equation can now be integrated directly, noting that the flux of oil at any level z is simply equivalent to the rate of oil release at the discharge point, Q_{oil} . Then the center line oil concentration $C(z)$ can be expressed as

$$C(z) = \frac{Q_{oil}}{\frac{\pi(\lambda_c b)^2 v}{\lambda_c + 1} + \pi(\lambda_c b)^2 W_s} \quad (2-7)$$

Equation 2-7 assumes that the oil in the plume is conservative and ignores dissolution or biodegradation.

E2.4 Conservation of momentum

Assuming the Boussinesq approximation (density variations are only important for the body force term) adequately describes the influence of density variations, the conservation of momentum equation for the plume is given by

$$\frac{d}{dz} (1/2 b^2 v^2) = \lambda^2 b^2 g' \quad (2-8)$$

E2.5 Conservation of buoyancy

Taking into account the effects of local density stratification in the environment, as well as the increase in volume flow rate of gas with height, the conservation of buoyancy is given by

$$\frac{d}{dz} \left(\frac{\pi \lambda^2 b^2 v g'}{\lambda^2 + 1} \right) = -\pi b^2 v N^2 + \frac{d}{dz} \left(\frac{Q_0 P_{av}}{(H - z) \rho_r (v + U_B)} \right) \quad (2-9)$$

where the bubble velocity U_B is related to the slip velocity U_s by $U_B = U_s(\lambda^2 + 1)$, has been introduced to account for the relative motion of the plume bubbles to the plume water and

$N^2(z) = (-g/\rho_r) d\rho_o/dz$ is the local buoyancy frequency. This slip velocity reduces the effective buoyancy flux in the plume. A value of 0.3 m/s has been shown by Cederwall and Ditmars (1974) to give good agreement to Kobus' (1968) data.

The second term on the right hand side of Equation 2-9 describes the change of buoyancy flux associated with (1) the change in volume flow rate of gas with height due to gas expansion as the hydrostatic pressure decreases, (2) the change of gas volume due to gas loss by dissolution, (3) the oil buoyancy flux. Specifically, Q_0 denotes an equivalent gas flow rate (in m^3/s at surface standard pressure and temperature conditions), including the remaining gas volume flow from the original release (determined based on initial Black Oil Table, BOT properties) and after gas dissolution (see Section 2.6), hydrate formation if applicable (see Section 2.7) and gas separation if applicable (see Section 2.8). The equivalent gas fluxes of oil volume flux and hydrate volume flux are also calculated to account for their respective contribution to the change of plume buoyancy using the non-ideal equation-of-state of gas compressibility factor applicable for deep water with high pressure and low temperature effects (e.g., Zheng and Yapa 2002).

Equations (2-5) through (2-9), with appropriate boundary conditions, completely describe the plume model. It is convenient to reformulate the governing equations in dimensionless form. Using the dimensionless relations

$$\begin{aligned} z &= Hx \\ b &= 2\alpha HB \\ v &= U_B M^{1/3} V \\ g' &= GU_B^2 M^{2/3} / \lambda^2 H \end{aligned}$$

where $M = Q_0 P_a (\lambda^2 + 1) / 4 \pi \alpha^2 \rho_r H^2 U_B^3$. The governing equations become

$$\frac{d}{dx}(B^2 V) = BV \quad (2-10)$$

$$\frac{d}{dx}(BV) = \frac{BG}{V} \quad (2-11)$$

$$\frac{d}{dx}(B^2 VG) = -\frac{N^2 (\lambda^2 + 1) H^2}{U_B^2 M^{2/3}} B^2 V + \frac{d}{dx} \left(\frac{V}{(1-x)(V + M^{-1/3})} \right) \quad (2-12)$$

Following the assumption of Morton et al. (1956) that at small heights an ordinary plume is not greatly influenced by stratification, the initial value of B, V, and G can be expressed in a power series solution in the form

$$B = z [0.6 + 0.01719M^{1/3} z^{1/3} - 0.002527M^{2/3} z^{2/3} - z(-0.04609 + 0.000031M^1) + \dots] \quad (2-13)$$

$$V = z^{-1/3} [1.609 - 0.3195M^{1/3} z^{1/3} + 0.0669M^{2/3} z^{2/3} + z(0.4536 - 0.0105M^1) + \dots] \quad (2-14)$$

$$G = V / (B^2 V(1-z)(V + M^{1/3})) \quad (2-15)$$

Equations (2-10) through (2-12) can now be solved numerically by a Runge Kutta method (White 1974) with initial conditions obtained from the power series solutions at some small starting value of z.

E2.6 Gas Dissolution

The blowout model formulation includes gas dissolution. The rate of dissolution is primarily a function of the amount of gas in the release and the initial gas bubble size associated with the release. As the gas dissolves, it reduces the plume buoyancy and increases the dissolved gas (e.g. methane) concentration in the plume-entrained water. In addition, in deeper waters, dissolution can decrease bubble size faster than the pressure related to expansion of the bubbles as the plume rises.

The gas dissolution formulation employed in **OILMAP DEEP** is based on that developed by Zheng et al. (2002) and Zheng and Yapa (2002). The formulation used here updates existing models through the development of analyses to take very deep, high pressure environments into account, specifically the impact of the high pressure and low temperatures on the deviation from ideal gas behavior.

The dissolution mass transfer rate for a gas bubble is calculated as a function of the molecular weight of the gas, a mass transfer coefficient, the surface area of the bubble and the temperature dependent solubility of the gas (e.g. methane) in water, given by:

$$\frac{dm}{dt} = KMA (C_s - C_0) \quad (2-16)$$

where m = mass of a gas bubble (kg)
 K = mass transfer coefficient (m/s)
 M = molecular weight of gas (kg/mole)
 A = surface area of a gas bubble (m²)
 C_0 = concentration of dissolved gas (mole/m³)
 C_s = saturated value of C_0 (mol/m³)

In the model, the deviation of a real gas from the ideal gas (law) can be described by the compressibility factor (z) defined as follows:

$$z = \frac{PV}{nRT} \quad (2-17)$$

where P = ambient pressure (Pa)
 V = gas volume (m³)
 n = number of moles of gas (-)
 R = universal gas constant = 1.9858 (cal/K mol)
 T = ambient temperature (K)

For an ideal gas, $z = 1$.

The gas solubility in water is commonly calculated by the conventional Henry's law. In deep water, where the pressure is high and temperatures are low, Zheng et al. (2002) found that the solubility computations can be improved by using a modified form of Henry's law:

$$f^g = Hx^l \exp\left(\frac{Pv^l}{RT}\right) \quad (2-18)$$

where H = water temperature dependent Henry's law constant (atm)
 x^l = mole fraction of dissolved gas in solution
 f^g = fugacity of gas in the gas phase
 v^l = partial molar volume of gas in solution

Henry's law constant and the fugacity are then calculated by a correlation for gas in water and the Peng-Robinson equation-of-state and v^l is specified as 36.5 cm³/mol for methane:

$$-\ln(H) = \frac{A_1}{R} + \frac{A_2}{RT} + \frac{A_3}{R} \ln T + \frac{A_4}{R} T \quad (2-19)$$

In this analysis methane is assumed to be the dominant gas of interest. For methane, Sloan (1997) gives the coefficients $A_1 - A_4$ as:

$A_1 = -365.183$
 $A_2 = 18,106.7$
 $A_3 = 49.7554$
 $A_4 = -0.000285$

The mass transfer coefficient of gas bubbles in liquids, K (m/s) is a function of gas diffusivity and the gas bubble size (surface area). The diffusivity of methane in water is taken as a constant $\sim 1.1\text{E-}9$ m²/s in the equations following. Gas bubbles in liquid are approximated as spheres for

small sizes, ellipsoids for intermediate sizes, and spherical-caps for large sizes. The transition diameter between small and intermediate size ranges is 5 mm and 13 mm between intermediate and large size ranges.

Formulations, originally from Johnson et al. (1969) and Clift et al. (1978), are used to form general formulations for mass transfer coefficient of bubbles in contaminated liquids, for three size ranges as presented in the following equations.

The small size range (less than 5 mm), assumes bubbles with a spherical shape:

$$K = 1.13 \left(\frac{UD}{0.45 + 0.2d_e} \right)^{\frac{1}{2}} \quad (2-20)$$

where K = mass transfer coefficient (cm/s)

U = terminal velocity of bubbles (cm/s)

D = molecular diffusivity of a gas in a liquid (cm²/s)

d_e = equivalent diameter of bubbles (cm)

Medium size range (between 5 and 13 mm) assumes bubbles with an ellipsoidal shape and a simple relationship to the diffusivity:

$$K = 6.5 D^{\frac{1}{2}} \quad (2-21)$$

And for the large size range (greater than 13 mm) the model assumes bubbles with a spherical-cap shape and the following relationship:

$$K = 6.94 d_e^{-\frac{1}{4}} D^{\frac{1}{2}} \quad (2-22)$$

The mass loss calculated by Equation 2-16 through 2-22 is implemented in the plume model to determine the potential gas loss at each level of the vertical integration through the plume. The loss is converted to a fraction of gas remaining at depth, and removed from the surface gas flux on which the buoyancy Equation 2-9 is based.

E2.7 Hydrate Formation

Equilibrium hydrate formation and dissociation for methane gas are determined by a multi-phase flash calculation developed by Bishnoi et al. (1979, 1989). The modeler must choose whether or not they want to allow hydrate formation; this has been implemented as a choice since hydrate formation in the water column is not well understood and the Bishnoi equilibrium curve defines the conditions that have the potential for formation only. In the present implementation when enabled the model calculates the fraction of gas that has formed hydrates, based on the ambient water temperature and the water to gas ratio (R_{w-g}). The ambient water temperature must be less than the methane equilibrium temperature at that depth (pressure) as seen in Figure E-4, showing the phase equilibrium boundary that marks the transition from a system of co-existing free methane gas and water/ice solid methane hydrate.

The methane equilibrium temperature (T_e , degrees K) is given as a function of depth (z) by:

$$T_e = 8.8189 \ln(z) - 48.499 \quad (2-23)$$

For water to gas ratios less than 5.82, the fraction of hydrates formed is given by:

$$F_{hyd} = 0.171 R_{w-g} \quad (2-24)$$

after which point hydrate formation is assumed to be complete.

An example of the effect of hydrate formation on the predicted trap height is shown in Figure E-5 to demonstrate the relative difference of enabling hydrate formation for a subsurface release that had temperature and depth such that the pressure was sufficient for hydrate formation in accordance with the Bishnoi equilibrium curve. The trap height for the hydrate formation case is significantly lower than that of the no hydrate formation case. As the methane gas is “frozen” (converted to hydrates), the gas associated with that conversion is removed from the buoyant plume and therefore the buoyancy force driving the plume up through the water column, is reduced and quickly disappears.

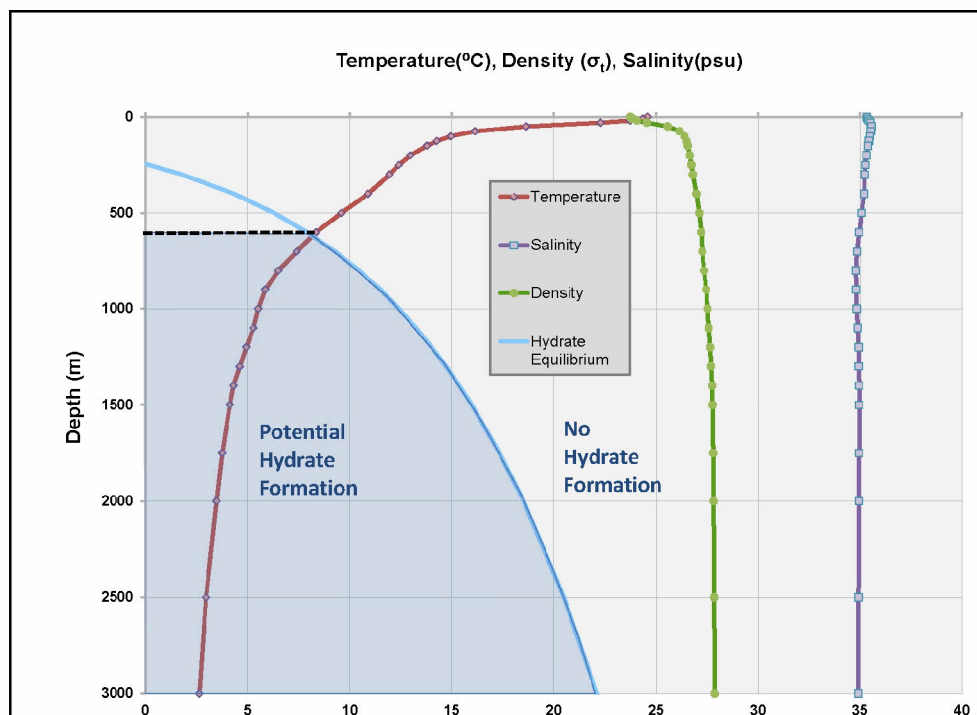


Figure E-4. Methane phase equilibrium plot as a function of water depth and temperature for the formation of methane hydrates.

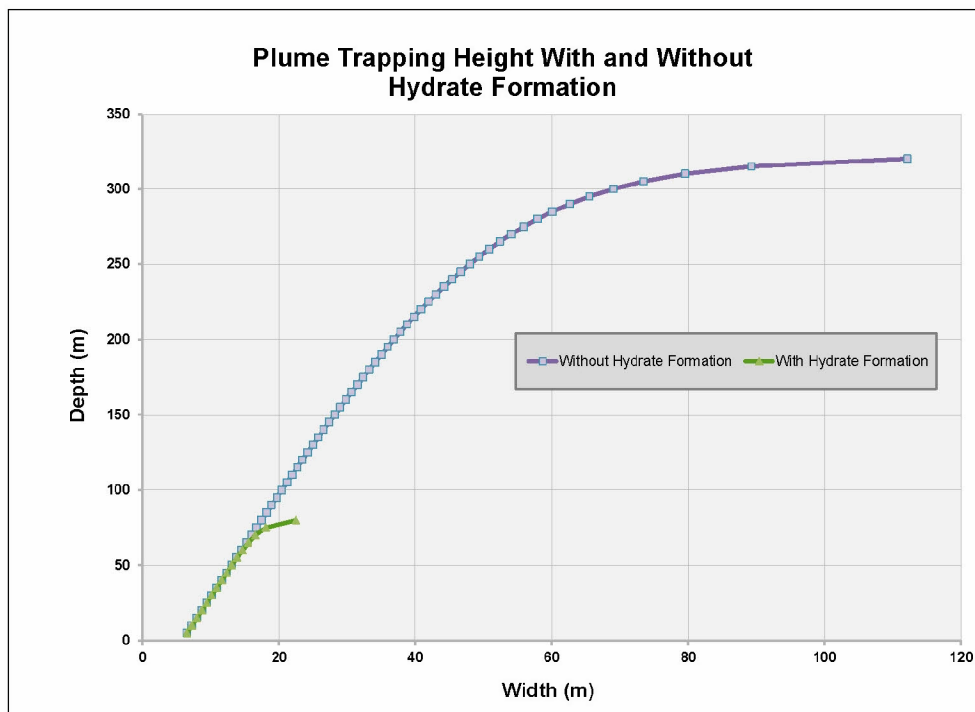


Figure E-5. Example of plume trapping height with and without hydrate formation.

The *blowout plume model* formulation includes the formation and dissolution of methane hydrates, which can form under certain conditions. A combination of pressure and temperature are necessary as well as saturation of the water column with dissolved methane. The temperature and pressure regime at the DWH release sites was sufficient for potential hydrate formation, however the methane concentration in the water column was found to be too low to support stable hydrate formation. As shown in Figure 6, the model predicted peak methane concentrations are approximately 30 mol/m^3 or 0.030 mol/L . Figure 6 illustrates the necessary concentration for stable hydrate formation in the range of conditions near the release sites. This figure illustrates that at 4°C (roughly the ambient water temperature at the depth of the blowout), the necessary concentration is a minimum of 0.040 mol/L and increases to over 0.10 mol/L at 18°C . The anticipated temperatures of the water column in the region of the plume (between 1,100 to 1,500 m below the surface) is between $4\text{--}6^\circ\text{C}$, and therefore the plume concentrations are below saturation and stable hydrate formation is not predicted to occur.

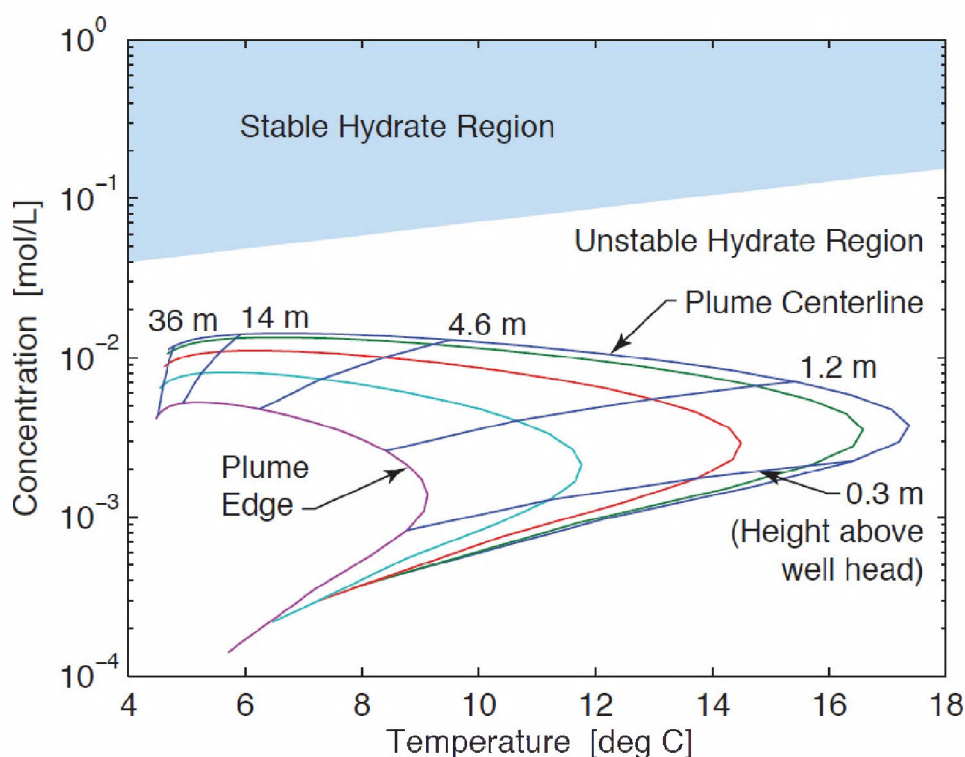


Figure E-6. Illustration of conditions for stable hydrate formation for approximately 1,500 m of water (Anderson et al. 2012).

E2.8 Plume Separation

In the presence of a strong ambient cross current, the bubble rise velocity may be sufficiently great to force the bubbles out of the upper boundary of the plume, as depicted in Figure E-7. Because the gas bubbles and their associated buoyancy forces the plume up through the water column, loss of gas bubbles can serve to reduce the bulk plume rise rate. The height above the blowout well head at which the bubbles rise out of the top side of the plume is called the separation height.

The loss of gas from the plume through separation is controlled by the difference between the calculated plume rise velocity and the bubble slip velocity. If the plume rise velocity is less than the slip velocity, some bubbles may escape through the top of the plume if the plume is sufficiently bent by an ambient cross current. The fraction of gas lost ($F_{gas\ lost}$) is assumed proportional to the plume width (twice the plume half width b) and the horizontal plume displacement due to the ambient current as given by:

$$F_{gas\ lost} = (x_h / 2b)^2 \quad (2-25)$$

where x_h = horizontal plume displacement due to ambient currents
 b = plume half width

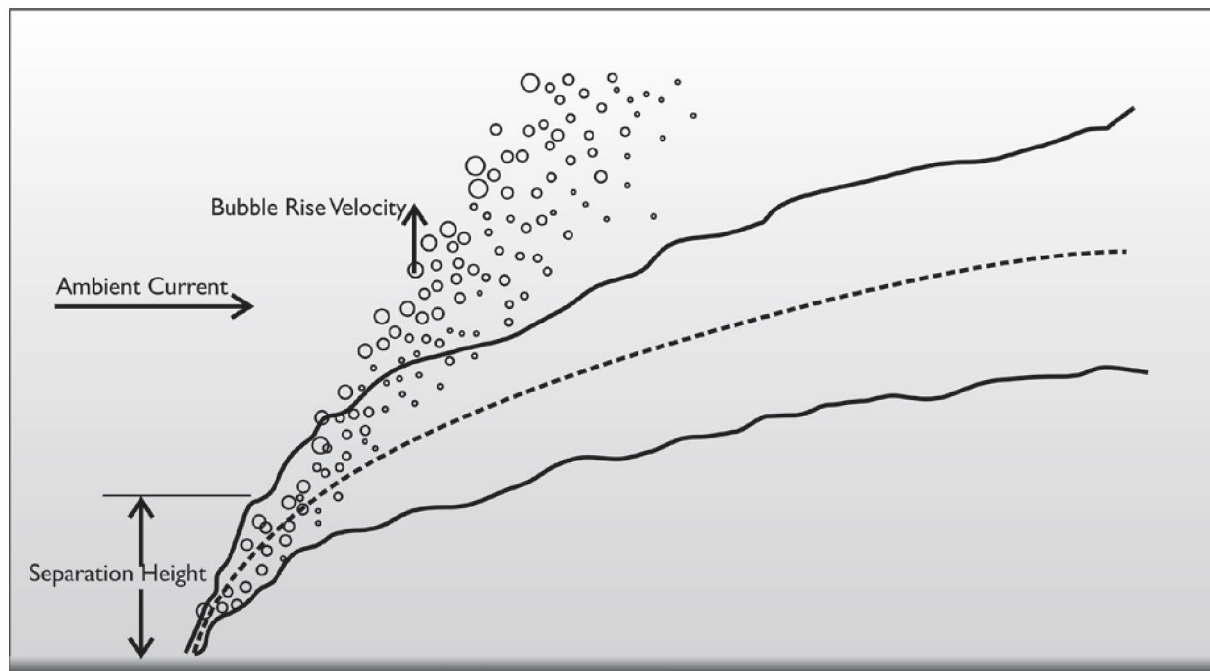


Figure E-7. Blowout plume in a cross-flow, showing bubble plume separation.

E2.9 Droplet Size Distribution

The subsurface blowout model oil droplet size distribution algorithm is used to initialize the subsurface oil spill particle trajectory model. It is assumed that oil droplets are formed shortly after the release and are transported along the plume until the trap depth. At this point their transport is determined by their rise velocity and the ambient currents and turbulence. The plume model assumes that there is no dissolution or biodegradation of oil droplets, based on the fact that typical transit times in blowout plumes are relatively short (minutes).

The blowout model's predicted droplet size distribution is reported in detail in Appendix G: Development of **OILMAP DEEP** Droplet Size Model. Application of the plume model to the DWH release is provided in Section 5.6 of the main report.

E3. Model Implementation

The results of the near-field blowout model provide information to the far field fates model about the plume (the three dimensional extent of the mixture of gas/oil/water) and a characterization of the initial dispersion / mixing of the oil discharged during the blowout. Key factors in this analysis are the volume flux of oil and gas, gas-to-oil ratio (GOR), depth, exit flow velocity, and environmental water column conditions (the depth profile of water temperature and salinity/density) which affect both the trap height and the potential for hydrate formation. Other factors such as duration of the blowout and ambient currents are also included but are less important.

The **OILMAP DEEP** blowout model implementation is done in two parts; the first is the plume model described in the previous section, based on the McDougall bubble plume model; the second is the oil droplet size distribution and volume fraction calculation. While they are based on the same scenario blowout specifications (e.g., oil type and flow rate, GOR, and depth), the model predictions are treated separately and do not interact. The two parts of the model

predictions only come together at the collapse of the near field plume, at the trap height, where the depth and droplet distribution predictions are used for initialization of the far field particle model simulation, **SIMAP**. The implementation of the plume model will be described here; the droplet size distribution model is described in Appendix G: Development of **OILMAP DEEP** Droplet Size Model.

The blowout plume model solves equations for conservation of water mass, momentum, buoyancy, and gas mass, using integral plume theory. An additional equation for the conservation of oil at the plume centerline is also solved. A flow chart of the model solution steps is presented in Figure E-8. The plume model is generally applicable and the specific blowout for simulation is defined by the model Input Parameters entered by the user. The two areas to the right on the flow chart are the model interaction with the user; the specification of the input parameters and generation of the model output data sets. The model reads in the blowout specifics then solves for the droplet size distribution and stores those results. The model then begins the simulation of the plume development, solving the partial differential equations using the Runge-Kutta method (White 1974) from the source until the trap height or water surface has been reached.

For the DWH blowout simulation the droplet size distribution and plume development is solved once a day for each day that oil was being released. The time history of daily, total oil release volumes was defined using the values given in the OBC report. The model was run individually for each location from which oil was released. Oil was released in one of two different configurations, the first configuration had varying percentages of the total release from two primary locations; at the end of the riser, and from a number of small holes in the vicinity of a kink that developed in the riser pipe, immediately above the BOP, and the second configuration reflected flow only from the cut riser pipe immediately above the BOP. The flow split estimates were based on application of the pipeline model described in Appendix D, using the gas-to-oil ratios at the surface and at depth as published in Zick (2013) as discussed below.

E3.1 Model Parameters

The specific plume model prediction is defined externally by the following set of parameters:

- Blowout release depth (m)
- Oil discharge rate (m^3/s)
- Oil density (kg/m^3)
- Gas : oil ratio (GOR) at the surface (-)
- Atmospheric pressure (Pa)
- Ambient seawater density profile (kg/m^3)
- Plume spreading coefficient, λ (-)
- Entrainment parameter, α (-)
- Slip velocity of gas bubbles in the oil plume (m/s)
- Ambient current velocity components (u and v) (m/s)
- Drag coefficient (-)

A few points about the specifics of the input parameters should be made here. Units for GOR are typically reported in Standard Cubic Feet (scf) of gas to Standard Barrel (stb) of oil. However, the GOR value used in the model is a dimensionless ratio, meaning that the gas and

oil volume units must be the same (e.g., cubic meters gas per cubic meters oil) and therefore must be converted.

Key factors in the plume analysis are the depth, oil discharge rate, and the GOR. The water column profile (given by temperature and salinity or density as a function of depth) will affect the trapping height and the gas dissolution rate, and indicate whether there is a potential for hydrate formation. The plume spreading, entrainment and the slip velocity are empirically derived parameters the exact function of which can be seen in the analytical equations presented in the Section 2 above. The plume spreading coefficient (λ) affects the rate at which the bulk plume spreads around the centerline as it is transported upwards. The entrainment parameter (α) controls the rate at which the bulk plume entrains water, by providing the proportionality between the plume vertical velocity and the rate at which water crosses the plume perimeter at a given element. Finally, the slip velocity is a measure of the difference in the rise velocity of the bulk plume and bubbles driving the buoyancy. A range of values for each of the parameters, found in the literature as well as values commonly used in **OILMAP DEEP** are presented in Table E-1.

Table E-1. Blowout plume model parameters.

Parameter	Literature Range	Commonly Used in <i>OILMAP DEEP</i>
Plume spreading coefficient (λ)	0.2 – 0.5	0.2
Entrainment parameter (α)	0.06 – 0.12	0.12
Slip velocity of gas bubbles in the oil plume (U_s)	0.25 – 0.35 m/sec	0.3 m/sec

Figure presents an example of the predicted plume half width (radius) and plume centerline velocity as a function of the height above the sea floor (well-head). Note that although this is for specific set of input parameters, it illustrates the trend in the typical relationship between centerline velocity and plume radius. The plume velocity defines the vertical movement of the bulk gas, oil and water mixture along the center of the plume.

The velocity of the plume decreases with distance from the discharge point as it entrains ambient seawater and the bulk density of the plume increases. As the plume continues to rise, additional seawater entrainment eventually brings the plume density close to the ambient density and therefore neutral buoyancy. As this progresses the centerline velocity decreases and approaches zero at which point the plume collapses and becomes trapped. The distance above the bottom (release point) at this point is called the trap height. From the trap height, the remaining gas and oil will ascend to the water surface as bubbles and droplets, respectively, controlled by their terminal rise velocities. The rise velocities of the oil droplets are significantly lower than that of the gas bubbles due to the smaller density difference between oil and water.

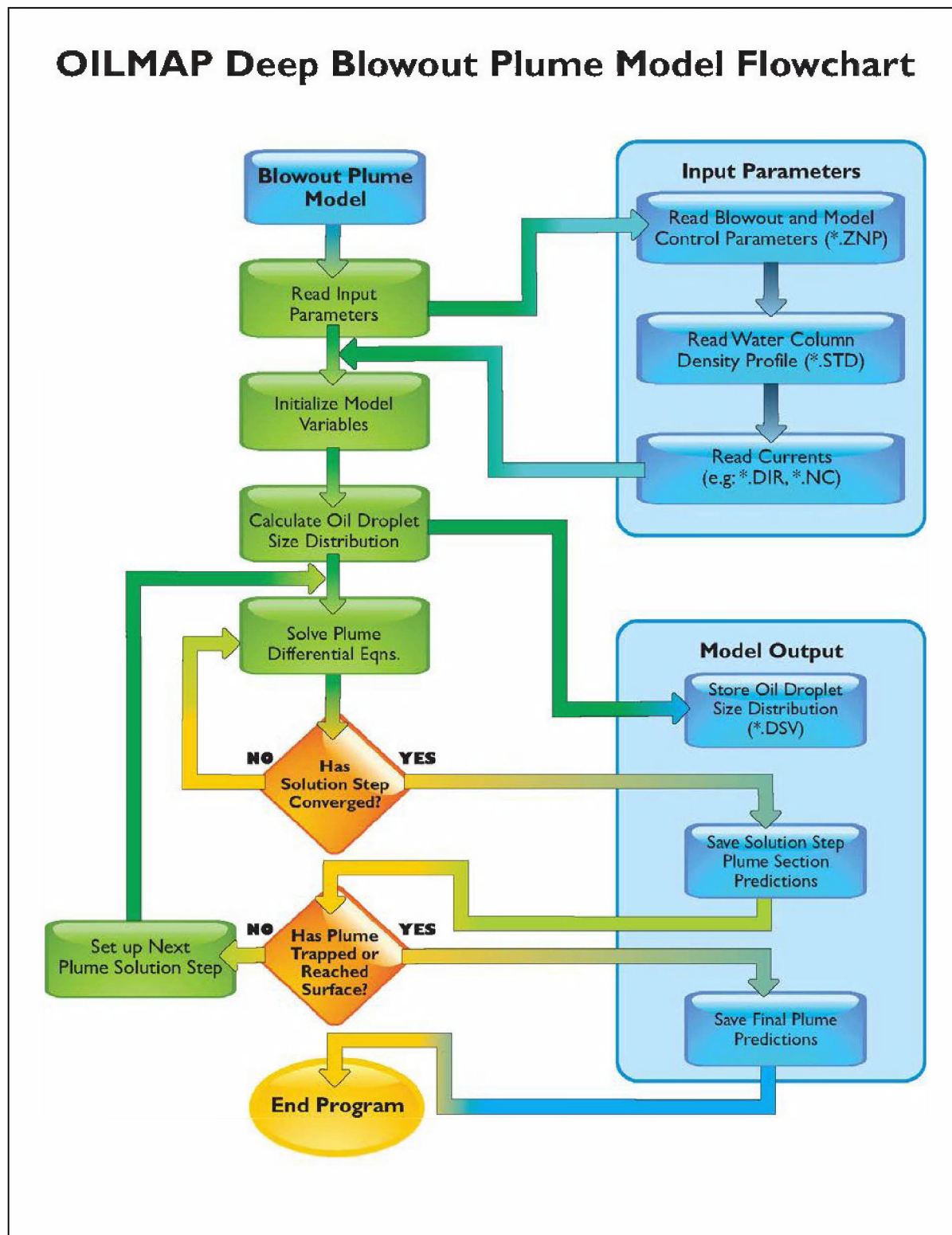


Figure E-8. Flowchart of the OILMAP Deep blowout plume model runtime execution.

While the blowout is initially defined by the oil discharge rate and the GOR, the plume dynamics and characteristics are controlled primarily by the buoyancy of the gas volume flux and to a lesser extent by the oil, due to the large density difference between gas and water and the much smaller density difference between oil and water. In the model, there are three processes that affect the gas volume; gas dissolution, hydrate formation for sufficiently deep blowouts and gas bubble/plume separation in the presence of strong ambient cross currents. For calculation of the plume dynamics, the loss of gas from dissolution, the potential for hydrate formation and bubble separation is multiplicative.

The plume calculations are terminated when the plume is neutrally buoyant, and occurs when the plume has entrained enough water and/or lost enough gas to reduce the density difference between the plume and the ambient water to near zero (neutral buoyancy).

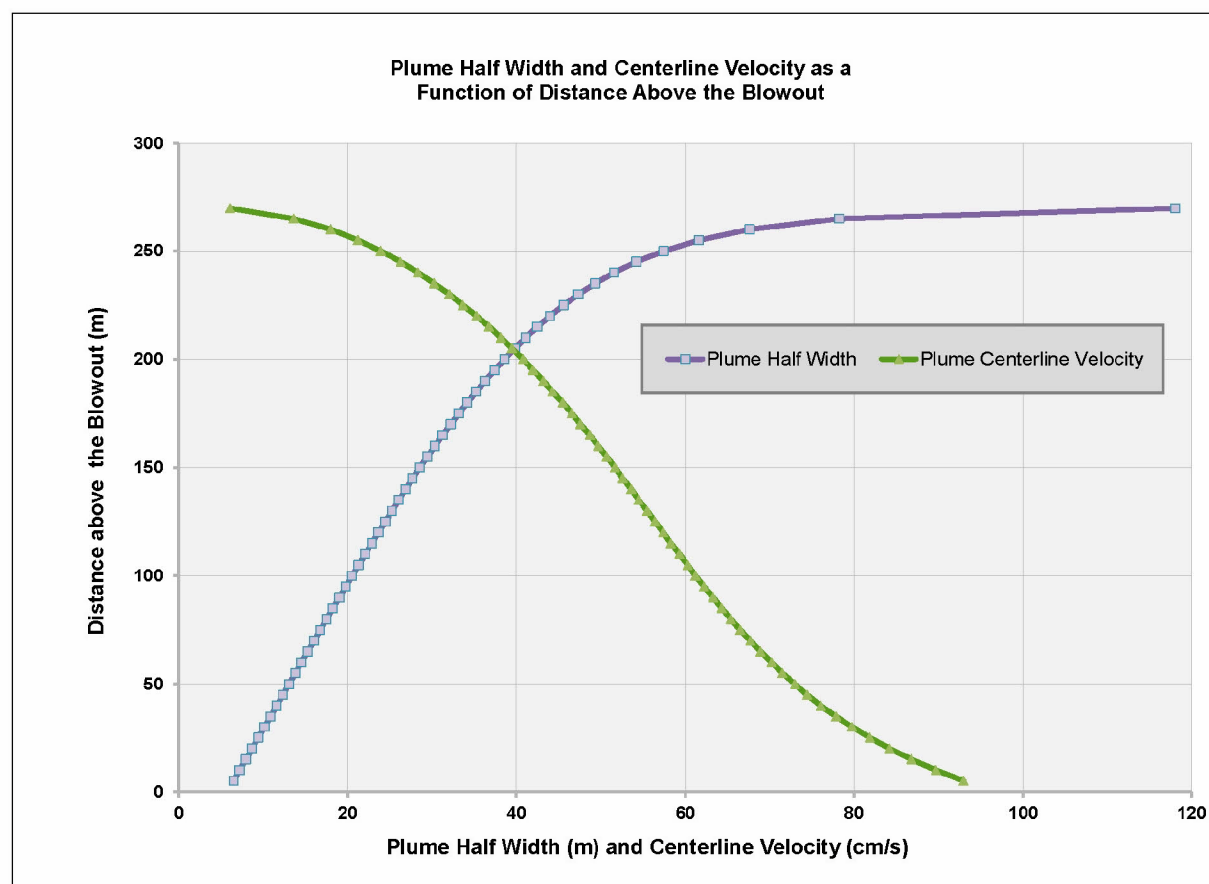


Figure E-9. Example plume half width and centerline rise velocity as a function of distance above the blowout.

E3.2 Implementation of the Macondo Crude Black Oil Tables

The Macondo Crude Black Oil Tables (BOT) equation of state were used to obtain the oil and gas properties for use in the droplet distribution and plume model, both at the surface and at depth. A phase behavior model, (an Equation of State [EOS] fluid characterization) for the Macondo reservoir fluids has been developed (Zick 2013) to predict the Macondo reservoir

fluids' physical, thermodynamic, and transport properties as functions of temperature, pressure, and fluid composition. These model predictions can be used to support engineering calculations such as the total flow of oil from the Macondo well, and to evaluate the gas to oil ratio (GOR) and therefore the volume flux at various pressures and temperatures. Appendix C provides details of the oil and gas properties based on the Macondo Crude Black Oil Tables (Zick 2013).

Several steps were taken to implement the BOT estimated properties in the DWH simulations. The first was to evaluate the Macondo crude EOS at "standard" conditions to obtain a value for the GOR at the surface, as that is a necessary input to the model to define the blowout. From the literature, a temperature of 60F and pressure of 14.7psi were selected to represent the standard (surface) conditions. The BOT EOS was evaluated at those conditions producing the values in Table E-2 following.

Table E-2. Black Oil Tables properties for "standard" surface conditions (Zick, 2013)

Temp (F)	Pres (psia)	Liq Vol Fraction (-)	Gas Vol Fraction (-)	Liq Den (kg/m3)	Gas Den (kg/m3)	Fluid Density (kg/m3)
60	14.7	0.001992	0.998	847.58	0.9791	2.666

These values result in the following GOR:

$$\text{GOR} = \frac{501}{2807} \quad \left(\frac{\text{m}^3/\text{m}^3}{\text{scf}/\text{bbl}} \right)$$

Using the Oil Budget Calculator (OBC) report (Lehr et al. 2010), estimated daily flow rates (assuming that they are represented at surface conditions) and the GOR calculated above, an estimate of the gas flux at the surface was made. The associated mass fluxes of gas and liquid oil were calculated using the BOT densities at surface conditions and a total mass flux estimated by combining the two. An example calculation for the first day of the blowout is presented in Table E-3.

Table E-3. Example oil and gas flow rates determined using Black Oil Tables properties for NOAA estimated blowout release rates at "standard" surface conditions

Date	OBC Discharge Estimate (bbls)	Oil Volume per day (m3)	Oil Volume flux avg. (m3/s)	Mass per day (kg)	Mass flux avg. (kg/s)	Surface Gas Volume per day (m3)	Surface Gas Volume flux avg. (m3/s)	Surface Gas Mass flux avg. (kg/s)	Total Mass flux avg. (kg/s)
4/22/2010	62200	9888.99	0.114456	8381711	97.01055	4954424	57.34288	56.14441	153.155

There are two basic conditions at which the oil and gas exit the riser pipe. At the beginning of the blowout, the full length of the riser was still basically intact, meaning the oil/gas fluid flowed roughly 1500m along the bottom before exiting the riser pipe. By the time the oil/gas reached the exit it is estimated that it would be at approximately ambient temperature and pressure, i.e. approximately 40°F and 2250 psia. For the oil/gas mixture exiting at the kink holes and through the riser once it was cut, it is assumed that the exiting fluid would be at the in-pipe temperature and pressure, i.e. approximately 180°F and 2650 psia. Based on estimates of McNutt et al.

(2011), for those two conditions, Table 4 shows the BOT EOS estimates the oil/gas fluid properties and the at depth GOR.

Table E-4. Black Oil Tables properties for the two conditions estimated at depth (Zick, 2013). Top line is for conditions in equilibrium with ambient; bottom line for in-pipe conditions.

Temp (F)	Pres (psia)	Liq Vol Fraction (-)	Gas Vol Fraction (-)	Liq Den (kg/m ³)	Gas Den (kg/m ³)	Fluid Density (kg/m ³)	Local GOR (-)
40	2250	0.597	0.40315	697.55	198.35	496.24	0.675
180	2650	0.423	0.5771	689.69	162.53	385.43	1.365

Following the estimation of fluid properties at depth, both inside and outside the riser pipe, it is possible to calculate the exit velocity using the mass flux estimated from “known” oil flow and GOR at surface conditions, and the local, at depth conditions just as the oil/gas fluid exits the riser or kink orifices, respectively. The fluid density at one of the two conditions, noted above, is divided into the mass flux for each day to estimate the local volume flux, (at depth). That value is then used with the opening area to calculate the exit velocity.

In addition, the momentum flux, buoyancy flux, transition height (from momentum jet to buoyant plume) and the plume half width at transition can also be estimated following Jirka (2004):

$$M_0 = U^2 A \quad \text{Momentum Flux}$$

$$B_0 = U g' A \quad \text{Buoyancy Flux}$$

$$g' = g (\rho_a - \rho_o) / \rho_{ref} \quad \text{Reduced Gravity}$$

$$Z_{transition} = C \frac{M_0^{3/4}}{B_0^{1/2}} = C L_m \quad \text{Transition height}$$

where A is the area of the opening, U is the exit velocity, and ρ is the density of the ambient, the fluid and a reference density with subscripts a, 0 and ref, respectively. The constant C is a scaling coefficient, for which Jirka (2004) suggests that the transition occurs between $1 < C < 5$. For a buoyant round jet, values of the half width (b) increase are

$$b = 0.110 Z_{transition} \quad \text{Jet half width increase}$$

where z is the distance from the release point.

Table E-5 provides an example of these calculations for the riser on the first day of the DWH blowout, for each of the values of the BOT EOS given in Table 4. The transition distances are seen to be quite short, less than 3.6 m, with the plume half widths below 0.6 m.

Table E-5. Calculations of the oil/gas fluid exit velocity, transition height and plume half width. Top line is for conditions in equilibrium with ambient; bottom line for in pipe conditions.

Temp (F)	Pres (psia)	Volume flux avg (m ³ /s) Q0	Exit Velocity (m/s) U0	Momentum Flux (m ⁴ /s ²) M0	Buoyancy Flux (m ⁴ /s ³) J0	Transition Height Range (m) z0	Plume Half width Range (m) b
40	2250	0.309	2.24	0.69	1.56	0.6 - 3.0	0.28 – 0.54
180	2650	0.397	2.88	1.14	2.44	0.7 - 3.6	0.29 – 0.60

The exit velocity (Table 5) can be used in the droplet distribution calculations to determine the energy available to break the oil into droplets. Details on the droplet size distribution model are discussed in Appendix G: Development of OILMAP DEEP Droplet Size Model.

E3.3 Initialization of the Plume Model

For the simulations, the properties estimated with the BOT EOS were used to initialize the pipe leak, plume and droplet size distribution models (Appendices D, E, and G, respectively). For the time period when there was outflow from both the end of the riser pipe and the holes in the area of the kink above the BOP, the pipe leak model was run and the output predictions of the flow split between the two was used as input to the plume and droplet size distribution models.

The plume model does not explicitly simulate the momentum jet phase of the blowout, but rather the buoyant plume phase is initialized with values obtained from the power series solution (Equations 2-13 through 2-15) at some small starting value of z (height above the blowout). The initial starting value is roughly equivalent to the dz (vertical integration step), however the model is fairly insensitive to this value in terms of the final trap depth, plume half width, and entrained volume predictions. Variation the initial value of z between 0.005 (the dz step used for the simulations) to 0.04 (the initial value used for the simulations), where in the original McDougal implementation a value of 0.025 was selected, produces a variability in the trap depth of 12m (1%), plume half width of 7m (7%) and total entrained volume of 100m³/s (5%).

E4. References

- Anderson, K., G. Bhatnagar, D. Crosby, G. Hatton, P. Manfield, A. Kuzmicki, N. Fenwick, J. Pontaza, M. Wicks, S. Socolofsky, C. Brady, S. Svedeman, A. K. Sum, C. Koh, J. Levine, R. P. Warzinski and F. Shaffer. 2012. Hydrates in the Ocean beneath, around, and above Production Equipment. *Energy & Fuels* 26(7):4167-4176.
- Bishnoi, P. R. and B.B. Maini. 1979. Laboratory study of behavior of oil and gas particles in salt water, relating to deepwater blowouts, *Spill Technology Newsletter* 4(1):24-36.
- Bishnoi, P.R., A.K. Gupta, P. Englezos, and N. Kalogerakis. 1989. *Fluid Phase Equilibria*, 83, 97.
- Cederwall, K. and J. Ditmars. 1974. Analysis of air bubble plumes, Report No. KH-R-24, W.M. Keck Laboratory of Hydraulics and Water Resources, Division of Engineering and Applied Science, California Institute of Technology Pasadena, California, September.
- Chen, F.H. and P.D. Yapa. 2001. Estimating hydrate formation and decomposition of gases released in a deepwater ocean plume. *Journal of Marine Systems* 30(1):21.
- Clift, R., J.R. Grace, and M.E. Weber. 1978. *Bubbles, Drops, and Particles*. Academic Press, NewYork.
- Fanneløp, T.K. and K. Sjoen. 1980a. Hydrodynamics of underwater blowouts, AIAA 8th Aerospace Sciences Meeting, January 14-16, Pasadena, California, AIAA paper, pp. 80-0219.
- Fanneløp, T. K. and K. Sjoen. 1980b. Hydrodynamics of underwater blowouts, *Norwegian Maritime Research* 4:17-33.
- Jirka, G.H. 2004. Integral model for turbulent buoyant jets in unbounded stratified flows. Part I: Single round jet. *Environ. Fluid Mech.* 4(1):1-56.
- Johnson, A.I., F. Besik and A.E. Hamielec. 1969. Mass transfer from a single rising bubble. *Can. J. Chem. Eng.* 47: 559-564,
- Kolluru, V.S.1993. Oil blowout model, Applied Science Associates, Inc., Narragansett, RI 02882.
- Kobus, H.E.1968. Analysis of the flow induced by air-bubble systems. *Proc. 11th Conference of Coastal Engineering London*, pp. 1016-1031.
- Lehr, B., S. Bristol and A. Possolo. 2010. Deepwater horizon oil budget calculator: A report to the national incident command. The Federal Interagency Solutions Group, Oil Budget Calculator Science and Engineering Team. http://www.restorethegulf.gov/sites/default/files/documents/pdf/OilBudgetCalc_FuII_HQ-Print_111110.pdf (Accessed on April 1, 2012).
- McNutt, M., R. Camilli, G. Guthrie, P. Hsieh, V. Labson, B. Lehr, D. Maclay, A. Ratzel and M. Sogge. 2011. Assessment of Flow Rate Estimates for the Deepwater Horizon / Macondo Well Oil Spill. Flow Rate Technical Group report to the National Incident Command, Interagency Solutions Group. Appendix D – Plume Calculation Team 2010; Particle Image Velocimetry Report. March 10, Available online: <https://www.doi.gov/sites/doi.gov/files/migrated/deepwaterhorizon/upload/FRTG-report-Appendix-D-Plume-Analysis-Report.pdf>.

- McDougall, T.J. 1978. Bubble plumes in stratified environments, *Journal of Fluid Mechanics*, 85(4):655-672.
- Milgram, J.H. 1983. Mean flow in round bubble plumes, *Journal of Fluid Mechanics* 133: 345-376.
- Morton, B.R., G.I. Taylor, and J.S. Turner. 1956. Turbulent gravitational convection from maintained & instantaneous sources, *Proceedings of the Royal Society, A* 234, pp. 1-23.
- Rye, H. 1994. Model for calculation of underwater blowout plume, *Proceedings of the 17th Arctic and Marine Oilspill Program Technical Seminar, Canada*, p. 849-865.
- Rye, H. P. Brandvik, and M. Reed. 1996. Subsurface oil release field experiment- observations and modeling of subsurface plume behavior, *Proceedings of the 19 th Arctic Marine Oilspill Program, Technical Seminar, Calgary, Alberta, Canada*, p 1417-1435.
- Sloan, E.D. 1997. *Clathrate Hydrates of Natural Gases*, Marcel Dekker, Inc., NewYork.
- Spaulding, M.L., P.R. Bishnoi, E. Anderson, and T. Isaji. 2000. An Integrated Model for Prediction of Oil Transport from a Deep Water Blowout.
- Topham, D.R. 1975. Hydrodynamics of an oil well blowout, *Beaufort Sea Technical Report*, Institute of Ocean Sciences, Sidney, B.C, No.33.
- Topham, D.R. 1977. Observations of the formation of hydrocarbon gas hydrates at depth in seawater. *Spill Technology Newsletter*.
- White, F.M. 1974, *Viscous Fluid Flow*, Mc-Graw Hill Book Company.
- Yapa, P.D. and F.H. Chen. 2003. CDOG 2.0, Clarkson Deepwater Oil and Gas Model User's Guide. Department of Civil and Environmental Engineering, Clarkson University, Box 5710, Potsdam, NY 13699.
- Yapa, P.D and L. Zheng. 1997. Simulation of oil spills from underwater accidents I: model development, *Journal of Hydraulic Research, International Association of Hydraulic Research, The Netherlands* 35(5): 673-688.
- Zheng, L. and P.D. Yapa. 1997. A numerical model for buoyant oil jets and smoke plumes, *Proceedings of the 20 th Arctic Marine Oilspill Program, Technical Seminar, Vancouver, BC, Canada*, p. 963-979.
- Zheng, L. and P.D. Yapa. 1998. Simulation of oil spills from underwater accidents II: Model verification, *Journal of Hydraulic Research, International Association of Hydraulic Research, The Netherlands*, 36(1):117-134.
- Zheng, L. and P.D. Yapa. 1999. A deepwater jet/plume model and a parametric analysis, p. 285-299.
- Zheng, L., P.D. Yapa, and Chen, F. H. 2002. A model for simulating deepwater oil and gas blowouts – Part I: Theory and model formulation. *Journal of Hydraulic Research* 41(4):339–351. International Association of Hydraulic Engineering and Research.
- Zheng, L. and P.D. Yapa. 2002. Modeling gas dissolution in deepwater oil/gas spills. *J. Marine Systems* 31(4): 299–309.
- Zick, A. 2013. Equation of state fluid characterization and analysis of the Macondo reservoir fluids, Expert report in matter of U.S. vs BP Exploration & Production, Inc. et al, submitted to the US Department of Justice, March 22, 2013.

Technical Reports for Deepwater Horizon Water Column Injury Assessment

WC_TR.13: Application of OILMAP DEEP to the Deepwater Horizon Blowout

Appendix F: Model of dispersant treatment

Authors: Malcolm Spaulding, Daniel Mendelsohn, Deborah Crowley,
Zhengkai Li, Andrew Bird

Revised: September 30, 2015

Project Number: 2011-144

RPS ASA 55 Village Square Drive, South Kingstown, RI 02879

Table of Contents

F1.	Background	1
F2.	Model framework and assumptions	4
F2.1	Premix	7
F2.2	Injected	7
F2.3	Entrained	7
F2.4	Plume	9
F2.4.1	Conservation of mass	10
F2.4.2	Conservation of momentum	10
F2.5	Jet	11
F3.	Model application and validation	12
F4.	Summary and conclusions	19
F5.	References	23

List of Figures

Figure F-1: ROV image of the application of dispersants to oil released above the cut riser pipe using the wand applicator, June 10, 2010 (left side of image). The dispersant plume (white billows) from the wand prior to its entry into the oil release is clearly evident. The dispersant plume path is strongly influenced by the entrained flow near the oil jet, bending almost 70 to 80 degrees from the wand injection direction.	1
Figure F-2: ROV image of the trident dispersant application device being held by ROV manipulator above the cut riser pipe above the BOP, June 13, 2010. No dispersants are being applied in this image.	2
Figure F-3: ROV image of dispersants being applied by the trident (foreground) to oil escaping from the cut riser above the BOP and flowing around the top hat, June 30, 2010. The white plumes along the tine of the trident are the result of dispersants being sprayed through small holes on the inner face of the tine.	2
Figure F-4: ROV image of dispersants being applied by the trident (left side) to oil escaping from the cut riser above the BOP and flowing around the top hat, June 21, 2010. The white plumes are the result of dispersants being sprayed through small holes on the inner face of the tine.....	3
Figure F-5: Number of hours per day of dispersant pumping at the specified rates (8, 10, and 12 gpm) to obtain the daily amount of dispersant applied through the spill period.	3
Figure F-6: Circular jet discharging from a pipe into a quiescent ambient fluid. The Zone of Flow Establishment (ZFE) and Zone of Established Flow (ZEF) are shown. The transition between the two occurs at approximately 6 to 10 pipe diameters (D_o). The velocity profile changes from a top hat distribution at the release location to Gaussian at the end of the ZFE. It is noted that the plume growth increases at a faster rate in the ZEF than in the ZFE.	8
Figure F-7: Thin cross section of plume from z to $z + dz$ (Roisin-Cushman 2004).	9

Figure F-8: Release from the end of the riser pipe on May 14, 2010 from the <i>Skandi Neptune</i> . The dispersant wand is noted at the lower right of the image.	12
Figure F-9: Schematic of top hat containment system.....	14
Figure F-10: Flow of oil around the rim of the top hat from ROV images on June 30, 2010.....	15
Figure F-11: Fraction treated (solid line, left axis) and DOR (right axis) vs number of diameters downstream from the release with varying sector fractions treated. The effective DOR is estimated by dividing the target DOR by the dispersant effectiveness (DE).	16
Figure F-12: Fraction treated (solid line, left axis) and DOR (right axis) vs distance downstream from the release with varying sector fractions treated. The effective DOR is estimated by dividing the target DOR by the dispersant effectiveness (DE).	17
Figure F-13: Fraction treated (solid line) and DOR (dashed line) vs time during the JF3 cruise for sectors treated ranging from 20 to 40%. The estimated DORs for the JF3 dives are provided. The distance from the wellhead to the sampling location for each dive is also shown (see Appendix G for additional details).....	18
Figure F-14: Hologram of “octopus” oil droplets created when dispersant is added to oil (David Murphy and Cheng Li, JHU; http://gulfresearchinitiative.org/mesocosm-experiments-look-oil-spill-bottom/)	21
Figure F-15: LES simulations of the initial stages of the release from a buoyant plume into quiescent receiving water. The figure shows contours of the velocity and associated variances (Source: T. Ozgokmen, University of Miami).	22
Figure F-16: LES predicted mixing of oil (red) and entrained dispersant (green –gray) with non- dimensional distance ($Y = \text{distance from release} / \text{release diameter}$) from the release location. (Source: T. Ozgokmen, University of Miami).....	23

List of Tables

Table F-1: Summary of test results of chemical dispersant effectiveness (DE) under standard laboratory testing conditions (SFT, swirling flask test; BFT, baffled flask test; WSL, Warren Springs Laboratory; Exdet, Exxon dispersant effectiveness test)	5
---	---

F1. Background

Dispersants were applied to the DWH release in immediate proximity to the oil discharge point using two basic methodologies: a wand consisting of a single pipe through which dispersant was applied (Figure F-1) and a two-tined fork (trident with two tines) diffuser system with spray holes located along the inner sides of the tines (Figure F-2). A review of the ROV video shows many variations of the application method and location but the basic pattern that emerges is that when the wand was used it was typically held by the ROV immediately outside the edge of the release point (Figure F-1) or inserted directly into the discharge. When the trident was used it was typically placed immediately above the release location so that the tines were on either side of the release, thus maximizing the amount of dispersant applied to the jet circumference (Figure F-2 – Figure F-4). The wand was the principal dispersant application tool used from the start of dispersant application in late April until June 15, 2010. After this date, the trident was primarily used until dispersant application ceased at the end of the spill, July 15, 2010.

Application rates based on analysis of the amount of dispersant applied per day appear to be approximately 10 gpm (Figure F-5). Dispersant application was primarily at the end of the riser pipe until June 4, 2010 when the riser pipe was cut and then at the cut riser pipe above the BOP and adjacent to the top hat from June 4 until the end of the spill. A close review of the ROV imagery suggests that the strategy that eventually evolved was to place the dispersant applicator (no matter its type) immediately adjacent to the oil release and allow plume entrainment to bring the dispersant into the jet and then mix it with the escaping oil and gas mixture. Figure F-3 shows a good example of this on June 30, 2010. Dispersant is being sprayed on the release from several small holes located on the inner face of the tines. The dispersant is clearly entrained into the oil jet. Figure F-4 shows that the same behavior is observed further from the release. The dispersant is continuing to being entrained and mixed with the oil. The video shows that once entrained the oil-dispersant mixture continued to move vertically at about the same azimuthal location. Subsequent mixing in the azimuthal direction was not observed.



Figure F-1: ROV image of the application of dispersants to oil released above the cut riser pipe using the wand applicator, June 10, 2010 (left side of image). The dispersant plume (white billows) from the wand prior to its entry into the oil release is clearly evident. The dispersant plume path is strongly influenced by the entrained flow near the oil jet, bending almost 70 to 80 degrees from the wand injection direction.

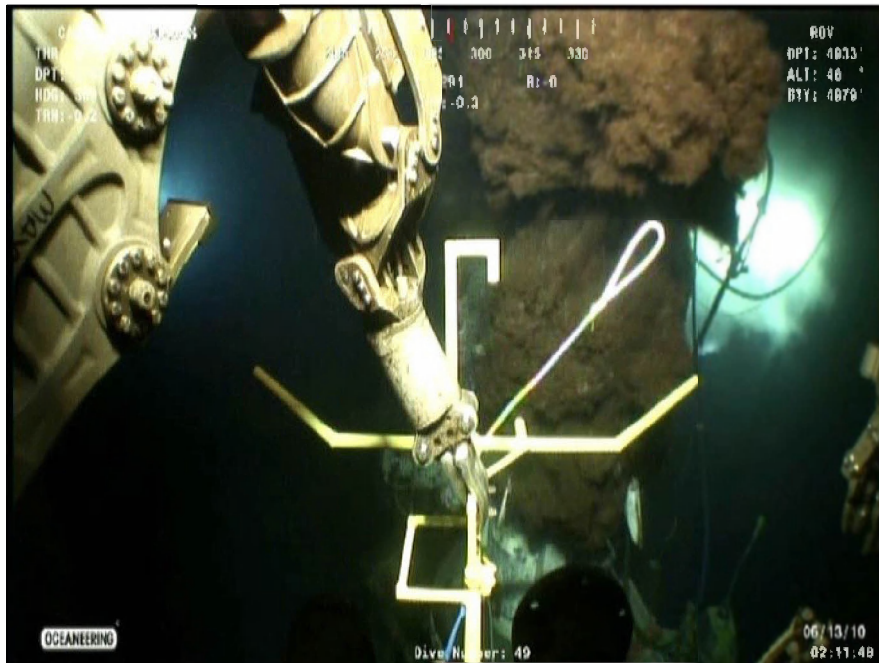


Figure F-2: ROV image of the trident dispersant application device being held by ROV manipulator above the cut riser pipe above the BOP, June 13, 2010. No dispersants are being applied in this image.



Figure F-3: ROV image of dispersants being applied by the trident (foreground) to oil escaping from the cut riser above the BOP and flowing around the top hat, June 30, 2010. The white plumes along the tine of the trident are the result of dispersants being sprayed through small holes on the inner face of the tine.

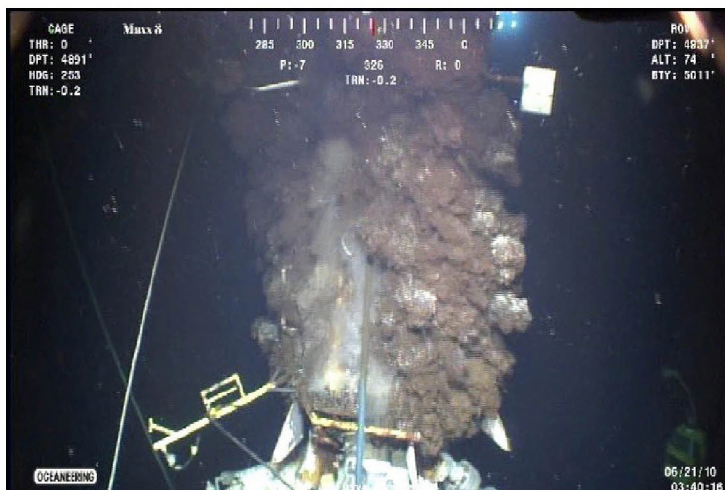


Figure F-4: ROV image of dispersants being applied by the trident (left side) to oil escaping from the cut riser above the BOP and flowing around the top hat, June 21, 2010. The white plumes are the result of dispersants being sprayed through small holes on the inner face of the tine.

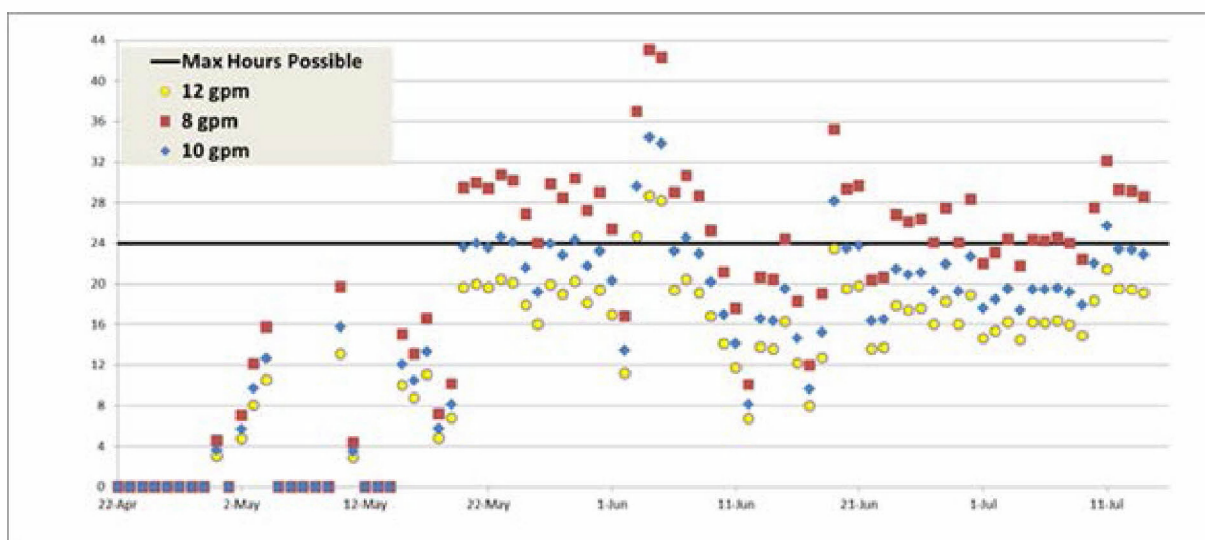


Figure F-5: Number of hours per day of dispersant pumping at the specified rates (8, 10, and 12 gpm) to obtain the daily amount of dispersant applied through the spill period.

In order to understand the effectiveness of the dispersant application an estimate is needed of how much oil was actually dispersed. Unfortunately no field data on oil droplet size pre and post dispersant application are available from inside or immediately adjacent to the buoyant plumes to document the effectiveness. One of the clearest sets of evidence of the impact of the dispersant was the appearance, disappearance, and re-appearance of oil at the sea surface above the spill during a period from May 10 to 12, 2010. During this period no dispersants were initially applied, then they were applied for approximately one day and then they ceased to be applied. This event is described in more detail in Appendix K.

It is the goal of this effort to develop a simplified method that will provide some quantitative guidance on the amount of oil that was treated and the associated Dispersant to Oil Ratio (DOR). To maximize the utility of this dispersant treatment model several different application methods will be addressed: (1) PREMIX- dispersant pre-mixed with oil before being released from the riser, 2) INJECTED- dispersant injected into the blowout plume and (3) ENTRAINED - dispersants entrained into the plume. The entrained is the option most often used in the DWH spill, with two application methods: wand and trident.

F2. Model framework and assumptions

The method for each application strategy is presented below. Each method estimates the fraction of oil treated and the associated DOR, and the dispersant effectiveness (DE). The DE is normally approximated as the product of operational, chemical, and hydrodynamic effectiveness (NRC, 2005) or

$$[DE]_{total} = [DE]_{operational} * [DE]_{chemical} * [DE]_{hydrodynamic} \quad (1)$$

where:

DE _{operational}	percent of dispersant that is mixed with oil based on the application method.
DE _{chemical}	percent of dispersant that is chemically effective in reducing oil water interfacial tension.
DE _{hydrodynamic}	percent of dispersant that is mixed with oil dependent on dilution and mixing energy that are present at the application site.

As noted by NRC (2005), (see quote below) there is some confusion in the use of the terminology and which term above includes which effect.

"Chemical effectiveness has been investigated in the laboratory, in wave tanks, and at sea. In many of these studies, effectiveness was defined based on chemical effectiveness, which was quantified as the mass fraction of oil that was measured in samples collected from the water column or the mass fraction that was not recovered from the water surface as floating oil. This definition has resulted in some confusion when attempting to compare studies conducted using different experimental systems, because these effectiveness metrics are operationally defined and measure different things in different systems. For example, some experimental designs include oil droplets that are large enough to resurface relatively quickly in the dispersed-oil concentration (e.g., those that measure water-column oil concentrations during periods of intense mixing), whereas others do not (e.g., those that include a settling period before measurement of dispersed-oil concentrations). Similarly, oil that is not recovered on the water surface may have been transferred to any of several compartments, of which the water column is only one. The droplet-size distribution of dispersed oil is a particularly important factor for chemical and hydrodynamic effectiveness, because it will determine whether the entrained oil will remain in the water column or float back to the surface under low energy conditions, which are unlikely to be the same during spill-response operations and effectiveness tests, regardless of the scale of the test. Future studies should include measurement of droplet-size distribution or some related metric to facilitate comparison among treatments. Lunel (1995b) has suggested that effectiveness tests should produce droplet-size distributions similar to those observed at sea, because this indicates similarity in the droplet-formation mechanisms."

For the purposes of the present analysis, the goal is to have a bulk effectiveness which includes all aspects of the application, chemistry, and mixing processes. The total amount of oil that is dispersed and the effective DOR, where the mixing energy, dispersant-oil chemistry, and

application method allow the dispersant to effectively lower the oil water interfacial tension, are then:

$$\text{Total treated} = \text{oil released} * \text{fraction of oil treated}$$

$$\text{DOR}_{\text{effective}} = \text{DOR} * \text{DE}$$

Table F-1 provides a summary of test results of chemical dispersant effectiveness (Chemical DE) under standard laboratory testing conditions, including lower mixing energy Swirling Flask Test (SFT), moderate mixing energy Exxon dispersant effectiveness test (Exdet), and vigorous mixing energy Baffled Flask Test (BFT) and Warren Spring Laboratory (WSL) test. The arithmetic mean value of the reported DE is 54%, and the median value is 55%, with a standard deviation of 22%. In the absence of data for subsea application, the mean value and associated standard deviation can be used as first estimate for effectiveness.

Table F-1: Summary of test results of chemical dispersant effectiveness (DE) under standard laboratory testing conditions (SFT, swirling flask test; BFT, baffled flask test; WSL, Warren Springs Laboratory; Exdet, Exxon dispersant effectiveness test)

Oil type	API Gravity	Oil density (g/ml)	Temperature (°C)	Dispersant type	Chemical DE	Test Apparatus	References
South Louisiana		0.839	15.6	Corexit 9527	55%	SFT	EC 2008
South Louisiana (2001)	32.72	0.8562	15	Corexit 9500	27%	SFT	EC 2008
Arabian Light	31.8-33.4	0.858-0.866	15	Corexit 9527	25%	SFT	EC 2008
Arabian Light	31.8-33.4			Corexit 9500	21%	SFT	EC 2008
Arabian Light (2000)	31.3	0.864	15	Corexit 9500	19%	SFT	EC 2008
South Louisiana Crude				Corexit 9500 A	55%	SFT	USEPA 2012
South Louisiana Crude				Corexit 9527 A	63%	SFT	USEPA 2012
South Louisiana Crude				Dispersant A	85%	BFT	Venosa et al. 2002
South Louisiana Crude				Dispersant E	87%	BFT	Venosa et al. 2002
South Louisiana Crude				Dispersant D	70%	BFT	Venosa et al. 2002
South Louisiana Crude				Dispersant F	67%	BFT	Venosa et al. 2002
South Louisiana Crude				Dispersant G	15%	BFT	Venosa et al. 2002

Oil type	API Gravity	Oil density (g/ml)	Temperature (°C)	Dispersant type	Chemical DE	Test Apparatus	References
South Louisiana Crude				Dispersant H	30%	BFT	Venosa et al. 2002
South Louisiana Crude				Dispersant A	55%	BFT	Sorial et al. 2004
South Louisiana Crude				Dispersant B	65%	BFT	Sorial et al. 2004
South Louisiana Crude				Dispersant C	44%	BFT	Sorial et al. 2004
South Louisiana Crude				Dispersant (18 dispersant average)	19%	SFT	Sorial et al. 2004
South Louisiana Crude				Dispersant (18 dispersant average)	66%	BFT	Sorial et al. 2004
South Louisiana Crude			5	Dispersant A	55%	BFT 150rpm	Chandrasekar et al. 2005
South Louisiana Crude			5	Dispersant A	75%	BFT 200rpm	Chandrasekar et al. 2005
South Louisiana Crude			5	Dispersant A	90%	BFT 250rpm	Chandrasekar et al. 2005
South Louisiana Crude			5	Dispersant b	28%	BFT 150rpm	Chandrasekar et al. 2005
South Louisiana Crude			5	Dispersant b	72%	BFT 200rpm	Chandrasekar et al. 2005
South Louisiana Crude			5	Dispersant b	81%	BFT 250rpm	Chandrasekar et al. 2005
South Louisiana Crude		0.84 (15°C)	5	Corexit 9500	81%	BFT 200rpm	Venosa & Holder 2013
South Louisiana Crude		0.84 (15°C)	25	Corexit 9500	78%	BFT 200rpm	Venosa & Holder 2013
Arab Light			15	Corexit 9527	45%	WSL LR 448	Venosa & Holder 2013
Kuwait			15	Corexit 9500	45%	WSL LR 448	Stevens & Roberts 2003
Kuwait			15	Corexit 9527	52%	WSL LR 448	Stevens & Roberts 2003

Oil type	API Gravity	Oil density (g/ml)	Temperature (°C)	Dispersant type	Chemical DE	Test Apparatus	References
MC252				Corexit 9500	43%	Exdet	Aurand et al. 2010
MC252				Corexit 9500	50%	SFT	Belore et al. 2011
MC252			21	Corexit 9500	61%	BFT	Li et al. 2011
Mean					54%		
Median					55%		
STD					22%		

F2.1 Premix

For this application method, dispersants are directly injected into the piping system before the oil gas mixture is released to the environment (e.g., within BOP). Given the high turbulence levels in the piping system, the small cross sectional area of the pipe, and premixing, it is assumed that the dispersant is completely mixed with the oil (hydrodynamic and operational DEs – 100%). The total DE is then dependent only on the chemical effectiveness.

F2.2 Injected

In this application method, dispersants are directly injected into the jet/plume exiting the release. The operational effectiveness is dependent on the application method. The mixing energy is typically high so the hydrodynamic effectiveness is likely 100%. The chemical effectiveness is dependent on the ability of the dispersant to coat the oil droplets.

F2.3 Entrained

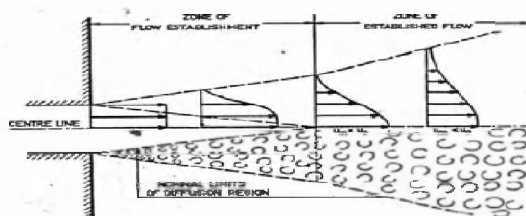
A review of the ROV imagery shows that for the majority of time for the DWH, the application strategy was to place the dispersant applicator immediately adjacent to the release location and at the outer edge of the oil-gas jet. This approach takes advantage of the normal jet/plume entrainment process to enable the dispersant to mix with the oil. Once in the jet/plume, the mixing processes in the shear layer continue to mix dispersants with the escaping oil and allow sufficient time for the dispersants to coat the surface of the oil droplets. This process continues as the entrained water/dispersant rises in the plume.

In order to keep the analysis simple, the following major assumptions are made.

1. Dispersant is mixed with sea water and then entrained into the rising oil/water jet/plume.
2. Mixing between the dispersant and oil is rapid within the entrained flow fluid (numbers of seconds).
3. All oil releases can be approximated as a simple jet or plume discharging from a pipe and mixing with ambient sea water (for a jet, the release is dominated by the momentum; for a plume, the release is dominated by buoyancy). A comparison of the dispersant application location to the momentum length scale (the ratio of momentum to buoyancy flux) can be used to determine whether to use the jet or plume formulation.
4. The impact of the plume bending from non-vertical discharge and buoyant effects is considered as secondary.

Assuming this basic entrainment based dispersant application strategy and the fact that dispersants are applied very near the discharge, the primary region of interest is where the oil jet/plume is under development and transitioning from the Zone of Flow Establishment (ZFE) to the Zone of Established Flow (ZEF) (Figure F-5). The transition distance is typically 6 to 10 times the diameter of the discharge pipe, D . The oil released transitions from a *top hat* distribution (for velocity or other variables) at the blowout location to a *Gaussian or normal distribution* at the end of the ZFE. In the ZFE region, the flows can either be a jet or plume or some combination of the two dependent on the momentum and buoyancy fluxes of the release. As the oil in the jet moves away from the release point, ambient water is entrained due to the strong shear between the jet core and the surrounding fluid. This results in an oil water mixture with decreasing oil concentrations with distance from the release due to continued dilution by the entrained water. At the end of the ZFE, the entrained seawater has been mixed to the center of the jet, as evidenced by the shape of the velocity profile (Figure F-6). In the ZEF the velocity profile in the jet or plume is Gaussian and the plume continues to grow.

Circular Jet



Zone of flow establishment (jet development; $6-10D_o$)

Zone of established flow (fully developed jet)

Figure F-6: Circular jet discharging from a pipe into a quiescent ambient fluid. The Zone of Flow Establishment (ZFE) and Zone of Established Flow (ZEF) are shown. The transition between the two occurs at approximately 6 to 10 pipe diameters (D_o). The velocity profile changes from a top hat distribution at the release location to Gaussian at the end of the ZFE. It is noted that the plume growth increases at a faster rate in the ZEF than in the ZFE.

It seems reasonable to assume that if dispersants are applied to the ambient sea water, immediately adjacent to the jet/plume, then they are mixed into the water that is ultimately entrained into the jet/plume.

To pursue this idea, an estimate is needed of the entrained water that is mixed with oil or alternately the ratio of the total flow (oil and water) to the flow (oil) at the release location, which provides an estimate of the dilution of the oil with water.

The total flow, Q_t , at any distance, z , is comprised of the oil flow rate, Q_o , plus the entrained water flow rate or Q_e .

$$Q_t = Q_o + Q_e \quad (2a)$$

or rewritten in terms of the entrained flow

$$Q_e = Q_t - Q_o \quad (2b)$$

The oil from the release is diluted by the entrained ambient water with a dilution, D , of

$$D = Q_t / Q_o \quad (3)$$

From Eq 1 and 3, it is noted that dilution (D) equals 1 at the release location, thus no dilution, and increases with distance from the release. At the end of the ZFE, nominally 6 to 10 release pipe diameters, D_o , the resulting mixture is part oil and part entrained water (dispersant) with the exact ratio dependent on whether the release is in the form of a plume or a jet. The rate of dilution is dependent on both the exit velocity and buoyancy of the release. The growth rate of the release (cross sectional area) is controlled by its effectiveness in entraining sea water. The dilution process continues after the ZFE into the ZEF, often at an increased rate, as shown schematically in Figure F-6.

If dispersant is introduced into the entrained water then the total oil flow rate treated, $Q_{treated}$, is the product of the entrained flow rate times the dilution given in Eq 3 or

$$Q_{treated} = Q_e / D = Q_e Q_o / Q_t \quad (4)$$

The untreated oil flow rate, $Q_{untreated}$, is the complement of this and given by

$$Q_{untreated} = Q_o / D = Q_o Q_o / Q_t \quad (5)$$

The sum of treated and untreated oil (Eq 4 and 5) gives the total oil release rate, Q_o .

An estimate of the DOR can be made by dividing the dispersant application rate, Q_{dis} , by the flow rate of the treated oil, $Q_{treated}$

$$DOR = Q_{dis} / Q_{treated} \quad (6)$$

It should be noted that the value of DOR in Eq (6) needs to be multiplied by the dispersant effectiveness, DE , to obtain the effective DOR $DOR_{effective}$ for the given application.

To apply the method described above one needs to determine whether the release is a jet (momentum) or plume (buoyancy), since the dilution (entrainment rate) is different depending on which dominates. For the oil and gas releases of interest here the dynamics are likely to be momentum dominated immediately after the release and then rapidly transition to buoyancy dominated as the release momentum is dissipated and the buoyancy dominates.

The relative flow rates for each release type are provided below. The plume case is provided first followed by the jet. The underlying theory is well known for these two cases (Hirst 1971 and Jirka 2004); the development here follows Roisin-Cushman (2004). The focus here is to obtain first order estimates in the near field of the release.

F2.4 Plume

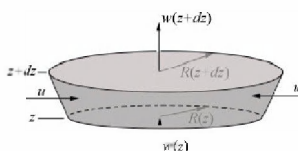


Figure F-7: Thin cross section of plume from z to $z + dz$ (Roisin-Cushman 2004).

To address this problem one needs to solve the conservation of mass and momentum equations for a release discharging into an ambient fluid.

F2.4.1 Conservation of mass

The conservation of mass equation on thin section of the release (Figure F-7), from z to $z + dz$, requires that the mass flow rate exiting the plume at $z + dz$ equal the sum of mass flow entering at z plus the fluid entrained between z and $z + dz$ entering at a velocity u . In differential form this can be expressed as

$$\frac{d(wR^2)}{dz} = 2uR \quad (7)$$

Where w is the vertical velocity and R is the radius of the plume at z . It has been assumed that the ambient fluid is entrained at the rate u times the surface area of the plume given by $2\pi R dz$.

F2.4.2 Conservation of momentum

The conservation of momentum equation requires that the momentum exiting the plume at $z + dz$ equals the momentum entering the plume plus the upward buoyancy force. The entrained fluid has no momentum itself so does not need to be considered. The buoyancy is due to the fact that oil/gas mixture has a lower density than the receiving water. In differential form this can be expressed as

$$\frac{dw^2 R^2}{dz} = g' R^2 \quad (8)$$

Where w and R are as previously defined and g' is the reduced gravity, defined as $g' = (\rho_a - \rho_o)g/\rho_a$ where ρ is density, of oil(o) and ambient(a) and g is gravity. In the absence of buoyancy, Eq 8 shows that momentum is conserved along the plume.

Assuming the entrainment flow rate is linearly dependent on the center velocity,

$$u = aw \quad (9)$$

Where a is constant

The most general solution to Eq 7 and 8 is

$$\begin{aligned} R &= \tan\theta \, z \\ w &= b \frac{B^{1/3}}{z^{1/3}} \\ g' &= c \frac{B^{2/3}}{z^{5/3}} \end{aligned} \quad (10a, b, \text{ and } c)$$

Where B is the buoyancy flux defined as $wg'\pi R^2$ and θ is the growth angle of the plume, and a , b , and c are constants. Equation 10a, b, and c can be solved simultaneously to determine the value of the three constants. These are given in Eq 11. All constants depend on the plume growth angle, θ . As an example, selecting a growth angle of 8.9 degrees, based on experimental observations, gives the values on the right side of Eq 10.

$$\begin{aligned} a &= \frac{5}{6} \tan^2 \theta = 0.130 \\ b &= \left(\frac{3}{4\pi \tan^2 \theta} \right)^{\frac{1}{3}} = 2.14 \\ c &= \left(\frac{4}{3\pi^2 \tan^4 \theta} \right)^{\frac{1}{3}} = 6.08 \end{aligned} \quad (11)$$

The flow rate at location z can be estimated as

$$Q_t = w\pi R^2 \quad (12)$$

Where w is provided in Eq 10b. At $z = 0$ there is no flow, thus a virtual origin. R in Eq 12 varies linearly with z ; $R = z \tan\theta$. To establish a reference frame for the actual flow at the origin of the release, R is assumed equal to the radius of the release location and the corresponding z estimated, z_o , where the 0 subscript denotes the effective origin of the release. The total flow rate in the plume, divided by the release flow rate, is

$$Q_t/Q_o = (z/z_o)^{5/3} \quad (13)$$

In the ZEF, the velocity profile assumes a Gaussian distribution and can be approximated by (Papanicolaou and List 1988).

$$w = 3.85 \frac{B^{3/2}}{z^{3/2}} \exp\left(-90\left(\frac{r^2}{z^2}\right)\right) \quad (14)$$

Where, B is the buoyancy flux.

Equation 14 can be multiplied by the cross sectional area, πR^2 and integrated over R to estimate the flow rate at any location z .

F2.5 Jet

For the case of the jet, the conservation of mass and momentum equations are formulated in differential form as in Eqs 7 and 8, but in this case the reduced gravity term in the conservation of momentum equation disappears, since the fluid is assumed to have the same density as the receiving water. Solving Eqs 7 and 8, the center line velocity is given as

$$w = R_o w_o / R \quad (15)$$

Where R_o and w_o are the radius and exit velocity of the release, respectively. R is the radius of the release at z . Assuming a linear growth rate, $R = \tan\theta z$. It is noted that $z = 0$ at the release location and thus has a radius of R_o .

The relative flow rate for the jet is then given by

$$Q_t/Q_o = 1 + \tan\theta z/R_o \quad (16)$$

Comparing Eq 13 and 16, it is observed that the total flow rate increases with z for a jet and with $z^{5/3}$ for a plume. The plume hence has a much faster dilution rate due to the buoyant forces acting on the discharge.

The growth angle θ is based on empirical observations and is ideally selected for the problem of interest. In some derivations an entrainment coefficient, α , is employed; which is equal to $\tan\theta/2$.

In the ZEF, the velocity profile assumes a Gaussian distribution and can be approximated by (Papanicolaou and List 1988).

$$w = 7.58 \frac{\sqrt{M}}{z} \exp\left(-86\frac{r^2}{z^2}\right) \quad (17)$$

Where M is the momentum flux.

Equation 17 can be multiplied by the cross sectional area, πR^2 and integrated across R to estimate the flow rate at any location z .

For the problem of interest the release starts as a jet and quickly transitions to a plume. To determine the characteristic location of the transition point, the momentum length scale of the release, L , is estimated. L is defined as ratio of the two fluxes,

$$L = M^{3/4}/B^{1/2} \quad (18)$$

Where M is the momentum flux ($M = wQ_t$) and B is the buoyancy flux ($B = Q_t g'$). If the location of application of dispersant is closer to the release than L , then the jet formulation should be used and if further, then the plume formulation employed.

F3. Model application and validation

In the DWH spill the video evidence indicates that the principal dispersant application strategy was via the entrainment based method described above. From the beginning of the spill to approximately the date of the riser being cut, dispersants were applied via a wand at the end of the riser pipe. After the riser was cut the most common application method was via the trident. Analysis of the ROV imagery suggests that the single wand had a radial reach of perhaps 10 to 15 degrees at the circumference of the release and two 45 degree segments for trident (90 degrees total). The dispersant applications for both were very close to the exit of the release, typically within 1 m.

Figure F-8 shows the release from the end of the riser pipe prior to the riser being cut. The release is dominated by buoyancy shortly after exiting the riser as evidenced by the curvature in the plume.



Figure F-8: Release from the end of the riser pipe on May 14, 2010 from the *Skandi Neptune*. The dispersant wand is noted at the lower right of the image.

The release from the riser, post the cut, is considerably more complicated than for pre-cut conditions. Oil exits the riser with a portion of the oil being recovered via the top hat containment system, through the recovery pipe, and another portion being diverted downward, around the rim of the top hat and exiting the top hat. This oil is transported upward (Figure F-10) parallel to

the outer radius of the top hat. ROV imagery shows that the radius of the outer edge of the plume is approximately 10 cm greater than the radius of the outer edge of the top hat. The imagery also shows that the plume shows no tendency to neck down above the height of the top hat but instead is approximately the same radius as at the lower lip of the top hat. The release is then observed, based on an analysis of ROV imagery, (Appendix C) to grow linearly with distance at a rate of about 10.5 degrees.

The key dimensions for the pre and post riser cut used in the analysis are:

Pre riser cut

Inner riser diameter – 0.42 m (FRTG, Flow Rate Technical Group report)

Post riser cut

Outer diameter of top hat - 1.22 m (FRTG)

Inner diameter of cut riser – 0.45 m (Inspection of cut riser, A. Bird, May 2012)

Height of top hat – 1 m

Outer diameter of recovery pipe – 0.245 m ROV Ima

Radial thickness of flow around top hat – 0.1 to 0.15 m (Δr) (ROV imagery)

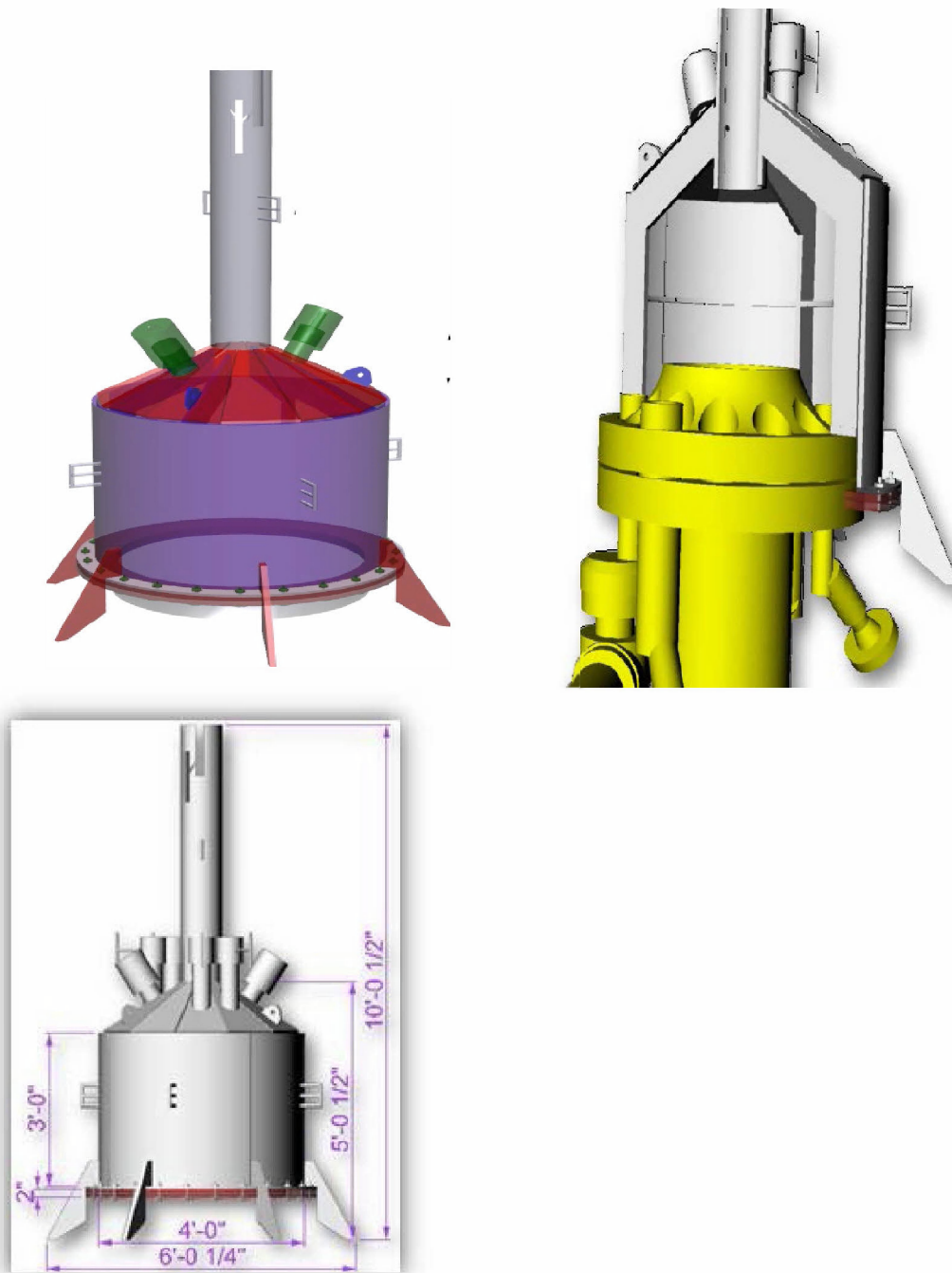


Figure F-9: Schematic of top hat containment system.



Figure F-10: Flow of oil around the rim of the top hat from ROV images on June 30, 2010.

The dispersant treatment model was applied to the DWH spill. As a first step the momentum length scale was calculated for the pre and post cut riser releases on a daily basis. This calculation was performed to determine the length scale at which the flow regime changes from a jet to a plume based on the ratio of the release momentum to buoyancy fluxes. This distinction is of key importance to choosing the proper analytical solution for entrainment calculations. The calculated length scale for the riser ranged from 0.5 to 0.8 m, depending on the assumption about the flow rate and release opening geometry. Estimates were also made for the kink release and gave values of 3 to 5 m, depending on the number of holes and the associated flow rates. Camilli et al. (2011) gave estimates of the momentum length scale for the pre-cut riser of 0.6 m for May 31, 2010, in very good agreement with the analysis presented here. Estimates of the length scale for the kink are not of interest since no dispersants were applied at this location. Based on this analysis and the observation from the ROV imagery that the dispersants were typically applied near the end of the riser and that entrainment and subsequent mixing proceeded with distance from the release point, it is reasonable to assume that the release can be best approximated as a buoyant plume, with the density of the oil and gas driving the plume.

To illustrate the predictions, the dispersant treatment model was applied to a simple test case with an oil release rate of 50,000 barrels per day and a dispersant application rate of 300 barrels per day. These values are typical of the ratio of oil to subsurface dispersants used during the spill. If the dispersant is completely mixed with the oil then the DOR is 1:167 (alternately written as 167).

Figure F-11 shows model-predicted fraction treated (solid line, left axis) and DOR (dashed line, right axis) as a function of distance from the release for post riser cut conditions. Distance is measured downstream from the release and non-dimensionalized by the diameter of the release at the source. Figure F-12 is the same plot but as a function of distance from the origin. Curves are shown assuming 6.25, 10, 12.5, 25, 30, 50, and 100% of the circumferential sector

is treated. These values include the azimuthal angle of the original treatment plus an internal growth rate in the plume. As an example, if the dispersant application device has an angular reach of 20 degrees at the application point and the azimuthal internal entrainment rate is 10 degrees, then the total angular sector treated is 40 degrees or in percent of circumference $(40/360) = 11.1\%$. If the internal growth rate is assumed constant then the sector percentage is independent of distance from the release. The DOR is given in terms of the target DOR divided by the Dispersant Effectiveness (DE). As an example, if the target application DOR is 1:50 and DE is 0.5 then the effective DOR is 1:100. The fraction treated increases with distance from the release and asymptotically approaches a constant value. The amount treated increases with sector treatment percentage. For low sector ranges (less than 30%) the fraction treated is close to its asymptotical value by 4 to 6 diameters from the release. For higher sector ranges (50 to 100%) asymptotic values are reached at greater distances. The DOR curves all have similar shapes to the fraction treated curves. In general, the fraction treated increases and the DOR decreases with distance from the release and with increasing percent of sector treated. For analysis purposes it appears that mixing is approximately complete by about 6 diameters. The zone of flow establishment (ZFE) is typically 5- 7 diameters from the release. Assuming a DE of 50%, a distance of 6 diameters, and application by the wand, the fraction treated is 6.5 % and the DOR is 1:20 or DOR/DE of 1:40. Similar assumptions for the trident gives a fraction treated of 26% and a DOR of 1:55 or DOR/DE of 1:110.

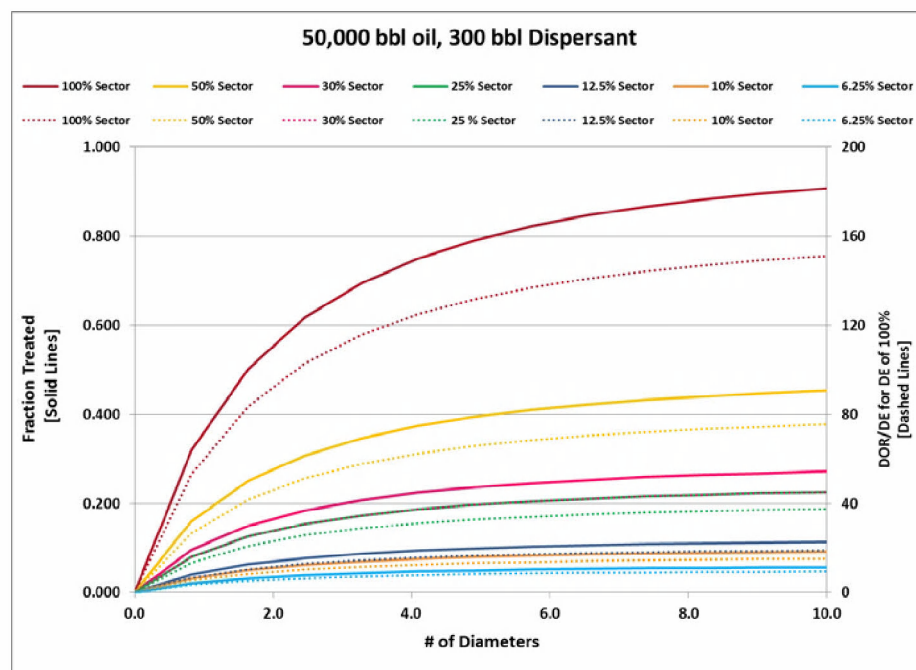


Figure F-11: Fraction treated (solid line, left axis) and DOR (right axis) vs number of diameters downstream from the release with varying sector fractions treated. The effective DOR is estimated by dividing the target DOR by the dispersant effectiveness (DE).

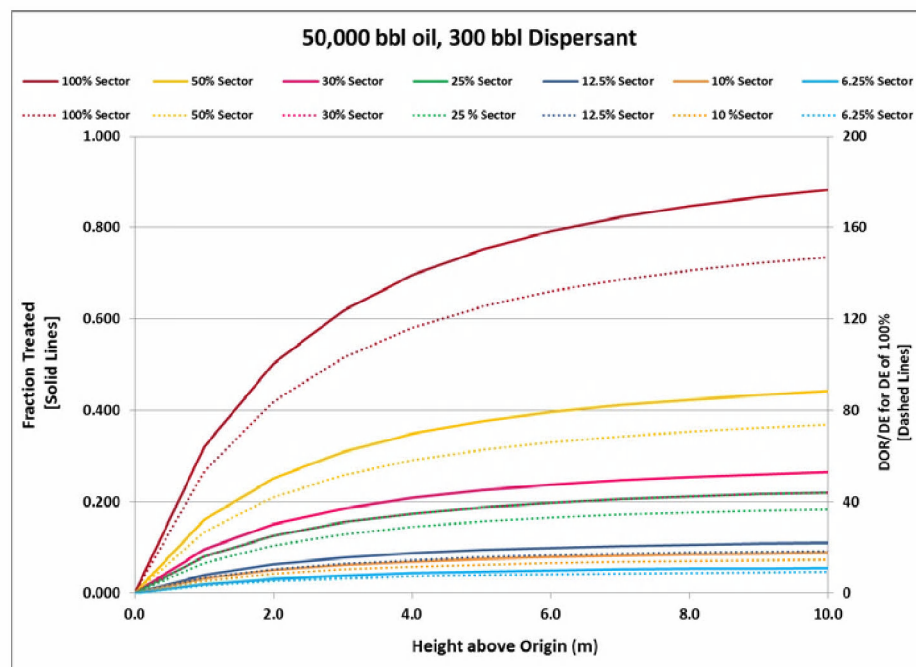


Figure F-12: Fraction treated (solid line, left axis) and DOR (right axis) vs distance downstream from the release with varying sector fractions treated. The effective DOR is estimated by dividing the target DOR by the dispersant effectiveness (DE).

To assess the model's predictive performance it was applied to predict the fraction treated and DOR during the time period when oil droplet sizes were being measured by *Holocam* during various dives from the R/V Jack Fritz cruises. This droplet size data set is summarized in Section 5.6 and described in detail in Appendix G and the *Holocam* data in Appendix J. During this period dispersants were primarily being applied via the trident immediately above the release and in close proximity to the mouth of the top hat. Dispersant treatment model simulations were performed for June 14 to 20, 2010, with a time step of one day. Daily oil release and dispersant application rates, as provided in Appendix B, were used.

Figure F-13 shows model predictions of fraction treated and DOR as a function of time assuming 20, 30, and 40% of the sector was treated. The 30% value is a reasonable estimate for the trident. The results are shown at approximately 6 diameters from the release origin. The model predicts fractions treated of 0.16, 0.25 and 0.34 for the 20, 30, and 40% sector cases, respectively. These values are invariant with time. The DOR for each sector case is also shown and varies daily throughout the period; the higher the percent of sector treated, the lower the DOR. The variations are caused by daily variations in the oil release and dispersant application rates. Fraction treated and DOR both scale linearly with percent of sector. The average DORs during the period are 1:33, 1:49, and 1:65 for the 20, 30, and 40% cases, respectively.

The DORs for dives #5 and #6 of the *Holocam* data were estimated using the droplet size model. Specifically an assumed log normal distribution was fit to the observations from each dive and the volume median diameter (VMD) determined for each. The VMD vs Weber/Ohnesorge number correlation equation was then used to estimate the necessary oil-water interfacial tension associated with the observed VMD. This value in turn was used to determine the DOR based on laboratory based observations of DOR vs oil water interfacial tension (Venkataraman et al. 2013). The DORs for the various dives are shown in Figure F-13.

The value next to the dive number is the distance between the sampling site and the wellhead. The *Holocam* data-based DOR for dives # 5 and 6 were 1:69 and 1:114.5, respectively. Model predictions are hence in reasonable agreement with the observations. The model of observed conditions predicts a variation in the DOR with time, which is in general agreement with the overall trend of the observational data.

The variation of field data is not surprising, given the quite different distances (dive #5 at 1.15 km from the wellhead vs dive #6 at 2.12 km) and depth into the water column (dive #5 at 1,459m vs dive #6 at 1,059m). As the droplet size data were collected at substantial distance from the wellhead, they may not represent the portion of release that was in the form of larger droplets which could have reached the surface before being sampled.

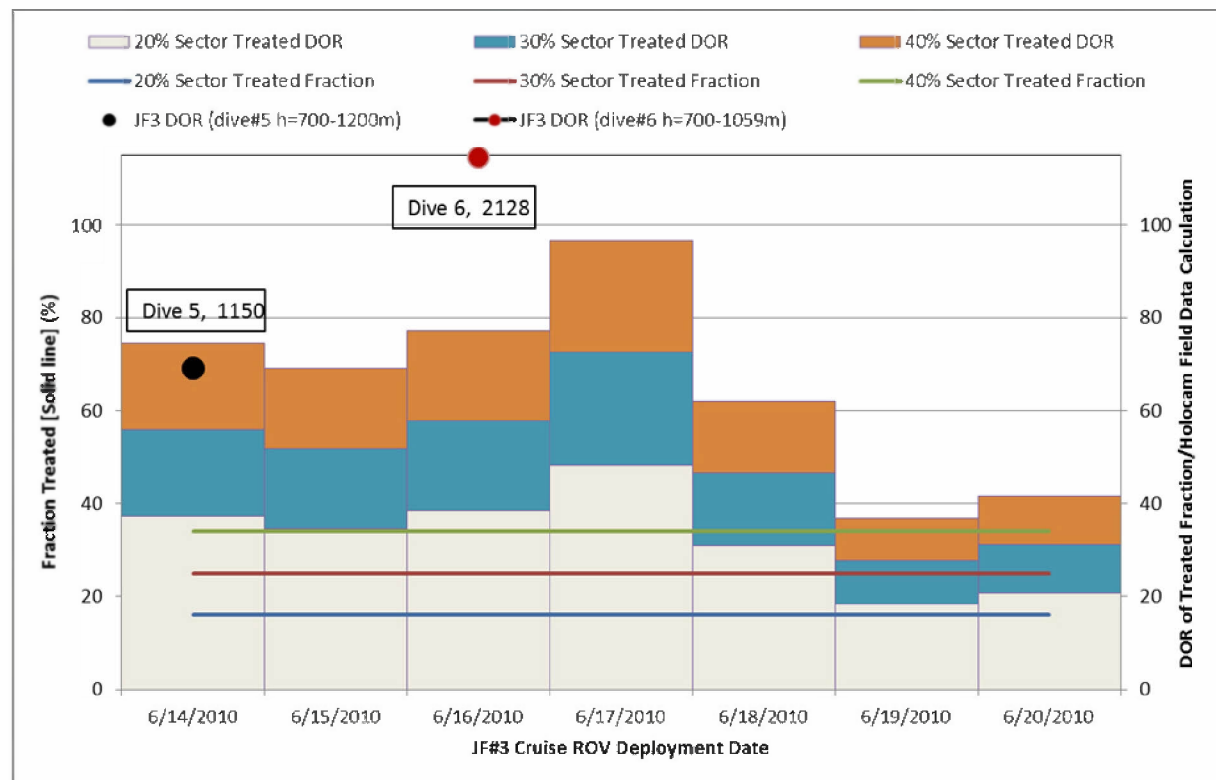


Figure F-13: Fraction treated (solid line) and DOR (dashed line) vs time during the JF3 cruise for sectors treated ranging from 20 to 40%. The estimated DORs for the JF3 dives are provided. The distance from the wellhead to the sampling location for each dive is also shown (see Appendix G for additional details).

The dispersant treatment model described above has been applied to the DWH spill using a daily time step. Data on the spill release rate and amount of dispersant applied subsurface is provided in Appendix B. Simulations have been performed for three different assumptions about the dispersant application method and its effectiveness. The results are provided in Section 6 of the main report.

F4. Summary and conclusions

A simplified methodology has been developed and implemented based on well-known jet and buoyant plume theory to estimate the fraction of oil treated and associated DOR with distance from the release for a variety of treatment options including: premix, injected, and entrained. The concept of dispersant effectiveness, including chemical, operational and hydrodynamic considerations, has been incorporated into the analysis methodology.

The dispersant treatment model was applied to the DWH during mid June 2010 when oil droplet size measurements were being made using *Holocam* techniques near the spill site to validate the approach. It was assumed that the principle dispersant application method was an entrainment based approach. Validation of the fraction treated was performed with data on the observed oil and DOSS concentrations at the trapping depth and an analysis of the chemistry data. These results are given in the main report (Section 6).

Application of the dispersant treatment model to the DWH spill was extremely challenging given the complicated release geometries (e.g., top hat collecting a portion of the release above the BOP, with the remainder of the release escaping around the outer edge of the top hat and being transported upward as a buoyant plume) and the complex mixing of the entrained dispersant from point (wand) or sector (trident) application methods with the escaping oil and gas mixture. The internal mixing of entrained fluid (and dispersant) within the plume is also of key importance. The effectiveness of the dispersant application in this case is also quite uncertain given the complicated mixing regimes and water-oil-dispersant chemistry. There is very little information in the literature on this problem since subsurface application of dispersant to a buoyant, multi-phase flow has been historically been extremely limited. Subsurface dispersant use during the DWH represents the first and only large scale application to a blowout. Little data was collected in the immediate vicinity of the release to help validate the treatment model.

The greatest uncertainty in the application of the dispersant treatment model is estimating the effective mixing between the entrained dispersant and the oil within the buoyant plume, the most critical issue being internal mixing within the plume from discrete applications on the plume circumference.

Several investigations are currently in progress at this time that will help provide additional insight into the dispersant treatment process. These are briefly summarized below.

SINTEF Laboratory Experiment

With support from the BP and the API Joint Industry Oil Spill Preparedness & Response Task Force (Oil Spill JITF), subsea dispersant injection program, SINTEF has performed a number of laboratory based experiments in their newly constructed, 7 m deep test basin. Each experiment consisted of releasing an oil or oil and gas mixture through a 0.5, 1.5, or 3.0 mm orifice at the bottom of the test tank. Droplet sizes were measured using PVM and LISST/LaserCam techniques. Experiments varied the oil release rate, heating, presence of gas, and the dispersant application approach (in line, injected near release and sprayed from above). DORs were varied from 1:25, 50, 100, 250, 500, to 1000. Video were collected at the location of the release point. Analyses of both the BP and API studies have been completed. The prior work has been presented in the form of two papers in the Journal of Marine Pollution Bulletin (Brandvik et al. 2013; Johansen et al. 2013), one on the experiments and results, and the second on an application of a droplet size distribution model to the data. The API study has been completed and summarized in a report (Brandvik et al. 2014). These data sets have been used to validate the oil droplet size model. The study investigated the influence of the way in

which dispersants were injected into the plume on the oil droplet size distribution, including pre-mixing, where dispersants were injected into the release pipe 3 m (2000 nozzle diameters) upstream of the release, injection horizontally into the plume at various distances from the release, and injection adjacent to the jet and allowed to entrain into the plume. Surprisingly the premix experiments showed that there was insufficient mixing of the dispersant into the oil despite the long length for mixing in the pipe. For the horizontal injection at different heights above the release, the effectiveness of treatment decreased with distance along the plume. The report attributed this to the following: droplets are already formed, reduced turbulence/shear forces in the ZEF establishment compared to the ZFE closer to the nozzle, further splitting into smaller droplets demands higher turbulence and the less effective use of dispersant since some is injected into the water instead of the oil phase. The entrainment based injection method was not successful since the injection rate of the dispersant was so large that it was directly injected into ZFE, not adjacent to it.

The results of the dispersant treatment model are consistent with these large scale laboratory experiments showing that rate of change of dilution (rate of mixing) decreases with increasing distance from the release location and that mixing is significantly impacted by how and where the dispersant is applied. Both show that complete mixing, regardless of the injection method, is difficult to achieve.

UHI Laboratory Experiment

Through funding from Chevron-MIT University Partnership, the Gulf of Mexico Research Initiative, and the U.S. Office of Naval Research APRISES program, Dr. Stephen Masutani at the University of Hawai'i, Mānoa and his graduate student S. I. Nagamine conducted a study on "*The effect of dispersants on the evolution of buoyant oil droplets*" (Nagamine 2014). The experimental study aimed to investigate the effects of dispersants on the evolution of droplets in the rising buoyant plume of oil droplets through monitoring the droplets with video cameras and chemical analysis of dissolved and dispersed oil concentrations. During the study, the oil droplets, treated with dispersants at a range of DOR's, were suspended by a downward flow of synthetic seawater in a vertical water tunnel to simulate their free-rise conditions. The results indicated that the addition of dispersant to oil promoted reduction of droplet size during free rise through a "tip-streaming" process, where larger droplets at sufficiently high DOR's shed filaments of oil from their edges, or by tearing events. The rate and extent of the droplet size reduction were found to dependent on DOR.

Similar research project is being conducted in Dr. Joseph Kats team at John Hopkins University, funded by GOMRI Dispersion Research on Oil: Physics and Plankton Studies (DROPPS) consortium, which has also been awarded for additional funding for the 2015-2017. Figure F-14 displays an example of holographic imagery that captures time-series a "tip-streaming" of tiny daughter droplets as the parent drop rises in the water column.

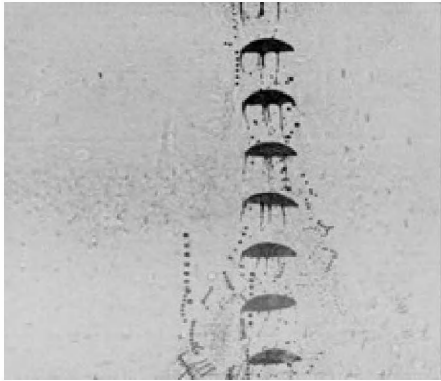


Figure F-14: Hologram of “octopus” oil droplets created when dispersant is added to oil (David Murphy and Cheng Li, JHU; <http://gulfresearchinitiative.org/mesocosm-experiments-look-oil-spill-bottom/>)

Gulf of Mexico Research Initiative Project (T. Ozgokmen, University of Miami)

With funding from GOMRI, Dr. Ozgokmen is undertaking Large Eddy Simulations (LES) of the release from the DWH blowout. One line of their investigation is to study the very near field with a particular focus on the very near field development of the flow field and the entrainment of water and its subsequent mixing into the plume. The approach allows one to explore the mixing between the oil and entrained fluid (dispersant) in great detail and provides a method to validate the dispersant treatment model. Figure F-15 shows initial simulations of the buoyant release into quiescent receiving water. The velocity and velocity variance contours are shown.

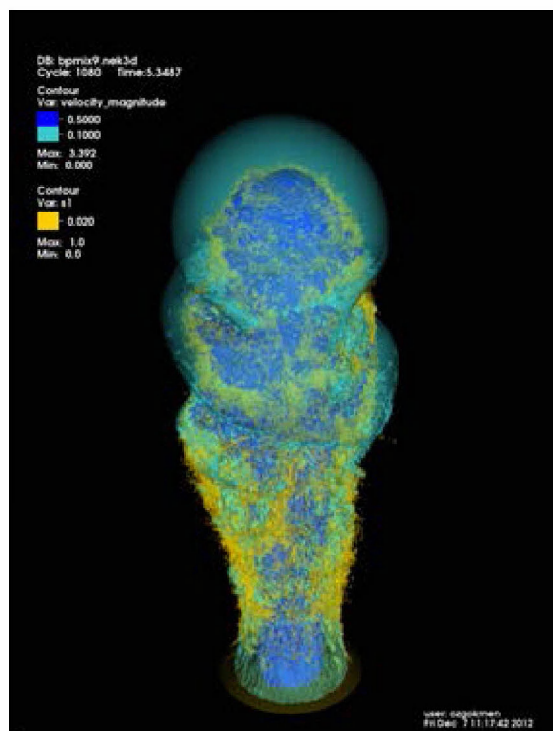


Figure F-15: LES simulations of the initial stages of the release from a buoyant plume into quiescent receiving water. The figure shows contours of the velocity and associated variances (Source: T. Ozgokmen, University of Miami).

A feasibility simulation was performed using this LES model to demonstrate the mixing between a jet/plume release and an adjacent release of a tracer (dispersant) in the immediate vicinity of the jet discharge location. This mimics the strategy used in most of dispersant application to the DWH blowout where the dispersant is entrained but not directly injected into the oil release. Figure F-16 shows the model predicted cross section of the two releases (oil located in the center and dispersant applied to the right) with distance (Y) from the discharge point in release diameters. A fixed contour of the original plume is shown in red and the dispersant release in green and gray. The tracer contours show dilution of the release. While the dispersant release is in close proximity to the oil release they are separated. Close to the discharge point ($Y=0.5$) this separation remains clear. At a distance of $Y=2$ the dispersant is clearly being entrained into the oil plume. With increasing distance along the plume center line the model predicts continued mixing of the dispersant ($Y=5$ and 10). The dispersant is seen to mix toward the center of the oil plume and increase its azimuthal mixing. The mixing in the azimuthal direction is limited and appears to become slower as the distance from the entrainment point increases (comparing contours at $Y=5$ and 10). The features of these demonstrative LES model predictions are consistent with the simplified dispersant treatment model developed here: namely limited azimuthal mixing and increasing dispersant dilution with distance from the release but asymptotically approaching an upper limit. The simulations appear to show almost complete mixing by 10 diameters.

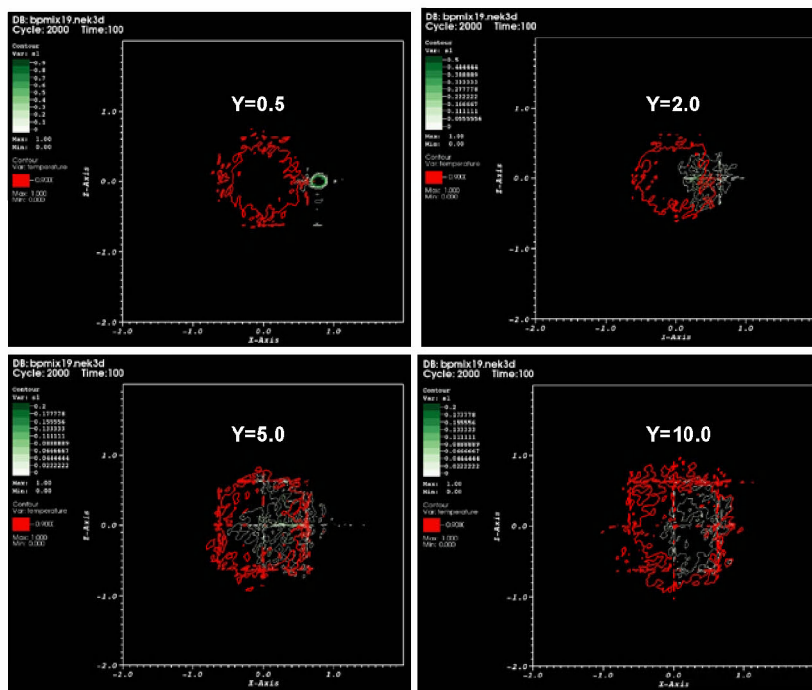


Figure F-16: LES predicted mixing of oil (red) and entrained dispersant (green –gray) with non-dimensional distance (Y = distance from release/ release diameter) from the release location. (Source: T. Ozgokmen, University of Miami).

F5. References

- Aurand, D., R. Belore, B. C. Jones, G. Coelho, M. Fraker, A. Lewis and O. Peltz. 2010. Dispersant Studies of the Deepwater Horizon Oil Spill Response: Vol 1. June 2010.
- Belore, R.C., I. Buist, B.K. Trudel and J. Morrison. 2011. Wave tank and swirling flask dispersant effectiveness testing on fresh Mississippi Canyon 252 oil. In: 2011 International Oil Spill Conference, IOSC 2011.
- Brandvik, P. J., Ø. Johansen, F. Leirvik, U. Farooq and P. S. Daling. 2013. Droplet breakup in subsurface oil releases – Part 1: Experimental study of droplet breakup and effectiveness of dispersant injection. *Marine Pollution Bulletin* (73):319-326.
- Brandvik, P. J., Ø. Johansen, U. Farooq, G. Angell and F. Leirvik. 2014. Sub-surface oil releases – Experimental study of droplet distributions and different dispersant injection techniques- version 2. A scaled experimental approach using the SINTEF Tower basin. SINTEF report no: A26122. Trondheim Norway 2014. ISBN: 9788214057393.
- Camilli, R., D.Di Iorio, AaBowen, C.M. Reddy, A.H. Techet, D.R. Yoerger, L.L. Whitcomb, J.S. Seewald, S.P. Sylva, and J. Fenwick. 2011. Acoustic measurement of the Deepwater Horizon Macondo well flow rate, *Proceedings of National Academy of*

- Sciences, www.pnas.org/cgi/doi/10.1073/pnas.1100385108 and supplementary material at www.pnas.org/lookup/suppl/doi:10.1073/pnas.1100385108/-/DCSupplemental.
- Chandrasekar, S., G.A. Sorial and J.W. Weaver. 2005. Dispersant effectiveness on three oils under various simulated environmental conditions. *Environmental Engineering Science* 22(3):324-336.
- EC. 2008. Environment Canada Oil Properties Databases and Software. Available online, http://www.etc-cte.ec.gc.ca/databases/OilProperties/oil_prop_e.html
- Hirst, E.A. 1971. Analysis of round turbulent buoyant jets discharged to flowing stratified ambient. ORNL- 4685, Oak Ridge National Laboratory, Oak Ridge, TN.
- Johansen, Ø., P. J. Brandvik and U. Farooq. 2013. Droplet breakup in subsea oil releases – Part 2: Predictions of droplet size distributions with and without injection of chemical dispersants. *Marine Pollution Bulletin* 73(1):327-335.
- Jirka, G. 2004. Integral Model for Turbulent Buoyant Jets in Unbounded Stratified Flows. Part I: Single Round Jet, *Environmental Fluid Mechanics* 4: 1–56, 2004.
- Li, Z., K. Lee, P. E. Kepkay, O. Mikkelsen and C. Pottsmith. 2011. Monitoring dispersed oil droplet size distribution at the Gulf of Mexico Deepwater Horizon spill site. In: 2011 International Oil Spill Conference, May 23-26, 2011, Portland, OR. Americal Petroleum Institute, Washington D.C.
- Lunel, T. 1995b. Understanding the mechanism of dispersion through oil droplet size measurements at sea. In: Lane, P.,eds. *The Use of Chemicals in Oil Spill Response*, ASTM STP 1252. American Society for Testing and Materials, Philadelphia, PA. Pp. 240-270.
- Nagamine, S.I. 2014. The effects of chemical dispersants on buoyant oil droplets, Master of Science In Mechanical Engineering, University of Hawai'i, Mānoa, Hawaii. 122 pg
- NRC. 2005. National Research Council: *Understanding Oil Spill Dispersants: Efficacy and Effects*. National Academies Press, Washington, D.C.
- Papanicolaou, P.N. and E. List. 1988. Investigations of round vertical turbulent buoyant jets. *J Fluid Mech.* 195:341–391.
- Roisin-Cushman, B. 2004. Environmental transport and fate, Chapter 3 Turbulent Jets and Chapter 10 Plumes and Thermals. Dartmouth College, Hannover, NH.
- Sorial, G.A., A.D. Venosa, K.M. Koran, E. Holder and D.W. King. 2004. Oil spill dispersant effectiveness protocol. II: Performance of revised protocol. *Journal of Environmental Engineering-ASCE* 130(10):1085-1093.
- Stevens, L. and J. Roberts. 2003. Dispersant effectiveness on heavy fuel oil and crude oil in New Zealand. In: *Proceedings of the 2003 International Oil Spill Conference*. American Petroleum Institute.
- USEPA. 2012. The United States Environment Protection Agency's list of authorized dispersants (NCP product schedule): The chemical components of the dispersants COREXIT 9500 and COREXIT 9527. Internet website: <http://www.epa.gov/bpspill/dispersants-qanda.html#list>

- Venkataraman, P., J. Tang, E. Frenkel, G.L. Mcpherson, J. He, S. R. Raghavan, V. L. Kolesnichenko, A. Bose and V. T. John. 2013. Attachment of a Hydrophobically Modified Biopolymer at the Oil-Water Interface in the Treatment of Oil Spills. *Applied Materials & Interfaces* 5(9):3572-3580.
- Venosa, A.D., D.W. King and G.A. Sorial. 2002. The baffled flask test for dispersant effectiveness: A round robin evaluation of reproducibility and repeatability. *Spill Science & Technology Bulletin* 7(5-6):299-308.
- Venosa, A.D. and E.L. Holder. 2013. Determining the dispersibility of South Louisiana crude oil by eight oil dispersant products listed on the NCP Product Schedule. *Marine Pollution Bulletin* 66(1-2):73-77.

Technical Reports for Deepwater Horizon Water Column Injury Assessment

WC_TR.13: Application of OILMAP DEEP to the Deepwater Horizon Blowout

Appendix G: Development of OILMAP DEEP droplet size model

Authors: Malcolm Spaulding, Daniel Mendelsohn, Deborah Crowley,
Zhengkai Li, Andrew Bird

Revised: September 30, 2015

Project Number: 2011-144

RPS ASA 55 Village Square Drive, South Kingstown, RI 02879

Table of Contents

G1.	Introduction and background	1
G2.	Review of gas and droplet size measurements: laboratory and field observations	3
G2.1	Laboratory experiments	3
G2.1.1	Blowout – University of Hawai'i	3
G2.1.2	Subsurface oil release – SINTEF API Study of Droplet Size Distributions and Dispersant Injection Techniques	6
G2.1.3	SL Ross BSEE Subsea Chemical Dispersant Research	10
G2.1.4	Delvigne's natural dispersion experiments and droplet size distribution	12
G2.1.5	SINTEF wave tank experiments on natural entrainment of weathered high viscosity oil	15
G2.1.6	BIO wave tank experiments on chemical dispersion of oil	17
G2.2	Deep Spill Field Experiments on Blowout Releases of Oil and Gas	18
G2.2.1	Methane gas bubble size distribution	19
G2.2.2	Diesel oil droplet size distribution	22
G2.3	Deep Water Horizon measurements	26
G2.3.1	ROV Video particle size	26
G2.3.2	Holographic Camera (Appendix I)	26
G3.	Impact of dispersant treatment on oil droplet size distribution	26
G4.	Review of oil droplet size models in existing blowout models	31
G4.1	CDOG, DEEP BLOW and OILMAP DEEP	31
G4.1.1	Determining the maximum drop size (d_{95}) based on Weber number method	31
G4.1.2	Determining the Rosin-Rammler type droplet size distribution	32
G4.2	SINTEF Modified Blowout Oil Droplet Size Model	32
G4.2.1	Determining the volume median diameter of drop size (vd_{50}) based on the modified Weber number method	32
G4.2.2	Droplet size distribution	33
G5.	New Oilmap Deep oil droplet size model	33
G5.1	Lognormal distribution with Weber number and Ohnesorge number dependent VMD	33
G5.1.1	Definition of dimensionless groups	33
G5.1.2	Volume median diameter formula	34
G5.1.3	Droplet size distribution	35
G5.2	Model validation	37
G5.2.1	Comparison of existing and developed oil droplet model with laboratory testing results	37

G5.2.2	Comparison of lognormal and Rosin- Rammler distributions with laboratory and field data	41
G5.2.3	Comparison of treated and untreated oil droplet size distributions using the new droplet size model	43
G6.	Summary and conclusions	48
G7.	References	50

List of Figures

Figure G-1: Different modes of jet breakup in the oil injection experiments. Jet velocity increased sequentially from left to right, corresponding to oil breakup mode as (A) Rayleigh instability, (B) sinuous wave breakup, (C) filament core breakup, (D) wave atomization and (E) turbulent atomization (Masutani & Adams, 2000; Tang, 2004).	4
Figure G-2: Liquid-liquid jet breakup regimes. Data points correspond to 175 oil and silicone fluid injection tests (upper two sets) and 85 CO ₂ injection tests (lower set) (Masutani & Adams, 2000; Tang, 2004).	5
Figure G-3: Representative droplet size distribution spectra for the five modes of breakup, velocity and Re increasing from left to right. Data are from experiments of liquid CO ₂ jet discharged through a 5 mm (i.d.) nozzle into water at about 60 atm pressure, with measurements performed about 70 cm (or 140 times nozzle diameter) from the release (Masutani & Adams, 2000; Tang, 2004).	6
Figure G-4: Representative rising oil plume in the SINTEF Tower Basin Experiment with release nozzle diameter 1.5mm and the oil flow rate at 1.2 L/min: (A) rising plume prior to dispersant injection (similar to the oil only droplet size distribution curve in Figure 5), (B) Immediately after dispersant injection started at an intended DOR of 1:50, and (C) 30 seconds after injection started (similar to solid green curve in Figure G-5).	7
Figure G-5: Relative oil droplet size distribution (volume %) recorded with the LISST-100X particle size analyzer in the SINTEF Tower tank experiment. These data were generated with dispersant injected at different DORs (the first ratio value next to DOR in the legend) and from the side at different distances (the second value in unit of mm in the legend) into the rising oil plume released from a 1.5 mm nozzle at 1.5 L/min flow rate for all the dispersant treated tests, but at 1.2 L/min flow rate for the non-treated oil only release test.	8
Figure G-6: SL Ross subsea dispersant experimental study. The facility includes a horizontally oriented underwater nozzle connected to pressurized gas and oil supply lines and two LISST-100X particle size analyzers positioned at different depths to capture oil droplet size distribution	11
Figure G-7: Entrainment coefficients as a function of initial oil viscosity (Delvigne & Hulsén, 1994).	13
Figure G-8: Mean droplet size d_{50} versus oil viscosity for submerged oil in turbulent energy dissipation rate (Delvigne & Sweeney(1988).	14
Figure G-9: Oil droplet size distribution in breaking-wave experiment (Delvigne & Sweeney, 1988).	15
Figure G-10: Droplet number distribution from image analysis together with best fits of the lognormal (black line) and Rosin-Rammler (red line) distribution functions. The Rosin-Rammler distribution does not fit well at the smaller droplet size ($d < 0.5$ mm), since it is weighted by volume rather than number distribution. The Rosin-Rammler distribution was therefore not used in Reed <i>et al.</i> (2009) droplet size analysis.	16

Figure G-11: Cumulative volume droplet size distribution of crude oil in an experimental wave tank (Lee, <i>et al.</i> , 2009, Li, <i>et al.</i> , 2009c); lognormal distribution parameters are listed in Table G-3.....	18
Figure G-12: The methane bubble number size distribution observed by Johansen et al. (2001) from cases (upper panel) (1) 9-19 m, (2) 19-23 m, (lower panel) (3) 39-58 m, and (4) 65-85 m above the release.	20
Figure G-13: The methane bubble volume size distribution observed by Johansen et al. (2001) cases (upper panel) (1) 9-19 m, (2) 19-23 m, (lower panel) (3) 39-58 m, and (4) 65-85 m, above the release.	21
Figure G-14: Distribution of the diesel oil droplet number size distribution observed by Johansen et al. (2001) at the <i>Deep Spill</i> field trials (upper panel) (5) 5-6 m, (6) 10-11 m, (lower panel) (7) 15-23 m, and (8) 35-56 m above the release.	23
Figure G-15: Distribution of the diesel oil droplet volume size distribution observed by Johansen et al. (2001) at the <i>Deep Spill</i> field trials (upper panel) (5) 5-6 m, (6) 10-11 m, (lower panel) (7) 15-23 m, and (8) 35-56 m above the release.	24
Figure G-16: The measured methane gas bubble median diameters at four different depths.....	25
Figure G-17: The measured diesel oil droplet median diameter at four different depths.	25
Figure G-18: Measured variation (upper) and fitted equations (middle) of oil-brine interfacial tension with dispersant concentration (in DOR) for MC252 and Corexit 9500 dispersant (Venkataraman et al 2013); and for three crude oils and Corexit 9500 dispersant (Khelifa and So, 2009).	30
Figure G-19: Comparison of observed volume median diameter data (circles) and the calculated values (mesh grid and color bar) based on Equation 17 with the best-estimate parameters ($r = 1.791$, $p=0.460$, and $q=-0.518$; $R^2=0.861$).	35
Figure G-20: SINTEF model predicted and the reported VMD of jet/plume oil releases with and without dispersant treatment. Upper panel, model based on earlier coefficients ($A = 15$, $B = 0.8$); Lower panel, based on later updated coefficients ($A = 24.8$, $B = 0.08$). The laboratory experimental datasets include 23 tests from SINTEF tower basin (Brandvik et al 2014), 12 tests from OHMSETT tank (Belore 2014), and 6 tests from SL Ross tank tests (Belore 2014).	38
Figure G-21: Oilmap Deep oil droplet size model predicted and the lab reported VMD of jet/plume oil releases with and without dispersant treatment. Upper panel, New OILMAP DEEP model: Solid lines are regression of SINTEF data and SL Ross data, respectively, dashed line is the regression with all data; For the SINTEF results, blue squares are untreated, and red squares and green triangles are all treated. Lower panel, Model prediction based on commercial version OILMAP DEEP oil droplet size model; (Experimental data are the same as in the upper panel, data source: Brandvik et al 2014; Belore 2014)	40
Figure G-22: Summary of observed cumulative droplet size distribution of five different data sets and the fitted lognormal and Rosin-Rammler droplet size distributions.	41
Figure G-23: <i>Deep Spill</i> field data and fitted lognormal distribution ($R^2 = 0.956 - 0.999$) and Rosin-Rammler distribution ($R^2 = 0.905 - 0.991$) of oil droplet size distribution data at four different depths. The fitted parameters are listed in Table G-9.	42

Figure G-24: Cumulative volume distribution of the chemically (purple) and physically (cyan) dispersed oil and their combined distribution (green) for DOR 1:40 with an assumed 73% (red) to 27% (blue) split between the untreated and treated oil, respectively.	44
Figure G-25: RPS ASA droplet size model predicted oil droplet volume distribution assuming varying percent of oil treated (0 to 100%) for DOR: 1:40 (upper panel), 1:90 (center panel), and 1:150 (lower panel). A 38,700 barrel/day release rate at an exit velocity of 2 m/sec was assumed.	46
Figure G-26: RPS ASA droplet size model predicted cumulative oil droplet volume distribution assuming varying percent of oil treated (0 to 100%) for DOR: 1:40 (upper panel), 1:90 (center panel), and 1:150 (lower panel). A 38,700 barrel/day release rate at an exit velocity of 2 m/sec was assumed.	47

List of Tables

Table G-1: Summary of the data from SINTEF tower basin tests (where D is the nozzle diameter, Q is the oil flow rate, DOR is the dispersant to oil ratio, IFT is the interfacial tension, U is the exit velocity, We is the Weber number, Vi is the viscosity number, and dp is the peak droplet diameter recorded in the LISST-100X analyzer.) Data of the shaded tests were excluded from droplet size model development or validation (see text for the reasoning of this practice).	9
Table G-2: Large scale OHMSETT tank (#33-44) and SL Ross wave tank (TN1-7) test conditions and volume median diameter (VMD) results.	11
Table G-3: Fitted parameters of the lognormal (volume) droplet size distribution for dispersion of MESA oil at four time points in an experimental wave tank (Lee, <i>et al.</i> , 2009, Li, <i>et al.</i> , 2009c).	18
Table G-4: Counts of methane gas bubbles at release experiment #4 carried out on 29 June 2000. In each second represents 25 pictures were recorded for bubble size analysis. A total of 667 bubbles were counted from a total of 3400 pictures (Johansen et al. 2001).	19
Table G- 5: Counts of diesel oil droplet sizes at release #2 carried out 27 June 2000. Each second represents 25 pictures evaluated for bubble sizes. A total of 667 droplets were evaluated by Johansen et al. (2001) from a total of 5325 pictures.	22
Table G-6: The Chemical components of Corexit 9500 and Corexit 9527 (EPA 2013)	28
Table G-7: CDOG, DEEP BLOW, and OILMAP DEEP parameters used in droplet size equation.	31
Table G-8: Fitted parameters of lognormal versus Rosin-Rammler distribution of five different droplet size data sets.	42
Table G-9: Fitted parameters of lognormal versus Rosin-Rammler distribution of the droplet size distributions observed at four different depths above the release spot of the <i>Deep Spill</i> field trial.	43
Table G-10: Values for variables used for the DWH release conditions	44
Table G-11: The fraction of treated (at DOR 1:40) and non-treated oil and estimated lognormal distribution parameters.	45

G1. Introduction and background

Oil droplets are generated by turbulence and turbulent shear flow under surface breaking wave conditions and in subsurface blowout release jet and buoyant plumes. The oil droplet size distribution is determined by the physical-chemical properties of the dispersed and continuous phases (e.g., viscosity, density, and interfacial tension) and the hydrodynamic characteristics of the flow field. Delvigne and Sweeney's (1988) algorithm is frequently used for natural dispersion of oils under breaking wave conditions. In practice, the characteristic droplet size (average or maximum diameter) is estimated based on its dependence on the mean energy dissipation rate and the viscosity of oil. In natural dispersion of oil, there appears to be a generally good agreement between the theoretical relationship, of oil droplet size and upper ocean turbulence as proposed by Li and Garrett (1998), and the dependence of the maximum droplet size on the energy dissipation rate and the oil viscosity as in Delvigne and Sweeney's (1988) algorithm. However, Delvigne and Sweeney's (1988) algorithm has no mechanism to account for the change of interfacial tension - often in orders-of-magnitude, when a chemical dispersant is applied. In case of a successful application of dispersants, an oil droplet size may be reduced to such an extent that the droplet Reynolds number decreases to the regime in which the shear forces (rather than the pressure force) turn out to be the dominant mechanism for droplet break up. In this viscous shear regime, the interfacial tension, energy dissipation rate, and the dispersed and continuous phase viscosity are all important variables that dictate the maximum droplet size (Li and Garrett 1998).

Oil droplet size distributions resulting from subsurface releases are currently modeled in most existing blowout models (e.g., OILMAP DEEP, DEEP BLOW, and CDOG) with a modification of liquid-liquid dispersion in pipe flow (Karabelas 1978) as described by (Johansen 2003). In practice, the first step is to calculate the maximum droplet size based on the Weber number where the length scale is the diameter of the release. The Weber number represents the ratio of fluid's inertia to surface tension. The second step is to determine the droplet size distribution based on the empirically estimated degree of spreading of an empirical distribution function. Rosin-Rammler and lognormal distributions are typically used. Most of the blowout droplet size model parameters have been calibrated against the Deep Spill field trial data (Johansen et al. 2001). The underlining assumption of the existing blowout oil droplet size model is that the breakup of oil into oil droplets is predominantly by Hinze (1955)'s disruptive pressure force mechanism, given that the turbulence level in the blowout jet flow mixing zone is strong, and the viscous force of the dispersed phase is relatively weak. Although this appears reasonable for typical blowout oil and gas release, this assumption has been challenged in the presence of subsurface dispersant injection (Johansen 2013), in which case the oil-water interfacial tension may be reduced by orders-of-magnitude. As a result, the coherent force of the oil phase viscosity may become significant, so that oil would not break up further into smaller droplets, even when the interfacial tension force becomes small due to the effect of the surfactant. A modified Weber number model has been adapted by Johansen et al. (2013) from a mixing tank reactor model developed by Wang and Calabrese (1986) to account for the viscosity effect in the case of low oil-water interfacial tension. The Wang and Calabrese model as adopted by Johansen et al. (2013), however, has some internal inconsistencies in terms of the parameter estimates and overestimates the size of dispersant treated oil droplets (Belore 2014; Lehr 2014).

In addition to the equilibrium droplet size models, population balance approaches have been applied to simulate the dynamic droplet distribution for oil droplets and gas bubbles at the subsurface (e.g., Bandara and Yapa 2011; Zhao et al. 2014). However, conflicting results have

been generated by different groups. For example, Bandara and Yapa (2011) predicted that the most active breakup and coalescence of droplets occurs within the first few meters, presumably due to the highest energy dissipation rates predicted to occur in this area, and the breakup and coalescence in the far-field can be ignored. Conversely, Zhao et al. (2014) predicted that relatively large oil droplets would form in the close proximity to the blowout release, and the oil droplets would continue to break up into smaller and smaller droplets as the plume ascended into the far field. Measurements of diesel oil droplets in the *Deep Spill* field experiments (Johansen et al. 2001) show that formation of droplets seems to have started relatively close to the release location (a few pipe diameters), followed by an increase in size to a peak large value, and then a gradual decrease in size further along the plume. Nevertheless, the authors of the report cautioned that *“it is difficult to conclude on the possible change in droplet size distribution as a function of the distance from the source, due to (1) relatively fewer number of large droplets counted at the upper locations than the lower depths, (2) difference in rising velocity of oil droplets and the ascending velocity of the image-acquisition ROV, and (3) loss of large droplet at distant vertical locations because of the separation of large droplets from a bent plume.”* Therefore, while the time- and space-dependent population balance equation approach provides a comprehensive picture of oil droplet size distribution, many aspects of the breakup and coalescence processes in the blowout release plume after the dispersant injection are still poorly understood. The current state-of-knowledge is insufficient to develop a sophisticated dynamic, population based droplet distribution model for practical application purpose.

In the OILMAP DEEP blowout model the *oil droplet size distribution model* is used to initialize the subsurface, far-field, oil spill particle trajectory and fate model (SIMAP). Earlier versions of the oil droplet size model are similar to the droplet size model in DeepBlow (Johansen 2003) and CDOG (Yapa et al. 2001) models. Review of laboratory studies and field observations, including the Deepwater Horizon (DWH) oil spill field measurements, revealed that (1) the maximum droplet size may not necessarily be dependent on the release orifice diameter, particularly when it is large, (2) the breakup of oil droplets may not be only dependent on the Weber number, but potentially other dimensionless groups representing the ratio of the dispersed phase viscous force to the restorative interfacial tension force may also be important, and (3) the distribution function of the droplets in the water column may be better represented by a lognormal droplet size distribution than the Rosin-Rammler distribution used in earlier models. Recently, new insight has been gained through intensive analysis of the field monitoring data following the Deepwater Horizon oil spill, and new data have been generated from several subsurface dispersant injection studies (Belore 2014, Brandvik et al. 2014). It is necessary to synthesize the data from these laboratory- and field-investigations, including the Deepwater Horizon field data, in order to evaluate the predictive performance of the present oil droplet models, and if warranted based on this review and evaluation, to develop a new oil droplet size model by taking advantage of the comprehensive laboratory and field data of both naturally and chemically dispersed oil droplet sizes.

In developing oil droplet size prediction models for blowouts, the conventional approach has been to focus on the dynamics of the blowout jet/plume and how the hydrodynamic and chemical processes occurring within the plume result in the formation of droplets in the presence of a release of an oil and gas mixture, with or without the addition of dispersants. Data to support the development, calibration, and verification of the model is typically derived from small and large scale laboratory studies of blowout like releases, from full scale field experiments, and from actual blowout events. In the present effort this basic strategy is extended to include oil droplet formation from breaking wave events at the sea surface that entrain oil in the water column, with the idea that the formation processes (turbulent shear) and

the controlling factors (interfacial tension and viscous effects) are very similar for both cases. The conceptual idea is that there should be a *universal* oil droplet model that would be applicable to both blowouts and the entrainment of surface oil due to breaking waves with the dependence on the same key processes. In the presentation to follow, this conceptual framework is employed and the resulting model then tested against available laboratory and field observations.

In the DWH blowout modeling report, the various components of the model are described in Appendix D (*Pipeline release model*), E (*Blowout plume model*), and Appendix H (*Fountain model*). This appendix (G) summarizes the development of OILMAP DEEP's *oil droplet size distribution model*. Section 2 reviews droplet size distribution data from laboratory and field observations; Section 3 discusses the impact of dispersant application on oil droplet size distribution; Section 4 provides a review of the current oil droplet size distribution models in existing blowout oil spill models. Section 5 presents the development of a new droplet size distribution model based on review of theoretical and lab studies and field measurement data. Finally, Section 6 gives a summary of the key findings and the implication of the developed new droplet size model in oil spill impact analysis and risk assessment. References are provided in Section 7.

G2. Review of gas and droplet size measurements: laboratory and field observations

This section provides an overview of laboratory and field observations on the formation and size distribution of oil droplets resulting from blowouts, as well as from breaking wave induced entrainment at the sea surface. While it is not conventional to include the later in such an overview, one will see that the droplet formulation processes from breaking wave turbulence shares a close similarity to that from a blowout.

G2.1 Laboratory experiments

G2.1.1 Blowout – University of Hawai'i

Oil and gas released from deep water blowouts form a rising plume, consisting of dissolved hydrocarbons, oil droplets, and gas bubbles, in a mixture with the entrained ambient seawater. On its ascending route, some of the oil separates from the plume due to the effects of ambient current and/or stratification; the separating oil tends to rise to the surface as individual diffusing oil droplets. The behavior of oil and gas in the plume and diffusion phases depends on the droplets/bubble size distribution, which is ultimately determined by droplet formation. For deep water blowouts at high pressure and low temperature, natural gas bubbles may also react with ambient seawater to form gas hydrates, which are less buoyant than gas bubbles and hence reduce plume buoyancy. Conversely, partial formation of hydrates in the form of a thin film surrounding the gas bubbles would reduce the gas dissolution rate and hence maintain the buoyancy of the affected bubbles.

A series of lab experiments were conducted at the University of Hawai'i (UH) (Masutani & Adams 2000, Tang 2004) to investigate these processes. The UH study evaluated the dependency of the break-up of oil discharged through an orifice into water on the release velocity from the orifice, U , the orifice diameter, D ; the oil density, ρ ; and viscosity, μ ; and the oil-water interfacial tension, σ . The researchers represented these variables in the form of two dimensionless parameters, the Reynolds number, $Re = \rho UD/\mu$, and the Ohnesorge number, $Z = \mu/(\rho\sigma D)^{0.5}$. UH researchers conducted 260 experiments over a wide range of Re - Z space by using a variety of orifice diameters and fluid types (crude oils, liquid CO_2 , and silicone fluids). The breakup pattern of the oil in jet releases was classified as occurring within one of the five modes – Rayleigh instability, sinuous wave breakup, filament core breakup, wave atomization, and full (turbulent) atomization. These are illustrated, from left to right, in Figure G-1.

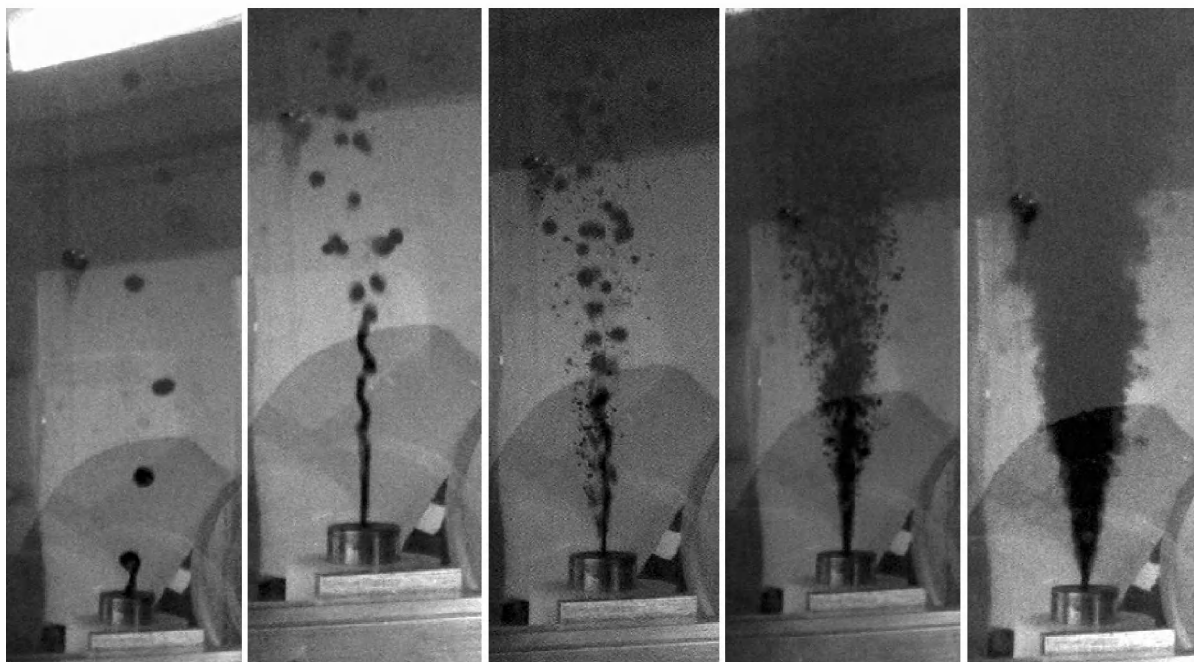


Figure G-1: Different modes of jet breakup in the oil injection experiments. Jet velocity increased sequentially from left to right, corresponding to oil breakup mode as (A) Rayleigh instability, (B) sinuous wave breakup, (C) filament core breakup, (D) wave atomization and (E) turbulent atomization (Masutani & Adams 2000, Tang 2004).

Liquid-liquid jet breakup regimes, as a function of Re and Z , are illustrated in Figure G-2. The dashed line indicates the boundary of the Rayleigh instability and the transitional modes (sinuous wave, filament core, and wave atomization), and the dashed-dotted line represents the boundary of the transition modes and the full turbulent atomization mode. These boundaries correspond to (a) $Z < 5.5/Re$ for laminar Rayleigh instability and (b) $Z > 18/Re$ for the turbulent atomization mode.

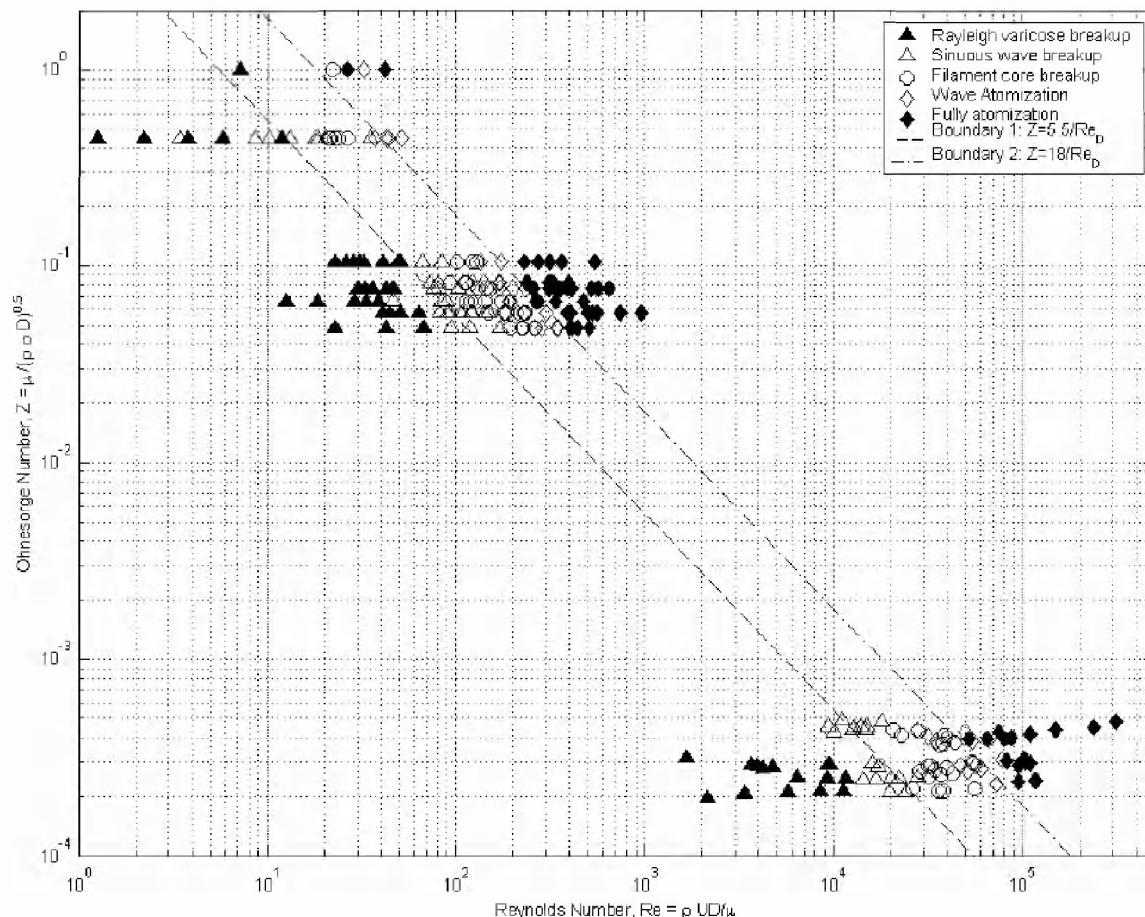


Figure G-2: Liquid-liquid jet breakup regimes. Data points correspond to 175 oil and silicone fluid injection tests (upper two sets) and 85 CO₂ injection tests (lower set) (Masutani & Adams 2000; Tang 2004).

Figure G-3 shows representative droplet size distributions corresponding to the different breakup modes for a liquid CO₂ jet discharging into water at high pressure. The data indicated the prevalence of large droplets (5-7 mm) along with fewer small droplets (0-5 mm) at the lowest speed (left panel) (Rayleigh mode), a wide range of droplet sizes at intermediate speeds (panel 2 and 3 from left) (transitional modes), and the dominance of small droplets (< 2 mm, with majority within 0.3-0.6 mm) at the highest speeds (wave and full atomization modes) (right two panels). The UH study has shown that the larger droplet sizes were correlated with the orifice diameter, while the smaller droplets were independent of orifice diameter. It has been suggested that the formation mechanism of the small droplets becomes relatively scale-independent once a threshold droplet diameter is reached. Note that while multi-modal distribution spectra were displayed for the Rayleigh and transitional stability breakup modes, mono-modal distributions tend to form in the atomization breakup regime, with the uneven arithmetic probability distributions. Further discussion below will show that the droplet size distribution is best described by a lognormal distribution for the atomization regime.

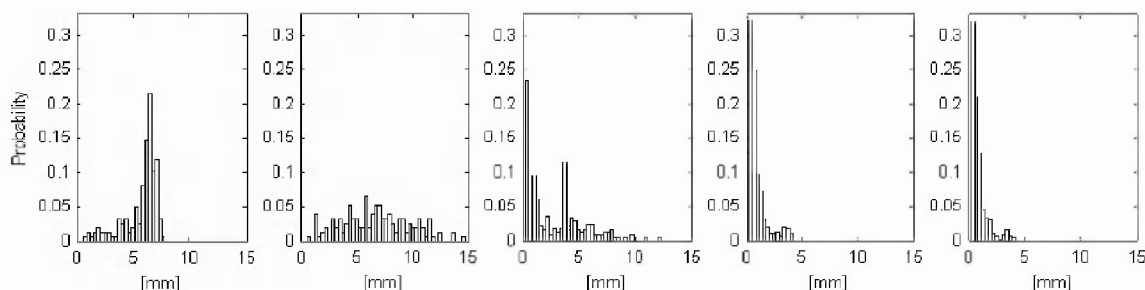


Figure G-3: Representative droplet size distribution spectra for the five modes of breakup, velocity and Re increasing from left to right. Data are from experiments of liquid CO₂ jet discharged through a 5 mm (i.d.) nozzle into water at about 60 atm pressure, with measurements performed about 70 cm (or 140 times nozzle diameter) from the release (Masutani & Adams 2000, Tang, 2004).

There are important implications in identifying the boundary between the Rayleigh instability breakup mode, the three transition modes, and the boundary between the transition modes and the turbulent atomization mode. These boundaries provide scale-independent dimensionless parameters to predict characteristics of the initial droplet size distribution, whether mono- or multi-modal distributions, the predominance of coarse or fine droplets, etc. under a wide range of flow conditions. A closer inspection of the dimensionless parameters given in Re-Z space (Figure G-1) shows that the dimensionless numbers can be further simplified in terms of the Weber number, noting that $(We)^{0.5} = Z \cdot Re$. 'We' is the ratio of disruptive momentum (hydrodynamic) forces to restoring surface tension and is directly related to the droplet breakup mechanisms (Hinze, 1955). In a blowout oil and gas release, the Weber number can be expressed as, $We = \rho U^2 D / \sigma$. Note that the diameter of the orifice was used in the analysis of the UH experimental results. The deep water blowout release opening diameter is typically used in existing blowout models (e.g., CDOG, DeepBlow). When the release opening size is large, the maximum stable droplet size under the Rayleigh-Taylor instability regime should be used in the calculation of Weber number, rather than the opening diameter.

Using the Weber number criteria, it is apparent that the boundary between Rayleigh instability and transitional breakup modes is about $We \leq 30$, whereas the boundary between atomization breakup mode and the transitional modes is about $We \geq 324$. Based on the calculated Weber number under various release velocity and oil properties, it will be found in the present analysis of the Deep Water Horizon oil spill that, all of the spill release scenarios (Appendix A: Release configurations) fall into the full turbulent atomization category, allowing one to develop and apply a mechanistic droplet size distribution function for use in OILMAP DEEP.

G2.1.2 Subsurface oil release – SINTEF API Study of Droplet Size Distributions and Dispersant Injection Techniques

As part of the American Petroleum Institute – Joint Industry Task Force (API-JITF) D3 "Evaluation of subsea dispersant injection methods/ equipment and effectiveness" program, an experimental study was conducted in SINTEF Tower Basin in Trondheim, Norway. The experimental facility consisted of a 6 m high by 3 m diameter cylindrical tank that had a seawater holding capacity of 42 m³. The main objectives of the project were to generate data that would help to answer questions regarding dispersant injection during a subsea blowout such as, 1) How does the dispersant injection method, dispersant to oil ratio (DOR), and dispersant type, affect the oil droplet size distribution (Volume Median Diameter – VMD)?; 2)

How does the dispersant-oil mixing vary as a function of distance from the orifice for different injection methods?, and 3) How does this mixing affect the oil droplet size distributions?

Figure G-4 displays side view photographs of a typical rising oil plume from the tower basin experiment, before and after the injection of dispersant (from left to right) The oil was released from a nozzle that was connected to the pressurized oil and/or air supply tubing. Figure G-5 shows the typical oil volume droplet size distribution generated from a series of oil release experiments at different Dispersant to Oil Ratio's (DOR) and at various downstream distances from the nozzle. The data were recorded using a laser *in situ* scattering and transmissiometry (LISST-100X, Sequoia Scientific Inc., Seattle, WA). Besides flow rate and DOR, the impact of other release conditions, such as the oil temperature, dispersant constituents, different dispersant injection techniques, nozzle diameter, and the co-release of oil and gas, were also tested in the series of experimental studies.

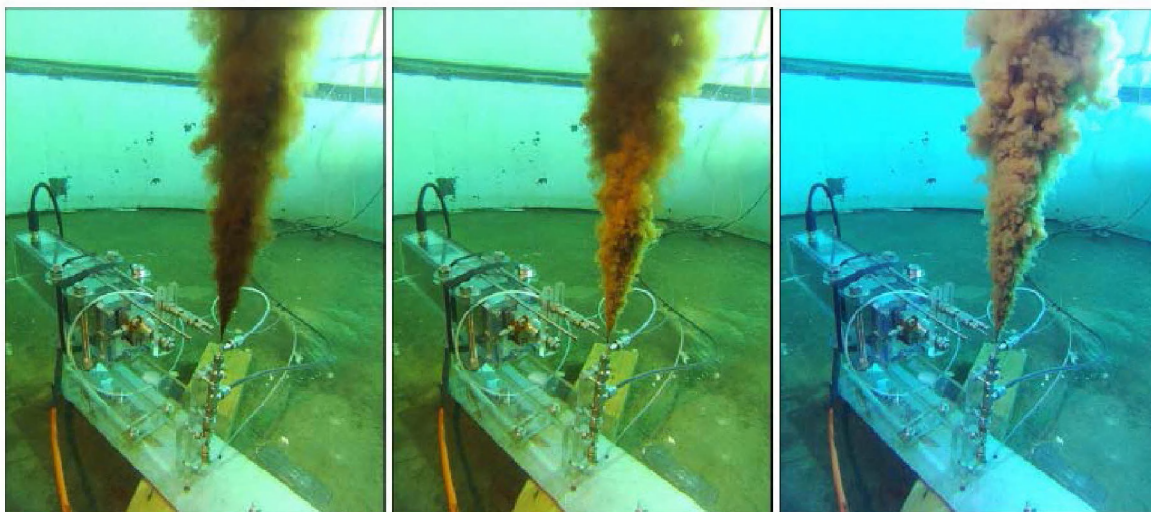


Figure G-4: Representative rising oil plume in the SINTEF Tower Basin Experiment with release nozzle diameter 1.5mm and the oil flow rate at 1.2 L/min: (A) rising plume prior to dispersant injection (similar to the oil only droplet size distribution curve in Figure 5), (B) Immediately after dispersant injection started at an intended DOR of 1:50, and (C) 30 seconds after injection started (similar to solid green curve in Figure G-5)

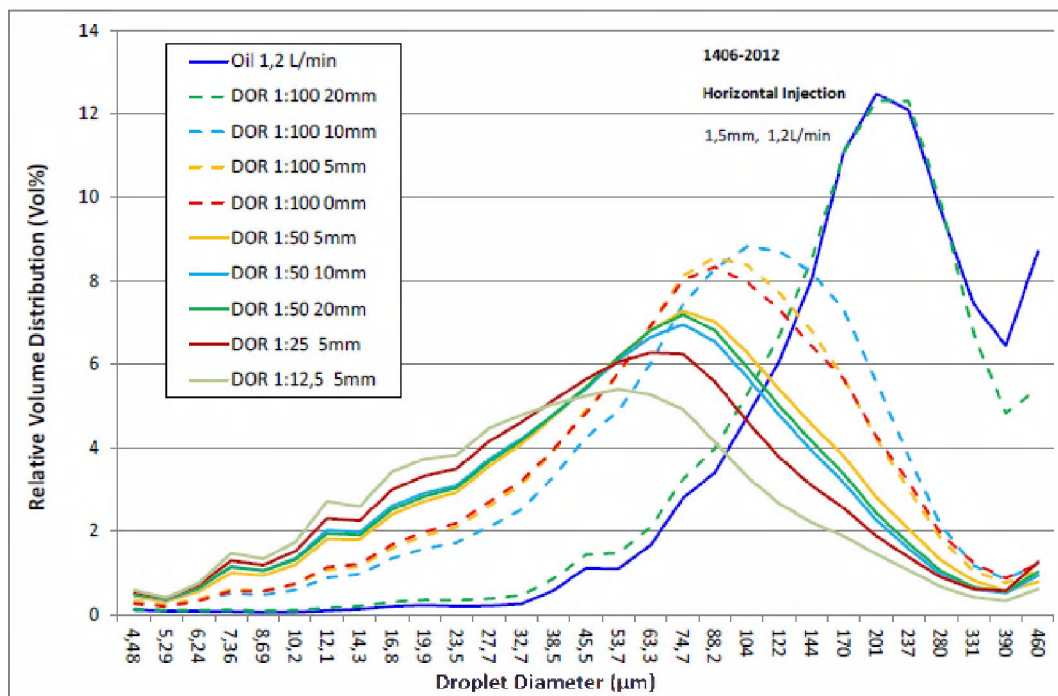


Figure G-5: Relative oil droplet size distribution (volume %) recorded with the LISST-100X particle size analyzer in the SINTEF Tower tank experiment. These data were generated with dispersant injected at different DORs (the first ratio value next to DOR in the legend) and from the side at different distances (the second value in unit of mm in the legend) into the rising oil plume released from a 1.5 mm nozzle at 1.5 L/min flow rate for all the dispersant treated tests, but at 1.2 L/min flow rate for the non-treated oil only release test.

Table G-1 summarizes the data from the SINTEF tower basin tests that were used in development of SINTEF's modified Weber Number based oil droplet size model (Johansen et al. 2013, see Section 3.2). Generally, the test results of the flow rate experiments are in agreement with the established empirical relationship. For instance the volume mean diameter (VMD) of the oil droplets in the rising plume was found to be inversely correlated with the oil release flow rate. The VMD of dispersant treated oil droplets were inversely correlated with the amount of dispersant. However, SINTEF tower basin tests have revealed that the previous droplet size models that are commonly used in oil spill models (such as CDOG, and DEEP BLOW) tend to underestimate the VMD of successfully treated oil at relatively low DOR's (i.e., the model calculated dispersant-treated oil droplet sizes appear to be smaller than the measured oil droplet sizes from the dispersant- treated tests). Note that in Table G-1, the three very low DOR tests (highlighted in green) on 28/06/2012 were excluded from the original SINTEF droplet size model development due to uncertainties in the recorded IFT(interfacial tension) values; The other two DOR=1:50 tests (highlighted in yellow), one on 17/04/2012 and the other on 06/06/2012, were further excluded from the following model and data comparison (Section 5.2), for the following reasons: (1) the IFT of these two tests are nearly two orders-of-magnitude lower than the other two tests at the same DOR (one simulated injection tool, the other on 28/06/2012); (2) the IFT of these two tests are nearly an order-of-magnitude lower than the higher DOR (1:25) tests; and (3) the IFT of these two tests are also two orders-of-magnitude lower than the laboratory measurements of the same source oil IFT at the corresponding DOR (Venkataraman et al. 2013), which is about 0.12 mN/m.

Table G-1: Summary of the data from SINTEF tower basin tests (where D is the nozzle diameter, Q is the oil flow rate, DOR is the dispersant to oil ratio, IFT is the interfacial tension, U is the exit velocity, We is the Weber number, Vi is the viscosity number, and dp is the peak droplet diameter recorded in the LISST-100X analyzer.) Data of the shaded tests were excluded from droplet size model development or validation (see text for the reasoning of this practice).

<u>Date</u>	<u>D, mm</u>	<u>Q, L/min</u>	<u>DOR</u>	<u>IFT, mN/m</u>	<u>U, m/s</u>	<u>We</u>	<u>Vi</u>	<u>dp, um</u>
17.04 2012	1.5	1.5	-	16.5	14.1	1.53E+04	9	144.0
	1.5	1.5	1:1000	14.7	14.1	1.72E+04	10	144.0
	1.5	1.5	1:500	13.2	14.1	1.91E+04	11	104.0
	1.5	1.5	1:250	4.5	14.1	5.60E+04	31	88.2
	1.5	1.5	1:100	1.5	14.1	1.68E+05	94	88.2
	1.5	1.5	1:50	0.002	14.1	1.26E+08	70736	74.7
	1.5	1.5	1:25	0.07	14.1	3.60E+06	2 021	53.7
26.04 2012	1.5	0.5	-	15	4.7	1.87E+03	3	391.0
	1.5	1.2	-	15	11.3	1.08E+04	8	237.0
	1.5	2.8	-	15	26.4	5.86E+04	18	104.0
Simulated	1.5	1.2	1:100	0.66	11.3	2.45E+05	172	74.7
inj. tool	1.5	1.2	1:50	0.056	11.3	2.88E+06	2021	53.7
	1.5	1.2	1:25	0.055	11.3	2.93E+06	2058	27.7
03.05 2012	0.5	0.1	-	15	8.5	2.02E+03	6	170.0
	0.5	0.2	-	15	17.0	8.07E+03	11	88.2
	0.5	0.5	-	15	42.4	5.04E+04	28	27.6
Injection	0.5	0.2	-	0.658	17.0	1.84E+05	258	32.7
above	0.5	0.2	-	0.056	17.0	2.16E+06	3032	19.9
06.06 2012	1.5	1.2	-	18.2	11.3	8.87E+03	6	237.0
Injection	1.5	1.2	1:100	0.5	11.3	3.23E+05	226	74.5
1.5 mm ab.	1.5	1.2	1:50	0.001	11.3	1.61E+08	113177	63.3
28.06 2012	1.5	1.2	-	18.1	11.3	8.92E+03	6	237.0
	1.5	1.2	1:1000	7.5	11.3	2.15E+04	15	237.0
	1.5	1.2	1:500	2.4	11.3	6.72E+04	47	237.0
	1.5	1.2	1:250	0.7	11.3	2.31E+05	162	170.0
	1.5	1.2	1:100	0.09	11.3	1.79E+06	1 258	104.0
	1.5	1.2	1:50	0.07	11.3	2.31E+06	1 617	63.3
	1.5	1.2	1:25	0.05	11.3	3.23E+06	2 264	53.7

G2.1.3 SL Ross BSEE Subsea Chemical Dispersant Research

This study was conducted by SL Ross Environmental Research Ltd (SL Ross 2014, Belore 2014) and sponsored by the U.S. Department of the Interior, Bureau of Safety and Environmental Enforcement (BSEE). The primary objective was to determine if the presence of natural gas or methane in a subsea oil and gas discharge would reduce the effectiveness of a dispersant injected into the gas-oil mixture. The impact of dispersant-to-oil ratio (DOR), location of dispersant injection, gas-to-oil ratio (GOR), oil type, and orifice diameter on oil droplet sizes were also evaluated in the study. The size of the oil drops generated in the subsea release, specifically the volume median diameter (VMD) of the oil drop size distribution, was used as the indication of oil chemical dispersant effectiveness; the lower the VMD the more effective the dispersant treatment.

Tests were conducted at the SL Ross laboratory facilities in Ottawa, Ontario, Canada and the BSEE Oil and Hazardous Materials Simulated Environmental Test Tank (OHMSETT) facilities in Leonardo, NJ. The wave tank tests utilized a horizontal jet release to allow for a separation of the rising oil drops from gas bubbles, making it possible for the direct measurement of the oil drops using a laser, in-situ particle size analyzer (LISST-100X). The liquid and gas delivery systems developed and tested in small scale facilities in Ottawa were then implemented in the larger scale tests conducted at the OHMSETT (Figure G-6).

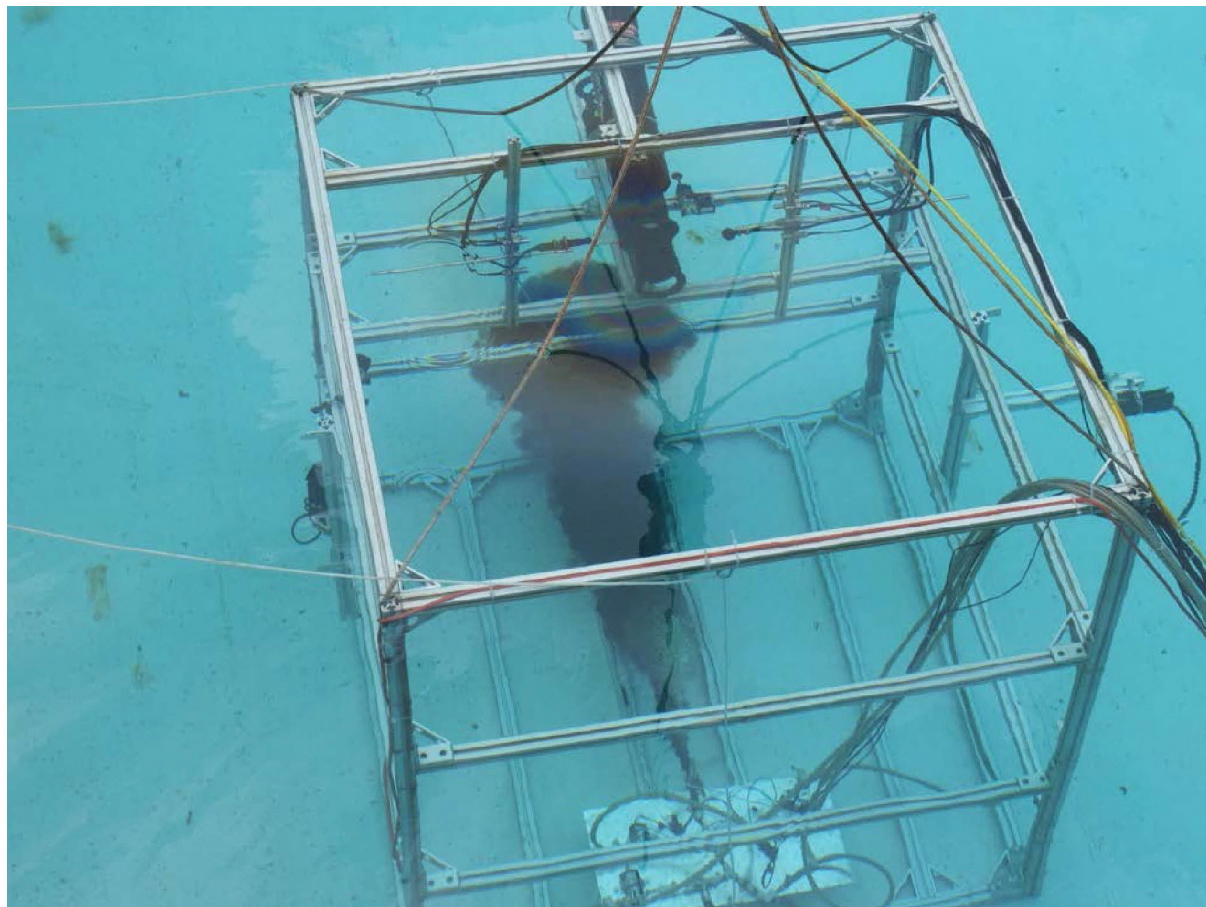


Figure G-6: SL Ross subsea dispersant experimental study. The facility includes a horizontally oriented underwater nozzle connected to pressurized gas and oil supply lines and two LISST-100X particle size analyzers positioned at different depths to capture oil droplet size distribution

The test results, summarized in Table G-2, show that oil type, release nozzle diameter and dispersant-to-oil ratio (DOR) all had an effect on dispersed oil volume median diameter. The most significant change was the observed decrease in VMD with an increase in DOR.

Table G-2: Large scale OHMSETT tank (#33-44) and SL Ross wave tank (TN1-7) test conditions and volume median diameter (VMD) results.

Test#	ID (mm)	Oil	Oil flow (ml/min)	Gas	Gas flow (ml/min)	DOR	VMD (μm)
33	4.5	Dorado	1500	Air	8280	1:50	37
34	4.5	Dorado	1500	Methane	8280	1:50	45
35	4.5	Dorado	1500	Air	13500	1:50	50
36	4.5	Dorado	1500	Methane	13500	1:50	53
37	4.5	Dorado	1500	Air	8280	1:100	105
38	4.5	Dorado	1500	Methane	8280	1:100	110
39	4.5	Dorado	1500	Air	13500	1:100	100
40	4.5	Dorado	1500	Methane	13500	1:100	150

Test#	ID (mm)	Oil	Oil flow (ml/min)	Gas	Gas flow (ml/min)	DOR	VMD (μm)
41	4.5	Dorado	1500	Air	8280	1:200	300
42	4.5	Dorado	1500	Methane	8280	1:200	300
43	4.5	Dorado	1500	Air	13500	1:200	300
44	4.5	Dorado	1500	Methane	13500	1:200	300
TN 6	1.5	Terra Nova	380	Air	1350	1:50	17
TN3 & 5	1.5	Terra Nova	380	Air	1350	1:95	60
TN1	1.5	Terra Nova	380	Air	1350	1:190	170
TN7	1.5	Terra Nova	380	Methane	1350	1:50	50
TN4	1.5	Terra Nova	380	Methane	1350	1:95	80
TN2	1.5	Terra Nova	380	Methane	1350	1:190	200

G2.1.4 Delvigne's natural dispersion experiments and droplet size distribution

Based on laboratory and flume experiments, Delvigne and Sweeney (1988) developed a relation for oil entrainment rate as a function of oil droplet size at the surface under breaking wave conditions:

$$Q_d = C^* D_d^{0.57} S F d^{0.7} \Delta d \quad \text{Eq 1}$$

Where:

- Q_d - the entrainment rate (oil mass entrained per unit area per unit time, in kg/m²-sec);
- C^* - empirical entrainment constant which depends on oil type and weathering state;
- D_d - dissipated breaking wave energy per unit surface area (J/m²);
- S - Fraction of sea surface covered by oil;
- F - Fraction of sea surface hit by breaking waves (s⁻¹);
- d - Oil particle diameter (m); and
- Δd - Oil particle interval diameter (m).

Equation 1 shows that the entrainment rate is dependent on wave conditions and oil properties. Wave conditions are represented by the strength of breaking wave energy per unit surface area (D_d) and the fraction and frequency of sea surface hit by breaking waves (F). The effect of oil properties is reflected by: (1) the empirical entrainment constant C^* as a function of oil viscosity (Figure G- 7), and (2) the droplet size distribution as a function of viscosity (Figure G-8 and Equation 2). The entrainment constant C^* was reported by Delvigne & Sweeney (1988) and Delvigne & Hulsen (1994) from their flume and laboratory experiments and is illustrated in Figure G-7. The entrainment coefficients (C^*) were slightly different within 100 cSt (Figure G-7), but decreased substantially for oil viscosities above 500 cSt.

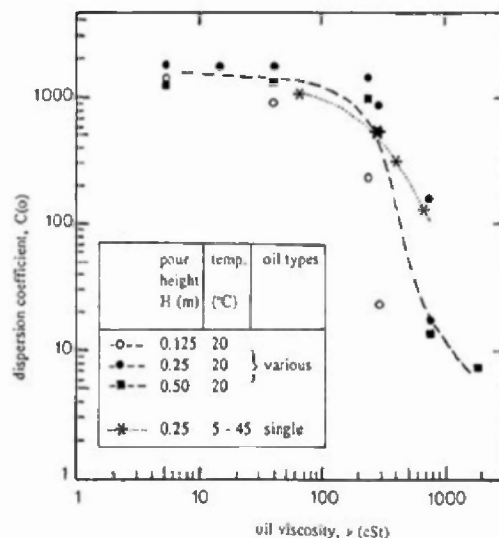


Figure G-7: Entrainment coefficients as a function of initial oil viscosity (Delvigne & Hulsen 1994).

To investigate the effects of oil properties on formation of oil droplets in turbulence (Delvigne & Sweeney 1988) conducted experiments in a grid column to produce oil droplets in homogeneous turbulence. The size distribution of the formed droplets was measured using a laser-beam particle size analyzer (LBPS). The mean droplet size (d_{50} , μm) was assumed dependent on the viscosity of the test oil and the turbulent energy levels (illustrated in Figure G-8) and fit to the following equation:

$$d_{50}, d_{max} \sim e^{-0.5} * \nu^{0.34} \quad \text{Eq 2}$$

Where:

e - wave energy dissipation rate per unit volume of seawater (W/m^3), and

ν - kinematic viscosity of oil (cSt).

This relation is applicable to oil in the Newtonian viscosity range, but not to high viscosity, non-Newtonian oil.

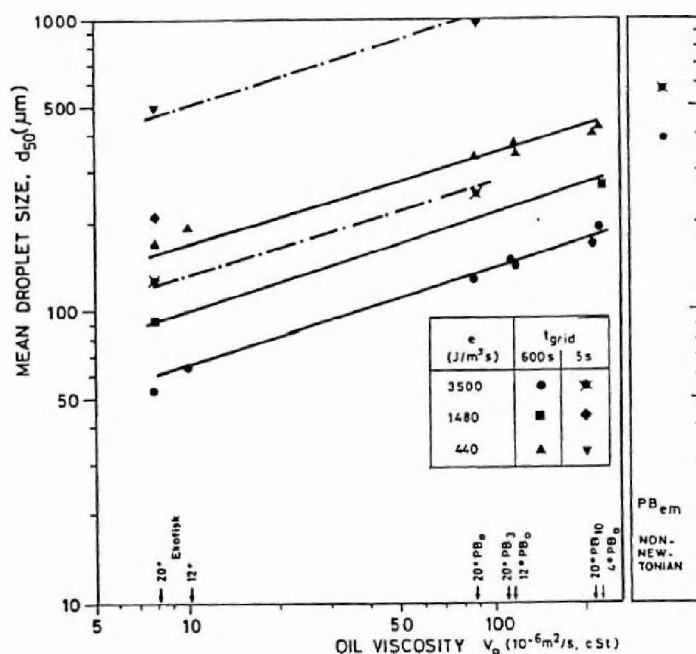


Figure G-8: Mean droplet size d_{50} versus oil viscosity for submerged oil in turbulent energy dissipation rate (Delvigne & Sweeney 1988).

The energy dissipation rate values recommended by Delvigne and Sweeney (1988) based on a comprehensive literature review were:

- 10^3 to 10^4 (J/m³-sec) for breaking waves;
- 1 to 10 (J/m³-sec) for surface layer;
- 10^{-1} to 1 (J/m³-sec) for estuaries; and
- 10^{-4} to 10^{-2} (J/m³-sec) for deep sea.

In terms of the dispersed oil droplet size distribution function, Delvigne and Sweeney (1988) proposed a power law relationship between the number of droplets in a size interval and the average size of the droplet size interval. In other words, there is a linear relation between $\log(N_i)$ and $\log(d_i)$, where N_i is the number of particles in the size interval $0.5 d_i$ to d_i , and d_i is particle diameter. These droplet size distribution data were observed from breaking wave experiments. The droplet sizes were measured using a microscope. A representative droplet size distribution is illustrated in Figure G-9. Delvigne and Sweeney (1988) pointed out that in the grid column experiments all detectable oil droplets were taken into account in the droplet size distribution analysis because the surfacing of large droplets could generally be neglected. In the flume experiments under breaking waves, however, the dispersed oil was generally only a small fraction of the total oil mass in the surface slick; although all surface oil may be submerged by the breaking wave, the oil lumps and large droplets resurfaced almost immediately after the breaking wave event. The maximum droplet diameter in the water column of the flume experiments was observed to be independent of the turbulent break-up processes, but instead, was dependent on resurfacing parameters, e.g., intrusion depth, rise velocity, and vertical turbulent diffusion coefficient. The proposed power law distribution was used again in Delvigne & Hulsén (1994). The curve-fit was restricted to droplets $\leq 200 \mu\text{m}$, based on the argument that these droplets had not been reduced in their counts by resurfacing during sampling.

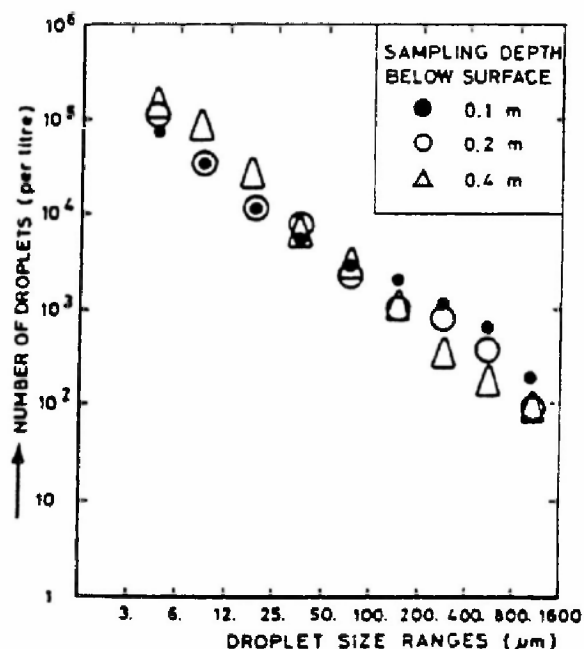


Figure G-9: Oil droplet size distribution in breaking-wave experiment (Delvigne & Sweeney 1988).

Reed et al. (2009) questioned Delvigne's suggestion that the power-law droplet size distribution function could be extrapolated to large droplet sizes. It is worth noting that while Delvigne's focus was on the entrained oil droplets that are relatively stable in suspension in the water column, Reed et al. (2009) focused at estimating the distribution of the entire range of oil droplets, including those that penetrated deep into the water column and those suspended near the surface slick (See Section 2.2.2).

Delvigne's measurements of the entrained oil droplets size distribution is more common in the oil spill community in characterizing oil droplet size distribution created by surface breaking waves (Jasper et al. 1978, Byford et al. 1984, Lewis et al. 1985, Lunel 1995). However, the full range droplet size distribution of Reed et al. (2009)'s experiment and Delvigne and Sweeney (1988)'s grid column experiment would be more suitable in a mass balance analysis. Therefore, the following oil droplet distribution model aims to estimate the full range of droplet size distribution.

G2.1.5 SINTEF wave tank experiments on natural entrainment of weathered high viscosity oil

Reed et al. (2009) conducted a comprehensive flume study to develop a numerical algorithm to compute the surface oil dispersion under breaking wave conditions. The flume tests included four different types of crude oil subjected to weathering times ranging from 1 hour to 3 days, with and without sunlight, and at two temperatures (5 °C and 13 °C). The four selected oils were North Slope, a paraffinic oil; Troll, a naphthalic oil; Norne, a waxy oil; and Grane, an asphaltenic oil.

The experimental measurements showed the lognormal distribution provided a good fit to the dispersed (number) droplet size distributions for the paraffinic North Slope and naphthalic Troll oil, as illustrated in Figure G-10 (Reed et al. 2009). The waxy Norne oil and the asphaltenic oil, however, were found to produce droplets with smaller values of median droplet size and

geometric standard deviations. This was attributed to incomplete dispersion of the surface slick; even the highest plunging jet used in their test was not able to break up the slick. The resistance of the surface slick to breakup is not necessarily due to high viscosity, but may be caused by other high yield stress rheological properties of the oil. As a result, the waxy Norne oil and the asphaltenic oil were not addressed in their droplet size analysis.

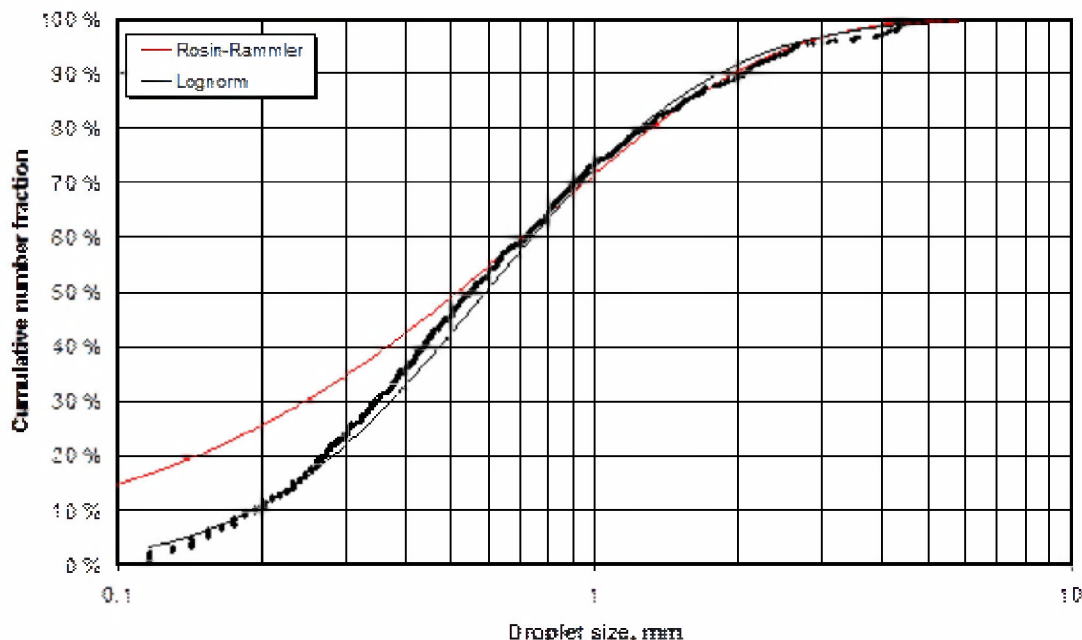


Figure G-10: Droplet number distribution from image analysis together with best fits of the lognormal (black line) and Rosin-Rammler (red line) distribution functions. The Rosin-Rammler distribution does not fit well at the smaller droplet size ($d < 0.5$ mm), since it is weighted by volume rather than number distribution. The Rosin-Rammler distribution was therefore not used in Reed et al. (2009) droplet size analysis.

Reed et al. (2009) postulated that the size distribution be defined by two parameters: (1) the mean logarithmic diameter ($\ln d_{50}$), which is dependent on wave parameters and oil properties (e.g. density, viscosity, interfacial tension), and (2) the logarithmic geometric standard deviation ($\ln \sigma$), which was constant based on their experiments. The median diameter of the droplet size distribution (normalized by the thickness of oil), D_{50} , as a function of oil properties and the wave height parameters was expressed as:

$$\frac{D_{50}}{h} = F W e^{-p} \quad \text{Eq 3}$$

where: F is a coefficient dependent on the viscosity of the oil,

$$Vi = \mu_o / \sqrt{\rho_o \sigma h} \quad \text{Eq 4}$$

where, Vi is the dimensionless viscosity group (i.e., Ohnesorge number, see Section G4.1); h is the oil film thickness (m), μ_o is the viscosity of oil (kg/m/s) and ρ_o is the density of oil (kg/m³), and σ is the interfacial tension (N/m, or kg/s²). Note that the dimensionless viscosity group is similar to the dimensionless Ohnesorge number (Z) that was introduced in the UH study of jet discharge of oil into water (See Section G2.1.1). The difference between the two is that oil

thickness was used as the characteristic length scale in Reed et al. (2009) compared to the orifice diameter that was used by UH researchers.

The viscosity coefficient term was empirically determined as,

$$F = C e^{aV_i} \quad \text{Eq 5}$$

where the empirical constants were $C = 1.154$ and $a = 0.0253$.

We is the Weber number defined by Reed et al. (2009) as:

$$We = \rho g H h / \sigma \quad \text{Eq 6}$$

where ρ is the density of water (kg/m^3), g is the gravitational acceleration rate (m/s^2), H is the free fall height or the wave amplitude (m), σ is the interfacial tension between oil and water (N/m); and h is the oil film thickness (m). In contrast to the Weber number definition in UH study, the product of g and H was used to replace the kinetic energy term (U^2) for the jet discharge. Similar to the definition of the Vi number, the thickness of oil slick was again used in place of the diameter of the orifice or release pipe diameter. Equations 3-6 lead to the following explicit equation for the median droplet size.

$$D50 = F H^{-p} h^{1-p} (\sigma / g \rho)^p \quad \text{Eq 7}$$

The exponent “ p ” is empirically determined to be 0.5. The logarithmic standard deviation (base₁₀) of the common logarithm normal droplet size distribution function is estimated to be $s = 0.40$, equal to 0.92 for base e .

The volume median diameter (VMD) of oil droplets can be determined from the count median diameter (CMD) by the following relation (Hatch and Choate 1929):

$$VMD = CMD \exp(3s^2) \quad \text{Eq 8}$$

Where: s is the natural logarithmic standard deviation. From the empirical data $s = 0.92$ in \log_e format. Therefore, the conversion factor from CMD to VMD is to multiply CMD by 12.7. Note a change of geometric standard deviation is possible for different oil types, under different hydrodynamic conditions, and in the presence of chemical dispersants.

G2.1.6 BIO wave tank experiments on chemical dispersion of oil

The Bedford Institute of Oceanography (BIO) wave tank was used to evaluate chemical dispersant effectiveness under different wave conditions. The wave tank was operated under regular and breaking wave conditions to test dispersion of different oils, including light, medium crude, and heavy fuel oils (Lee et al. 2009, Li et al. 2009a, Li et al. 2009b, Li et al. 2009c, Li et al. 2010). The experimental design included dispersant-treated effectiveness tests and non-treated control experiments. In the control experiments, the oil was dispersed physically by wave action alone. Natural dispersion of the two crude oils (MESA and ANS) under regular waves resulted in the entrainment of approximately 5 to 10% of the oil under regular waves and 10 to 20% under breaking wave conditions. Tests on the higher viscosity IFO180 oil (kinematic viscosity of 1,800 to 4,000 cSt at the ambient experimental temperatures from 9.8 to 16.9°C) resulted in about 5% entrainment of oil under regular wave conditions and 10% under breaking waves (Lee et al. 2009, Li et al. 2010).

Figure G-11 illustrates the representative droplet size distribution curves obtained from the wave tank study on MESA crude oil dispersion under regular waves. The figure shows the measured cumulative volume droplet size distributions and a lognormal droplet size distribution function fit to the data at four different time points. The fit parameters (logarithmic median and geometric

standard deviation) are summarized in Table G-3. As shown in the graph and table, the entrained droplet size distributions are well described using a lognormal droplet size distribution function ($R^2 > 0.95$). The volume median diameters are around 100 μm during the first 10 min but gradually decreased to around 70 μm as the time allowed for dispersion increased to 100 min. For natural dispersion of the high viscosity IFO180 oil, the entrained oil droplets were $\geq 300 \mu\text{m}$, and were larger than the naturally entrained crude oils.

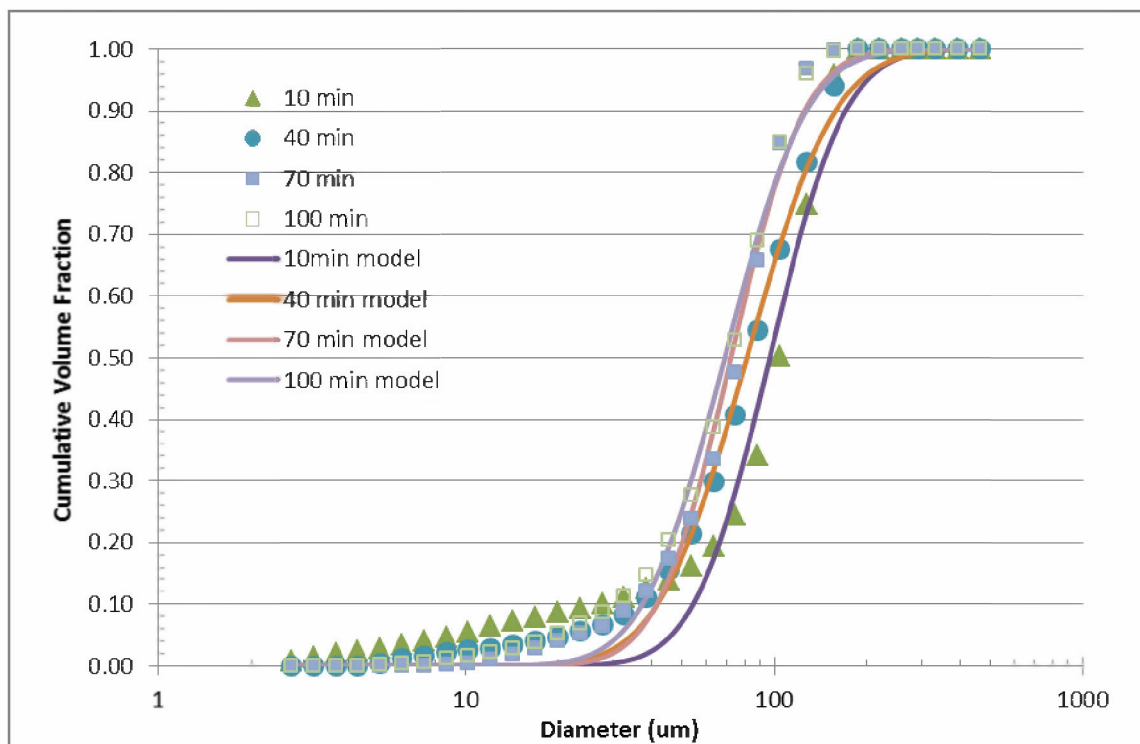


Figure G-11: Cumulative volume droplet size distribution of crude oil in an experimental wave tank (Lee et al. 2009, Li et al. 2009c); lognormal distribution parameters are listed in Table G-3.

Table G-3: Fitted parameters of the lognormal (volume) droplet size distribution for dispersion of MESA oil at four time points in an experimental wave tank (Lee et al. 2009, Li et al. 2009c).

Time	10 min	40min	70min	100min
$\ln(d)$	4.57	4.40	4.28	4.23
$\ln(\sigma_g)$	0.45	0.52	0.43	0.48
R^2	0.9777	0.9959	0.9955	0.9954
$d (\mu\text{m})$	96	81	72	69
σ_g	1.56	1.68	1.54	1.61

G2.2 Deep Spill Field Experiments on Blowout Releases of Oil and Gas

Deep Spill field experiments were conducted during June 26-29, 2000, at the Helland Hansen site in the Norwegian Sea (at 65°N, 4°50' E) and the results documented in a series of reports

and papers (Johansen et al. 2000, Johansen et al. 2001, Johansen et al. 2003). The prime goal of the field study was to obtain data for verification of numerical models for simulating accidental releases in deep water, as well as to test monitoring equipment and evaluate safety measures. Field experiments were conducted with controlled releases of (1) nitrogen, (2) a mixture of diesel oil and natural gas, (3) a mixture of crude oil and natural gas, and (4) natural gas release, at 845 m from a 12 cm diameter orifice (Johansen et al. 2000). Three of the four release experiments were surveyed by an ROV; only release Experiment #3 was not surveyed.

The size distributions of the blowout oil droplets and gas bubbles were determined based on the manual analysis of the video images taken by the ROV. During the surveys of the plumes, the color camera took close-up photographs while the ROV was ascending inside the plume. Measurements were made of methane bubble size distributions from release number #4 and of diesel droplet size distributions from release number #2. Imageries were sampled quite frequently from the video. It became evident that the same bubble/droplet appeared on many pictures in a sequence. The analyst then had to manually keep track of the different bubbles/droplets that appeared on the screen, in order to avoid double counting the same droplet/bubble.

G2.2.1 Methane gas bubble size distribution

Gas bubble size distributions were counted for release experiment # 4 at four selected distances above the release source in an effort to evaluate the impact of distance from the source on the size distribution. Gas bubble size data of reasonable quality were counted and sized from the pictures found between about 9-85 m above the release source (Table G-4, Figure G-12).

Table G-4: Counts of methane gas bubbles at release experiment #4 carried out on 29 June 2000. In each second represents 25 pictures were recorded for bubble size analysis. A total of 667 bubbles were counted from a total of 3400 pictures (Johansen et al. 2001).

Case No.	Time interval, local time	Depth interval	Distance above source of release	Number of gas bubbles counted
1	11-17-45 --- 11-18-15	836 – 826	9 – 19	124
2	11-18-16 --- 11-18-27	826 – 822	19 – 23	184
3	11-19-15 --- 11-20-05	806 – 787	39 – 58	201
4	11-43-50 --- 11-44-35	780 – 760	65 – 85	158

Figure G-12 shows the methane bubble number size distributions measured by Johansen et al. (2001). The number distributions are typically in the range 1-5 mm diameters, with some gas bubbles having sizes closer to 8 mm. A similar distribution is shown in Figure G-13 for the volume of the gas bubbles. This volume distribution is based on the same bubbles that have been counted as for the number diameter distribution, except that the diameter is taken to the third power (in order to arrive at volume estimates). In Figure G-13, the volume distribution is skewed towards larger gas bubbles, compared to the distribution shown in Figure G-12. The reason for this distortion is that bubbles increase in volume faster than their corresponding increase in diameter.

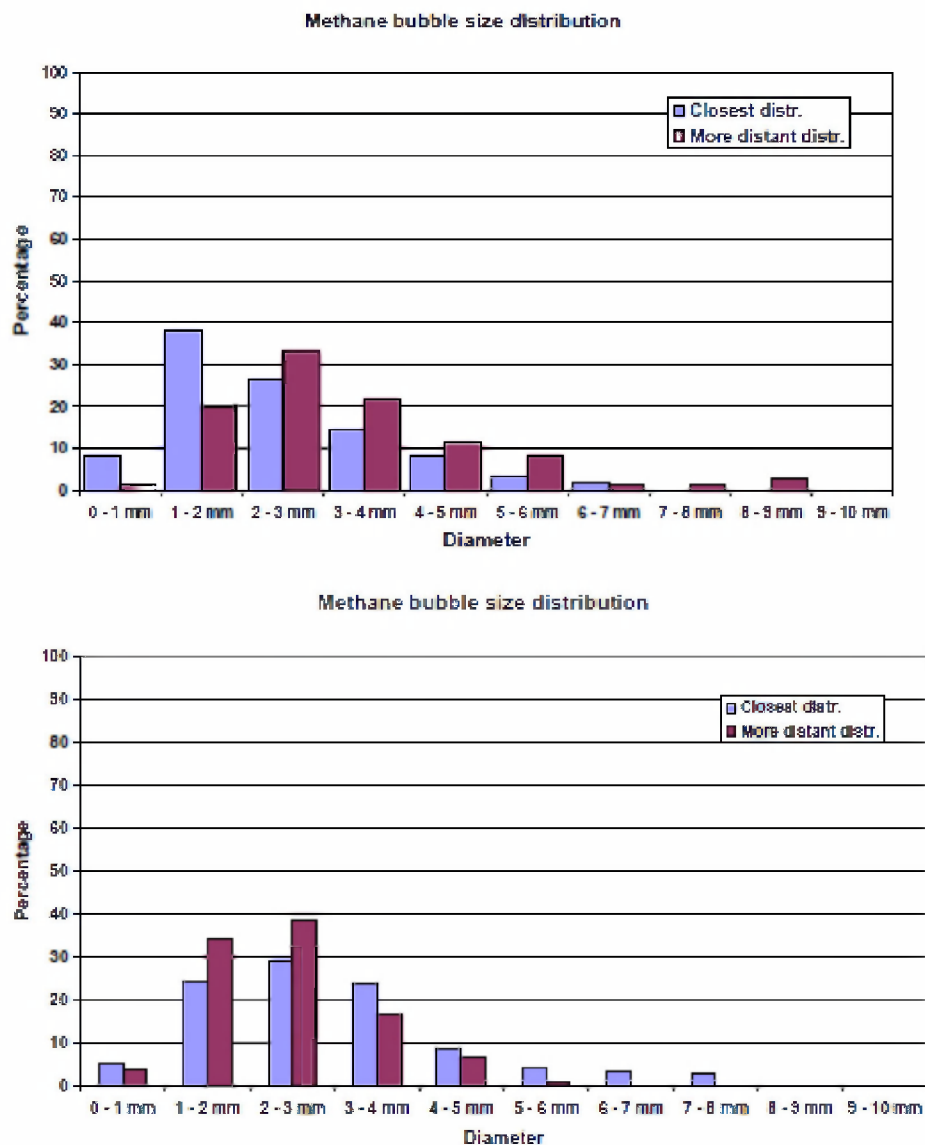


Figure G-12: The methane bubble number size distribution observed by Johansen et al. (2001) from cases (upper panel) (1) 9-19 m, (2) 19-23 m, (lower panel) (3) 39-58 m, and (4) 65-85 m above the release.

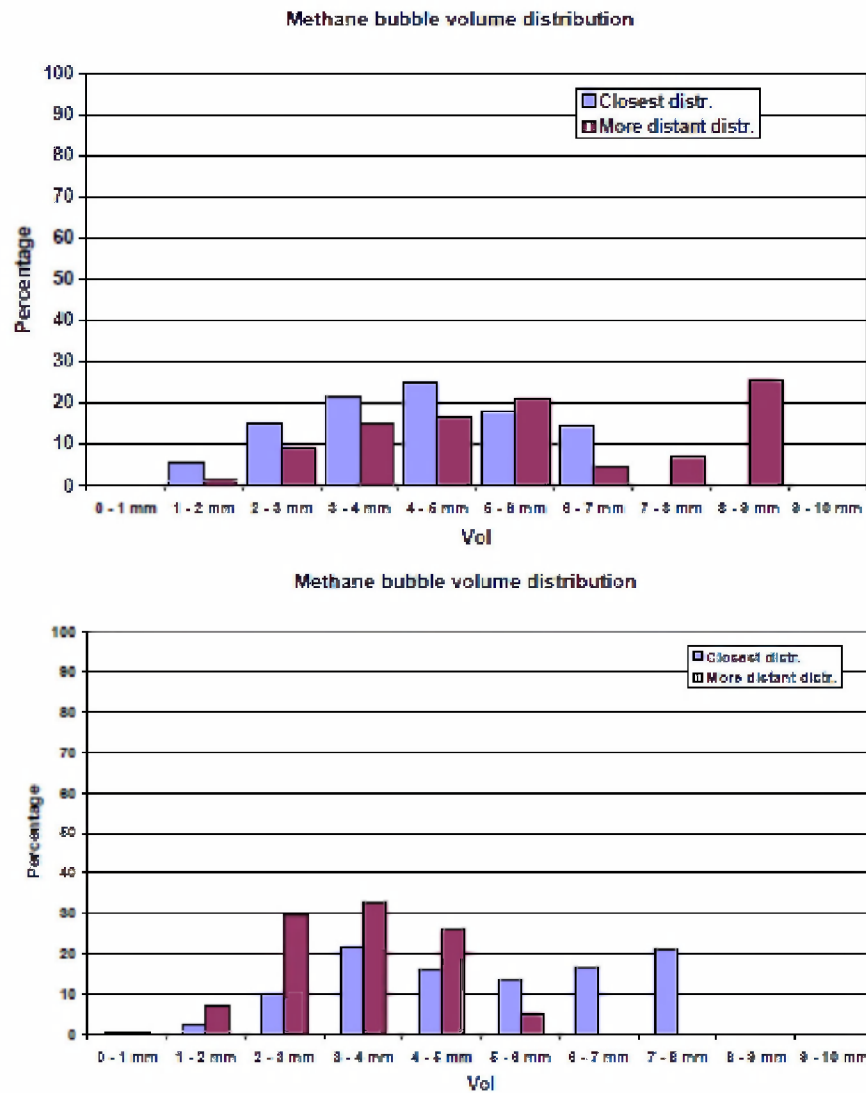


Figure G-13: The methane bubble volume size distribution observed by Johansen et al. (2001) cases (upper panel) (1) 9-19 m, (2) 19-23 m, (lower panel) (3) 39-58 m, and (4) 65-85 m, above the release.

G2.2.2 Diesel oil droplet size distribution

Diesel (in combination with natural gas (principally methane), release experiment number #2 was conducted on 27 June 2000. The water temperature at the release point was about - 0.82°C. Diesel oil droplet size distributions were reported by Johansen et al. (2001) at four selected distances above the release source. The criterion for selecting the cases was the same as for the gas bubble size distribution, that is, to look at the size distribution at various distances from the source. The number of diesel droplets, by count, between about 5 and 56 m above the release are provided in Table G-5.

Table G- 5: Counts of diesel oil droplet sizes at release #2 carried out 27 June 2000. Each second represents 25 pictures evaluated for bubble sizes. A total of 667 droplets were evaluated by Johansen et al. (2001) from a total of 5,325 pictures.

Case No.	Time interval, local time	Depth interval (m)	Distance above source of	Number of oil droplets counted
5	09-16-29 --- 09-16-32	840 – 839	5 – 6	215
6	09-16-48 --- 09-16-52	835 – 834	10 – 11	129
7	09-21-50 --- 09-22-40	830 – 822	15 – 23	139
8	09-28-14 --- 09-30-49	810 – 789	35 – 56	194

Figure G-14 and G-15 illustrate the number size and volume size distribution of diesel oil droplets, respectively. Johansen et al. (2001) concluded that it was not possible to assess the change in droplet or bubble size distribution as a function of the distance from the source (Johansen et al. 2001).

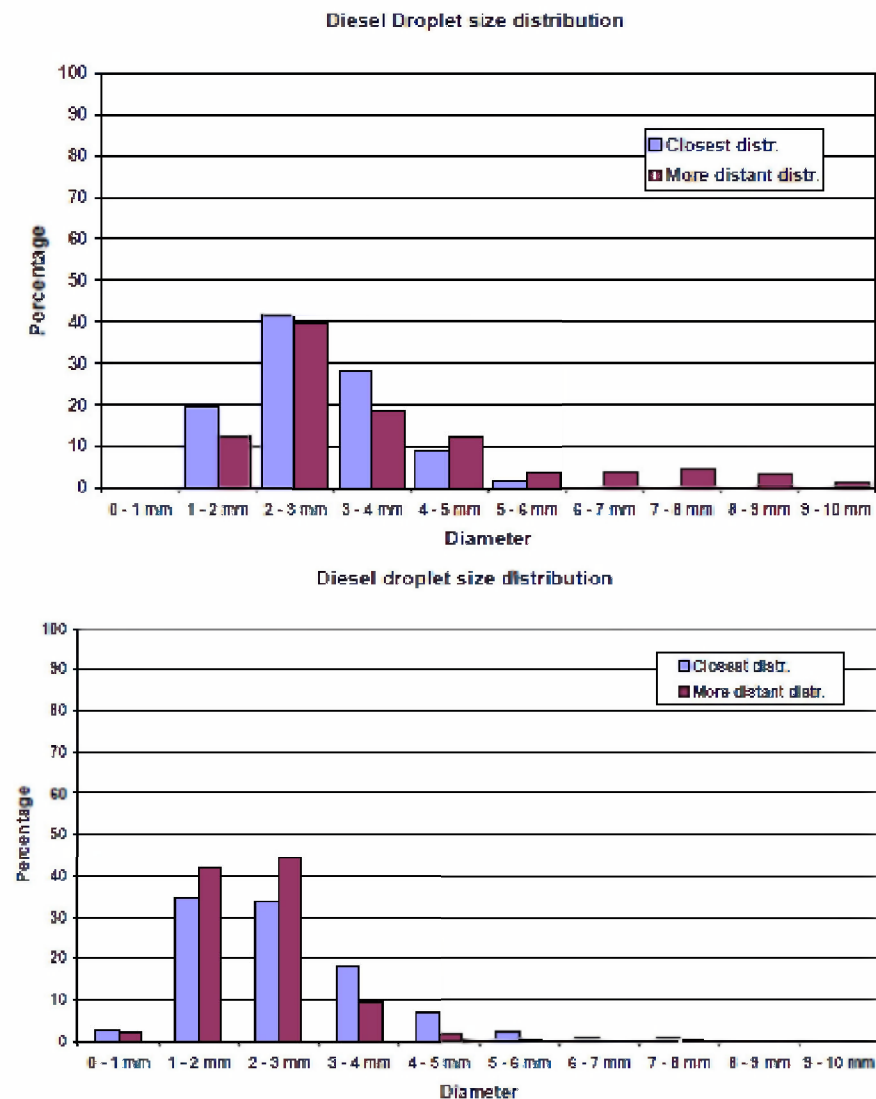


Figure G-14: Distribution of the diesel oil droplet number size distribution observed by Johansen et al. (2001) at the *Deep Spill* field trials (upper panel) (5) 5-6 m, (6) 10-11 m, (lower panel) (7) 15-23 m, and (8) 35-56 m above the release.

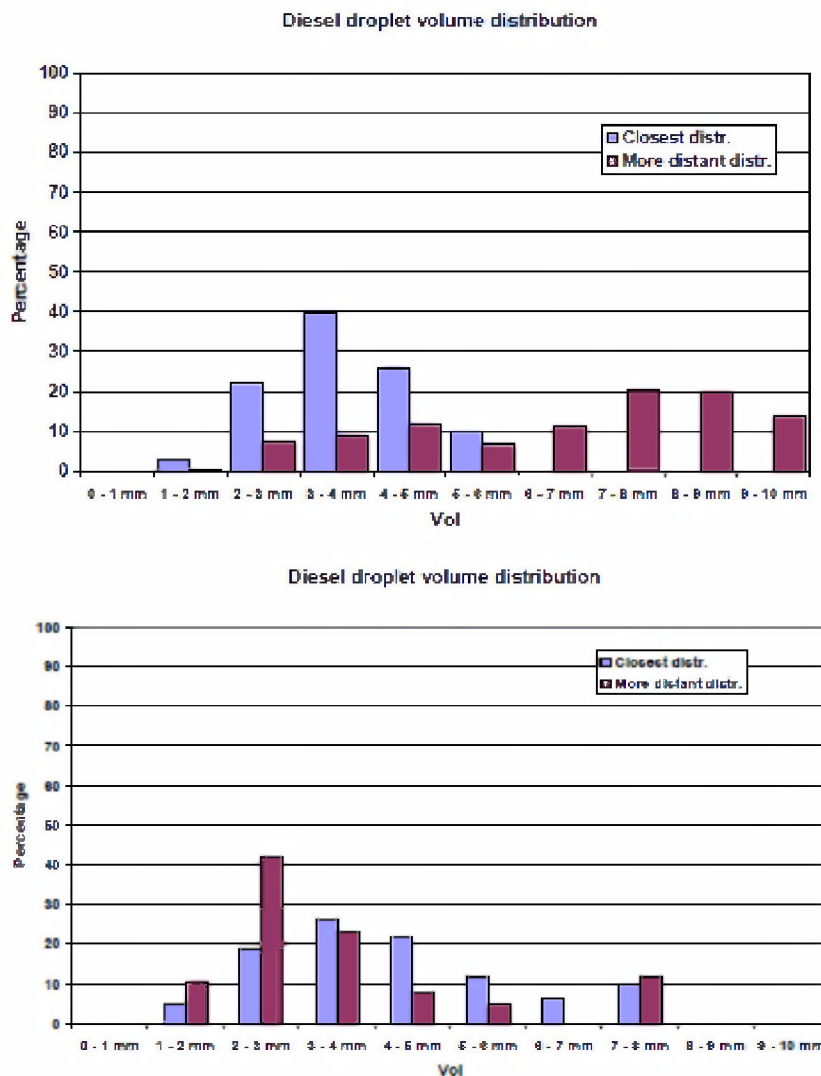


Figure G-15: Distribution of the diesel oil droplet volume size distribution observed by Johansen et al. (2001) at the *Deep Spill* field trials (upper panel) (5) 5-6 m, (6) 10-11 m, (lower panel) (7) 15-23 m, and (8) 35-56 m above the release.

During experiment # 2, the release of natural gas (CH_4/CO_2 0.55 Nm^3/s) and diesel ($1\text{m}^3/\text{min}$) resulted in a composite release velocity of 1.62 m/s at a depth of 845 m. ROV recordings resulted in good quality plume photographs that allowed for both bubble and droplet size distribution analyses. The release contained 73% by volume of diesel and 27% by volume of natural gas. The k value for the Weber number method (see Eq. 10) was determined by a fit to the volume distribution data (Johansen et al. 2001) and the n value of the Rosin-Rammler distribution (see Eq. 12) was estimated based on a fit a lognormal volume distribution of two parameter (logarithmic median and log geometric standard deviation (see below)). For both methane gas bubbles and diesel oil droplets, there appears to be an initial increase of median diameter, followed by decrease, as a function of distance above the release (Figures G-16 and G-17, the distance above the release values provided in these figures were averaged over the

various depths). However, according to the original report, “it is difficult to conclude on the possible change in droplet size distribution as a function of the distance from the source. This was caused by a number of reasons discussed by the report, including (1) relatively fewer number of large droplets counted at the two upper locations than the two lower depths, (2) difference in rising velocity of oil droplets and the ascending velocity of the image-acquisition ROV, and (3) loss of large droplet at distant vertical location of the data-recording because of the separation of large droplets from a bent plume during the rise of the plume.”

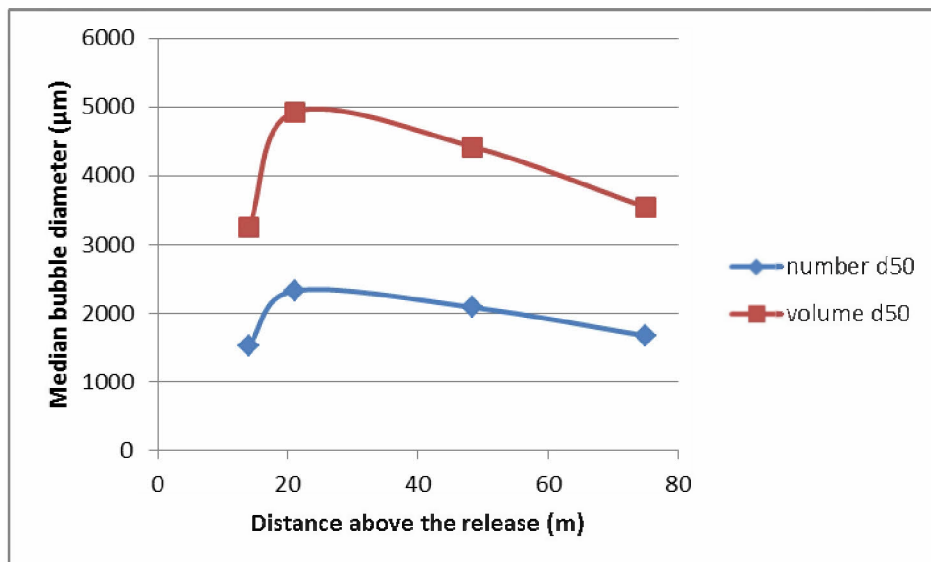


Figure G-16: The measured methane gas bubble median diameters at four different depths

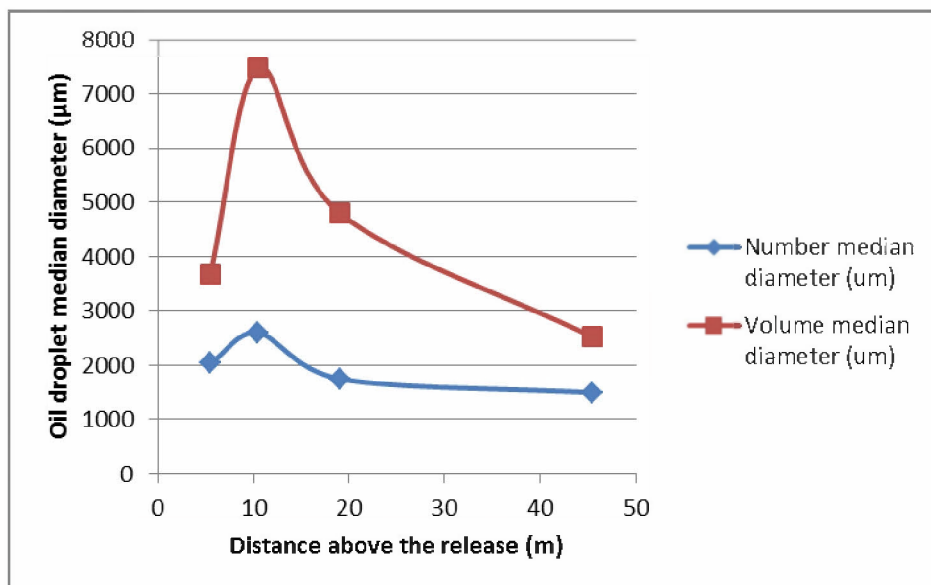


Figure G-17: The measured diesel oil droplet median diameter at four different depths.

G2.3 Deep Water Horizon measurements

G2.3.1 ROV Video particle size

There were two *M/V Jack Fitz* cruises that had Remotely Operated Vehicle (ROV) surveillance images and videos of suspended oil droplets and/or particulates in the water column. The *Jack Fitz 2* cruise took place between May 22 and 31, 2010, and the *Jack Fitz 3* cruise took place between June 14 and 20, 2010. These cruises deployed and collected CTD profiles along with ROV observations of oil in the water column. The *Jack Fitz 2* cruise included 17 ROV dives at horizontal distances ranging from within a couple of kilometers to over 100 km from the well head and at depths from the surface to 1,600 meters. Dispersants were being applied to the riser release during the first cruise and to the release above the BOP during the second. The riser was cut on June 2, 2010. The analysis of this data is included in RPS ASA Draft Physical-Chemical Technical Reports for DWH Water Column Trustees: Volume III, Oil Particle Data from the DWH Oil Spill (Li et al. 2014).

G2.3.2 Holographic Camera (Appendix I)

As part of the particle sampling program related to the DWH oil spill in the Gulf of Mexico, a unique set of data on the size distribution of oil droplets was collected and processed by Cabell Davis and Nick Loomis (Woods Hole Oceanographic Institute, WHOI) during the *M/V Jack Fitz* Cruise 3 (JF3) using an *in situ* digital holographic camera (*Holocam*). The particle sizes were determined for *in situ* holograms that were recorded from 9 dives (7 deep dives and 2 shallow dives) with a horizontal distance of 1 to 10 km from the well and depths from the sea surface to the seabed. Among these dives, two dives (#5 and #6) were identified to have “much oil” in the deep water column by Davis and Loomis (2014). A lognormal number and/or volume droplet size distribution function was fit to the *in situ* droplet size data of these two dives (#5 and #6) with very favorable goodness-of-fit ($R^2 > 0.96$). The observed volume median droplet diameters from dive #5 and #6 were in the range of 70 - 218 μm and 73-250 μm , respectively. Details of the process of fitting the lognormal distribution function to these data are presented in Appendix I.

G3. Impact of dispersant treatment on oil droplet size distribution

Dispersants are mixtures of solvents, surfactants, and other additives that are applied to oils slicks or blowout release sources to reduce the oil-water interfacial tension (NRC 1989, Clayton et al. 1993, NRC 2005). Reduction of oil-water interfacial tension promotes the formation of small oil droplets under either surface breaking wave or the blowout jet/plume turbulent shear flow that provides high mixing energy to break up oil. The effectiveness of dispersant on oil dispersion is largely dependent on reducing the overall droplet size distribution, and especially the formation of large numbers of small droplets. The dispersant effectiveness is a function of various factors, including dispersant chemistry, oil chemistry and their weathering behavior, dispersant and oil physical-chemical, and turbulence mixing energy either from the surface breaking waves or subsurface blowout turbulence.

A typical commercial dispersant is a mixture of three types of chemicals - solvents, additives, and surfactants (NRC 2005). Solvents are added for three purposes: (1) to enhance the

dissolution of surfactants and additives into a homogeneous dispersant mixture, (2) to reduce the product's viscosity and modify the dispersant's solubility in water, and (3) to determine the extent which dispersants may be premixed with water for some spray applications (and possibly impact on effectiveness when applied subsurface). Additives may also improve the dissolution of the surfactants into an oil slick and increase the long-term stability of the dispersant formulation. Surfactants are the most important compounds in a dispersant product. Surfactants contain both lipophilic (hydrophobic) and hydrophilic (water-compatible) groups, and hence tend to reside at the oil-water interface to reduce the oil-water interfacial tension. This is caused by the amphiphilic nature of surfactants at the oil-water interface, with an orientation with the hydrophilic groups interacting with the water phase and the hydrophobic groups interacting with the oil. The extent of such orientation is determined by the commercial formulations of the chemical dispersant product. This is often comprised of two or more surfactant molecules that have different solubility in both water and oil, and is characterized by the Hydrophilic-Lipophilic Balance (HLB) parameter. The blend of surfactant in commercial dispersant formulations tend to be hydrophilic and the current formulations usually consist of surfactant mixtures with an overall HLB in the range of 9 to 11 (Clayton et al. 1993, NRC 2005).

Precise compositions for commercial dispersant formulations are proprietary (NRC 2005). Corexit products are the most prevalent of all dispersants stockpiled in the United States and Canada. Table G-6 summarizes the main components of Corexit dispersants. Corexit 9527 and 9500 (Nalco, TX) include the same surfactants (a mixture of 48% nonionic and 35% anionic surfactants) incorporated into a different solvent. The major nonionic surfactants include ethoxylated sorbitan mono- and tri-oleates and sorbitan mono-oleate; the major anionic surfactant is sodium dioctyl sulfosuccinate. A different solvent was used in the two Corexit products: Corexit 9527 contains glycol ether solvent (2-butoxyethanol), whereas Corexit 9500 has replaced that with a mixture of aliphatic hydrocarbons (Norpar 13; n-alkanes ranging from nonane to hexadecane).

Table G-6: The Chemical components of Corexit 9500 and Corexit 9527 (EPA 2013)

CAS Registry Number	Chemical Name	Short Name	Function
57-55-6	Propylene glycol	PG	Solvent
111-76-2*	2-Butoxyethanol	2-BE	Solvent
577-11-7	Dioctyl sodium sulfosuccinate	DOSS	Surfactant
1338-43-8	Sorbitan, mono-(9Z)-9-octadecenoate	Span 80	Surfactant
9005-65-6	Sorbitan, mono-(9Z)-9-octadecenoate, poly(oxy-1,2-ethanediyl) derivatives	Tween 80	Surfactant
9005-70-3	Sorbitan, tri-(9Z)-9-octadecenoate, poly(oxy-1,2-ethanediyl) derivatives	Tween 85	Surfactant
29911-28-2	Dipropylene Glycol Monobutyl Ether	DPnB	Solvent
64742-47-8	Petroleum distillates		Solvent

* Not a component of Corexit 9500

The physical chemistry of dispersant-oil interactions and the energy requirements for effective oil-droplet formation and dispersion can be expressed using a simple relation,

$$W_k = \sigma_{o-w} A_{o-w} \quad \text{Eq 9}$$

where W_k is the mixing energy (Joule or Nm or $\text{kg}\cdot\text{m}^2/\text{s}^2$), σ_{o-w} is the oil-water interfacial tension (N/m or kg/s^2) and A_{o-w} is the total oil-water interfacial area (m^2). This equation shows that reduction of the interfacial tension allows creation of a larger oil-water interfacial area, meaning that a larger number of smaller droplets can be produced, with the same level of energy input.

The impact of dispersant treatment on oil droplet size distribution is addressed through the variation of oil and water interfacial tension as a function of the type and amount of dispersant applied. Figure G-18 provides an estimate of the interfacial tension as a function of dispersant-to-oil ratio DOR. The values in the upper panel are taken from Venkataraman et al. (2013) while those in the lower panel are from Khelifa et al. (2009).

The objective in using chemical dispersants on oil is to reduce the oil-water interfacial tension, hence increasing the ratio of disruptive inertial to cohesive interfacial forces (Weber number). However, adding dispersant also increases the ratio of two cohesive forces: dispersed phase viscous to interfacial tension (Ohnesorge number). As a result, three parameters are simultaneously changed as a function of oil-water interfacial tension (IFT): (1) Instability length scale is dependent on the square root of IFT, i.e., $d_o \sim f(\sigma^{0.5})$, (2) Ohnesorge number changes to

the inverse 3/4th order of IFT, i.e., $Oh \sim g(\sigma^{-0.75})$, and (3) Weber number varies as a function of inverse square root of IFT, i.e., $We \sim (\sigma^{-0.5})$. Taken together, the volume median diameter changes to the inverse 0.413th order of IFT, i.e., $vd50 \sim (\sigma^{0.413})$.

The oil water interfacial tension can be estimated from laboratory studies as a function of DOR (e.g., Khelifa and So 2009, Khelifa et al. 2011, and Venkataraman et al. 2013) (Figure G-18). For weathered oil, the effect of dispersant on IFT reduction is decreased (Khelifa et al 2011). For example, the ANS oil weathered by 22.5% has an initial IFT of 24.2 mN/m at a DOR of 1:100, IFT is reduced to 2.73 mN/m at DOR of 1:40 and 0.32 mN/m, at DOR 1:20, IFT is 2.03×10^{-2} mN/m. Similar results of the impact of dispersant on IFT reduction are also reported by Venkataraman et al. (2013).

In the present application, the original data of Venkataraman et al. (2013) were used to fit the curves of IFT vs DOR relationship. These fitted equations were selected for the DWH simulations as it was generated from fresh source oil MC252 oil and Corexit 9500 dispersant and hence most closely matched the conditions for subsurface dispersant applications during the spill.

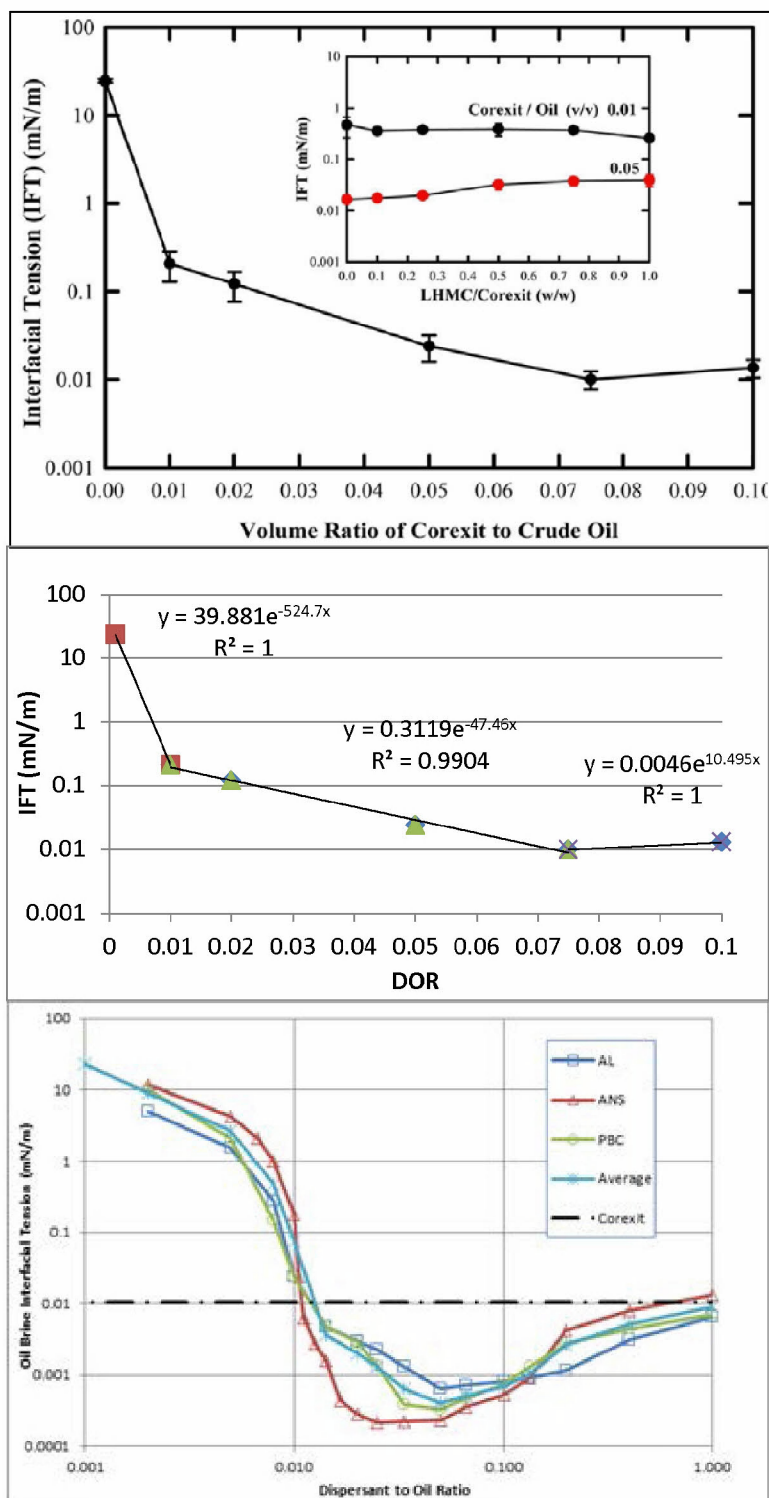


Figure G-18: Measured variation (upper) and fitted equations (middle) of oil-brine interfacial tension with dispersant concentration (in DOR) for MC252 and Corexit 9500 dispersant (Venkataraman et al. 2013); and for three crude oils and Corexit 9500 dispersant (Khelifa and So 2009).

G4. Review of oil droplet size models in existing blowout models

G4.1 CDOG, DEEP BLOW and OILMAP DEEP

In the existing blowout models, including CDOG, DEEP BLOW and OILMAP DEEP (i.e., earlier versions), the same droplet size description model is used as reported by Johansen (2002) and Yapa and Chen (2004). The method involves two steps: the first step is the computation of the maximum droplet size, and the second is to determine the droplet size distribution using a Rosin-Rammler type formulation.

G4.1.1 Determining the maximum drop size (d_{95}) based on Weber number method

The existing droplet size method describes the multi-phase flow conditions at the release location (prior to the oil release out of the nozzle) according to the local void fraction and gas to oil ratio (GOR) as follows (based on the two-phase pipe flow experiments of Gould et al. (1974)): (a) if the local void fraction > 0.95 (at high GOR, i.e., $GOR > 19$), it is a mist flow; in this case, inside the pipe, the continuous phase is gas and the dispersed phase is oil droplets; (b) if the local void fraction ≤ 0.95 (at low GOR, i.e., $GOR < 19$), it is an oil flow; in this case, the continuous phase is oil and the dispersed phase is gas, as gas bubbles or slugs. The maximum droplet size d_{max} in both cases are determined by the diameter of the nozzle D_o and the dimensionless Weber number, We (Karabelas 1978):

$$d_{max} = k D_o We^{-0.6} \quad \text{Eq 10}$$

The values of coefficient k and the physical parameters are different dependent on the void fraction (Table G-7). The exit Weber number is defined as:

$$We = \frac{\rho_w U_o^2 D_o}{\sigma} \quad \text{Eq 11}$$

where ρ_w (kg/m^3) is the density of seawater, D_o (m) is the diameter of the release, and U_o (m/sec) is its speed, and σ (N/m) is the interfacial tension between oil and sea water.

Table G-7: CDOG, DEEP BLOW, and OILMAP DEEP parameters used in droplet size equation.

Parameters	Case a (high GOR)	Case b (low GOR)
Continuous phase	Gas	Oil
K (droplet size scaling)	4	27.5
N (size distribution parameter)	2.5	1.6
Density of continuous phase	Density of gas	Density of water
Interfacial tension	Gas-oil, 0.005 N/m	Oil-water, 0.03 N/m

G4.1.2 Determining the Rosin-Rammler type droplet size distribution

The droplet size distribution in the existing models is computed from the Rosin-Rammler distribution. That is, the fraction of the total volume contained in droplets with diameter less than d_i is given as,

$$V(d_i) = 1 - \exp\left[-2.996 * \left(\frac{d_i}{d_{95}}\right)^n\right] \quad \text{Eq 12}$$

Where n is an index corresponding to the spread of the droplet size distribution; the larger the value of n the narrower the distribution. The CDOG user's manual recommends that two parameters k and n have to be calibrated with experimental data, and more experimental work is needed to improve the confidence level for these values. Default values are provided in Table G-7.

G4.2 SINTEF Modified Blowout Oil Droplet Size Model

The experimental data of SINTEF tower tank tests (Brandvik et al. 2013, 2014) were used by Johansen et al. (2013) and Brandvik et al. (2014) to derive a new empirical model for predicting oil droplet sizes. The model formulation once again involves two steps: (1) development of an algorithm for predicting droplet sizes in oil jets based on Wang and Calabrese's (1986) empirical model, and (2) prediction of oil droplet size distribution based on lognormal or Rosin-Rammler droplet size distributions.

G4.2.1 Determining the volume median diameter of drop size (vd_{50}) based on the modified Weber number method

Johansen et al. (2013) argued that the Weber number scaling of the characteristic droplet size generated by a turbulent oil jet injection into water (i.e., $d_{50}/D = A We^{-3/5}$) is valid for interfacial tension limited breakup. However, under certain conditions (such as high exit velocities, high oil viscosities, or for low interfacial tensions), viscous forces may be of importance, and in these cases the characteristic droplet size will scale as a function of the exit Reynolds number rather than the Weber number. In the transitional region, when both interfacial tension and viscous forces are important in influencing droplet breakup, a semi-empirical equation for the droplet size has been proposed by Wang and Calabrese (1986) based on attempting to estimate oil droplet size distributions from a series of completely stirred tank reactor experiments:

$$\left(\frac{d_{50}}{D}\right) = A * We^{-0.6} * \left[1 + B * Vi \left(\frac{d_{50}}{D}\right)^{1/3}\right]^{0.60} \quad \text{Eq 13}$$

Where A and B are empirical coefficient and Vi is the tank viscosity group number, which is defined as $Vi = \mu U / \sigma$. This is an implicit equation since the value being sought, d_{50} , is on both sides of the equation and hence must be solved by iterative methods.

Equation 13 forms the basis for the new SINTEF oil droplet size derived from the Tower Basin experimental data. There are two versions of the empirical coefficients that are published based

on their experimental data. In Johansen et al. (2013) the coefficients ($A = 15$ and $B = 0.8$) were derived from a few of the early dispersant treated and non-treated test results (Brandvik et al. 2013). A second set of empirical coefficients ($A = 24.8$ and $B = 0.08$) were estimated by SINTEF based on the more comprehensive dataset of oil jet breakup experiments, with and without dispersant, that became available after the tower experiments were completed (Brandvik et al. 2014).

G4.2.2 Droplet size distribution

After estimating the median droplet size depending on outlet conditions and interfacial tension, the lognormal distribution and Rosin-Rammler distribution functions was used to represent the oil droplet size distribution. The SINTEF model has been fitted to both distributions and the findings point in favor of the lognormal distribution, but with the provision that variations in standard deviations might depend on field release conditions, including the subsurface dispersant injection method.

G5. New Oilmap Deep oil droplet size model

G5.1 Lognormal distribution with Weber number and Ohnesorge number dependent VMD

Given the availability of data from recent laboratory and large scale laboratory experiments for both treated and untreated releases a new oil droplet size model has been developed and included in **OILMAP DEEP** and used in the application to the DWH release. An overview of the new model follows.

G5.1.1 Definition of dimensionless groups

It is clear from recent experiments that in the most general case the oil droplet size depends on disruptive and viscous effects and the interfacial tension between oil and water; the latter being strongly impacted by the addition of dispersants. This naturally leads to a model formulation that is dependent on the We and Oh (or dispersed phase viscosity number, which is also related to the dispersed phase Reynolds numbers). In the interest of simplicity the model formulation is based on the We and Oh numbers.

Weber Number (We) is the ratio of disruptive momentum (hydrodynamic) forces to restorative (interfacial tension) forces and defined as:

$$We = \frac{\rho_w * U^2 * d_o}{\sigma_{o-w}} \quad \text{Eq 14}$$

Where, ρ_w is the density of seawater ($\text{kg} \cdot \text{m}^{-3}$); U is the exit velocity of the oil ($\text{m} \cdot \text{s}^{-1}$); σ_{o-w} is the oil-water interfacial tension ($\text{N} \cdot \text{m}^{-1}$ or $\text{kg} \cdot \text{s}^{-1}$), and d_o is the characteristic length scale (m).

Ohnesorge Number (Oh) (Ohnesorge 1936, Lefebvre 1989) is the ratio of dispersed phase viscous to interfacial tension forces:

$$Oh = \frac{\mu_o}{\sqrt{\rho_o \sigma_{o-w} d_o}} \quad \text{Eq 15}$$

Where μ_o is the dynamic viscosity of oil ($\text{Pa}\cdot\text{s}$ or $\text{N}\cdot\text{m}^{-2}\cdot\text{s}$ or $\text{kg}\cdot\text{m}^{-1}\cdot\text{s}^{-1}$); ρ_o is the density of oil ($\text{kg}\cdot\text{m}^{-3}$), σ_{o-w} is the oil-water interfacial tension ($\text{N}\cdot\text{m}^{-1}$), and d_o is the characteristic length scale (m).

The characteristic length scales in these two dimensionless numbers are determined by the Rayleigh - Taylor (R-T) instability maximum diameter (Grace et al. 1978) or the release nozzle diameter, whichever is smaller. The R-T instability maximum diameter is given by

$$d_o = 4 * \left[\frac{\sigma_{o-w}}{\Delta \rho * g} \right]^{0.5} \quad \text{Eq 16}$$

where, $\Delta \rho = \rho_w - \rho_o$ is the density difference between seawater (ρ_w) and oil (ρ_o) ($\text{kg}\cdot\text{m}^{-3}$); g is gravity acceleration rate ($\text{m}\cdot\text{s}^{-2}$); and σ_{o-w} is the oil-water interfacial tension ($\text{N}\cdot\text{m}^{-1}$).

G5.1.2 Volume median diameter formula

The proposed non-dimensional volume median droplet diameter is dependent on the We and Oh numbers and is given by the following.

$$\frac{vd_{50}}{d_o} = r * (1 + 10 * Oh)^p * We^q \quad \text{Eq 17}$$

Where: vd_{50} is the volume median diameter (VMD) (m); d_o is either the maximum oil droplet diameter of Rayleigh-Taylor Instability (m) or the release nozzle diameter, whichever is smaller. The ratio of the VMD and the characteristic length scale is calculated through an empirical relationship of the dependence of the ratio on the Oh and We number.

The exponential constant coefficients (p and q) with base Oh and We , respectively, are determined based on surface entrainment of oil droplets under breaking wave conditions. A multivariate regression analysis was performed to determine the values of r , p , and q in Equation 17, using 28 laboratory tests (18 datasets from Delvigne et al. (1994) study, and 10 from Reed et al. (2009)'s study). For the surface entrainment of oil, the least square best fit parameters were estimated as $r = 1.791$, $p = 0.460$, and $q = -0.518$, with $R^2 = 0.861$ and $n = 28$. Figure G-19 shows the goodness of fit of the observed non-dimensional volume median diameters versus the two dimensionless groups, Weber and Ohnesorge number. Within the range of these parameters, the fit results agree very well with the measurements. This step serves to calibrate the model under surface breaking wave conditions. Then, the model coefficients are calibrated with the Deep Spill blowout release conditions, and finally, the model was validated against the SINTEF tower basin and DWH field data. Model validation with SINTEF and DWH data are described below.

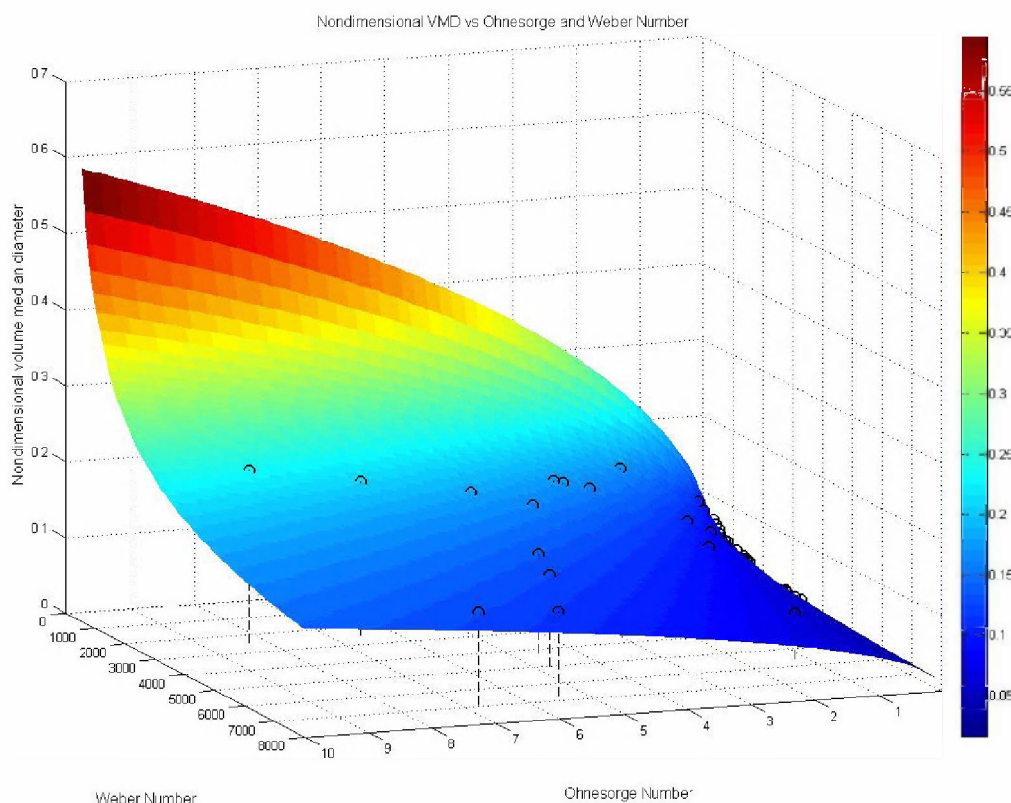


Figure G-19: Comparison of observed volume median diameter data (circles) and the calculated values (mesh grid and color bar) based on Equation 17 with the best-estimate parameters ($r = 1.791$, $p=0.460$, and $q=-0.518$; $R^2=0.861$).

For the blowout oil droplet size distribution volume median diameter, it is assumed that the exponential function dependence with respect to Oh and We is the same as under the surface breaking wave conditions, whereas the linear scaling coefficient term (r) must be fit to the blowout conditions. The reason for doing this is the difference in the Weber number definition: While the disruptive momentum is quantified in terms of the average exit speed in the blowout model (Eq. 14), it is determined based on the significant wave height under surface breaking waves. Therefore, the linear scaling coefficient (r) is determined based on the Deep Spill field trial data to be 9.67. Based on Hinze's (1955) argument, the minimum effective viscosity (i.e., Oh number) is 0.1.

Equations 14-17 can be applied to estimate the gas bubble droplet size distribution using gas phase relevant coefficients. The gas-brine interfacial tension was reported to be 0.0728 N/m (Bandara & Yapa 2011). The scaling coefficient in Eq 17 is determined to be 2.988 from the field observation data of *DeepSpill* experiment. The Oh number is replaced with a constant value because of the low value of the gas phase viscosity.

G5.1.3 Droplet size distribution

The field and laboratory experimental data summarized above suggest that the oil droplet size distribution of the blowout release and the surface breaking wave conditions can be simulated

using a lognormal distribution function. The lognormal distribution was introduced by Mugele & Evans, (1951) to describe droplet size distribution of sprays. Mugele & Evans (1951) compared four different types of spray droplet size distribution functions including Rosin-Rammler, Nukiyama-Tanasawa, log-probability, and upper-limit lognormal distribution, and concluded that the lognormal distribution most accurately described the spray droplet size distribution throughout the entire distribution range. The upper-limit lognormal distribution function was applied to liquid-liquid dispersion in pipe flow (Karabelas et al. 1978, Simmons and Azzopardi 2001).

Given the median diameter, a lognormal distribution was fit to droplet size data from *DeepSpill* and DWH and gave lognormal standard deviations for *DeepSpill* of $\log \sigma_g = 0.51 \pm 0.09$ and for DWH of $\log \sigma_g = 0.59 \pm 0.08$. A value of 0.5 has been selected for general use, since it is independent of the present application.

The lognormal particle size distribution involves the use of the logarithmic transformation of size data to obtain the lognormal distribution. The logarithm of particle size (normalized by $d_0 = 1\mu\text{m}$), is plotted along the x-axis, and the frequency or cumulative fraction is plotted along the y-axis.

$$df = \frac{1}{\sqrt{2\pi} d_p \ln \sigma_g} \exp\left(-\frac{(\ln d_p - \ln d_g)^2}{2(\ln \sigma_g)^2}\right) dd_p \quad \text{Eq 18}$$

The oil droplet (number) size distribution may be characterized by two parameters, the logarithmic mean, d_g , and the logarithmic standard deviation, σ_g . The logarithmic mean is expressed as a geometric mean diameter, d_g ,

$$\ln d_g = \frac{\sum n_i \ln d_i}{N} \quad \text{Eq 19}$$

For the number distribution, the geometric mean diameter can be customarily replaced by the number median diameter; the geometric mean is the arithmetic mean of the distribution of $\ln(d_i)$, which is a symmetrical normal distribution, and hence its mean and median are equal. The median of the distribution of $\ln(d_i)$ is also the median of the distribution d_i , as the order of values does not change in converting to logarithms. The logarithmic standard deviation is expressed as the geometric standard deviation σ_g ,

$$\ln \sigma_g = \left(\frac{\sum n_i (\ln d_i - \ln d_g)^2}{N-1} \right)^{1/2} \quad \text{Eq 20}$$

The lognormal distribution is most useful where the distribution covers a wide range of values, where the ratio of the largest to the smallest value is greater than 10. The lognormal droplet size distribution has many convenient attributes for the present application (Hinds 1999) including (1) all moment distributions of any lognormal distribution are lognormal and have the same geometric standard deviation, (2) the geometric mean is the arithmetic mean of the distribution of logarithmic particle diameter, which is a symmetrical normal distribution, and hence, its mean and median are equal, and (3) all moment distributions (means, medians, moment averages, etc.) can be calculated directly using conversion equations.

The current formulation has significant benefits over the earlier formulation used in previous applications of OILMAP DEEP (and other blowout models) including: Weber number that depends on maximum stable oil droplet size rather than blowout pipe diameter, the dispersed phase viscosity, lognormal distribution substantially improved fit to droplet size data ($R^2=0.994$ to 0.995) compared to the Rosin-Rammler distribution ($R^2 = 0.876$ to 0.996), and a single

parameter droplet size distribution model since the standard deviation of the lognormal model is fixed.

G5.2 Model validation

G5.2.1 Comparison of existing and developed oil droplet model with laboratory testing results

The volume median diameters (VMD) of oil droplets in the jet and/or plume generated under laboratory testing conditions and those calculated with existing and alternate oil droplet size prediction models are compared to validate and evaluate the model. The datasets that are used for this comparison include 23 tests from SINTEF tower basin experiments (Table G-1), 12 tests from OHMSETT tank tests (Table G-2) and 6 tests from SL Ross tank tests (Table G-2). The droplet size prediction models that are assessed include the SINTEF modified Weber number method (Johansen et al. 2013; Brandvik et al. 2014) and the OILMAP DEEP Weber/Ohnesorge number method (see Section 5.1).

Figure G-20 shows the comparison of the reported VMD and the model predicted VMD using the SINTEF modified Weber number method. There are two sets of empirical model coefficients that were derived from the SINTEF tower basin experimental studies. The first set of coefficients ($A = 15$, $B = 0.8$) were fitted based on a limited number of experiments that were published in the Journal of Marine Pollution Bulletin (Johansen et al 2013). The second set of coefficients ($A = 24.8$, $B = 0.08$) were fitted to additional experimental data that were included in the project final report (Brandvik et al 2014). Not surprisingly, there is a good correlation of the reported VMD's of SINTEF tower basin experiments and the model prediction based on the second set updated coefficients (Figure G-20, lower panel). Model predictions based on the earlier set of coefficients (Figure G-20, upper panel) does not agree with the experimental data when observed droplet VMD's are small. In addition, Figure G-20 also clearly shows that the SINTEF model, based on either set of model coefficients, is incapable of predicting the reported VMD from the SL Ross study. The model in general over-predicts the VMD of oil droplets from the SL Ross experiments. This was also pointed out by the SL Ross researcher (Belore 2014) when comparing their data to the earlier version of the SINTEF model (Johansen et al. 2013):

"SINTEF model... over estimates the drop sizes for the high dispersant dosage tests completed both in the SL Ross tank and in the large scale tests at OHMSETT... The SINTEF model is not sensitive to interfacial tension reductions greater than 500 to 1000 times. It would appear that the SINTEF model does not predict the oil drop size reduction that was measured with successful dispersant application in this project's experiments. The authors of the SINTEF paper recognized that their model is preliminary and could require parametric adjustment once additional test data becomes available."

While the SINTEF model, with the most recent set of coefficients, compares well with their data, its performance against the other two data sets is generally very poor. Even with the newer set of constant coefficients, the model shows a low correlation to the data and a predictive bias of 1.578 for the SL Ross data sets. Model predicted values for dispersant treated oil are substantially larger than the observed.

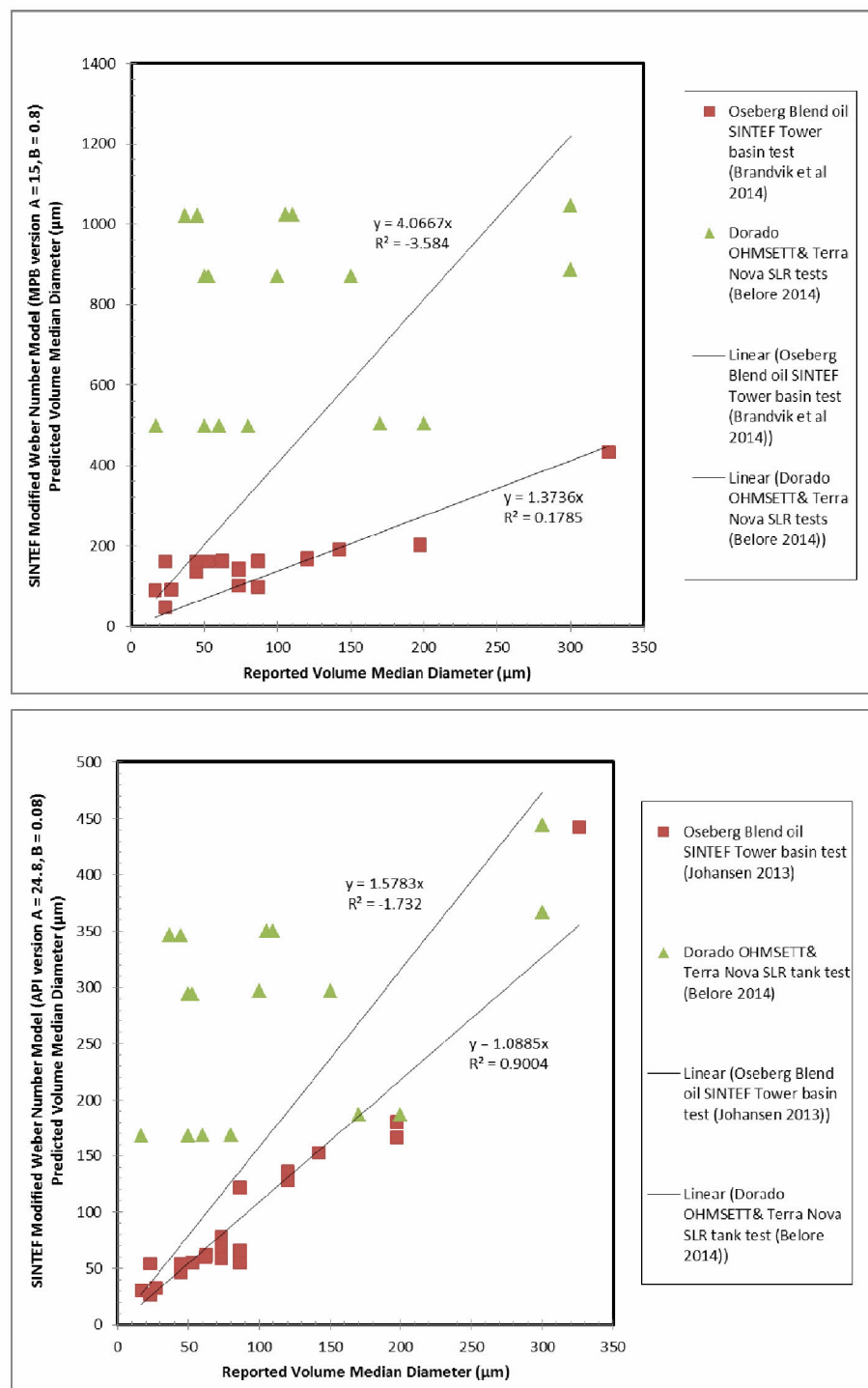


Figure G-20: SINTEF model predicted and the reported VMD of jet/plume oil releases with and without dispersant treatment. Upper panel, model based on earlier coefficients (A = 15, B = 0.8); Lower panel, based on later updated coefficients (A = 24.8, B = 0.08). The laboratory experimental datasets include 23 tests from SINTEF tower basin (Brandvik et al. 2014), 12 tests from OHMSETT tank (Belore 2014), and 6 tests from SL Ross tank tests (Belore 2014).

Figure G-21 compares the new and existing OILMAP DEEP predictions with the experimental observations of the VMD. The upper panel is for the case where the droplet model is dependent on both the Weber and Ohnesorge numbers (new model, as described in, Section 5.1), while the lower panel shows the case if the dependence is only on the We number (existing), as in current commercial version of OILMAP DEEP (Crowley et al. 2014). The solid lines show the fit of the model to the individual data sets, while the dashed line shows the fit to all of the data. This comparison shows that the correlation (based 41 data points for both treated and untreated oil) of the model prediction and the lab results for the new method is very high for data obtained from the SINTEF tower basin experiments ($R^2=0.90$) and the two different sets of data obtained by SL Ross ($R^2=0.83$); one in the large scale OHMSETT test tank and the other in the smaller scale SL Ross test tank. The overall relation of the model predicted VMD and the reported VMD can be expressed as $y = 0.9871x$, with the correlation coefficient $R^2 = 0.867$ when all data is used in this validation.

It is worth noting that 41 tests used in the validation included a large variety of different testing conditions, namely, 3 nozzle diameters (0.5 mm, 1.5 mm, and 4.5 mm), 3 different oil types (Oseberg Blend, Dorado, and Terra Nova), 2 flow phase conditions (oil release in the presence and absence of gas phase), various DOR's (from no dispersant control to 1:1000 to 1:25), and a range of different nozzle oil exit velocities (from 4.01 to 42 m/s).

The commercial version of OILMAP DEEP droplet size model performs reasonably well in predicting the sizes for the untreated oil (blue squares) (lower panel Figure G-21), but underestimates the sizes for the treated oil. The R^2 are 0.83, 0.84, and 0.75 for SINTEF, SL Ross, and all data, respectively.

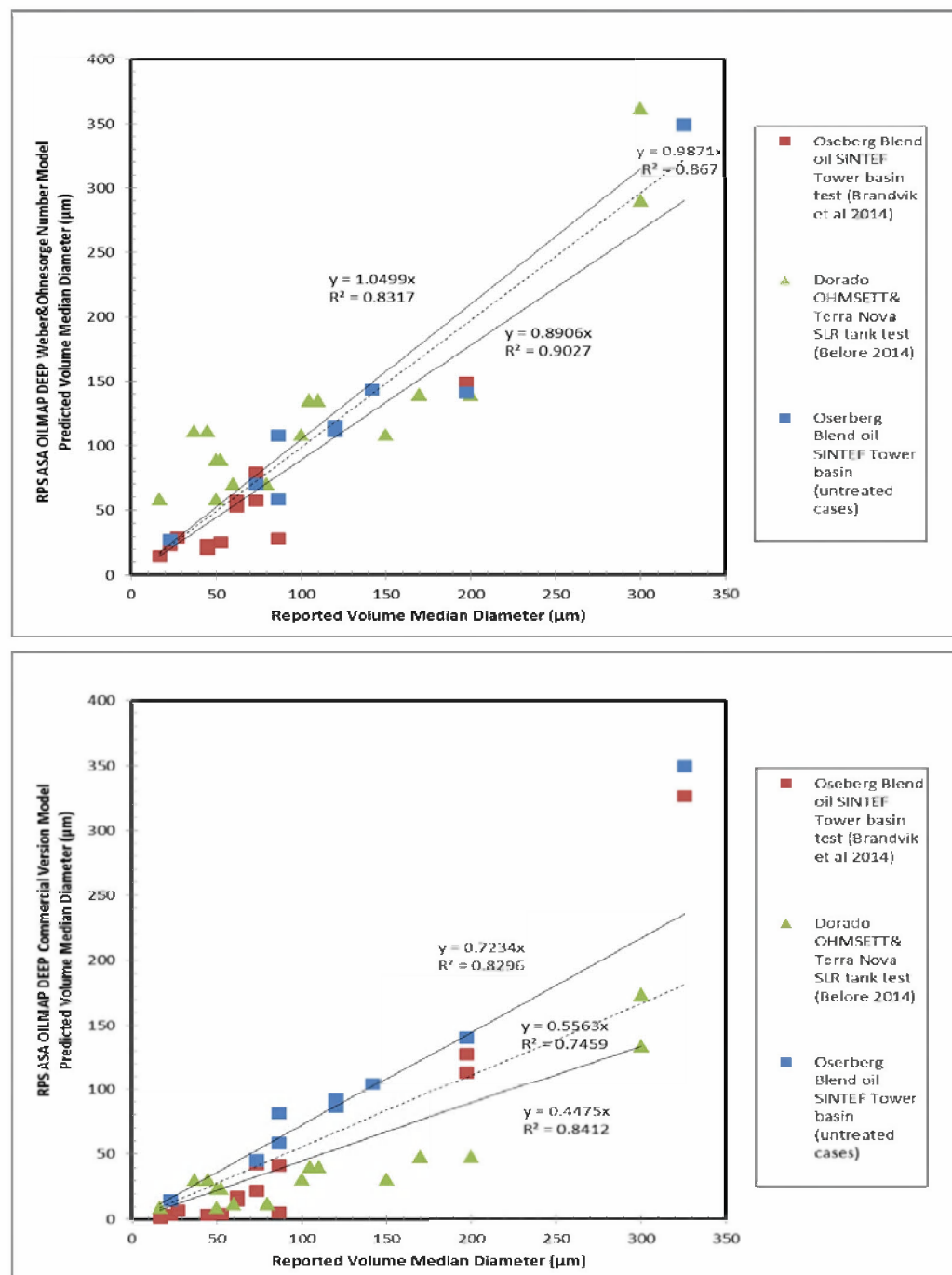


Figure G-21: Oilmap Deep oil droplet size model predicted and the lab reported VMD of jet/plume oil releases with and without dispersant treatment. Upper panel, New OILMAP DEEP model: Solid lines are regression of SINTEF data and SL Ross data, respectively, dashed line is the regression with all data; For the SINTEF results, blue squares are untreated, and red squares and green triangles are all treated. Lower panel, Model prediction based on commercial version OILMAP DEEP oil droplet size model; (Experimental data are the same as in the upper panel, data source: Brandvik et al. 2014; Before 2014)

G5.2.2 Comparison of lognormal and Rosin-Rammler distributions with laboratory and field data

A large number of laboratory and field measurements of droplet size distribution data have been reported (Lewis et al. 1985, Delvigne & Sweeney 1988, Daling et al. 1990, Lunel 1995, Khelifa & So 2009, Li et al. 2009). The comparison of lognormal and Rosin-Rammler distributions with the laboratory droplet size distribution data was performed to compare the goodness of fit. The fit of Rosin-Rammler distribution needs to be carried out with the volume distribution, whereas the fit of lognormal distribution can be done either with the number or volume distribution. Here, in order to allow for comparison, all the observational data were transformed to volume distributions first and then the selected distribution function was fit to the transformed data.

Figure G-22 illustrates the size distribution data of the laboratory measurements and model results. The field measurements include: (1) *In situ* Holographic camera of Deepwater Horizon JF3 cruise; (2) the ROV image analysis of the JF2 cruise data; (3) field trial of the *DeepSpill* (Johansen et al. 2000); and (4) the laboratory experimental study conducted in UH (Tang 2004). The observational data are fit with both lognormal and Rosin-Rammler droplet size distribution functions using Microsoft Excel's built-in Solver data analysis tool. Based on correlation coefficient (Table G-8) the lognormal distribution fits all five data sets very well. Rosin-Rammler distribution reasonably fits most of the data sets, but the fit is not as good as the lognormal.

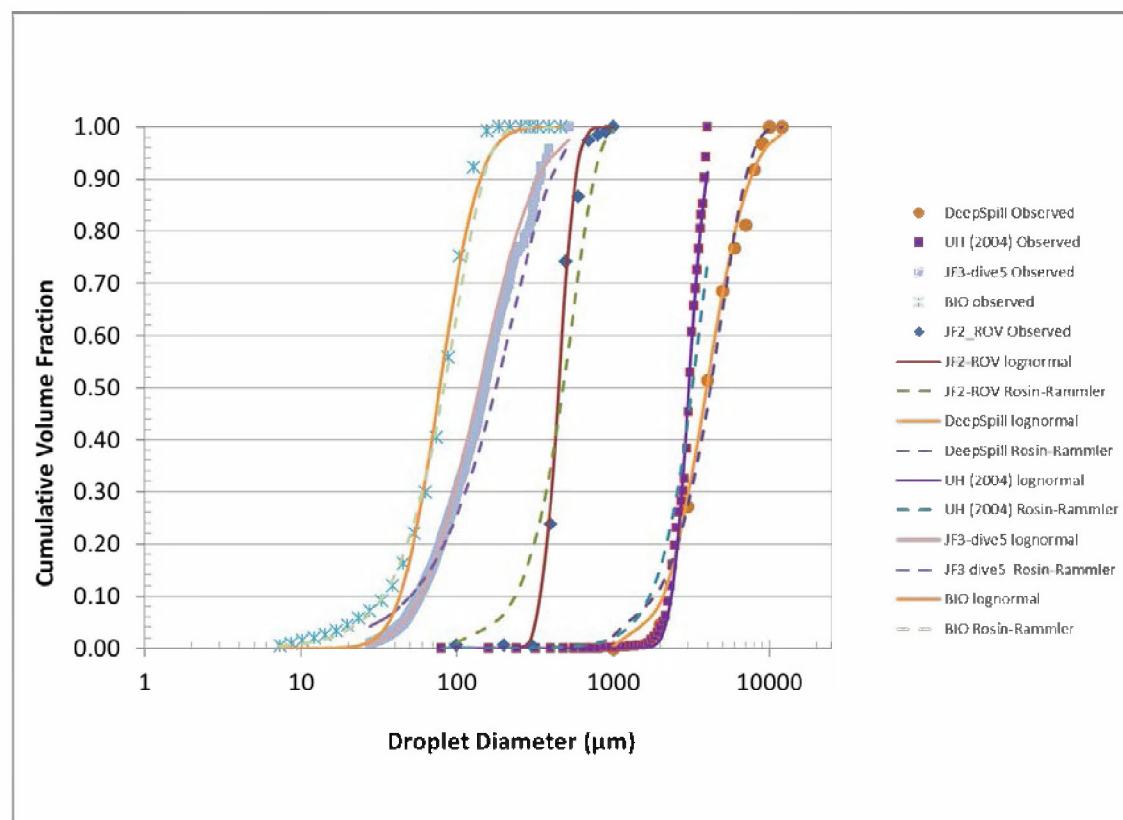


Figure G-22: Summary of observed cumulative droplet size distribution of five different data sets and the fitted lognormal and Rosin-Rammler droplet size distributions.

Table G-8: Fitted parameters of lognormal versus Rosin-Rammler distribution of five different droplet size data sets.

Data set	lognormal			Rosin Rammler		
	v.m.d	log(gsd)	r^2	v.d95	n	r^2
UH	3046	0.20	0.994	5494	2.76	0.876
DeepSpill	3953	0.50	0.994	7843	2.33	0.986
JF3-dive5	138	0.67	0.995	471	1.50	0.945
JF-2	447	0.19	0.995	828	2.66	0.933
BIO	78	0.46	0.994	167	2.08	0.996

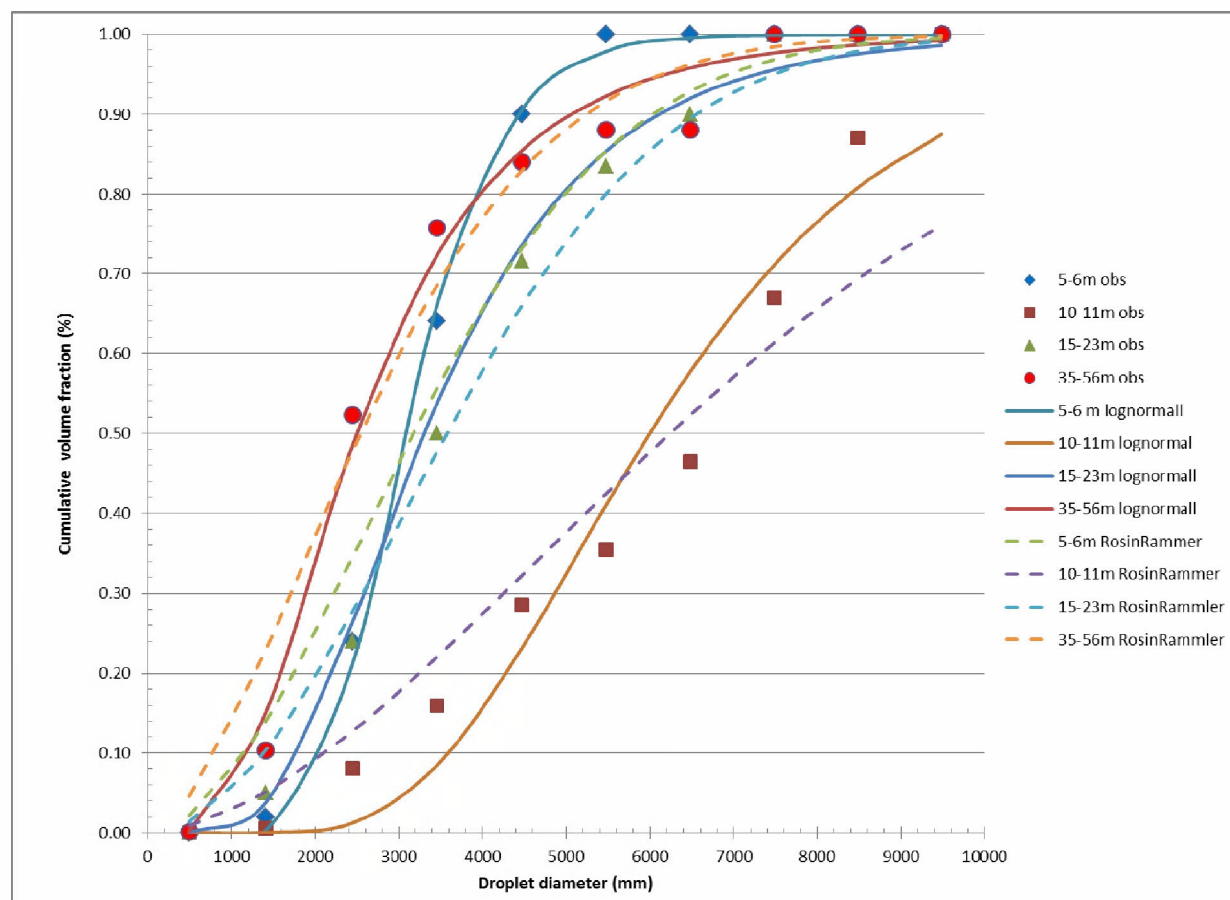
**Figure G-23: *Deep Spill* field data and fitted lognormal distribution ($R^2 = 0.956 - 0.999$) and Rosin-Rammler distribution ($R^2 = 0.905 - 0.991$) of oil droplet size distribution data at four different depths. The fitted parameters are listed in Table G-9.**

Figure G-23 presents the diesel oil droplet size distributions measured at four different depths above the release point during the *Deep Spill* field trial. Also shown in the figure are the correspondingly optimum lognormal and Rosin-Rammler size distribution fits to the data. For the lognormal volume distribution, the volume median diameter ranged from 2496 to 5994 μm , and the logarithmic geometric standard deviation ranged from 0.286 to 0.552. For comparison, the

Rosin-Rammler distribution predicts the d_{95} of oil droplets to be 6139 – 14,505 μm (or $8,766 \pm 3,865 \mu\text{m}$), with a spreading coefficient (n) of 1.666 to 1.985 (or 1.814 ± 0.145). The average R^2 of the fits for the lognormal distribution and the Rosin-Rammler distribution were 0.985 and 0.954, respectively.

Table G-9: Fitted parameters of lognormal versus Rosin-Rammler distribution of the droplet size distributions observed at four different depths above the release spot of the *Deep Spill* field trial.

Distance	lognormal			Rosin Rammler		
	v.m.d	log(gsd)	r^2	v.d95	n	r^2
5-6m	3073	0.286	0.999	6938	1.875	0.946
10-11 m	5994	0.399	0.956	14505	1.735	0.905
15-23 m	3306	0.479	0.996	7483	1.985	0.991
35-56 m	2496	0.552	0.989	6139	1.660	0.973

G5.2.3 Comparison of treated and untreated oil droplet size distributions using the new droplet size model

The new oil droplet size model was applied to compare predictions and observations of droplets for the DWH spill for the JF3 cruise time period (see details about the field observation in Appendix I, Analysis of *Holocam* oil droplet size distribution data). Among the nine ROV dives, there were five deep dives where the maximum ROV deployment depths were more than 1,000 m from the surface, or within approximately 500 m depth from the oil release depth (well head blowout preventer). Two dives (#5 and #6) were identified to have *much oil* in the deep water column based on manual analysis methods (Davis and Loomis 2014). The observed volume median droplet diameters from dives #5 and #6 were in the range of 70 - 218 μm and 73-250 μm , respectively, based on the surveyed oil droplets (i.e., Class 1 particles identified in Davis and Loomis 2014 automatic processing data). These droplets are probably mostly produced from the treated fraction, which is a reasonable assumption based on the well-separated treated versus untreated fractions (see Figures G-24 and G-25 and discussion below).

Figure G-24 shows the model-predicted cumulative volume oil droplet size distribution for the two bounding cases: either all oil treated or all oil untreated. If all the oil is treated, the median droplet size ranges from 20 to 200 μm , while if it is untreated, the range is from 800 to 10,000 μm . Figure G-24 also shows the cumulative volume distribution curves for a hypothetically partially treated case: 27% treated and 73% untreated. Finally the cumulative distribution is shown for the mixture of treated and untreated oil. The analysis indicates that more than 95 % of the dispersant treated oil droplets would have had droplet diameter small enough ($d \leq 300 \mu\text{m}$) so that they may be retained in the subsurface plume. Oil droplets up to 300 μm have been frequently measured at the JF3 ROV dives, all of which had the maximum volume diameter (d_{95}) around 300 μm (see Table G-4 of Appendix I). Conversely, more than 95% of non-treated oil droplets would be large enough ($d \geq 1,000 \mu\text{m}$) to escape from the plume in the near field, once the conic-shape buoyant blowout plume bent towards the horizontal orientation due to trapping. Droplets above 1,000 μm rise rapidly, and it takes less than 7 hours for these droplets to ascend from the trapping depth (1,100 m) to the surface (see Table 6-1 of the main report).

Table G-10: Values for variables used for the DWH release conditions

Variable	Value	Unit
σ_o	0.019	N/m
U	2.01	m/s
ρ_w	1027.76	kg/m ³
ρ_o	856	kg/m ₃
d_o	13432	μm

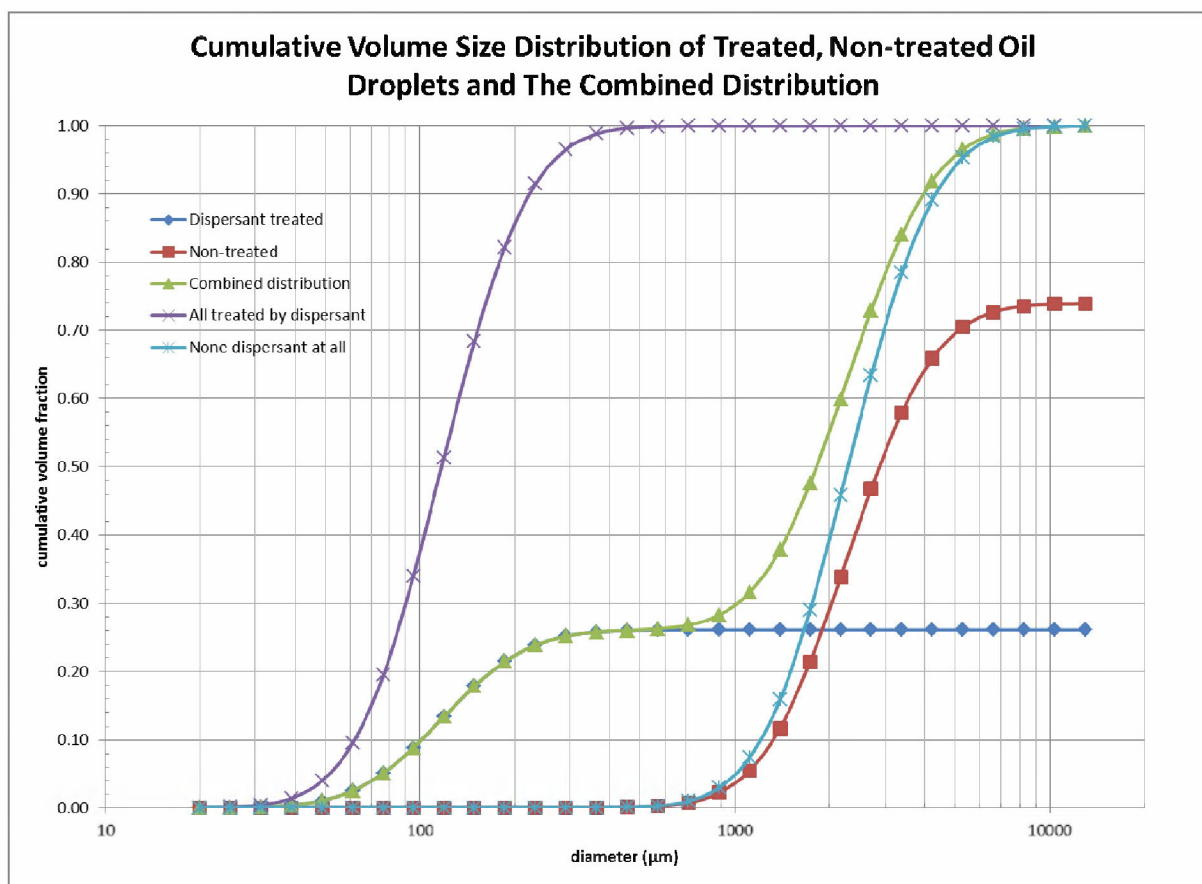


Figure G-24: Cumulative volume distribution of the chemically (purple) and physically (cyan) dispersed oil and their combined distribution (green) for DOR 1:40 with an assumed 73% (red) to 27% (blue) split between the untreated and treated oil, respectively.

Table G-11: The fraction of treated (at DOR 1:40) and non-treated oil and estimated lognormal distribution parameters.

	bbls	fraction	We	Oh	$\ln(\sigma_g)$	vmd (μm)
treated	10,360	0.27	41,465	1.24	0.5	119
non-treated	28,340	0.73	2,935	0.02	0.5	2,286

To explore the impact of DOR and the percent of oil treated, simulations were performed assuming DORs of 1:40, 1:90, and 1:150, with percent treated ranging from 0 to 100%. The first two values represent DOR cases explored in the Oil Budget Calculator (Lehr et al. 2010) and the last is representative of the approximate average value assuming all oil is treated for the *Jack Fitz 3* (JF3) cruise period (Appendix I). These DORs imply that 26.8% (1:40), 60% (1:90), 67% (1:100) and 100% (1:150) of the oil was treated given the dispersants that were available. Note, however, the application of chemical dispersant at subsurface was primarily accomplished using a wand device during pre-cut or trident device post-cut. In either case the best-estimate is that less than 1/3 cross-sectional area of the entire plume would be treated, rendering an *in situ* DOR quite different from the complete-mixing assumption.

Figure G-25 shows the model-predicted volume based droplet size distribution versus percent of oil treated, while Figure G-26 shows the corresponding cumulative volume distribution versus droplet size distribution. Cases are presented for DORs of 1:40, 1:90, and 1:150. These simulations used the same flow rate as for the JF3 cruise period (June 14 – 20, 2010) but assumed that the dispersant application is not limited by the dispersant available. If that limit was imposed, 26.5 (DOR: 1:40), 60 (1:90) and 100 % (1:150) would have been treated, as noted above. Figure G-26 shows that the droplet distributions for the treated and untreated oil are well separated for the 1:40 and 1:90 cases, and show very limited overlap even for the case at DOR 1:150. The degree of overlap is predicted to increase as the DOR increases, but doesn't become significant until values reach DORs of 1:150 or greater. In studying the distributions (Figure G-26), it is clearly seen that as the amount of oil treated increases, the amount of untreated oil decreases correspondingly. These simulations clearly show that for practical applications, the droplet size distribution remaining in the water column (droplets below 300 μm) is dominated by the treated oil.

The cumulative droplet size distributions show the expected shape for a compound distribution with the left side dominated by the treated oil and the right side by the untreated oil. The separation between the two decreases as the DOR decreases. At a DOR 1:150 the distributions partially overlap and the cumulative distribution smoothly transitions from treated to untreated oil.

In Figures G-25 – G-26, it was assumed that all the dispersants applied were 100% effective to achieve the DOR at a specific dispersant flow rate for a certain oil flow rate. This represents the optimum in terms of the volume of oil that can be treated for the amount of dispersant applied. However, in the real-world, subsurface blowout oil spill dispersant treatment application, the dispersant might be applied at dispersant efficiencies (or effectiveness) lower than 100%. This can be due to variations in the application strategy, logistic challenges, mixing behavior in the treatment plume, among many other reasons.

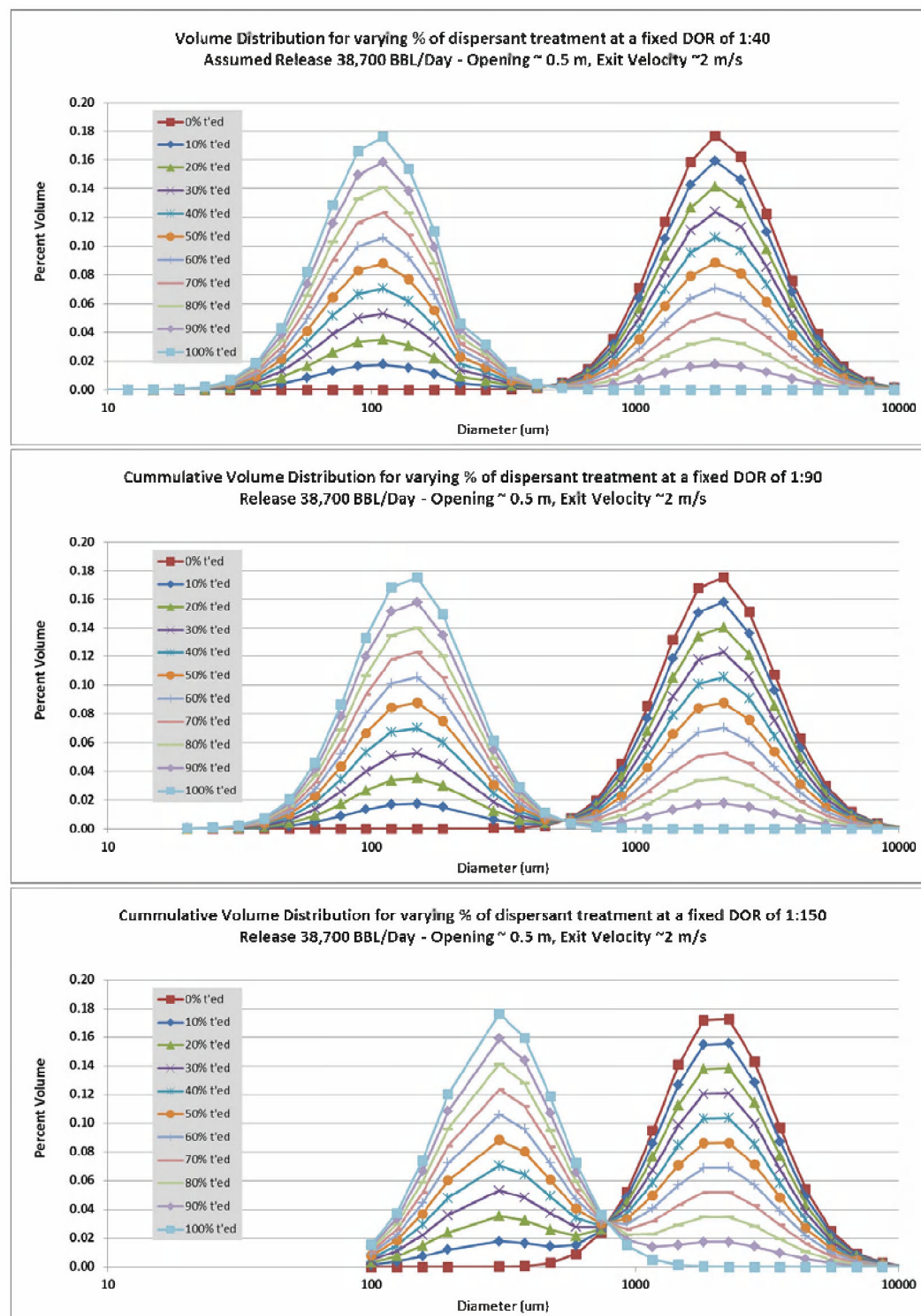


Figure G-25: RPS ASA droplet size model predicted oil droplet volume distribution assuming varying percent of oil treated (0 to 100%) for DOR: 1:40 (upper panel), 1:90 (center panel), and 1:150 (lower panel). A 38,700 barrel/day release rate at an exit velocity of 2 m/sec was assumed.

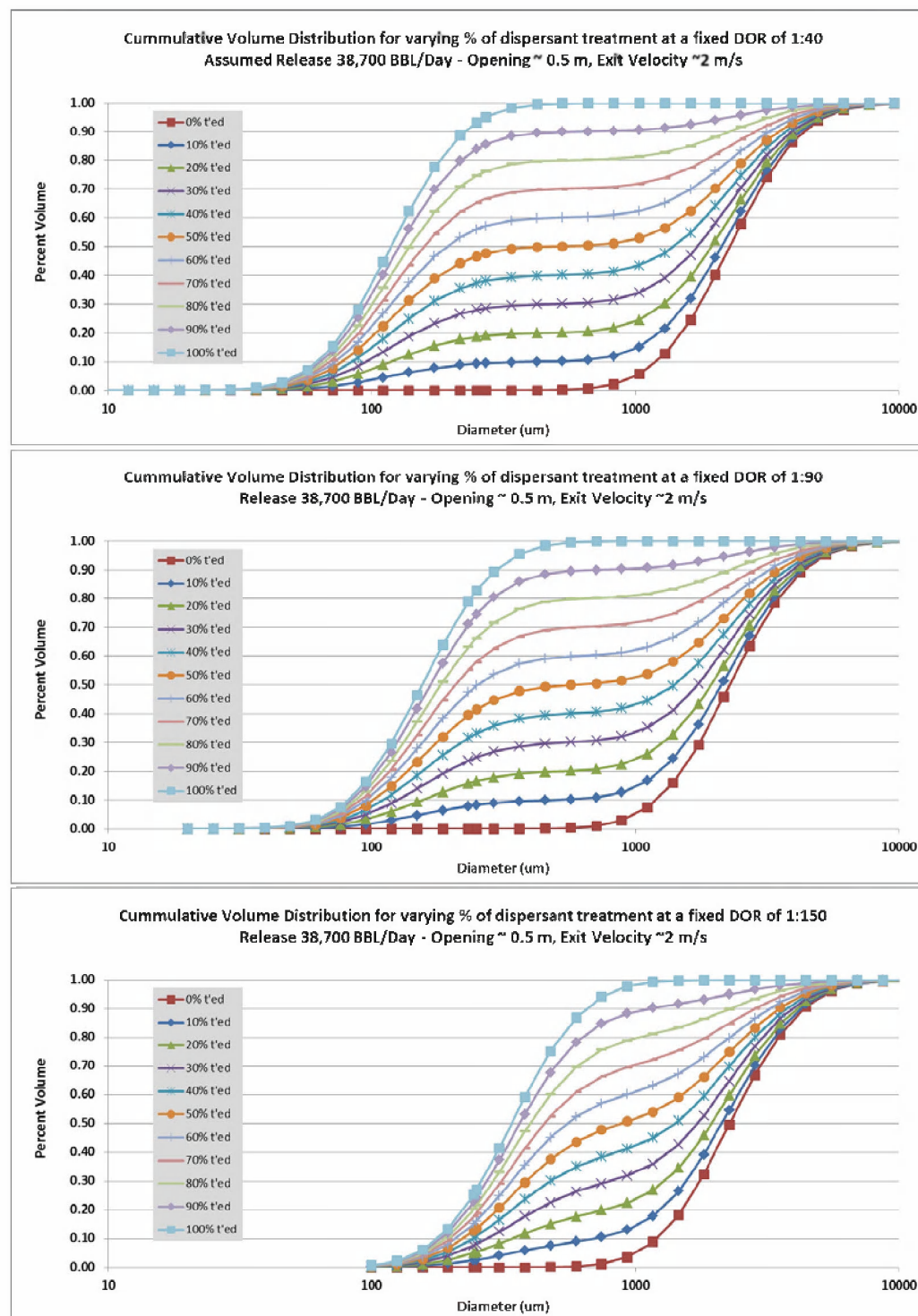


Figure G-26: RPS ASA droplet size model predicted cumulative oil droplet volume distribution assuming varying percent of oil treated (0 to 100%) for DOR: 1:40 (upper panel), 1:90 (center panel), and 1:150 (lower panel). A 38,700 barrel/day release rate at an exit velocity of 2 m/sec was assumed.

G6. Summary and conclusions

In this appendix, data of oil droplet (and few gas bubble) size distributions associated with blowouts and breaking wave turbulence at the sea surface have been reviewed from several small and large scale laboratory studies (including UHI, SINTEF, SL Ross, Delvigne and Sweeney, and BIO) and field measurements (including Deep Spill experiment and Deepwater Horizon oil spill field monitoring program). The oil droplet size data have been thoroughly reviewed and synthesized for the purposes of the evaluating, developing, calibrating, and validating a new oil droplet size distribution model.

Existing (including CDOG, Deep Blow, and an earlier version of OILMAP DEEP) and recently developed (such as SINTEF's modified Weber number method) oil droplet size distribution models have been reviewed, in an effort to evaluate their ability to predict the oil droplet and gas bubble distribution from a blowout under realistic field conditions, including application of dispersants for a subsurface blowout release.

The predictions of existing models, based on Weber number method, perform reasonably well in predicting the median droplet size for oil droplets generated in blowouts without treatment by dispersants. However, the predictions underestimate the median size of the dispersant-treated oil droplets, probably caused by the fact that there is no parameter in the models to account for the dispersed phase viscosity effect, which may suppress the further breakup and formation of small droplets. The SINTEF modified Weber number method introduced a viscosity number, to address the viscous effects, which become more important when oil-water interfacial tension is greatly reduced as a result of dispersant treatment. Comparison of the model prediction and experimental results, however, indicates that SINTEF modified Weber number method tends to over-predict the treated oil droplet sizes, even when the treatment has been conducted at an optimum DOR.

As a result of the critical review of data and existing droplet size models, a new OILMAP DEEP oil droplet size distribution model was developed that can be used to provide a more accurate prediction of oil droplet formation in the turbulent blowout release, under the complex balance mechanism of different forces, including inertia, buoyancy, interfacial tension, and viscous forces among the dynamic dispersed and continuous multi-phase flows. Based on the oil droplet formation mechanism, the new oil droplet size distribution model accounts for the forces relating the disruptive inertial momentum and buoyancy, and the restorative oil-water interfacial tension and the viscosity of the dispersed phase. The model has been developed based on the prediction of the volume median diameter of the generated oil droplets in turbulent shear flow. The VMD prediction is formulated based on the system characterization using two non-dimensional groups, the Weber and Ohnesorge numbers, which broadly define the disruptive and restorative forces acting in a blowout plume. The model constant coefficients were calibrated against a variety of experimental measurements, including data from surface oil entrainment due to breaking wave turbulence and the Deep Spill field experimental results. The oil droplet size distribution model was developed based on thorough review of the field data, which shows that the lognormal droplet size distribution, with a constant geometric standard deviation of the distribution, can best describe the distribution function of the blowout oil droplet sizes.

The new OILMAP DEEP oil droplet size model was also validated through comparison of model predictions and the small and large scale laboratory experimental results and the oil droplet size data obtained from the Deepwater Horizon oil spill field monitoring JF3 cruise ROV *Holocam* in

situ measurements. All these comparisons have demonstrated an excellent goodness-of-fit of the new droplet model predictions and the observational data. The comparison has clearly shown that the new droplet model provides good quality predictions of the observed size distributions for both treated and non-treated oil, if the DOR and oil flow rate is accurately specified.

G7. References

- Bandara, U.C. and P.D. Yapa. 2011. Bubble Sizes, Breakup, and Coalescence in Deepwater Gas/Oil Plumes. *Journal of Hydraulic Engineering-ASCE* 137: 729-738.
- Belore, R. 2014. Subsea chemical dispersant research. *Proceedings of The 37th AMOP Technical Seminar on Environmental Contamination and Response*, Environment Canada, Canmore, Alberta, Canada. Pp. 618-650.
- Brandvik, P. J., Ø. Johansen, F. Leirvik, U. Farooq and P. S. Daling. 2013. Droplet breakup in subsurface oil releases – Part 1: Experimental study of droplet breakup and effectiveness of dispersant injection. *Marine Pollution Bulletin* (73):319-326.
- Brandvik, P.J., Ø. Johansen, U. Farooq, G. Angell and F. Leirvik. 2014. Sub-surface oil releases – Experimental study of droplet distributions and different dispersant injection techniques- version 2. A scaled experimental approach using the SINTEF Tower basin. SINTEF report no: A26122. Trondheim Norway 2014. ISBN: 9788214057393.
- Byford, D.C., P.R. Laskey and A. Lewis. 1984. Effect of low temperature and varying energy input on the droplet size distribution of oils treated with dispersants. pp. 208-228 *Ottawa, ON, Canada*.
- Clayton, J.R.J., J.R. Payne and J.S. Farlow. 1993. *Oil Spill Dispersants: Mechanisms of Action and Laboratory Tests*. CRC Press, Inc. Boca Raton, FL.
- Crowley, D., D. Mendelsohn, N.W. Mulanaphy, Z. Li and M. Spaulding. 2014. Modeling Subsurface Dispersant Applications for Response Planning and Preparation. *International Oil Spill Conference Proceedings 2014(1)*:933-948.
- Daling, P.S., D. Mackay, N. Mackay and P.J. Brandvik. 1990. Droplet size distributions in chemical dispersion of oil spills: toward a mathematical model. *Oil and Chemical Pollution* 7: 173-198.
- Davis, C.S. and N.C. Loomis. 2014. Description of data processing methods used to determine oil droplet size distributions from in situ holographic imaging during June 2010 on cruise M/V Jack Fitz 3. Cabell S. Davis, Woods Hole Oceanographic Institution; Nick Loomis, MIT/WHOI Joint Program in Oceanography. 33 pages.
- Delvigne, G.A.L and L.J.M. Hulsen. 1994 Simplified laboratory measurement of oil dispersion coefficient - Application in computations of natural oil dispersion. *Proceedings of the Seventeenth Arctic and Marine Oil Spill Program (AMOP) Technical Seminar*, Vancouver, B.C., Environmental Protection Service, Environment Canada, pp.173-187.
- Delvigne, G.A.L and C.E. Sweeney. 1988. Natural dispersion of oil. *Oil and Chemical Pollution* 4: 281-310.
- EPA. 2013. EPA's list of authorized dispersants (NCP product schedule): The chemical components of the dispersants COREXIT 9500 and COREXIT 9527. Internet website: <http://www.epa.gov/bpspill/dispersants-qanda.html#list>. Accessed on October 14, 2014
- Gould, T.L., M.R. Tek and D.L. Katz. 1974. Two-phase flow through vertical, inclined, or curved pipe. *Journal of Petroleum Technology* 8: 915-926.
- Grace, J. R., T. Wairegi and J. Brophy. 1978. Break-up of drops and bubbles in stagnant media. *The Canadian Journal of Chemical Engineering* 56(1):3-8.

- Hatch, T. and S. Choate. 1929. Statistical description of the size properties of nonuniform particulate substances. *J. Franklin Inst.* 207: 369–387.
- Hinds, W.C. 1999. Particle Size Statistics. In: *Aerosol Technology: Properties, Behavior, and Measurement of Airborne Particles*, Chapter 4. Pp 75-109. John Wiley & Sons, Inc, New York, NY.
- Hinze, J. O. 1955. Fundamentals of the hydrodynamic mechanism of splitting in dispersion processes. *Journal of AIChE* 1:289-295.
- Jasper, W.L., T.L. Kim and M.P. Wilson. 1978. Droplet size distributions in a treated oil-water system. *Chemical Dispersants for the Control of Oil Spills*, ASTM STP 659, (McCarthy LTJ, Lindblom GP & Walter HF, . 203-216. American Society for Testing and Materials, Philadelphia, PA.
- Johansen, Ø. 2003. Development and verification of deep-water blowout models. *Marine Pollution Bulletin* 47(9-12):360-368
- Johansen, Ø., P.J. Brandvik and U. Farooq. 2013. Droplet breakup in subsea oil releases – Part 2: Predictions of droplet size distributions with and without injection of chemical dispersants. *Marine Pollution Bulletin* 73(1):327-335.
- Johansen, Ø, H. Jensen and A. Melbye. 2000. ROV Sonar and Visual Pictures from the Field Trial 'Deep Spill', June 2000, Technical Report, SINTEF Applied Chemistry, Trondheim, Norway.
- Johansen, Ø., H. Rye and C. Cooper. 2003. DeepSpill - Field study of a simulated oil and gas blowout in deep water. *Spill Science & Technology Bulletin* 8: 433-443.
- Johansen, Ø., H. Rye, A. Melbye, H. Jensen, B. Serigstad and T. Knutsen. 2001. Deep spill JIP experimental discharges of gas and oil at Jelland Hansen - June 2000, Technical Report, SINTEF Applied Chemistry, Trondheim, Norway.
- Karabelas, A.J. 1978. Droplet size spectra generated in turbulent pipe flow of dilute liquid/liquid dispersions. *AIChE Journal* 24: 170-180.
- Khelifa, A and L.L.C. So. 2009. Effects of chemical dispersants on oil-brine interfacial tension and droplet formation. In: *32nd Proceedings of Arctic and Marine Oil Spill Program Technical Seminar*, Environment Canada, Ottawa, Canada, pp. 383-396.
- Khelifa, A., D.M. Charron, T.-S. Tong and N.R. Singh. 2011. Effects of chemical dispersants on oil-brine interfacial tension and droplet formation: New results using new high resolution imaging setup and weathered oils. In: *34nd Proceedings of Arctic and Marine OilSpill Program Technical Seminar*, Environment Canada, Ottawa, Canada, pp. 865-879.
- Lee, K., Z. Li, M.C. Boufadel, A.D. Venosa and S.M. Miles. 2009. Wave tank studies on dispersant effectiveness as a function of energy dissipation rate and particle size distribution. Final report submitted to NOAA/CRRC/UNH. Pp67+ appendix..
- Lefebvre, A. H. 1989. *Atomization and Sprays*. New York, NY: Hemisphere Publishing Corporation.
- Lehr, B. 2014. Review of recent studies on dispersed oil droplet distribution. *Proceedings of the 37th AMOP Technical Seminar on Environmental Contamination and Response*, Environment Canada, Canmore, Alberta, Canada. In: 1 Pp. 1-8.

- Lehr, B, S. Bristol, and A. Possolo. 2010. Deepwater horizon oil budget calculator: A report to the national incident command. The Federal Interagency Solutions Group, Oil Budget Calculator Science and Engineering Team.
http://www.restorethegulf.gov/sites/default/files/documents/pdf/OilBudgetCalc_Full_HQ-Print_111110.pdf (Accessed on April 1, 2012).
- Lewis, A, D.C. Byford and P.R. Laskey. 1985. The significance of dispersed oil droplet size in determining dispersant effectiveness under various conditions.. American Petroleum Institute, Washington D.C.
- Li, M. and C. Garrett. 1998. The relationship between oil droplet size and upper ocean turbulence. *Marine Pollution Bulletin* 36:961-970
- Li, Z., K. Lee, T. King, M.C. Boufadel and A.D. Venosa. 2009a. Evaluating Chemical Dispersant Efficacy in an Experimental Wave Tank: 2, Significant Factors Determining In Situ Oil Droplet Size Distribution. *Environmental Engineering Science* 26: 1407-1418.
- Li, Z., K. Lee, T. King, M.C. Boufadel and A.D. Venosa. 2009b Evaluating crude oil chemical dispersion efficacy in a flow-through wave tank under regular non-breaking wave and breaking wave conditions. *Marine Pollution Bulletin* 58: 735-744.
- Li, Z., K. Lee, T. King, P. Kepkay, M.C. Boufadel and A.D. Venosa. 2009c. Evaluating Chemical Dispersant Efficacy in an Experimental Wave Tank: 1, Dispersant Effectiveness as a Function of Energy Dissipation Rate. *Environmental Engineering Science* 26: 1139-1148.
- Li, Z., K. Lee, T. King, M.C. Boufadel and A.D. Venosa. 2010. Effects of temperature and wave conditions on chemical dispersion efficacy of heavy fuel oil in an experimental flow-through wave tank. *Marine Pollution Bulletin* 60: 1550-1559.
- Li, Z., A. Bird, J. R. Payne, N. Vinhateiro and Y. Kim. 2014. Draft Physical-Chemical Technical Reports for Deepwater Horizon Water Column Trustees: Volume III. Oil Particle Data from the Deepwater Horizon Oil Spill. Date of Draft: January 18, 2013; Project No, 2011-144. RPS ASA, 55 Village Square Drive, South Kingstown, RI 02879
- Lunel, T. 1995. Understanding the mechanism of dispersion through oil droplet size measurements at sea. *The Use of Chemicals in Oil Spill Response*, ASTM STP 1252, (Lane P, ed.), pp. 240-270. American Society for Testing and Materials, Philadelphia, PA.
- Masutani, S.M. and E.E. Adams.. 2000. Experimental study of multiphase plumes with application to deep ocean oil spills. Final report to U.S. Dept. of Interior, Mineral Management Service, Contract no. 1435-01-98-CT-30946. pp147.
- Mugele, R.A. and H.D. Evans. 1951. Droplet size distribution in sprays. *Industrial and Engineering Chemistry* 43: 1317-1325.
- NRC. 1989. National Research Council: Using oil spill dispersant on the sea. Pp. 78-80. National Academy Press, Washington D.C.
- NRC. 2005. National Research Council: Understanding Oil Spill Dispersants: Efficacy and Effects. National Academies Press, Washington, D.C.
- Ohnesorge, W. 1936. Formation of drops by nozzles and the breakup of liquid jets. *Journal of Applied Mathematics and Mechanics* 16:355-358.

- Reed, M., Ø. Johansen, F. Leirvik, and B. Brors. 2009. Numerical algorithm to compute the effects of breaking waves on surface oil spilled at sea. Final report submitted to NOAA/UNH Coastal Response Research Center. Vol. 19 + appendices. SINTEF Institute for Materials and Chemistry.
- S.L. Ross. 2014. S.L. Ross Environmental Research Ltd, Subsea chemical dispersant research. Final Report, submitted to the Bureau of Safety and Environmental Enforcement (BSEE), U.S. Department of the Interior, Washington, D.C., under Contract E13PC00045.
- Simmons, M.J.H. and B.J. Azzopardi. 2001. Drop size distributions in dispersed liquid-liquid pipe flow. *International Journal of Multiphase Flow* 27(5):843-859.
- Tang, L. 2004. Cylindrical liquid-liquid jet instability. August 2004 Ph.D. Dissertation, University of Hawai'i.
- Venkataraman, P., J. Tang, E. Frenkel, G.L. Mcpherson, J. He, S.R. Raghavan, V.L. Kolesnichenko, A. Bose and V.T. John. 2013. Attachment of a Hydrophobically Modified Biopolymer at the Oil-Water Interface in the Treatment of Oil Spills. *Applied Materials & Interfaces* 5(9):3572-3580.
- Wang, C.Y. and R.V. Calabrese. 1986. Drop breakup in turbulent stirred-tank contactors, Part II: Relative influence of viscosity and interfacial tension. *AIChE Journal* 32(4):667-676.
- Yapa, P.D., L. Zheng and F.H. Chen. 2001. A model for deepwater oil/gas blowouts. *Marine Pollution Bulletin* 43(7-12):234-241.
- Yapa, P.D. and F.H. Chen. 2004. Behavior of oil and gas from deepwater blowouts. *Journal of Hydraulic Engineering, ASCE* 130(6): 540-553.
- Zhao, L., M.C. Boufadel, S.A. Socolofsky, E. Adams, T. King and K. Lee. 2014. Evolution of droplets in subsea oil and gas blowouts: Development and validation of the numerical model VDROD-J. *Marine Pollution Bulletin* 83(1):58-69.

Technical Reports for Deepwater Horizon Water Column Injury Assessment

WC_TR.13: Application of OILMAP DEEP to the Deepwater Horizon Blowout

Appendix H: Fountain and Intrusion Model Development

Authors: Malcolm Spaulding, Daniel Mendelsohn, Deborah Crowley,
Zhengkai Li, Andrew Bird

Revised: September 30, 2015

Project Number: 2011-144

RPS ASA 55 Village Square Drive, South Kingstown, RI 02879

Table of Contents

H1.	Introduction	1
H2.	Fountain and Intrusion model Theory	1
H2.1	Fountain and intrusion model defined for a quiescent environment without ambient currents	1
H2.2	Fountain and Intrusion flow in the presence of ambient currents	5
H3.	Extent and Flow Rate of the Intrusion Layer	6
H3.1	Plume Model Outputs as Input to the Fountain and Intrusion model	6
H3.2	Solution Method of Fountain and Intrusion Layer Flows in the Presence of Ambient Currents	7
H3.3	Results of Intrusion layer flows with Ambient Currents	8
H4.	Comparison to <i>in situ</i> Hydrocarbon Concentrations	13
H4.1	Hydrocarbon Chemistry Data of the Field Measurements	13
H4.2	Post-cut Period BTEX Mass Balance Analysis	18
H4.3	Summary of Hydrocarbon (BTEX) Mass Balance Analysis Results	21
H5.	Comparison to <i>In Situ</i> DOSS Concentrations during Post-cut Period	23
H5.1	Dispersant DOSS Chemistry Data of the Field Measurements	24
H5.2	Post-cut Period DOSS Mass Balance Analysis	27
H5.3	DOSS Data Summary	29
H6.	Summary	30
H7.	References	31

List of Figures

Figure H-1. Schematic of the interfacial spreading currents (intrusion layer) from Ansong et al. (2008).	2
Figure H-2. Conceptual scheme of intrusion layer deformation, spreading and transport in the presence of an ambient current (direction from left to right).....	5
Figure H-3. Plume model predicted total entrained volume flux at trap height for the riser (both pre- and post-cut) and the kink releases.	7
Figure H-4. Sensitivity analysis of the Fountain and intrusion model predicted intrusion layer volume flux as a function of distance from the wellhead for entrainment coefficients of 0.0625, 0.083, and 0.094 during pre-cut and post-cut period of the riser flow.	9
Figure H-5. Intrusion model predicted intrusion layer cross-sectional dimension (width, thickness) and mean velocity as a function of distance from the wellhead: Pre-cut riser (upper panel), Kink flow (middle panel), and Post-cut riser (lower panel). The entrainment coefficient was assumed as 0.083 (corresponding to a round buoyant plume) in these predictions.	11
Figure H-6. Model predicted intrusion layer volume flux and cross-sectional area as a function of distance from the wellhead. An entrainment coefficient of 0.083 (corresponding to round buoyant plume) was assumed for these predictions.	12
Figure H-7. BTEX observations over the course of the blowout period: (upper) BTEX concentrations as a function of distance from the wellhead, (b) BTEX concentrations as a function of date. Both pre and post cut values are shown.	15
Figure H-8. Direction effects on the BTEX sampling locations in the intrusion layer: Upper panel, Pre- cut versus post-cut sampling locations in the intrusion layer over the course of the blowout; Lower Panel, All sampling sites during the pre-cut and post-cut period between 1 and 10 km distance from the wellhead, and sampling depth between 1000 and 1200 m.	17
Figure H-9. Percent of detectable measurements in each direction from the wellhead (Spier et al. 2013).	18
Figure H-10: Intrusion model predicted daily post-cut intrusion layer water volume flux (based on an entrainment coefficient of 0.083 and at a distance of 1.5 km from the wellhead)	19
Figure H-11. Intrusion model predicted fraction of BTEX retained in the intrusion layer each day during the Post-cut period. Prediction was based on horizontal water entrainment coefficient of 0.083.	21
Figure H-12. Comparison of the pre-cut and post-cut cumulative fraction vs droplet diameter for various treatment assumptions. The intrusion layer is assumed to trap all droplets below a cut-off size of $d \leq 300 \mu\text{m}$. Displayed here are predictions from three dispersant-treatment cases: low-efficiency estimate, best-estimate, and high-efficiency estimate.	22
Figure H-13. Application rate of Corexit 9500A dispersant at the well (upper panel) and resultant DOSS mass flux (lower panel), from data in the Oil Budget Calculator (Lehr et al. 2010).	23
Figure H-14. Log (Concentration) (ppb) of DOSS vs depth (m) and distance from the well head are displayed. Note the data are presented in natural logarithm, hence in the subsurface	

intrusion layer the likely range of maximum DOSS concentration was about e^3 - e^4 (i.e., 20-55 $\mu\text{g/L}$).	24
Figure H-15. DOSS concentrations in the plume layer (see Figure H-14) from NRDA cruise post-cut cruises (upper panel), and the linear correlation of the paired BTEX and DOSS concentrations (lower panel).	26
Figure H-16. Fountain and intrusion model predicted fraction of DOSS retained in the intrusion layer each day during the post-cut period.....	29

List of Tables

Table H-1: Descriptive statistics of the plume layer BTEX concentrations ($\mu\text{g/L}$) during pre-cut (April 20 to June 2, 2010) and post-cut (June 3 to July 14, 2010) period.	14
Table H-2. Post-cut period (June 3 – July 14, 2010) mass balance analysis of trapped BTEX fraction in the intrusion layer.	20
Table H-3. The Pre-cut (April 22 to June 2, 2010) water column DOSS concentrations ($\mu\text{g/L}$) ..	25
Table H-4. Descriptive statistics of the plume layer DOSS concentrations ($\mu\text{g/L}$) during the post-cut (June 3 to July 14, 2010) period for all directions and from the southwest only	27
Table H-5. Post-cut period (June 3 – July 14, 2010) mass balance analysis of trapped DOSS fraction in the plume intrusion layer	28

H1. Introduction

One of the key questions in understanding the effects of the blowout is how much of the oil rose to the surface and how much remained trapped at depth. During early stages of the oil transport and fates, the initial plume rises rapidly through surrounding seawater as it is driven upwards by buoyancy forces. Within a few hundred meters of the release, the plume has lost sufficient gas through dissolution and entrained enough water to become neutrally buoyant and traps (i.e., stops rising). There is still a substantial volume flux associated with the plume however, which after overshooting the trap depth (fountain) is eventually forced laterally into an intrusion layer. The characteristics, transport and fate of the oil in the fountain and intrusion layer are the focus of this analysis.

There are many similarities between the trapping of the plume, its initial overshoot and subsequent development of an intrusion layer and a traditional fluid fountain in an un-stratified or stratified environment, reaching a maximum height and falling back and forming an intrusion layer. These similarities will be used to evaluate the fate of oil and other chemicals in the trapped plume.

In addition, during the course of the spill event, a significant amount of data was collected, including the concentrations in the water column of various chemicals associated with oil and the dispersants applied at the blowout that were used to track the oil. Validating the model predictions with observations will also provide confidence in using the model to estimate the total amount of oil that must have remained in the intrusion layer. In order to accomplish this, the bounding values of the thickness (height), width and spreading rates of the intrusion layer must be determined, over which the concentrations can be estimated. The following sections provide a description of theory, development, and application of the *fountain and intrusion model*, and a comparison of the model predicted results of intrusion layer flows and concentrations to the DWH spill observations.

H2. Fountain and Intrusion model Theory

H2.1 Fountain and intrusion model defined for a quiescent environment without ambient currents

The fountain and intrusion model, as developed for this application, is a series of analytical formulae that were integrated to describe the characteristics and fate of the blowout plume after it has become neutrally buoyant, trapped, and begins to flow laterally in the intrusion layer.

An estimate of the thickness of the intrusion layer and the flow rate in a quiescent environment can be determined using a simple fountain and intrusion model approach. Based on the work of Ansong et al. (2008), a relationship can be established between the intrusion layer spreading velocity, the initial buoyancy flux of a fountain impinging on a density interface, and the radial distance from the fountain centerline. A schematic of the formation of the fountain and intrusion layer is presented in Figure H-1.

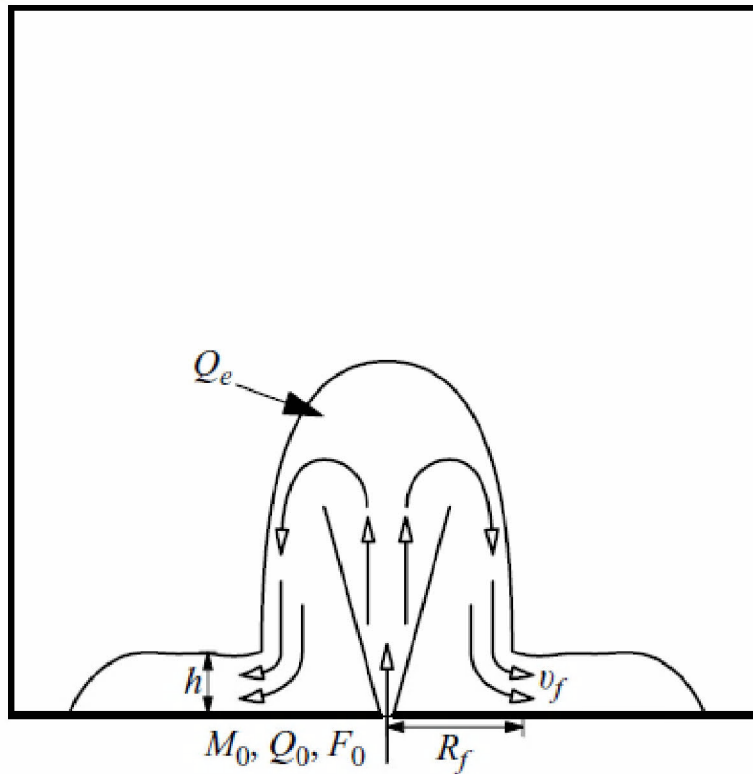


Figure H-1. Schematic of the interfacial spreading currents (intrusion layer) from Ansong et al. (2008).

Using Ansong et al's (2008) method, the total volume flux at the level of the source, just as the flow begins to spread outward is given by

$$Q_T = Q_e + Q_0 \quad \text{H.1}$$

where Q_T = total volume flux (m^3/s)
 Q_e = entrained volume flux (m^3/s)
 Q_0 = initial volume flux (m^3/s)

Ansong et al. (2008) also related the thickness of the intrusion layer as it spreads outward and extrudes, to the spreading velocity and the total plume volume flux (initial plus entrained) of a fountain, where the return flow redirects from a vertical to a horizontal flow (at the level of the source, just as the flow begins to spread outward) as

$$Q_T = 2\pi R_f h v_f \quad \text{H.2}$$

where R_f = radius of the return flow (m)
 h = corresponding thickness of the spreading layer (m)
 v_f = initial spreading velocity at a radial distance R_f (m/s)

Assuming a top-hat-shaped plume of radius r and mean vertical velocity w_o , the buoyancy flux can be written as:

$$F_0 = \pi r_0^2 w_0 g' \quad \text{H.3}$$

where F_0 = buoyancy flux (m^4/s^3)

$$g' = \frac{(\rho_a - \rho)}{\rho_0} g = \text{reduced gravity } (\text{m/s}^2)$$

r_0 = source radius (m)

w_0 = average vertical velocity at the source (m/s)

ρ_a = ambient density (kg/m^3)

ρ = density of the fountain at a given height (kg/m^3)

ρ_0 = reference density taken as the initial density of the fountain (kg/m^3)

For a buoyancy-driven flow, and using Equation H.2, dimensional analysis gives a relationship for the flow velocity of the form

$$v_r \propto \left(\frac{Q_T g'}{R_f} \right)^{1/3} \quad \text{H.4}$$

and since conservation of buoyancy requires that $g' Q_T = F_0$, Equation H.4 can be recast as

$$v_r \propto \left(\frac{F_0}{R_f} \right)^{1/3} \quad \text{H.5}$$

By balancing the driving buoyancy force and the retarding inertia force, Chen (1980) obtained the position of the front, R , as a function of time, t $R(t) = c F_0^{1/4} t^{3/4}$, (where $c=0.84$ is an experimental constant), thus the velocity term in Equation H.5 can be written as

$$v_r = 0.59 \left(\frac{F_0}{R_f} \right)^{1/3} \quad \text{H.6}$$

where conservation requires that $Q_T t = \pi R^2 h$. The radial velocity is evaluated first using Eq H.6 after which the intrusion layer thickness is calculated from the conservation Equation H.2.

Assuming a Gaussian profile for the velocity and that the plume density is not significantly different from the ambient, the mass flow, \dot{m} , and momentum flux, \dot{M} , of the intrusion layer can be written as:

$$\dot{m} = \pi^{3/2} \rho h v_r r \quad \text{H.7}$$

$$\dot{M} = \frac{\pi^{3/2}}{\sqrt{2}} \rho h v_r^2 r \quad \text{H.8}$$

At some distance from the turning region (where the falling fountain plume turns from an essentially vertical plume to the horizontal intrusion layer), viscous effects and in particular viscous entrainment becomes important. As ambient seawater is entrained into the intrusion layer, the thickness of the layer grows and the radial velocity decreases. In analyzing the viscous entrainment, it is convenient to assume the entrainment rate is proportional to the radial velocity, the contact surface ($2\pi r dr$) and an entrainment coefficient, β , such that the conservation of water mass and momentum can be written following Kolluru (1993) as:

Conservation of mass

$$\frac{d}{dr} \left(\pi^{3/2} \rho h v_r r \right) = 2\pi \rho \beta v_r \quad \text{H.9}$$

Conservation of momentum

$$\frac{d}{dr} \left[\frac{\pi^{3/2}}{\sqrt{2}} \rho h v_r^2 r \right] = 0.0 \quad \text{H.10}$$

The solution to Equations H.9 and H.10 are given, respectively, by

$$\frac{v_r}{v_{r_i}} = \left[1 + \frac{2\beta}{\sqrt{\pi}} \frac{r_i}{h_i} \left(\frac{r^2}{r_i^2} - 1 \right) \right]^{-1/2} \quad \text{H.11}$$

$$\frac{h}{h_i} = \frac{r_i}{r} \left[1 + \frac{2\beta}{\sqrt{\pi}} \frac{r_i}{h_i} \left(\frac{r^2}{r_i^2} - 1 \right) \right] \quad \text{H.12}$$

where v_{r_i} = initial horizontal velocity (m/s)

h_i = initial layer thickness (m)

r_i = initial radius (m)

Fannelop and Sjoen (1980) found that for the lateral spreading layer, a change in the character of the radial flow occurred at $r = 2b$, (twice the trapped plume half width, b) and therefore the mass flow and momentum flux Equations H.7 and H.8 can be written as

$$\dot{m} = \pi \rho w 2b^2 \quad \text{H.13}$$

$$\dot{M} = \frac{\pi}{2} \rho w^2 b^2 \quad \text{H.14}$$

which relates the vertical plume to the horizontal intrusion layer. The unknown initial conditions can now be determined at $r_i = 2b$ from Equations H.11 and H.12 as follows

$$v_i = w/\sqrt{2} \quad \text{H.15}$$

$$h_i = b/\sqrt{2\pi}$$

Defining a new set of dimensionless variables for the radius, R , radial velocity, V , and layer thickness, H , as

$$V = v_r/w$$

$$H = h/b \quad \text{H.16}$$

$$R = r/b$$

and combining Equations H.11, H.12, H.15, and H.16 and solving, the final forms of the dimensionless radial velocity and layer thickness are:

$$V = \left[2 \left(1 + \beta \sqrt{2} (R^2 - 4) \right) \right]^{-1/2} \quad \text{H.17}$$

$$H = \left[\frac{2}{\pi} \right]^{-1/2} R^{-1} \left(1 + \beta \sqrt{2} (R^2 - 4) \right) \quad \text{H.18}$$

which, for $R > 1$ (i.e. $r > b$) reduces to

$$V = R^{-1} (2\beta \sqrt{2})^{-1/2} \quad \text{H.19}$$

$$H = \beta R \frac{2}{\sqrt{\pi}} \quad \text{H.20}$$

Equations H.19 and H.20 are then easily employed to predict the decreasing radial intrusion velocity and increasing thickness of the layer as a function of radius. At larger distances from the vertical plume fountain area, the radial flow becomes analogous to a two dimensional source.

H2.2 Fountain and Intrusion flow in the presence of ambient currents

It should also be noted that the preceding intrusion layer radial velocity and thickness are both defined for a quiescent environment, i.e. no ambient currents. In the case of an ambient current, the symmetrical, expanding radial intrusion layer would be forced in the direction of the currents, as illustrated in Figure H-2.

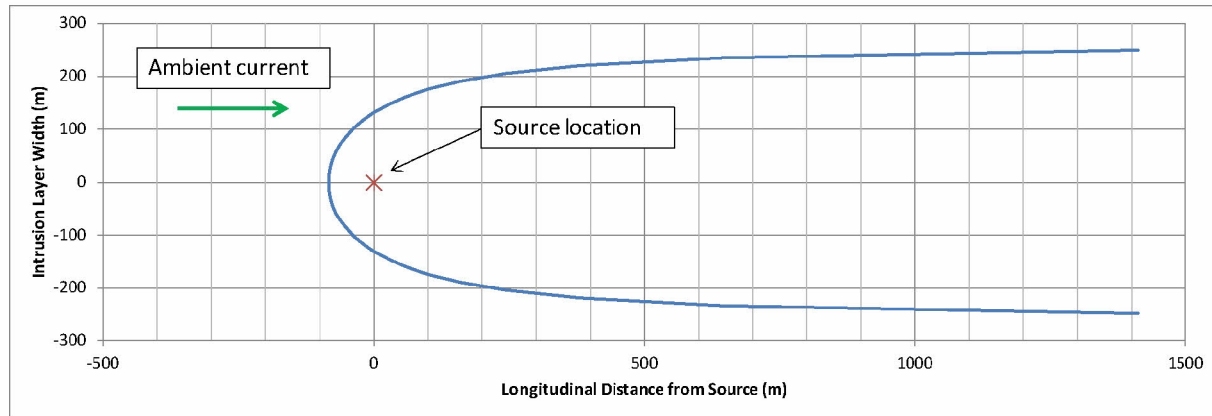


Figure H-2. Conceptual scheme of intrusion layer deformation, spreading and transport in the presence of an ambient current (direction from left to right).

Using the notion of a two dimensional source as seen from the far field, it is possible to develop a solution to the intrusion layer flow field in the presence of an ambient current using potential flow analysis methods (White 1979). The stream function, ψ , in the horizontal direction, for a two dimensional vertical line source (intrusion layer) can be represented as

$$\psi = \left(\frac{m}{2\pi}\right) \theta + U_{\infty} y \quad \text{H.21}$$

where U_{∞} = ambient current (m/s)
 m = line source strength (m^2/s)
 θ = angle (radians)
 y = cross-stream half width (m)

and the source strength m is a function of the plume radial velocity, v_r , from the fountain model calculations (Eq. H.6), evaluated at the plume half width, and the plume half width, b such that

$$m = bv_r \quad \text{H.22}$$

The radial coordinates for the edge of the bent intrusion layer can now be defined in terms of the angle and the radial distance from the source, the source strength, and the ambient velocity as

$$r = \frac{m(\pi - \theta)}{U_{\infty} \sin \theta} \quad \text{H.23}$$

The Cartesian coordinates are then simply

$$x = r \cos \theta, \quad y = r \sin \theta \quad \text{H.24}$$

And the Cartesian velocity components are found by differentiation of the stream function, ψ

$$u = \frac{\partial \psi}{\partial y} = U + \frac{m}{r} \cos \theta, \quad v = -\frac{\partial \psi}{\partial x} = \frac{m}{r} \sin \theta \quad \text{H.25}$$

The upstream extent of the intrusion, is a “stagnation” point where $u = v = 0$, and is located at $(x, y) = (-a, 0)$, where $a = m/U_\infty$.

The horizontal dimension and velocity of the intrusion through the ambient, defined by Eqs H.24 and H.25 can now be used in concert with the intrusion layer thickness estimates defined by Eq H.20 to estimate the dimensions and extent of the intrusion layer. The velocity of the intrusion is initially in excess of the ambient velocity, so the absolute intrusion layer velocity is found by adding the two. The entrainment and therefore the growth of the intrusion layer is based on the velocity difference between the intrusion and the ambient and would thus decrease over time as the intrusion velocity decreased, approaching a theoretical asymptote. In practice, the intrusion layer transitions to passive advection at some nominal excess velocity.

H3. Extent and Flow Rate of the Intrusion Layer

H3.1 Plume Model Outputs as Input to the Fountain and Intrusion model

Assuming a fixed release rate of 62,000 barrels per day ($0.114 \text{ m}^3/\text{s}$), which is an estimate for flow from the well in the early stages of the blowout (McNutt et al. 2011); the *blowout plume model* predicted a trap height of 350 m above the bottom. The total entrained volume flow rate at the trap height was predicted to be approximately, $2,200 \text{ m}^3/\text{s}$. Figure H-3 presents the blowout-plume model predicted total entrainment volume flux at the trap height for the riser (pre and post cut) and the kink release over the blowout period. For the 62,200 bbl/day oil release rate early in the blowout, a total entrained volume flux of the plume at trap height would be $2,200 \text{ m}^3/\text{s}$, decreasing gradually to approximately $1,500 \text{ m}^3/\text{sec}$, corresponding to the decreasing amount of oil and gas released into the water column as the blowout spill progressed daily and oil recovery operations were instituted. The transition between the pre-cut riser and the post-cut periods is clearly seen in the peak value of the riser flow on June 3. The entrained volume flux from the kink is about $500 \text{ m}^3/\text{sec}$ and increases slightly with time as the number of holes at the kink increases, from 2 to 6, particularly immediately before the riser was cut. These daily volume fluxes were used as input to the *fountain and intrusion model*.

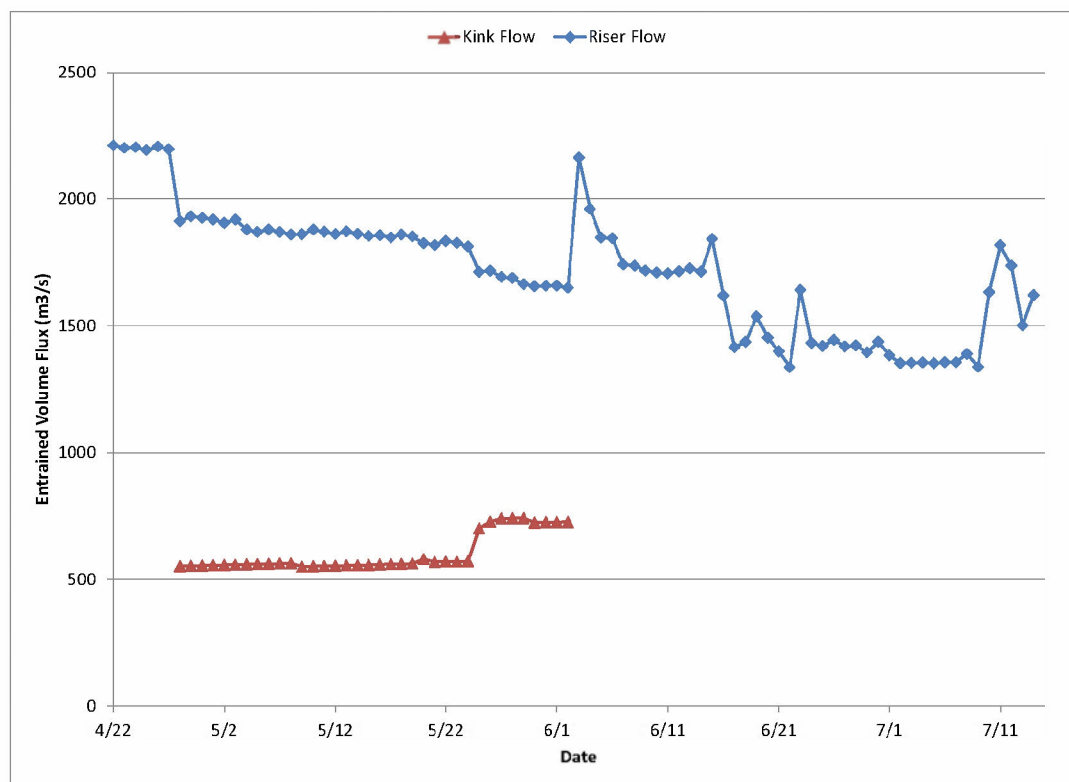


Figure H-3. Plume model predicted total entrained volume flux at trap height for the riser (both pre- and post-cut) and the kink releases.

H3.2 Solution Method of Fountain and Intrusion Layer Flows in the Presence of Ambient Currents

The fountain and intrusion model were applied to predict the intrusion flows for three release scenarios, namely riser pre-cut, kink flow, and riser post-cut flow. The transition of the returning overshooting fountain to a level of neutral buoyancy and horizontal intrusion flow was assumed to occur at twice the half-width of the descending blowout plume at the trap height (i.e., $R_f = 2b$). Based on this transitional distance, the initial buoyancy flux (F_0), the buoyancy-driven horizontal velocity (v_r), and the corresponding height of the spreading layer (h) were calculated for each day of each release scenario using Eq. H.3, H.6, and H.2, respectively.

The intrusion layer variables, including the source strength (m), the radial coordinates for the edge of the bent intrusion layer plume (\vec{r}), the plume downstream distance (x) and half-width (y), and the velocity components (u and v) can be calculated using Eq. H.22, 23, 24, and 25, respectively.

The calculation of the intrusion layer thickness also started at the assumed transition from the returning fountain to the lateral flow at $R_f=2b$. The calculation was performed using Eq. H.19-20, based on the definition of the dimensionless variables in Eq. H.16. The horizontal entrainment coefficient (i.e., β in Eq. H.19-20) was initially taken as an empirical constant (see Section H3.3). As the intrusion layer plumes were carried downstream by the ambient current flow, the plume volume flux increased and the velocity decreased due to the continually entrained ambient

seawater and the loss of inertia to overcome viscous forces. To simulate this effect, the horizontal entrainment was assumed to decrease as a function of the velocity difference between the intrusion layer and ambient current flow. Therefore the horizontal entrainment asymptotically approached zero eventually after the intrusion layer reached the same velocity as the ambient current flow.

H3.3 Results of Intrusion layer flows with Ambient Currents

The average ambient currents at the 350 m trap height above the bottom are estimated to be in the range of 6.7 to 6.9 cm/sec with a standard deviation of 4.7 to 5.2 cm/sec, based on ADCP measurements at the release location (see Blowout Main Report). The mean ambient current speed is therefore estimated to be 6.8 cm/sec. Given the ambient currents the spreading intrusion layer is expected to be deformed and forced in the direction of the ambient flow. Kolluru (1993) presented a horizontal spreading plume model that accounted for entrainment, using a coefficient similar to the buoyant plume entrainment value, and recommended a value of 0.083, as presented in Equations H.19 and H.20. For comparison Jirka (2004) reviewed equations for five self-similar asymptotic regimes of turbulent round buoyant jets in unbounded stratified flows, and proposed entrainment coefficients of 0.055, 0.083, 0.11, 0.5, and 0.5 for single source round jet, plume, wake, advected line puff, and advected thermal puff, respectively. In a later paper, Jirka (2006) also reviewed the plane jet dynamics resulting from multipoint diffuser jets, and proposed entrainment coefficients of 0.0625, 0.125, 0.094, 0.5, and 1.5 for a pure plane jet, pure plane plume, pure plane wake, advected line puff, and advected thermal puff, respectively.

It is clear that the selection of the entrainment coefficient of the horizontal plume in the intrusion model may have a significant impact on the prediction of the growth of the plume cross sectional areas and the volume fluxes. It is also clear that immediately prior to the trap depth the plume is likely a round buoyant plume, which results in a fountain, and ultimately converts into a plane wake flow as the distance from the centerline of the trapping location increases (Figures H-1 and 2) and the momentum of the plume is dissipated. A sensitivity analysis was therefore conducted to show the effect of the selection of the entrainment coefficient on the intrusion volume layer flux. Figure H-4 presents the predicted kink-flow and post-cut riser flow related horizontal plume intrusion layer fluxes as a function of distance, for three different entrainment coefficients: 0.0625, 0.083, and 0.094. The predictions start at a distance of $R = 2b$ downstream from the release location. These entrainment coefficients were selected based on Jirka (2004, 2006) review of integral model for turbulent buoyant jets in unbounded stratified flows, including single round jet (Jirka 2004) and multipoint diffuser plane jet dynamics (Jirka 2006). Jirka (2006) identified five asymptotic regimes for plane jet geometry formed from a finite length slot discharged into unbounded ambient stratified flow. In an environment with constant velocity (u_a) and constant gradient of buoyancy ($\epsilon = (g/\rho_a)(dp_a/dz)$) and beyond the initial zone of flow establishment (ZOF), the plane buoyant jet behavior is controlled by the parameters including ambient current speed (u_a), ambient fluid buoyancy (ϵ), specific source flow buoyancy flux, as well as the specific source transverse momentum flux (m_{ot}) and the excess longitudinal momentum flux (m_{oe}). The five regimes (and their entrainment coefficients) were (i) pure plane jet (0.0625), (ii) pure plane plume (0.125), (iii) pure plane wake (0.094), (iv) advected plane puff (0.5), and (v) advected plane thermal (1.5). Among these, the first and the third regimes have common conditions with present analysis in terms of ambient current speed, source buoyancy flux, and source momentum flux. The entrainment coefficients for these two cases are 0.0625 and 0.094, respectively. The third coefficient (0.083), which is between the two bounds, was

recommended by Kolluru (1993) in the prediction of surface horizontal intrusion layer as a result of blowout release of oil and gas, and hence was also included here. The real flow transition in the present analysis could be very complex and might be mixed processes of round buoyant plume, pure plane jet, and pure plane wake. A possible scenario for the transition from vertical buoyant plume to horizontal intrusion layer may be as follows. As the fountain flow descends (Figure H-1) it behaves like a negatively buoyant round plume; when it starts to spread radially it becomes a pure plane jet, since it has lost its buoyancy but still has some momentum, and eventually the plane jet converts to a pure plane wake (Figure H-2); so, the related entrainment coefficient is initially 0.083 and, in the near field of the intrusion layer, changes to 0.0625 (if it behaves more of a plane jet) or 0.0904 (if it behaves as a plane wake). In the far field of the intrusion layer, however, the entrainment is restrained by ambient density stratification which inhibits entrainment, so 0.094 is upper bound and likely only applies for a short distance. If one assumes a constant value of entrainment coefficient, the bounding values are between low 0.0625 and high 0.094, with a best estimate of 0.083.

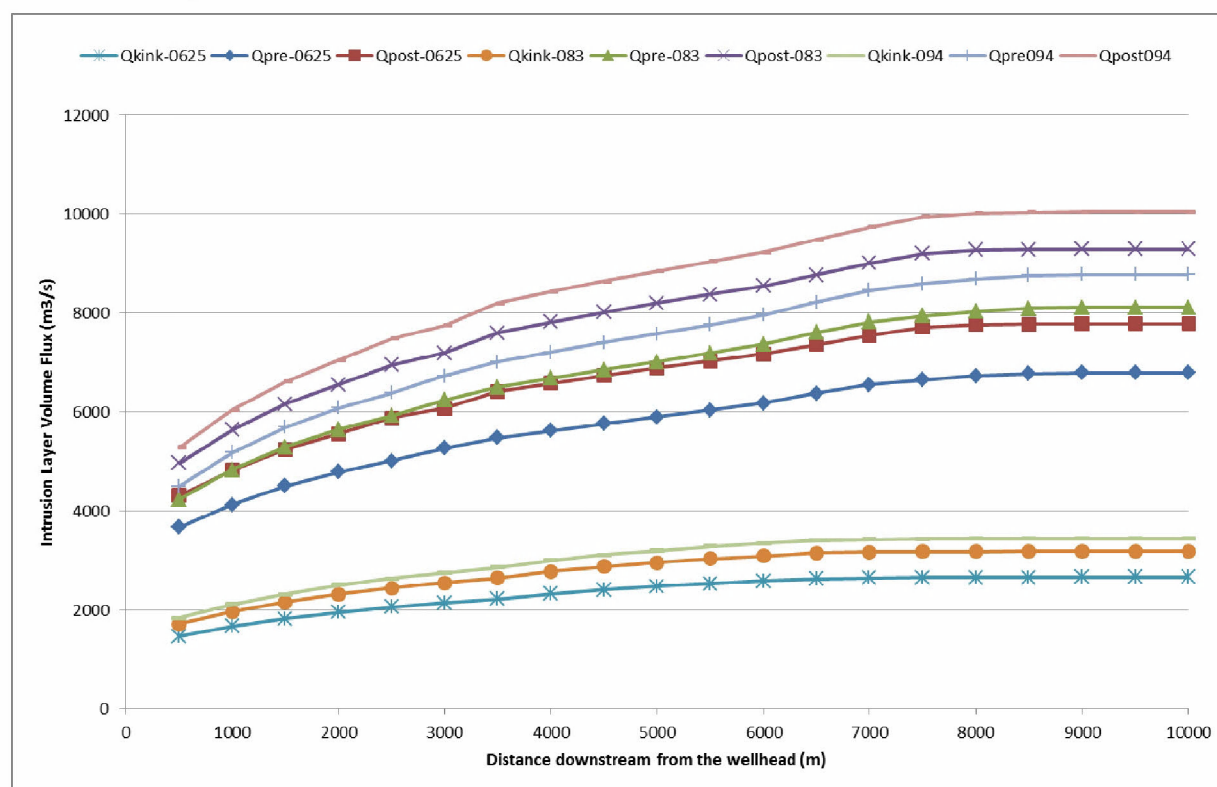


Figure H-4. Sensitivity analysis of the Fountain and intrusion model predicted intrusion layer volume flux as a function of distance from the wellhead for entrainment coefficients of 0.0625, 0.083, and 0.094 during pre-cut and post-cut period of the riser flow.

The oil release rates for this simulation are: Pre-cut average 49,334 bbls/day, post-cut average 38,548 bbls/day, and kink average 12,263 bbls/day. The predicted plume volume fluxes, for entrainment coefficients of 0.0625 ~ 0.094, range from 6,500 to 10,000 m^3/s (Figure H-4) and compare reasonably well with the corresponding near field deep water plume volume flux values estimated by Camilli et al. (2010) and Kujawinski et al. (2011). Camilli et al. (2010)'s analysis falls into the post-cut period, whereas Kujawinski et al. (2011) reported time (May/June) may fall in pre-cut or post-cut time. Camilli et al. (2010) defined the subsurface plume cross section

detected at 16 km down-range of the source on June 26, 2010 (within the post-cut period) to be 778 m wide (estimated based on the mass spectrometer methane data) and 116 m high (estimated based on the gas chromatography Benzene, Toluene, Ethylbenzene, and o-, m-, and p-Xylene (BTEX) data). Assuming the average current flow speed of 0.078 m/s that they used, the volume flux is estimated to be 7039.3 m³/s. Kujawinski et al. (2011) assumed the deep water plume (between 1 to 10 km distance from the wellhead) to be 100 m high based on their measured vertical region of high dispersant constituent (DOSS, see below) concentrations during May/June 2010 cruises, and 1 km wide referenced from Camilli et al. (2010) mass spectrometry methane data; once again assuming the mean current flow speed of 0.078 m/s, the volume flux is estimated as 7,800 m³/s. These estimated water volume fluxes values are in general agreement with the asymptotic intrusion layer volume fluxes from the present model. For example, the asymptotic flux was predicted 8105 m³/s and 9283 m³/s, respectively, for the pre-cut and post-cut period with entrainment coefficient of 0.083; and 6783 m³/s and 7777 m³/s, respectively, for the pre-cut and post-cut period with an assumed entrainment coefficient of 0.0625.

Assuming the mean entrainment coefficient of 0.083, representative of a round plume, and using the intrusion model entrainment equations presented in Section 2, the intrusion layer flow parameters were calculated including the cross-sectional width, thickness, area, mean velocity, and volume flux. Figure H-5 presents the model predicted intrusion layer cross-sectional dimensions (width, thickness) and mean cross sectional velocity as a function of downstream distance from the well head for the pre-cut riser, post-cut riser, and kink- associated horizontal intrusion layers, respectively. Figure H-6 shows the mean values of the intrusion layer flux and cross-sectional area as a function of downstream distance from the well head for the pre-cut riser, post-cut riser, and kink- associated horizontal intrusion layer, respectively. The pre and post riser cut plume volume fluxes are shown for reference. In Figure H-6, the term “plume” refers to the buoyant, rising plume prior to trapping, and “intrusion” refers to the horizontally flowing, trapped intrusion layer.

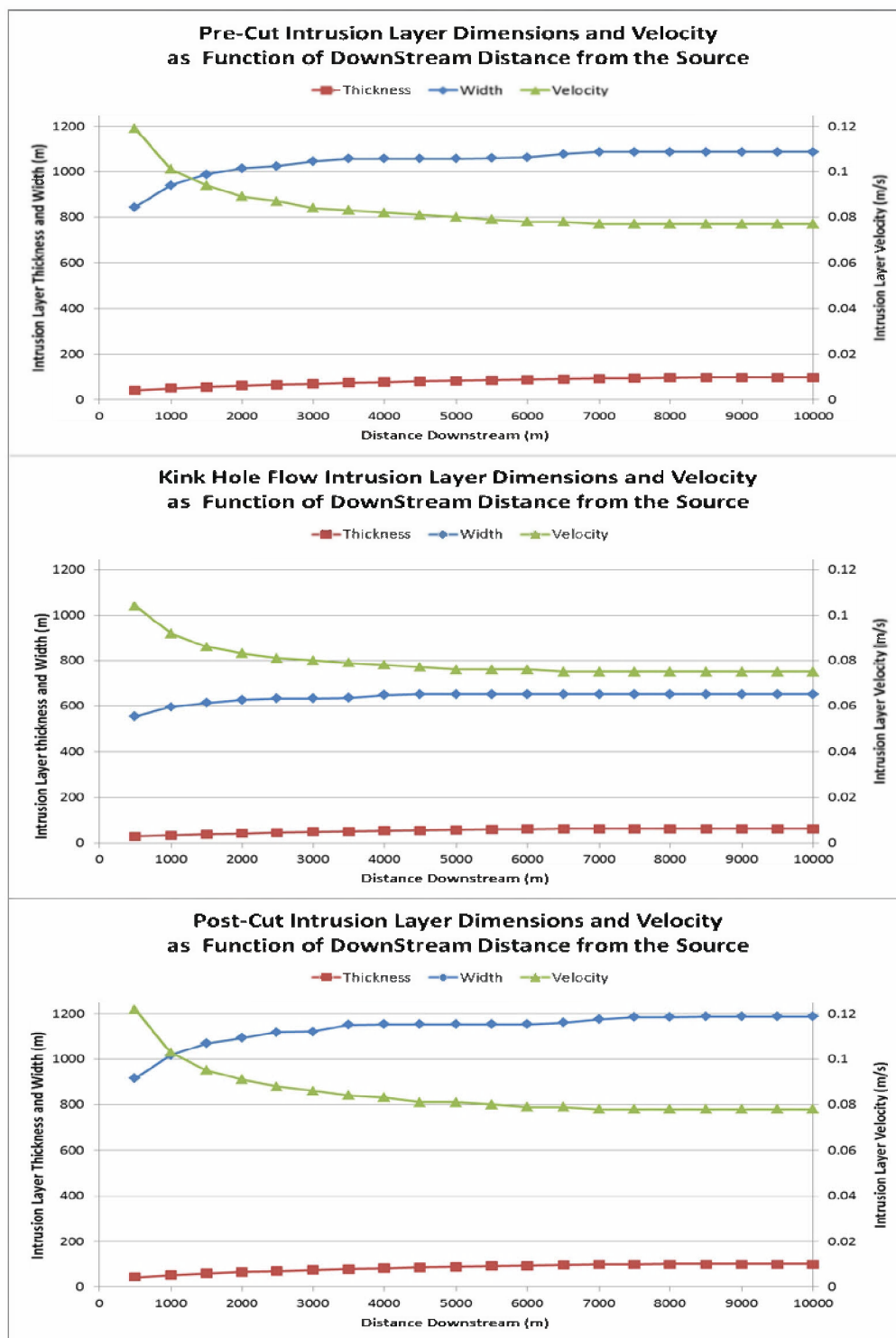


Figure H-5. Intrusion model predicted intrusion layer cross-sectional dimension (width, thickness) and mean velocity as a function of distance from the wellhead: Pre-cut riser (upper panel), Kink flow (middle panel), and Post-cut riser (lower panel). The entrainment coefficient was assumed as 0.083 (corresponding to a round buoyant plume) in these predictions.

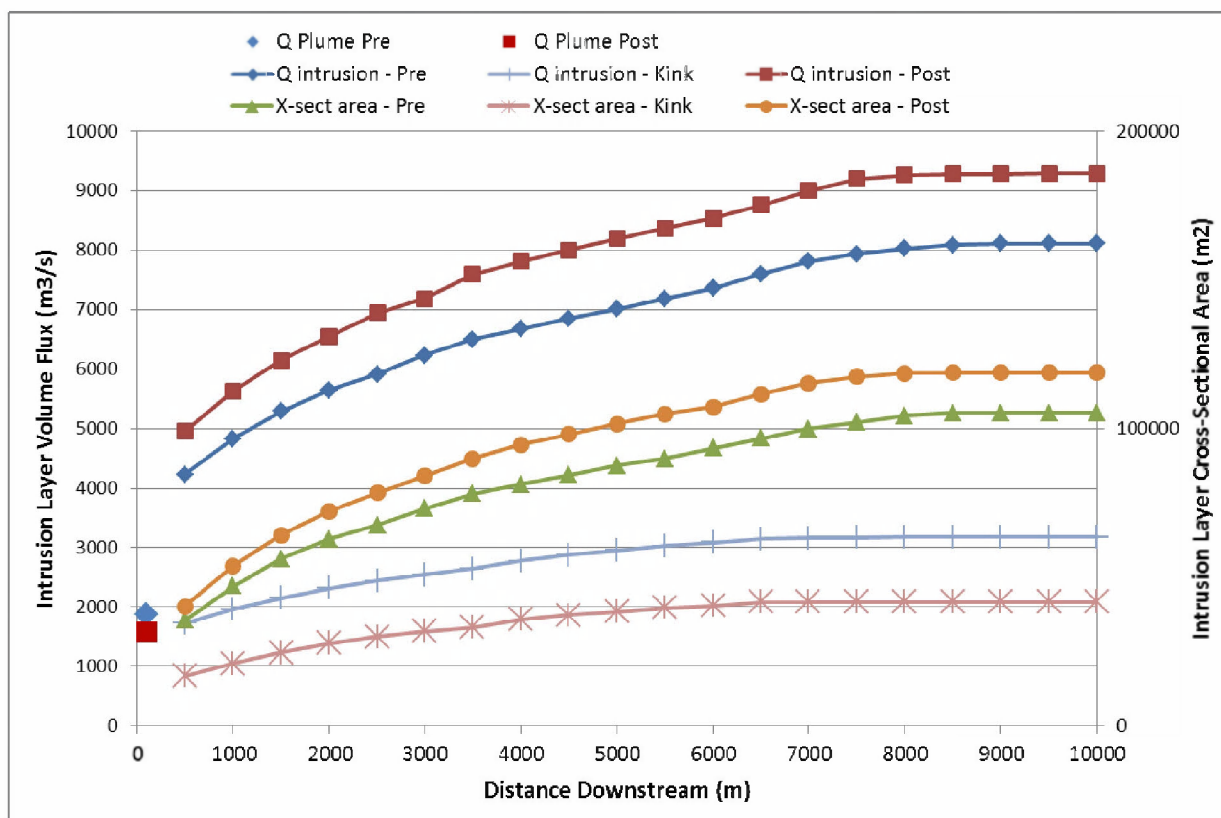


Figure H-6. Model predicted intrusion layer volume flux and cross-sectional area as a function of distance from the wellhead. An entrainment coefficient of 0.083 (corresponding to round buoyant plume) was assumed for these predictions.

H4. Comparison to *in situ* Hydrocarbon Concentrations

To determine the percent of oil retained in the intrusion layer, an analysis was performed based on the hydrocarbons released from the source and those that were observed to trap. Due to the inhomogeneous distribution of hydrocarbon compounds in the water column in the area surrounding the well head and the difficulties in measuring concentrations in a temporally and spatially varying release from surface deployed instruments, it is a significant challenge to perform a very accurate mass balance analysis based on the comparison of the measured *in situ* hydrocarbon concentrations and the results of model prediction. Therefore, the uncertainty in this type of analysis must be appreciated in the interpretation of the results.

In the following comparison of field data and model predictions, the entire spill duration (from April 22 to July 14, 2010) was divided into two major time periods – pre-cut and post-cut. The pre-cut period corresponds to the dates between April 22 and June 2, 2010; post-cut period includes the dates between June 3 and July 14, 2010. During the pre-cut period, the cumulative amount of oil released into the environment accounted for about 60.61% of the total oil mass released over the entire duration of the spill. During the post-cut period, the remaining 39.39% was released. In addition, there was considerable daily variation of the amount of oil released, and dispersants applied at the wellhead. The dispersant application method also varied with time. To consider these varying conditions, the amount of oil retained in the plume intrusion layer was calculated for each day, based on the daily variation of the amount of oil released, and the amount and application method of the subsurface dispersant applied. The average percentage of the oil fraction retained in the plume layer during the post-cut time period was then estimated. Uncertainties for the analyses were represented by the prediction of intrusion layer flow rate estimation (based on the intrusion model prediction) and the intrusion layer hydrocarbon compound group concentration estimation (based on the analysis of chemistry samples collected from the field).

H4.1 Hydrocarbon Chemistry Data of the Field Measurements

BTEX includes a group of hydrocarbon compounds that are ideal candidates for the analysis of mass balance based on their availability from field measurements. The un-weathered DWH source oil contained about 1.9 % by weight of total BTEX (19,124 µg BTEX /g oil), which in turn included 0.24% (2,351 µg/g oil) benzene. Published literature shows that the subsurface intrusion layer is comprised of highly soluble components such as BTEX (Reddy et al. 2012) and a smaller fraction of insoluble hydrocarbons (Ryerson et al. 2011). BTEX, along with polycyclic aromatic hydrocarbons, are also thought to be responsible for the CDOM fluorometry measurement anomalies and indications of the subsurface hydrocarbon plume. These groups have very different water-solubility. BTEX are most soluble in water, with a DWH MC252 source oil fraction weighted - solubility of 495 mg/L at 25°C. As the primary focus of the present analysis was on the fraction of oil retained in the subsurface intrusion layer, predictions based on the most soluble compounds, namely BTEX, would likely best represent the fraction of oil retained in the subsea intrusion layer.

Field samples collected in close proximity to the DWH well head were screened for this analysis based on the following criteria: (1) sampling collected between April 20 and June 2, 2010 for the pre-cut period, and between June 3 and July 14, 2010 for the post-cut period; (2) sampling depths between 1,000 m and 1,200 m, the observed depth range of plume trapping; (3) sampling distance between 1 km and 10 km from the well head (representing near field

conditions where sampling is most likely to capture the intrusion layer) ; (4) positive (detectable) values of BTEX; and (5) for post-cut period, positive values of DOSS (a constituent of Corexit 9500 dispersant, see below) (DOSS is used in an additional analysis presented later in the text as a proxy for the amount of dispersant trapped).

Among all the available DWH NRDA chemistry BTEX data, there were 40 samples pre-cut and 83 samples post-cut that were found to meet these screening criteria. Figure H-7 displays the measured BTEX concentrations in the intrusion layer plotted as a function of distance and time. This plot clearly indicates the large variability in BTEX concentrations both as a function of distance from the wellhead (Figure H-7, upper panel) and date of sampling (Figure H-7, lower panel). There is no clear trend with distance within approximately 6 km, but the values beyond this distance, especially post-cut, appear to be lower on average than the average closer than 6 km. With respect to sampling time, the measured BTEX concentrations pre-cut, on average, are higher (103 µg/L) than the post-cut values (51 µg/L). Table H-1 summarizes the descriptive statistics of the field measurements for the pre-cut and post-cut periods. The analysis includes all directions as well as just from the predominant drift direction to the southwest.

Table H-1: Descriptive statistics of the plume layer BTEX concentrations (µg/L) during pre-cut (April 20 to June 2, 2010) and post-cut (June 3 to July 14, 2010) period.

	<i>Pre-cut</i>		<i>Post-cut</i>	
	<i>All Direction</i>	<i>Southwest only</i>	<i>All Direction</i>	<i>Southwest only</i>
Mean	103.300	100.80	51.085	60.069
Standard Error	11.750	12.48	4.995	7.638
Median	94.045	91.73	40.703	48.920
Mode	#N/A	#N/A	#N/A	#N/A
Standard Deviation	70.502	71.72	45.503	47.698
Sample Variance	4970.480	5143.31	2070.566	2275.108
Kurtosis	-1.125	-1.14	0.460	-0.002
Skewness	0.227	0.28	1.139	0.936
Range	223.250	223.25	171.853	171.337
Minimum	4.450	4.45	4.347	4.863
Maximum	227.700	227.70	176.200	176.200
Sum	3718.812	3326.55	4240.035	2342.697
Count	36	33	83	39
Confidence Level (95.0%)	23.854	25.43	9.936	15.462

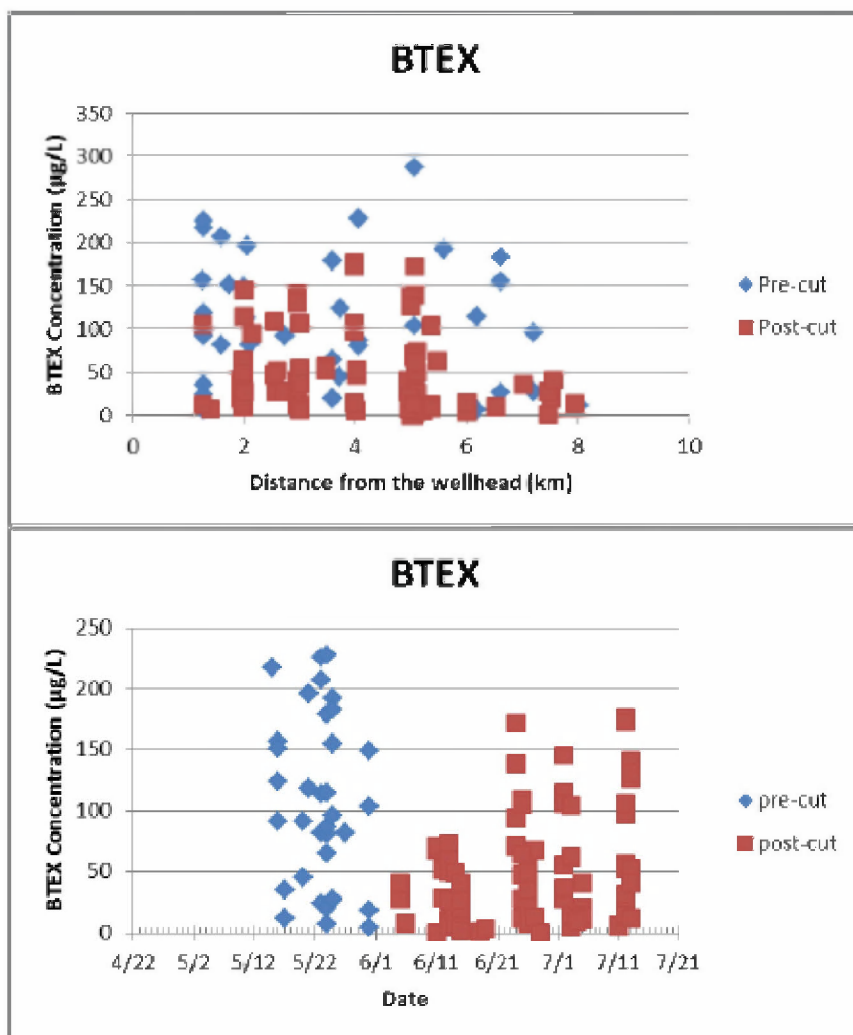


Figure H-7. BTEX observations over the course of the blowout period: (upper) BTEX concentrations as a function of distance from the wellhead, (b) BTEX concentrations as a function of date. Both pre and post cut values are shown.

The difference between pre-cut and post-cut plume layer BTEX concentrations can be attributed to a variety of factors including: (1) pre-cut kink flow (as 18% to 28% of total flow, see Table 5-5 of the Blowout main report) at high exit velocity, (2) pre-cut wand-application of dispersants in treating smaller fraction of oil at the un-cut riser end (see Section 5.6 Application of the Dispersant Treatment Model of the Blowout main report); (3) post-cut trident-application of dispersants, potentially more effective in dispersing oil and (4) post-cut oil recovery operations via the top hat containment system, and therefore resulting in less oil released per unit of time post-cut than pre-cut.

In addition to the effects of distance and sampling time period, the potential impact of the direction of sampling sites relative to the wellhead was also evaluated. To this end, the longitudinal and latitudinal distances of these sampling locations, relative to the DWH wellhead (longitude, -88.3659453; latitude, 28.73814) as the point of origin, were plotted and are shown

in Figure H-8. This plot illustrates the effect of direction (from the wellhead) on probable locations where plume water samples. The direction of the sampling locations relative to the wellhead shows a marked difference between pre-cut versus post-cut sampling. During the pre-cut period, only the samples collected from the westerly and southwesterly direction from the wellhead showed detectable values in BTEX, with the majority (36 out of 40) of the samples collected within a narrow range of angles between 180° and 225° . The trend of the high concentrations of samples retrieved southwest of the wellhead, during the pre-cut period, is consistent with the data analysis made by Spier et al. (2013), as shown in the Figure H-9. Conversely, during the post-cut sampling period, samples collected from a much wider range of directions (angles from 0° to 270°) were shown to have elevated BTEX concentrations. On the other hand, the lower panel of Figure H-8 shows a plot of all sampling stations in which water column samples have been collected within the intrusion layer (1000 ~ 1200 m deep) and within a distance between 1 km and 10 km from the wellhead, whether or not any BTEX compounds were detected. This plot shows that there was a much higher sampling frequency during the post-cut than the pre-cut period. During the post-cut period, sampling stations were almost evenly distributed throughout all directions from the wellhead. In contrast, during the pre-cut period, sampling stations were predominantly in the southwesterly direction, with only 8 out of 70 sampling stations in the northern and southeast directions. Such uneven spatial deployment of sampling stations during the pre-cut period has made it complicated to delineate the source of the detected BTEX compounds in the intrusion layer – i.e. whether these were mainly from the kink flow or from the end of the riser flow or both had made some contribution, in the latter case, to what extent these BTEX values might be attributable to the kink flow or the riser flow. Given the fact that the post-cut sampling period has a greater number of samples, that directional distribution of the intrusion layer is better represented with this sampling design, and that the pre-cut period convoluted intrusion layer fluxes of kink and un-cut riser flows is not well known, the retention analysis was performed for the post cut period only.

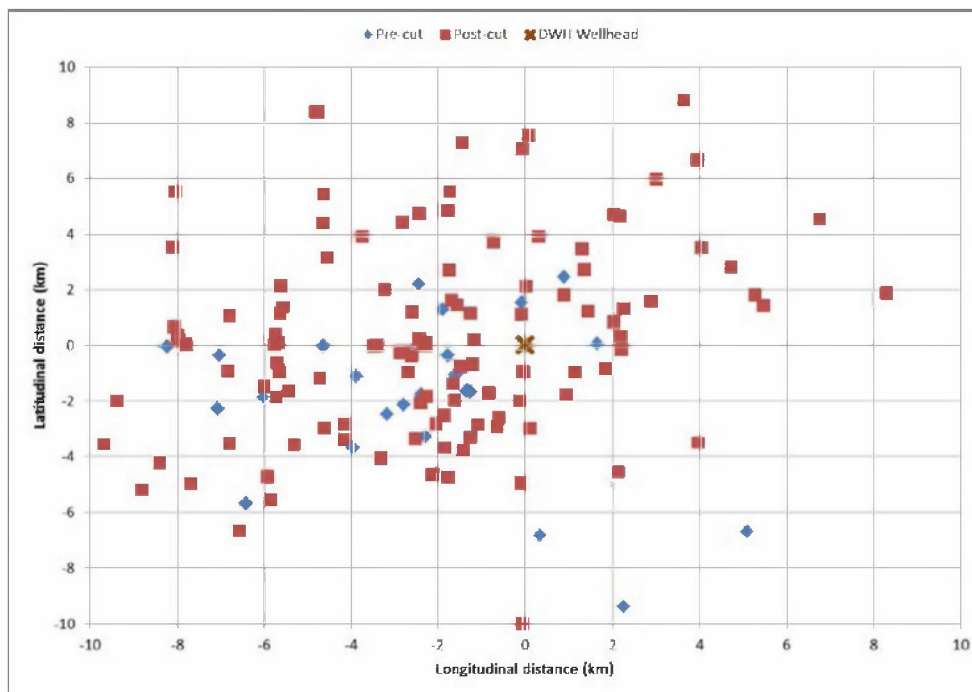
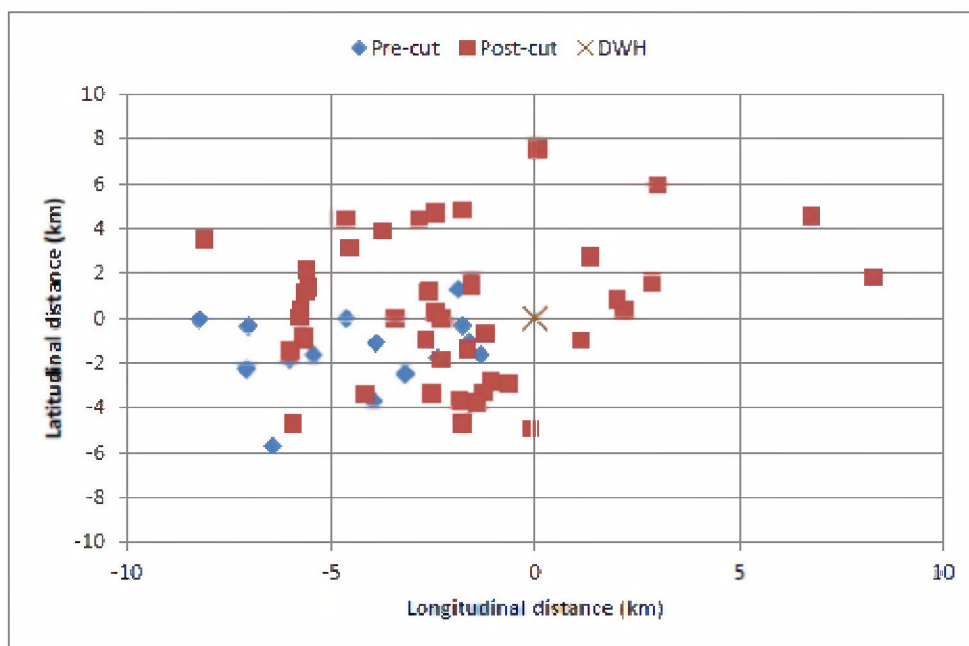


Figure H-8. Direction effects on the BTEX sampling locations in the intrusion layer: Upper panel, Pre- cut versus post-cut sampling locations in the intrusion layer over the course of the blowout; Lower Panel, All sampling sites during the pre-cut and post-cut period between 1 and 10 km distance from the wellhead, and sampling depth between 1000 and 1200 m.

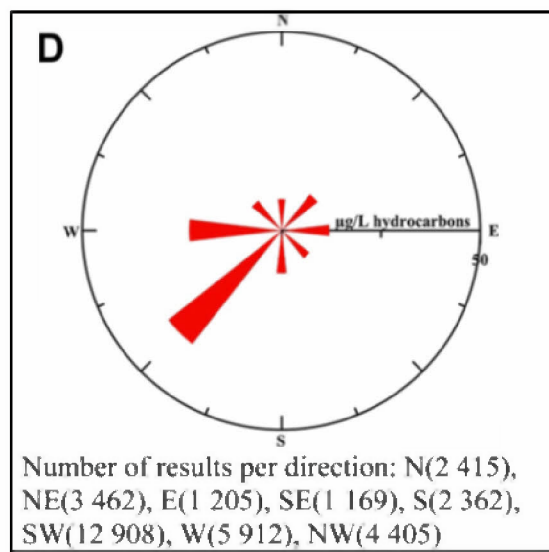


Figure H-9. Percent of detectable measurements in each direction from the wellhead (Spier et al. 2013).

H4.2 Post-cut Period BTEX Mass Balance Analysis

In order to make an estimate of the total mass flux of oil trapped in the deep water intrusion layer, the layer volume flux needs to be multiplied by the intrusion layer cross-sectional average concentration of the dispersed BTEX.

For the post-cut period, the release was from a single source (i.e., post-cut riser opening, just above the Lower Marine Riser Package or LMRP) and the dispersed oil components were observed to be present mostly in dissolved and finely dispersed phases (Reddy et al. 2012). The volume flux of BTEX contained in the intrusion layer was estimated based on the total oil BTEX released in the environment from the post-cut riser, and the results are presented in Figure H-10.

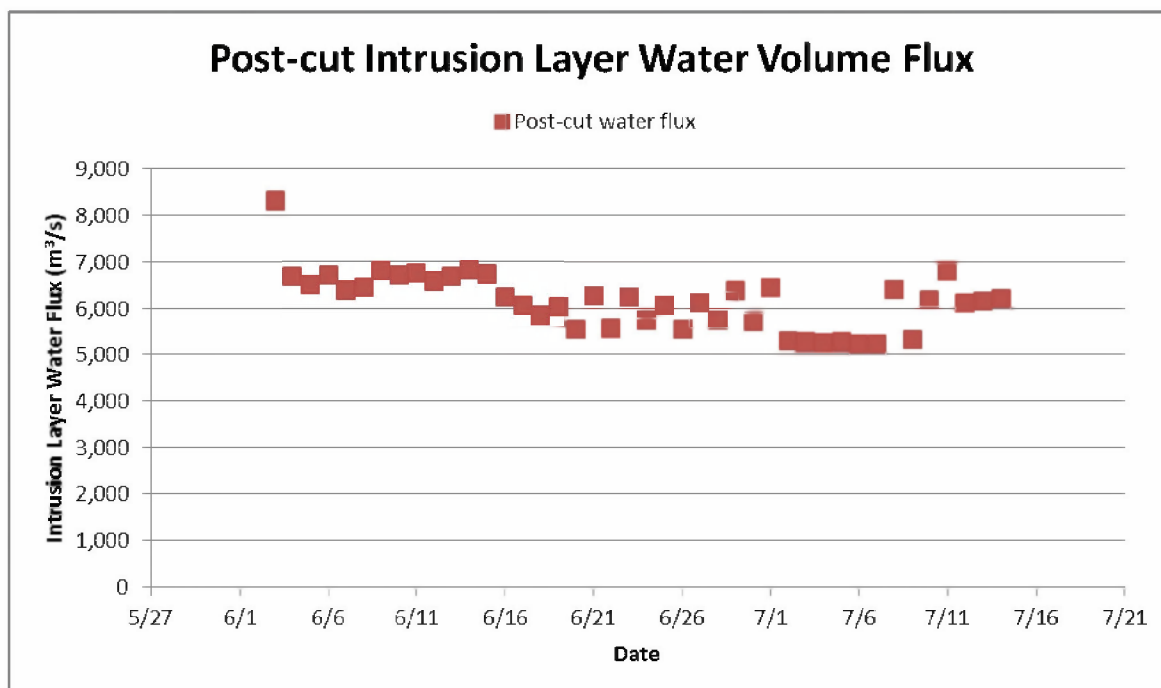


Figure H-10: Intrusion model predicted daily post-cut intrusion layer water volume flux (based on an entrainment coefficient of 0.083 and at a distance of 1.5 km from the wellhead)

After the total post-cut volume flux was determined, the flow cross-sectional average BTEX concentrations was estimated based on the measured oil chemistry data in the intrusion layer. Theory (e.g., OILMAP DEEP) and DWH field measurements (Camilli et al. 2010) indicate that the distribution of hydrocarbons in the deep water intrusion layer would follow a Gaussian-like distribution across the central axis of the intrusion layer. Assuming that the samples collected from the trapped intrusion layer were sampled randomly from a Gaussian (i.e., normal) distribution of concentration, the mean value would likely represent the spatial mean value of the plume cross-sectional distribution of hydrocarbons. Therefore, the mean values of BTEX in all horizontal directions (Table H-1) were used to estimate the post-cut mass flux of the hydrocarbons. The calculated mass flux in the deep water intrusion layer was then compared with the total mass flux of the hydrocarbon group within the total release of the source oil from the wellhead. The ratio of the mass flux of the BTEX hydrocarbons trapped in the intrusion layer flow, and the initial total mass of the BTEX hydrocarbons released at the wellhead, would then provide an estimate of the fraction of the release oil components (groups or compounds) that were retained in the deep water intrusion layer.

The model predicted horizontal intrusion layer water volume flux and the mean BTEX concentrations measured in the field were used to calculate the daily variation of the retained fraction of BTEX in the layer. Table H-2 summarizes the estimated values during the post-cut period. The results are also shown in Figure H-11. During the post-cut period, approximately 21% to 35% of the released BTEX was retained in the deep water intrusion layer, with an average level of $27 \pm 5\%$.

Table H-2. Post-cut period (June 3 – July 14, 2010) mass balance analysis of trapped BTEX fraction in the intrusion layer.

Wellhead Oil Release flow to Water Col				DOR (norm)	Plume layer water flux and BTEX concentrations				Source oil release		Trapped Fraction		
Kink	Riser	Total	Subs. Disp		Water flux	BTEX mean	BTEX 95% CI	BTEX mass flux	BTEX in source		Mean	95% C.I	
Date (bpd)	(bpd)	(bpd)	(bpd)		(m3/s)	(ug/L)	(ug/L)	(g/s)	(%)	(g/s)	(%)	(%)	
6/3/2010	0	60000	60000	423	142	8309	51.08	9.94	424	1.91%	1807	23.48%	4.57%
6/4/2010	0	53813	53813	492	109	6680	51.08	9.94	341	1.91%	1621	21.05%	4.09%
6/5/2010	0	49304	49304	483	102	6500	51.08	9.94	332	1.91%	1485	22.36%	4.35%
6/6/2010	0	48581	48581	332	146	6694	51.08	9.94	342	1.91%	1463	23.37%	4.54%
6/7/2010	0	44658	44658	351	127	6370	51.08	9.94	325	1.91%	1345	24.19%	4.70%
6/8/2010	0	44394	44394	328	135	6453	51.08	9.94	330	1.91%	1337	24.65%	4.79%
6/9/2010	0	43484	43484	288	151	6805	51.08	9.94	348	1.91%	1310	26.54%	5.16%
6/10/2010	0	43798	43798	242	181	6699	51.08	9.94	342	1.91%	1319	25.94%	5.05%
6/11/2010	0	43546	43546	201	217	6761	51.08	9.94	345	1.91%	1312	26.33%	5.12%
6/12/2010	0	43961	43961	116	381	6586	51.08	9.94	336	1.91%	1324	25.41%	4.94%
6/13/2010	0	43692	43692	236	185	6680	51.08	9.94	341	1.91%	1316	25.93%	5.04%
6/14/2010	0	43379	43379	233	186	6819	51.08	9.94	348	1.91%	1307	26.66%	5.19%
6/15/2010	0	48152	48152	279	172	6731	51.08	9.94	344	1.91%	1450	23.71%	4.61%
6/16/2010	0	40273	40273	209	193	6243	51.08	9.94	319	1.91%	1213	26.29%	5.11%
6/17/2010	0	33105	33105	137	241	6059	51.08	9.94	310	1.91%	997	31.04%	6.04%
6/18/2010	0	33748	33748	218	155	5846	51.08	9.94	299	1.91%	1017	29.38%	5.71%
6/19/2010	0	37159	37159	403	92	6035	51.08	9.94	308	1.91%	1119	27.54%	5.36%
6/20/2010	0	34809	34809	335	104	5557	51.08	9.94	284	1.91%	1049	27.07%	5.27%
6/21/2010	0	32164	32164	339	95	6261	51.08	9.94	320	1.91%	969	33.01%	6.42%
6/22/2010	0	30703	30703	233	132	5567	51.08	9.94	284	1.91%	925	30.75%	5.98%
6/23/2010	0	40834	40834	236	173	6227	51.08	9.94	318	1.91%	1230	25.86%	5.03%
6/24/2010	0	33865	33865	306	111	5743	51.08	9.94	293	1.91%	1020	28.76%	5.59%
6/25/2010	0	32952	32952	299	110	6067	51.08	9.94	310	1.91%	993	31.22%	6.07%
6/26/2010	0	34642	34642	301	115	5536	51.08	9.94	283	1.91%	1044	27.10%	5.27%
6/27/2010	0	32845	32845	275	119	6101	51.08	9.94	312	1.91%	989	31.50%	6.13%
6/28/2010	0	33800	33800	314	108	5741	51.08	9.94	293	1.91%	1018	28.80%	5.60%
6/29/2010	0	31877	31877	275	116	6378	51.08	9.94	326	1.91%	960	33.93%	6.60%
6/30/2010	0	33821	33821	324	104	5715	51.08	9.94	292	1.91%	1019	28.66%	5.57%
7/1/2010	0	31646	31646	251	126	6456	51.08	9.94	330	1.91%	953	34.60%	6.73%
7/2/2010	0	31409	31409	263	119	5292	51.08	9.94	270	1.91%	946	28.57%	5.56%
7/3/2010	0	31402	31402	279	113	5287	51.08	9.94	270	1.91%	946	28.55%	5.55%
7/4/2010	0	31540	31540	248	127	5246	51.08	9.94	268	1.91%	950	28.21%	5.49%
7/5/2010	0	31418	31418	278	113	5272	51.08	9.94	269	1.91%	946	28.46%	5.53%
7/6/2010	0	31539	31539	278	114	5234	51.08	9.94	267	1.91%	950	28.14%	5.47%
7/7/2010	0	31522	31522	280	112	5227	51.08	9.94	267	1.91%	950	28.12%	5.47%
7/8/2010	0	31621	31621	274	115	6416	51.08	9.94	328	1.91%	953	34.41%	6.69%
7/9/2010	0	31108	31108	256	122	5329	51.08	9.94	272	1.91%	937	29.05%	5.65%
7/10/2010	0	40601	40601	315	129	6177	51.08	9.94	316	1.91%	1223	25.80%	5.02%
7/11/2010	0	47465	47465	367	129	6805	51.08	9.94	348	1.91%	1430	24.31%	4.73%
7/12/2010	0	44698	44698	334	134	6106	51.08	9.94	312	1.91%	1346	23.17%	4.51%
7/13/2010	0	35836	35836	333	108	6168	51.08	9.94	315	1.91%	1079	29.19%	5.68%
7/14/2010	0	39857	39857	327	122	6202	51.08	9.94	317	1.91%	1201	26.39%	5.13%
Post-cut average												27.06%	5.26%

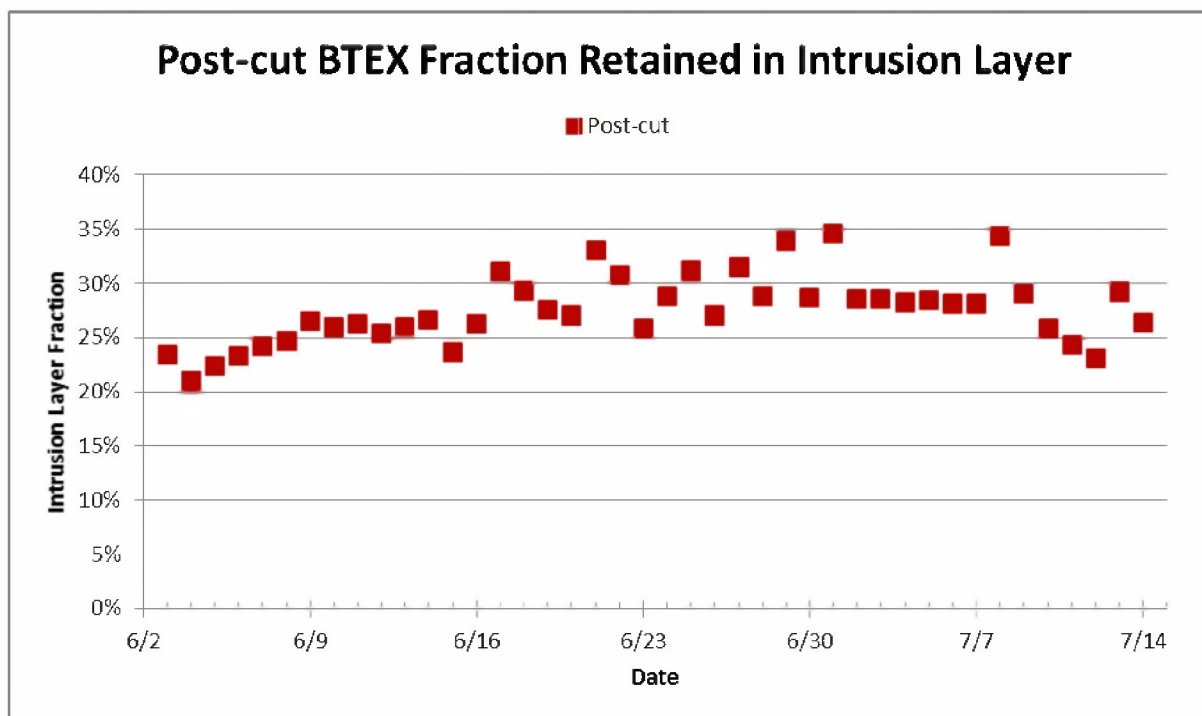


Figure H-11. Intrusion model predicted fraction of BTEX retained in the intrusion layer each day during the Post-cut period. Prediction was based on horizontal water entrainment coefficient of 0.083.

H4.3 Summary of Hydrocarbon (BTEX) Mass Balance Analysis Results

In summary, a mass balance analysis of the oil (BTEX) fraction retained in the plume layer was performed based on the estimated volume flux of water in the intrusion layer derived from the intrusion model, and the measured hydrocarbon concentrations within the deep water trapped intrusion layer in the near field (i.e., between about 1 to 10 km away from the wellhead). The analysis showed for the post-cut period, approximately $27 \pm 5\%$ of oil mass flux was trapped in the intrusion layer resulting from released oil at the wellhead. An independent estimate was made based on an application of the dispersant treatment (Appendix F) and droplet size distribution models (Appendix G) for the best estimate of the actual treatment and a low and high efficiency treatment cases. Figure H-12 shows the cumulative oil fraction vs droplet diameter for the low, best and high treatment efficiency cases, for both pre and post cut periods. Efficiency, in this context, means how effective the dispersant is in treating the oil, so that the sufficiently small droplets may be trapped in the intrusion layer at least in the near field downstream of the wellhead. Assuming a droplet cut-off diameter to be 300 μm for oil to remain in the water column, the high efficiency case shows 22% pre and 55% post cut oil retained in the water column, while the values for the best estimate are 18% and 28%, respectively. The low estimate case gives values of 5% and 15%, for pre and post cut periods respectively. The best estimate of the post cut period (28%) is in good agreement with the present analysis of 27% for the post cut period.

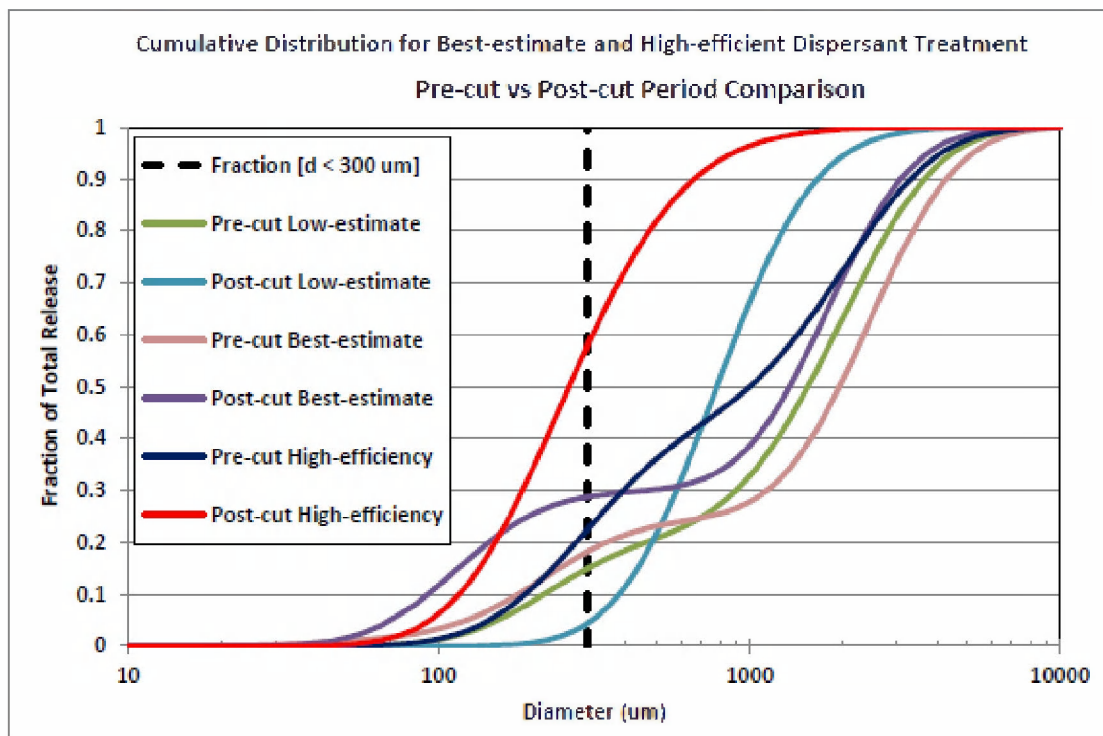


Figure H-12. Comparison of the pre-cut and post-cut cumulative fraction vs droplet diameter for various treatment assumptions. The intrusion layer is assumed to trap all droplets below a cut-off size of $d \leq 300 \mu\text{m}$. Displayed here are predictions from three dispersant-treatment cases: low-efficiency estimate, best-estimate, and high-efficiency estimate.

H5. Comparison to *In Situ* DOSS Concentrations during Post-cut Period

An independent assessment of the amount of mass trapped in the intrusion layer was also made using one key ingredient associated with the application of subsurface dispersant Corexit 9500A, namely the anionic surfactant DOSS (dioctyl sodium sulfosuccinate). DOSS concentrations were analyzed throughout the entire duration of the DWH spill as part of the water column chemical analysis for the NOAA NRDA monitoring program. A benefit of using DOSS is that the source strength is well documented, as it is a direct function of the amount of dispersant applied. A time-series of the dispersant application rate and the resulting mass flux of DOSS are presented in Figure H-13. The average DOSS application mass flux was reported as 4,376 kg/day for the post cut period.

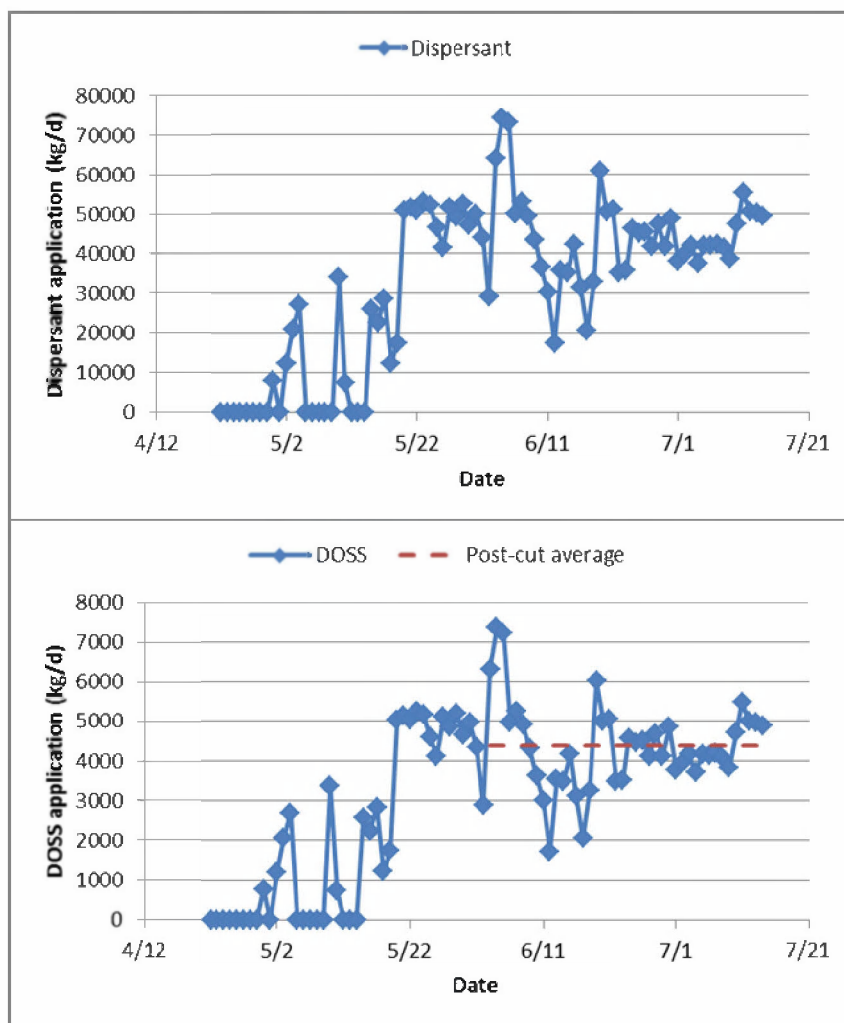


Figure H-13. Application rate of Corexit 9500A dispersant at the well (upper panel) and resultant DOSS mass flux (lower panel), from data in the Oil Budget Calculator (Lehr et al. 2010).

H5.1 Dispersant DOSS Chemistry Data of the Field Measurements

Figure H-14 shows the concentrations of DOSS for each sample vs depth and distance from the source collected over the duration of the release.

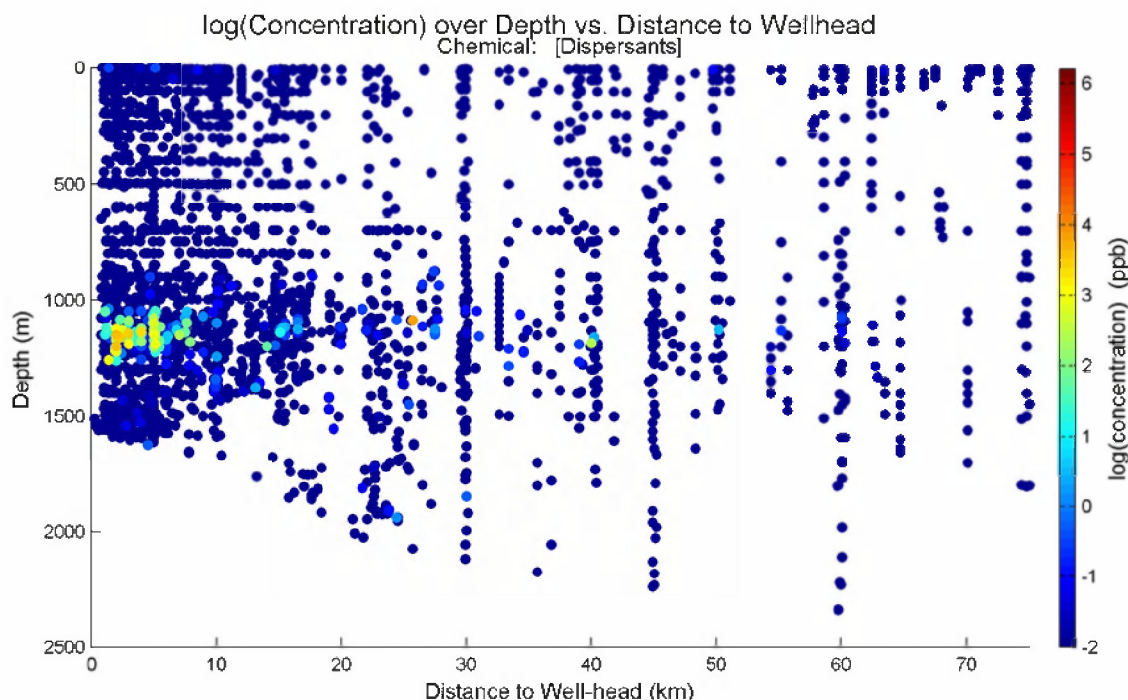


Figure H-14. Log (Concentration) (ppb) of DOSS vs depth (m) and distance from the well head are displayed. Note the data are presented in natural logarithm, hence in the subsurface intrusion layer the likely range of maximum DOSS concentration was about e^3 - e^4 (i.e., 20-55 $\mu\text{g/L}$).

Table H-3 shows that during the pre-cut period, the only measured DOSS values in the intrusion layer was found in a sample collected at depths of 1175.6 m and distances of 2 km from the wellhead on May 30, 2010, with a very low DOSS concentration of 0.00609 $\mu\text{g/L}$; a second sample was found at depth of 1219.2 m and distance of 2.1 km from the wellhead on May 27, 2010, with DOSS concentration also low at 0.01060 $\mu\text{g/L}$. Expanding the vertical profile throughout the entire depth from surface to bottom, three more samples were found to have elevated DOSS concentrations in depth between 700 and 1300m, and the remaining two surface layer samples less than 10 m from the surface, with DOSS concentrations all less than 0.2 $\mu\text{g/L}$.

Table H-3. The Pre-cut (April 22 to June 2, 2010) water column DOSS concentrations (µg/L)

Date	Depth (m)	Distance (km)	Phases	DOSS (ug/L)
5/30/2010	1175.6	1.99	Filter/Particulate	0.00609
5/27/2010	1219.2	2.10	Filter/Particulate	0.01060
5/30/2010	758	1.96	Filter/Particulate	0.02150
5/27/2010	867.5	2.10	Filter/Particulate	0.00831
5/27/2010	867.5	2.10	Filter/Particulate	0.01190
5/30/2010	1	2.44	Filter/Particulate	0.03700
5/12/2010	9.14	7.76	Filter/Particulate	0.15500

The post-cut period DOSS concentrations of the plume layer water column samples within 10 km distance from the wellhead are plotted in Figure H-15 (upper panel). Also presented in Figure H-15 (lower panel) is a linear correlation of the DOSS and BTEX concentrations of the paired samples. The correlation of BTEX and DOSS measurements is low but statistically significant. The descriptive statistics of the data are presented in Table H-4. The values of the DOSS concentrations in the field plume samples are generally in agreement with independent measurements made by academic cruises primarily within 10 km of the well in the May-June 2010 time period (Kujawinsky et al. 2011).

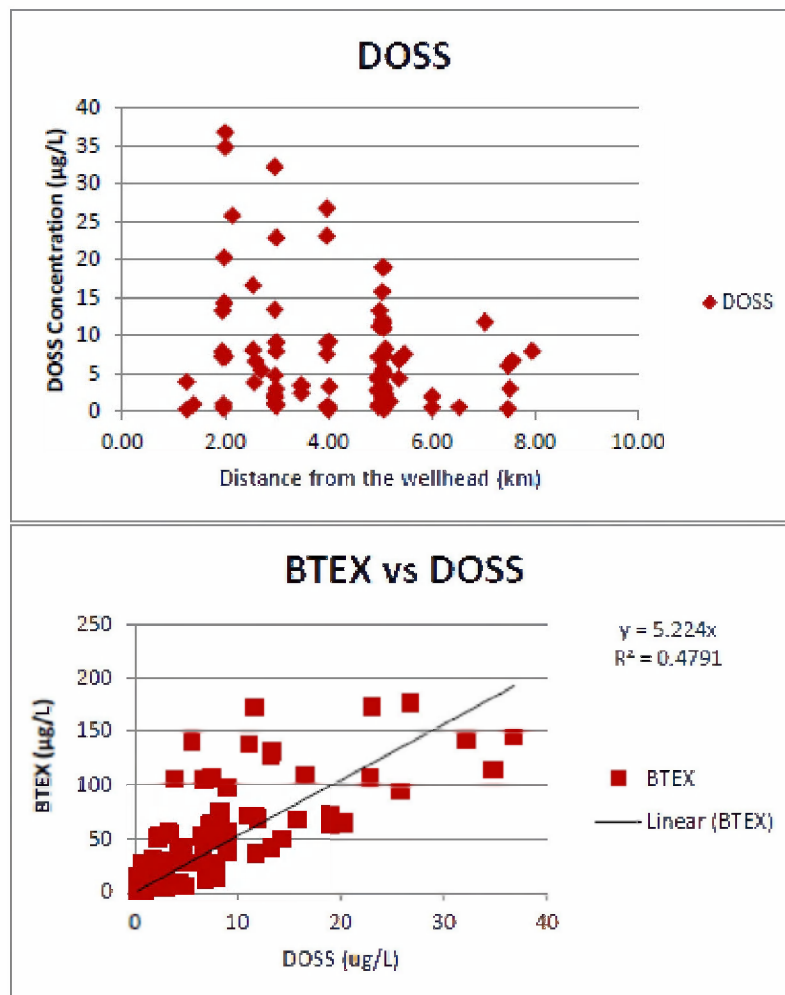


Figure H-15. DOSS concentrations in the plume layer (see Figure H-14) from NRDA cruise post-cut cruises (upper panel), and the linear correlation of the paired BTEX and DOSS concentrations (lower panel).

Table H-4. Descriptive statistics of the plume layer DOSS concentrations (µg/L) during the post-cut (June 3 to July 14, 2010) period for all directions and from the southwest only

	<i>Post-cut</i>	
	<i>All Direction</i>	<i>Southwest only</i>
Mean	7.942	8.272
Standard Error	0.899	1.280
Median	6.040	5.410
Mode	11.700	#N/A
Standard Deviation	8.188	7.992
Sample Variance	67.036	63.869
Kurtosis	2.795	1.102
Skewness	1.687	1.228
Range	36.531	31.931
Minimum	0.269	0.269
Maximum	36.800	32.200
Sum	659.167	322.608
Count	83	39
Confidence Level (95.0%)	1.788	2.591

The mass balance analysis for DOSS was therefore only conducted for the post-cut period, since only two measurements with very low DOSS concentrations were observed during the pre-cut period.

H5.2 Post-cut Period DOSS Mass Balance Analysis

The mass balance of the DOSS fraction retained in the plume was analyzed using the data as presented in Figure H-15 and Table H-4. The mass balance analysis was performed based on the intrusion layer DOSS mass flux, which was estimated from the intrusion layer water flux and the mean DOSS concentrations. These intrusion layer DOSS mass flux values were then divided by the daily DOSS mass flux at the source to estimate the fraction of DOSS retained in the horizontal intrusion layer. The results of the analysis are presented in Table H-5 and Figure H-16. During the post-cut period, the fraction of dispersant applied subsurface that would be retained in the intrusion layer ranged from 62% to 100 %, with the average estimated as approximately $90 \pm 23\%$ ¹ suggesting that the majority of dispersants applied at the subsea were trapped in the subsurface horizontal intrusion layer. The uncertainty value is given in terms of the mean 95 % confidence limit over all sampling days.

¹ Confidence interval 67%-100%

Table H-5. Post-cut period (June 3 – July 14, 2010) mass balance analysis of trapped DOSS fraction in the plume intrusion layer

Date	Wellhead Oil Release			Plume layer water flux and DOSS concentrations				Wellhead dispersant application				Trapped Fraction	
	Kink	Riser	Total	Water flux	DOSS mean	DOSS 95% CI	DOSS mass flux	Disp app.	DOR	DOSS in disp.	DOSS mass flux	Mean	95% C.I
	(bpd)	(bpd)	(bpd)	(m3/s)	(ug/L)	(ug/L)	(g/s)	(bpd)	(norm)	(%)	(g/s)	(%)	(%)
5/3/2010	0	60000	60000	8309	7.942	1.788	66	423	142	9.90%	73	90.21%	20.31%
6/4/2010	0	53813	53813	6680	7.942	1.788	53	492	109	9.90%	85	62.33%	14.03%
6/5/2010	0	49304	49304	5500	7.942	1.788	52	483	102	9.90%	84	61.69%	13.89%
6/6/2010	0	48581	48581	5694	7.942	1.788	53	332	146	9.90%	57	92.57%	20.84%
6/7/2010	0	44658	44658	6370	7.942	1.788	51	351	127	9.90%	61	83.34%	18.76%
6/8/2010	0	44394	44394	6453	7.942	1.788	51	328	135	9.90%	57	90.37%	20.34%
6/9/2010	0	43484	43484	6805	7.942	1.788	54	288	151	9.90%	50	100.00%	24.38%
6/10/2010	0	43798	43798	6609	7.942	1.788	53	242	181	9.90%	42	100.00%	28.60%
6/11/2010	0	43546	43546	6761	7.942	1.788	54	201	217	9.90%	35	100.00%	34.73%
6/12/2010	0	43961	43961	6586	7.942	1.788	52	116	381	9.90%	20	100.00%	58.89%
6/13/2010	0	43692	43692	6680	7.942	1.788	53	236	185	9.90%	41	100.00%	29.23%
6/14/2010	0	43379	43379	6819	7.942	1.788	54	233	186	9.90%	40	100.00%	30.19%
6/15/2010	0	48152	48152	6731	7.942	1.788	53	279	172	9.90%	48	100.00%	24.91%
6/16/2010	0	40273	40273	6243	7.942	1.788	50	209	193	9.90%	36	100.00%	30.86%
6/17/2010	0	33105	33105	6059	7.942	1.788	48	137	241	9.90%	24	100.00%	45.62%
6/18/2010	0	33748	33748	5846	7.942	1.788	46	218	155	9.90%	38	100.00%	27.73%
6/19/2010	0	37159	37159	6035	7.942	1.788	48	403	92	9.90%	70	68.78%	15.48%
6/20/2010	0	34809	34809	5557	7.942	1.788	44	335	104	9.90%	58	76.12%	17.14%
6/21/2010	0	32164	32164	6261	7.942	1.788	50	339	95	9.90%	59	84.78%	19.09%
6/22/2010	0	30703	30703	5567	7.942	1.788	44	233	132	9.90%	40	100.00%	24.66%
6/23/2010	0	40834	40834	6227	7.942	1.788	49	236	173	9.90%	41	100.00%	27.31%
6/24/2010	0	33865	33865	5743	7.942	1.788	46	306	111	9.90%	53	86.00%	19.36%
6/25/2010	0	32952	32952	6067	7.942	1.788	48	299	110	9.90%	52	93.25%	20.99%
6/26/2010	0	34642	34642	5536	7.942	1.788	44	301	115	9.90%	52	84.32%	18.98%
6/27/2010	0	32845	32845	6101	7.942	1.788	48	275	119	9.90%	48	100.00%	22.90%
6/28/2010	0	33800	33800	5741	7.942	1.788	46	314	108	9.90%	54	83.99%	18.91%
6/29/2010	0	31877	31877	6378	7.942	1.788	51	275	116	9.90%	48	100.00%	23.94%
6/30/2010	0	33821	33821	5715	7.942	1.788	45	324	104	9.90%	56	80.94%	18.22%
7/1/2010	0	31646	31646	6456	7.942	1.788	51	251	126	9.90%	44	100.00%	26.53%
7/2/2010	0	31409	31409	5292	7.942	1.788	42	263	119	9.90%	46	92.18%	20.75%
7/3/2010	0	31402	31402	5287	7.942	1.788	42	279	113	9.90%	48	87.11%	19.61%
7/4/2010	0	31540	31540	5246	7.942	1.788	42	248	127	9.90%	43	96.95%	21.82%
7/5/2010	0	31418	31418	5272	7.942	1.788	42	278	113	9.90%	48	86.94%	19.57%
7/6/2010	0	31539	31539	5234	7.942	1.788	42	278	114	9.90%	48	86.55%	19.48%
7/7/2010	0	31522	31522	5227	7.942	1.788	42	280	112	9.90%	48	85.59%	19.27%
7/8/2010	0	31621	31621	6416	7.942	1.788	51	274	115	9.90%	47	100.00%	24.18%
7/9/2010	0	31108	31108	5329	7.942	1.788	42	256	122	9.90%	44	95.56%	21.51%
7/10/2010	0	40601	40601	6177	7.942	1.788	49	315	129	9.90%	54	90.12%	20.29%
7/11/2010	0	47465	47465	6805	7.942	1.788	54	367	129	9.90%	64	85.06%	19.15%
7/12/2010	0	44698	44698	6106	7.942	1.788	48	334	134	9.90%	58	83.83%	18.87%
7/13/2010	0	35836	35836	6168	7.942	1.788	49	333	108	9.90%	58	84.93%	19.12%
7/14/2010	0	39857	39857	6202	7.942	1.788	49	327	122	9.90%	57	86.96%	19.58%
Post-cut average				6245								90.11%	23.37%

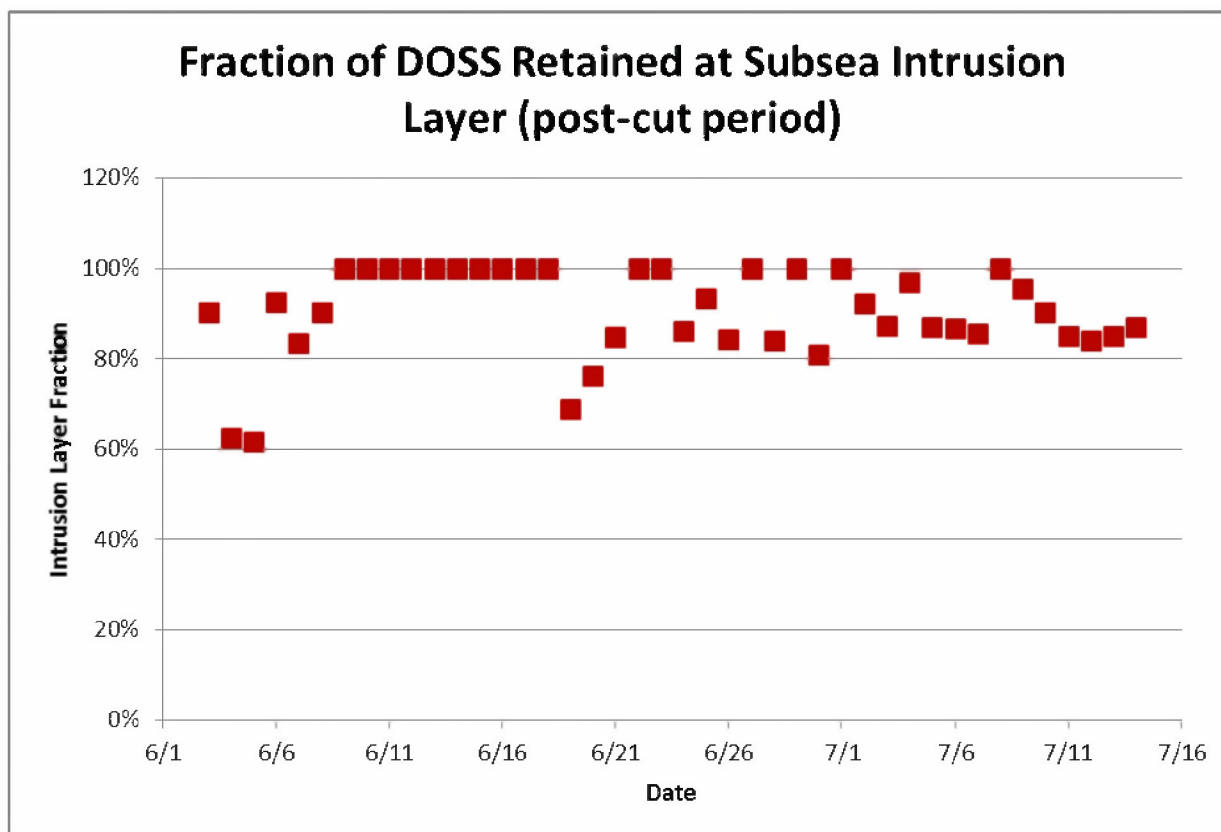


Figure H-16. Fountain and intrusion model predicted fraction of DOSS retained in the intrusion layer each day during the post-cut period.

H5.3 DOSS Data Summary

In summary, the mass balance of the DOSS constituent in dispersant was analyzed using the NRDA dataset. The mean concentration of DOSS in the 83 samples collected from the intrusion layer in the near field was 7.94 ± 0.90 $\mu\text{g/L}$, and the median value was 6.04 $\mu\text{g/L}$. These values are consistent with the Kujawinski et al. (2011) analysis, that predicted that the plume layer average concentration of DOSS would be approximately 7 $\mu\text{g/L}$, if the dispersants applied subsea were retained in the intrusion layer. Based on the estimated water volume flux in the intrusion layer, approximately $90 \pm 23\%^2$ of the applied dispersant would have been retained in the deep water plume. This is consistent with the best-estimated dispersant effectiveness value of 80% that was used in the dispersant treatment model (Appendix F).

Several caveats must be considered for this mass balance analysis. The first is in regards to the biodegradation of the dispersant constituent, DOSS, in the marine environment (Campo et al 2013; Kujawinski et al 2011; White et al 2014). Kujawinski et al. (2011) reported that the degradation rate of DOSS was slow in the deep ocean, and therefore it would behave as a

² Confidence interval 67%-100%

conservative tracer in the intrusion layer. Campo et al. (2013) found that although there was measurable biodegradation of DOSS at room temperature (25°C), biodegradation of DOSS at deep sea temperature (5°C) was not detectable over the duration of their 42 day laboratory experimental period. For a point of reference, the model predicted intrusion layer travel time to a radius of 1.5 km from the well site, where the preceding estimates were made, is on the order of 10-15 hours. More recently, White et al. (2014) reported that DOSS was discovered through analysis of DWH oil samples found on coral 6 months after the spill and on beaches in the Gulf of Mexico more than 24 months after the spill, suggesting that DOSS was very persistent in the environment.

Second, the "Dispersant Indicators" in the NRDA processed forensic data (Horn et al. 2015) is technically not only DOSS, but may contain two compounds that have been investigated for dispersants. This included glycol ethers and DOSS (in solution only). Other dispersants, including 1) 2-Butoxyethanol, 2) Dioctyl sulfosuccinate sodium salt, and 3) Bis-(2-ethylhexyl) fumarate were excluded from analysis, as there were significant problems with contamination (cleaners used on sampling apparatus). Therefore, interpretation of the analysis can only be made towards the fraction retained of the DOSS fraction, rather than of all the dispersant constituents in their entirety.

H6. Summary

The key results from the above analyses are:

- The Fountain and intrusion model was applied to estimate the horizontal intrusion layer water volume fluxes downstream of the DWH wellhead, in the direction of ambient current flow.
- The estimated intrusion layer water volume fluxes were applied to estimate the mass flux of both a hydrocarbon component of the source oil (i.e., BTEX group) and the constituents (i.e., DOSS) of the dispersants directly applied at the wellhead during the post cut period. These were compared to the field measurement data of BTEX and DOSS in the depth intervals co-incident with the intrusion layer and near field distance downstream of the well head (i.e., within 1 – 10 km in horizontal distance). Both analyses were restricted to the post cut period given the limited number of samples or directional bias in sampling and the intermingling of releases from both kink and riser during the pre-cut period.
- The mass balance of BTEX results indicated that on average, approximately an average of 27 ± 5 % of the BTEX from the source oil was retained in the intrusion layer during post-cut period.
- The dispersant constituent, DOSS, mass balance analysis estimated that approximately $90 \pm 23\%$ ³ of DOSS, applied at the well head, was retained in the subsurface intrusion layer, during the post-cut period.

³ Confidence interval 67%-100%

H7. References

- Ansong, J, P.J. Kyba, and B.R. Sutherland. 2008. Fountains impinging on a density interface, *J. Fluid Mech.* 595:115–139.
- Camilli, R., C.M. Reddy, D.R. Yoerger, B.A S. Van Mooy, M.V. Jakuba, J.C. Kinsey, C P. McIntyre, S.P. Sylva and J.V. Maloney. 2010. Tracking hydrocarbon plume transport and biodegradation at Deepwater Horizon. *Science* 330: 201-204.
- Campo, P., A.D. Venosa and M.T. Suidan. 2013. Biodegradability of Corexit 9500 and Dispersed South Louisiana Crude Oil at 5 and 25 °C. *Environmental Science & Technology* 47(4):1960-1967.
- Chen, J.C. 1980. Studies on gravitational spreading currents. PhD thesis, California Institute of Technology, Pasadena, CA
- Fannelop, T.K. and K.Sjoen. 1980. Hydrodynamics of Underwater Blowouts. *Norwegian Maritime Research*, No. 4, 1980.
- Horn, M., D. French McCay, J. Payne, W. Driskell, Z. Li, M. Grennan, L. Decker, and S. Zamorski, 2015. Technical Reports for Deepwater Horizon Water Column Injury Assessment –Water Column Chemical and Physical Data from the Deep Water Horizon Blowout. RPS ASA, South Kingstown, RI, USA.
- Jirka, G. 2004. Integral Model for Turbulent Buoyant Jets in Unbounded Stratified Flows. Part I: Single Round Jet. *Environmental Fluid Mechanics* 4(1):1-56.
- Jirka, G. 2006. Integral Model for Turbulent Buoyant Jets in Unbounded Stratified Flows Part 2: Plane Jet Dynamics Resulting from Multiport Diffuser Jets. *Environmental Fluid Mechanics* 6(1):43-100.
- Kolluru, V.S. 1993. Oil blowout model. Internal report, Applied Science Associates, Inc., Narragansett, RI 02882 [Now RPS ASA, South Kingstown, RI, USA 02879].
- Kujawinski, E.B., M.C. Kido Soule, D.L. Valentine, A.K. Boysen, K. Longnecker and M. C. Redmond. 2011. Fate of Dispersants Associated with the Deepwater Horizon Oil Spill. *Environmental Science & Technology* 45(4):1298-1306.
- Lehr, B., S. Bristol and A. Possolo. 2010. Deepwater horizon oil budget calculator: A report to the national incident command. The Federal Interagency Solutions Group, Oil Budget Calculator Science and Engineering Team.
http://www.restorethegulf.gov/sites/default/files/documents/pdf/OilBudgetCalc_Full_HQ-Print_111110.pdf (Accessed on April 1, 2012).
- McNutt, M., R. Camilli, G. Guthrie, P. Hsieh, V. Labson, B. Lehr, D. Maclay, A. Ratzel and M. Sogge. 2011. Assessment of Flow Rate Estimates for the Deepwater Horizon / Macondo Well Oil Spill. Flow Rate Technical Group report to the National Incident Command, Interagency Solutions Group, March 10, 2011.
- Reddy, C.M., J.S. Arey, J.S. Seewald, S P. Sylva, K.L. Lemkau, R.K. Nelson, M.A.S. Van Mooy and R. Camilli, 2012. Composition and fate of gas and oil released to the water column during the Deepwater Horizon oil spill. *Proceedings of National Academy of Sciences* 109(5): 20229-20234.

- Spier, C., W.T. Stringfellow, T.C. Hazen and M. Conrad. 2013. Distribution of hydrocarbons released during the 2010 MC252 oil spill in deep offshore waters. *Environmental Pollution* 173: 224-230.
- White, F.M., 1979. *Fluid Mechanics*. McGraw-Hill, Inc.
- White, H.K, S.L. Lyons, S.J. Harrison, D.M. Findley, Y. Liu, and E.B. Kujawinski. 2014. Long-Term Persistence of Dispersants following the Deepwater Horizon Oil Spill. *Environ. Sci. Technol. Lett.* 1, 295–299.

Technical Reports for Deepwater Horizon Water Column Injury Assessment

WC_TR.13: Application of OILMAP DEEP to the Deepwater Horizon Blowout

Appendix I: WHOI *Holocam* oil droplet size distribution data from JF3 cruises

Authors: Malcolm Spaulding, Daniel Mendelsohn, Deborah Crowley,
Zhengkai Li, Andrew Bird

Revised: September 30, 2015

Project Number: 2011-144

RPS ASA 55 Village Square Drive, South Kingstown, RI 02879

Table of Contents

I1.	<i>Holocam</i> oil droplet size distribution data from JF3 cruises.....	1
I2.	Lognormal distribution fit to the data	6
I2.1	Number median diameter and standard deviation of each dive	6
I2.2	Volume median diameter (VMD) and standard deviation of each dive	9
I3.	Summary	11
I4.	References	11

List of Figures

Figure I-1. Upper Panel, A. Cruise M/V Jack Fitz 3. Holographic camera (*Holocam*) mounted on the ROV. B. Locations of ROV dives 5-13, for which holograms were processed; Lower Panel, Time and Location (Latitude, Longitude, and Depth Range) of each dive..... 1

Figure I-2: Upper panel, Figure 9 of Davis and Loomis (2014), Dive 5, (hologram A1009566) size distribution of oil droplets determined by manual (Class 0 = no oil, Class 1 = oil, Class 2 = possible oil) and automatic (Class 1 = oil droplets, Class 2 = non-oil particles) methods; for the manual method, objects were class 1 or 2 with ≥ 6 pixel diameter. Lower panel, Figure 10 of Davis and Loomis (2014) Dive 5, (hologram A1009566) size distribution of oil droplets determined by manual and automatic methods; for the manual method, objects were class 1 only..... 4

Figure I-3: Figure 11 of Davis and Loomis (2014), Dive 5, Diameters of oil droplets (class 1, open circles) and possible droplets (class 2, black dots) versus depth..... 5

Figure I-4: Figure 12 of Davis and Loomis (2014), Dive 6, Diameters of oil droplets (class 1, open circles) and possible droplets (class 2, black dots) versus depth..... 5

Figure I-5. Cumulative number distribution of dives #5 and 6 throughout entire depth of in situ measurements and the fitted lognormal distribution functions 6

Figure I-6. An example of the observed (dots) and fitted (lines) cumulative lognormal droplet size number distribution of the JF3 dive #5 droplet size data. The left panel shows the data of the whole range as reported by Davis and Loomis (2014), and all the data were used to fit the lognormal size distribution function; the right panel displays only droplets $d \geq 30 \mu\text{m}$, a cutoff size that was used by Davis and Loomis (2014) in calibrating the algorithm for automatic size measurement of the holographic particles. The fitted number median diameters for the all data fit (left) and partial data fit (right) were 34.2 and 34.1 μm , respectively; and the geometric standard deviations are 0.65 and 0.66, respectively. The same comparisons were made for dive #6..... 7

Figure I-7: Summary of the lognormal number median diameter of dives #5 and #6 at different depth intervals. The depth range of each depth interval is calculated as, $100 \cdot (n-1)$ to $100 \cdot n$, where n is the sequential order of the depth interval as shown on the label of the x-axis, except the greatest depth interval of each dive, which should be the maximum depth of each dive (given in Table I-1). 8

Figure I-8: Summary of the logarithmic geometric standard deviation of dives #5 and #6 at different depth intervals. The depth ranges are the same as given in Figure I-7.....	8
Figure I-9. Cumulative volume distribution of dives #5 and 6 throughout the entire depth of <i>Holocam</i> measurements and the fitted lognormal distribution functions	9
Figure I-10: Observed (dots) and fitted (lines) cumulative lognormal droplet size volume distribution of the JF-3 dive# 5 droplet size data. The left panel shows the data for the whole range as reported by Davis and Loomis (WHOI), and all the data were used to fit the lognormal size distribution function; the right panel displays only droplets $d \geq 30 \mu\text{m}$, a cutoff size that was used by Davis and Loomis in calibrating the algorithm for automatic size measurement of the holographic particles. The fitted volume median diameters for the all data fit (left) and partial data fit (right) are both $148 \mu\text{m}$	10
Figure I-11: The volume median diameter of droplets at different depths (binned into 100m intervals) for dives #5 and #6.	11

List of Tables

Table I-1. Summary of daily flow rate (total and oil released to the water column, bbl), dispersants applied (gal) and the maximum depth and distance of the JF3 dives from the Davis and Loomis (2014) study.....	2
Table I-2: Summary of hologram data that was manually analyzed from each dive (Table 4 of Davis and Loomis, 2014)	4
Table I-3: The observed maximum number and volume droplet diameters (d_{95} and d_{99}) of each individual dive	10

11. *Holocam* oil droplet size distribution data from JF3 cruises

As part of the Natural Resource Damage Assessment (NRDA) sampling program in response to the DWH oil spill in the Gulf of Mexico, a unique set of data on size distribution of oil droplets was collected and processed by Davis and Loomis (2014; also Loomis, 2011). The data was collected during a cruise on the M/V *Jack Fitz* Cruise 3 (JF3) using an *in situ* digital holographic camera (*Holocam*). The size distributions of the oil droplets present in the water column were estimated using the *Holocam*, which was mounted on the front of a remotely operated vehicle (ROV). The data were collected between June 14 and 20, 2010, post riser-cut, at distances ranging from 1,150 m to 9,323 m from the wellhead throughout the depth of the water column, from the surface to the sea bed (Figure I-1). A summary of key information for each dive is provided in Table I-1. The data on oil release rates and dispersant application rates are from Lehr et al. (2010) and the data on the dives depths and locations from Davis and Loomis (2014). Data from dives #1 to #3 were corrupted and not reported and dive #4 was a test dive.

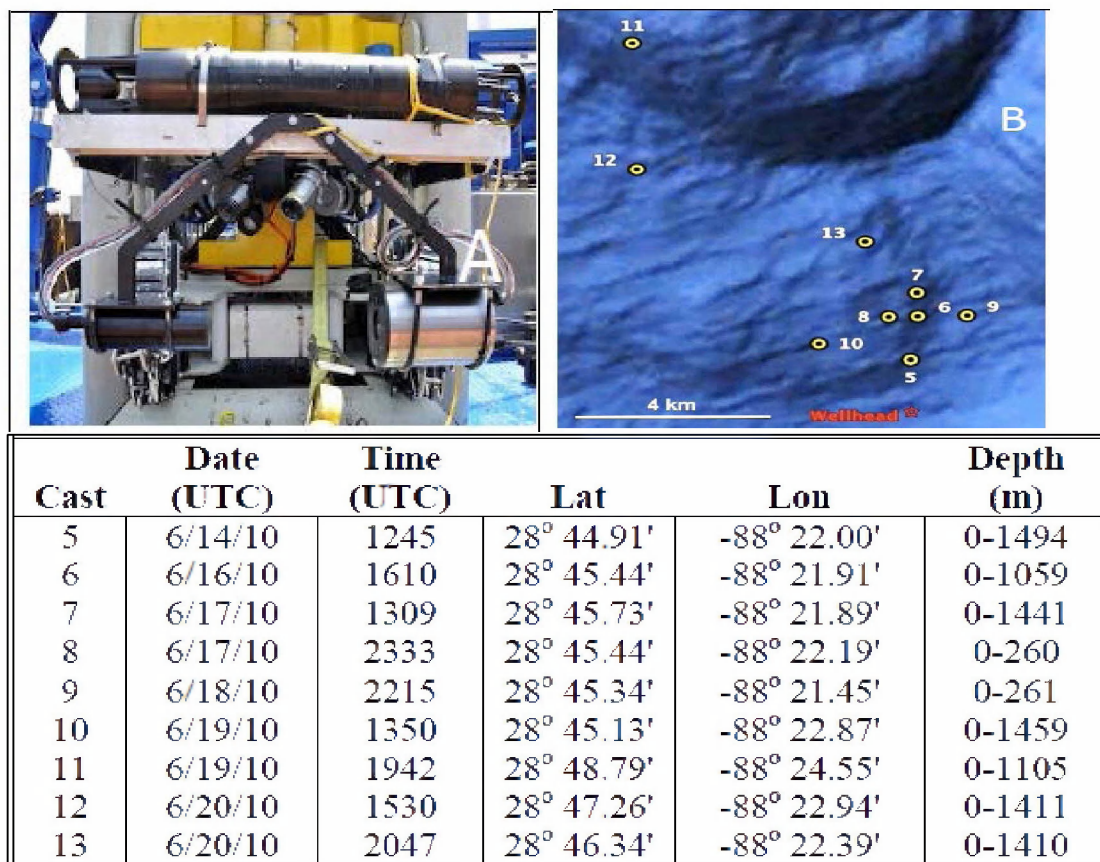


Figure I-1. Upper Panel, A. Cruise M/V Jack Fitz 3. Holographic camera (*Holocam*) mounted on the ROV. B. Locations of ROV dives 5-13, for which holograms were processed; Lower Panel, Time and Location (Latitude, Longitude, and Depth Range) of each dive.

Davis and Loomis (2014) developed an automated method to analyze the *Holocam* data from each dive to facilitate data processing. To validate the automated method they performed manual analyses of a sub-set of holograms from each dive. They developed a classification system to determine the presence of oil: for the manual method: Class 0 = no oil, Class 1 = oil, Class 2 = possible oil and for the automated method: Class 1 = oil droplets, Class 2 = non-oil particles. The manual method has been used as the definitive standard for selecting data for the present study. The results of the manual analysis are provided in Table I-2, showing dives with *no oil*, *little oil*, and *much oil*. A review of the table, with a focus on the amount of oil at the trapping depths (deep stations), shows that dives # 5 and 6 had *much oil*; dives #7, 10, 12, and 13 *little oil*; and dive #11 *no oil*. Dives # 8 and 9 were sampled in shallow depths only. Given the low number of oil droplets observed in the manual analysis for the dives with *little oil* (30 droplets or less) and to minimize uncertainty in identifying oil droplet sizes, only data from dives # 5 and 6 where *much oil* was observed are included in the present analysis.

Table I-1. Summary of daily flow rate (total and oil released to the water column, bbl), dispersants applied (gal) and the maximum depth and distance of the JF3 dives from the Davis and Loomis (2014) study.

		Maximum Depth (h) and Distance (s) from Well Head		OBC Total Oil Release (TR), Recovered Oil (RC), and Net Release to the Water Column (WC)			Surface (Surf), Subsurface (Sub), and Total (Total) Dispersant applied		
Date	Dive	h (m)	s (m)	TR (bbl)	RC (bbl)	WC (bbl)	Surf (gal)	Sub (gal)	Total (gal)
6/14/2010	5	1494	1150	58800	15421	43379	10741	9800	20541
6/16/2010	6	1059	2128	58500	18227	40273	13593	8777	22370
6/17/2010	7	1441	2664	58400	25295	33105	12423	5763	18186
6/17/2010	8	260	2160	58400	25295	33105	12423	5763	18186
6/18/2010	9	261	2110	58300	24552	33748	15711	9148	24859
6/19/2010	10	1459	2150	58200	21041	37159	8510	16911	25421
6/19/2010	11	1105	9323	58200	21041	37159	8510	16911	25421
6/20/2010	12	1411	5716	58100	23291	34809	19576	14070	33646
6/20/2010	13	1410	3854	58100	23291	34809	19576	14070	33646

A summary of the key findings of the Davis and Loomis (2014) study are provided below using direct quotes from their report:

- “A total of 7697 holograms were automatically processed from these dives. A total of 1651 holograms were manually scanned, with an additional 172 manually scanned and then fully analyzed in detail, for a total of 1823 holograms manually processed.”
- “The manual analysis revealed that oil droplets were found primarily on Dives 5 and 6, with few droplets observed on other dives (Table I-2). Most of the oil droplets were observed in the deep plume during Dives 5 and 6. While little oil was observed in upper layer on Dive 5, substantial numbers of oil droplets were observed in shallow waters on Dive 6 (Table-2).”
- “For the initial hologram (A1009566), the size distribution of oil droplets and possible droplets (class 1 and 2 combined) was similar to that found using the automated method, with mean diameters not significantly different between methods for objects ≥ 6 pixels in diameter (Figure 9 (Figure I-2 upper panel) of Davis and Loomis, 2014).”
- “For objects manually sorted to class 1 (oil droplets), the mean size (of the manual method) was larger, as expected, due to the greater number of pixels required to positively identify oil droplets (Figure 10 (Figure I-2, lower panel) of Davis and Loomis, 2014). For droplets $\geq 30\mu\text{m}$, no significant difference in mean diameter was found between those manually versus automatically sorted (manual mean = $54.0\mu\text{m}$, automatic mean = $55.0\mu\text{m}$, t-test $p = 0.87$, hologram A1009566).”
- “Droplet diameter (μm) varied by nearly 3 orders of magnitude on Dives 5 and 6 with oil droplets observed at localized depths (Figure 11 (Figure I-3) and Figure 12 (Figure I-4) of Davis and Loomis 2014). Within the deep plume observed in Dives 5 and 6, oil droplet diameter (μm) increased with decreasing depth. For example, on Dive 5, the mean diameter of oil droplets (category 1) located between 1100-1200 m was $54\pm 3\mu\text{m}$ (mean $\pm 2\text{sd}$), whereas the mean diameter of droplets between 850-950 m was $349\pm 4\mu\text{m}$. Similarly, on Dive 6, the mean diameter of oil droplets (category 1) located in the deeper portion of the plume (>1020 m) was $150\pm 3\mu\text{m}$, whereas the mean diameter of oil droplets in the 950-1020 m layer was $315\pm 2\mu\text{m}$, and the mean diameter of oil droplets in the 850-950 m layer was $368\pm 3\mu\text{m}$.”
- “On both dives #5 and #6, oil droplets were not commonly observed between 250-850 m. At depths <250 m, few oil droplets were observed on Dive 5, but many were observed on Dive 6. The mean diameter of droplets (category 1) in the upper layer for Dive 6 was $156\pm 6\mu\text{m}$.”
- “In general, the manual and automatic methods to determine oil droplet size agreed well for Dives 5 and 6.”

Table I-2: Summary of hologram data that was manually analyzed from each dive (Table 4 of Davis and Loomis, 2014)

Dive	NUMBER OF HOLOGRAMS			Notes	Concentration (Droplets/liter)
	Depth layer	Analyzed	Scanned		
5	Shallow	19		Little oil (2 droplets)	1.1567
	Deep	44	57	Much oil (577 droplets)	62.7788
6	Shallow	27		Much oil (73 droplets)	29.7110
	Deep	32		Much oil (194 droplets)	66.6209
7	Shallow	1	101	Little oil (13 droplets)	1.4006
	Deep		203	Little oil (6 droplets)	0.3248
8	Shallow		225	No oil	<0.0488
9	Shallow	1	176	Little oil (18 droplets)	1.1175
10	Shallow	13	148	Little oil (3 droplets)	0.2048
	Deep	1	215	Little oil (3 droplets)	0.1526
11	Shallow	13	64	No oil	<0.1427
	Deep	2	112	No oil	<0.0964
12	Shallow		55	No oil	<0.1998
	Deep		19	Little oil (1 droplet)	0.5784
13	Shallow	16	61	Little oil (4 droplets)	0.5709
	Deep	3	215	Little oil (30 droplets)	1.5122
Total all dives		172	1651		

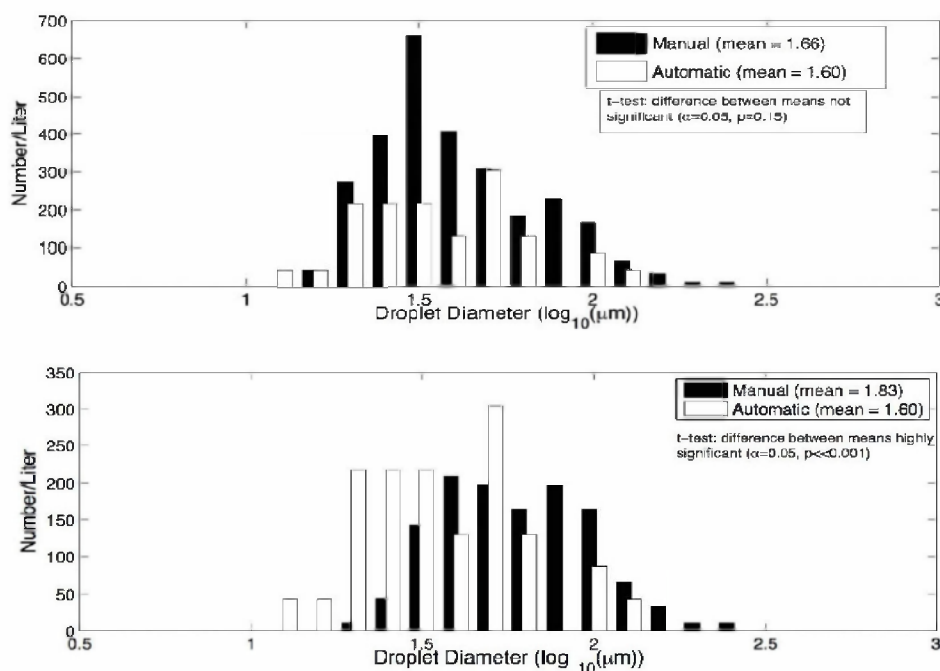


Figure I-2: Upper panel, Figure 9 of Davis and Loomis (2014), Dive 5, (hologram A1009566) size distribution of oil droplets determined by manual (Class 0 = no oil, Class 1 = oil, Class 2 = possible oil) and automatic (Class 1 = oil droplets, Class 2 = non-oil particles) methods; for the manual method, objects were class 1 or 2 with ≥ 6 pixel diameter. Lower panel, Figure 10 of Davis and Loomis (2014) Dive 5, (hologram A1009566) size distribution of oil droplets determined by manual and automatic methods; for the manual method, objects were class 1 only.

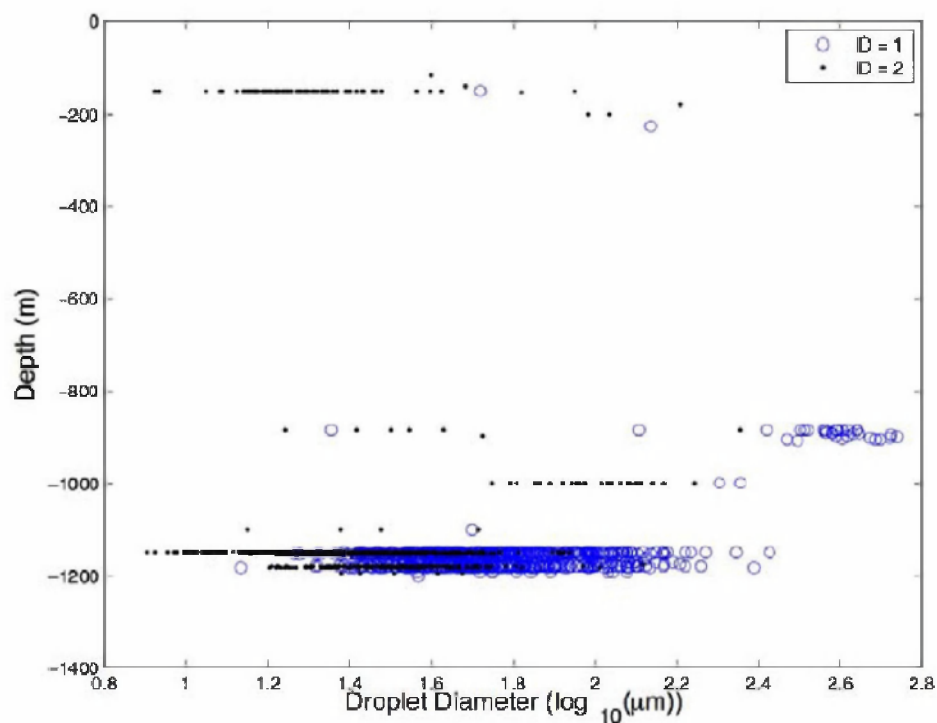


Figure I-3: Figure 11 of Davis and Loomis (2014), Dive 5, Diameters of oil droplets (class 1, open circles) and possible droplets (class 2, black dots) versus depth.

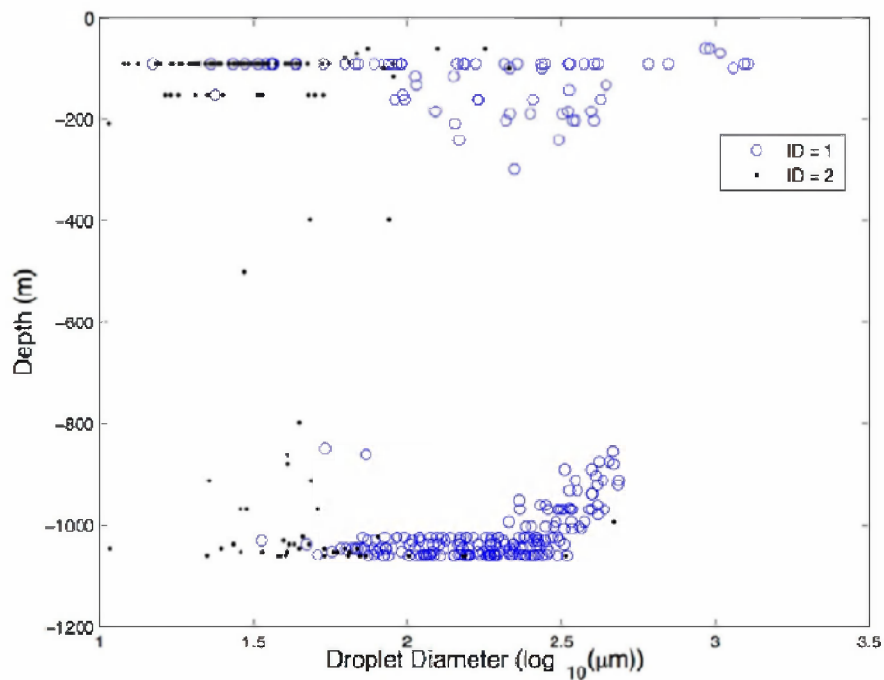


Figure I-4: Figure 12 of Davis and Loomis (2014), Dive 6, Diameters of oil droplets (class 1, open circles) and possible droplets (class 2, black dots) versus depth.

12. Lognormal distribution fit to the data

12.1 Number medium diameter and standard deviation of each dive

Figure I-5 presents the cumulative droplet size number distribution of JF3 dives #5 and #6 Class 1 particles (identified by Davis and Loomis (2014) as oil droplets). The other Class 2 particles (accounting for more than 90% of the total number of measured particles for each dive) were excluded from the analysis, as they were determined by Davis and Loomis (2014) to be non-oil particles.

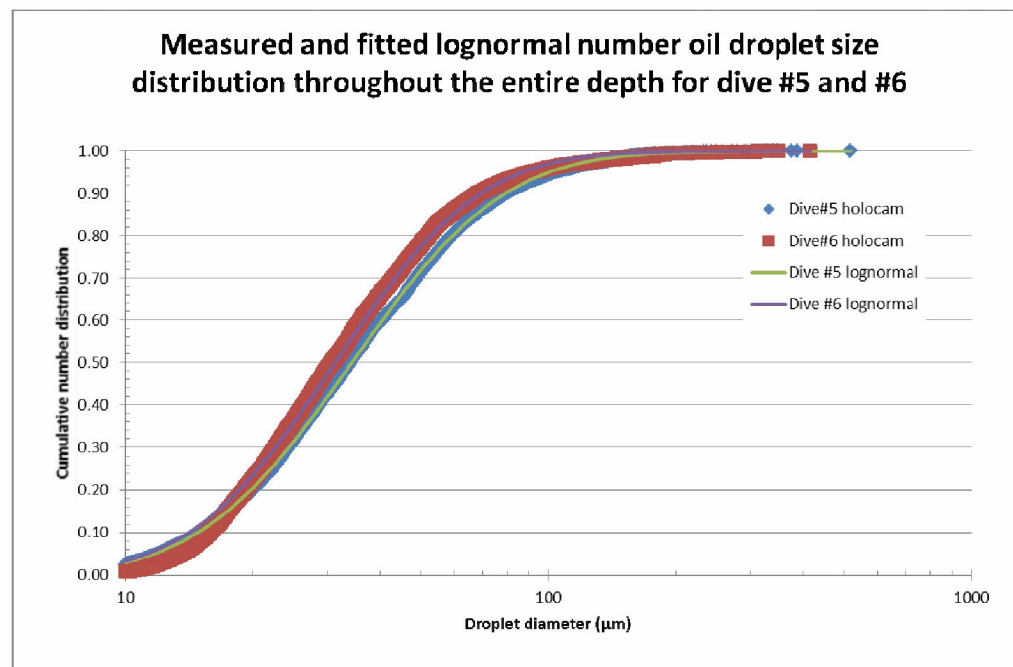


Figure I-5. Cumulative number distribution of dives #5 and 6 throughout entire depth of in situ measurements and the fitted lognormal distribution functions

The two-parameter (median number diameter and geometric standard deviation) lognormal *oil droplet distribution* function was fit to the *Holocam* data of dives #5 and #6. The goodness-of-fit is extremely good with R^2 of 0.9997 and 0.9972 for dive #5 and #6, respectively.

In Davis and Loomis work the training set developed to identify droplets did not include droplets smaller than 30 μm. To determine the sensitivity of the lognormal fit to droplet size data, droplet diameter data below 30 μm was then excluded in the re-analysis of the dive #5 and #6 *Holocam* data. As shown in Figure I-6, lognormal distribution fits are almost identical, with and without accounting for the exact diameter of the droplets $d \leq 30$ μm, and the number median diameter sizes and standard deviations are almost identical for the two fits.

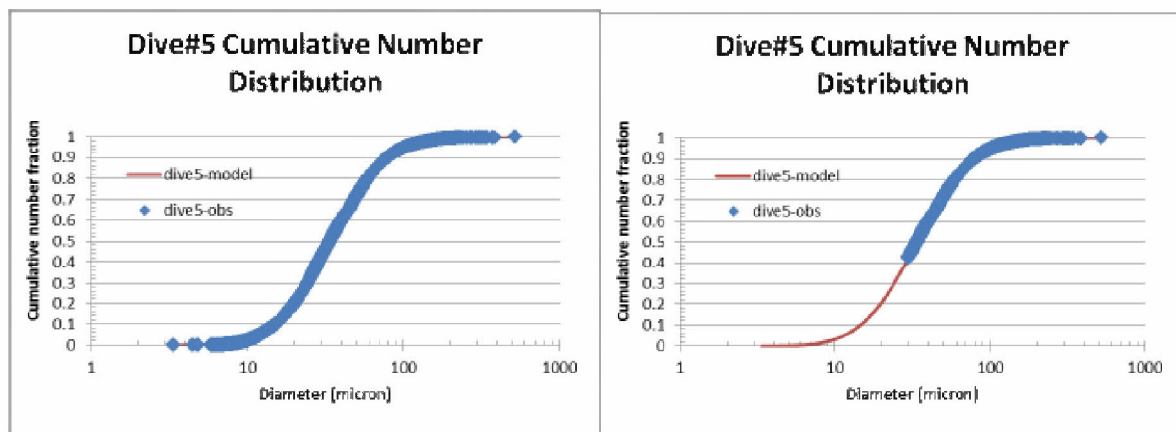


Figure I-6. An example of the observed (dots) and fitted (lines) cumulative lognormal droplet size number distribution of the JF3 dive #5 droplet size data. The left panel shows the data of the whole range as reported by Davis and Loomis (2014), and all the data were used to fit the lognormal size distribution function; the right panel displays only droplets $d \geq 30 \mu\text{m}$, a cutoff size that was used by Davis and Loomis (2014) in calibrating the algorithm for automatic size measurement of the holographic particles. The fitted number median diameters for the all data fit (left) and partial data fit (right) were 34.2 and 34.1 μm , respectively; and the geometric standard deviations are 0.65 and 0.66, respectively. The same comparisons were made for dive #6.

The droplet size data for dive #5 and #6 were then binned vertically every 100 m (except the last bin of each dive, which includes the remaining depth of the water less than 100 m) into 11 and 15 depth intervals, from the surface to the maximum depth for additional data analysis. Figure I-7 shows the number median diameters for dive #5 and #6 at different depth intervals. The majority of the median diameters are less than or equal to 45 μm .

The corresponding values for the standard deviations are shown in Figure I-8. The average logarithmic geometric standard deviation (GSD or σ_g) of the lognormal number distribution is 0.60 ± 0.08 . This is in very good agreement with the logarithmic GSD when fit ($\log \sigma_g = 0.51 \pm 0.09$, Appendix G) to the *Deep Spill* field observations (Johansen et al. 2001). This suggests that as a general modeling approach, a simple constant logarithmic geometric standard deviation can be used in describing oil droplet size distribution when using the lognormal size distribution function.

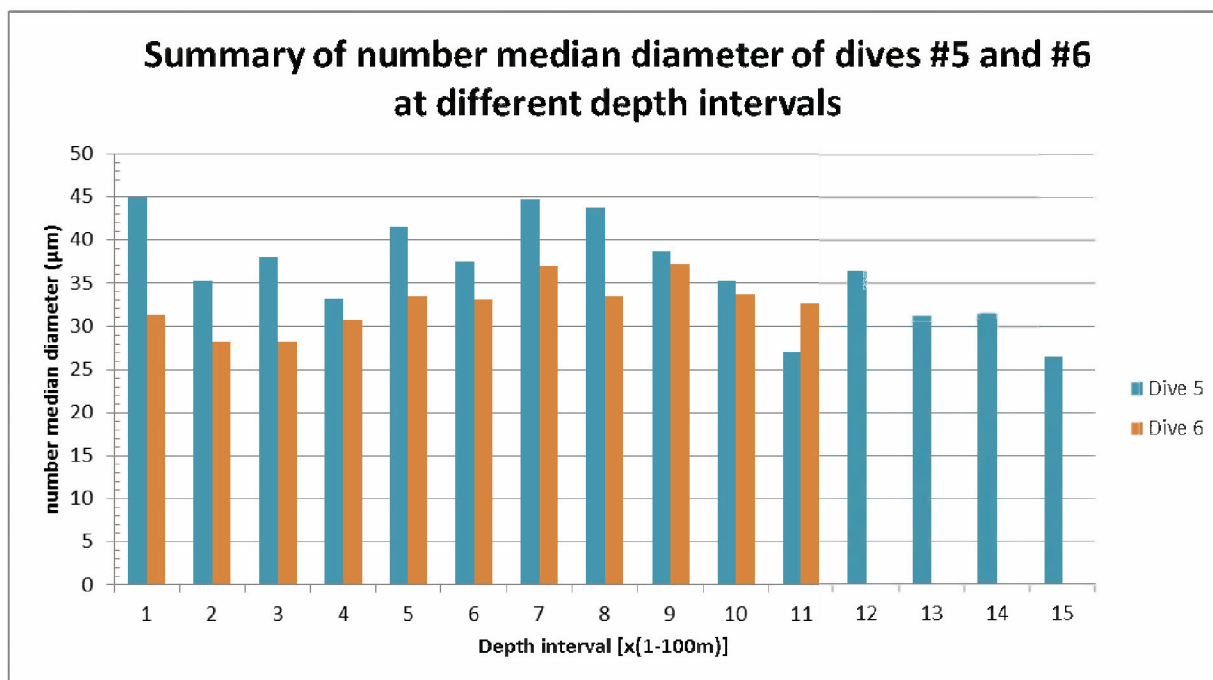


Figure I-7: Summary of the lognormal number median diameter of dives #5 and #6 at different depth intervals. The depth range of each depth interval is calculated as, $100 \cdot (n-1)$ to $100 \cdot n$, where n is the sequential order of the depth interval as shown on the label of the x-axis, except the greatest depth interval of each dive, which should be the maximum depth of each dive (given in Table I-1).

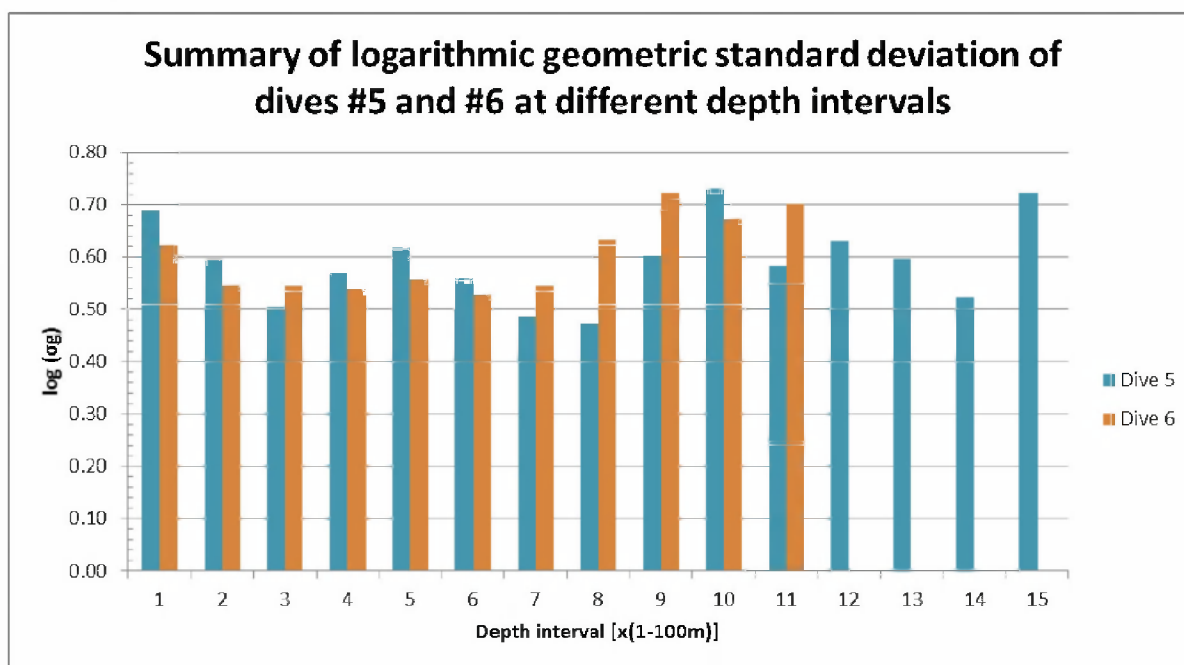


Figure I-8: Summary of the logarithmic geometric standard deviation of dives #5 and #6 at different depth intervals. The depth ranges are the same as given in Figure I-7.

12.2 Volume median diameter (VMD) and standard deviation of each dive

The same data sets of the JF3 dive #5 and #6 number distributions were used to calculate the cumulative volume droplet size distributions. Figure I-9 presents plots of the cumulative volume droplet size distributions and fitted lognormal distribution functions for JF3 dives #5 and #6 Class 1 particle data (identified by Davis and Loomis (2014) as oil droplets), and with an R^2 of 0.9992 and 0.9670, for dives #5 and #6, respectively.

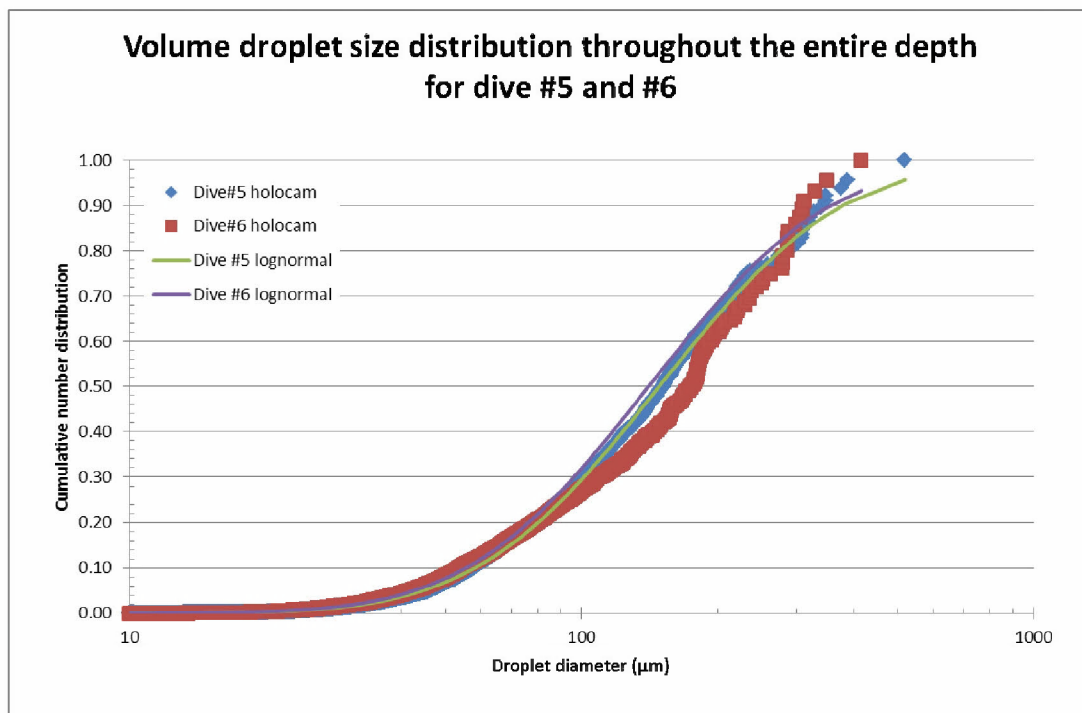


Figure I-9. Cumulative volume distribution of dives #5 and 6 throughout the entire depth of Holocam measurements and the fitted lognormal distribution functions

Figure I-10 presents a comparison of the computed and the model fit cumulative volume distribution of dive #5 including (left-hand side) and excluding (right-hand side) the exact sizes of smaller droplets ($d \leq 30 \mu\text{m}$). Similar comparisons were made for dive #6, indicating that the sizing of smaller droplets ($d \leq 30 \mu\text{m}$) has no significant impact on the overall cumulative volume size distribution parameters.

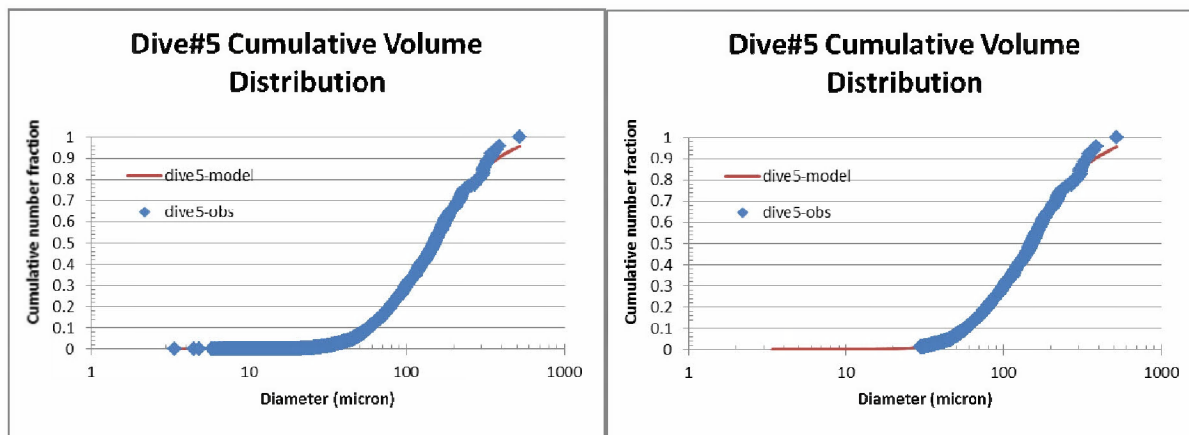


Figure I-10: Observed (dots) and fitted (lines) cumulative lognormal droplet size volume distribution of the JF-3 dive# 5 droplet size data. The left panel shows the data for the whole range as reported by Davis and Loomis (WHOI), and all the data were used to fit the lognormal size distribution function; the right panel displays only droplets $d \geq 30 \mu\text{m}$, a cutoff size that was used by Davis and Loomis in calibrating the algorithm for automatic size measurement of the holographic particles. The fitted volume median diameters for the all data fit (left) and partial data fit (right) are both $148 \mu\text{m}$.

Table I-3 summarizes the maximum (d_{95} or d_{99}) number diameters and volume diameters observed for each of the JF3 dives; these values serve as the upper boundary of the droplet diameters that are likely to be encountered in the environment. For dive #5 on volume distribution basis, 95% of the oil droplets have diameters less than $388 \mu\text{m}$, whereas 99% of those are less than $519 \mu\text{m}$. On a number basis, these two boundaries are $103 \mu\text{m}$ and $171 \mu\text{m}$, respectively. For dive # 6 similar values were obtained. The volume diameters are $350 \mu\text{m}$ and $417 \mu\text{m}$ and the number diameters are 91 and $179 \mu\text{m}$, for the 95% and 99% values, respectively.

Table I-3: The observed maximum number and volume droplet diameters (d_{95} and d_{99}) of each individual dive

Dive #	Number diameter (μm)		Volume diameter (μm)	
	d_{95}	d_{99}	d_{95}	d_{99}
Dive5	103	171	388	519
Dive6	91	179	350	417

Figure I-11 presents the volume median diameters for dive #5 and #6 at different depth intervals. The ranges of the volume median diameters of dive # 5 data for each depth interval, excluding the maximum depth interval, were $70 - 218 \mu\text{m}$. The ranges of the volume median diameters of dive # 6 data were $73-250 \mu\text{m}$. The trends of the diameters changing with depth intervals are generally consistent with the manual processing data results of Davis and Loomis (2014; see summary above).

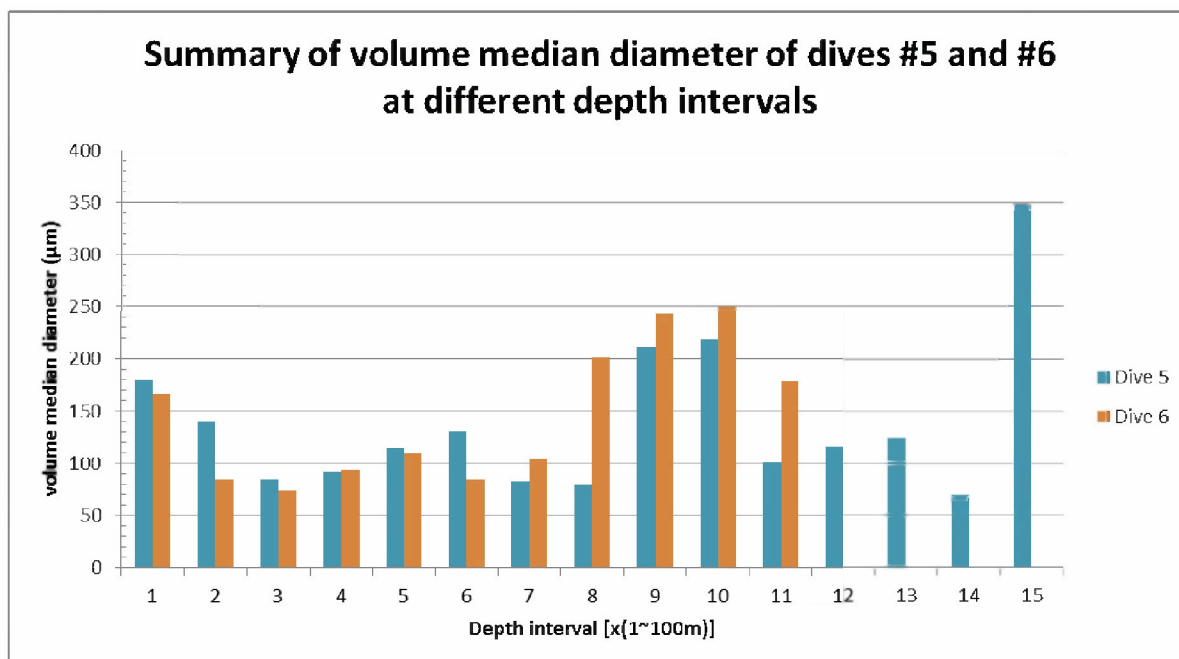


Figure I-11: The volume median diameter of droplets at different depths (binned into 100m intervals) for dives #5 and #6.

13. Summary

Davis and Loomis (2014) reported *Holocam*-based measurements of the oil droplet size distribution during the M/V *Jack Fitz* (JF) 3 cruise. Among those ROV deployment dives, two dives, dive #5 and #6 were reported to have *much oil* in the deep water column; dive #6 was also shown to have much oil in the shallow water layer. Lognormal (number and volume) oil droplet size distribution function fits the measured oil droplet size distribution data very well. The observed volume median droplet diameter from the JF3 cruise dive #5 and #6 were in the range of 70 - 218 μm and 73-250 μm, respectively.

14. References

- Davis, C. S. and N. C. Loomis, 2014. Deepwater Horizon Oil Spill (DWHOS) Water Column Technical Working Group Image Data Processing Plan: *Holocam*, Description of data processing methods used to determine oil droplet size distributions from in situ holographic imaging during June 2010 on cruise M/V Jack Fitz 3. Woods Hole Oceanographic Institution; MIT/WHOI Joint Program in Oceanography. 15 pages + Appendices.
- Johansen, O., H. Rye, A. Melbye, H. Jensen, B. Serigstad, and T. Knutsen, 2001. Deep Spill JIP experimental discharges of gas and oil at Jelland Hansen - June 2000, Technical Report, SINTEF Applied Chemistry, Trondheim, Norway.
- Lehr, W., S. Bristol, and A. Possolo, 2010. Deepwater horizon oil budget calculator: A report to the national incident command. The Federal Interagency Solutions Group, Oil Budget Calculator Science and Engineering Team.

http://www.restorethegulf.gov/sites/default/files/documents/pdf/OilBudgetCalc_Full_HQ-Print_111110.pdf (Accessed on April 1, 2012).

Loomis, N. C., 2011. Computational imaging and automated identification for aqueous environments. PhD dissertation, Massachusetts Institute of Technology and the Woods Hole Oceanographic Institute, Cambridge, Massachusetts, USA.

Technical Reports for Deepwater Horizon Water Column Injury Assessment

WC_TR.13: Application of OILMAP DEEP to the Deepwater Horizon Blowout

Appendix J: OILMAP DEEP Output to SIMAP Input

Authors: Malcolm Spaulding, Daniel Mendelsohn, Deborah Crowley,
Zhengkai Li, Andrew Bird

Revised: September 30, 2015

Project Number: 2011-144

RPS ASA 55 Village Square Drive, South Kingstown, RI 02879

Table of Contents

J.1	Background	1
J.2	Blowout Plume Model Output for SIMAP Input	1
J.3	Droplet Size Model Output for SIMAP Input.....	2
J.4	Model Results Post-Processing for SIMAP Input.....	4
J.5	References	15

List of Figures

Figure J-1: Illustration of daily distribution of mass in various bin sizes throughout the release for the no treatment case.	8
Figure J-2: Illustration of daily distribution of mass in various bin sizes throughout the release for the low treatment case.	9
Figure J-3: Illustration of daily distribution of mass in various bin sizes throughout the release for the high treatment case.....	9
Figure J-4: Illustration of daily distribution of mass in various bin sizes throughout the release for the best estimate case.	10
Figure J-5: Illustration of time history of release of oil to the water column (first panel), time history of dispersant applied (second panel), and time history of fraction of total oil released from various regrouped bin sizes for the no treatment case (third and fourth panel). Note that the third panel covers fractions between 0-1 and the fourth panel covers only fractions 0-0.05 to facilitate viewing.	11
Figure J-6: Illustration of time history of release of oil to the water column (first panel), time history of dispersant applied (second panel), and time history of fraction of total oil released from various regrouped bin sizes for the low treatment case (third and fourth panel). Note that the third panel covers fractions between 0-1 and the fourth panel covers only fractions 0-0.05 to facilitate viewing.	12
Figure J-7: Illustration of time history of release of oil to the water column (first panel), time history of dispersant applied (second panel), and time history of fraction of total oil released from various regrouped bin sizes for the high treatment case (third and fourth panel). Note that the third panel covers fractions between 0-1 and the fourth panel covers only fractions 0-0.05 to facilitate viewing.	13
Figure J-8: Illustration of time history of release of oil to the water column (first panel), time history of dispersant applied (second panel), and time history of fraction of total oil released from various regrouped bin sizes for the best estimate case (third and fourth panel). Note that the third panel covers fractions between 0-1 and the fourth panel covers only fractions 0-0.05 to facilitate viewing.	14

List of Tables

Table J-1. Summary of droplet size bin characteristics for initial period April 22 – April 27, 2010.	3
Table J-2. Summary of mass total (BBL, barrels and MT, metric tons) and fractional breakdown (K- kink, RD- riser dispersed and RND- riser not dispersed) for four different cases.	5

J.1 Background

RPS ASA's **OILMAP DEEP**, an integrated system of sub-model components, was applied to the Deepwater Horizon (DWH) oil spill to simulate the near field transport and fate of the oil and gas released into the northeastern Gulf of Mexico. The output of **OILMAP DEEP** was provided as input to **SIMAP** to characterize the subsurface oil release; **SIMAP** in turn is used to determine the far field transport, fate, exposures, and effects of the oil in the environment.

In the present application, simulations from the *blowout plume model* (trapping height) and the *oil droplet size model* (volume-weighted oil droplet size distribution), were provided as input to **SIMAP**. Predictions of the *pipeline release model* were used as input to the *blowout plume model* and those from the dispersant treatment model as input to the *droplet size model*. The blowout and droplet size simulations were performed on a daily time step. This time step was used to be consistent with the temporal resolution of the input data describing the oil that was released and the subsurface dispersant that was applied. The time step used in the **SIMAP** simulations is nominally a half-hour, but has an option of defining the mass released at any time step, regardless of the **SIMAP** solution time step. For this study input files were generated with mass released from each discrete oil droplet size on a two hour time step, though half the bin sizes were released every hour (half on odd hours, half on even hours) to both minimize the number of original spilllets and to release mass in a continuous manner. The daily release, which was assumed constant throughout the day, was used to determine the appropriate mass released per time step.

The end product of the blowout model was input data to **SIMAP** that defined the release in the form of an *.spt file which is an input file recognized by **SIMAP**. The input to **SIMAP** is in the form of oil released throughout the spill event and consists of the position (latitude, longitude), depth (below the surface), the time of release (relative to event onset) and the amount of mass (MT) in varying droplet sizes for each time step. The three major components to generating the **SIMAP** input are: running the *Blowout Plume Model*, running the *Droplet Size Model*, and then post-processing the model results into **SIMAP**-ready format.

Four (no dispersant treatment, low dispersant treatment, best estimate of dispersant treatment, and high estimate of dispersant treatment) cases were simulated, as described in the Technical Report: Application of OILMAP DEEP to the Deepwater Horizon Blowout (hereafter referred to as the Technical Report), which varied in the estimate of mass treated with dispersant and the efficiency of the treatment.

J.2 Blowout Plume Model Output for SIMAP Input

The Blowout Plume model used input characterizing the DWH release on a daily basis and returned detailed resulting plume information, most importantly for generating **SIMAP** input was the plume 'trap height or depth' for that daily release condition. The trap height is the height (above the release location) at which the plume becomes neutrally buoyant, after which point the droplets rise based on their free rise velocity (the free rise of the droplets is simulated in **SIMAP**).

The plume modeling was described in detail within Section 5.6 of the Technical Report, however an overview will be provided here as well. Appendix E contains a detailed description of the blowout plume model theory and development. As previously established, the DWH spill

consisted of two release locations: (1) end of the broken riser and (2) above the BOP at the wellhead (at slightly variable heights depending on whether kink flow or cut riser flow), and three different release types: riser not dispersed (RND), riser dispersed (RD), and kink (K).

The present application predicted the plume dynamics resulting from the riser and kink separately over the entire event, 84 days from April 22 through July 14, 2010 from the riser (either end of broken riser or cut riser), and 36 days from April 28 through June 2nd from the kink. Note that the riser pipe cut was completed early on the morning of June 3rd, however since the majority of that day reflected the post cut riser condition; the entire day was represented as having no kink flow. The blowout plume model did not discern between the non-dispersed and dispersed fractions of the riser release, therefore the riser is modeled as a bulk release for trap height calculations. The model inputs varied mainly with respect to the amount of oil and gas released as well as the release exit opening diameter (or equivalent diameter such as in the case of the kink holes). The plume model simulates the evolution of the plume, the oil and gas mixture that entrains an increasing amount of water with increasing height above the release. The output of the model includes details of the plume characteristics (location, size, and centerline oil and gas concentrations) and the trap height.

For each release (riser and kink) the trap height for each day was used as input to the **SIMAP** model. Details on the implementation of this height into the input file are described in Section J.4.

J.3 Droplet Size Model Output for SIMAP Input

The *oil droplet size model* was used to determine the volume (mass) distribution of oil within a set of droplet size 'bins' on a daily basis for the three different release types (RND, RD, K) for each day of the DWH spill event. Appendix G contains details on the *Oil Droplet Size Model* methodology and Section 5.7 of the Technical Report presents details on the application of the Droplet Model to the DWH event.

For each release type, the Droplet Size Model required an input file describing the total oil flow from the release, GOR (to calculate gas flow), estimated exit velocity based on the Black Oil Table analysis (Zick 2013), and oil-water interfacial tension for each day. The plume model was based on the amount released to the water column, while the droplet size model used the total release including the amount collected to determine the exit velocity which is used as input to the *Oil Droplet Size Model*. This difference is due to the fact that the droplet size model is dependent on a velocity representative of the conditions of the release, and while some oil and gas is collected above the release point, the velocity at the release opening (with all oil and gas) is the representative of the velocity responsible for droplet formation. Use of the total flow provides the appropriate exit velocity, and results in the proper distribution of percent mass in the droplet size bins. The actual mass is a function of the mass released to the water column from each release type and is described in more detail in Section J.4.

The oil-water interfacial tension differs between the riser dispersed fraction and the riser non-dispersed fraction, thus the reason this release source (riser) was modeled as two separate releases. The oil-water interfacial tension for the treated fraction for each day was calculated based on the relationship between the dispersant-to-oil ratio (DOR) and the interfacial tension. The details of this relationship are documented in Appendix G.

In the present model application, the model solved for the volume (mass) fraction in a set of 100 discrete prescribed droplet size bins for each release type for each day. Table J-1 illustrates the minimum, maximum, and representative size for the bins. The droplet size model solved for the

amount of mass between the minimum and maximum of the bin, and the representative size is the size assigned to the associated mass in the **SIMAP** input file. Note that the representative size was assigned to the bin arithmetic mean, with the exception of the largest bin captured all sizes greater than 9,500 μm .

Table J-1. Summary of droplet size bin characteristics for initial period April 22 – April 27, 2010.

Bin #	Minimum Size (um)	Maximum Size (um)	Representative Size (um)	Bin #	Minimum Size (um)	Maximum Size (um)	Representative Size (um)
1	0	10	5	51	500	525	512
2	10	20	15	52	525	550	537
3	20	30	25	53	550	575	562
4	30	40	35	54	575	600	587
5	40	50	45	55	600	625	612
6	50	60	55	56	625	650	637
7	60	70	65	57	650	675	662
8	70	80	75	58	675	700	687
9	80	90	85	59	700	725	712
10	90	100	95	60	725	750	737
11	100	110	105	61	750	775	762
12	110	120	115	62	775	800	787
13	120	130	125	63	800	825	812
14	130	140	135	64	825	850	837
15	140	150	145	65	850	875	862
16	150	160	155	66	875	900	887
17	160	170	165	67	900	925	912
18	170	180	175	68	925	950	937
19	180	190	185	69	950	975	962
20	190	200	195	70	975	1000	987
21	200	210	205	71	1000	1100	1050
22	210	220	215	72	1100	1200	1150
23	220	230	225	73	1200	1300	1250
24	230	240	235	74	1300	1400	1350
25	240	250	245	75	1400	1500	1450
26	250	260	255	76	1500	1600	1550
27	260	270	265	77	1600	1700	1650
28	270	280	275	78	1700	1800	1750
29	280	290	285	79	1800	1900	1850
30	290	300	295	80	1900	2000	1950
31	300	310	305	81	2000	2300	2150
32	310	320	315	82	2300	2600	2450

Bin #	Minimum Size (um)	Maximum Size (um)	Representative Size (um)	Bin #	Minimum Size (um)	Maximum Size (um)	Representative Size (um)
33	320	330	325	83	2600	2900	2750
34	330	340	335	84	2900	3200	3050
35	340	350	345	85	3200	3500	3350
36	350	360	355	86	3500	3800	3650
37	360	370	365	87	3800	4100	3950
38	370	380	375	88	4100	4400	4250
39	380	390	385	89	4400	4700	4550
40	390	400	395	90	4700	5000	4850
41	400	410	405	91	5000	5500	5250
42	410	420	415	92	5500	6000	5750
43	420	430	425	93	6000	6500	6250
44	430	440	435	94	6500	7000	6750
45	440	450	445	95	7000	7500	7250
46	450	460	455	96	7500	8000	7750
47	460	470	465	97	8000	8500	8250
48	470	480	475	98	8500	9000	8750
49	480	490	485	99	9000	9500	9250
50	490	500	495	100	9500	-	10000

The end product of the *Oil Droplet Size Model* application was the percent of volume (mass) in the prescribed droplet bin set for each release type, for each day of the release. Note that not all days had mass in every bin size.

J.4 Model Results Post-Processing for SIMAP Input

The model results from the *blowout plume model* and the *oil droplet size model* were used to generate the **SIMAP** model input.

For each day, the total mass released to the water column was known based on inputs defined by the OBC (Appendix A) and the total mass was determined based on an assumed oil density of 856 kg/m³ (Appendix C). The fraction of the release from each release type was calculated based on the amount of oil released to the water column from each source using a combination of the total released to the water column (Appendix A), the *pipeline release model* (Appendix D) and estimates of the amount treated with dispersant from either generalizations of the amount treated (e.g., none or all) with dispersant or from the *dispersant treatment model* (Appendix F) depending on the Case. The result of this analysis was the fraction of the release to the water column from the three different release types, for each day and for each case. Table J-2 illustrates this result for the four different treatment cases.

Table J-2. Summary of mass total (BBL, barrels and MT, metric tons) and fractional breakdown (K- kink, RD- riser dispersed and RND- riser not dispersed) for four different cases.

Date	Day of Release	Release to Water Column (BBL)	Release to Water Column (MT)	None Treated			High/Low Treatment			Best Estimate Treatment		
				Fraction K	Fraction RD	Fraction RND	Fraction K	Fraction RD	Fraction RND	Fraction K	Fraction RD	Fraction RND
4/22/2010	1	62200	8381.71	0.000	0.000	1.000	0.000	0.000	1.000	0.000	0.000	1.000
4/23/2010	2	62100	8368.24	0.000	0.000	1.000	0.000	0.000	1.000	0.000	0.000	1.000
4/24/2010	3	61900	8341.29	0.000	0.000	1.000	0.000	0.000	1.000	0.000	0.000	1.000
4/25/2010	4	61800	8327.81	0.000	0.000	1.000	0.000	0.000	1.000	0.000	0.000	1.000
4/26/2010	5	61700	8314.33	0.000	0.000	1.000	0.000	0.000	1.000	0.000	0.000	1.000
4/27/2010	6	61600	8300.86	0.000	0.000	1.000	0.000	0.000	1.000	0.000	0.000	1.000
4/28/2010	7	61500	8287.38	0.209	0.000	0.791	0.209	0.000	0.791	0.209	0.000	0.791
4/29/2010	8	61400	8273.91	0.209	0.000	0.791	0.209	0.000	0.791	0.209	0.000	0.791
4/30/2010	9	61300	8260.43	0.209	0.000	0.791	0.209	0.791	0.000	0.209	0.064	0.727
5/1/2010	10	61200	8246.96	0.209	0.000	0.791	0.209	0.000	0.791	0.209	0.000	0.791
5/2/2010	11	61000	8220.01	0.210	0.000	0.790	0.210	0.790	0.000	0.210	0.064	0.726
5/3/2010	12	60900	8206.53	0.210	0.000	0.790	0.210	0.790	0.000	0.210	0.064	0.726
5/4/2010	13	60800	8193.06	0.211	0.000	0.789	0.211	0.790	0.000	0.211	0.064	0.726
5/5/2010	14	60700	8179.58	0.211	0.000	0.789	0.211	0.000	0.789	0.211	0.000	0.789
5/6/2010	15	60600	8166.1	0.211	0.000	0.789	0.211	0.000	0.789	0.211	0.000	0.789
5/7/2010	16	60500	8152.63	0.211	0.000	0.789	0.211	0.000	0.789	0.211	0.000	0.789
5/8/2010	17	60400	8139.15	0.212	0.000	0.788	0.212	0.000	0.788	0.212	0.000	0.788
5/9/2010	18	60200	8112.2	0.212	0.000	0.788	0.212	0.000	0.788	0.212	0.000	0.788
5/10/2010	19	60100	8098.73	0.212	0.000	0.788	0.212	0.788	0.000	0.212	0.064	0.724
5/11/2010	20	60000	8085.25	0.213	0.000	0.787	0.213	0.787	0.000	0.213	0.064	0.724
5/12/2010	21	59900	8071.78	0.213	0.000	0.787	0.213	0.000	0.787	0.213	0.000	0.787
5/13/2010	22	59800	8058.3	0.213	0.000	0.787	0.213	0.000	0.787	0.213	0.000	0.787
5/14/2010	23	59700	8044.83	0.214	0.000	0.786	0.214	0.000	0.786	0.214	0.000	0.786
5/15/2010	24	59100	7963.97	0.216	0.000	0.784	0.216	0.784	0.000	0.216	0.063	0.721
5/16/2010	25	58500	7883.12	0.218	0.000	0.782	0.218	0.782	0.000	0.218	0.063	0.719
5/17/2010	26	58270	7852.13	0.219	0.000	0.781	0.219	0.781	0.000	0.219	0.063	0.718
5/18/2010	27	58000	7815.74	0.220	0.000	0.780	0.220	0.781	0.000	0.220	0.063	0.717
5/19/2010	28	56100	7559.71	0.227	0.000	0.773	0.227	0.773	0.000	0.227	0.062	0.711
5/20/2010	29	56800	7654.04	0.241	0.000	0.759	0.241	0.759	0.000	0.241	0.061	0.697

Date	Day of Release	Release to Water Column (BBL)	Release to Water Column (MT)	None Treated			High/Low Treatment			Best Estimate Treatment		
				Fraction K	Fraction RD	Fraction RND	Fraction K	Fraction RD	Fraction RND	Fraction K	Fraction RD	Fraction RND
5/21/2010	30	56725	7643.93	0.242	0.000	0.758	0.242	0.758	0.000	0.242	0.061	0.697
5/22/2010	31	57439	7740.15	0.239	0.000	0.761	0.239	0.762	0.000	0.239	0.062	0.700
5/23/2010	32	57580	7759.15	0.238	0.000	0.762	0.238	0.762	0.000	0.238	0.062	0.701
5/24/2010	33	58500	7883.12	0.234	0.000	0.766	0.234	0.766	0.000	0.234	0.062	0.704
5/25/2010	34	52322	7050.61	0.352	0.000	0.648	0.352	0.648	0.000	0.352	0.052	0.596
5/26/2010	35	55704	7506.35	0.338	0.000	0.662	0.338	0.662	0.000	0.338	0.054	0.609
5/27/2010	36	58200	7842.69	0.334	0.000	0.666	0.334	0.666	0.000	0.334	0.054	0.612
5/28/2010	37	58100	7829.22	0.334	0.000	0.666	0.334	0.666	0.000	0.334	0.054	0.612
5/29/2010	38	58000	7815.74	0.335	0.000	0.665	0.335	0.665	0.000	0.335	0.054	0.611
5/30/2010	39	57900	7802.27	0.336	0.000	0.664	0.336	0.665	0.000	0.336	0.054	0.611
5/31/2010	40	57700	7775.32	0.337	0.000	0.663	0.337	0.663	0.000	0.337	0.054	0.610
6/1/2010	41	57600	7761.84	0.337	0.000	0.663	0.337	0.663	0.000	0.337	0.054	0.609
6/2/2010	42	57500	7748.37	0.338	0.000	0.662	0.338	0.662	0.000	0.338	0.054	0.609
6/3/2010	43	60000	8085.25	0.000	0.000	1.000	0.000	1.000	0.000	0.000	0.300	0.700
6/4/2010	44	53813	7251.53	0.000	0.000	1.000	0.000	1.000	0.000	0.000	0.300	0.700
6/5/2010	45	49304	6643.92	0.000	0.000	1.000	0.000	1.000	0.000	0.000	0.300	0.700
6/6/2010	46	48581	6546.49	0.000	0.000	1.000	0.000	1.000	0.000	0.000	0.300	0.700
6/7/2010	47	44658	6017.85	0.000	0.000	1.000	0.000	1.000	0.000	0.000	0.300	0.700
6/8/2010	48	44394	5982.28	0.000	0.000	1.000	0.000	1.000	0.000	0.000	0.300	0.700
6/9/2010	49	43484	5859.65	0.000	0.000	1.000	0.000	1.000	0.000	0.000	0.300	0.700
6/10/2010	50	43798	5901.96	0.000	0.000	1.000	0.000	1.000	0.000	0.000	0.300	0.700
6/11/2010	51	43546	5868.01	0.000	0.000	1.000	0.000	1.000	0.000	0.000	0.300	0.700
6/12/2010	52	43961	5923.93	0.000	0.000	1.000	0.000	1.000	0.000	0.000	0.300	0.700
6/13/2010	53	43692	5887.68	0.000	0.000	1.000	0.000	1.000	0.000	0.000	0.300	0.700
6/14/2010	54	43379	5845.5	0.000	0.000	1.000	0.000	1.000	0.000	0.000	0.300	0.700
6/15/2010	55	48152	6488.68	0.000	0.000	1.000	0.000	1.000	0.000	0.000	0.300	0.700
6/16/2010	56	40273	5426.96	0.000	0.000	1.000	0.000	1.000	0.000	0.000	0.300	0.700
6/17/2010	57	33105	4461.04	0.000	0.000	1.000	0.000	1.000	0.000	0.000	0.300	0.700
6/18/2010	58	33748	4547.68	0.000	0.000	1.000	0.000	1.000	0.000	0.000	0.300	0.700
6/19/2010	59	37159	5007.33	0.000	0.000	1.000	0.000	1.000	0.000	0.000	0.300	0.700
6/20/2010	60	34809	4690.66	0.000	0.000	1.000	0.000	1.000	0.000	0.000	0.300	0.700

Date	Day of Release	Release to Water Column (BBL)	Release to Water Column (MT)	None Treated			High/Low Treatment			Best Estimate Treatment		
				Fraction K	Fraction RD	Fraction RND	Fraction K	Fraction RD	Fraction RND	Fraction K	Fraction RD	Fraction RND
6/21/2010	61	32164	4334.23	0.000	0.000	1.000	0.000	1.000	0.000	0.000	0.300	0.700
6/22/2010	62	30703	4137.36	0.000	0.000	1.000	0.000	1.000	0.000	0.000	0.300	0.700
6/23/2010	63	40834	5502.55	0.000	0.000	1.000	0.000	1.000	0.000	0.000	0.300	0.700
6/24/2010	64	33865	4563.45	0.000	0.000	1.000	0.000	1.000	0.000	0.000	0.300	0.700
6/25/2010	65	32952	4440.42	0.000	0.000	1.000	0.000	1.000	0.000	0.000	0.300	0.700
6/26/2010	66	34642	4668.16	0.000	0.000	1.000	0.000	1.000	0.000	0.000	0.300	0.700
6/27/2010	67	32845	4426	0.000	0.000	1.000	0.000	1.000	0.000	0.000	0.300	0.700
6/28/2010	68	33800	4554.69	0.000	0.000	1.000	0.000	1.000	0.000	0.000	0.300	0.700
6/29/2010	69	31877	4295.56	0.000	0.000	1.000	0.000	1.000	0.000	0.000	0.300	0.700
6/30/2010	70	33821	4557.52	0.000	0.000	1.000	0.000	1.000	0.000	0.000	0.300	0.700
7/1/2010	71	31646	4264.43	0.000	0.000	1.000	0.000	1.000	0.000	0.000	0.300	0.700
7/2/2010	72	31409	4232.49	0.000	0.000	1.000	0.000	1.000	0.000	0.000	0.300	0.700
7/3/2010	73	31402	4231.55	0.000	0.000	1.000	0.000	1.000	0.000	0.000	0.300	0.700
7/4/2010	74	31540	4250.15	0.000	0.000	1.000	0.000	1.000	0.000	0.000	0.300	0.700
7/5/2010	75	31418	4233.71	0.000	0.000	1.000	0.000	1.000	0.000	0.000	0.300	0.700
7/6/2010	76	31539	4250.01	0.000	0.000	1.000	0.000	1.000	0.000	0.000	0.300	0.700
7/7/2010	77	31522	4247.72	0.000	0.000	1.000	0.000	1.000	0.000	0.000	0.300	0.700
7/8/2010	78	31621	4261.06	0.000	0.000	1.000	0.000	1.000	0.000	0.000	0.300	0.700
7/9/2010	79	31108	4191.93	0.000	0.000	1.000	0.000	1.000	0.000	0.000	0.300	0.700
7/10/2010	80	40601	5471.16	0.000	0.000	1.000	0.000	1.000	0.000	0.000	0.300	0.700
7/11/2010	81	47465	6396.11	0.000	0.000	1.000	0.000	1.000	0.000	0.000	0.300	0.700
7/12/2010	82	44698	6023.24	0.000	0.000	1.000	0.000	1.000	0.000	0.000	0.300	0.700
7/13/2010	83	35836	4829.05	0.000	0.000	1.000	0.000	1.000	0.000	0.000	0.300	0.700
7/14/2010	84	39857	5370.9	0.000	0.000	1.000	0.000	1.000	0.000	0.000	0.300	0.700

The volume (mass) fraction, for each bin size, for each day, from each release type was multiplied by the fraction of the total release for that day for each release type to get the adjusted volume (mass) fraction of the daily total in each bin size for each release type. This adjusted volume (mass) distribution was then multiplied by the daily released mass to calculate the mass in each bin size for each of the release types. The daily mass per representative bin size was then adjusted to be consistent with the desired 2 hour time step of bin size release used in **SIMAP**. An illustration of the time history of mass distribution in the varying droplet size bins is presented in Figures J1 through J4 for the no treatment, low treatment, high treatment and the best estimate of dispersant treatment case, respectively. The time history of percent total event mass within varying regrouped (fewer) bin sizes throughout the release is presented in Figures J5 through J8 for the no treatment, low treatment, high treatment and the best estimate of dispersant treatment case.

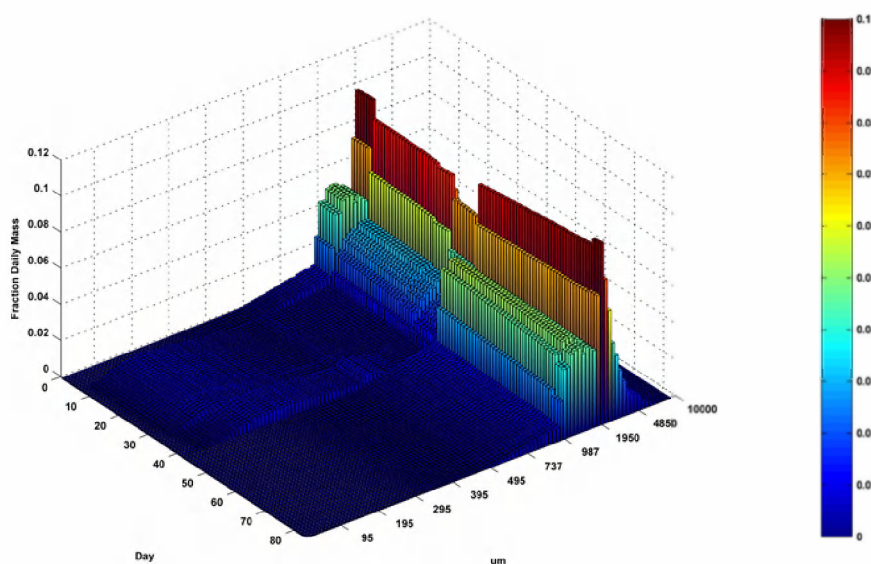


Figure J-1: Illustration of daily distribution of mass in various bin sizes throughout the release for the no treatment case.

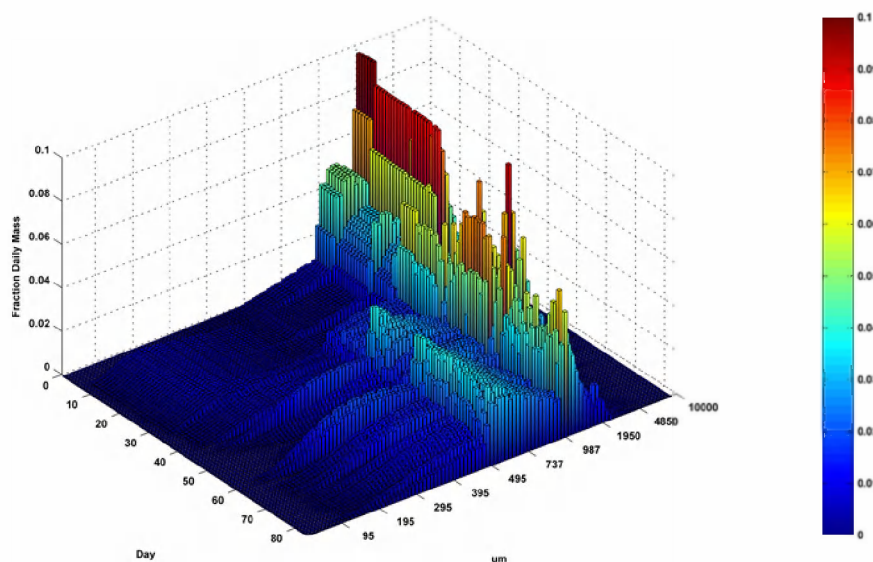


Figure J-2: Illustration of daily distribution of mass in various bin sizes throughout the release for the low treatment case.

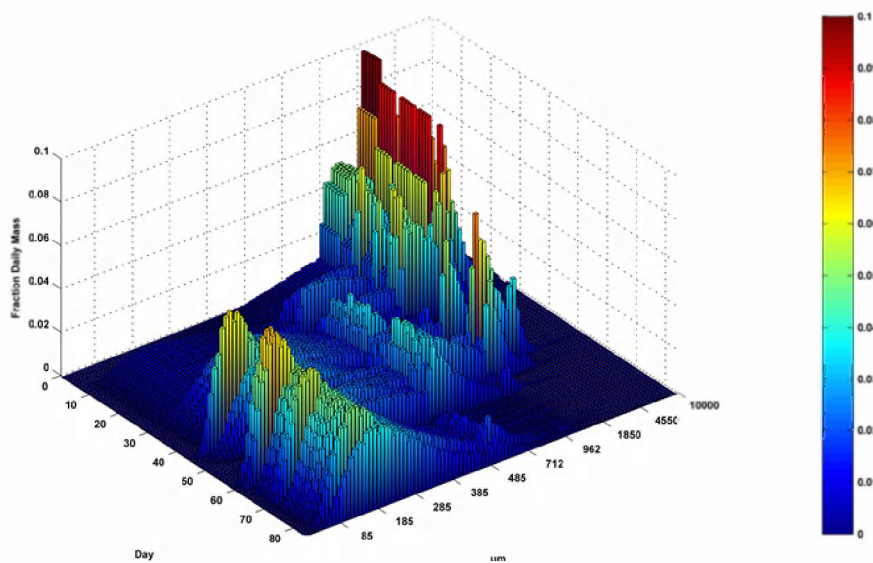


Figure J-3: Illustration of daily distribution of mass in various bin sizes throughout the release for the high treatment case

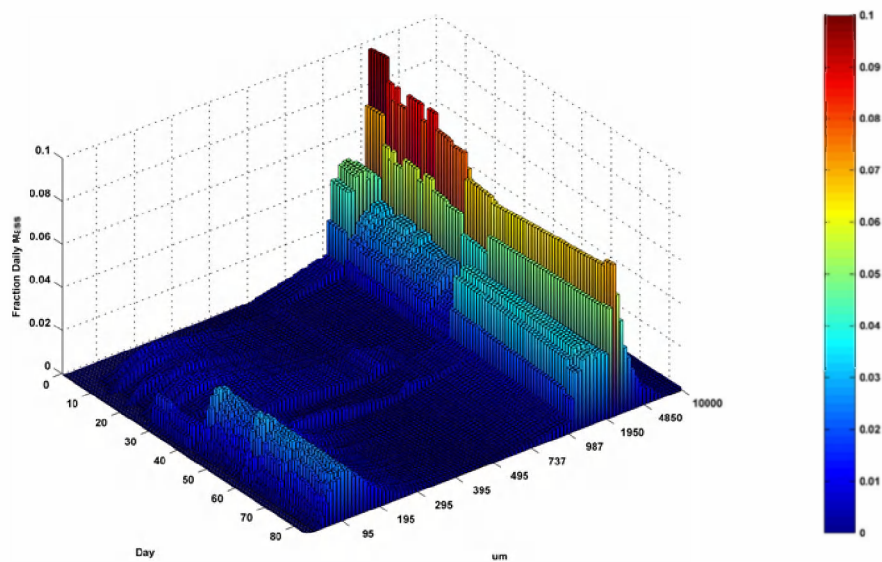


Figure J-4: Illustration of daily distribution of mass in various bin sizes throughout the release for the best estimate case.

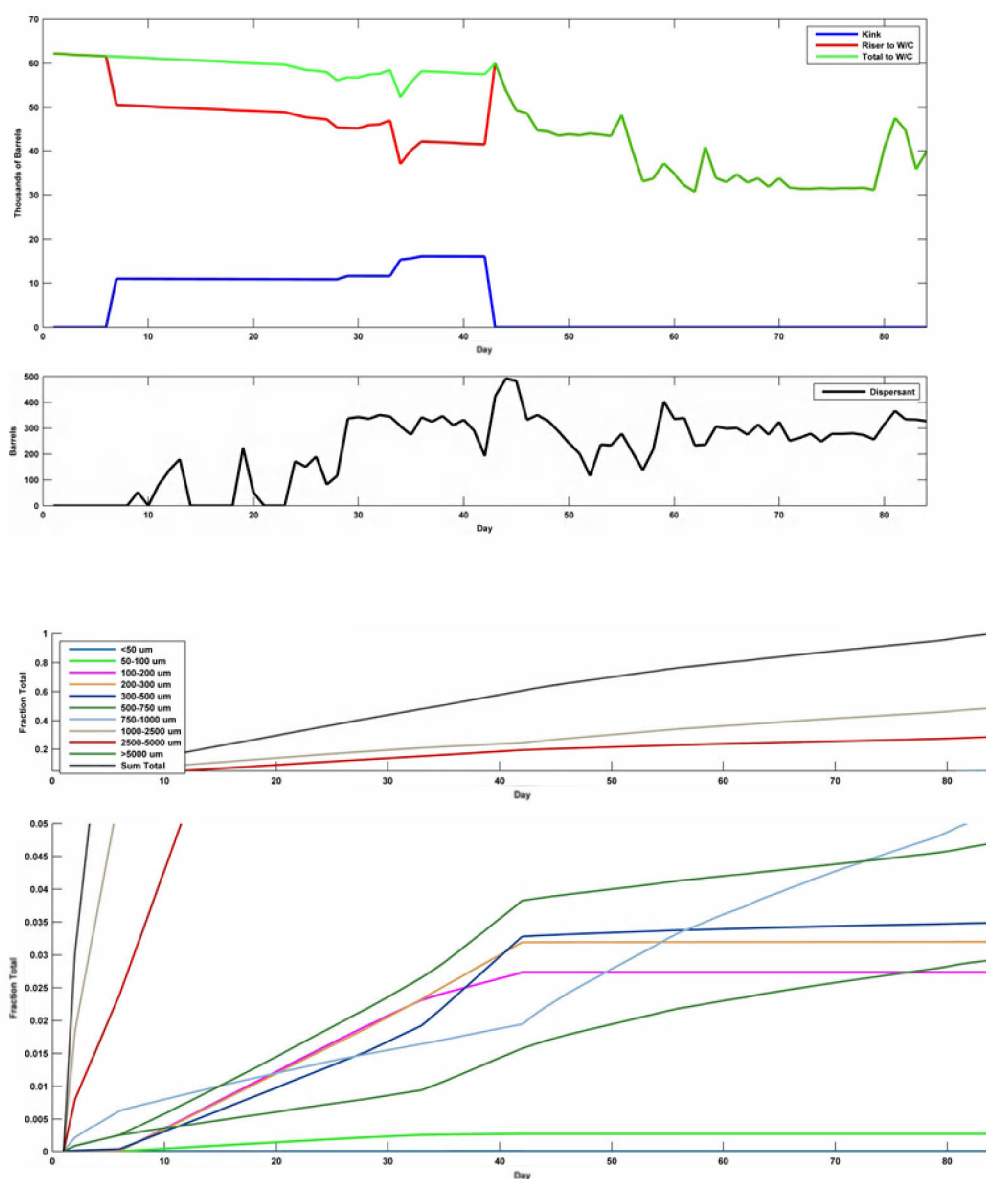


Figure J-5: Illustration of time history of release of oil to the water column (first panel), time history of dispersant applied (second panel), and time history of fraction of total oil released from various regrouped bin sizes for the no treatment case (third and fourth panel). Note that the third panel covers fractions between 0-1 and the fourth panel covers only fractions 0-0.05 to facilitate viewing.

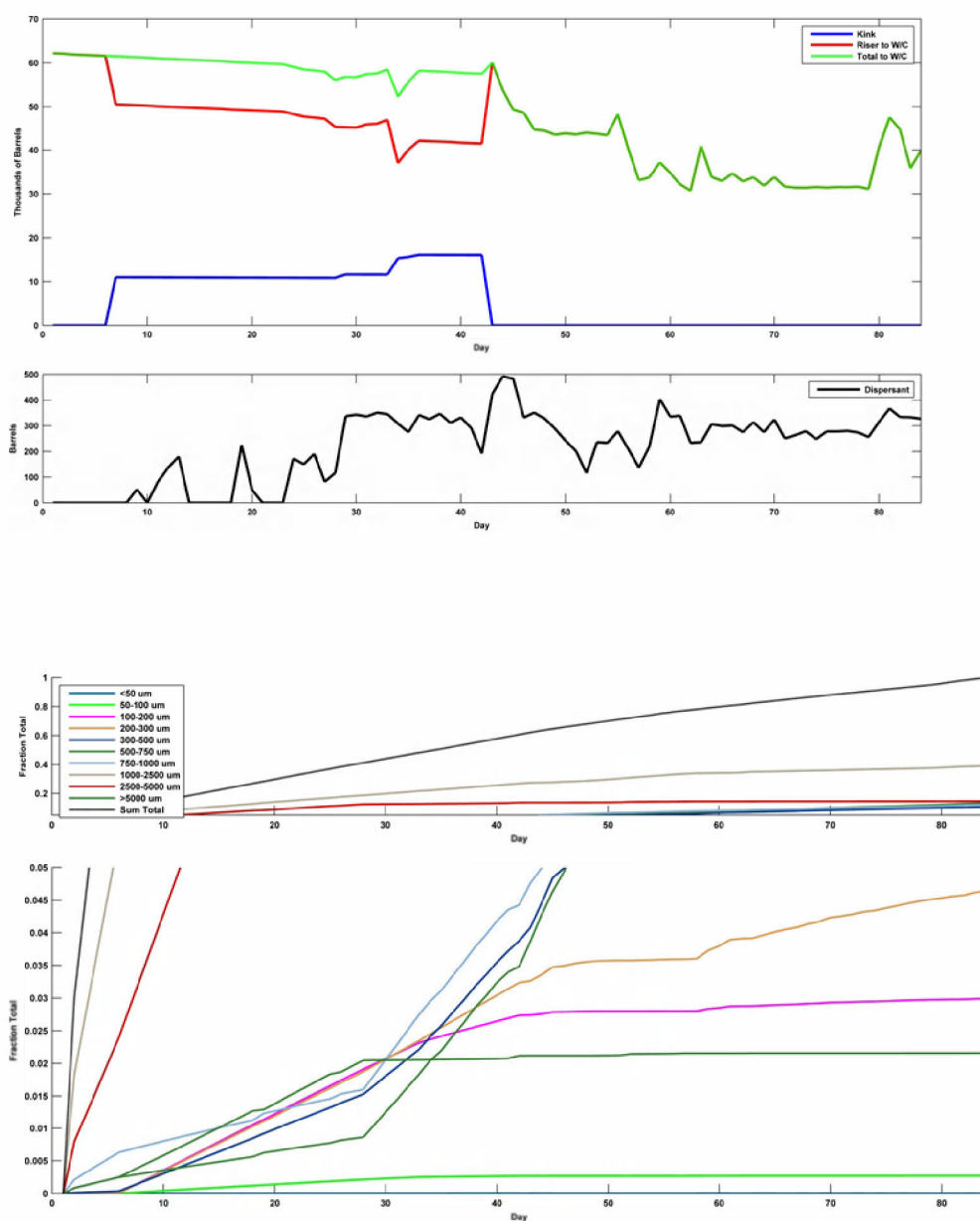


Figure J-6: Illustration of time history of release of oil to the water column (first panel), time history of dispersant applied (second panel), and time history of fraction of total oil released from various regrouped bin sizes for the low treatment case (third and fourth panel). Note that the third panel covers fractions between 0-1 and the fourth panel covers only fractions 0-0.05 to facilitate viewing.

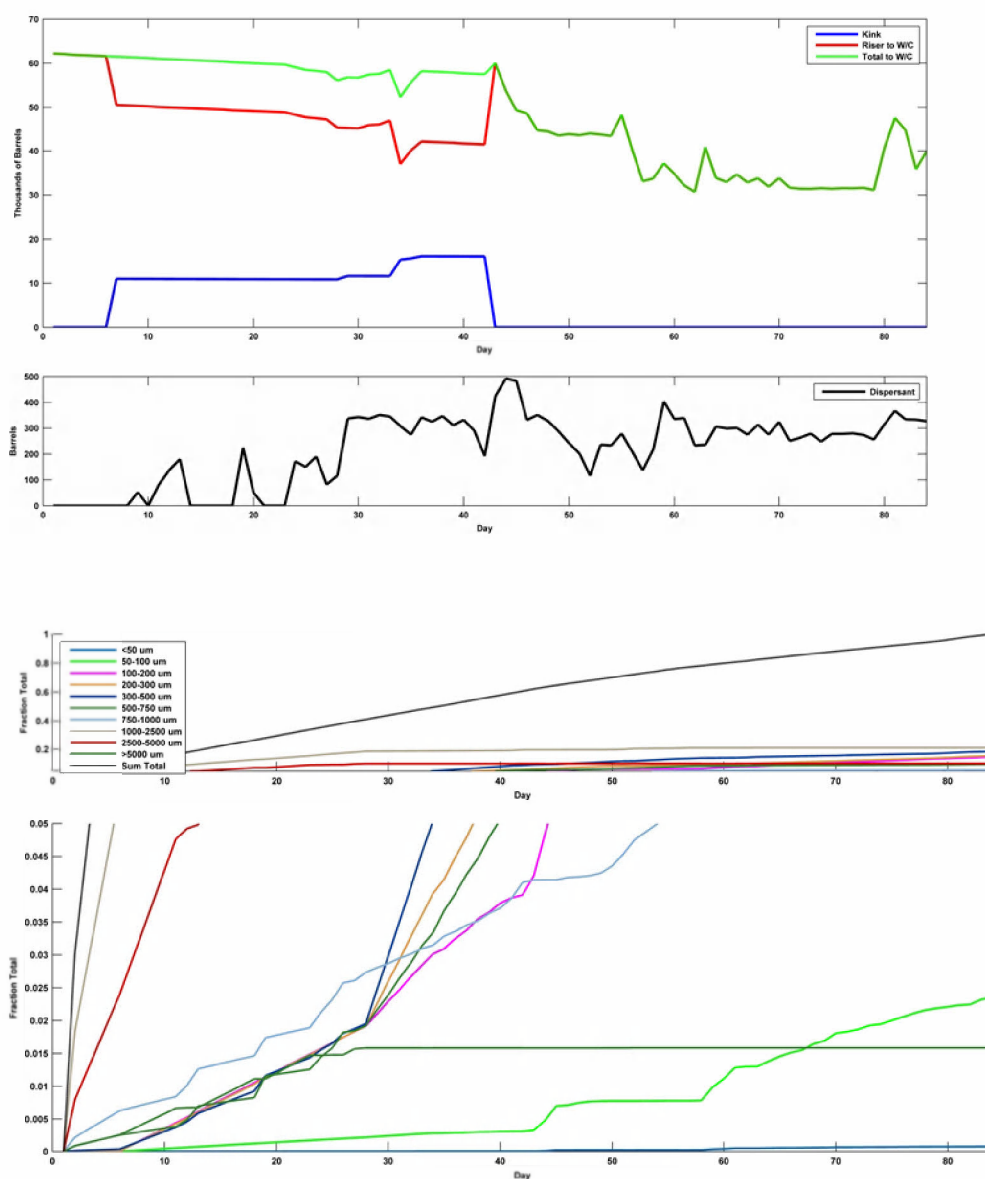


Figure J-7: Illustration of time history of release of oil to the water column (first panel), time history of dispersant applied (second panel), and time history of fraction of total oil released from various regrouped bin sizes for the high treatment case (third and fourth panel). Note that the third panel covers fractions between 0-1 and the fourth panel covers only fractions 0-0.05 to facilitate viewing.

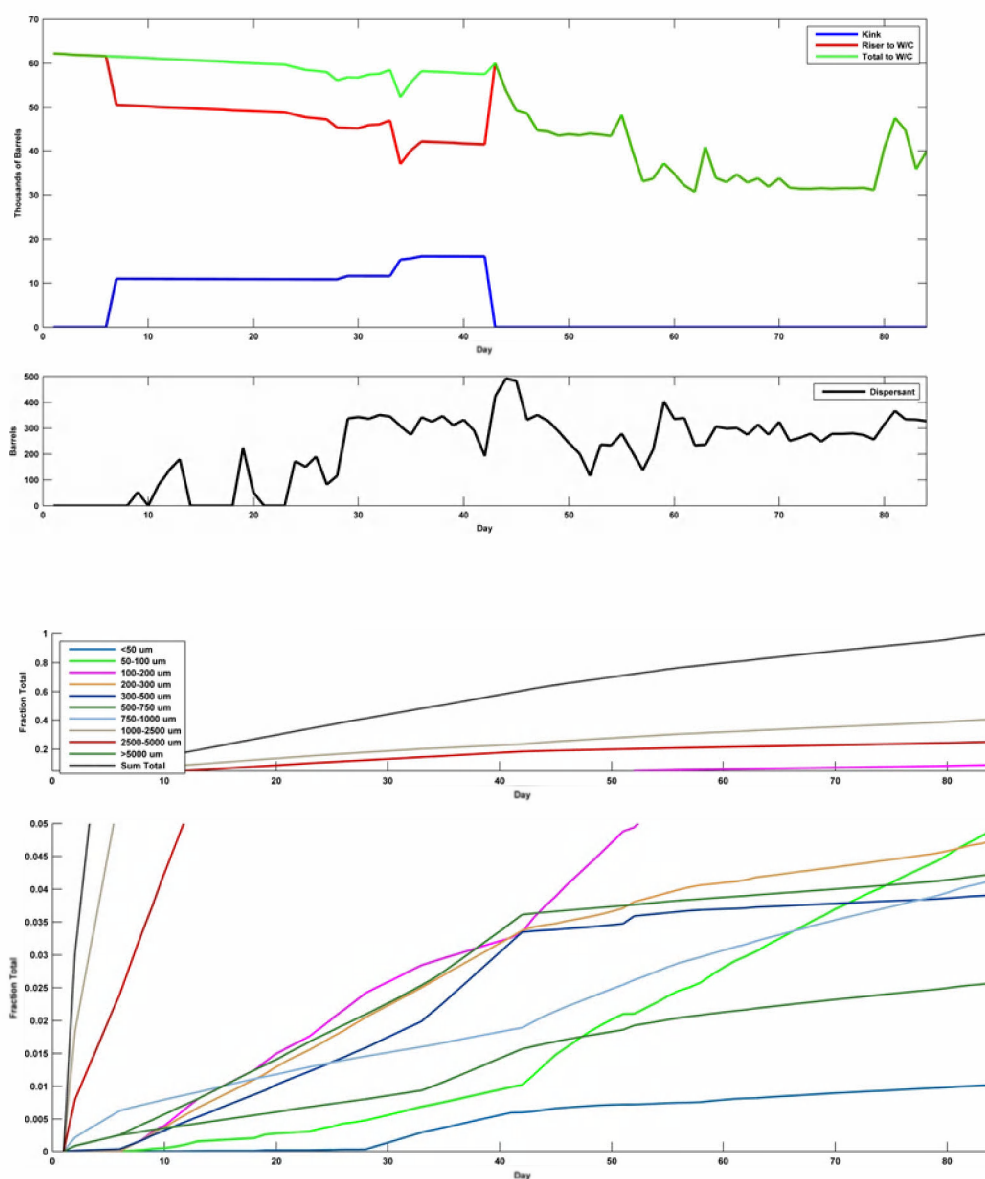


Figure J-8: Illustration of time history of release of oil to the water column (first panel), time history of dispersant applied (second panel), and time history of fraction of total oil released from various regrouped bin sizes for the best estimate case (third and fourth panel). Note that the third panel covers fractions between 0-1 and the fourth panel covers only fractions 0-0.05 to facilitate viewing.

The input to **SIMAP** requires the oil droplet position in terms of latitude and longitude. The position of the mass for the riser, prior to June 3rd when cutting operations ceased, was defined as position 1 per Appendix A and from June 3rd on was defined as position 2 per Appendix A. The vertical position for each day was assigned based on the resulting trap height from the *blowout plume model* for that day, from either the riser or kink flow, depending on the day and the bin size. All bins were assigned the position based on riser position for that day and riser trap height, except for bin sizes 300-1000 μm during the kink period. These bin sizes were predominantly associated with the kink flow and as such they were assigned the location (latitude, longitude) associated with the kink (site 1 per Appendix A) and the vertical position associated with the trap height predicted for the kink flow during the time period associated with the kink release.

The culmination of all the above described steps is a list of the position (latitude, longitude, and vertical), mass of representative droplet sizes, representative droplet size and time of release from time 0 hrs (onset of the release) to hour 2,015.5 (onset of the last half hour of the release on July 15, 2010).

J.5 References

Zick, A.A. 2013. Expert Report, U.S. v. BP Exploration & Production, Inc. et al., Equation-of-State Fluid Characterization and Analysis of the Macondo Reservoir Fluids. Prepared on behalf of the United States. Prepared by: Aaron A. Zick, Zick Technologies, Inc., 6335 SW Dolph Drive, Portland, OR. March 22, 2013.